



**HAL**  
open science

# Characterization and impact of the hydrodynamics on the performance of umbilical-cord derived stem cells culture in stirred tank bioreactors

Céline Loubière

## ► To cite this version:

Céline Loubière. Characterization and impact of the hydrodynamics on the performance of umbilical-cord derived stem cells culture in stirred tank bioreactors. Chemical and Process Engineering. Université de Lorraine, 2018. English. NNT : 2018LORR0220 . tel-02122902

**HAL Id: tel-02122902**

**<https://hal.univ-lorraine.fr/tel-02122902v1>**

Submitted on 11 Dec 2019

**HAL** is a multi-disciplinary open access archive for the deposit and dissemination of scientific research documents, whether they are published or not. The documents may come from teaching and research institutions in France or abroad, or from public or private research centers.

L'archive ouverte pluridisciplinaire **HAL**, est destinée au dépôt et à la diffusion de documents scientifiques de niveau recherche, publiés ou non, émanant des établissements d'enseignement et de recherche français ou étrangers, des laboratoires publics ou privés.



## AVERTISSEMENT

Ce document est le fruit d'un long travail approuvé par le jury de soutenance et mis à disposition de l'ensemble de la communauté universitaire élargie.

Il est soumis à la propriété intellectuelle de l'auteur. Ceci implique une obligation de citation et de référencement lors de l'utilisation de ce document.

D'autre part, toute contrefaçon, plagiat, reproduction illicite encourt une poursuite pénale.

Contact : [ddoc-theses-contact@univ-lorraine.fr](mailto:ddoc-theses-contact@univ-lorraine.fr)

## LIENS

Code de la Propriété Intellectuelle. articles L 122. 4

Code de la Propriété Intellectuelle. articles L 335.2- L 335.10

[http://www.cfcopies.com/V2/leg/leg\\_droi.php](http://www.cfcopies.com/V2/leg/leg_droi.php)

<http://www.culture.gouv.fr/culture/infos-pratiques/droits/protection.htm>



Ecole Doctorale 608 : Sciences et Ingénierie des Molécules, des Produits,  
des Procédés et de l'Énergie

# THÈSE

Présentée et soutenue publiquement pour l'obtention du grade de

## Docteur de l'Université de Lorraine

Spécialité Génie des Procédés, des Produits et des Molécules

Par

**Céline Loubière**

le 10 Décembre 2018

### Characterization and impact of the hydrodynamics on the performance of umbilical-cord derived stem cells culture in stirred tank bioreactors

#### Jury

<b>Pr. Jack Legrand</b>	Professeur (Université de Nantes)	Rapporteur
<b>Pr. Giuseppina Montante</b>	Professeur (Università di Bologna)	Rapporteur
<b>Dr. Emma Petiot</b>	Maître de Conférences (CPE Lyon)	Examinateur
<b>Dr. Marie-Laure Collignon</b>	Chercheur (Pall Life Sciences)	Examinateur
<b>Pr. Eric Olmos</b>	Professeur (Université de Lorraine)	Examinateur
<b>Dr. Emmanuel Guedon</b>	Directeur de Recherche (CNRS)	Examinateur
<b>Pr. Isabelle Chevalot</b>	Professeur (Université de Lorraine)	Invité
<b>Dr. Loïc Reppel</b>	Maître de Conférences (CHRU Nancy)	Invité
<b>Dr. Angélique Delafosse</b>	Chercheur (Université de Liège)	Invité

Université de Lorraine  
Laboratoire Réactions et Génie des Procédés (LRGP)  
UMR CNRS 7274, Nancy, France



# Acknowledgements

Les travaux présentés dans ce manuscrit ont été effectués au sein du Laboratoire Réactions et Génie des Procédés (LRGP), dans l'équipe Bioprocédés-Biomolécules (BioProMo), dans l'Université de Lorraine. Je tiens donc en premier lieu à remercier Dr. Laurent Falk de m'avoir accueillie au LRGP pendant ces trois années de thèse.

Je souhaite ensuite adresser mes plus sincères remerciements envers mes directeurs Pr. Eric Olmos, Dr. Emmanuel Guedon et mes encadrants Pr. Isabelle Chevalot et M. Fabrice Blanchard. Pour leurs conseils scientifiques et pédagogiques, leur rigueur, leur disponibilité et leur confiance, je leur adresse ma reconnaissance. Les échanges que nous avons eus m'ont confortée dans mon choix de travailler dans le monde de la recherche scientifique.

Je tiens aussi à transmettre mes respectueux remerciements au Pr. Giuseppina Montante de l'Università di Bologna et au Pr. Jack Legrand de l'Université de Nantes pour avoir accepté de juger ces travaux de thèse. Je remercie également Dr. Emma Petiot de CPE Lyon, Dr. Marie-Laure Collignon de Pall Life Sciences (Belgique), Dr. Loïc Reppel du CHRU de Nancy et Dr. Angélique Delafosse de l'Université de Liège, d'avoir accepté d'examiner ces travaux.

Ces travaux ont été financés par l'Agence Nationale de la Recherche (ANR) dans le cadre du projet STEMCellREAcTOR. Ils n'auraient pu être menés à bien sans le support du Dr. Angélique Delafosse et du Pr. Dominique Teye de l'équipe PEPs de l'Université de Liège, du Pr. Jean-Luc Six du laboratoire LCPM, du Dr. Natalia De Isla du laboratoire IMoPA, du Dr. Loïc Reppel du CHRU de Nancy et du Pr. Danièle Bensoussan de l'UTCT, tous les quatre de l'Université de Lorraine, ainsi que les sociétés partenaires Global Process Concept (GPC, La Rochelle) et BioInox (Bergerac), envers qui j'exprime ma profonde gratitude pour leurs compétences en génie chimique, en culture de cellules et en biotechnologies.

Je remercie mes collègues pour l'atmosphère conviviale dans laquelle j'ai évoluée pendant ces trois années. Merci Aline, Léna, Mengyao, Jonathan, Chafik, Felipe, Daniel, Amani, mes chers collègues de thèse, mais aussi merci à toute la famille BioProMo, et à notre dernier arrivant l'Orque voyageur, pour ce soutien et ces moments chaleureux et conviviaux le midi, et lors des soirées. La vie au laboratoire fut animée, avec toujours une surprise qui fait sourire en passant le pas de la porte du 2<sup>e</sup>. Merci pour votre joie, votre naturel, mais aussi pour votre bienveillance (je me souviendrai des bonbons qui apparaissaient après une culture de cellules capricieuses). Je réserve des remerciements plus particuliers envers ma voisine de bureau, Caroline, avec qui j'ai particulièrement apprécié travailler, discuter sur des sujets plus ou moins scientifiques, mais aussi pour tout son soutien une fois en-dehors du laboratoire.

Merci aussi aux étudiants que j'ai eu l'occasion d'encadrer lors de stages et projets de recherche, Victoria, Anaïs, Olivier, Amine et Charif, qui se sont impliqués pour ces travaux de recherche.

Je remercie également mes amis de toujours, Flora et Anne Hélène, mes contrebandiers de coeur Kelly, Carine et Jeannot, ainsi que Mathilde qui révolutionnera les batteries.

Enfin, je souhaite remercier ma famille pour son soutien, et plus particulièrement ma mère Michèle, mon père Joël, mes deux frères Bruno et Florent, ma belle-soeur Sophie et mes deux neveux Arthur et Zacharie, dont l'aîné a su apprécier mes imitations du cycle de vie d'une cellule souche. Mon Nono, j'aurai partagé avec toi la grande épreuve de la rédaction, prétendant tous deux au titre de docteur à quelques semaines d'intervalle.

---

*Expliquer toute la nature est une tâche trop ardue pour un seul homme ou une seule époque. Il est plus sage de faire peu en étant sûr de soi et laisser le reste à ceux qui viendront après, que présumer de tout sans être sûr de rien.*

- Isaac Newton

# List of publications and presentations

The following contributions are presented according to their chronological publication, with the most recent ones in first places. Speakers of oral presentations are written in bold.

## Journal publications

### Accepted

Delafosse, A., Loubière, C., Calvo, S., Toye, D., Olmos, E. (2018). Solid-liquid suspension of microcarriers in stirred tank bioreactor - Experimental and numerical analysis. *Chemical Engineering Science*, 180, 52-63.

### In revision

Pourchet, L., Petiot, E., Dos Santos, M., Thépot, A., Blum, L., Olmos, E., Loubière, C., Marquette, C. (2018). Large 3D bioprinted tissue: Dynamic maturation and vascularization. *Bioprinting*.

### Submission in 2018

Loubière, C., Delafosse, A., Guedon, E., Chevalot, I., Olmos, E. (2018). Dimensional analysis and CFD simulations of microcarrier 'just-suspended' state in MSC bioreactors. *Chemical Engineering Science*.

Loubière, C., Sion, C., Guedon, E., Chevalot, I., De Isla, N., Reppel, L., Olmos, E. (2018). Establishment of a process strategy dedicated to hMSC cultures derived from umbilical cords on microcarriers on a hPL supplemented culture medium. *Biochemical Engineering Journal*.

Loubière, C., Guedon, E., Chevalot, I., Olmos, E. (2019). CFD-based strategy to optimize the impeller design for MSC cultures in bioreactors. In preparation for the special issue of Mixing 16 in *Chemical Engineerring and Technology*.

## Oral presentations

**Olmos, E.**, Chéron, J., Loubière, C., Delaunay, S., Guezennec, A.G. (2018). Hydrodynamic modelling of bioleaching reactors. *3<sup>rd</sup> Promethee Workshop*, October 10<sup>th</sup> 2018, Orléans, France.

**Loubière, C.**, Delafosse, A., Toye, D., Guedon, E., Chevalot, I., Olmos, E. (2018). CFD-based strategy to optimize the impeller design adapted to microcarrier suspension in stirred tank bioreactors. *16<sup>th</sup> European Conference on Mixing*, September 9-12<sup>th</sup>, 2018, Toulouse, France.

**Sion, C.**, Loubière, C., Guedon, E., Chevalot, I., Olmos, E. Control of microcarrier feed time by quantitative determination of bead-to-bead transfer during hMSC cultures. *12<sup>th</sup> European Symposium on Biochemical Engineering Sciences (ESBES)*, September 9-12<sup>th</sup>, 2018, Lisbon, Portugal.

**Loubière, C.**, Guedon, E., Chevalot, I., Olmos, E. CFD-based strategy to optimize the impeller design for mesenchymal stem cells cultures in bioreactors. *5<sup>th</sup> BioProScale Symposium 2018*, March 20-22<sup>th</sup>, 2018, Berlin, Germany.

**Loubière, C.**, Olmos, E., Guedon, E., Chevalot, I., Toye, D., Delafosse, A. New models to predict microcarriers 'just-suspended' state in bioreactors for stem cell culture. *10<sup>th</sup> World Congress of Chemical Engineering - 4<sup>th</sup> European Congress of Applied Biotechnology*, October 1-5<sup>th</sup>, 2017, Barcelona, Spain.

**Loubière, C.**, Guedon, E., De Isla, N., Chevalot, I., Olmos, E. Impact du mode de culture sur les performances d'expansion de cellules souches mésenchymateuses issues de cordons ombilicaux. *16<sup>ème</sup> congrès de la Société Française du Génie des Procédés (SFGP)*, July 11-13<sup>th</sup>, 2017, Nancy, France.

**Loubière, C.**, Olmos, E., Guedon, E., Chevalot, I., Toye, D., Delafosse, A. Nouveaux modèles de prédiction de l'état de juste mise en suspension de microporteurs en bioréacteurs de culture de cellules souches. *16<sup>ème</sup> congrès de la Société Française du Génie des Procédés (SFGP)*, July 11-13<sup>th</sup>, 2017, Nancy, France.



Loubière, C., De Isla, N., Guedon, E., Chevalot, I., Toyé, D., Delafosse, A., **Olmos, E.** Bioreactor development for umbilical-cord-mesenchymal stem cell (MSC) culture. *Symposium of the French Federation of Biotechnology (FFB)*, May 15-16<sup>th</sup>, 2017, Lille, France.

### Poster presentations

Delafosse, A., Loubière, C., Olmos, E., Toyé, D. Experimental validation of solid-liquid simulations of microcarrier suspension in a stirred-tank bioreactor. *16<sup>th</sup> European Conference on Mixing*, September 9-12<sup>th</sup>, 2018, Toulouse, France.

Loubière, C., Sion, C., Guedon, E., Chevalot, I., Olmos, E. Quantitative image analysis of microcarrier colonization and cell expansion during hMSC cultures. *12<sup>th</sup> European Symposium on Biochemical Engineering Sciences (ESBES)*, September 9-12<sup>th</sup>, 2018, Lisbon, Portugal.

Loubière, C., Chevalot, I., De Isla, N., Sion, C., Reppel, L., Guedon, E., Olmos, E. Establishment of a process strategy dedicated to hMSC cultures derived from umbilical cords on microcarriers in a hPL supplemented culture medium. *5<sup>th</sup> BioProScale Symposium 2018*, March 20-22<sup>th</sup>, 2018, Berlin, Germany.

Delafosse, A., Loubière, C., Calvo, S., Olmos, E., Toyé, D. Development of an optical technique to characterize solid-liquid suspension in stirred tank bioreactors. *16<sup>ème</sup> congrès de la Société Française du Génie des Procédés (SFGP)*, July 11-13<sup>th</sup>, 2017, Nancy, France.

Loubière, C., Olmos, E., Guedon, E., Chevalot, I., Toyé, D., Delafosse, A. New models for predicting microcarrier just-suspended state in bioreactors. *25<sup>th</sup> European Society for Animal Cell Technology (ESACT) Meeting*, May 14-17<sup>th</sup>, 2017, Lausanne, Switzerland.



# Contents

<b>Acknowledgements</b>	<b>iii</b>
<b>List of publications and presentations</b>	<b>v</b>
<b>Contents</b>	<b>ix</b>
<b>List of Figures</b>	<b>xi</b>
<b>List of Tables</b>	<b>xix</b>
<b>Nomenclature</b>	<b>xxiii</b>
<b>Introduction</b>	<b>1</b>
<b>1 State of the Art</b>	<b>9</b>
1.1 Introduction . . . . .	10
1.2 Mesenchymal stem / stromal cells and their therapeutic benefits . . . . .	11
1.3 MSC sources and population heterogeneities . . . . .	24
1.4 Expansion process challenges . . . . .	27
1.5 Microcarrier-based cultures . . . . .	37
1.6 Hydrodynamics potential impact on MSC . . . . .	53
1.7 Thesis aims and objectives . . . . .	73
<b>2 Improvement of WJ-MSC culture on microcarriers</b>	<b>91</b>
2.1 Introduction . . . . .	92
2.2 Preliminary results . . . . .	94
2.3 Development of an automatic cell counting method on microcarriers using image analysis . . . . .	99
2.4 Impact of the type of microcarrier in different agitation modes on the ex- pansion performances . . . . .	104

---

2.5	Cell culture on home-made microcarriers . . . . .	135
2.6	Chapter conclusions . . . . .	140
<b>3</b>	<b>Modelling of microcarriers just-suspended state in a stirred tank bioreactor</b>	<b>147</b>
3.1	Introduction . . . . .	148
3.2	CFD models investigation for simulation of microcarriers suspension in stirred-tank bioreactors . . . . .	150
3.3	Dimensional analysis and CFD simulations of microcarrier just-suspended state . . . . .	163
3.4	Chapter conclusions . . . . .	185
<b>4</b>	<b>Optimization of the impeller design for MSC culture on microcarriers in a stirred tank bioreactor</b>	<b>193</b>
4.1	Introduction . . . . .	194
4.2	Impeller design comparison according to the hydromechanical stress encountered by the microcarriers . . . . .	196
4.3	CFD-based strategy to optimize the impeller design adapted to microcarrier suspension in a minibioreactor . . . . .	203
4.4	WJ-MS culture in STR using selected EE impeller designs . . . . .	226
4.5	Chapter conclusions . . . . .	232
	<b>Conclusions</b>	<b>237</b>
	<b>Résumé détaillé de la thèse</b>	<b>245</b>
	<b>Appendices</b>	<b>263</b>
	Appendix A: Supplementary materials and methods . . . . .	265
	Appendix B: Solid-liquid suspension of microcarriers in stirred tank bioreactor - Experimental and numerical analysis . . . . .	274
	Appendix C: Design of experiments of the impeller design optimization . . . . .	287
	<b>Abstract / Résumé</b>	<b>289</b>

# List of Figures

1	Conceptual illustration of a technology S-curve showing the evolution of expansion technologies used in cell therapy manufacture. . . . .	2
2	Global architecture of the STEMCellREAcTOR ANR project. . . . .	4
3	Global methodology applied in the present PhD thesis, linking experimental and numerical results together. . . . .	6
1.1	Mesenchymal stem cells discovery from guinea-pig bone marrow . . . . .	12
1.2	Increase of the number of MSC-based scientific publications for 25 years . .	12
1.3	Criteria defining MSC according to the International Society for Cellular Therapy (ISCT). . . . .	13
1.4	Development overview of a regenerative medicine applied to hMSC therapy	14
1.5	Historical timeline of MSC discoveries and main developments. . . . .	15
1.6	Potency of cell level and differentiation capabilities according to the cell development stage after ESC and MSC isolation . . . . .	16
1.7	Systemic administration of mesenchymal stem cells can trigger distal (endocrine) or local (paracrine) effects that include cell-mediated actions .	17
1.8	Multilineage potential of MSC . . . . .	18
1.9	Evolution of the number of starting clinical studies based on MSC . . . . .	19
1.10	Clinical studies involving MSC distribution according to the clinical phase and the type of disease treated . . . . .	20
1.11	Clinical studies involving MSC distribution in the world . . . . .	20
1.12	Body-map of MSC sources in the human body. . . . .	24
1.13	Transversal histological cut of a human umbilical cord . . . . .	26
1.14	Global manufacturing process for adherent-dependent cell therapeutics with each step main challenges . . . . .	28
1.15	Basic configuration of a monitored and controlled bioreactor for MSC culture. . . . .	30

---

1.16	Suitable bioreactors for MSC expansion, classified according to the power input type. . . . .	33
1.17	Planar bioreactors in static mode for MSC expansion . . . . .	34
1.18	Bioreactors for MSC expansion on microcarriers in dynamic mode . . . . .	35
1.19	Cell adhesion force evolution during during life cycle, from cell attachment to cell detachment. . . . .	39
1.20	Comparison of static and agitated conditions for microcarrier-based culture using hBM-MSC from 3 different donors, and a comparison of different microcarriers in 100 mL spinner flasks. . . . .	46
1.21	Morphological characterization of BM-MSC cultured in different media and population doubling time in days of adherent cells cultures in different expansion media between passage 1 and passage 2. . . . .	48
1.22	Parameters influencing particle suspension in STR. . . . .	49
1.23	Particle suspension states and distribution in STR according to the agitation . . . . .	50
1.24	Flow patterns and particle bed shapes observed at agitation rates $N < N_{js}$ depending on mixing structures . . . . .	50
1.25	Schematic representation of the intermediate phenomena from the impeller rotation to its impact on cells adhered on particles. . . . .	54
1.26	Flow regime and turbulence evolution with the Reynolds number. . . . .	55
1.27	Energy transfer from large eddies to small eddies according to the turbulent energy cascade theory. . . . .	58
1.28	Dimensionless stress in fully developed turbulent flow given by the theory of isotropic turbulence. . . . .	59
1.29	Turbulent energy dissipation rate spatial fluctuation in STR . . . . .	62
1.30	Hydro-biological coupling in a monitored stirred-tank bioreactor. . . . .	63
1.31	Description of the hydromechanical stress applied on colonized microcarriers. . . . .	64
1.32	Time-averaged distributions within the entire bioreactor volume of stress and Kolmogorov length scale. . . . .	69
1.33	Dimensionless fluid magnitude and axial velocities in the standard and modified Univessel® SU. . . . .	70
1.34	Dimensionless spatial distributions of the logarithm of turbulent dissipation rate simulated by LES for EED, EEU, RT, MPD and MPU. . . . .	71
2.1	Presentation of the different steps of this work for the improvement of a WJ-MSC expansion process on microcarriers. . . . .	93
2.2	Non-systematic WJ-MSC behaviour in planar static cultures when cells are locally close to confluence. . . . .	95

2.3	Jelly matrix formation entrapping all microcarriers during dynamic cultures at $t_0 + 1$ day. . . . .	96
2.4	Kinetics of the metabolite concentrations using the <i>hep - M</i> culture medium, and according to the type of microcarrier. . . . .	98
2.5	Kinetics of the metabolite concentrations using the <i>FD - M</i> culture medium, and according to the type of microcarrier. . . . .	98
2.6	Photo post-treatment to detect and count cells after Live / Dead staining. . . . .	100
2.7	Photo treatment to detect and count microcarriers and cells after DAPI staining. . . . .	101
2.8	Distributions of the number of cells per microcarrier, calculated by the Matlab script, after 3 days of culture and 13 days of culture. . . . .	103
2.9	Example of photo treatment by image analysis after DAPI staining and microcarriers recognition . . . . .	116
2.10	Comparison of the mean cell number per microcarrier determined by automatic post-treatment and by visual counting. . . . .	116
2.11	Cell nuclei DAPI coloration at $t_0 + 5$ days in static mode. . . . .	118
2.12	Kinetics of metabolite concentrations over time in static mode and according to the type of microcarrier used. . . . .	119
2.13	Mean number of cells per microcarrier cultivated with an orbital agitation and according to the type of microcarrier at $t_0 + 2$ days and $t_0 + 5$ days . . . . .	121
2.14	Fraction of microcarriers containing at least one cell in culture with an orbital agitation and according to the type of microcarrier at $t_0 + 2$ days and $t_0 + 5$ days. . . . .	121
2.15	Coefficient of variation of the distribution characterizing the number of cell per microcarrier with an orbital agitation and according to the type of microcarrier at $t_0 + 2$ days and $t_0 + 5$ days. . . . .	122
2.16	Cell morphology grown on microcarriers at $t_0 + 2$ days according to the type of microcarrier and the agitation mode. . . . .	123
2.17	Kinetics of metabolite concentrations during cultures stirred with an orbital agitation and according to the type of microcarrier used. . . . .	125
2.18	Mean number of cells per microcarrier cultivated with a mechanical agitation and according to the type of microcarrier at $t_0 + 2$ days and $t_0 + 5$ days. . . . .	126
2.19	Fraction of microcarriers containing at least one cell in culture with a mechanical agitation and according to the type of microcarrier at $t_0 + 2$ days and $t_0 + 5$ days . . . . .	126

2.20	Coefficient of variation of the distribution characterizing the number of cell per microcarrier with a mechanical agitation and according to the type of microcarrier at $t_0 + 2$ days and $t_0 + 5$ days . . . . .	127
2.21	Kinetics of metabolite concentrations during cultures stirred with a mechanical agitation and according to the type of microcarrier used. . . . .	128
2.22	DAPI cell nuclei staining after cell detachment and filtration. . . . .	130
2.23	Characterization of GW-MS-C immunophenotype, expanded under various dynamic conditions, by flow cytometry. . . . .	131
2.24	Differentiated WJ-MS-C: adipocytes stained with Oil Red, osteocytes stained with Alizarin Red, chondrocytes stained with Alcian blue. . . . .	132
2.25	Home-made microcarriers formulation by the LCPM laboratory. . . . .	136
2.26	Macroscopic comparison of WJ-MS-C static cultures in 6 well-plates with commercial and home-made microcarriers. . . . .	136
2.27	Kinetics of the metabolite concentrations WJ-MS-C cultures on commercial and home-made microcarriers in static 6 well-plates. . . . .	137
2.28	Live / Dead and DAPI cell staining on the commercial Cytodex-1 and the home-made PLA1 and PLA1-hPL microcarriers, from static cultures in 6 well-plates at $t_0 + 7 d$ . . . . .	138
2.29	Number of harvested cells after the detachment and separation from microcarriers steps performed at $t_0 + 7 d$ and from static cultures in 6 well-plates using commercial and home-made microcarriers. . . . .	139
3.1	Presentation of the different steps of this work for the establishment of methods to predict microcarriers just-suspended state in stirred tank bioreactors. . . . .	149
3.2	Minibioreactor used for CFD simulations: Experimental apparatus and example of mesh discretization. . . . .	150
3.3	TRYTON bioreactor used for CFD simulations: Experimental apparatus and example of mesh discretization. . . . .	151
3.4	Comparison of the impact of the wall function selected for near-wall treatment with the $k-\varepsilon$ model on $y^+$ values displayed on the vessel wall: Standard Wall Function and Scalable Wall Function. . . . .	155
3.5	Comparison of the impact of the wall function selected for near-wall treatment with the $k-\varepsilon$ model on the turbulent energy dissipation rate: Standard Wall Function and Scalable Wall Function. . . . .	156
3.6	Interphase momentum exchange coefficient $K_{SL}$ evolution with the particle volume fraction from different models. . . . .	159



3.7	Comparison of the impact of the turbulent dispersion force on the particle volume fraction distribution in the bioreactor: Solid volume fraction fields from simulations run without turbulent dispersion model and with the diffusion in VOF model. . . . .	161
3.8	Variables used in the design of experiments. . . . .	167
3.9	Mesh discretization of the vessel for the CFD simulations. . . . .	172
3.10	Evolution of the experimentally determined $S$ coefficients from the Zwietering correlation with the microcarrier volume fraction in the bioreactor, for Cytodex-1 and Star-Plus. . . . .	174
3.11	Flow patterns and particle bed shapes observed at agitation rates $N < N_{js}$ depending on mixing structures: axial flow, radial flow and mixed-flow. . . . .	175
3.12	Comparison of the deviation between the experimental $N_{js}$ and the $N_{js}$ predicted by the model for operating conditions out of the design of experiment and model resolution, according to the impeller design. . . . .	177
3.13	Comparison of experimental $N_{js}^{exp}$ and modeled $N_{js}^{mod}$ , depending on the impeller design. . . . .	179
3.14	Comparison of modeled $N_{js}$ and numerically adapted $N_{js,Zwietering}$ . . . . .	182
3.15	Comparison of experimental $N_{js}$ and modeled $N_{js}$ with the CFD-based method. . . . .	184
4.1	Presentation of the different steps of this work for the geometrical optimization of an impeller design, in order to improve MSC culture on microcarriers in STR. . . . .	195
4.2	Impeller designs used for CFD simulations: four-blade Rushton turbine, three-blade Elephant Ear impeller and three-blade marine propeller. . . . .	196
4.3	Volumetric distributions of the turbulent energy dissipation rate $\varepsilon$ in the whole fluid volume in the bioreactor, at $N = N_{js}$ for different impeller designs. . . . .	198
4.4	Experimental spatial distribution of microcarriers at $N = N_{js}$ with the EED, the EEU, the MPU and the RT. . . . .	198
4.5	Relative comparison between four impeller designs (EED, RT, EEU and MPU) at $N = N_{js}$ , according to the power per unit of volume based on the whole liquid volume $\langle (P/V) \rangle$ and encountered by the microcarriers $\langle (P/V)_{@p} \rangle$ , and the Energy Dissipation / Circulation function $EDC$ . . . . .	201
4.6	Microcarrier distribution within the minibioreactor equipped with an EE impeller ( $C/T = 0.41$ , $D/T=0.4$ , $\beta = 45^\circ$ ) at $N = 0$ rpm and $N = N_{js} = 75$ rpm. . . . .	207

4.7	Flowchart presenting the global strategy applied for the impeller design optimization coupling CFD simulations with a multi-objective optimization.	208
4.8	Mesh discretization of the vessel for the CFD simulations and visualization of the geometrical variables involved in the design optimization. . . . .	209
4.9	EE impellers built using 3D-printing for $N_{js}$ experimental measurements. .	213
4.10	Comparison between experimental $N_{js}^{exp}$ and modelled $N_{js}^{predicted}$ using the 31-design points responses surfaces and using the reduced-design points response surface. . . . .	215
4.11	Linear relationship between the Power number $N_{p,js}$ and the blade slope angle $\beta$ , regardless the impeller size and position in the reactor. . . . .	216
4.12	Comparison of the calculated Power numbers at the just-suspended state $N_{p,js}$ according to the blade slope angle of EE impellers with values from common impellers in fully-turbulent regime. . . . .	217
4.13	Relationship between $N_{js}$ and $\langle \lambda_K \rangle$ calculated within all the fluid volume, and $\langle \lambda_{K,@p} \rangle$ calculated according to the local particle concentration within the bioreactor. . . . .	218
4.14	3-D heatmap graphic displaying $N_{js}$ value according to the 3 impeller geometrical parameters. . . . .	219
4.15	3-D heatmap graphic displaying $\langle (P/V)_{@p} \rangle$ value according to the 3 impeller geometrical parameters. . . . .	220
4.16	Comparison of $\langle (P/V)_{@p} \rangle$ and $\langle (P/V) \rangle$ calculated for the impeller designs of the DOE. . . . .	221
4.17	3-D heatmap graphic displaying $EDC$ value according to the 3 impeller geometrical parameters. . . . .	222
4.18	Geometry of the optimal impeller designs. . . . .	223
4.19	Particle volume fraction $\alpha_S$ and turbulent energy dissipation rate $\varepsilon$ distributions within the minibioreactor equipped with the optimal impeller design. . . . .	224
4.20	Kinetics of glucose and lactate concentrations according to the stirred system. . . . .	227
4.21	Cell morphology on microcarriers at $t_0 + 1$ day and $t_0 + 5$ days, and according to the stirred system used: Minibioreactor and Erlenmeyer flask. .	228
4.22	Selected EED impellers in minibioreactors, without agitation and at the just-suspended state ( $N = N_{js}$ ). . . . .	229
4.23	Kinetics of metabolite concentrations according to the EED impeller used in minibioreactor. . . . .	230
4.24	Evolution of the mean number of cells per microcarrier $\langle N_{cell/\mu C} \rangle$ over time with the three EED impeller designs. . . . .	231

4.25	Global methodology and main contributions on the improvement of WJ-MSC cultures on microcarriers (Chapter 2 summary). . . . .	238
4.26	Global methodology and main contributions about the microcarrier just-suspended state modelling in a stirred tank bioreactor (Chapter 3 summary). . . . .	240
4.27	Global methodology and main contributions about the optimization of an impeller design for MSC culture on microcarriers in a stirred tank bioreactor (Chapter 4 summary). . . . .	241
5.1	Illustration conceptuelle de type courbe en S, des technologies de culture de CSM. . . . .	247
5.2	Méthodologie globale appliquée dans les présents travaux de thèse, reliant les résultats expérimentaux aux résultats numériques. . . . .	249
5.3	Formation de matrice gélifiée piégeant les microporteurs lors d'une culture dynamique à $t_0 + 1$ jour. . . . .	250
5.4	Traitement d'une photo par le script Matlab pour détecter et compter les cellules et microporteurs, après coloration DAPI. . . . .	251
5.5	Stratégie scientifique mise en place pour l'amélioration des performances du procédé d'expansion cellulaire de CSM sur microporteurs (chapitre 2). . . . .	253
5.6	Parametres influençant la suspension de particules en bioréacteur agité. . . . .	254
5.7	Stratégie scientifique mise en place et contributions pour modéliser l'état de juste mise en suspension de microporteurs en bioréacteur agité (chapitre 3). . . . .	255
5.8	Comparaison relative entre quatre types de mobiles (EED, RT, EEU and MPU) à $N = N_{js}$ , selon la puissance par unité de volume calculée sur l'ensemble du fluide $\langle (P/V) \rangle$ et perçue par les microporteurs $\langle (P/V)_{@p} \rangle$ , et la fonction <i>EDC</i> . . . . .	257
5.9	Distributions de la fraction volumique en microporteurs $\alpha_S$ et du taux de dissipation de l'énergie turbulente $\varepsilon$ dans le bioréacteur équipé du mobile optimisé. . . . .	257
5.10	Stratégie scientifique mise en place et contributions autour de l'optimisation de la géométrie d'un mobile d'agitation pour la culture de CSM sur microporteurs en bioréacteur agité (chapitre 4). . . . .	258
A.1	WJ-MSC culture in Erlenmeyer flasks. . . . .	268
A.2	Spinner flask used for MSC culture on microcarriers. . . . .	268
A.3	WJ-MSC culture in a minibioreactor. . . . .	270



# List of Tables

1.1	Current MSC-based products with marketing authorization . . . . .	22
1.2	Comparison of MSC from bone marrow, adipose-tissue and Wharton’s jelly of the umbilical cord according to their isolation ease, their proliferative capability and their differentiation potency. . . . .	25
1.3	Characteristics of cell culture media . . . . .	29
1.4	Volume comparison of different dynamic systems for MSC culture on microcarriers. . . . .	36
1.5	Commercial microcarriers used for hMSC cultures (based on manufacturer data). . . . .	38
1.6	Overview of the MSC cultures performed on microcarriers. . . . .	42
1.7	Impact of agitation geometry and phase properties on the minimal agitation rate ensuring complete suspension, by considering all other parameters fixed. . . . .	50
1.8	Kolmogorov hypothesis for turbulence description . . . . .	57
1.9	Characterization of the turbulent ranges based on the eddy sizes. . . . .	58
1.10	Examples of Power number values for different impeller designs in turbulent regime. . . . .	60
1.11	Time-averaged parameters characterizing the hydrodynamics in STR for MSC cultures on microcarriers. . . . .	60
1.12	Current CFD-based studies on microcarriers suspensions in bioreactors. . . . .	67
2.1	Comparison of the number of cells harvested and the ease of detachment according to the cell origin and the culture medium used . . . . .	94
2.2	Potential of jelly matrix formation for different sets of culture conditions. . . . .	96
2.3	Glucose consumption ratios between the two culture media $FD - M$ and $hep - M$ for paired cultures at various operating conditions. . . . .	97

2.4	Thresholds values for cell recognition according to the staining and the type of microcarrier used. . . . .	102
2.5	Microcarrier physical properties (based on manufacturer data) and concentrations used in this study. . . . .	110
2.6	Stirred systems and agitation conditions chosen for cultures in dynamic mode. . . . .	111
2.7	List of antibodies used for the flow cytometry analyses. . . . .	114
2.8	Kinetic parameters calculated for cultures involving an orbital agitation and according to the type of microcarrier used. . . . .	124
2.9	Kinetic parameters calculated for cultures involving a mechanical agitation and according to the type of microcarrier used . . . . .	127
2.10	Cell number counted after detachment according to the type of microcarrier	130
2.11	Cell viability after detachment according to the type of microcarrier . . . .	131
2.12	Microcarriers performances summary according to the agitation mode. . .	134
3.1	Water and microcarriers material properties for CFD simulations. . . . .	151
3.2	Constants involved in the $k$ and $\varepsilon$ equations during CFD simulations. . . .	154
3.3	Impact of near-wall turbulence modelling on CFD results at the microcarrier just-suspended state and for different impeller designs in a minibioreactor. . . . .	157
3.4	Brief description of the drag force models proposed in Fluent and compared for microcarrier just-suspended state. . . . .	158
3.5	Calculation of the Brucato and Pinelli corrections for drag force models at different vessel levels. . . . .	160
3.6	Summary of the final models selection for microcarrier just-suspended state during CFD simulations. . . . .	162
3.7	Microcarrier physical properties: manufacturer and experimental data. . .	168
3.8	$K_i$ and $a_i$ parameters of the three models predicting $N_{js}$ , according to the impeller design. . . . .	176
3.9	Mean errors between $N_{js}$ predicted by the models and experimental values at $T = 20^\circ\text{C}$ , according to the impeller design and the model used. . . . .	177
3.10	Mean errors between $N_{js}$ predicted by the models and experimental values, at $37^\circ\text{C}$ according to the impeller design and the model used. . . . .	178
3.11	Mean errors between $N_{js}$ predicted by the models and experimental values at 20 rpm, in a 20 L vessel equipped with a EE down-pumping impeller, according to the impeller design and the model used. . . . .	178
3.12	Impact of the impeller design on $N_{js}$ and classification. . . . .	179

3.13	Adapted Zwietering coefficients $S_{calc}$ values according to the impeller design and the $D/T$ ratio. . . . .	181
4.1	Comparison of the experimental $N_{js}^{exp}$ and the modelled $N_{js}^{mod}$ and fluid turbulence characteristics at the microcarrier just-suspended state for different impeller designs in a minibioreactor, according to $\langle \varepsilon \rangle$ ascending order. . . . .	197
4.2	Fluid turbulence determination at the microcarrier just-suspended state for different impeller designs in a minibioreactor, according to $\langle \varepsilon \rangle$ ascending order. . . . .	199
4.3	Fluid turbulence characterization at the microcarrier just-suspended state for different impeller designs in a minibioreactor, according to $\langle \varepsilon \rangle$ ascending order. . . . .	200
4.4	Geometrical characteristics of the 3D-printed impeller designs. . . . .	213
4.5	Comparison of the robustness of the response surfaces obtained with the different algorithms. . . . .	214
4.6	Geometrical parameters and corresponding $N_{js}$ and objective function values predicted as optimal impellers. Results are presented from single-objective optimizations and from the final multi-objective function. . . . .	223
4.7	Geometrical characteristics of the selected EED impellers and modelled parameters related to the hydromechanical stress encountered by the particles at the just-suspended state. . . . .	228
5.1	Résumé des performances obtenues avec différents microporteurs selon le mode de culture. . . . .	252
5.2	Paramètres $K_3$ et $a_3$ du modèle prédisant $N_{js}$ , selon le type de mobile. . . . .	255
A.1	Stirred systems and agitation conditions chosen for cultures in dynamic mode in this thesis. . . . .	267





# Nomenclature

## *Variables*

$A$	Adhesion surface	(m <sup>2</sup> )
$a_{1,2,3}$	Model constants	(-)
$b_{1,2,3}$	Model constants	(-)
$c_{1,2,3}$	Model constants	(-)
$C$	Off-bottom clearance	(m)
$C_{1\varepsilon}$	Constant involved in the $k$ and $\varepsilon$ equations	(-)
$C_{2\varepsilon}$	Constant involved in the $k$ and $\varepsilon$ equations	(-)
$C_{\mu}$	Constant involved in the $k$ and $\varepsilon$ equations	(-)
$C_D$	Drag coefficient	(-)
$c_v$	Coefficient of variation of the cell number per micro-carrier distribution	(%)
$d_{1,2,3}$	Model constants	(-)
$d$	Diameter	(m)
$D$	Impeller diameter	(m)
$EDC$	Energy Dissipation / Circulation function	J m <sup>-3</sup>
$f_{t,Brucato}$	Brucato corrective coefficient	(-)
$f_{t,Pinelli}$	Pinelli corrective coefficient	(-)
$F^{exp}$	Cell expansion factor	(d <sup>-1</sup> )
$g$	Gravity constant	(m s <sup>-2</sup> )
$H$	Tank height	(m)
$k$	Turbulence kinetic energy	(m <sup>2</sup> s <sup>-2</sup> )
$K_{1,2,3}$	Model impeller constants	(-)
$K_{SL}$	Interphase momentum exchange coefficient	(-)
$Lac/Glu$	Lactate concentration on glucose concentration ratio	(-)
$n_{exp}$	Number of experiments	(-)
$N$	Impeller agitation rate	(s <sup>-1</sup> )
$N_{DOE}$	Total number of design points of the design of experiments	(-)
$n_{mesh}$	Total mesh number	(-)
$\langle N_{cell/\mu C} \rangle$	Mean number of cell per microcarrier	cell / $\mu C$

$p$	Pressure	(Pa)
$P$	Global power input	(W)
$PF$	Packed fraction criterion	(-)
$\langle (P/V) \rangle$	Global power input per unit of volume	(W m <sup>-3</sup> )
$Q_{p,net}$	Particle volume flow rate in the mesh cell	(m <sup>3</sup> s <sup>-1</sup> )
$S$	Zwietering coefficient	(-)
$SF$	Still fraction criterion	(-)
$T$	Tank diameter	(m)
$\mathbf{v}$	Velocity vector	(m s <sup>-1</sup> )
$v_{r,S}$	Terminal velocity of particles in settling bed	(m s <sup>-1</sup> )
$V$	Volume	(m <sup>3</sup> )
$X$	Mass concentration of particles	(%)
$x_{colo}$	Colonized microcarrier fraction	(%)
$Y_{Glu}$	Glucose consumption yield	(-)

*Greek letters*

$\alpha$	Volume fraction	(-)
$\beta$	Blade slope angle	(°)
$\varepsilon$	Turbulent energy dissipation rate	(m <sup>2</sup> s <sup>-3</sup> )
$\gamma$	Diffusion coefficients	(-)
$\lambda_K$	Kolmogorov length scale	(m)
$\mu$	Dynamic viscosity	(Pa s)
$\nu$	Kinematic viscosity	(m <sup>2</sup> s <sup>-1</sup> )
$\Psi$	Smoothing function of the Huilin-Gidaspow model	(-)
$\rho$	Density	(kg m <sup>-3</sup> )
$\sigma$	Standard deviation of the number of cell per microcarrier distribution	cell / $\mu C$
$\sigma_k$	Constant involved in the $k$ and $\varepsilon$ equations	(-)
$\sigma_\varepsilon$	Constant involved in the $k$ and $\varepsilon$ equations	(-)
$\tau$	Hydrodynamic stress	(Pa)
$\tau_p$	Particle residence time	(s)
$\bar{\bar{\tau}}$	Reynolds stress tensor	(Pa)
$\omega$	Optimization criterion	(-)

*Dimensionless number*

$Ar$	Archimede number	(-)
$Fr$	Froude number	(-)
$N_p$	Power number	(-)

## NOMENCLATURE

---

$N_q$	Pumping capacity	(-)
$Re$	Reynolds number	(-)
$y^+$	Dimensionless distance from the vessel wall	(-)
$y^*$	Dimensionless distance from the vessel wall	(-)

### *Subscripts*

@ $p$	Encountered by the particles
5-95	Confidence interval
50	Median
crit	Critical
down	Determination of $N_{js}$ by $N$ decrease
exp	Experimental
js	Just-suspended state
L	Liquid phase
$m$	Mixture
max	Maximal
min	Minimal
mod	Modeled
o	Orbital
p	Particle
ref	Reference
S	Solid phase
t	Turbulent
tot	Total
up	Determination of $N_{js}$ by $N$ increase

### *Abbreviations*

$\mu$ C	Microcarrier
ASC	Adipose-derived Stem Cell
BM	Bone Marrow
CFD	Computational Fluid Dynamics
CFU-F	Colony-Forming Units Fibroblast
DEM	Discrete Element Method
EED	Elephant Ear impeller in Down-pumping mode
EEU	Elephant Ear impeller in Up-pumping mode
ESC	Embryonic Stem Cell
FBS	Fetal Bovine Serum
FD-M	Fibrin-Depleted culture Medium

GLU	Glucose
GMP	Good Manufacturing Practices
hep-M	Culture medium containing heparin
hPL	Human Platelet Lysate
ISCT	International Society for Cellular Therapy
LDH	Lactate DesHydrogenase
MOGA	Multi-Objective Genetic Algorithm
MPD	Marine Propeller in Down-pumping mode
MPU	Marine Propeller in Up-pumping mode
MRF	Moving Reference Frame
MSC	Mesenchymal Stem / Stromal Cell
PLA	PolyLactic Acid
RANS	Reynold-Averaged Navier-Stokes
RT	Rushton Turbine
STR	Stirred Tank (bio)Reactor
UC	Umbilical Cord
WJ	Wharton's Jelly

# Introduction

**S**INCE the last decades, many efforts based on the use of mesenchymal stem cells (MSC) were initiated. Due to their promising therapeutic functions (differentiation capability, bioactive factors secretion, immunomodulatory properties...), new applications in cell therapies were investigated. Parts of the ongoing clinical trials are notably focused on diseases for which current treatments are not sufficiently effective (heart failures, cancers, type I and II diabetes...). MSC are adherent-dependent cells, namely they need an attachment to a surface to grow. This adherence surface limitation must be thus carefully taken into account for the expansion process development and scale-up. In the clinical environment, current culture systems are however still limited to 2D planar cultures (T-flasks), despite higher operating costs (technical maintenance) and contamination risks, as well as the need of larger space in incubators, in comparison to '3D' bioreactors. It is clear that planar cultures will be not sufficient to meet the increasing demand for MSC, from  $10^9$  to  $10^{12}$  cells / lot [1], and that expansion processes must be intensified, by taking care of both the number of harvested cells, and the cell quality [2]. In this way, the whole process, from cell isolation to the delivery to the patient, must be carefully designed and controlled, through scalable, cost-effective and closed GMP culture systems and protocols [3].

The present PhD thesis is specifically focused on the cell expansion phase, with an attention on the microcarrier technology, as it offers the theoretical greatest performance of expansion (Fig. 1). For this technology, cells adhere on the surface of particles, which display a diameter  $d_p \approx 200 \mu\text{m}$  and a density  $\rho_S \approx 1,020 \text{ kg m}^{-3}$  close to the liquid phase density ; particles are then suspended by an agitation in a bioreactor. The production of a dose containing  $10^9$  cells would require 150 T-175 flasks (based on a final cell density of  $40,000 \text{ cell / cm}^2$ ), which would be tricky to implement. The specific adherence surface available for cell expansion is greatly enhanced in microcarrier-based cultures, where

$10^9$  cells may be produced in a 2.4 L bioreactor, and where the addition of monitoring / control loop is made easier, in accordance with GMP specifications. However, cell response to its biochemical / physical environment still has to be investigated in such systems [4]. For MSC cultures, this should include the interactions with:

- The culture medium formulation, which must display a clinical grade [5].
- The microcarrier properties (material, diameter, porosity, coating...) and concentration [6].
- The physical and chemical parameters of the environment, such as the temperature, the pH or the dissolved oxygen [2].
- The nutrient and metabolite concentrations [7].
- The hydrodynamics and stress generated by the agitation [8, 9, 10].

Cell biological and physiological responses to this environment must be first understood and controlled for the expansion process scale-up, including the bioreactor design, the feeding strategy, as well as the culture conditions.

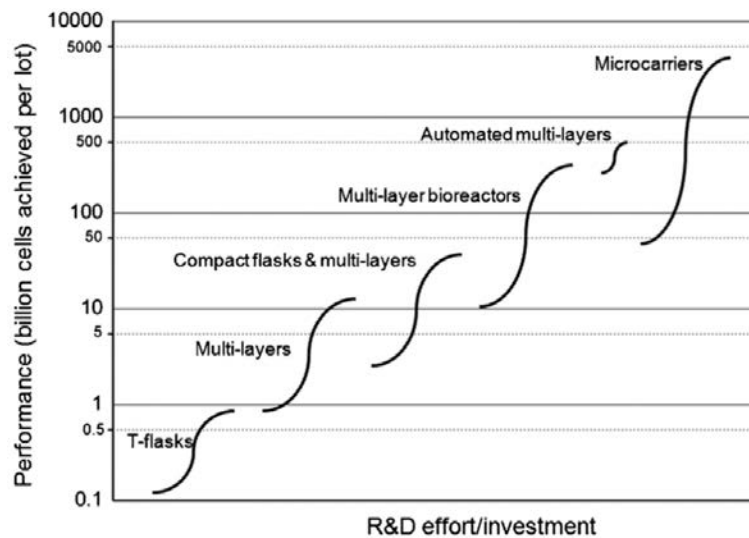


Figure 1: Conceptual illustration of a technology S-curve showing the evolution of expansion technologies used in cell therapy manufacture. The limits of each S-curve correspond to the amount of cells achieved by the smallest and largest size of each technology type when using the maximum number of units (80 for planar and 8 for microcarriers). The x-axis represents qualitatively the R&D effort required for a company currently using T-flasks to change to other cell expansion technologies. Figure reproduced from Simaria *et al.* (2014) [11].

In this context, the multidisciplinary STEMCellREAcTOR project (2014-2018, <http://stemcreator-project.com>), funded by the ANR (French national agency for research) and coordinated by the LRGP, was conducted to address the main scientific questions

related to this topic. Studies were thus performed in collaboration with the other partners of this project, namely three national and international laboratories (LCPM-Nancy, ULg-Liège, IBC-Moscow) and two SME (Global Process Concept-La Rochelle, Bio-Inox-Bergerac). Fig. 2 presents the global architecture of the STEMCellREAcTOR project. This thesis was mainly involved in the coupling of hydrodynamics and MSC culture performance part. Since adherent-dependent animal cells are known to be particularly sensitive to shear stress [12], our studies were carried out in order to get more knowledge on the hydrodynamics at the microcarrier just-suspended state in STR. Data about the potential damaging zones in the bioreactor were then related to the MSC physiological response during the expansion process. MSC expansion process on microcarriers was also conducted with the support of the IMoPA laboratory (Nancy), directly involved into MSC clinical applications, and based on works of two previous PhD thesis performed in the laboratory and from the literature data. The first thesis, conducted by Caroline Ferrari (2012), concerned the expansion of bone marrow MSC from pig, while the second one, defended by Céline Martin (2016), used human bone marrow MSC ; both studies used culture media supplemented with FBS.

Three main objectives were defined through this PhD thesis. The first one aimed **to improve the expansion of MSC from umbilical cords** (Wharton’s jelly) on microcarriers, in a clinical grade medium. Secondly, **the hydrodynamics in stirred bioreactors was investigated at the microcarrier just-suspended state** and modelled, depending on the operating conditions (agitation design, particle properties). The last objective consisted in the **determination of an optimal impeller design for MSC culture on microcarriers** in a bioreactor, by minimizing the particle exposure to potentially damaging zones. The present report is thus divided into four chapters, relying on the scientific methodology summarized in Fig. 3:

- **Chapter 1** presents a **global literature review**, relating the MSC expansion process with the hydrodynamics in stirred tank bioreactors. It should be emphasized that **specific and more detailed literature reviews, and materials and methods are presented in each result chapters, through scientific publications.**
- **Chapter 2** displays results about the **improvement of WJ-MSc culture on microcarriers**. To meet the need of a robust cell counting method, an automatic and *in situ* method was developed, providing cell distribution on microcarriers. Then, the impact of the type of microcarrier on the expansion performance was investigated, according to different agitation modes. It allowed the selection of two commercial microcarriers, which were then compared to home-made microcarriers,

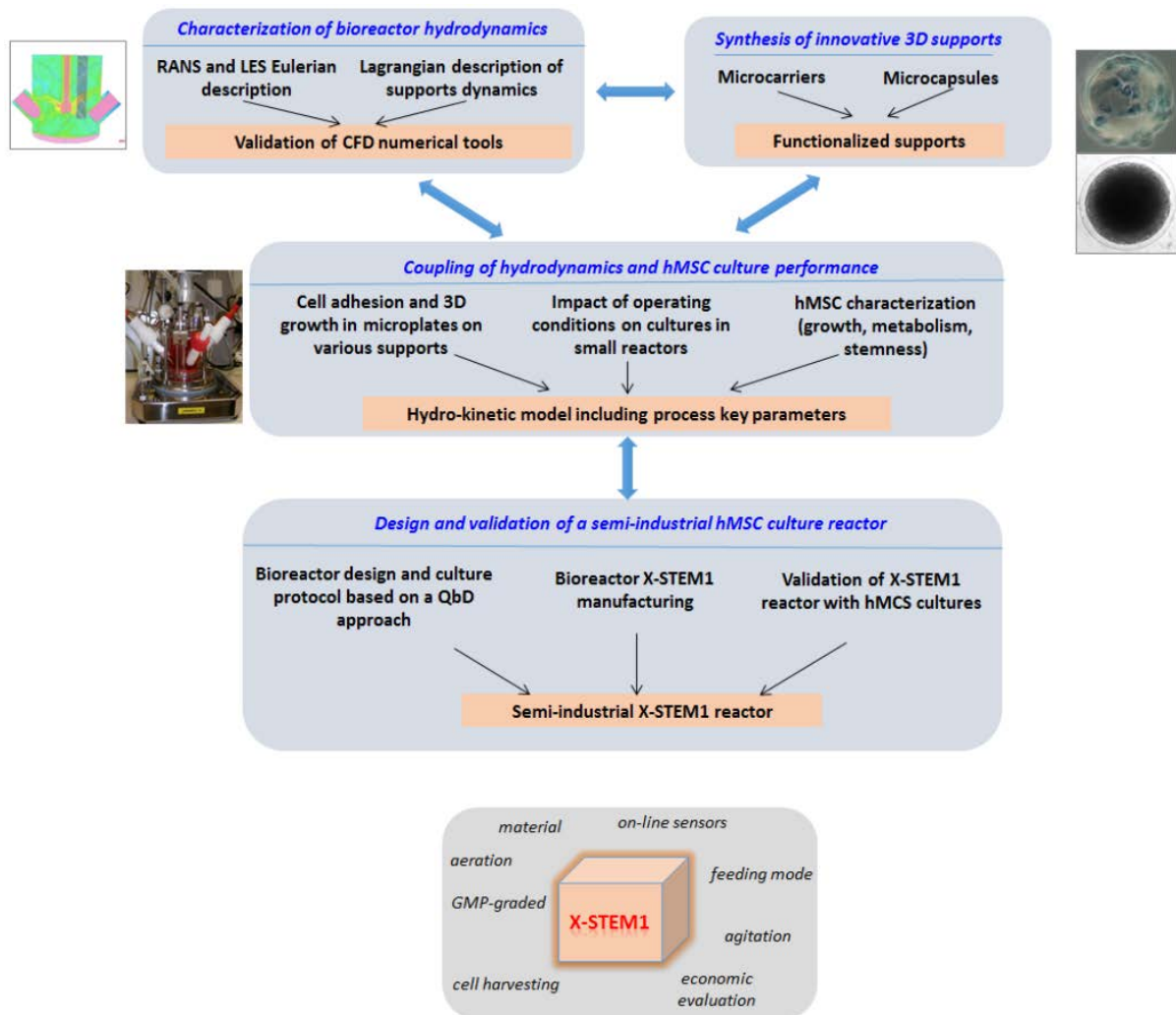


Figure 2: Global architecture of the STEMCellREACTOR ANR project.

synthesized by the LCPM laboratory partner, in terms of cell attachment, expansion and detachment potentialities.

- **Chapter 3** presents results about the **modelling of the microcarrier just-suspended state in stirred-tank bioreactors**. Two models were established to predict the minimal agitation rate ensuring all particles suspension ( $N_{js}$ ). The first one arises from a dimensional analysis. The second one is based on Computational Fluid Dynamics (CFD) simulations, after a preliminary model validation.
- **Chapter 4** finally aims at **comparing different impeller designs according to the hydromechanical stress encountered by microcarriers using CFD simulations**. To this end, comparisons were based on the particle exposure to the potentially damaging zones. Then, it allowed the development of a CFD-based strategy coupled to a multi-objective optimization in order to predict the optimal impeller geometrical parameters (blade slope angle, size, position) to



minimize potential cell damages due to the agitation. At last, WJ-MSC expansion performances were compared in 200 mL STR equipped with impellers displaying different geometrical parameters leading to different energy levels on microcarriers.

- For the sake of clarity and simplicity, it was chosen not to detail all materials and methods used in this present work in a 'Materials and methods' chapter, since dedicated sections are presented in each result chapters, through scientific publications. Experimental and numerical approaches related to the preliminary and complementary works are detailed in Appendix A.
  
- The design and validation task of the ANR project were also achieved during this PhD work, but were not detailed in the present manuscript for clarity reasons.

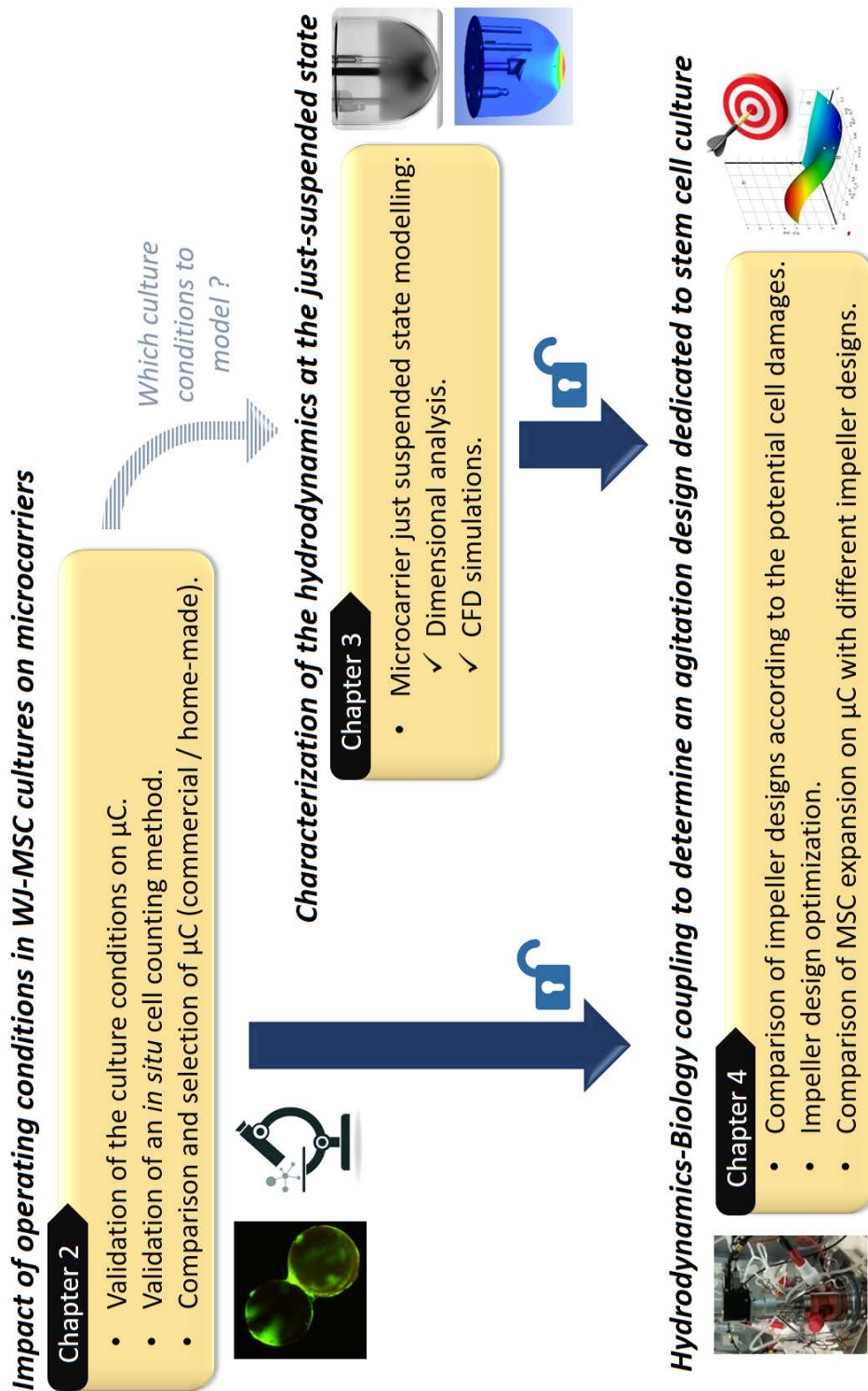


Figure 3: Global methodology applied in the present PhD thesis, linking experimental and numerical results together.

## References

- [1] J. Rowley, E. Abraham, A. Campbell, H. Brandwein, S. Oh, Meeting lot-size challenges of manufacturing adherent cells for therapy, *BioProcess International* 10 (2012) 16–22.
- [2] C. Martin, É. Olmos, M.-L. Collignon, N. De Isla, F. Blanchard, I. Chevalot, A. Marc, E. Guedon, Revisiting MSC expansion from critical quality attributes to critical culture process parameters, *Process Biochemistry* 59 (2017) 231–243.
- [3] V. Jossen, C. van den Bos, R. Eibl, D. Eibl, Manufacturing human mesenchymal stem cells at clinical scale: process and regulatory challenges, *Applied Microbiology and Biotechnology* (2018) 1–14.
- [4] A. C. Schnitzler, A. Verma, D. E. Kehoe, D. Jing, J. R. Murrell, K. A. Der, M. Aysola, P. J. Rapiejko, S. Punreddy, M. S. Rook, Bioprocessing of human mesenchymal stem/stromal cells for therapeutic use: Current technologies and challenges, *Biochemical Engineering Journal* 108 (2016) 3–13.
- [5] S. Gottipamula, M. Muttigi, U. Kolkundkar, R. Seetharam, Serum-free media for the production of human mesenchymal stromal cells: a review, *Cell Proliferation* 46 (2013) 608–627.
- [6] Q. A. Rafiq, K. Coopman, A. W. Nienow, C. J. Hewitt, Systematic microcarrier screening and agitated culture conditions improves human mesenchymal stem cell yield in bioreactors, *Biotechnology Journal* 11 (2016).
- [7] C. Ferrari, E. Olmos, F. Balandras, N. Tran, I. Chevalot, E. Guedon, A. Marc, Investigation of growth conditions for the expansion of porcine mesenchymal stem cells on microcarriers in stirred cultures, *Applied Biochemistry and Biotechnology* 172 (2014) 1004–1017.
- [8] C. J. Hewitt, K. Lee, A. W. Nienow, R. J. Thomas, M. Smith, C. R. Thomas, Expansion of human mesenchymal stem cells on microcarriers, *Biotechnology Letters* 33 (2011) 2325–2335.
- [9] A. W. Nienow, C. J. Hewitt, T. R. Heathman, V. A. Glyn, G. N. Fonte, M. P. Hanga, K. Coopman, Q. A. Rafiq, Agitation conditions for the culture and detachment of hMSCs from microcarriers in multiple bioreactor platforms, *Biochemical Engineering Journal* 108 (2016) 24–29.
- [10] T. R. Heathman, A. W. Nienow, Q. A. Rafiq, K. Coopman, B. Kara, C. J. Hewitt, Agitation and aeration of stirred-bioreactors for the microcarrier culture of human mesenchymal stem cells and potential implications for large-scale bioprocess development, *Biochemical Engineering Journal* 136 (2018) 9–17.
- [11] A. S. Simaria, S. Hassan, H. Varadaraju, J. Rowley, K. Warren, P. Vanek, S. S. Farid, Allogeneic cell therapy bioprocess economics and optimization: Single-use cell expansion technologies, *Biotechnology and Bioengineering* 111 (2014) 69–83.

- [12] N. Ma, K. W. Koelling, J. J. Chalmers, Fabrication and use of a transient contractional flow device to quantify the sensitivity of mammalian and insect cells to hydrodynamic forces, *Biotechnology and Bioengineering* 80 (2002) 428–437.

# Chapter 1

## State of the Art


### Contents

---

<b>1.1</b>	<b>Introduction</b>	<b>10</b>
<b>1.2</b>	<b>Mesenchymal stem / stromal cells and their therapeutic benefits</b>	<b>11</b>
1.2.1	MSC background and definition evolution	11
1.2.2	Therapeutic benefits and prospective	15
1.2.3	Current limits	21
<b>1.3</b>	<b>MSC sources and population heterogeneities</b>	<b>24</b>
1.3.1	MSC niches in the human body and MSC functional differences	24
1.3.2	Wharton's Jelly as promising source of MSC	25
<b>1.4</b>	<b>Expansion process challenges</b>	<b>27</b>
1.4.1	Cell quality and safety requirements	28
1.4.2	Cell quantity enhancement	32
<b>1.5</b>	<b>Microcarrier-based cultures</b>	<b>37</b>
1.5.1	Microcarrier characteristics	37
1.5.2	Cell - microcarrier interactions	39
1.5.3	MSC culture on microcarriers: an outlook	41
1.5.4	Particles just-suspended state	49
<b>1.6</b>	<b>Hydrodynamics potential impact on MSC</b>	<b>53</b>
1.6.1	Hydromechanical stress and turbulence description	53
1.6.2	Hydrodynamics characterization in STR	58
1.6.3	Hydro-biological coupling	62
1.6.4	Fluid flow characterization using CFD	65
1.6.5	Impeller design optimization	68
<b>1.7</b>	<b>Thesis aims and objectives</b>	<b>73</b>

---

## 1.1 Introduction

 IN recent years, a particular attention has been paid to mesenchymal stem / stromal cells (MSC) for their application in regenerative medicine. According to the U.S. National Institute of Health, more than 800 clinical trials are indeed completed or ongoing to treat cancers, heart failures and Parkinson's disease as some of many examples (ClinicalTrials.gov database, on May 22<sup>th</sup>, 2018). However, in order to reach the high cell dose requirements, corresponding to  $10^9$  and  $10^{12}$  cells/lot [1], these adherent-dependent cells may be cultivated on microcarriers (100-400  $\mu\text{m}$  diameter solid particles), in agitated bioreactors [2]. When mixing this solid-liquid suspension, a compromise has to be found between sufficient mixing to suspend the microcarriers, and negligible cell damages. It is generally assumed that working at the microcarrier just-suspended state is a good compromise between sufficient nutrients homogenization, mass transfer and reasonable hydromechanical stress encountered by the cells. However, assuming that MSC are shear stress sensitive [3], the hydrodynamics and more particularly the hydromechanical stress generated need to be studied and quantified to ensure cells quality during the whole expansion process.

The present thesis take place at the interface between MSC expansion improvement and the impact of the hydrodynamics on cell biological response. This first chapter introduces a global introduction supported by studies of literature, in order to contextualize and clarify these thesis attempts. Specific and more detailed literature reviews are proposed in each results chapter, as first part of studies presented as scientific publications.

This global context overview will be firstly dedicated to the MSC definition and the therapeutic context dealing with MSC, before presenting their different sources and the specificities of Wharton's Jelly MSC. Then, main challenges for the expansion process will be highlighted, concerning both the product quantity and quality. This will lead to the microcarrier characteristics and prospectives as a way to overcome the current limits. Hence, microcarriers and their related culture performances will be presented. The last part will finally focus on the impact of the hydrodynamics on MSC and the potential cell damages generated.

## 1.2 Mesenchymal stem / stromal cells and their therapeutic benefits

In order to understand the issues related to MSC and their role in the medical field, it is proposed here to present their definition through their historical background. Their properties and also their name evolved many times during the last decades. Today, their name is still under discussion in the scientific world, with names based either on their origin or on their application. In a second time, their therapeutic benefits will be presented with a close link to the medical needs, including both clinical trials and commercialized MSC-based drugs.

### 1.2.1 MSC background and definition evolution

In 1867, the German pathologist Cohnheim suggested the presence of non-hematopoietic stem cells in the bone marrow [4]. The bone marrow was hence considered as a source of fibroblast cells, which may contribute to wound healing. In 1869, the French physiologist Goujon performed bone marrow transplantations on heterotrophic anatomic sites to demonstrate the ectopic novo-generation of bone and marrow [5]. However, a century passed before the therapeutic application of these cells. In 1968, Tavassoli and Crosby defined an osteogenic potential, inherent to the bone marrow [6]. These results were however limited by the difficulty in the identification of progenitor cells from cells differentiated in bone cells, due to experiments involving entire bone marrow fragments.

The studies led by Alexander Friedenstein and his colleagues in the 60's and 70's are considered as pioneer work in the cell identification as stem cells [7, 8]. Two major breakthroughs were established. First, the osteogenic capacity was associated to a cell minority, different from the hematopoietic cells by their relative quick adherence on culture flask surfaces and by their morphology comparable to fibroblasts, as shown in Fig 1.1. This first discovery allowed to determine the cell origin, namely the medular stroma. In a second time, Friedenstein *et al.* demonstrated the clonogenicity capacity. Combined with the capability to generate skeletal tissue cells (bone, cartilage, adipose tissue, fibrous tissue), Friedenstein and Owen attributed to these cells the name of osteogenic stem cells [9] or stromal stem cells from bone marrow [10]. At the beginning of the 90's, Arnold Caplan gave them the name of mesenchymal stem cells, widely used today to qualify them [11].

In 1999, as part of his works in the Osiris Therapeutics, Inc. company, Mark Pittenger isolated homogeneous MSC populations and controlled their differentiation *in vitro* and their clonal isolation [12]. During the next years, various studies demonstrated the MSC therapeutic capacities, including, '*inter alia*', their immunomodulatory properties [13, 14].

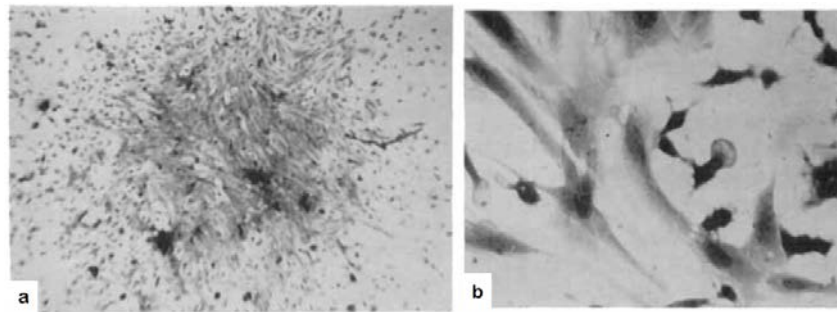


Figure 1.1: Mesenchymal stem cells discovery from guinea-pig bone marrow: Cover slide cultures of bone marrow cells at 12<sup>th</sup> day of explantation (a) 10 × objective; (b) 20 × objective. Figure reproduced from Friedenstein *et al.*, 1970 [8].

Moreover, MSC were found in other sources than the bone marrow, like in the adipose tissues or the umbilical cord [15]. All these biological and technological advancements led to an increasing number of studies on MSC, as presented in Fig. 1.2.

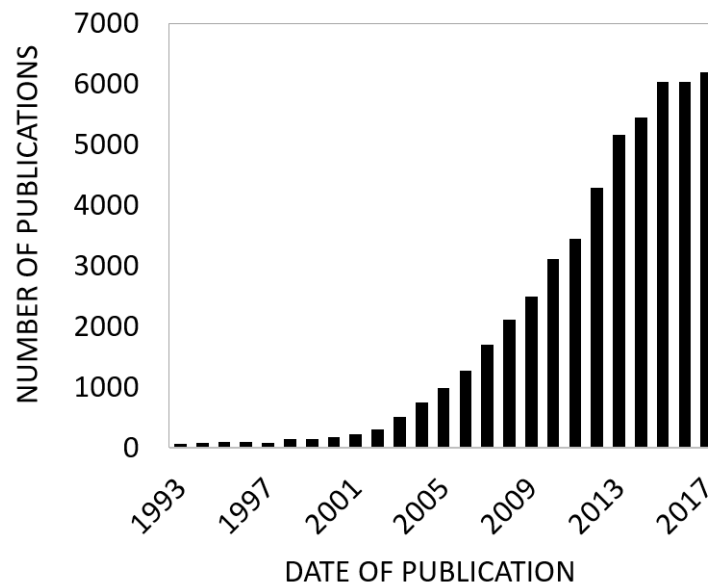


Figure 1.2: Increase of the number of MSC-based scientific publications for 25 years (PubMed data base, with 'Mesenchymal stem cells' or 'Mesenchymal stromal cells' search term).

In 2000, a non-hematopoietic mesenchymal stem cells committee was organized under the direction of E. Horwitz and A. Keating and involved 250 participants. One of the objectives concerned the need to clearly define the MSC. It has emerged that the stemness was questionable according to the expression of surface antigens related to multiple cell lines and thus with questions about these cells engagement in a cell line and their stem identity [16]. Following this debate, Horwitz and his colleagues showed the need to clarify the nomenclature defining the MSC in a paper handled by the ISCT (International Society for Cellular Therapy). The name 'multipotent mesenchymal stromal cells' was chosen, based



on the tissue nature from which the cells were coming [17]. This designation permitted to keep the MSC acronym, already embedded in the scientific world. The ISCT proposed thereafter, through the publication of Dominici *et al.* in 2006, 3 criteria to define MSC, as summarized in Fig. 1.3 [18]. Since then, they are considered as the reference criteria for MSC studies. It is also admitted that these 3 criteria are defined as minimal criteria, despite potential heterogeneities in MSC populations, either between two different sources or within a given source.

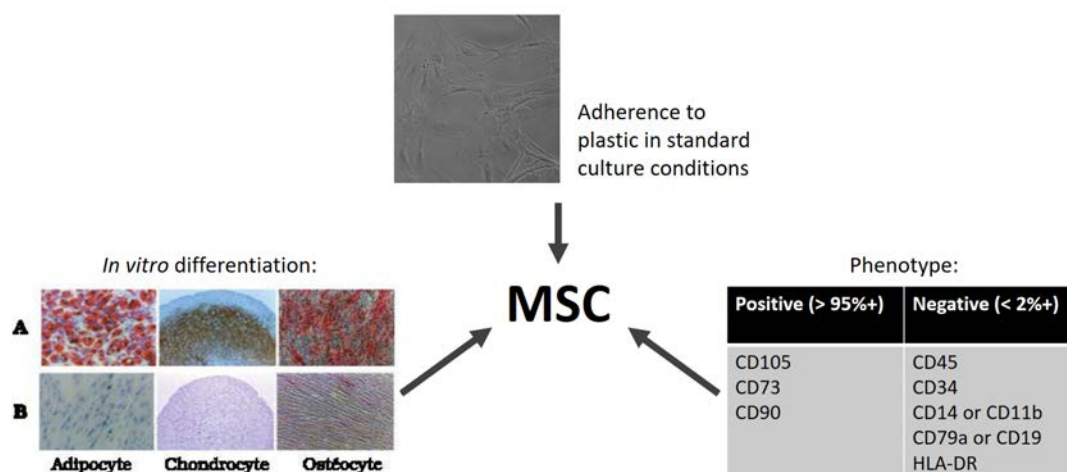


Figure 1.3: Criteria defining MSC according to the International Society for Cellular Therapy (ISCT).

Although it was previously validated for bone marrow MSC, the 'mesenchymal' term became questionable as presented by Bianco *et al.* in 2009 [19]. This term was indeed based on the hypothesis that multiple tissues from skeletal lines may be generated from adult MSC. Nevertheless, the non-skeletal capacity of a single MSC has not been formally proved *in vivo*. However, Bianco and his colleagues specified that the name of mesenchymal stromal cell was already widely used and that it would be futile to replace it by a more appropriate term following the biological point of view, as 'skeletal stem cell' for bone marrow MSC. Changing the name would entail more disorder and confusion than to admit some imprecisions with the current terms, and to well define the cell origin and properties according to the applications.

It has been then reproach to the definition given by the ISCT the lack of cell immunological properties among the criteria. In 2013, through the paper of Krampera *et al.*, the ISCT proposed some guidelines to characterize MSC in the clinical applications [20]. It was performed with the aim of a global discussion to lead to comparable and non-ambiguous results on MSC efficiency for clinical use.

More recently, MSC began to be considered through the expansion process. The paper of Martin *et al.* in 2017 presented these aspects, establishing direct relations between

cell characterisation, process expansion and final therapeutic use [21]. It was also shown that, to allow a regulatory approbation for therapeutic applications, it is necessary to define MSC according to: (i) the potential cell damages occurring during the isolation and expansion processes, (ii) *in vivo* data obtained from pre-clinical studies, and (iii) *in vitro* characterization via their identity, their senescence state and their multipotent, immunomodulatory and angiogenic properties (Fig. 1.4).

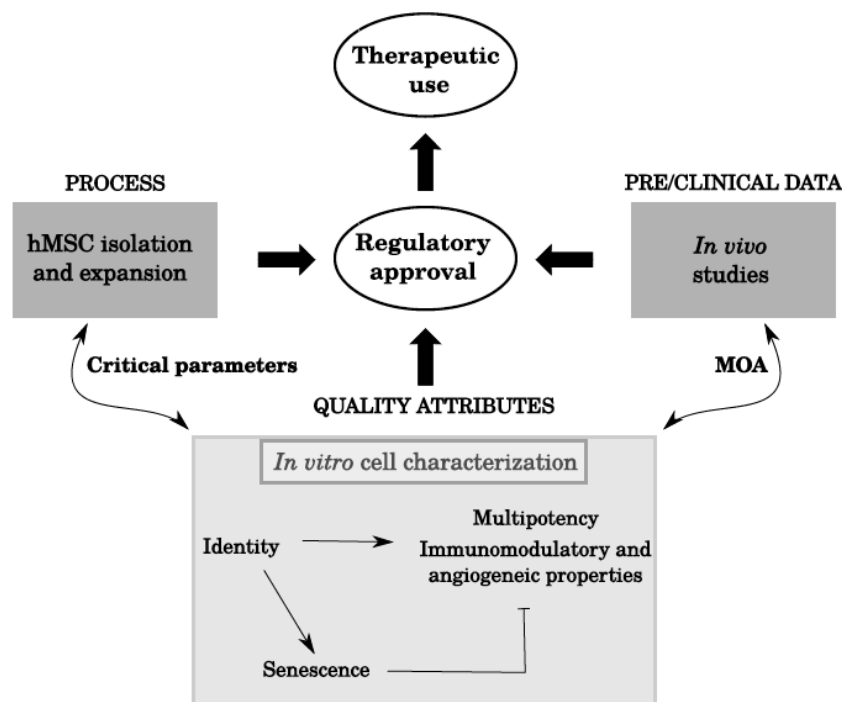


Figure 1.4: Development overview of a regenerative medicine applied to hMSC therapy (MOA: Mode Of Actions). Figure reproduced from Martin *et al.*, 2017 [21].

As a result of the regenerative medicine development, commercially-available working MSC banks emerged to meet the cell demand for both clinical and research applications. These banks should notably be manufactured under current Good Manufacturing Practices (cGMP) and conform to xeno-free guidelines. They mainly involve hBM-MSCs (RoosterBio Inc., Waisman Biomanufacturing) or hASCs (RoosterBio Inc.). They were developed with the aim of decreasing the time spent for investigational new drug submissions and getting closer to results standardization.

Figure 1.5 proposes to resume this historic, highlighting the sharp acceleration observed in the MSC study over time.

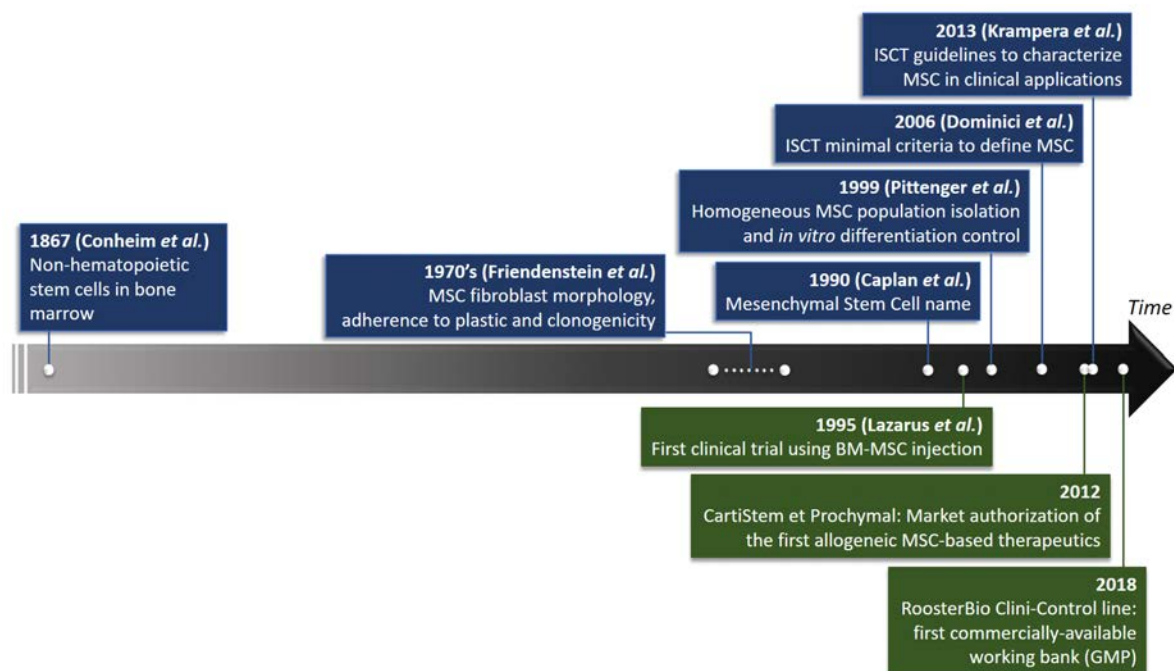


Figure 1.5: Historical timeline of MSC discoveries and main developments.

## 1.2.2 Therapeutic benefits and prospective

### Ethical conduct

Human stem cells are generally classified as either embryonic or adult stem cells. MSC belong to the second category, whereas human embryonic stem cells (hESC) are isolated from inner cell mass of a blastocyst. This corresponds to a hundred cells recovered from an embryo after 5 to 7 days following the fecundation. As presented in Fig. 1.6, hESC are pluripotent and are thus able to produce more lineages of differentiated cells than MSCs. Their use is however controversial. Initially, hESC isolation led to the embryo destruction, considered to be equivalent to a human life in most of countries [22]. Since then, efforts have been made to avoid embryo destruction, by using a single blastomere isolated before the blastocyst stage [23]. Following ethical charts, adult stem cells, including MSC, are still considered to present a better alternative. Their isolation is performed with the donor approval, and *in vitro* expansion is performed in order to obtain sufficient cells for therapeutic applications. Regarding the cell multipotency, the source of adult stem cells is generally chosen according to the final application.

### Therapeutic functions

Many efforts are underway in the field of the regenerative medicine, defining a branch of medicine involving methods to regrow, repair or replace damaged or diseased cells,

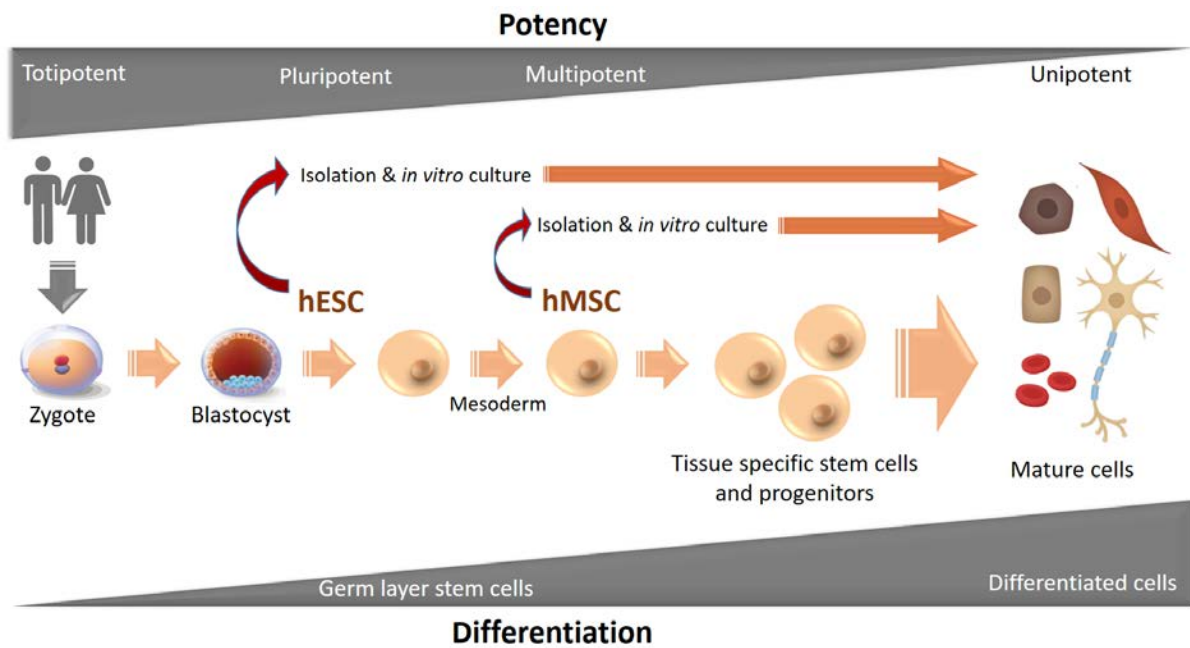


Figure 1.6: Cell level of potency and differentiation capability according to the cell development stage for ESC and MSC isolation. Figure inspired from Prodinge *et al.* [24].

organs or tissues. Stem cells are strongly related to this field of study through tissue engineering and cell therapy. As shown in Fig. 1.7, they indeed present specific advantages involving: (i) differentiation into various cell lineages, (ii) secretion of crucial factors for cell survival and proliferation, (iii) immunomodulatory properties, (iv) exosome transfer and (v) capacity to migrate to the exact site of injury.

#### *a - Cell differentiation*

MSC applications were first focused on the multipotent properties, with both differentiation and transdifferentiation potential, for tissue engineering as replacement therapies. The different lineages induced by MSC are presented in Fig. 1.8. These cells were notably integrated in three dimensional (3D) scaffolds for the replacement of 3D pieces in *in vivo* tissues. MSC differentiation into distinctive end-stage cell types was used for tissue cultivation including bone, cartilage, muscle, bone marrow stroma, tendon, ligament, and other connective tissues [26, 27, 28, 29].

#### *b - Trophic activity*

Today, most of consideration of MSC therapeutic effects concerns their capacity to secrete a wide variety of cytokines and growth factors with both paracrine (cell-to-cell communication) and autocrine (hormonal or chemical communication) activities. MSC act thus as trophic mediators, by analogy with the 'nurturing'. Neurobiologists used the term 'trophic', meaning 'nutritional' to define the enhancing secretions by nerve terminals to

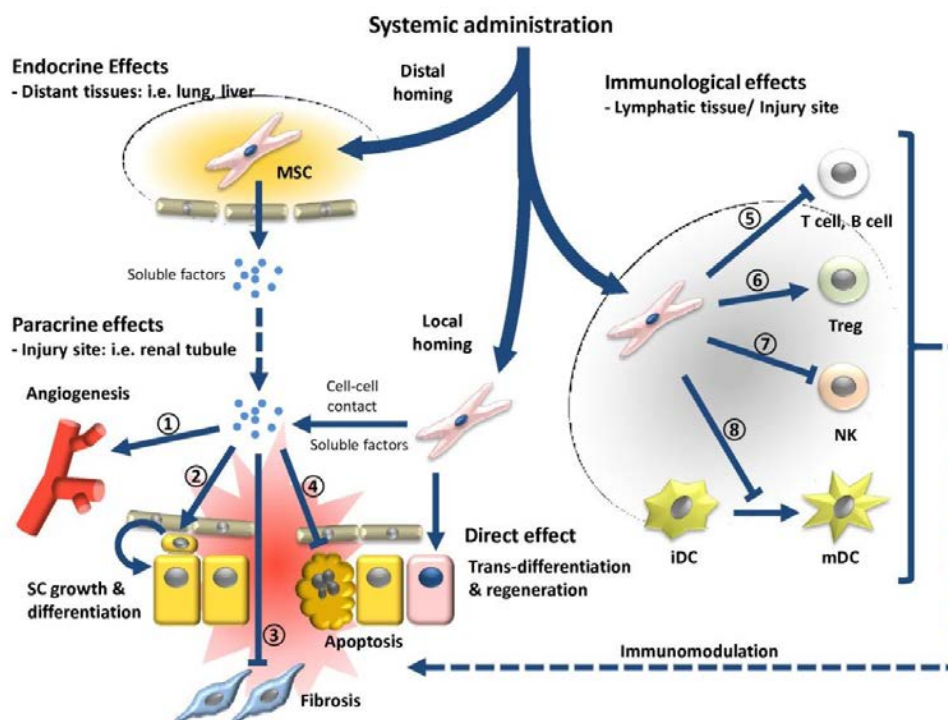


Figure 1.7: Systemic administration of mesenchymal stem cells can trigger distal (endocrine) or local (paracrine) effects that include cell-mediated actions. 1) Promotion of angiogenesis. 2) Stem cell growth and differentiation. 3) Inhibition of fibrosis. 4) Inhibition of apoptosis. 5) Suppression of T and B cells. 6) Induction of regulatory T cell (Treg) differentiation and expansion. 7) Inhibition of natural killer (NK) cells. 8) Inhibition of dendritic cell (DC) maturation. Figure reproduced from Carrion and Figueroa, 2011 [25].

end organs that are not neurotransmitters [30, 31, 32]. Hence, secreted bioactive factors act in MSC vicinity and lead to the following benefits [33]:

- Fibrosis (scar formation) and apoptosis (programmed cell death) inhibition.
- Angiogenesis (blood vessel formation) enhancement.
- Stimulation of mitosis, proliferation and differentiation of organ-intrinsic precursor or stem cell.

All these factors participate in tissue maintenance and make MSC as an injury-site sensitive and / or response therapeutics.

### *c - Immunomodulatory properties*

A particular attention is also paid to MSC immunomodulatory properties and inflammation reduction. These cells have indeed the ability to affect the immune system through cytotoxic T-cell-mediated lysis escape, as well as B-cell proliferation inhibition or promotion, and modulation of cytokine secretion profiles of dendritic and macrophages [33, 34]. Moreover, according to their environment, MSC may induce different immune responses with either inflammation inhibition or stimulation by releasing proinflammatory molecules if the level of inflammatory cytokines is low, making them 'guardians' against excessive

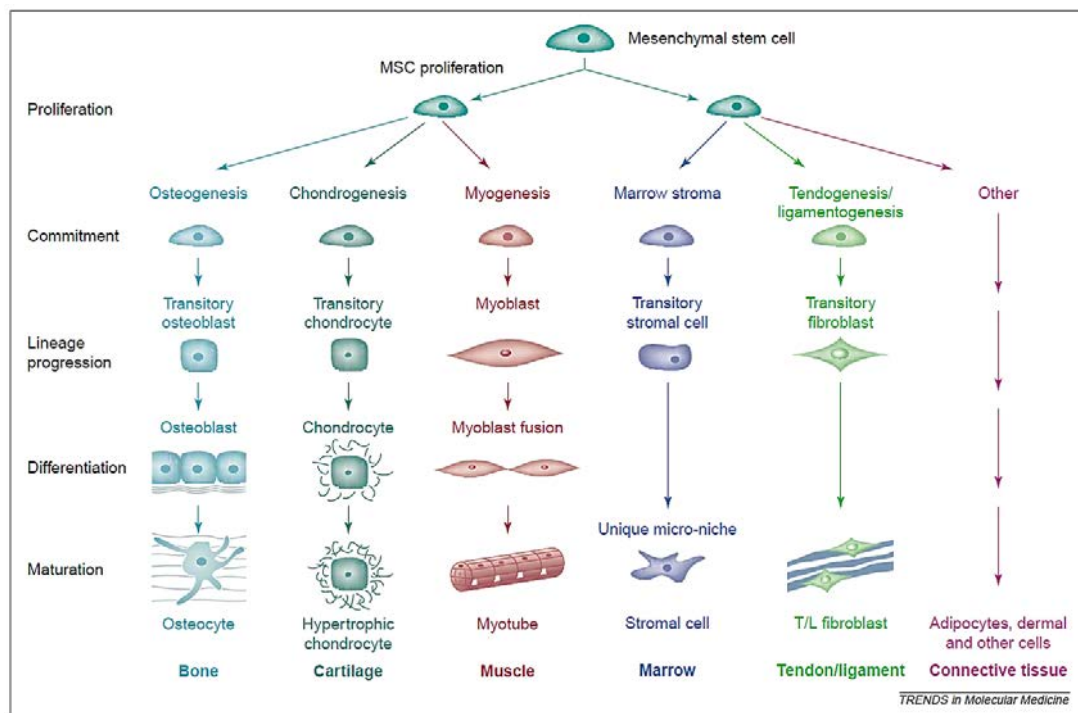


Figure 1.8: Multilineage potential of MSC. Figure reproduced from Caplan *et al.*, 2001 [26].

inflammatory responses [35, 36]. In this way, MSC are able to suppress the local immune system, making them good candidates for autoimmune diseases and allogeneic treatments.

#### *d - Exosome transfer*

A novel MSC use has recently been discovered, through exosome transfer. These secreted vesicles carry nucleic acids, proteins and lipids involved in diverse biochemical and cellular processes such as communication, structure and mechanics, inflammation, exosome biogenesis, tissue repair and regeneration, and metabolism [37, 38]. MSC exosomes appeared thus to be able to interact with many cell types while conferring cellular and immune responses. As for MSC, they remain independent from the tissue source and present an immunomodulatory role.

#### *e - Homing mechanism*

One of the main interest for cell therapies is the capacity of MSC to reach the injured site [39]. This mechanism is currently not fully understood, but seems to result from a correct combination of signals between molecules of the injured tissue and corresponding receptors on MSCs [40, 33]. Chemokines signal proteins play a role in the migration of cells from the immune system to the site of infection. In the case of MSC, it was shown that MSCs were able to migrate differently towards different growth factors and chemokines *in vitro*, and that the MSC migration to injured tissues may depend on the systemic and local inflammatory state [41].

### Clinical trials: Current state and outlook

As a promising future in regenerative medicine, the number of clinical trials has been rising since the turn of the century, as shown in Fig. 1.9. This number is directly related to the different scientific breakthroughs, involving therapeutic properties and benefits discovery as well as the improvement of MSC isolation, expansion and analysis techniques. So far, up to 843 clinical trials involving the term "Mesenchymal stem cells" are referenced in the ClinicalTrials.gov database (U.S. National Library of Medicine, on May 22th, 2018), with more than half of them starting during the five last years. Most of MSC-based studies were elaborated in order to evaluate the biomedical potential for the treatment of neurological, bone and cartilage, and cardiovascular diseases (Fig. 1.10 (A)). MSC brought a novel approach to treat complex diseases, in which traditional medications present little clinical effect, like Graft Versus Host Diseases (GVHD), both Type I and Type II Diabetes, liver, kidney, lung and Crohn's diseases as significant examples.

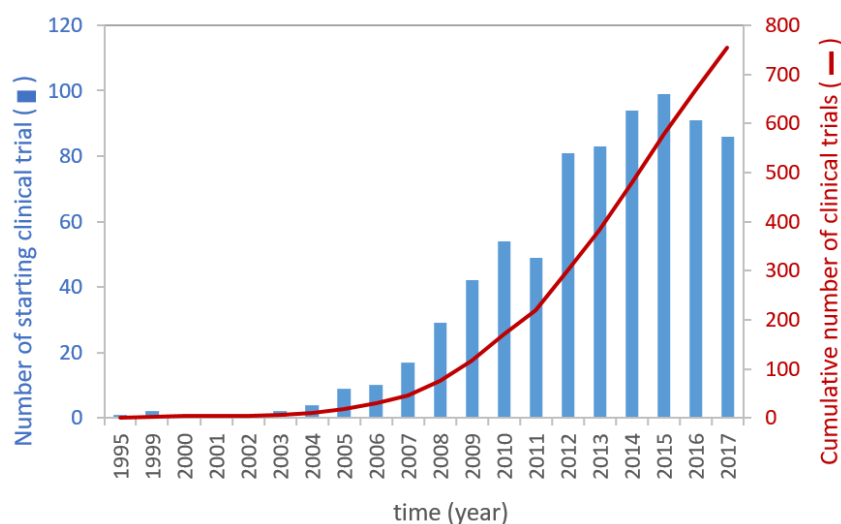


Figure 1.9: Evolution of the number of starting clinical studies based on MSC (www.clinicaltrials.gov, May 22<sup>nd</sup>, 2018).

Despite the high interest for MSC clinical applications, it should be remembered that long time is necessary to complete a clinical trial until the last phase. At the present time, only few studies are in Phase IV and the majority of them remains in phase I or Phase II (Fig. 1.10 (B)). By admitting that the entire drug development may take between 12 to 18 years from preclinical research to marketing, and may cost over \$1 billion [42, 43], more clinical studies are expected during next years.

In addition to the time, phase state and application distributions, MSC clinical studies may be considered across the world and according to country policies. As presented in

## 1.2. MESENCHYMAL STEM / STROMAL CELLS AND THEIR THERAPEUTIC BENEFITS

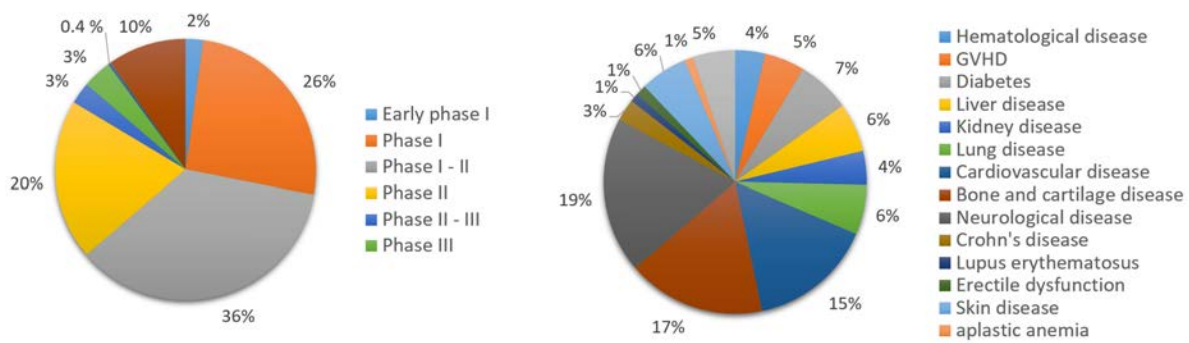


Figure 1.10: Clinical studies involving MSC distribution according to (A) the clinical phase and (B) the type of disease treated (www.clinicaltrials.gov, May 22<sup>nd</sup>, 2018).

Fig. 1.11, 3 main areas are standing out from the crowd: East Asia, the United-States and Europe with respectively 260, 166 and 161 clinical studies.

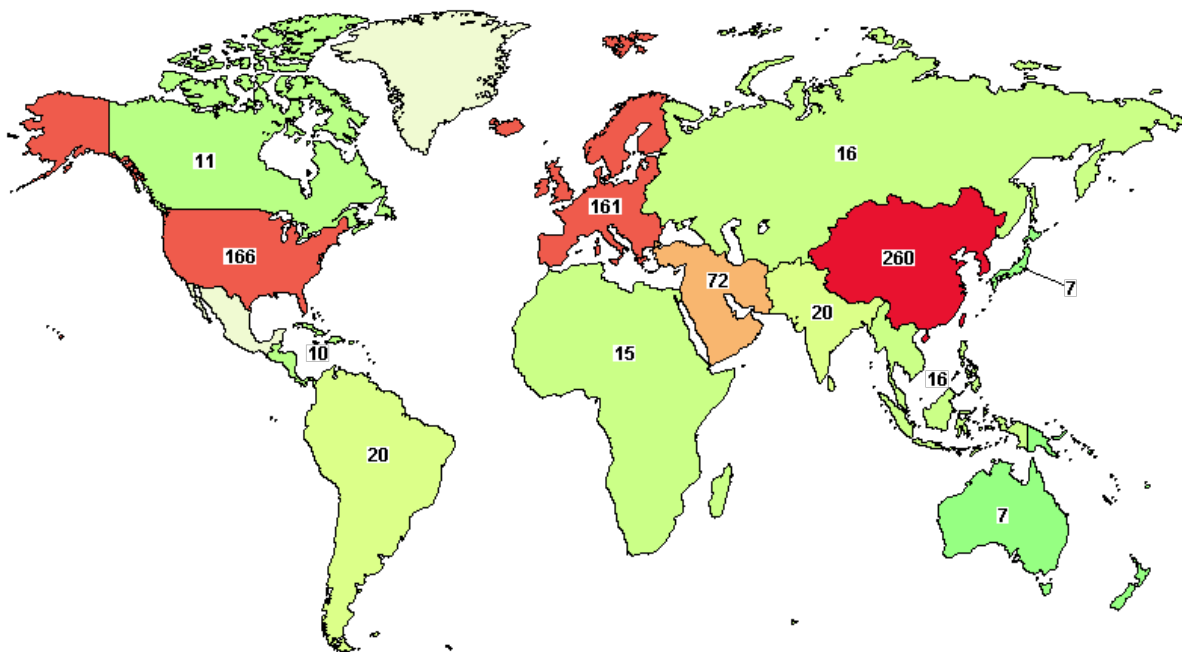


Figure 1.11: Clinical studies involving MSC distribution in the world (www.clinicaltrials.gov, May 22<sup>nd</sup>, 2018).

East Asia studies mainly take place in China (171 studies) and South Korea (70 studies). As presented in Table 1.1, almost 6 MSC-based therapeutics holding market authorization are carried on in Korea, including the Cartistem<sup>®</sup>, the first approved allogeneic MSC-based drug in the world in 2012. Very recently, China has clearly defined its position supporting global stem cell research. The first official policy in this way was announced in 2015 with the aim of regulation and supervision improvement [44]. Since then, China emerged as a major player in the stem cell research, including MSCs, over the last few years and is



expected to invest in the next years.

In north America, the Prochymal / TEMCELL<sup>®</sup> (Mesoblast Limited company, bought from Osiris Therapeutics) case study may be highlighted. This product is one of the first allogeneic MSC-therapeutics by getting the Canadian market authorization a few months after the Korean authorization for Cartistem<sup>®</sup> and was the first allogeneic cellular medicine to receive full approval in Japan [45].

In Europe, most studies are performed in Spain with 59 registered studies, followed by France with 26 studies. A Phase IV clinical study was however recorded in Italy, involving autologous bone marrow concentrate to treat bone marrow edema. This recent study is estimated to be completed in 2024. Still recently, the biopharmaceutical company TiGenix developed a single-dose allogeneic Adipose-derived stem cells product (Alofisel<sup>®</sup> / Cx601 (darvadstrocel)) to treat complex perianal fistulas in Crohn's disease. This product was validated in phase III through an international collaboration (ADMIRE-CD: Spain, Austria, Belgium, Germany, Italy, Netherlands, France, Israel) and is the first MSC-drug in the European market.

**The present decade thus shows the emergence of the first MSC-based therapeutics.** The spatial distribution of clinical studies shows the country policies with the definition of 3 hotspots, with increasing investments and thus increasing gap with the rest of the world.

### 1.2.3 Current limits

Today, MSC appears as a promising therapeutic product, but scientific and clinical studies remain relatively recent. Fast MSC therapeutic applications on the human body has to be carefully controlled and validation of the product safety and efficiency may be very expensive, explaining the limited number of studies reaching the market approval. MSC quality is particularly questioned after *ex vivo* expansion, often necessary to reach the high cell dose requirements between  $10^9$  and  $10^{12}$  cells / lot [1]. There are still controversies about MSC use and the potential risks associated, necessitating more clinical data, and a better cell behaviour understanding during the whole process of isolation, expansion and clinical delivery [46]. MSC *in vitro* expansion involves isolation, expansion and harvest. This whole culture process is expected to submit MSC to a different environment than the one encountered in the cell niche ; that may induce cell physiology modifications:

- Therapeutic potential may be reduced by loss of self-renewal and multipotency capacity [47].

Table 1.1: Current MSC-based products with marketing authorization.

Product name	Company	hMSC type	Transplant	Indication	Location (Marketing authorization)
Allostem <sup>®</sup>	AlloSource	hASCs	Allogeneic	Spine fusion, orthopaedic bone graft	U.S. (FDA, medical device)
Alofisel <sup>®</sup> (darvadstrocel)	TiGenix & Takeda Pharmaceutical	hASCs	Allogeneic	Perianal fistulas in Crohn's disease	European Union (EMA)
Cartistem <sup>®</sup>	Medipost	UCB-MSC	Allogeneic	Knee cartilage defects (osteoarthritis)	Korea (MFDS)
Graftx <sup>®</sup>	Osiris Therapeutics	hBM-MSC	Allogeneic	hard-to-treat acute & chronic wounds	U.S. (FDA, medical device)
OsteoCel <sup>®</sup>	NuVasive	hBM-MSC	Allogeneic	Spinal Bone Regeneration	U.S. (FDA, medical device)
OvationOS <sup>®</sup>	Osiris Therapeutics	hBM-MSC	Allogeneic	Bone regeneration	U.S. (FDA, medical device)
Prochymal / TEMCELL HS <sup>®</sup>	Mesoblast & JCR Pharmaceuticals	hBM-MSC	Allogeneic	GvHD	Canada, New Zealand (HC)
Stempeucel <sup>®</sup>	Stempeucis	hBM-MSC	Allogeneic	Critical limb ischemia due to Buerger's disease	Japan (PMDA) India (DCGI)
Trinity Evolution <sup>®</sup>	Orthofix	hBM-MSC	Allogeneic	Musculoskeletal defects	U.S. (FDA, medical device)
Trinity Elite <sup>®</sup>	Orthofix	hBM-MSC	Allogeneic	Musculoskeletal defects	U.S. (FDA, medical device)
Hearticellgram <sup>®</sup> -AMI	Pharmicell	hBM-MSC	Autologous	Acute myocardial infarction	Korea (MFDS)
Cupistem <sup>®</sup>	Anterogen	hASC	Autologous	Crohn's fistula	Korea (MFDS)
Neuronata-R	Corestem	hBM-MSC	Autologous	Lou Gehrig's Disease	Korea (MFDS)
QueenCell <sup>®</sup>	Anterogen	hASC	Autologous	Regeneration of subcutaneous adipose tissue	Korea (MFDS)
Ossron <sup>TM</sup>	RMS	hBM-MSC	Autologous	Bone regeneration	Korea (MFDS)

MFDS : Ministry of Food and Drug Safety (previously Korea Food and Drug Administration).

FDA : Food and Drug Administration.

EMA : European Medicines Agency.

HC : Health Canada.

PMDA : Pharmaceuticals, Medical Devices Agency.

DCGI : Drug Controller General of India.

- Rapidly dividing cells cultures may increase the risk of genetic and epigenetic mutation, leading to potential spontaneous transformations like tumours [48, 49], and a high number of population doubling may undergo senescence and genetic instability.
- Long-term *in vitro* expansion was found to alter MSC karyotype and gene expression, and notably cell apoptosis [50]. MSC lifetime is thus limited to a few number of passages or population doublings.
- Cell apoptosis may be generated by the biochemical / physical environment of cultures (hypoxia, low serum concentration, shear stress) [51, 52].

Risks of MSC carcinogenesis is still in debate according to clinical studies [53]. Some of them demonstrated the safety of *in vitro* MSC expansion with no malignant transformation with inhibition of tumour growth in some cases [54], whereas others reported that MSC promoted tumour growth or led to tumour formation [55, 56]. By concern of cell safety validation, a systematic study on the trials was proposed by Lalu *et al.*, but more information are necessary to understand the nature of the factors leading to a potential carcinogenesis, and how it operates [57].

#### Section summary

- MSC demonstrate promising applications in regenerative medicine, leading to a significant increase of research studies and clinical trials for the two last decades.
- However, the process to develop a drug from preclinical research to marketing is laborious (time-consuming and expensive), limiting the number of completed clinical trials. Majority of them are thus actually on phase I or II.
- 15 autologous or allogeneic MSC-based products obtained marketing authorization in different countries across the world.
- MSC quality has to be verified after *ex vivo* expansions, in particular after long-term cultures.

## 1.3 MSC sources and population heterogeneities

### 1.3.1 MSC niches in the human body and MSC functional differences

Historically, MSC were extracted from bone marrow, but cells from other adult and neonatal tissues appeared to also fulfil the ISCT *in vitro* criteria required for the MSC designation. This notably included sources as the bone-marrow [58], adipose-tissues [59], synovium [60], lung [61], muscles [62], umbilical-cord blood [63] or umbilical-cord matrix (Wharton's jelly) [64]. Regarding the wide range of sources, presented in Fig. 1.12, MSC tend to be considered ubiquitous. In the human body, MSC are stored in niches corresponding to a microenvironment, composed of extracellular matrix, chimiokines, cytokines, adhesion molecules and growth factors, under hypoxia (between 1 and 6 % of oxygen). This particular environment acts as a 'reservoir', maintaining MSC stemness. But, while MSC from all sources share common characteristics, they differ in some cases as for BM-MS, ASC and WJ-MS, that are listed in Table 1.2 [65, 66, 67, 68, 69, 70, 71].

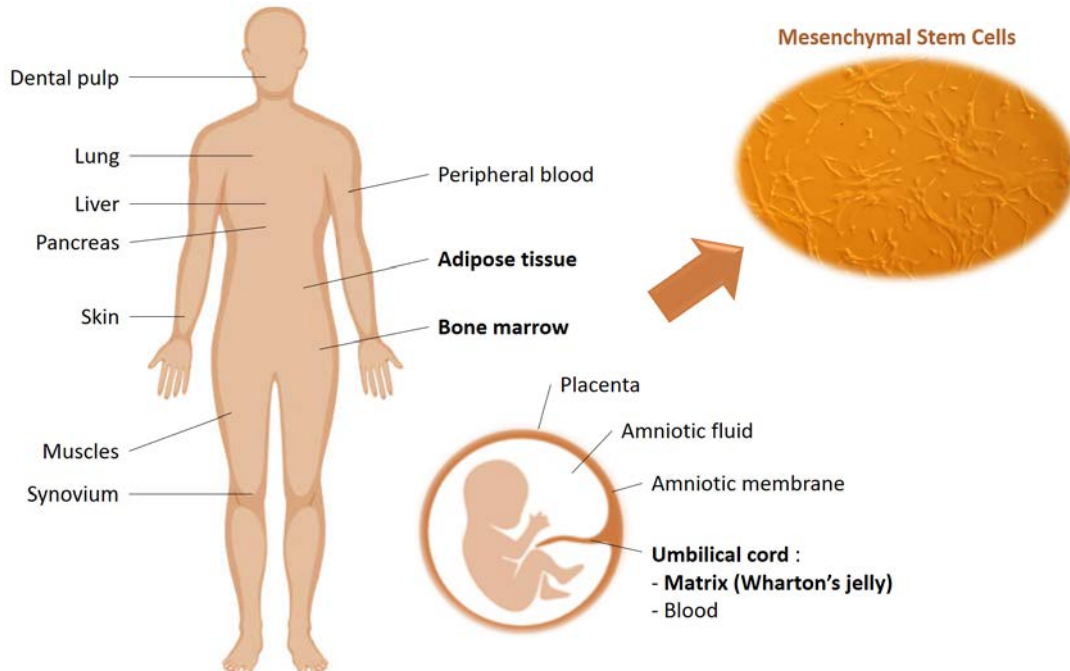


Figure 1.12: Body-map of MSC sources in the human body.

In addition to these functional differences due to the cell source, heterogeneity is also observed in MSC sub-populations. This heterogeneity involves different expression of

Table 1.2: Comparison of MSC from bone marrow, adipose-tissue and Wharton’s jelly of the umbilical cord according to their isolation ease, their proliferative capability and their differentiation potency.

	BM-MSC	ASC	WJ-MSC
Isolation method	Often recovered from the iliac crest of consenting patients treated for transplantation. This procedure is invasive and the number of cells harvested is strongly dependant on the donor age (between 500 to 50 000 cells per gram).	Mainly derived from fat tissues obtained from surgically resected material of liposuction. The procedure is less invasive than for BM-MSC and more cells are recovered, between 350 000 and $10^6$ cells per gram.	Isolation methods are non-invasive, but require clinics with storage and / or cell isolation capability. A high number of cells is recovered with around $85 \times 10^6$ cells per cm. The donor age is considered constant as the newborn one.
Proliferation	Mainly used in studies.	According to studies, proliferative potential is similar or higher to BM-MSC regarding the frequency of CFU-F (Colony Forming Units of Fibroblasts).	<ul style="list-style-type: none"> <li>- Faster doubling time and greater <i>in vitro</i> expansion.</li> <li>- Higher numbers of passages till senescence.</li> <li>- Higher frequency of CFU-F.</li> </ul>
Differentiation capacity	Mainly used in studies. Validation of differentiation into chondrocytes, osteoblasts and adipocytes. Acting as reference in this table.	Similar as BM-MSC, validation of differentiation into chondrocytes, osteoblasts and adipocytes	<ul style="list-style-type: none"> <li>- Slower differentiation into adipocytes.</li> <li>- Higher endothelial differential potential.</li> </ul>

regulatory proteins classes, and is supposed important for MSC therapeutic role. It was indeed suggested that isolation of the sub-populations may improve the treatment of specific diseases [72]. However this theory raises a question about cell nature of the *in vivo* precursor of MSC, which are then cultivated *in vitro*. MSC isolated from the human body could be only part of the MSC population in the niches [73].

### 1.3.2 Wharton’s Jelly as promising source of MSC

As shown in Table 1.2, the Wharton’s jelly, emerged as a reliable source of MSC. It corresponds to the matrix surrounding the vein and the two arteries in the umbilical cord, as presented in Fig. 1.13. It may be used as a regular source of cells, potentially unlimited. However, the umbilical cord must be treated within 48 hours after the newborn birth,

requiring equipments in the maternity hospitals. This criterion becomes important with the increasing needs of MSC for clinical trials and for a potential industrial implementation. Hence, regarding the number of cell recovered from the body, a great interest is paid to WJ-MSC in comparison to BM-MSC, but still mostly used. Moreover it was observed that extra-embryonic perinatal MSC (placenta, fetal membrane, umbilical cord, amniotic fluid) presented both adult MSC and embryonic stem cells properties. WJ-MSC notably present the following advantages in comparison with other adult MSC sources [74, 75, 67]:

- A lower doubling time (< 24 hours at first passages) leading to faster proliferation,
- A broader multipotent plasticity,
- A higher number of passages before senescence (> 10 passages expansion *ex vivo* in comparison to 6 passages expansion with other adult stem cells),
- A lower immunogenicity, notably with the HLA-G antigen expression (involved in avoidance of the maternal immune response against the fetus), making them very good candidates for allogeneic transplantations,
- No donor effect due to the donor age, considering the newborn age.

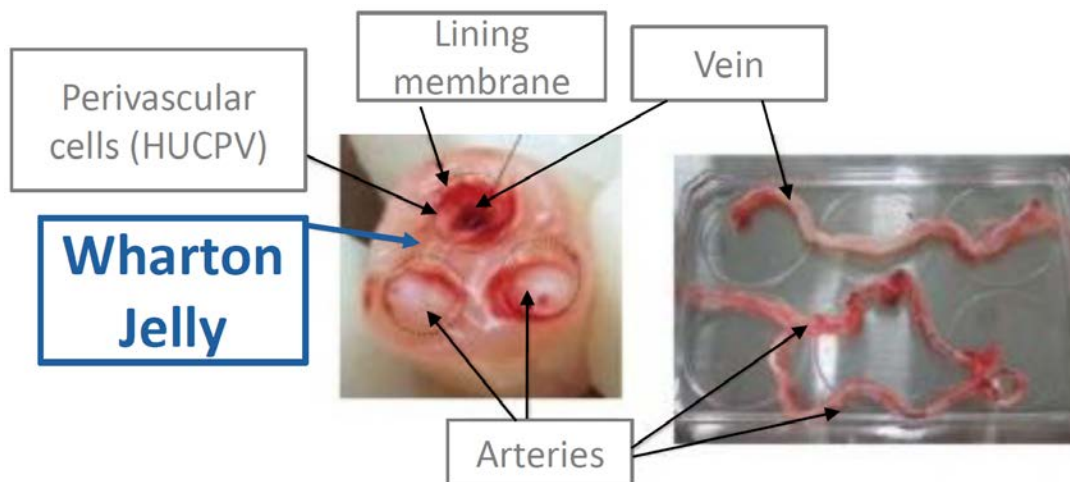


Figure 1.13: Transversal histological cut of a human umbilical cord. Figure reproduced from Nagamura-Inoue *et al.*, 2014 [74].

Although WJ-MSC seem to present more homogeneous populations than other adult sources, they still display heterogeneities. The perinatal environment was indeed found to affect fetus-derived MSC. For instance, WJ-MSC obtained from umbilical cord related to healthy and diabetic mothers were compared, expressed the same markers, but with different expression levels ; it was found that WJ-MSC from diabetic mothers displayed a higher adipocyte differentiation efficiency [76]. Differences may thus be observed between different umbilical cords, namely different donors.

## Section summary

- MSC are present in numerous zones in the human body, but the most currently used source is in the bone marrow, where it was originally discovered.
- Umbilical cord is considered as a suitable source substitute, with a non-invasive isolation method. Different studies demonstrated that a higher number of cells was recovered from the Wharton's jelly and that cells presented better proliferative and immunomodulatory properties. Moreover, low effect due to donor age is expected.

## 1.4 Expansion process challenges

Regarding the increasing demand of MSC for therapeutic applications from one side, and the poor number of cells recovered from the different available sources from the other side, expansion processes have to be scaled-up and intensified. For this purpose, two main challenges have to be overcome. First, cell harvested quantity may be enhanced by developing cultures in mixed bioreactors and by technological progress. In parallel, cell quality at the end of the process must be preserved, ensuring in one hand cell stemness and therapeutic properties [77, 2, 21], and on the other hand a high-quality and purity of the final product, remaining safe for patients.

Similarly to all bioprocesses aiming at therapeutic bioproducts production, MSC processes must be carefully designed. For this purpose, specific constraints have to be taken into account:

- MSC doubling time (about 24 h to more than 48 h according to cell source and cell passage) entails long cultures up to several weeks, requiring culture medium replacement.
- In contrast to the recombinant protein production process, MSC are the final product itself. Cell lysis must thus be avoided, as well as any phenotype modification.
- MSC are adherent-dependent cells. For large-scale productions, the total volume on the adherence surface ratio  $V_{tot} / S_{available}$  must be minimized to dispose of compact systems.

It should also be noticed that cultures of MSC aggregates suspension were previously validated, but this culture strategy is still in development and seems to be applied for only specific categories of MSC [78, 79].

### 1.4.1 Cell quality and safety requirements

For the purpose of a cell-based drug launching, the product and the entire process must be approved by the competent authorities, as the Food and Drug Administration (FDA) in the USA or the European Medicines Agency (EMA) in Europe. As presented in Fig. 1.14, all steps involved from cell isolation to drug administration must be carefully controlled. Within the framework of this thesis, only the upstream process part, and more specifically the cell expansion step, will be detailed. However, downstream process, as well as storage and delivery systems should be anticipated if possible in order to ensure the drug quality and distribution.

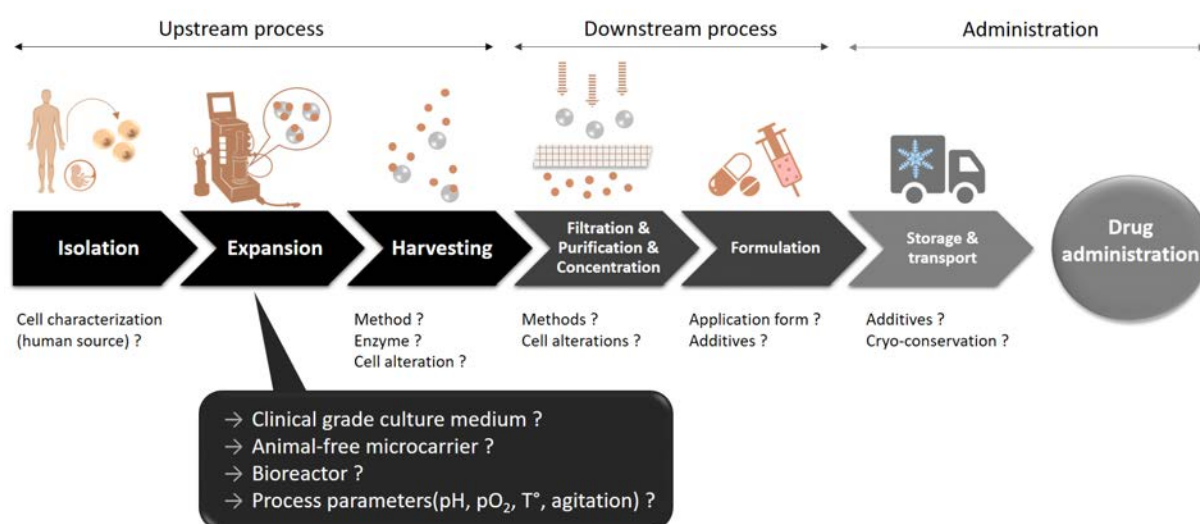


Figure 1.14: Global manufacturing process for adherent-dependent cell therapeutics with each step main challenges. Figure adapted from Schnitzler *et al.*, 2016, and Elseberg *et al.*, 2017 [80, 81].

#### Clinical grade culture medium

*In vitro* MSC cultures require growth media composed of a basal medium notably containing glucose, salts, amino acids and a buffer (e.g.,  $\alpha$ -MEM, DMEM), and generally supplemented with serum as a source of proteins, adhesion factors, vitamins, growth factors, hormones, fatty acids and lipids [82]. Although fetal bovine serum (FBS) is often used in research, it is generally non-compliant with the GMP guidelines, due to sanitary risks (virus and prion contaminations). Clinical grade FBS is produced in a few countries like New-Zealand, but its use in clinical applications is limited. In this way, effort were performed to dispose of reduced or serum-free culture media. Jayme and its colleagues classified culture media into 4 categories [83]:



- Reduced serum media: Serum use is reduced by nutrients and animal-derived factors addition.
- Serum-free media: Replacement of the serum by protein factors which do not require serum to support cellular function.
- Protein-free media: Formulation without polypeptide materials.
- Chemically-defined media: Formulation which may be protein-free and is composed of biochemically-defined low molecular weight components.

These different culture media were compared in Table 1.3 and demonstrated that the best safety confidence was obtained with the chemically-defined media, despite the need of more efforts in process and development.

Table 1.3: Characteristics of cell culture media. Table reproduced from Jayme *et al.*, 1999 [83].

Cell culture medium category	Reduced serum medium	Serum-free medium	Protein-free medium	Chemically-defined medium
Potential for introducing adventitious contaminants	+++	++	+	-
Complexity of downstream product purification	+++	++	+	+
Improved bioperformance (e.g. growth, product yield)	+/-	++	++	++
Ease of cell culture adaptation to novel formula	+++	+	+/-	+/-

(-): Negligible, (+/-): Slight, (+): Significant, (++) : Much greater, (+++) : Very much greater.

Today, the two main types of serum-free culture media are the chemically defined culture media or using human blood-derived alternatives, like human platelet lysate (hPL) [84, 85]. The use of hPL has been validated and led to higher expansion rates than with FBS, making it a good substitute at an affordable cost [86]. Rich in proteins and growth factors, no additional growth factor is required, in contrary to bFGF addition for FBS supplements. Nevertheless, heparin may be necessary to prevent gel formation, by reaction between the calcium of the basal medium and the fibrin of the hPL. Heparin at a concentration of 2 IU mL<sup>-1</sup> was found to prevent this coagulation without cell growth alteration, but higher concentration reduced cell growth [87]. Heparin use can be avoided by mechanical fibrin-depletion in the culture medium before use. This operation consists in successive thermal and mechanical shocks to force biogel formation. Then, this precipitate is removed and the medium is filtered [88, 89]. Although this clotting procedure limits the heparin addition, a supplementary preparation step of at least 18 hours is required to ensure process reliability.

### Bioreactor design for a more controlled environment

Cell environment must be carefully controlled to ensure cell growth and an efficient production. The various parameters requiring measurements and control are presented in Fig. 1.15 in a conventional closed stirred tank bioreactor. Analysis may be performed *off-line*, as generally performed for cell and substrates concentrations, or *on-line* with *in situ* probes or analysers integrated on a sampling loop, assuming homogeneity in the vessel. Based on these data, a distributed control system may be implemented to maintain the different parameters at fixed set-points. In the case of MSC cultures, the temperature is generally set at 37°C and the pH between 7.2 and 7.4. Concerning dissolved oxygen, either normoxia (21 % of oxygen) and hypoxia (between 1 and 6 % of oxygen) conditions may be found in the literature. Another advantage in the use of a control and monitored system is the recording of parameter variations occurring during the culture. It furnishes information to potential injuries to cells, and thus decreases the reaction time in case of a defective batch.

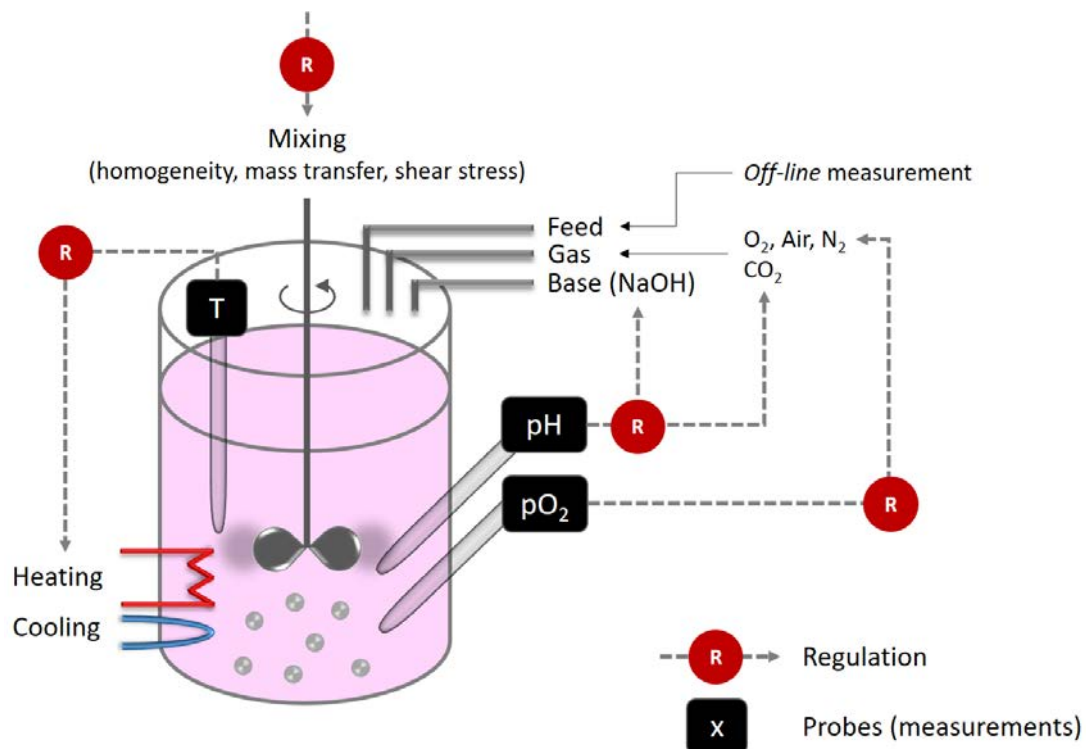


Figure 1.15: Basic configuration of a monitored and controlled bioreactor for MSC culture.

Bioreactors are also designed according to the feed strategy applied. In the case of MSC cultures on microcarriers, the following strategies were validated:

- **Batch** cultures involve no culture medium and / or microcarrier addition or removing during the whole culture time. Cultures are hence limited to a few days, generally related to a lack of nutrients and / or growth surface [90].
- **Fed-batch** cultures allow to start cell adhesion and expansion in a reduced culture medium volume. Fresh culture medium is then added to provide nutrients and to dilute metabolites produced by cells. Microcarriers supplement may also be performed, assuming cell bead-to-bead capability. Fed-batch cultures enable longer cultures than in batch systems, but are still limited by the total amount of supplemented culture medium [91].
- **Feed-harvest** strategy is currently used feeding system and consists in partial culture medium exchange. Agitation is stopped to allow microcarriers sedimentation and a certain amount of supernatant is removed. The same amount of fresh medium, with or without microcarriers, is finally added before agitation is restarted. In this case, parts of metabolites produced by cells are totally removed, allowing longer cultures than in fed-batch systems. However, cells and microcarriers remain in the vessel during the whole culture, limiting the total amount of microcarrier added. [92, 91, 93].
- **Continuous perfusion** systems require more efforts and specific technologies, but allow even longer cultures than with a feed / harvest feeding strategy. In this case, the culture is limited by cellular alterations, which may occur after a high number of population doublings. Two perfusion MSC cultures were already reported in the literature. First, Dos Santos *et al.* validated a perfusion system from day 3 to day 11 of cultures, using a feeding line and a removal line equipped with a stainless steel filter as cell retention device, allowing a flow rate of  $100 \text{ mL day}^{-1}$  for a working volume of 400 mL. A higher cell yield was obtained in this system in comparison to both fed-batch and feed / harvest cultures. However, no microcarrier addition was reported in this work[91]. In a second time, Cunha *et al.* proposed a strategy coupling a perfusion system with cell concentration and clearance for downstream processing. The ATF<sup>TM</sup> technology was used, which is based on alternating tangential flow created by a diaphragm moving upwards and downwards within a pump head and connected to a filter housing. The perfusion feeding strategy was automatically controlled by a gravimetric control system and allowed a flow rate of  $80 \text{ mL day}^{-1}$  starting from day 5 to day 14 of culture, for a working volume of 400 mL. Only one prompt microcarrier addition was performed on day 6 [93]. In these two studies, the perfusion system was used to overcome limitation of substrates, but was not focus on growth surface limitation.

## 1.4.2 Cell quantity enhancement

Various types of bioreactors were developed for industrial pharmaceutical applications. Following the classification of Eibl *et al.* for animal cell cultures, Jossen *et al.* proposed a MSC specific classification according to the energy transmission in the culture medium [94, 95]. Static planar systems were distinguished from dynamic systems, as presented in Fig. 1.16. The second category involves various bioreactors, which may be mechanically or hydraulically driven. The present state of art will focus on static planar systems and mechanically-driven dynamic cultures involving microcarriers. The dynamic cultures will be notably separated according to the use of internal or external devices for the agitation.

### Planar culture systems

Today, most cultures are still performed on planar surfaces in static mode, without any mechanical energy contribution. Hence, diffusive energy and mass transfer are mainly expected. Their main applications concern screening experiments and expansions for clinical trials. Using MSC capacity to adhere on plastic surfaces, single-use disposable systems made of plastic were found suitable and are currently widely used.

- **Mono-layer systems** are the simplest case to implement, such as Petri dishes, T-flasks and multi-well plates placed in incubators (Fig. 1.17 (A), (B) and (C)). Their low cost and ease of operation make them the mostly used system, despite limited available surface, and thus cell expansion. Moreover, these systems require operator interventions to replace the culture medium and to perform cell passages. At least, this type of reactors may quickly become bulky, and the operational costs may increase with related contamination risks.
- **Multi-layer planar flasks** like the Corning<sup>®</sup> CellSTACK<sup>®</sup> [96] or the Nunc<sup>TM</sup> Cell Factory<sup>TM</sup> (Thermo Scientific) [97] systems (Fig. 1.17 (D) and (E)), which are close to the previous case principle. In these systems, several parallel surfaces are placed in flasks in order to minimize the  $V_{tot} / S_{available}$  ratio. In this way, more growth surface is available, leading to a higher number of cell recovered, but most of limits of mono-layer systems remain. Moreover, cell detachment efficiency may be heterogeneous in a flask, leading to significant cell loss.
- **Closed multi-layer flasks** as Corning<sup>®</sup> HYPERFlask<sup>®</sup> systems [98] (Fig. 1.17 (F)) differ from the two previous designs by two characteristics. First, inoculation and culture medium replacement in a closed system reduce the contamination risks. Secondly, without headspace, the  $V_{tot} / S_{available}$  ratio is also reduced by using gas-permeable culture layers. However, this system may become cumbersome in incubators at larger scales and as for multi-layer planar systems, cell harvesting

may remain difficult.

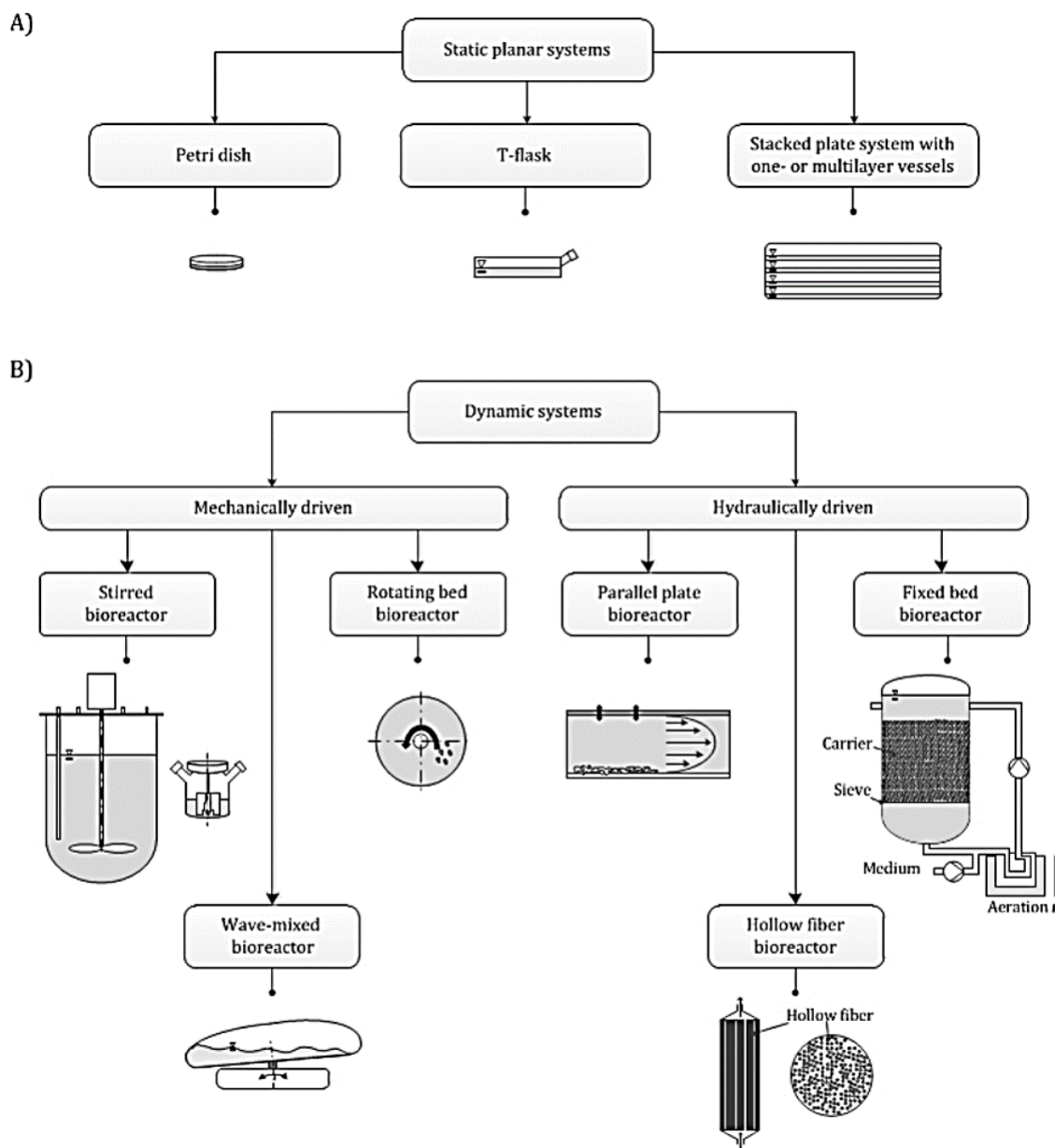


Figure 1.16: Suitable bioreactors for MSC expansion, classified according to the power input type. Figure reproduced from Jossen *et al.*, 2014 [95].

All these systems involve static cultures, but without fluid circulation, poor mass transfer would be expected, leading to potential pH, dissolved oxygen and substrate or metabolite concentration gradients [80].

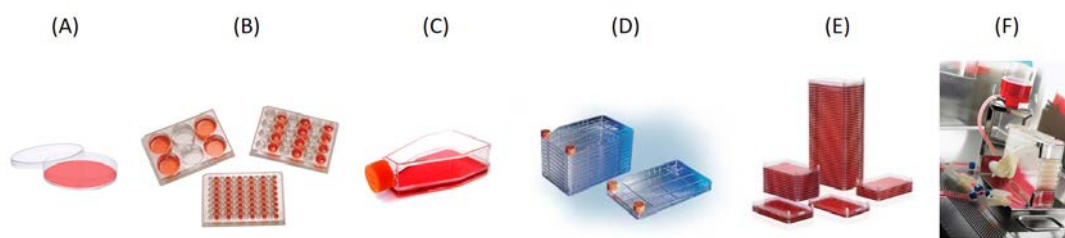


Figure 1.17: Planar bioreactors in static mode for MSC expansion: Petri dish (A), Multi-well plates (B), T-flask (C), Corning<sup>®</sup> CellSTACK<sup>®</sup> flasks (D), Nunc<sup>™</sup> Cell Factory<sup>™</sup> flasks (E) and HYPERFlask<sup>®</sup> systems (F).

### Dynamic systems for microcarrier mixing

To overcome the static cultures limits, culture may be transposed on microcarriers, consisting of spheres of about 200  $\mu\text{m}$  diameter with a density close to water one [99]. Once cells adhere on the surface of these particles, they are suspended in a bioreactor filled with the culture medium by a mechanical agitation. The addition of monitoring / control loops is made easier, in accordance with GMP specifications. Moreover, mixing allows a better culture homogenization, limiting  $\text{O}_2$ , pH and nutrients gradients, enhanced energy and mass transfer through convective transport, and available liquid-solid interface area maximization. It has been demonstrated that microcarriers led to a higher number of cells recovered by lot, despite they need more efforts and investments in R&D [100, 101]. Microcarrier-based cultures in stirred tank bioreactor will be presented in more details in section 1.5. Here, an outlook on the available culture systems is presented with the strengths and limits of each one.

#### *External agitation*

Mixing may be performed by vibrations or rotational movements directly applied on the bioreactor vessel. MSC cultures have been validated in three types of reactors belonging to this category. They are currently limited to small scales, but scale-up may be investigated by defining the proper limiting parameters.

- **Shaker culture systems** are based on an orbital agitation. Erlenmeyer flasks (Fig. 1.18 (A)) are commonly used for cell suspension in animal cell cultures. In the same manner, particles such as microcarriers may be suspended, generally at the just-suspended state. Despite the global field of mammalian cell cultures led to novel bioreactor developments such as disposable orbital shaken permitting culture from 50 mL to 1,000 L [102], MSC culture in such systems remains limited to only a few tens of millilitres. Microcarrier suspension would indeed require efforts to maintain cultures at gentle agitation rates, with the need to ensure reduced shear stress and avoid potential cell damages due to the hydromechanical stress generated.

BM-MSK cultures performed in a working volume of 20 mL in an Erlenmeyer flask was notably found to display a higher cell expansion after 7 days of culture (between 5-fold and 10-fold growth) than in Spinner flasks (< 5-fold growth). But UC-MSK cultures displayed similar expansions in the two systems [103].

- **Wave-mixing systems** involve disposable culture bag placed on a rocking platform (Fig. 1.18 (B)), promoting fluid wave-motion by one-dimensional oscillatory movements, enhancing gas transfer from surface aeration. This system was found to be suitable for shear-sensitive cells and scalable productions may be achieved with up to 100 L cultures. MSK cultures were validated in a 500 mL working volume with expansions of 15.7-fold and 16.3-fold over 7 days [104]. Another culture was performed in a 1500 mL working volume and displayed an expansion of 6.59-fold over 9 days, three times lower than the cell expansion obtained in a control spinner flask. However, the authors indicated that the attachment step performed in shake flasks was not optimized. Moreover, some cell-aggregates appeared after 3 days of culture [105].

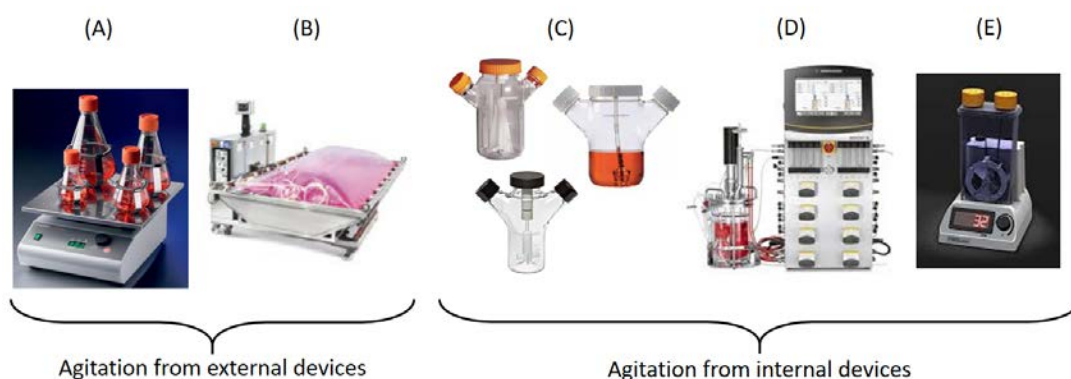


Figure 1.18: Bioreactors for MSC expansion on microcarriers in dynamic mode: Erlenmeyer flasks (A), Wave-mixing system (B), Spinner flasks (C), Stirred-tank bioreactor (D) and Vertical Wheel<sup>TM</sup> Pneumatic Bioreactor System (VW-PBS) (E).

### *Internal agitation*

The mixing device is placed in the vessel and generates fluid pumping and circulation movements. For the purpose of MSK cultures, the main issue is the production of shear stress, which must be controlled and minimized, but most of large scale cultures are performed in bioreactors from this category.

- **Stirred Tank (bio)Reactors (STR)** involve one or several impellers placed in the reactor vessel. According to the impeller shape and pumping mode, different

flow patterns may be generated. Until today, a lot of knowledges was indeed collected, presenting a relatively simple, scalable and well-documented development in mammalian cell cultures. Small-scale cultures may be performed in Spinner flasks (Fig. 1.18 (C)), placed in an incubator. For larger productions, STR in disposable bag or in glass vessel (Fig. 1.18 (D)) are necessary. They are often better controlled and monitored through probe implementation and regulation systems. Most of the current microcarrier-based cultures are performed in this type of reactor, and demonstrated up to a 43-fold growth after 11 days in a 50 L bioreactor [106].

- **Vertical Wheel<sup>TM</sup> Pneumatic Bioreactor System (VW-PBS)** (Fig. 1.18 (E)) were developed to promote fluid homogeneity with low shear stress. In these systems, displaying U-shaped bottom, a large wheel impeller is rotating around a vertical plane, lifting the fluid and suspended particles. It allow scalability with an available volume comprised between 50 mL and 500 L. MSC culture were validated from a 60 mL working volume, leading to a 3.4-fold growth after 4 days of culture [107], to a 2.2 L scale with a 12-fold growth obtained after 14 days of culture [108].

Microcarrier-based systems, both involving an internal or an external mechanical agitation, rarely exceed a few tens of liters. Deeper knowledge and development are indeed necessary to transpose the current technologies used for mammalian cells to the culture of MSC on suspended microcarriers. Scale-up of STR is indeed better controlled by specific parameters such as the mixing time, the impeller tip speed, the power input or the oxygen transfer performance. The current highest microcarrier-based cultures of 35 L [109] and 50 L [106] were both based on the minimal agitation rate ensuring all particle suspension  $N_{js}$ . Table 1.4 presents the comparison of the preceding dynamic systems according to their potential scalability.

Table 1.4: Volume comparison of different dynamic systems for MSC culture on microcarriers.

System	Min. volume	Max. volume	Highest current MSC culture volume achieved ( $V_{working}$ )	Scalable potential
Orbital shaken bioreactor	25 mL	1000 L	200 mL (present work)	++ ?
Wave-mixing	100 mL	100 L	1.5 L [105]	+
STR	15 mL	2500 L	50 L [106]	+++
VW-PBS	50 mL	500 L	2.2 L [108]	+



## Section summary

- Cell quality must be conformed to regulatory standards. This should be done by the use of a clinical grade culture medium, animal-free microcarriers, control and regulation of the environment (closed system, bio-physico-chemical parameters control).
- Cell quantity must be improved in order to reach the high cell dose requirements. Microcarriers furnish a lower  $V_{tot} / S_{available}$  ratio, making them good candidates for MSC culture intensification.
- Stirred-tank bioreactors are currently investigated to adress both quality and quantity challenges. Different process strategies were validated, including different feed strategies, static or dynamic modes and various culture system designs.

## 1.5 Microcarrier-based cultures

With scalable process prospective, MSC cultures on suspended microcarriers are considered as best choice for larger cell production. However, particle properties and interactions with the hydrodynamics must be intended to improve cell adhesion and expansion, to limit potential cell damages (cell death, detachment or differentiation) and to allow an efficient cell detachment. Cultures are generally performed at the just-suspended state, ensuring all particles suspension, to limit the hydromechanical stress generated. This section will first present microcarriers specific properties and cell adhesion mechanisms in order to introduce the agitation impact on cell growth. An outlook of the microcarrier-based MSC cultures and the current efforts will be then presented. Finally, just-suspended state relevancy and determination will be here developed in the case of stirred tank bioreactors.

### 1.5.1 Microcarrier characteristics

Microcarriers are spherical particles with a diameter comprised between 90 and 400  $\mu\text{m}$ . They were introduced in 1967 by Van Wezel as chromatography package [99], and since then are widely used for adherent-dependent cell cultures for vaccines or recombinant proteins production. Besides, many efforts were done to promote cell adhesion, leading to the commercialization of a wide variety of microcarriers, differing from their composition, potential coating, porosity, polarity and charge density. Properties of commercial microcarriers used for MSC cultures are enumerated in Table 1.5.

Table 1.5: Commercial microcarriers used for hMSC cultures (based on manufacturer data).

Product name	Manufacturer	Porosity	Material	Coating	Density (g/mL)	Diameter range $d_p$ ( $\mu\text{m}$ )
<b>Mammalian protein-coated microcarriers</b>						
Collagen	SoloHill	Non-porous	PS	Collagen	1.02	125 - 212
Cultispher-S <sup>®</sup>	Percell-Biolytica AB	Macroporous	Gelatin	None	1.02 - 1.04	130 - 380
Cultisphere-G <sup>®</sup>	Percell-Biolytica AB	Macroporous	Gelatin	None	1.02 - 1.04	130 - 380
Cytodex-3 <sup>™</sup>	GE Healthcare	Microporous	Dextran	Denatured collagen	1.04	141 - 211
FACT III	SoloHill	Non-porous	PS	Collagen	1.02 - 1.03	90 - 150
SphereCol <sup>®</sup>	Advanced BioMatrix	Non-porous	PS	Collagen	1.03	125 - 212
Denatured Collagen	Corning	Non-porous	PGA	Denatured collagen	1.01 - 1.03	200 - 300
<b>Dissolvable</b>						
<b>Recombinant protein-coated microcarriers</b>						
ProNectin <sup>®</sup> F	SoloHill	Non-porous	PS	Recombinant fibronectin	1.02	125 - 212
<b>Xeno-free microcarriers</b>						
Cytodex 1 <sup>™</sup>	GE Healthcare	Non-porous	Dextran	DEAE	1.03	147 - 248
Cytopore 1 <sup>™</sup>	GE Healthcare	Macroporous	Cellulose	DEAE	1.1	200 - 280
Cytopore 2 <sup>™</sup>	GE Healthcare	Macroporous	Cellulose	DEAE	1.1	200 - 280
Enhanced Attachment	Corning	Non-porous	PS	CellBIND	1.02	125 - 212
Glass	SoloHill	Non-porous	PS	High silica glass	1.02	125 - 212
Hillex <sup>®</sup> II	SoloHill	Non-porous	PS	Cationic amine	1.1 - 1.2	160 - 200
Hillex <sup>®</sup> CT	SoloHill	Non-porous	PS	Cationic amine	1.1 - 1.2	160 - 200
Plastic	SoloHill	Non-porous	PS	None	1.02	125 - 212
Plastic-Plus	SoloHill	Non-porous	PS	None	1.02	125 - 212
Star-Plus	SoloHill	Non-porous	PS	None	1.02	125 - 212
Synthemax II <sup>®</sup>	Corning	Non-porous	PS	Synthemax II	1.03	125 - 212
Synthemax II <sup>®</sup>	Corning	Non-porous	PS	Synthemax II	1.03	125 - 212
Dissolvable	Corning	Non-porous	PGA	Synthemax II	1.01 - 1.03	200 - 300
<b>PS: Polystyrene</b>						
<b>PGA: Polycalacturonic acid polymer chains cross-linked wia calcium ions</b>						
<b>DEAE: N,N'-diethylaminoethyl groups</b>						

## 1.5.2 Cell - microcarrier interactions

As presented in Fig. 1.19, MSC life cycle may be divided in three steps: (i) cell attachment, (ii) cell growth and (iii) cell detachment. Each phase involves different environments and constraints depending on culture strategies (static planar or suspended microcarrier-based cultures). The agitation has notably a significant impact on cell attachments and / or detachment during the culture (this will be discussed in more detail in section 1.6).

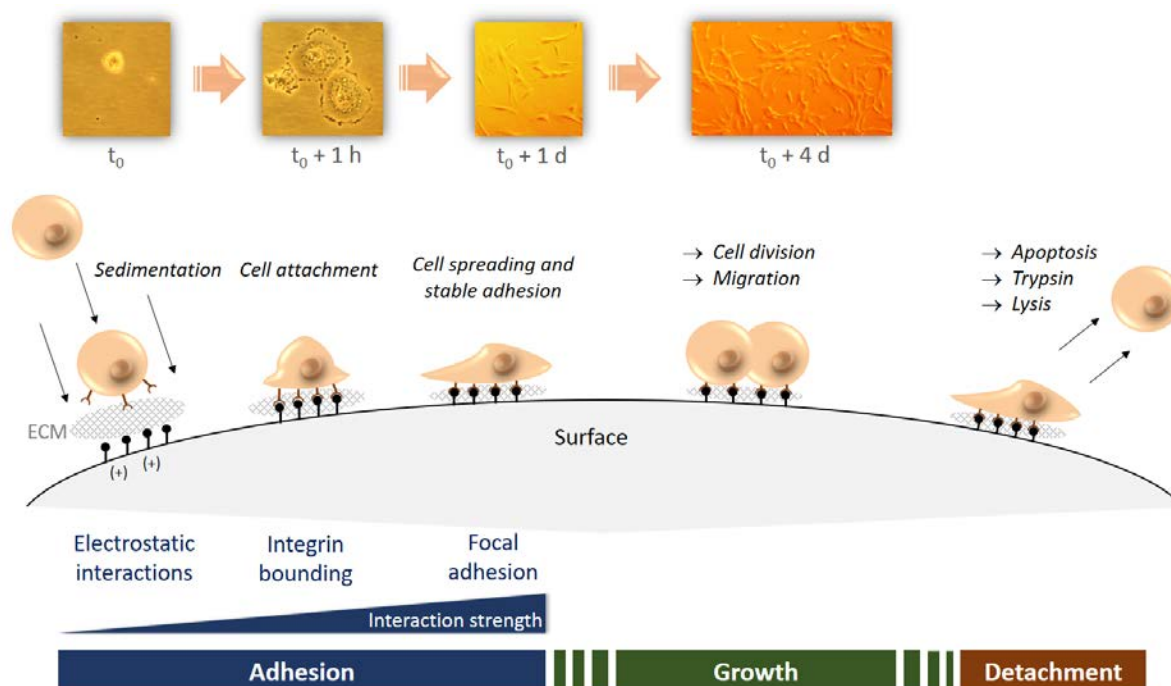


Figure 1.19: Cell adhesion force evolution during during life cycle, from cell attachment to cell detachment. Photos from a WJ-MS-C culture in T-flask.

### First phase: Cell adhesion

In suspension, MSC morphology is spherical. Due to gravity, cell sedimentation will allow contacts between cells and the solid substrate [110]. In the case of MSC cultures, the substrate is often made of plastic with potential specific charge and hydrophobic properties. Cells will thus attach to the solid surface through electrostatic and ionic forces between cell surface receptors named integrin and the growth surface charges. Then, integrin bounding between cell body and the surface leads to cell morphology change. Cell flattening and spreading is starting before focal adhesion formation and organization of the actin skeleton to stabilize the cell adhesion [111, 112]. Moreover, serum used in the culture medium contains many proteins, such as fibronectin and collagen, promoting the attachment.

According to cell source, donor age, cell passage and interactions with the substrate, the attachment step may require from 1 hour to 1 day. So, cells must have sufficient time to pass from electrostatic forces, easy to break, to stronger interactions of the integrin bounding. In static cultures, the environment is conducive to this whole mechanism. However, attention has to be paid in dynamic cultures, especially concerning fluid shear stress, which may break cells-substrate interactions. In this way, MSC cultures on microcarriers may involve, in the first hours of the culture, no agitation [109, 113], a gentle continuous agitation [114, 106], or a gentle discontinuous agitation [84, 115]. Once focal adhesion is established and cell adhesion is stable, cell will stay attached for several days. Focal adhesion point mechanism allows cell to migrate according to the environmental signalling. Cell movement is performed according to the following steps: (i) Cell cytoskeleton organization leads to a protusion, (ii) a new adhesion point is established between the protusion and the substrate, (iii) cytoskeleton organization and contractile forces pull the cell forward, (iv) the focal adhesion point opposite to the new one is disassembled leading to cell retraction [116].

### **Second phase: Cell growth**

Adhesion forces decrease during cell division [117, 118]. During this mechanism, cells stop moving and reduce their adhesion to the substrate. Still attached, cell rounding is observed before the division. Once the membrane separation between the cell and the daughter cell is finished, cell returns to a spreading morphology. Cell migration from a microcarrier to another is called *bead-to-bead*. This phenomenon has been validated for BM-MSC on different microcarriers [119].

### **Third phase: Cell detachment**

At the end of the cell life, cell membrane is no more able to maintain sufficient tension at the focal adhesion, leading to the cell detachment [120]. During cell cultures, induced detachments are performed before cell confluence, avoiding a total surface colonization and contact inhibition. This procedure is used to transfer cells on new surfaces or for the final harvesting. Different enzymatic and non-enzymatic detachment methods are available. Enzymatic digestion involves solutions like Trypsin, Accutase or TrypLE (animal-free recombinant enzyme), and are based on the cleaving of membrane proteins responsible of the cell adhesion. This procedure nevertheless affects cell viability and cell surface markers [121]. Cell contact with Trypsin must thus last no more than a few minutes, directly followed by an addition of protein excess, leading to both enzyme inhibition and dilution. In contrast, non-enzymatic methods may involve cell scrapping, as well as cell dissociation buffer (CDB) or EDTA. These two solutions contain chelating agents acting on calcium

and magnesium bonds used by cells for the adhesion [122]. All these detachment methods were compared and showed that enzymatic digestions, especially with TrypLE, were found more suitable than non-enzymatic methods. EDTA and scraping methods led to a lower cell viability and damaged morphologies, while CDB-detached cells presented lower immunosuppressive and multi-lineage differentiation capabilities [121].

Although enzymatic digestions present a better viability and stem properties, alteration of the surface markers involved in cell migration are observed. Recently, other animal cell detachment methods based on the substrate instead of the cell directly are investigated, using temperature-responsive materials [123, 124] or biodegradable vectors [125]. They were particularly studied for the need to avoid cell damages during the process, and to overcome the MSC detachment difficulty. Most of microcarriers were indeed developed to promote cell adhesion with no constraints on cell detachment, the targeted product often being released in the culture medium or from cell lysis.

### 1.5.3 MSC culture on microcarriers: an outlook

During the last decade, MSC cultures on microcarriers have been validated in a variety of reactor geometries, and at different scales. Representative examples are given in Table 1.6. MSC culture improvement passed through the optimization of different operating conditions, including the type of microcarrier, the culture medium or the bioreactor design. The feeding strategy was already addressed in section 1.4.1, with the use of a feed / harvest strategy to prevent metabolites concentrations limitation. The emergence of continuous perfusion systems was also reported as promising for longer cultures in a closed system.

#### Microcarrier type

Most of microcarrier comparisons are performed in static mode, but it is assumed that cell growth in static cultures on microcarrier is not necessarily correlated to growth in stirred systems and that early cell attachment and spreading on microcarriers do not necessarily predict efficiency of the cell expansion in agitated microcarrier culture [103]. Rafiq *et al.* recently presented the lack of robust and transferable methodology for microcarrier selection [113]. The poor number of studies explaining the reason of the use of a given microcarrier was deplored. Hence, Rafiq and its colleagues proposed a systematic microcarrier screening, involving 13 microcarriers under both static and dynamic conditions for BM-MSC culture. Comparison results are reproduced in Fig. 1.20. Micro-well screening was found sufficient by mean of high-throughput (multiple microcarrier comparison and long time cultures), but comparison in agitated bioreactor was still recommended for the definitive choice. In this study, higher viable cell numbers were obtained with Collagen,

Table 1.6: Overview of the MSC cultures performed on microcarriers.

Reactor	MSC source	Microcarrier	Working volume (mL)	Culture duration (day)	<i>in-line</i> monitoring	Reference
<b>Serum containing culture medium</b>						
STR	BM-MSC	Plastic P102-L	15	8	Yes	Rafiq <i>et al.</i> (2017) [126]
Spinner	BM-MSC	Home made	25	4	No	Leber <i>et al.</i> (2015) [119]
Spinner	BM-hMSC	Cytodex-3	30	5	No	Yang <i>et al.</i> (2010) [127]
Spinner	BM-hMSC	pNIPAAm-grafted Cytodex-3	30	5	No	Yang <i>et al.</i> (2010) [127]
Spinner	BM-pMSC	Cytodex-1	40	28	No	Frauentenschuh <i>et al.</i> (2007) [128]
Spinner	BM-hMSC	Cytodex-3	50	10	No	Caruso <i>et al.</i> (2014) [129]
Spinner	BM-hMSC	CultiSpher-G	50	6	No	Sum <i>et al.</i> (2010) [130]
PBS-VW	BM-MSC	PNIPAM	60	4	No	Yuan <i>et al.</i> (2018) [107]
Spinner	ASC	Cultispher-S	80	9	No	Dos Santos <i>et al.</i> (2011) [84]
Spinner	BM-hMSC	Cytodex-1	50 - 100	15	No	Schop <i>et al.</i> (2008) [114]
Spinner	Placental hMSC	Cytodex-3	80 to 100	13	No	Hewitt <i>et al.</i> (2011) [3]
Spinner	BM-MSC	PNIPAM	100	4	No	Yuan <i>et al.</i> (2017) [107]
Spinner	ASC	Hillex II	100	6	No	Kaiser <i>et al.</i> (2013) [131]
Spinner	ASC	ProNectin F	100	6	No	Kaiser <i>et al.</i> (2013) [131]
Spinner	BM-MSC	Plastic P102-L	100	8	No	Rafiq <i>et al.</i> (2017) [126]
Spinner	Amniotic membrane hMSC	CultiSpher-S	100	8	No	Chen <i>et al.</i> (2011) [132]
Spinner	fetal BM-hMSC	Cytodex-3	100	7	No	Chen <i>et al.</i> (2015) [133]
Spinner	fetal BM-hMSC	Cytodex-1	100	12	No	Goh <i>et al.</i> (2013) [134]
Spinner	fetal BM-hMSC	Cytodex-3	100	12	No	Goh <i>et al.</i> (2013) [134]
Spinner	fetal BM-hMSC	Cultispher GL	100	12	No	Goh <i>et al.</i> (2013) [134]

Reactor	MSC source	Microcarrier	Working volume (mL)	Culture duration (day)	<i>in-line</i> monitoring	Reference
Spinner	Fetal BM-hMSC	HyQSpheres P102-L	100	12	No	Goh <i>et al.</i> (2013) [134]
Spinner	BM-hMSC	Plastic P-102L	100	12	No	Rafiq <i>et al.</i> (2013) [135]
Spinner	BM-hMSC	Plastic P-102L	100	6	No	Heathman <i>et al.</i> (2016) [136]
Spinner	BM-hMSC	Cultispher-S	125	6	No	Yuan <i>et al.</i> (2014) [137]
Spinner	BM-MSC	Cytodex-1	200	12	No	Ferrari <i>et al.</i> (2012) [138]
Wave	Placental hMSC	Cultispher-S	500	7	Yes	Timmins <i>et al.</i> (2012) [104]
STR	fetal BM-hMSC	Cytodex-3	800	7	Yes	Shekaran <i>et al.</i> (2015) [133]
Spinner	Rat ear MSC	Cultispher-S	1,000	4	No	Sart <i>et al.</i> (2009) [139]
STR	fetal BM-hMSC	Cytodex-3	1,000	8	Yes	Goh <i>et al.</i> (2013) [134]
STR	UC-hMSC	Cytodex-1	1,500	10	Yes	Hupfeld <i>et al.</i> (2014) [140]
STR	AM-MSC	Cytodex-1	1,500	10	Yes	Hupfeld <i>et al.</i> (2014) [140]
Wave	hASC	Polystyrene	1,500	9	Yes	Jossen <i>et al.</i> (2016) [105]
STR	ASC	ProNectin F	2,000	7	Yes	Schirmaier <i>et al.</i> (2014) [109]
STR	BM-MSC	Collagen	2,400	13	Yes	Lawson <i>et al.</i> (2017) [106]
STR	BM-hMSC	Plastic P-102L	2,500	12	Yes	Rafiq <i>et al.</i> (2013) [135]
STR	ASC	Plastic collagen-coated	3,000	19	Yes	Siddiquee & Sha (2015) [141]
STR	ASC	ProNectin F	35,000	8	Yes	Schirmaier <i>et al.</i> (2014) [109]
STR	BM-MSC	Collagen	50,000	11	Yes	Lawson <i>et al.</i> (2017) [106]
Spinner	BM-hMSC	CultiSpher-S	NA	9	No	Eibes <i>et al.</i> (2010) [92]
STR	Placental hMSC	Cytodex-3	NA	6	<i>off-line</i>	Yu <i>et al.</i> (2009) [142]
Spinner	ASC	Alginate (porous)	NA	14	No	Turner <i>et al.</i> (2012) [143]
Spinner	WJ-hMSC	Cultispher-G	NA	16	No	Zhao <i>et al.</i> (2015) [144]

Reactor	MSC source	Microcarrier	Working volume (mL)	Culture duration (day)	<i>in-line</i> monitoring	Reference
<b>human platelet lysate or human serum containing culture medium</b>						
Spinner	ASC	Enhanced Attachment	70 - 100	7	No	Gadelorge <i>et al.</i> (2018) [145]
Spinner	ASC	Synthemax II	70 - 100	7	No	Gadelorge <i>et al.</i> (2018) [145]
Spinner	ASC	Plastic Plus	70 - 100	7	No	Gadelorge <i>et al.</i> (2018) [145]
Spinner	WJ-MSC	Plastic Plus	100	7	No	Petry <i>et al.</i> (2016) [146]
Spinner	WJ-MSC	Plastic	100	6	No	De Soure <i>et al.</i> (2017) [115]
STR	WJ-MSC	Plastic P-102L	800	8	Yes	Tozetti <i>et al.</i> (2017) [98]
STR	ASC	Enhanced Attachment	800	8	Yes	Gadelorge <i>et al.</i> (2018) [145]
STR	ASC	Enhanced Attachment	2,000	12	Yes	Gadelorge <i>et al.</i> (2018) [145]
STR	BM-MSC	Collagen	2,400	13	Yes	Lawson <i>et al.</i> (2017) [106]
STR	BM-MSC	Collagen	50,000	11	Yes	Lawson <i>et al.</i> (2017) [106]



Reactor	MSC source	Microcarrier	Working volume (mL)	Culture duration (day)	<i>in-line</i> monitoring	Reference
<b>Chemically-defined culture medium</b>						
STR	BM-MSC	Plastic P-102L	15	8	Yes	Rafiq <i>et al.</i> (2017) [126]
Erlen	BM-MSC	Cytodex-1	20	7	No	Tan <i>et al.</i> (2015) [103]
Spinner	BM-MSC	Cytodex-1	20	7	No	Tan <i>et al.</i> (2015) [103]
Erlen	UC-MSC	Cytodex-1	20	7	No	Tan <i>et al.</i> (2015) [103]
Spinner	UC-MSC	Cytodex-1	20	7	No	Tan <i>et al.</i> (2015) [103]
Spinner	BM-hMSC	Synthemax II	35	42	No	Hervy <i>et al.</i> (2014) [147]
Spinner	BM-hMSC	Cultispher-S	80	9	No	Dos Santos <i>et al.</i> (2011) [84]
Spinner	WJ-hMSC	Cultispher-S	80	6	No	Mizukami <i>et al.</i> (2011) [148]
Spinner	ASC	Cultispher-S	80	9	No	Dos Santos <i>et al.</i> (2011) [84]
Spinner	BM-hMSC	Synthemax II	80	8	No	Carmelo <i>et al.</i> (2015) [149]
Spinner	BM-hMSC	Enhanced attachment	80	8	No	Carmelo <i>et al.</i> (2015) [149]
Spinner	BM-hMSC	Plastic	80	8	No	Carmelo <i>et al.</i> (2015) [149]
Spinner	ASC	Plastic	80	8	No	Carmelo <i>et al.</i> (2015) [149]
Spinner	BM-MSC	Plastic P-102L	100	8	No	Rafiq <i>et al.</i> (2017) [126]
Spinner & STR	BM-hMSC	Plastic	100 & 800	4 + 7	Yes	Dos Santos <i>et al.</i> (2014) [91]
Spinner & STR	ASC	Plastic	100 & 800	4 + 7	Yes	Dos Santos <i>et al.</i> (2014) [91]
STR	BM-MSC	Plastic P-102L	100	6	Yes	Heathman <i>et al.</i> (2018) [150]
Spinner	BM-hMSC	Synthemax II	120	9	No	Cunha <i>et al.</i> (2017) [151]
Spinner	ASC	Synthemax II	120	7	No	Cunha <i>et al.</i> (2017) [151]
STR	BM-MSC	Synthemax II	250	14	Yes	Sousa <i>et al.</i> (2015) [108]
STR	BM-hMSC	Synthemax II	400	14	Yes	Cunha <i>et al.</i> (2017) [151]
STR	WJ-hMSC	Cultispher-S	800	6	Yes	Mizukami <i>et al.</i> (2011) [148]
STR	BM-hMSC	Synthemax II	1,000	7	Yes	Cunha <i>et al.</i> (2017) [151]
STR	ASC	Synthemax II	1,000	7	Yes	Cunha <i>et al.</i> (2017) [151]
PBS-VW	BM-MSC	Synthemax II	2,200	14	Yes	Sousa <i>et al.</i> (2015) [108]

Plastic and ProNectin F microcarriers. Some variations were found to be dependent on cell donor, but identical results were obtained for the three donors, leading the authors to suggest that a process would not need to be revalidated with a new microcarrier if a donor cell bank was exhausted. However, only bone marrow derived MSC were here compared, using one agitation condition (Spinner flask), and with the same culture medium (FBS supplement). Microcarriers found optimal may be different with other culture conditions.

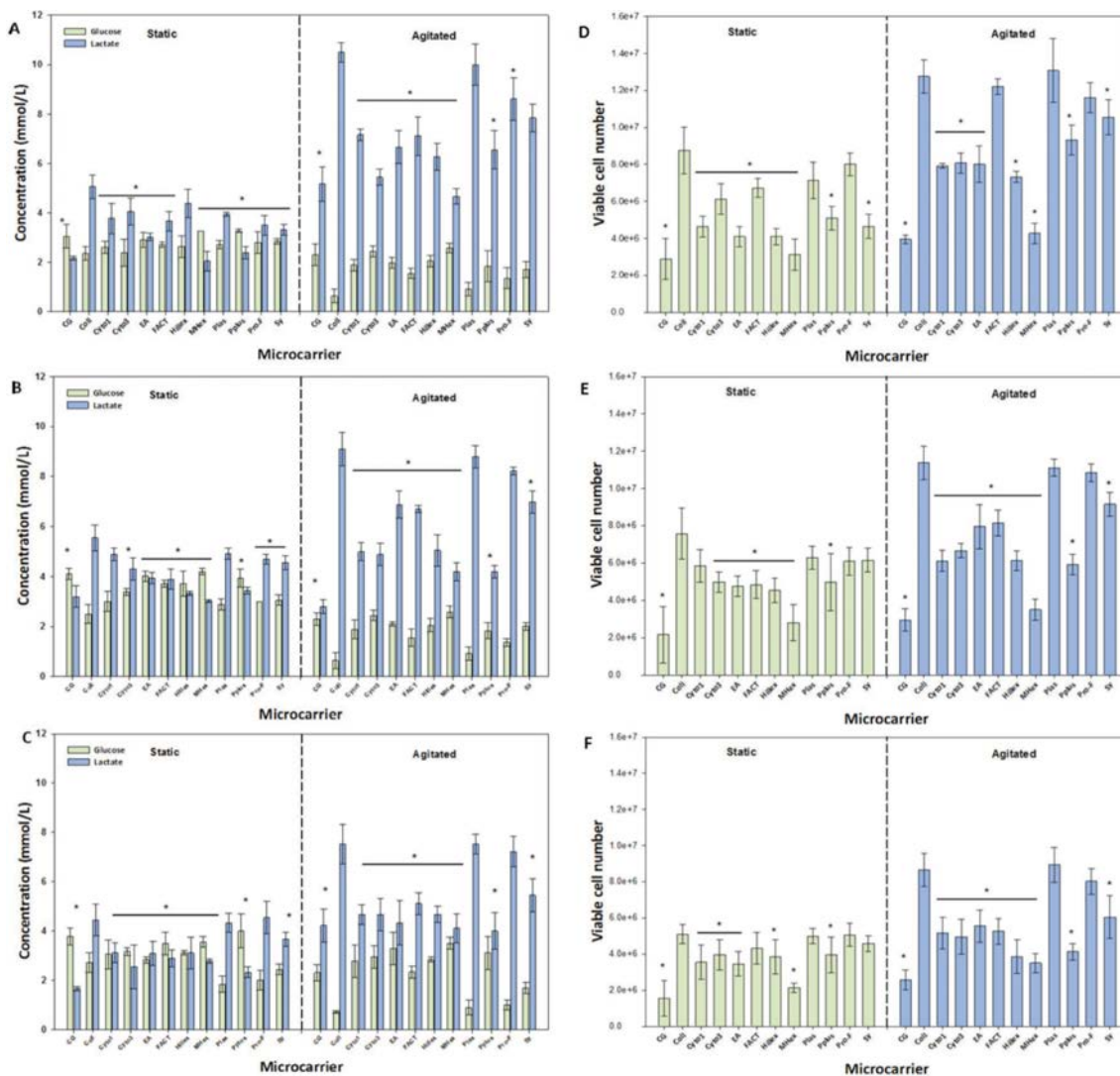


Figure 1.20: Comparison of static and agitated conditions for microcarrier-based culture using hBM-MSC from 3 different donors, and a comparison of different microcarriers in 100 mL spinner flasks. Glucose consumption and lactate production for hBM-MSC1 (A), hBM-MSC2 (B) and hBM-MSC3 (C). Viable cell number for hBM-MSC1 (D), hBM-MSC2 (E) and hBM-MSC3 (F). Data is presented as mean  $\pm$  standard deviation (SD) ( $n = 4$ ). Significant differences in values were noted with  $p$ -value < 0.05 (\*) in comparison to the highest respective value. Figure reproduced from Rafiq *et al.*, 2016 [113].

## Culture medium

As described in section 1.4.1, different culture medium were formulated for MSC cultures. New culture medium developments were motivated by the need of clinical-grade media. One way was the use of hPL. FBS and FGF2 replacement by hPL led to higher cell growth rate, as demonstrated by Azouna *et al.* [86]. Figure 1.21 showed that 5 % hPL was found sufficient to replace 10 % FBS. A population doubling time of  $5.8 \pm 1.03$  days was obtained with 5 % hPL. HPL concentration increase led to an even lower population doubling time, with  $3.8 \pm 0.7$  days for 10 % hPL, but a compromise had to be found between this time gain and hPL use. Most current hPL-based cultures use a 5 % hPL concentration [115, 106, 145].

Another way was the use of chemically-defined culture media. Gottipamula *et al.* reviewed culture characteristics of commercially available serum-free media [152]. It was notably indicated that these media supported higher cell growth rates and presented the advantage to allow modifications for target-specific MSC culture applications. As examples, MesenCult<sup>TM</sup> (Stem Cell Technologies), MesenGro<sup>®</sup> (StemRD) and StemPro<sup>®</sup> MSC SFM (Gibco) were presented as growth-promoting media, ensuring better cell quality (phenotype, specific surface marker expression, gene expression profiles, colony forming unit fibroblasts CFU-F and tri-lineage differentiation), in comparison to FBS-based culture media. Hervy *et al.* compared Mensencult and StemGro media for BM-MSK cultures in spinner flasks. StemGro medium demonstrated a higher fold expansion than with Mesencult-XF medium, with respectively population doubling times of  $2.3 \pm 0.4$  and  $3.6 \mp 0.4$  per passage. However, Tan *et al.* compared the impact of commercial serum-free media in both monolayer and microcarrier-based cultures [103]. It was shown that cell growth in monolayer culture did not furnish equivalent growth in static microcarrier cultures, making the culture medium formulation and the microcarrier surface composition co-dependent for cell growth improvement. It was hence suggested that the culture medium should be optimized in static microcarrier cultures before a definitive validation with agitation.

## Bioreactor scale-up

Using larger stirred tank bioreactors allow probes implementation and thus control and monitoring of physical parameters (pH, dissolved oxygen, temperature), in accordance with a more robust expansion process and GMP guidelines. These stirred-tank bioreactors involve nevertheless some factors influencing the hydrodynamic forces summarized in Fig. 1.22 [80]. With the aim of expansion process intensification, these parameters must be considered together for process design. A promising large scale expansion was conducted

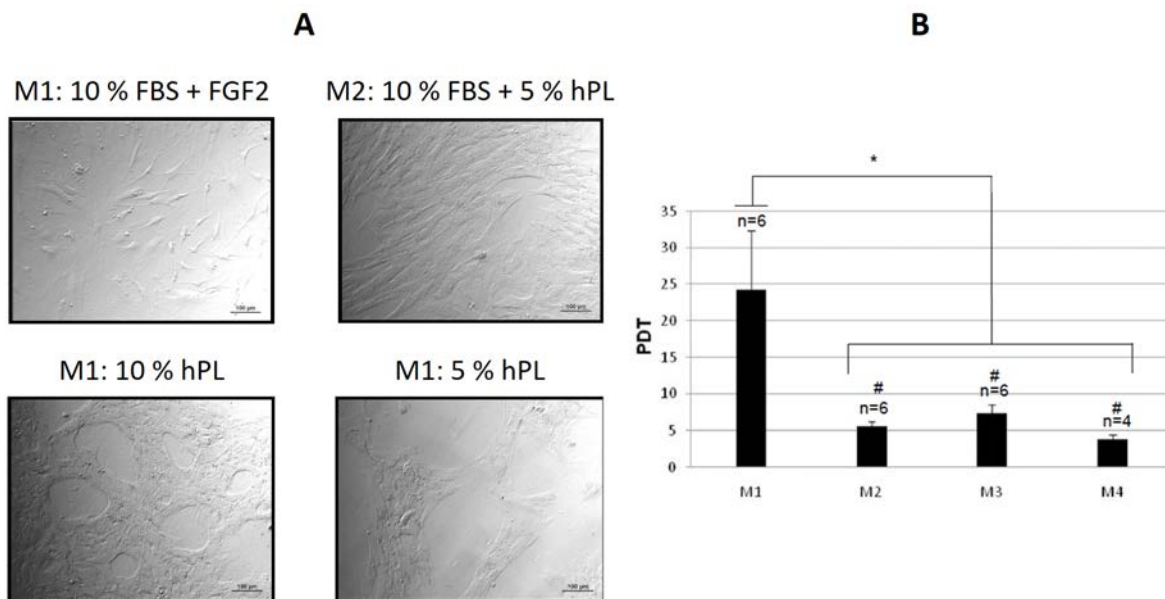


Figure 1.21: Morphological characterization of BM-MSC cultured in different media (representative results from 13 experiments are shown) (A) and Population doubling time (PDT) of adherent cells cultures in different expansion media between passage 1 and passage 2 (B). Figure reproduced from Azouna *et al.*, 2012 [86].

in 2017 in a 50 L pilot, as reported by Lawson *et al.* [106]. This work was based on a scale-down model performed in the 3 L Mobius STR. The strategy used the 3 L small scale to determine set-points, notably concerning pH and dissolved oxygen, and refined conditions applied on the 50 L bioreactor was reached. Large scale expansion was notably ensured by a progressive addition of microcarrier. Culture started in a volume of 20 L and fresh surfaces were added through two culture medium feeds until the final volume of 50 L. A 43-fold increase in cell yield was achieved after 11 days of cultivation.

### WJ-MSC microcarrier-based cultures using hPL

In the case of WJ-MSC, only two studies have been conducted on microcarriers, in a culture medium supplemented with hPL, adapted for clinical use. Petry *et al.* compared five different microcarriers (Hillex II, ProNectin F-coated, Plastic, Plastic-Plus and Glass-coated) in static mode and validated the dynamic culture in Spinner flasks with the one giving the best growth and attachment condition in static mode [146]. In parallel, De Soure *et al.* validated cells isolation and also dynamic cultures in spinner flasks with Plastic microcarriers precoated with a culture medium supplemented with 50 % hPL [115]. However, such conditions have only been validated at the laboratory scale (until 100 mL), and comparison of microcarriers have only been performed in static mode for WJ-MSC.

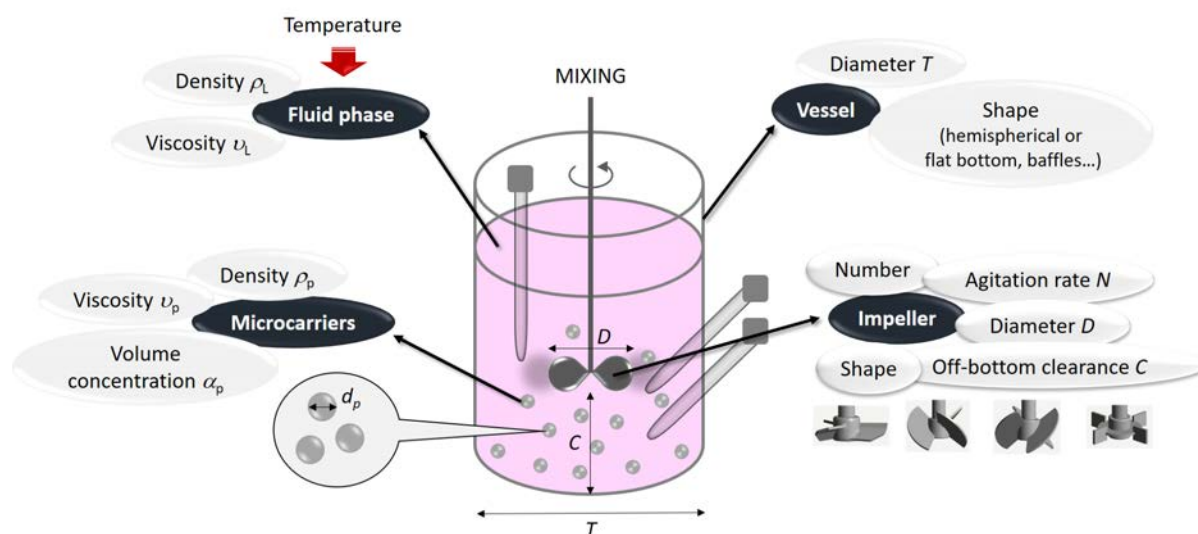


Figure 1.22: Parameters influencing particle suspension in STR.

### 1.5.4 Particles just-suspended state

Microcarrier suspension in stirred tank bioreactors is fundamental for MSC expansion. The agitation must be sufficient to allow culture medium homogenization and avoid  $O_2$ , pH and nutrient gradient limitations, to enhance mass transfer, and to maximize the available liquid-solid interfacial area. Hence, suspension of all particles is required to avoid microcarrier settling in the bottom and aggregation [138]. However, a too vigorous agitation may generate damages to the cells through cell lysis, cell detachment or by inducing their differentiation [153, 154]. One reasonable strategy to get a sufficient mixing performance and minimization of hydromechanical stress is to operate at the impeller just-suspended agitation rate  $N_{js}$  at which complete beads suspension is ensured (Fig. 1.23). This means that bioreactor hydrodynamics must therefore be intensively studied to guarantee cells viability and allow a process scale-up, leading to the need of reliable models.

The critical agitation rate  $N_{js}$  is function of the different parameters, presented in Fig. 1.22. In the case of microcarrier suspension in small scale bioreactor, no sparging is necessary. Table 1.7 presents the impacts of the different parameters, for a given vessel shape. In addition, the impeller design significantly impact  $N_{js}$  value, according to the fluid macroscopic flow pattern in the vessel. As presented in Fig. 1.24, axial flows are composed of large circulation loops, generally over the liquid height (axial downward pumping impellers), radial flows involve four circulation loops and often lead to fluid compartments, and mixed-flows involve a large circulation loop in the opposite direction of the one generated by axial flows and a potential small circulation loop above (axial inward pumping impellers). In the first case, in down-pumping mode, particles are pushed

down and suspended after sliding the slide wall, whereas in the two other cases, particles are pushed inward and entrained by the impeller.

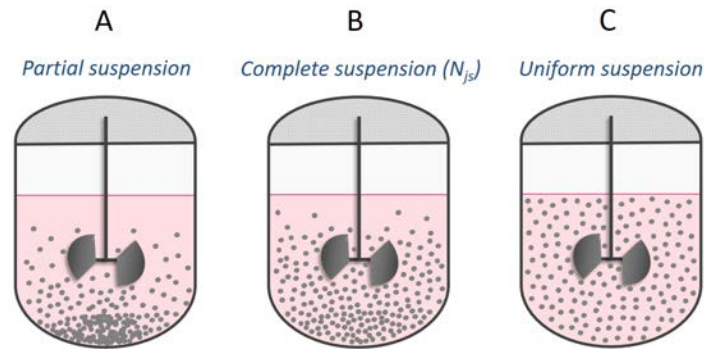


Figure 1.23: Particle suspension states and distribution in STR according to the agitation: A fraction of particles remains in the bottom (A), all particles are in suspension (B), the particle concentration is uniform (C).

Table 1.7: Impact of agitation geometry and phase properties on the minimal agitation rate ensuring complete suspension, by considering all other parameters fixed.

Parameter	Effect on $N_{js}$ when increasing
<b>Geometrical dimensions</b>	
Impeller diameter D	$N_{js} \searrow$
Off-bottom clearance C	$N_{js} \nearrow$
<b>Fluid-solid interactions</b>	
Particle Archimede number	$N_{js} \nearrow$
Particle volume fraction	$N_{js} \nearrow$

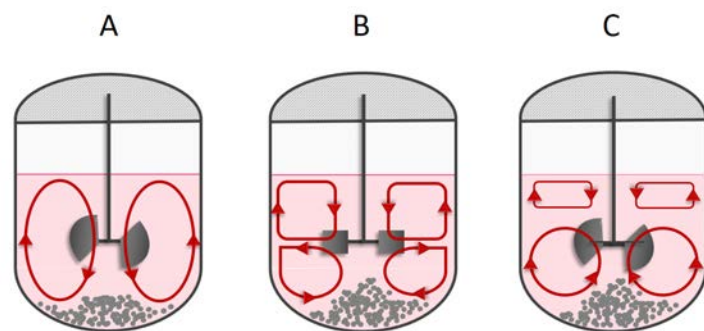


Figure 1.24: Flow patterns and particles bed shapes observed at agitation rates  $N < N_{js}$  depending on mixing structures: axial flow with impellers in down-pumping mode (A), radial flow (B) and mixed-flow impellers in up-pumping mode (C).

Many methods have been established to estimate  $N_{js}$ , and were classified in 4 categories by Tamburini *et al.*: (i) direct methods, (ii) indirect methods, (iii) computational methods, and (iv) theoretical methods [155]. Nevertheless, these methods were established and validated for particles that were significantly denser than microcarriers, like sand or glass beads, but not necessarily for microcarriers. A relevant example concerns the Zwietering equation, considered as the mostly used model to predict  $N_{js}$ . This equation, presented in Eq. (1.1), involves a  $S$  coefficient related to the impeller shape, size and location in the vessel.  $\nu_L$  is the kinematic viscosity,  $g$  is the gravity component,  $\rho_p$  and  $\rho_L$  are the densities of the solid and the liquid phase,  $X$  is the particle mass fraction,  $d_p$  is the particle diameter and  $D$  is the impeller diameter. It has been shown by Ibrahim and Nienow that the calculation of the  $S$  coefficients in the same operational conditions for sand particles and microcarriers, could present up to 50 % overestimation for microcarriers [156]. This difference was attributed to the low density difference between microcarriers and the liquid phase (around 40 kg m<sup>-3</sup>), which facilitates the lifting of particles from the tank bottom.

$$N_{js} = S \cdot \nu_L^{0.1} \cdot \left( \frac{g \cdot (\rho_p - \rho_L)}{\rho_L} \right)^{0.45} \cdot X^{0.13} \cdot d_p^{0.2} \cdot D^{-0.85} \quad (1.1)$$

To our knowledge, only a few determination and / or predictive methods have been applied to microcarrier suspensions:

- *Direct methods* may be both qualitative or quantitative. They are based on visualizations or measurements of the suspended or unsuspended particle amount. The well-known Zwietering visual determination considers that the just-suspended state is reached when particles do not stay longer than 1 or 2 seconds in the tank bottom [157]. This method has been validated for microcarriers and is the most commonly used for MSC dynamic cultures [156, 158, 3].
- *Indirect methods* are based on variables related to the impeller agitation rate. At the just-suspended state, these variables present particular behaviour. Recently, two teams developed different optical methods based on microcarrier local concentration, using Cytodex-1. These microcarriers have the specificity to be transparent, allowing light passage through the material and light scattering. For orbital shaken bioreactors, Perialisi *et al.* used a laser-light to illuminate an horizontal plane located just over the vessel bottom and a camera to record optical measurements through a mirror underneath the vessel [159]. Small brightness variation were analysed and directly correlated to the light scattering, found to be proportional to the amount of particles settled in the vessel bottom. The works of Delafosse *et al.* were performed in a stirred tank bioreactor equipped with a mechanical agitation [160]. A light attenuation technique was developed allowing measurement on the whole

reactor, and was validated for different impellers. Light attenuation was found to be function of the local particle concentration, and permitted to characterize the solid spatial distribution. By distinguishing the system in three zones (clear layer below the free surface, bulk zone with a homogeneous distribution and packed bed of motionless particles at the bottom),  $N_{js}$  determination was achieved when the particle concentration in the bulk zone was found equal to the mean particle concentration. Although it is limited to transparent microcarriers, these two methods may be used for just-suspended state prediction.

- *Computational methods* involves data recovered from CFD (Computational Fluid Dynamics) simulations. Microcarrier suspension modelling is very recent, and studies were generally focused on flow pattern and shear stress characterization, than on the development of a  $N_{js}$  predictive method. CFD was found to be complementary to PIV (Particle Image Velocimetry) studies and experimental cultures for microcarrier suspension in STR characterization [161, 131, 109, 162, 163, 164, 160]. These aspects are presented in more details in section 1.6.4.
- *Theoretical methods* are mainly based on the assumption of an equilibrium between particle settling and the off-bottom lifting and led to models derived from experimental results (often according to limited ranges of geometries and particle properties). As results of a dimensional analysis performed in the case of microcarrier suspension in orbital shaken bioreactors, Olmos *et al.* established a correlation involving  $N_{js}$  through a Froude number and other dimensionless numbers related to particle properties and geometrical parameters [165].

Although  $N_{js}$  prediction methods are well established for particles such as sand or glass beads, they are rare in the case of low density particles like microcarriers. For the majority of the MSC cultures on microcarriers,  $N_{js}$  parametrization is based on a visual determination, which has the advantage to be a quick and non-intrusive operation. Nevertheless, it may become impossible to use at large-scale cultures, as it was the case in the 50 L scale in the study of Lawson *et al.* Future large scale cultures will thus require methods adapted to large volumes as well as scalable and robust models.



## Section summary

- MSC culture on microcarriers was validated in different systems and using different types of microcarriers. The use of such particles is notably investigated for process scale-up.
- However, microcarriers were initially developed to improve cell attachment and expansion. In the case of MSC, cells are the product itself. Efforts are thus still necessary for cell detachment, with quality control.
- Numerous operating conditions were reported in STR, but only few compared microcarriers in order to determine the most suitable. A systematic comparison of microcarriers in static mode was recently proposed, which should then be definitively validated in agitated condition.
- The just-suspended state was investigated as a good compromise between culture medium homogenization and reduced hydromechanical stress. However, due to the low difference in densities between microcarriers and the liquid phase, predictive and characterization methods have to be adapted.

## 1.6 Hydrodynamics potential impact on MSC

### 1.6.1 Hydromechanical stress and turbulence description

As previously presented, agitation is required to fully suspend microcarriers in the bioreactor. It is nevertheless source of hydromechanical stress leading to potential damages to cells adhered the particle surfaces. MSC cultures are mostly performed in hypoxia and  $O_2$  consumption is sufficiently slow to ensure sufficient dissolved oxygen in the reactor only by surface aeration for small scales. Lavrentieva *et al.* reported a  $O_2$  consumption of  $0.024 \pm 0.002$  and  $0.095 \pm 0.005$   $\text{pmol h}^{-1} \text{ cell}^{-1}$ , respectively in hypoxia (1.5 %  $O_2$ ) and normoxia (21 %  $O_2$ ) [166]. Although dissolved oxygen in large-scale cultures should be controlled to avoid  $O_2$  limitations, it has been shown by Heathman *et al.* that direct sparging at the just-suspended state was detrimental to BM-hMSC growth [150]. So, unlike other mammalian cell cultures in STR, damages related to sparging will not be taken into account in the present state of art, which will focus on damages due to the agitation only. Before describing cell physiological and performance responses to hydromechanical stress

encountered in the bioreactor, impact of turbulence on suspended particles will be presented. The different length scales related to the turbulent phenomena are indeed crucial for understanding the link between turbulence and hydromechanical stress encountered by particles, related to the potential cell damages. Hence, the present section aims at describing the phenomena related to the turbulence and at drawing a parallel with their impact for MSC cultivated on suspended microcarriers at the different turbulence length scales. Considering microcarrier and cell sizes, these length scales will help to determine the critical damaging scales. Figure 1.25 summarize the relationship between the turbulence and the impact on microcarriers and cells, which will be developed in more details in the following sections.

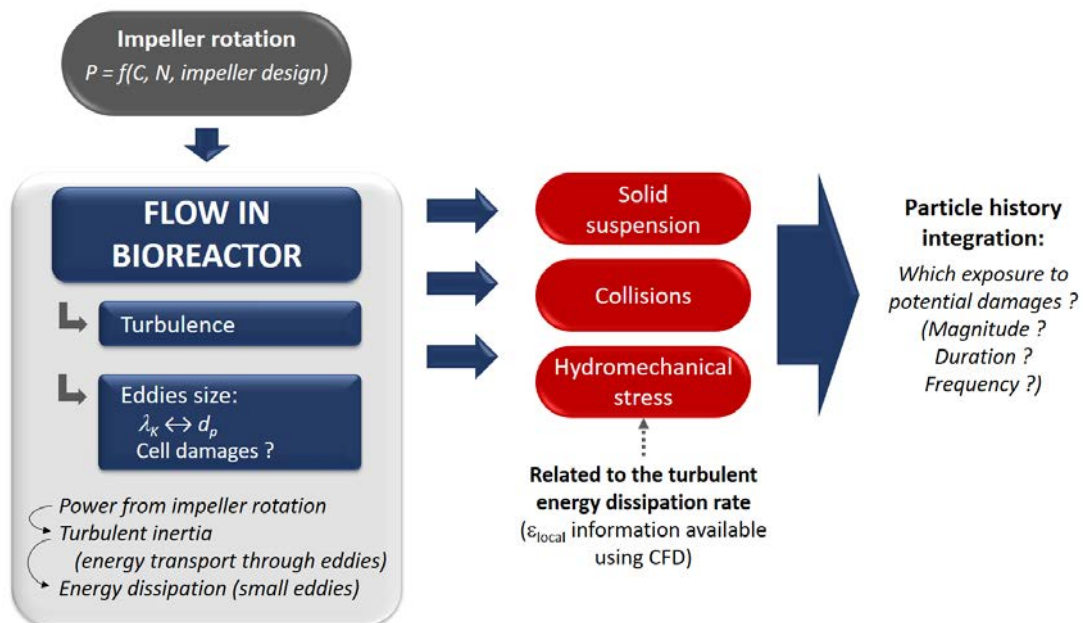


Figure 1.25: Schematic representation of the intermediate phenomena from the impeller rotation to its impact on cells adhered on particles (P: dissipated power, C: driving torque).

The agitation is characterized by flow patterns and flow regime. Laminar flow mainly involves diffusive mass and heat transfer. This transport is notably dominant for high kinematic viscosity. In contrast, transport in fully turbulent flow is mainly convective and induced by the fluid momentum. Turbulence may be defined as a state, at which the fluid flow is varying in all space, with random fluid velocity variations. It leads to complex and disorderly movements and to instabilities formation, closely linked to the agitation in stirred bioreactors. The dimensionless Reynolds number  $Re$  is introduced to determine which force is dominant in the system. For STR, it is calculated according to the Eq. (1.2), with  $\rho_L$  and  $\mu_L$  the fluid density and kinematic viscosity,  $D$  the impeller

diameter as characteristic length and  $N$  the impeller agitation rate. Fig. 1.26 presents the different flow regime according to the Reynolds number. First initiated instabilities, called Tollmien-Schlichting waves, are generated in 2-dimensions. They move to 3-dimensional instabilities in the transition regime until the fully turbulent regime establishment, with chaotic movements. Due to friction between the fluid and the reactor wall, the transition between the laminar and the turbulent flow occurs later in the boundary layer. For many impellers in STR, flow regimes may be defined according to the following values:

- $Re < 1$ : Stokes regime, notably involved in the microfluidic field.
- $Re < 10$ : Laminar regime.
- $10 < Re < 10^3 - 10^4$ : Transition regime.
- $Re > 10^3 - 10^4$ : Turbulent regime.

$$Re = \frac{\text{inertial forces}}{\text{viscous forces}} = \frac{\rho_L \cdot N \cdot D^2}{\mu_L} \quad (1.2)$$

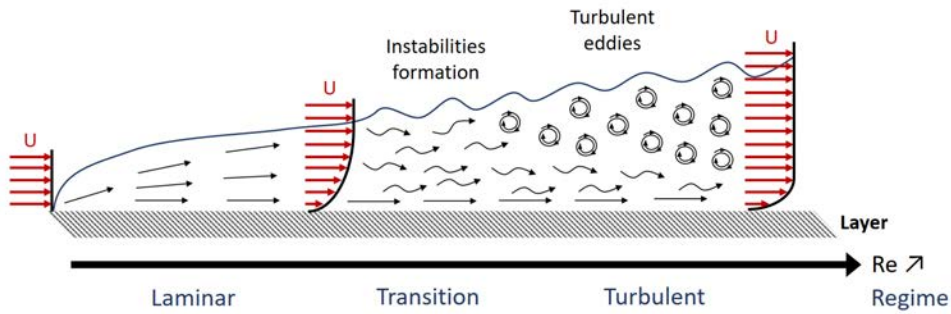


Figure 1.26: Flow regime and turbulence evolution with the Reynolds number.

The next subsections will describe these instabilities establishment and potential damaging effects. First, the energy cascade concept, developed by Richardson, allow to explain the turbulent eddies formation and energy transfer mechanisms. In a second time, the Kolmogorov's isotropic turbulence theory will be presented with the related different laws and turbulence characterization.

### The energy cascade mechanism

In the 1920's, the English mathematician, physicist and meteorologist Lewis Fry Richardson qualitatively explained the turbulence phenomenon through the formation of eddies of different sizes. Large eddies were defined by a characteristic length  $L$ , a characteristic velocity  $U$  and a characteristic time  $\tau_L = L/U$ . Their corresponding Reynolds number  $Re_L = (U \cdot L) / \mu$  presented high value, namely viscous forces were negligible. Richardson suggested that these large eddies were divided into smaller eddies in a turbulent flow, with

kinetic energy transfer from the large eddies to the small ones. These new eddies may then be also divided in smaller ones, until they became small enough to present significant viscous forces. At this point, the kinetic energy of turbulence is converted into heat. The global energy dissipation rate  $\langle \varepsilon \rangle$  was defined as a function of the large eddy properties as:

$$\langle \varepsilon \rangle = \frac{U^3}{L} \quad (1.3)$$

The kinematic energy of a large eddy is considered to be equal to the kinematic energy contained in all generated eddies, until part of this energy is transferred as heat. These divisions and sub-divisions led to the eddy cascade illustration, and were summarized in the rhyming verse from Richardson [167]:

*Big whirls have little whirls  
Which feed on their velocity  
And little whirls have lesser whirls  
And so on to viscosity  
- In the molecular sense.*

### The Kolmogorov's theory

In 1941, the russian mathematician Andreï Kolmogorov completed the cascade theory with an hypothesis on the local isotropy state (H0) and two similarity hypothesis (H1 and H2), presented in Table 1.8 and illustrated in Fig. 1.27 [168, 169]. The H1 statement involved the length  $\lambda_K$ , the velocity  $u_{\lambda_K}$  and the time  $\tau_{\lambda_K}$  scales according to the two parameters  $\varepsilon$  and  $\nu$ , as presented in Eqs. (1.4) to (1.6). They correspond to the Kolmogorov scale in the dissipation range, describing the smallest eddies in the flow. The Reynolds number  $Re_{\lambda_K}$  (Eq. (1.7)) is equal to 1 and displays comparable viscous and inertial effects, leading to kinetic energy dissipation as heat.

$$\text{length scale : } \lambda_K = \left( \frac{\nu^3}{\varepsilon} \right)^{1/4} \quad (1.4)$$

$$\text{velocity scale : } u_{\lambda_K} = (\varepsilon \cdot \nu)^{1/4} \quad (1.5)$$

$$\text{time scale : } \tau_{\lambda_K} = \left( \frac{\nu}{\varepsilon} \right)^{1/2} \quad (1.6)$$

$$Re_{\lambda_K} = \left( \frac{\lambda_K \cdot u_{\lambda_K}}{\nu} \right) = 1 \quad (1.7)$$

The second similarity hypothesis H2 introduced the inertial subrange, where viscous effects are negligible, with large enough Reynolds number  $Re_{\lambda_T}$ . As a consequence to this

Table 1.8: Kolmogorov hypothesis for turbulence description.

Hypothesis	Statement
H0	At sufficiently high Reynolds numbers, the small scale turbulent motions ( $l \ll L$ ) are statistically isotropic.
H1	In every turbulent flow at sufficiently high Reynolds number, the statistics of the small scale motion ( $l < l_{EI}$ ) have a universal form that is uniquely determined by $\varepsilon$ and $\nu$ .
H2	In every turbulent flow at sufficiently high Reynolds number, the statistics of the motions of scale $l$ in the range $L \gg l \gg \lambda_K$ have a universal form that is uniquely determined by $\varepsilon$ independently of $\nu$ .

$l$ : length scale of an eddy.

$L$ : length scale of the large eddies.

$l_{EI}$ : length scale of the transition between the large scale anisotropic eddies and the small scale isotropic eddies.

$l_{DI}$ : length scale of the transition to the dissipation range.

$\lambda_K$ : length scale of the smallest eddies in the flow.

assumption, the velocity and time scales are decreasing with the length scale. This range, between the smallest eddies and the large eddies, is the Taylor microscale, where the kinetic energy is transferred from larger eddies to smaller ones. The Taylor length scale  $\lambda_T$  is defined as:

$$\lambda_T = \left( \frac{10 \cdot \nu \cdot k}{\varepsilon} \right)^{1/2} \quad (1.8)$$

### Kinetic energy and eddies size impact during cell culture

Characteristic length scales and Reynolds numbers of each scale, previously described, are summarized in Table 1.9. Potential damages depend on the entity size in comparison with the Kolmogorov length scale  $\lambda_K$ . Concerning cells adhered on microcarriers, the microcarrier diameter  $d_p$ , typically around 200  $\mu\text{m}$ , is used, admitting that no cell damage due to flow associated stresses occurs if  $d_p < \lambda_K$ . Croughan *et al.* indeed reported lower FS-4 cells (human diploid fibroblasts cells) growth rates when  $\langle \lambda_K \rangle$  dropped below 125  $\mu\text{m}$  and no relative growth extent below 100  $\mu\text{m}$  ( $d_p = 185 \mu\text{m}$ ) [170]. The critical  $\langle \lambda_K \rangle$  value retained as a limit for potential cell damages was hence established around  $2/3 \times d_p$ . However, recent studies found that BM-MSC growth kinetics and stemness properties were not impaired for turbulent eddies around  $0.4 \times d_p$  and  $1/3 \times d_p$ . A significantly lower cell growth was nevertheless observed for  $\lambda_K \approx 1/4 \times d_p$  [171, 150].

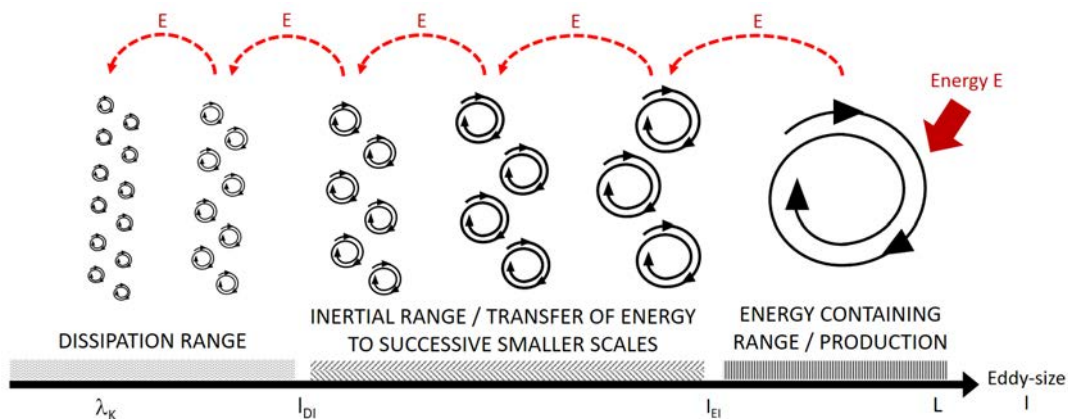


Figure 1.27: Energy transfer from large eddies to small eddies according to the turbulent energy cascade theory.

Table 1.9: Characterization of the turbulent ranges based on the eddy sizes.

	Integral length scale	Taylor microscale	Kolmogorov length scale
Predominant forces	Inertial » Viscous		Inertial $\approx$ Viscous
Length scale	$L = k^{3/2}/\varepsilon$	$\lambda_T = (10 \cdot \nu \cdot k/\varepsilon)^{1/2}$	$\lambda_K = (\nu^3/\varepsilon)^{1/4}$
Reynolds	$Re_L = k^2/(\varepsilon \cdot \nu)$	$Re_{\lambda_T} = (\lambda_T \cdot u_{\lambda_T})/\nu$	$Re_{\lambda_K} = (\lambda_K \cdot u_{\lambda_K})/\nu = 1$

## 1.6.2 Hydrodynamics characterization in STR

As described by Henzler *et al.*, particle stress is a consequence of a velocity difference between the particles and the fluid [172]. In laminar flow, the stress  $\tau$  is calculated using the Newton's law in Eq. 1.9. However, in the case of turbulent flow, the relative velocity that determines this stress comes from the turbulent fluctuations. The Reynolds decomposition allow to define the velocity field of a flow  $u$  as the sum of the mean velocity  $\bar{u}$  and a fluctuating term  $u'$ . The Reynolds stress tensor  $\tau_t$  is then calculated, using the turbulent fluctuation velocity  $\sqrt{u'^2}$ , as presented in Eq. 1.10. Stress determination is dependent on the turbulent energy dissipation rate  $\varepsilon$  and the Kolmogorov length scale  $\lambda_K$ , which allow to define the turbulent range. Relationships are presented in Fig. 1.28 for the different ranges. Regarding these results, and independently of the flow regime, the stress applied on particles  $\tau$  is only related to the turbulent energy dissipation rate  $\varepsilon$ .

$$\tau = \mu \frac{du}{dx} \quad (1.9)$$

$$\tau_t = \rho \sqrt{u'^2} \quad (1.10)$$

Turbulence analysis is classically performed with a single phase, although it is known that particle suspensions may affect the hydrodynamics. In the case of the STR, two regions

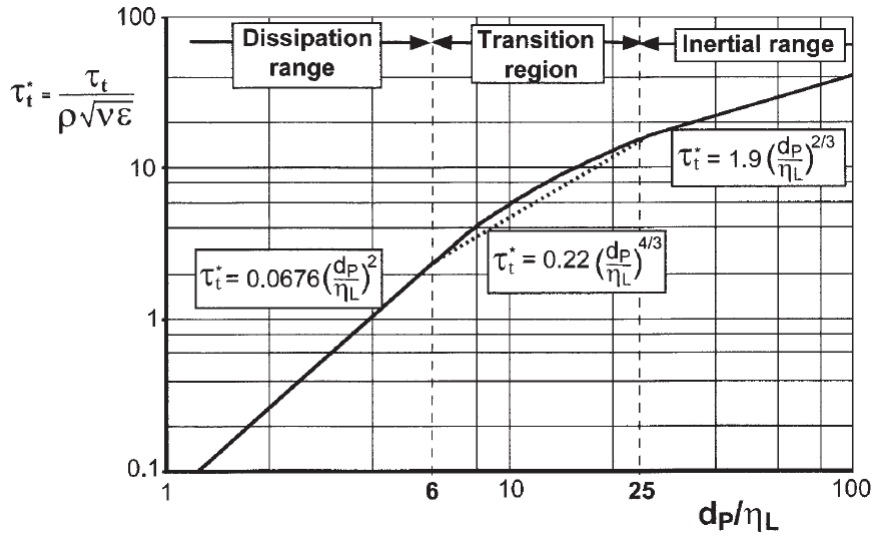


Figure 1.28: Dimensionless stress in fully developed turbulent flow given by the theory of isotropic turbulence. Figure reproduced from Henzler *et al.*, 2000 [172]. In this figure,  $\eta_L$  corresponds to the Kolmogorov length scale  $\lambda_K$ .

may be distinguished: (i) the impeller region and (ii) the rest of the vessel. Shear stress is much higher around the impeller, with local turbulent dissipation rates  $\varepsilon$  up to 100 times the mean value in the vessel  $\langle \varepsilon \rangle$ , while  $\varepsilon$  can lead to only  $0.25 \times \langle \varepsilon \rangle$  in the rest of the vessel [173]. The energy dissipation rate is mostly used to characterize the hydrodynamics. In contrast to the agitation rate, it allows the comparison of different bioreactor geometries.

### Time-averaged parameters


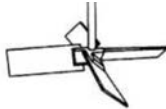


The energy balance on the bioreactor states that required power  $P_{req}$  should be equal to the dissipated power  $P$ . This amount of power corresponds to the power delivered at the shaft tip after deducting power loss by friction and transmission devices. It is then converted into turbulent inertia, and finally dissipated at the small eddy scales, leading to turbulence in the system.  $P$  is dependent on the impeller design and is generally characterized by the Power number  $N_p$ , defined in Eq. (1.11). It relates the friction forces to the inertial forces, involving the fluid density  $\rho_L$ , the agitation rate  $N$  and the impeller diameter  $D$ . In turbulent regime ( $Re > 10^3 - 10^4$ ), this number becomes constant. Examples of  $N_p$  values are given for different impeller design in Table 1.10.

$$N_p = \left( \frac{P}{\rho_L \cdot N^3 \cdot D^5} \right) \quad (1.11)$$

Using this power characterization, the volume-averaged turbulent energy dissipation rate  $\langle \varepsilon \rangle$  is calculated using Eq. (1.12), with  $(P/V)$  the input power dissipated per unit of

volume,  $\rho_L$  the fluid density,  $N_p$  the Power number,  $N$  the agitation rate, and  $D$  the impeller diameter.  $\langle \varepsilon \rangle$ , and also  $(P/V)$ , are directly correlated to different characteristics of mixing parameters, summarized in Table 1.11.

Table 1.10: Examples of Power number values for different impeller designs in turbulent regime.

				
Impeller design	Marine Propeller	Pitched Blade Turbine	Elephant Ear Impeller	Rushton Turbine
$N_p$	0.37 - 0.5	0.7 - 1.7	1.7 - 2.1	4 - 6

$$\langle \varepsilon \rangle = \frac{1}{\rho_L} \cdot \left( \frac{P}{V} \right) = \left( \frac{N_p \cdot N^3 \cdot D^5}{V} \right) \quad (1.12)$$

Table 1.11: Time-averaged parameters characterizing the hydrodynamics in STR for MSC cultures on microcarriers.

Key parameter	Equation of model	$\langle \varepsilon \rangle$ proportionality
Mixing time $t_M$	$t_M = 5.9 \cdot \left( \frac{T}{D} \right)^{1/3} \cdot \varepsilon^{-1/3} \cdot T^{2/3}$ (Nineow, 1997 [174])	$\langle \varepsilon \rangle^{-1/3}$
Kolmogorov length scale $\lambda_K$	$\lambda_K = \left( \frac{\nu^3}{\varepsilon} \right)^{1/4}$	$\langle \varepsilon \rangle^{-1/4}$
Maximum energy dissipation rate $\varepsilon_{max}$	$\varepsilon_{max} = E \cdot N^3 \cdot D^2 \cdot \rho$ (Zhou, 1996 [173])	$\langle \varepsilon \rangle$
Power number	$N_p = \frac{P}{\rho \cdot N^3 \cdot D^5}$	Independent
Pumping number	$N_Q = \frac{Q}{N \cdot D^3}$	Independent

Microcarrier cultures are known to be more sensitive to cell damages than suspended cell cultures. Lethal cell response was indeed observed for  $\langle \varepsilon \rangle$  values of  $1 \text{ kW m}^{-3}$  for anchored CHO cells, in comparison to  $10^5 \text{ kW m}^{-3}$  for suspended CHO cells [175]. The maximal energy dissipation rate  $\varepsilon_{max}$  may also be used as a relevant parameter, considering MSC to be sensitive to the local energy dissipation rate, especially in the impeller region and impeller stream. For microcarrier-based cell cultures, Croughan *et al.* reported that the size of the smallest turbulent eddies in the bioreactor were a better parameter for scale-up considerations and for systems that are not geometrically similar [153]. In turbulent regime, the Power number  $N_p$  and the Pumping capacity  $N_Q$  may be taken into account to characterize the impeller design and efficiency. They are respectively used for power consumption estimation and to describe the amount of liquid pumped out



from the rotor region of the impeller. However, the turbulent energy dissipation rate  $\langle \varepsilon \rangle$  is generally referred as the main source of information to describe the hydromechanical stress.

### Cell 'lifelines' impact

The previous parameters generally used time- or spatial-average values, but local heterogeneities may also be considered. In STR, due to the impeller rotation, turbulence is indeed strongly heterogeneous. Figure 1.29 presents an example of turbulent energy dissipation rate 'seen' by cells in a stirred-tank bioreactor. Cell history may include different shear stress by passing through different zones in the vessel, with a higher shear stress in the impeller influence zone [176]. The  $(\varepsilon_{max}/\bar{\varepsilon})$  ratio may be used to complete the mixing characterization in the bioreactor. It was notably found that lower  $(\varepsilon_{max}/\bar{\varepsilon})$  values were obtained with larger impellers (higher  $D/T$  ratios) [177]. Venkat *et al.* characterized fluid flow and microcarrier suspension in a spinner flasks, by calculating local specific energy dissipation rates. They suggested that the critical zones for potential microcarriers and cell damages were the trailing vortex region around the impeller, and the high energy converging (vortex) flow region [178].

Furthermore, a cumulative effect on the hydromechanical stress may occur for particles with a high exposure frequency. Hence,  $\langle \varepsilon \rangle$  may be not sufficient to characterize the impact of the hydrodynamics, and may require complementary information such as the time or frequency exposure, particularly in zones presenting the highest local  $\varepsilon$  values. In this way, Godoy-Silva *et al.* looked for the impact of the hydrodynamics, through repetitive and high levels of hydrodynamic stress and quantified according to the energy dissipation rate, on suspended CHO cell physiological response [179]. It was demonstrated in this case, that cell growth and monoclonal antibody production were resistant to the hydrodynamics stress with  $\varepsilon$  up to  $6.4 \times 10^6 \text{ m}^2 \text{ s}^{-3}$ , by displaying no significant variation in comparison to the control culture. However, a shift of glycosylation pattern was observed for  $\varepsilon \geq 6 \times 10^4 \text{ m}^2 \text{ s}^{-3}$ . Cells were thus also sensitive to the repetitive hydrodynamic stress applied.

This time / spatial-dependent incidence was also introduced into an energy dissipation / circulation function (*EDC*) by Jüsten *et al.* for filamentous fungi morphology investigation, during cultures submitted to different agitations [180]. This parameter calculation was then applied on other mycelial fragmentations and was related to protein production using a chemostat system [181]. More recently, Collignon *et al.* [164] used a similar energy dissipation / circulation function (Eq. (1.13)) to combine intensity and exposure frequency of MSC adhered on microcarriers to the hydromechanical stress in a bioreactor. Five impeller designs were compared using CFD LES and were found to generate

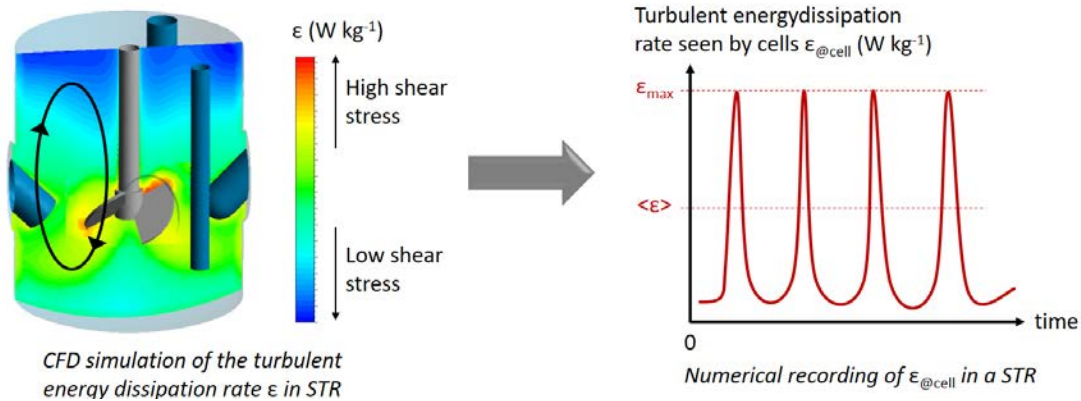


Figure 1.29: Turbulent energy dissipation rate spatial fluctuation in STR. Figure adapted from Master course of ENSAIA.

heterogeneous flows and different exposure frequencies to hydromechanical stress. *EDC* took into account exposure to critical zones, where the Kolmogorov length scale  $\lambda_K$  was inferior to the particle diameter. For a given power input, *EDC* values were compared for a Rushton turbine, Marine propellers and Elephant Ear impellers, both in up-pumping or in down-pumping modes, for a given  $(P/V)$ . Despite the marine propeller in up-pumping mode required the highest agitation rate, it provided the lowest *EDC* value.

$$EDC = \frac{1}{t_c} \cdot \frac{\rho_L}{V_{\mu C}(\lambda_K < d_p)} \cdot \iiint_{V_{\mu C}(\lambda_K < d_p)} \varepsilon dV \quad (1.13)$$

Hydromechanical stress impact should thus be jointly considered through stress intensity and frequency, but it is still difficult to weight these two contributions on physiological response.

### 1.6.3 Hydro-biological coupling

Macro- and micro-environments have a strong impact on biological activity, such as cell growth, cell viability, cell adhesion on microcarriers or cell differentiation. However, hydrodynamics and biological activity are coupled through non-linear relationships, making delicate the process optimization. Fig. 1.30 presents a simplified flow chart relating hydrodynamics to the cell biological responses. Biochemical inputs, hydromechanical stress and physical parameters have an impact on cell responses and potential population heterogeneities. Moreover, during the culture, cell response may affect the environment in the bioreactor. So, interconnection and time-dependent evolutions should be taken into account. According to the operating conditions, the agitation may influence cell biological response through the culture medium homogenization and mass transfer, and through the hydromechanical stress generated.

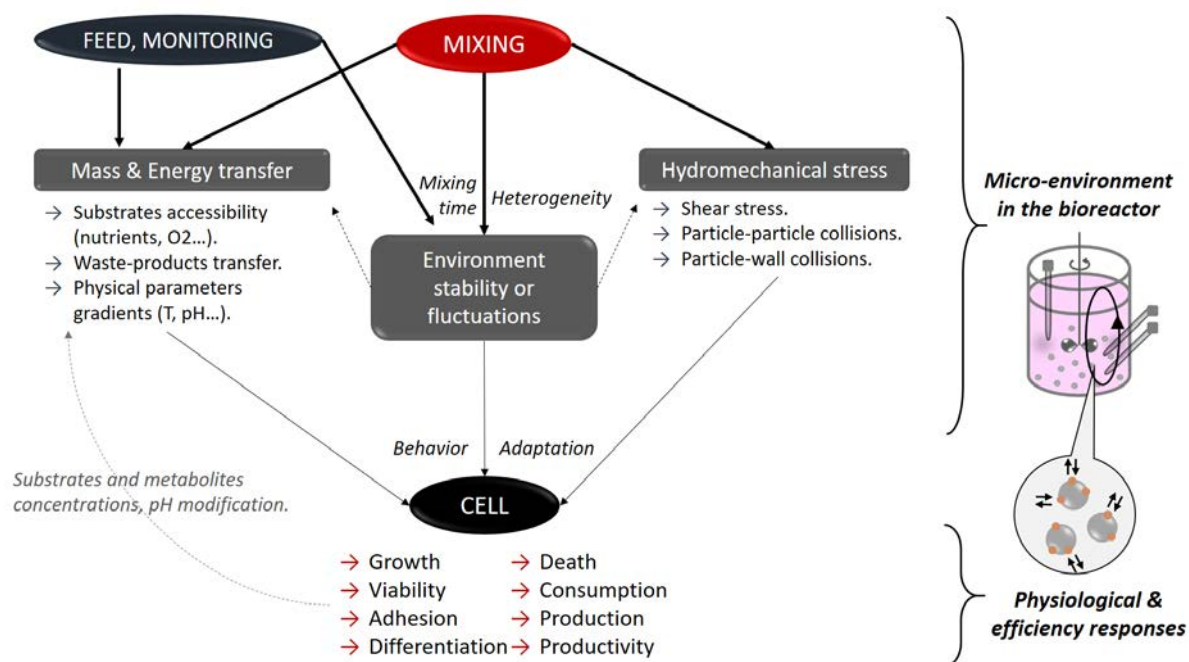


Figure 1.30: Hydro-biological coupling in a monitored stirred-tank bioreactor.

### Culture medium homogenization

The culture medium provides the carbon and the energy sources for cell activity. Glucose, glutamine, amino acids, growth factors and antioxidant molecules consumption are necessary for cell growth and metabolic activity. It has been shown that a lack of these nutrients led to a decrease of the cell growth and the cell production. An extended culture duration in this starving environment may lead to cell morphology modification with potential detachment, cell death and thus a decrease in cell viability. Concerning the dissolved oxygen, cell requirements are low, but must be sufficient to ensure metabolic activity. Furthermore, it was shown that dissolved oxygen concentration had an impact on cell pre-differentiation. Reppel *et al.* notably found that hypoxic cultures enhanced WJ-MSC chondrogenic differentiation potential [182]. In all cases, nutrients and oxygen accessibility is looked for efficient cultures. Related to the biochemical input consumption, cells produce waste-products such as lactic acid and ammonia. These products were reported to be toxic and inhibitory for cell cultures at high concentrations [183]. So, high local concentration should be avoided. According to the input and feed strategy, the agitation thus lead to the culture medium homogenization and mass transfer improvement and limit the local toxic compounds accumulation.

### Hydromechanical stress

As previously established, a too high or inadequate agitation may lead to cell damages, resulting in lower cell growth and / or cell death and cell viability decrease [153]. Cherry and Papoutsakis reported 3 main mechanisms, considered strong enough to affect cells adhered on microcarriers in stirred bioreactors [184]:

- Particle-particle collisions.
- Particle-bioreactor walls (wall of the vessel, impeller, probes...) collisions.
- Particle interactions with turbulent fluid eddies of the same size.

Based on the turbulent energy cascade concept and as shown in Fig. 1.31, turbulent eddies of different sizes are present in the bioreactor. On one hand, larger eddies have no direct detrimental effect on particles, but they are responsible of bead transport, which may end with collisions with another beads or with internal parts of the bioreactor, especially the impeller. On the other hand, eddies of the same size than particles are responsible for damages due to shear stress.

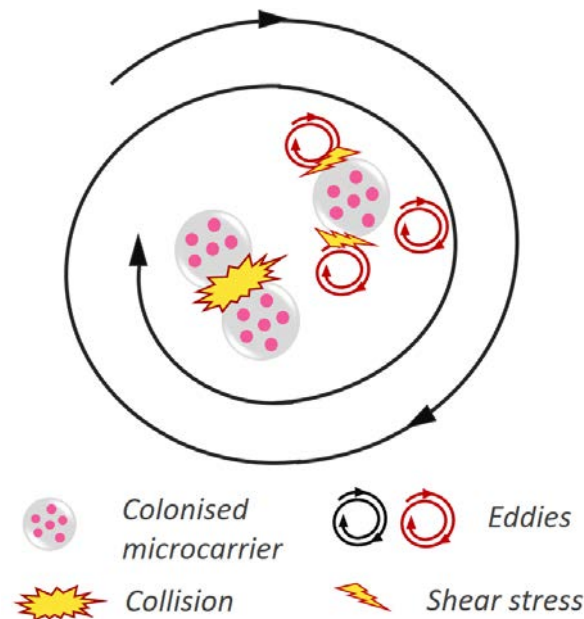


Figure 1.31: Description of the hydromechanical stress applied on colonized microcarriers.

The agitation effect on MSC growth and adhesion efficiency on microcarriers have been recently quantified by Heathman *et al.* [150]. They reported that growth rate significantly decreased at  $N = 2 \times N_{js}$ , but remained similar for  $N = N_{js}$  and  $N = 1.3 \times N_{js}$  in 250 mL DASGIP DASbox bioreactors (Eppendorf, Germany). It was also observed that cell quality remained unchanged after culture at  $N = 2 \times N_{js}$ , which thus suggested that the poor growth performances obtained were due to failure of the cells to attach on particle

surface rather than fluid shear stress. Interestingly, the Kolmogorov length scale  $\lambda_K$  was found under the microcarrier size  $d_p$  for agitation rates of the study, with around  $0.4 \times d_p$  at  $N = N_{js}$ . Severe performance loss were also observed when  $\lambda_K < 0.25 \times d_p$ , involving therefore a higher input power. In this case, cells were detached from beads but remained safe in suspension with turbulent eddies still larger than their own size. Based on these different scales, Nienow *et al.* developed a cell detachment strategy [171]. To overcome the cell detachment from microcarrier limitation, they proposed to apply an agitation rate at  $N = 5 \times N_{js}$  during the enzymatic digestion. This agitation rate was chosen to obtain a Kolmogorov length scale between the cell and the microcarrier sizes, so the agitation had an effect on cell attachment points to bead surfaces, but was not damaging for suspended cells.

Hydromechanical stress was finally found to potentially induce MSC differentiation, with shear stress conditions on MSC and their progenitors for specific applications. They mainly involved parallel-plate flow chamber to control the mechanical forces or in perfused systems, which notably revealed the impact of shear stress on MSC osteogenesis differentiation [185]. Osteogenic markers expression was found to increase with shear stress. Complementary studies looked at the effect of intermittent or continuous fluid shear stress on MSC osteogenic differentiation. Intermittent fluid shear stress promoted significantly higher osteogenic genes expression than cells under continuous fluid shear stress. Hence, the frequency and the variations with low intensity affect the potential cell differentiation, and should be considered as the fluid shear stress cumulative impact [186]. All these positive or potentially deleterious effects of the agitation on cell biological responses should be considered according to spatial distribution, with potential gradients and turbulent energy dissipation heterogeneities, and temporal evolution, with cell adaptation and cumulative effects or exposure.

#### 1.6.4 Fluid flow characterization using CFD

Computational Fluid Dynamics (CFD) may be used as a complementary approach to the experimental data. In the present case, CFD allows to better understand flow structures in bioreactors and their potential heterogeneity, affecting cell culture efficiency. It is notably used to complete the limited data in the literature for fluid flow and shear stress in stirred bioreactors, particularly at the particle just-suspended state where the system is not homogeneous. Concerning bioreactor designs and scale-up, CFD enables to understand and compare different design concepts from the bench to the industrial scale. So, for scale-up applications, the number of experiments at the pilot-plant level to valid or adapt a design may be reduced using preliminary numerical predictions.

CFD allows to solve the Navier-Stokes equations, that govern fluid flow, to furnish quanti-

tative analysis and prediction of fluid flow phenomena. Microcarrier suspension in stirred tank bioreactors involves two phases, namely the culture medium as the liquid phase and the microcarriers as the granular solid phase, whose interactions (drag force, turbulent dispersion) have to be modelled. Biological reactions may also be implemented to model cell growth or cell metabolic activity but, to our knowledge, it has never been applied for MSC cultures on microcarriers. Cell time scales (doubling time  $> 1$  day) are indeed much larger than hydrodynamic phenomena time scale, and cell growth modelling is complex, due to a high sensitivity to the environment (biochemical concentrations, available surface, hydromechanical stress...) and to differences according to the cell source. Current works are mainly based on microcarrier dispersion characterization and distribution of the shear stress encountered by the particles. Single-phase velocity fields may be experimentally validated using PIV (Particle Image Velocimetry).

Number of studies conducted CFD simulations of solid-liquid suspensions in stirred tank bioreactors at or close to the just-suspended state with particles significantly heavier than microcarriers, like sand [187, 188, 155, 189, 190, 191]. On this basis, recent studies adapted the models for microcarrier suspensions in different bioreactor design. They are summarized in table 1.12.

### Stirred tank bioreactors

Hydromechanical stress at microcarrier just-suspended state was first characterized at the small-scale in spinner flasks. Liovic *et al.* and Ponnuru *et al.* showed that higher shear stress was obtained near the impeller tips and behind the blades [161, 192]. They also calculated the Kolmogorov length scale and obtained minimal values on baffle surface, when the impeller magnet was aligned with baffles. They respectively found  $\lambda_{K,min} = 75 \mu\text{m}$  and  $\lambda_{K,min} = 50 \mu\text{m}$ , considered to potentially damaging cells on microcarriers.

Kaiser *et al.* used CFD for spinner flasks without baffles and observed mainly tangential flow, with low axial and radial components. In this work,  $\lambda_{K,min}$  was found around  $44 \mu\text{m}$ , but no cell death due to the hydromechanical stress was observed during cultures. They also revealed a nearly stagnant flow directly under the impeller, in the bottom of the vessel, leading to possible microcarrier sedimentation and agglomeration [131].

Berry *et al.* used an Euler-Lagrange approach for particle tracking and demonstrated the impact of particle spatial distribution on the shear stress encountered by the particles [194]. At the just-suspended state, namely  $N = N_{js}$ , they found potentially damaging zones with  $\lambda_K < d_p$  in only 0.75 % of the bioreactor volume.  $\lambda_{K,min}$  was notably found at  $112 \mu\text{m}$ . For  $N < N_{js}$ , they observed an overall stress decrease within the fluid, but and increase of the mean stress exposure. Microcarriers were redistributed in zones of high stress, in particular in the bottom of the bioreactor (Fig. (1.32)). Hence, working

Table 1.12: Current CFD-based studies on microcarriers suspensions in bioreactors.

Reference	Code	Bioreactor design (working volume)	Modelling approach	Turbulence modelling
Liovic et al. [161]	ANSYS CFX 14.0	Spinner flask (N/A)	Single-phase (Particle tracking)	k- $\omega$ BSL-RSM LES-WALE
Kaiser et al. [131]	ANSYS Fluent 13	Spinner flask (100 mL)	Multi-phase - Euler-Euler	Standard k- $\epsilon$
Ponnuru et al. [192]	Flow-3D	Spinner (50 mL)	Multi-phase - Euler-Lagrangian	k- $\epsilon$
Schirmaier et al. [109]	ANSYS Fluent 14.0	STR (2 L)	Multi-phase - Euler-Euler	k- $\epsilon$
		STR (35 L)		k- $\epsilon$
Jossen et al. [193]	ANSYS Fluent 14	STR (2L) (1 L)	Multi-phase - Euler-Euler	k- $\epsilon$
Delafosse et al. [163]	ANSYS Fluent 14.5	STR (1.12 L)	Multi-phase - Euler-Lagrangian	dispersed k- $\epsilon$
Jossen et al. [105]	ANSYS Fluent 15	Wave bioreactor (1 L)	Single-phase*	k- $\omega$ SST
Berry et al. [194]	ANSYS CFX 14.5	Spinner flask (100 mL)	Multi-phase - Euler-Lagrangian	k- $\omega$ in near-wall region and k- $\epsilon$ in far-wall region
Collignon et al. [164]	ANSYS Fluent 14.5	Minibioreactor (200 mL)	Single-phase*	LES-WALE-SGS LES-WALE-Smagorinsky SGS
Delafosse et al. [160]	ANSYS Fluent 16.2	STR (1.12 L)	Multi-phase - Euler-Euler granular	Realizable k- $\epsilon$ LES 'mixture' standard k- $\epsilon$

LES: Large Eddies Simulation.

WALE: Wall-Adapting Local Eddy-viscosity.

BSL-RSM: Baseline Reynolds Stress Model.

SGS: sub-grid scale.

\* Completed by experimental microcarrier distributions.

at an agitation rate under the just-suspended state may be investigated to reduce the turbulent energy dissipation in the fluid, but should be considered according to the particle distribution in the areas involving the highest local stress. It should be noticed that particle tracking simulations were limited to low particles concentrations. Here, it was run for a volume concentration of 1 % in a working volume of 100 mL, although MSC cultures generally involve concentrations between 1 and 5 %. This limitation was due to the maximal possible number of particles complying with computational resources. Such simulations are thus still limited to small scales.

For the purpose of scale-up, microcarrier suspension were also investigated in larger STR. In this way, Schirmaier *et al.* worked on bioreactors of 2 and 50 L, both equipped with 2 Elephant Ear impellers [109]. Based on the same models as Kaiser *et al.* for spinner flasks, they mainly found axial flow in such systems. As for spinner flasks, a nearly stagnant region was observed below the impeller. Minimum Kolmogorov length scales were found lower than for spinner flasks with respectively 15 and 28  $\mu\text{m}$  in the 50 and 2 L bioreactors. Despite the 50 L STR presented the smallest turbulent eddies, the spatial mean value  $\langle \lambda_K \rangle$  was found much higher than in the 2 L, with 230  $\mu\text{m}$  versus 102  $\mu\text{m}$ , and the dissipated power in the fluid ( $P/V$ ) was found lower, with 0.63  $\text{W m}^{-3}$  versus 1.5 to 4  $\text{W m}^{-3}$ . This work showed therefore the necessity to consider both volume-averaged values and the local potentially damaging zones (minimal  $\langle \lambda_K \rangle$  values).

### 1.6.5 Impeller design optimization

Bioreactor design, and more specifically impeller design, have a significant impact on hydromechanical stress encountered by cells on microcarriers. Based on the previous characteristic parameters, as the Kolmogorov length scale  $\lambda_K$  and the turbulent energy dissipation rate  $\varepsilon$ , some studies compared different impeller design for MSC cultures on microcarriers in stirred tank bioreactors, in order to determine the *a priori* most suitable. Two teams worked on axial impeller comparison. In one hand, Collignon *et al.* compared 7 impellers in a 20 L bioreactor, involving 4 designs (TTP Mixel, A310 Lightnin, 3 streamed-blades VMI-Rayneri, Elephant Ear Applikon) with different diameters [158]. At  $N = N_{js}$ , impellers inducing the largest swept volumes led to the lowest agitations rates. They finally proposed the TTP Mixel with a small diameter and the Elephant Ear impellers as the most suitable for cell cultures, presenting the lowest mechanical stress. On the contrary, the A310 impellers were found to generate more hydromechanical stress. In the other hand, Jossen *et al.* performed an impeller design optimization of a dual-impellers configuration in the 2 L UniVessel<sup>®</sup> SU Bioreactor [193]. They started from the standard design of the UniVessel<sup>®</sup> SU Bioreactor and compared 9 geometrical configurations using



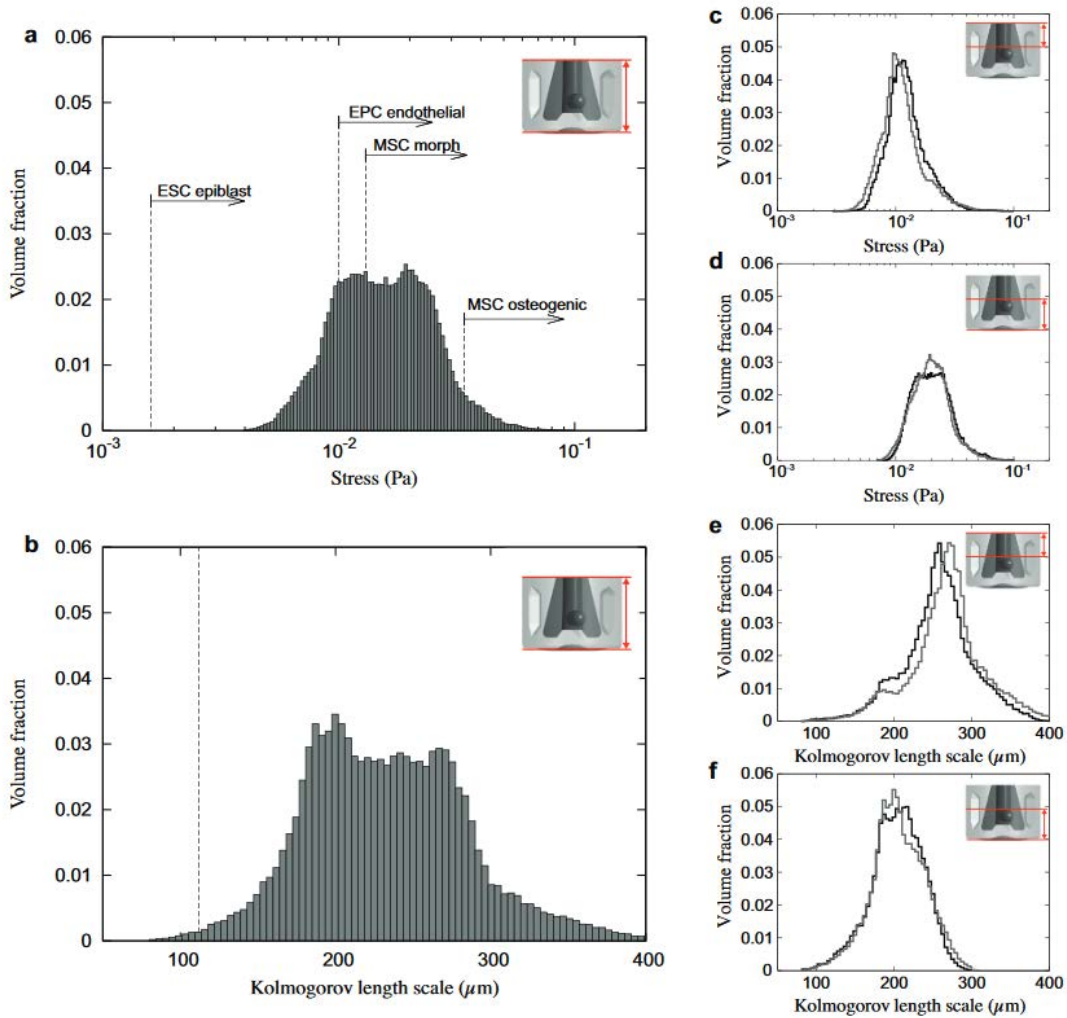


Figure 1.32: Time-averaged distributions within the entire bioreactor volume of a) stress (with shear stress thresholds at which stem cells have undergone morphological or biological changes), and b) Kolmogorov length scale  $\lambda_K$ , for the free-slip top boundary condition (dashed line for length of  $2/3$  the average microcarrier diameter). Time-averaged distributions in the bioreactor volume of stress for c)  $z > 27$  mm, and d)  $z < 27$  mm, and of Kolmogorov length scale for e)  $z > 27$  mm, and f)  $z < 27$  mm (grey line for distribution for the rigid free-slip top boundary condition ; black line for distribution for the outflow top boundary condition). For all subfigures, the ensemble-averaging time-period is  $t = 15$  s to  $t = 30$  s, and impeller speed  $N = 60$  rpm. Figure reproduced from Berry *et al.*, 2016 [194].

single-phase CFD at a constant agitation rate, by varying the impeller diameter, the blade slope angle and the off-bottom clearance. They aimed at enhancing axial discharge and minimizing the fluid shear stress. They finally demonstrated that the agitation rate to reach the just-suspended state was reduced by only slight modifications of the blade slope angle and the off-bottom clearance. For a particle concentration of 0.5 %,  $N_{js}$  passed from 122 rpm to 77 rpm after the optimization, and as a consequence,  $\varepsilon$  was significantly reduced. Multi-phase CFD was finally used to characterize the selected design at  $N = N_{js}$  for different particle concentrations. Examples of velocity fields are compared in Fig. 1.33,

between the initial and the modified configurations.

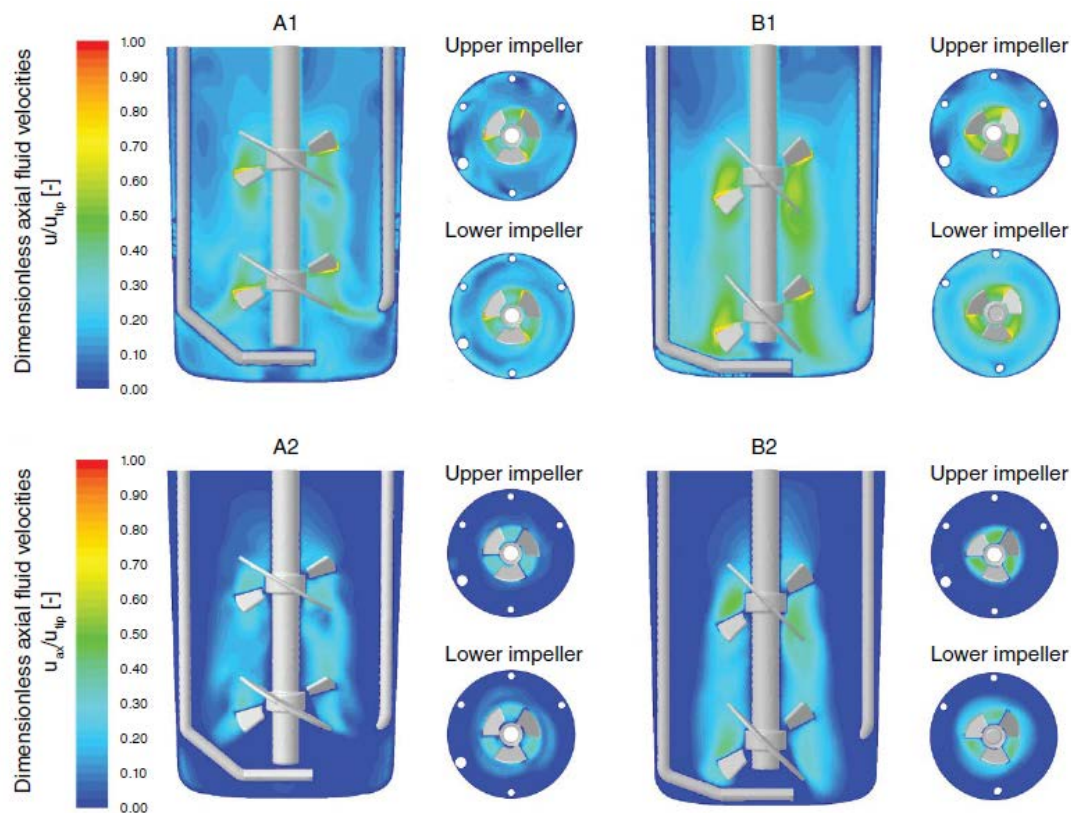


Figure 1.33: Dimensionless fluid magnitude (A1, B1) and axial (A2, B2) velocities in the standard (A) and modified (B) UniVessel<sup>®</sup> SU. Contour are given for the mid-reactor and mid-impeller planes. Figure reproduced from Jossen *et al.*, 2014 [193].

Other agitation modes were investigated, as in the work of Delafosse *et al.*, with a down-pumping impeller (HTPG impeller), an up-pumping impeller (Elephant Ear impeller) and a radial Rushton turbine in a 1.12 L bioreactor [163]. This study also presented novel results by taking into account the local shear stress related to the particle collisions. The impeller in down-pumping mode led to more potential damages to cells with 24 % of the fluid volume admitting  $(\lambda_K / d_p) < 1$  and was found to generate more collisions. A last study from Collignon *et al.* compared microcarrier suspensions at the just-suspended state with 5 impellers in a 200 mL bioreactor [164]. It involved a Rushton turbine (RT), an Elephant Ear impeller (EE-) and a Marine Propeller (MP-), both in up-pumping (-U) and down-pumping modes (-D). Agitation rates for the just-suspended state were found higher for impeller in up-pumping mode (130 rpm with the Elephant Ear impeller) than with the same designs in down-pumping mode (75 rpm with the Elephant Ear impeller). It may be noticed that axial impellers in up-pumping mode are generally used for mammalian cell cultures, regarding homogenization and gas dispersion. In the case of MSC cultures on microcarriers, these two conditions are not priority concerns. MSC are shear-stress

sensitive and so, the use of impellers in down-pumping mode may be investigated. In complementary, Collignon *et al.* compared the five impellers for a given  $\langle \varepsilon \rangle$  and found that the Elephant Ear impeller led to the highest exposure to both frequency and intensity of hydromechanical stress. However, for the specific application of MSC cultures, comparison may differ at  $N = N_{js}$ .

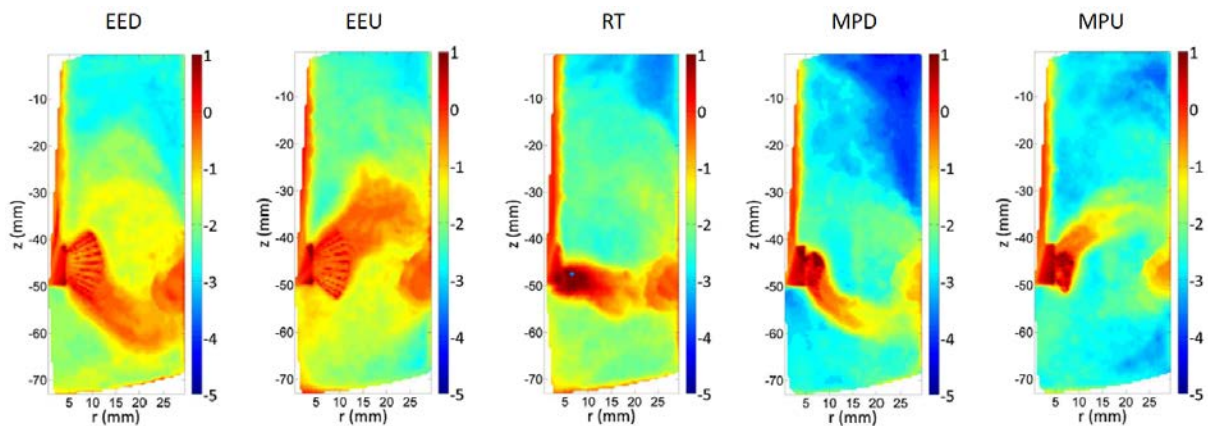


Figure 1.34: Dimensionless spatial distributions of the logarithm of turbulent dissipation rate  $\varepsilon/(N^3 \times d^2)$  simulated by LES for EED ( $N = 150$  rpm), EEU ( $N = 150$  rpm), RT ( $N = 173$  rpm), MPD ( $N = 308$  rpm) and MPU ( $N = 308$  rpm). All agitation conditions correspond to the same global power input of  $10^{-3} \text{ W kg}^{-1}$ . Figure reproduced from Collignon *et al.*, 2016 [164].

### Section summary

- In stirred systems, the impeller rotation induces fluid flow, with the formation of eddies with different sizes. The turbulence generated may nevertheless lead to potential cell damages. Eddies of approximately the same size than microcarriers are considered potentially damaging for adhered cells.
- The turbulent dissipation rate  $\varepsilon$  and the Kolmogorov length scale  $\lambda_K$  are generally used to relate the hydromechanical stress to the biological and physiological cell responses.
- The particle history should be integrated to the relationship between the hydrodynamics and the cell response, by taking into account stress intensity as well as duration and frequency exposure to the potentially damageable zones.
- The agitation design was found to strongly impact the hydromechanical stress encountered by the particles. CFD simulations were notably used to compare different designs for microcarrier suspension, or for the investigation of optimal configurations. CFD indeed allows to determine local parameters such as stress, turbulent dissipation rate  $\varepsilon$ , Kolmogorov length scale  $\lambda_K$  or fluid velocity.

## 1.7 Thesis aims and objectives

The present literature review clearly showed that MSC culture are more and more used in regenerative medicine, both in clinical trials and for new drug development. However, more investigations are still necessary to understand cell response to their environment and overcome some technological limits:

- *Ex vivo* MSC expansions involve an environment different from the cell niches of the human body, and often long term expansions in order to obtain a sufficient number of cells. The potential modifications of physiology due to these conditions still have to be fully characterized to ensure cell quality at the end of the process.
- With the imperative to preserve cell quality, the conditions used in the different process steps, from the cells isolation to their delivery, have to be carefully managed. Nowadays, studies tend to present results performed in clinical grade culture media and using animal-free microcarriers, but more information needs to be collected, for the different operating conditions involved. In parallel, closed bioreactors allowing the physical and chemical parameters control and monitoring are investigated, but more experimental and numerical investigations are needed to understand the whole process impact on cell quality.
- Another challenge concerns the cell quantity. MSC are anchorage-dependent and current expansion are performed in planar systems for clinical applications, limiting the process intensification. Other bioreactor designs are looked for to improve cell yields, with the use of microcarriers suspended by an agitation in some of them. More information on cell response to the environments induced by these designs have to be explored.
- Considered as a promising technology for scale-up, microcarriers are more and more studied, but efforts are still necessary to understand the relationship between cells and their environment (particle material impact on cell attachment, expansion and detachment capability, and on cell phenotype, hydromechanical stress and collisions due to the agitation...).

Aiming at proposing an integrated study, the objectives of the present thesis are distinguished into three result chapters. Each part will deal with specific questions related to the limits previously described:

- **Chapter 2:** WJ-MSK culture on microcarriers have to be improved and to be suitable for clinical grade applications. However, due to the difficulty to detach cells from microcarriers, information on cell distribution on particles is rare, and

most of the expansion results present in the literature are based on invasive or indirect methods leading to global values (nuclei counting after cell lysis, metabolite concentration kinetics, WST-1, MTT...). Based on this, is it possible to directly count cells on microcarriers and recover *in situ* local data? Then, which microcarrier would be the most suitable for WJ-MSC adhesion, expansion and detachments steps? Does it depend on the agitation mode? Finally, is it possible to develop a home-made microcarrier dedicated for MSC culture?

- **Chapter 3:** Current models to predict the just-suspended state are generally not developed for low-density particles such as microcarriers. Is it therefore possible to build a robust model to predict the microcarrier just-suspended state in STR by dimensional analysis? Moreover, studies already reported the use of CFD to characterize the hydrodynamics in STR during MSC cultures on microcarriers. Could a CFD-based approach also be able to predict the just-suspended state?
- **Chapter 4:** The agitation design is known to have an impact on the hydromechanical stress encountered by the particles, and also by the adhered cells. The literature review showed that most studies are based on volume-averaged values and do not systematically take into account the exposure frequency to this stress. How could it be integrated into CFD investigations for impeller design performance comparisons, with the aim of reduced stress applied on the solid phase? Is it then possible to optimize an impeller design, suitable for MSC cultures on microcarriers?

## References

- [1] J. Rowley, E. Abraham, A. Campbell, H. Brandwein, S. Oh, Meeting lot-size challenges of manufacturing adherent cells for therapy, *BioProcess International* 10 (2012) 16–22.
- [2] K. M. Panchalingam, S. Jung, L. Rosenberg, L. A. Behie, Bioprocessing strategies for the large-scale production of human mesenchymal stem cells: a review, *Stem Cell Research & Therapy* 6 (2015) 225–234.
- [3] C. J. Hewitt, K. Lee, A. W. Nienow, R. J. Thomas, M. Smith, C. R. Thomas, Expansion of human mesenchymal stem cells on microcarriers, *Biotechnology Letters* 33 (2011) 2325–2335.
- [4] J. Cohnheim, Über entzündung und eiterung, *Archiv für pathologische Anatomie und Physiologie und für klinische Medicin* 40 (1867) 1–79.
- [5] E. Goujon, Recherches expérimentales sur les propriétés physiologiques de la moelle des os, *Journal de l'Anatomie et de la Physiologie Normales et Pathologiques de l'Homme et des Animaux* 6 (1869) 399–412.
- [6] M. Tavassoli, W. H. Crosby, Transplantation of marrow to extramedullary sites, *Science* 161 (1968) 54–56.
- [7] A. J. Friedenstein, K. V. Petrakova, A. I. Kurolesova, G. P. Frolova, Heterotopic transplants of bone marrow, *Transplantation* 6 (1968) 230–247.
- [8] A. Friedenstein, R. Chailakhjan, K. Lalykina, The development of fibroblast colonies in monolayer cultures of guinea-pig bone marrow and spleen cells, *Cell Proliferation* 3 (1970) 393–403.
- [9] A. Friedenstein, R. Chailakhyan, U. Gerasimov, Bone marrow osteogenic stem cells: in vitro cultivation and transplantation in diffusion chambers, *Cell Proliferation* 20 (1987) 263–272.
- [10] M. Owen, A. Friedenstein, Stromal stem cells: marrow-derived osteogenic precursors, *Cell and Molecular Biology of Vertebrate Hard Tissues* 136 (1988) 42–60.
- [11] A. I. Caplan, Mesenchymal stem cells, *Journal of Orthopaedic Research* 9 (1991) 641–650.
- [12] M. F. Pittenger, A. M. Mackay, S. C. Beck, R. K. Jaiswal, R. Douglas, J. D. Mosca, M. A. Moorman, D. W. Simonetti, S. Craig, D. R. Marshak, Multilineage potential of adult human mesenchymal stem cells, *Science* 284 (1999) 143–147.
- [13] K. Le Blanc, Immunomodulatory effects of fetal and adult mesenchymal stem cells, *Cytotherapy* 5 (2003) 485–489.

- 
- [14] S. Aggarwal, M. F. Pittenger, Human mesenchymal stem cells modulate allogeneic immune cell responses, *Blood* 105 (2005) 1815–1822.
- [15] I. Ullah, R. B. Subbarao, G. J. Rho, Human mesenchymal stem cells-current trends and future prospective, *Bioscience Reports* 35 (2015) 1–18.
- [16] E. Horwitz, A. Keating, The nonhematopoietic mesenchymal stem cell committee workshop. nonhematopoietic mesenchymal stem cells: what are they?, *Cytotherapy* 2 (2000) 387–388.
- [17] E. Horwitz, K. Le Blanc, M. Dominici, I. Mueller, I. Slaper-Cortenbach, F. C. Marini, R. Deans, D. Krause, A. Keating, Clarification of the nomenclature for MSC: The international society for cellular therapy position statement, *Cytotherapy* 7 (2005) 393–395.
- [18] M. Dominici, K. Le Blanc, I. Mueller, I. Slaper-Cortenbach, F. Marini, D. Krause, R. Deans, A. Keating, D. Prockop, E. Horwitz, Minimal criteria for defining multipotent mesenchymal stromal cells. the international society for cellular therapy position statement, *Cytotherapy* 8 (2006) 315–317.
- [19] P. Bianco, P. G. Robey, P. J. Simmons, Mesenchymal stem cells: revisiting history, concepts, and assays, *Cell Stem Cell* 2 (2008) 313–319.
- [20] M. Krampera, J. Galipeau, Y. Shi, K. Tarte, L. Sensebe, Immunological characterization of multipotent mesenchymal stromal cells - the international society for cellular therapy (ISCT) working proposal, *Cytotherapy* 15 (2013) 1054–1061.
- [21] C. Martin, É. Olmos, M.-L. Collignon, N. De Isla, F. Blanchard, I. Chevalot, A. Marc, E. Guedon, Revisiting MSC expansion from critical quality attributes to critical culture process parameters, *Process Biochemistry* 59 (2017) 231–243.
- [22] J. A. Thomson, J. Itskovitz-Eldor, S. S. Shapiro, M. A. Waknitz, J. J. Swiergiel, V. S. Marshall, J. M. Jones, Embryonic stem cell lines derived from human blastocysts, *Science* 282 (1998) 1145–1147.
- [23] Y. Chung, I. Klimanskaya, S. Becker, T. Li, M. Maserati, S.-J. Lu, T. Zdravkovic, D. Ilic, O. Genbacev, S. Fisher, et al., Human embryonic stem cell lines generated without embryo destruction, *Cell Stem Cell* 2 (2008) 113–117.
- [24] C. M. Prodingler, J. Reichelt, J. W. Bauer, M. Laimer, Current and future perspectives of stem cell therapy in dermatology, *Annals of Dermatology* 29 (2017) 667–687.
- [25] F. A. Carrion, F. E. Figueroa, Mesenchymal stem cells for the treatment of systemic lupus erythematosus: is the cure for connective tissue diseases within connective tissue?, *Stem Cell Research & Therapy* 2 (2011) 1–8.
- [26] A. I. Caplan, S. P. Bruder, Mesenchymal stem cells: building blocks for molecular medicine in the 21st century, *Trends in Molecular Medicine* 7 (2001) 259–264.
- [27] A. I. Caplan, Mesenchymal stem cells: cell-based reconstructive therapy in orthopedics, *Tissue Engineering* 11 (2005) 1198–1211.



- [28] H. Petite, V. Viateau, W. Bensaid, A. Meunier, C. de Pollak, M. Bourguignon, K. Oudina, L. Sedel, G. Guillemain, Tissue-engineered bone regeneration, *Nature Biotechnology* 18 (2000) 959–963.
- [29] P. Bianco, P. G. Robey, Stem cells in tissue engineering, *Nature* 414 (2001) 118–121.
- [30] A. I. Caplan, J. E. Dennis, Mesenchymal stem cells as trophic mediators, *Journal of Cellular Biochemistry* 98 (2006) 1076–1084.
- [31] A. I. Caplan, Adult mesenchymal stem cells for tissue engineering versus regenerative medicine, *Journal of Cellular Physiology* 213 (2007) 341–347.
- [32] A. Forte, M. Cipollaro, U. Galderisi, Genetic, epigenetic and stem cell alterations in endometriosis: new insights and potential therapeutic perspectives, *Clinical Science* 126 (2014) 123–138.
- [33] L. da Silva Meirelles, A. M. Fontes, D. T. Covas, A. I. Caplan, Mechanisms involved in the therapeutic properties of mesenchymal stem cells, *Cytokine & Growth Factor Reviews* 20 (2009) 419–427.
- [34] K. Le Blanc, O. Ringden, Immunomodulation by mesenchymal stem cells and clinical experience, *Journal of Internal Medicine* 262 (2007) 509–525.
- [35] M. E. Bernardo, W. E. Fibbe, Mesenchymal stromal cells: sensors and switchers of inflammation, *Cell Stem Cell* 13 (2013) 392–402.
- [36] D. J. Prockop, J. Y. Oh, Mesenchymal stem/stromal cells (MSCs): Role as guardians of inflammation, *Molecular Therapy* 20 (2012) 14–20.
- [37] R. C. Lai, T. S. Chen, S. K. Lim, Mesenchymal stem cell exosome: a novel stem cell-based therapy for cardiovascular disease, *Regenerative Medicine* 6 (2011) 481–492.
- [38] R. C. Lai, R. W. Y. Yeo, S. K. Lim, Mesenchymal stem cell exosomes, in: *Seminars in Cell & Developmental Biology*, volume 40, Elsevier, pp. 82–88.
- [39] V. Sordi, Mesenchymal stem cell homing capacity, *Transplantation* 87 (2009) 42–45.
- [40] T. Squillaro, G. Peluso, U. Galderisi, Clinical trials with mesenchymal stem cells: an update, *Cell Transplantation* 25 (2016) 829–848.
- [41] A. L. Ponte, E. Marais, N. Gallay, A. Langonne, B. Delorme, O. Herault, P. Charbord, J. Domenech, The in vitro migration capacity of human bone marrow mesenchymal stem cells: comparison of chemokine and growth factor chemotactic activities, *Stem Cells* 25 (2007) 1737–1745.
- [42] J. Holland, Fixing a broken drug development process, *Journal of Commercial Biotechnology* 19 (2013) 5–6.
- [43] C. P. Adams, V. V. Brantner, Estimating the cost of new drug development: is it really \$802 million?, *Health Affairs* 25 (2006) 420–428.

- 
- [44] J.-w. Cao, L. Zhang, Y. Li, Q. Yang, W.-h. Fu, X.-c. Wang, W.-l. Huang, Trends and prospects of stem cell research in china, *Chinese Medical Sciences Journal* 31 (2016) 116–120.
- [45] Y. Najima, K. Ohashi, Mesenchymal stem cells: The first approved stem cell drug in japan, *Japanese Hematopoietic Cell Transplant Society* 6 (2017) 125–132.
- [46] I. Elboghady, H. Hassanzadeh, B. E. Stein, H. S. An, Controversies and potential risk of mesenchymal stem cells application, *Seminars in Spine Surgery* 27 (2015) 103–106.
- [47] J. Kim, J. W. Kang, J. H. Park, Y. Choi, K. S. Choi, K. D. Park, D. H. Baek, S. K. Seong, H.-K. Min, H. S. Kim, Biological characterization of long-term cultured human mesenchymal stem cells, *Archives of Pharmacal Research* 32 (2009) 117–126.
- [48] F. Casiraghi, G. Remuzzi, M. Abbate, N. Perico, Multipotent mesenchymal stromal cell therapy and risk of malignancies, *Stem Cell Reviews and Reports* 9 (2013) 65–79.
- [49] D. Rubio, S. Garcia, M. F. Paz, T. De la Cueva, L. A. Lopez-Fernandez, A. C. Lloyd, J. Garcia-Castro, A. Bernad, Molecular characterization of spontaneous mesenchymal stem cell transformation, *PLOS one* 3 (2008) 1–15.
- [50] R. Izadpanah, D. Kaushal, C. Kriedt, F. Tsien, B. Patel, J. Dufour, B. A. Bunnell, Long-term in vitro expansion alters the biology of adult mesenchymal stem cells, *Cancer Research* 68 (2008) 4229–4238.
- [51] W. Zhu, J. Chen, X. Cong, S. Hu, X. Chen, Hypoxia and serum deprivation-induced apoptosis in mesenchymal stem cells, *Stem Cells* 24 (2006) 416–425.
- [52] E. Kearney, P. Prendergast, V. Campbell, Mechanisms of strain-mediated mesenchymal stem cell apoptosis, *Journal of Biomechanical Engineering* 130 (2008) 061004.
- [53] A. H. Klopp, A. Gupta, E. Spaeth, M. Andreeff, F. Marini, Concise review: dissecting a discrepancy in the literature: do mesenchymal stem cells support or suppress tumor growth?, *Stem Cells* 29 (2011) 11–19.
- [54] M. E. Bernardo, N. Zaffaroni, F. Novara, A. M. Cometa, M. A. Avanzini, A. Moretta, D. Montagna, R. Maccario, R. Villa, M. G. Daidone, et al., Human bone marrow-derived mesenchymal stem cells do not undergo transformation after long-term in vitro culture and do not exhibit telomere maintenance mechanisms, *Cancer Research* 67 (2007) 9142–9149.
- [55] S. A. Bergfeld, Y. A. DeClerck, Bone marrow-derived mesenchymal stem cells and the tumor microenvironment, *Cancer and Metastasis Reviews* 29 (2010) 249–261.
- [56] Y.-r. Lu, Y. Yuan, X.-j. Wang, L.-l. Wei, Y.-n. Chen, C. Cong, S.-f. Li, D. Long, W.-d. Tan, Y.-q. Mao, et al., The growth inhibitory effect of mesenchymal stem cells on tumor cells in vitro and in vivo, *Cancer Biology & Therapy* 7 (2008) 245–251.

- [57] M. M. Lalu, L. McIntyre, C. Pugliese, D. Fergusson, B. W. Winston, J. C. Marshall, J. Granton, D. J. Stewart, Safety of cell therapy with mesenchymal stromal cells (safecell): a systematic review and meta-analysis of clinical trials, *PLOS one* 7 (2012) 1–21.
- [58] J. E. Dennis, A. I. Caplan, Bone marrow mesenchymal stem cells, in: *Stem Cells Handbook*, Springer, 2004, pp. 107–117.
- [59] B. Puissant, C. Barreau, P. Bourin, C. Clavel, J. Corre, C. Bousquet, C. Taureau, B. Cousin, M. Abbal, P. Laharrague, et al., Immunomodulatory effect of human adipose tissue-derived adult stem cells: comparison with bone marrow mesenchymal stem cells, *British Journal of Haematology* 129 (2005) 118–129.
- [60] C. De Bari, F. Dell’Accio, P. Tylzanowski, F. P. Luyten, Multipotent mesenchymal stem cells from adult human synovial membrane, *Arthritis & Rheumatology* 44 (2001) 1928–1942.
- [61] M. J. Griffiths, D. Bonnet, S. M. Janes, Stem cells of the alveolar epithelium, *The Lancet* 366 (2005) 249–260.
- [62] W. Jackson, A. Aragon, F. Djouad, Y. Song, S. Koehler, L. Nesti, R. Tuan, Mesenchymal progenitor cells derived from traumatized human muscle, *Journal of Tissue Engineering and Regenerative Medicine* 3 (2009) 129–138.
- [63] K. Bieback, S. Kern, H. Klüter, H. Eichler, Critical parameters for the isolation of mesenchymal stem cells from umbilical cord blood, *Stem Cells* 22 (2004) 625–634.
- [64] H.-S. Wang, S.-C. Hung, S.-T. Peng, C.-C. Huang, H.-M. Wei, Y.-J. Guo, Y.-S. Fu, M.-C. Lai, C.-C. Chen, Mesenchymal stem cells in the wharton’s jelly of the human umbilical cord, *Stem Cells* 22 (2004) 1330–1337.
- [65] J. Chahla, S. Mannava, M. E. Cinque, A. G. Geeslin, D. Codina, R. F. LaPrade, Bone marrow aspirate concentrate harvesting and processing technique, *Arthroscopy Techniques* 6 (2017) 441–445.
- [66] S. Schreml, P. Babilas, S. Fruth, E. Orsó, G. Schmitz, M. B. Mueller, M. Nerlich, L. Prantl, Harvesting human adipose tissue-derived adult stem cells: resection versus liposuction, *Cytotherapy* 11 (2009) 947–957.
- [67] D. L. Troyer, M. L. Weiss, Concise review: Wharton’s jelly-derived cells are a primitive stromal cell population, *Stem Cells* 26 (2008) 591–599.
- [68] H. Yoshimura, T. Muneta, A. Nimura, A. Yokoyama, H. Koga, I. Sekiya, Comparison of rat mesenchymal stem cells derived from bone marrow, synovium, periosteum, adipose tissue, and muscle, *Cell and Tissue Research* 327 (2007) 449–462.
- [69] S. Karahuseyinoglu, O. Cinar, E. Kilic, F. Kara, G. G. Akay, D. Ö. Demiralp, A. Tukun, D. Uckan, A. Can, Biology of stem cells in human umbilical cord stroma: in situ and in vitro surveys, *Stem Cells* 25 (2007) 319–331.

- 
- [70] M.-Y. Chen, P.-C. Lie, Z.-L. Li, X. Wei, Endothelial differentiation of wharton's jelly-derived mesenchymal stem cells in comparison with bone marrow-derived mesenchymal stem cells, *Experimental Hematology* 37 (2009) 629–640.
- [71] C. Rebelatto, A. Aguiar, M. Moretao, A. Senegaglia, P. Hansen, F. Barchiki, J. Oliveira, J. Martins, C. Kuligovski, F. Mansur, et al., Dissimilar differentiation of mesenchymal stem cells from bone marrow, umbilical cord blood, and adipose tissue, *Experimental Biology and Medicine* 233 (2008) 901–913.
- [72] D. G. Phinney, Biochemical heterogeneity of mesenchymal stem cell populations: clues to their therapeutic efficacy, *Cell Cycle* 6 (2007) 2884–2889.
- [73] M. Pevsner-Fischer, S. Levin, D. Zipori, The origins of mesenchymal stromal cell heterogeneity, *Stem Cell Reviews and Reports* 7 (2011) 560–568.
- [74] T. Nagamura-Inoue, H. He, Umbilical cord-derived mesenchymal stem cells: Their advantages and potential clinical utility, *World Journal of Stem Cells* 6 (2014) 195–202.
- [75] D.-W. Kim, M. Staples, K. Shinozuka, P. Pantcheva, S.-D. Kang, C. V. Borlongan, Wharton's jelly-derived mesenchymal stem cells: phenotypic characterization and optimizing their therapeutic potential for clinical applications, *International Journal of Molecular Sciences* 14 (2013) 11692–11712.
- [76] L. Pierdomenico, P. Lanuti, R. Lachmann, G. Grifone, E. Cianci, L. Gialò, S. Pacella, M. Romano, E. Vitacolonna, S. Miscia, et al., Diabetes mellitus during pregnancy interferes with the biological characteristics of wharton's jelly mesenchymal stem cells, *The Open Tissue Engineering and Regenerative Medicine Journal* 4 (2011).
- [77] K. Cierpka, C. L. Elseberg, K. Niss, M. Kassem, D. Salzig, P. Czermak, hMSC production in disposable bioreactors with regards to GMP and PAT, *Chemie Ingenieur Technik* 85 (2013) 67–75.
- [78] D. Baksh, J. E. Davies, P. W. Zandstra, Adult human bone marrow-derived mesenchymal progenitor cells are capable of adhesion-independent survival and expansion, *Experimental Hematology* 31 (2003) 723–732.
- [79] S. Sart, A.-C. Tsai, Y. Li, T. Ma, Three-dimensional aggregates of mesenchymal stem cells: cellular mechanisms, biological properties, and applications, *Tissue Engineering Part B: Reviews* 20 (2013) 365–380.
- [80] A. C. Schnitzler, A. Verma, D. E. Kehoe, D. Jing, J. R. Murrell, K. A. Der, M. Aysola, P. J. Rapiejko, S. Punreddy, M. S. Rook, Bioprocessing of human mesenchymal stem/stromal cells for therapeutic use: Current technologies and challenges, *Biochemical Engineering Journal* 108 (2016) 3–13.
- [81] C. Elseberg, J. Leber, T. Weidner, P. Czermak, The challenge of human mesenchymal stromal cell expansion: Current and prospective answers, in: *New Insights into Cell Culture Technology*, InTech, 2017, pp. 99–134.

- [82] N. Fekete, M. T. Rojewski, R. Lotfi, H. Schrezenmeier, Essential components for ex vivo proliferation of mesenchymal stromal cells, *Tissue Engineering Part C: Methods* 20 (2013) 129–139.
- [83] D. W. Jayme, S. R. Smith, Media formulation options and manufacturing process controls to safeguard against introduction of animal origin contaminants in animal cell culture, *Cytotechnology* 33 (2000) 27–36.
- [84] F. d. Santos, P. Z. Andrade, M. M. Abecasis, J. M. Gimble, L. G. Chase, A. M. Campbell, S. Boucher, M. C. Vemuri, C. L. d. Silva, J. M. Cabral, Toward a clinical-grade expansion of mesenchymal stem cells from human sources: a microcarrier-based culture system under xeno-free conditions, *Tissue Engineering Part C: Methods* 17 (2011) 1201–1210.
- [85] C. Tekkate, G. P. Gunasingh, K. Cherian, K. Sankaranarayanan, Humanized stem cell culture techniques: the animal serum controversy, *Stem Cells International* 2011 (2011) 1–14.
- [86] N.B. Azouna, F. Jenhani, Z. Regaya, L. Berraeis, T. B. Othman, E. Ducrocq, J. Domenech, Phenotypical and functional characteristics of mesenchymal stem cells from bone marrow: comparison of culture using different media supplemented with human platelet lysate or fetal bovine serum, *Stem Cell Research & Therapy* 3 (2012) 6–20.
- [87] H. Hemeda, J. Kalz, G. Walenda, M. Lohmann, W. Wagner, Heparin concentration is critical for cell culture with human platelet lysate, *Cytotherapy* 15 (2013) 1174–1181.
- [88] S. Laner-Plamberger, T. Lener, D. Schmid, D. A. Streif, T. Salzer, M. Öller, C. Hauser-Kronberger, T. Fischer, V. R. Jacobs, K. Schallmoser, et al., Mechanical fibrinogen-depletion supports heparin-free mesenchymal stem cell propagation in human platelet lysate, *Journal of Translational Medicine* 13 (2015) 354.
- [89] K. Pachler, T. Lener, D. Streif, Z. A. Dunai, A. Desgeorges, M. Feichtner, M. Öller, K. Schallmoser, E. Rohde, M. Gimona, A good manufacturing practice–grade standard protocol for exclusively human mesenchymal stromal cell–derived extracellular vesicles, *Cytotherapy* 19 (2017) 458–472.
- [90] S. Sart, Y.-J. Schneider, S. N. Agathos, Influence of culture parameters on ear mesenchymal stem cells expanded on microcarriers, *Journal of Biotechnology* 150 (2010) 149–160.
- [91] F. dos Santos, A. Campbell, A. Fernandes-Platzgummer, P. Z. Andrade, J. M. Gimble, Y. Wen, S. Boucher, M. C. Vemuri, C. L. da Silva, J. Cabral, A xenogeneic-free bioreactor system for the clinical-scale expansion of human mesenchymal stem/stromal cells, *Biotechnology and Bioengineering* 111 (2014) 1116–1127.
- [92] G. Eibes, F. dos Santos, P. Z. Andrade, J. S. Boura, M. M. Abecasis, C. L. da Silva, J. M. Cabral, Maximizing the ex vivo expansion of human mesenchymal stem cells

- using a microcarrier-based stirred culture system, *Journal of Biotechnology* 146 (2010) 194–197.
- [93] B. Cunha, T. Aguiar, M. M. Silva, R. J. Silva, M. F. Sousa, E. Pineda, C. Peixoto, M. J. Carrondo, M. Serra, P. M. Alves, Exploring continuous and integrated strategies for the up-and downstream processing of human mesenchymal stem cells, *Journal of Biotechnology* 213 (2015) 97–108.
- [94] D. Eibl, R. Eibl, R. Pörtner, Mammalian cell culture technology: an emerging field, *Cell and Tissue Reaction Engineering* (2009) 3–11.
- [95] V. Jossen, R. Pörtner, S. C. Kaiser, M. Kraume, D. Eibl, R. Eibl, Mass production of mesenchymal stem cells-impact of bioreactor design and flow conditions on proliferation and differentiation, *Cells and Biomaterials in Regenerative Medicine* (2014) 119–174.
- [96] N. Fekete, M. T. Rojewski, D. Fürst, L. Kreja, A. Ignatius, J. Dausend, H. Schrezenmeier, GMP-compliant isolation and large-scale expansion of bone marrow-derived MSC, *PLOS one* 7 (2012) 1–14.
- [97] K. Falkowitz, J. Staggert, V. Wedege, A system approach to improving yields in a disposable bioreactor, *BioProcess International* 4 (2006) 56–62.
- [98] P. Aparecida Tozetti, S. R. Caruso, A. Mizukami, T. Risque Fernandes, F. B. da Silva, F. Traina, D. T. Covas, M. D. Orellana, K. Swiech, Expansion strategies for human mesenchymal stromal cells culture under xeno-free conditions, *Biotechnology Progress* 33 (2017) 1358–1367.
- [99] A. Van Wezel, Growth of cell-strains and primary cells on micro-carriers in homogeneous culture, *Nature* 216 (1967) 64–65.
- [100] A. S. Simaria, S. Hassan, H. Varadaraju, J. Rowley, K. Warren, P. Vanek, S. S. Farid, Allogeneic cell therapy bioprocess economics and optimization: Single-use cell expansion technologies, *Biotechnology and Bioengineering* 111 (2014) 69–83.
- [101] T. Ma, A.-C. Tsai, Y. Liu, Biomanufacturing of human mesenchymal stem cells in cell therapy: Influence of microenvironment on scalable expansion in bioreactors, *Biochemical Engineering Journal* 108 (2016) 44–50.
- [102] X. Zhang, M. Stettler, D. De Sanctis, M. Perrone, N. Parolini, M. Discacciati, M. De Jesus, D. Hacker, A. Quarteroni, F. Wurm, Use of orbital shaken disposable bioreactors for mammalian cell cultures from the milliliter-scale to the 1,000-liter scale, *Disposable Bioreactors* (2009) 33–53.
- [103] K. Y. Tan, K. L. Teo, J. F. Lim, A. K. Chen, S. Reuveny, S. K. Oh, Serum-free media formulations are cell line-specific and require optimization for microcarrier culture, *Cytotherapy* 17 (2015) 1152–1165.
- [104] N. Timmins, M. Kiel, M. Günther, C. Heazlewood, M. Doran, G. Brooke, K. Atkinson, Closed system isolation and scalable expansion of human placental mesenchymal stem cells, *Biotechnology and Bioengineering* 109 (2012) 1817–1826.

- [105] V. Jossen, C. Schirmer, D. Mostafa Sindi, R. Eibl, M. Kraume, R. Pörtner, D. Eibl, Theoretical and practical issues that are relevant when scaling up hMSC microcarrier production processes, *Stem Cells International* 2016 (2016).
- [106] T. Lawson, D. E. Kehoe, A. C. Schnitzler, P. J. Rapiejko, K. A. Der, K. Philbrick, S. Punreddy, S. Rigby, R. Smith, Q. Feng, J. R. Murrell, M. S. Rook, Process development for expansion of human mesenchymal stromal cells in a 50 L single-use stirred tank bioreactor, *Biochemical Engineering Journal* 120 (2017) 49–62.
- [107] X. Yuan, A.-C. Tsai, I. Farrance, J. A. Rowley, T. Ma, Aggregation of culture expanded human mesenchymal stem cells in microcarrier-based bioreactor, *Biochemical Engineering Journal* 131 (2018) 39–46.
- [108] M. F. Sousa, M. M. Silva, D. Giroux, Y. Hashimura, R. Wesselschmidt, B. Lee, A. Roldão, M. J. Carrondo, P. M. Alves, M. Serra, Production of oncolytic adenovirus and human mesenchymal stem cells in a single-use, vertical-wheel bioreactor system: Impact of bioreactor design on performance of microcarrier-based cell culture processes, *Biotechnology Progress* 31 (2015) 1600–1612.
- [109] C. Schirmaier, V. Jossen, S. C. Kaiser, F. Jüngerkes, S. Brill, A. Safavi-Nab, A. Siehoff, C. Bos, D. Eibl, R. Eibl, Scale-up of adipose tissue-derived mesenchymal stem cell production in stirred single-use bioreactors under low-serum conditions, *Engineering in Life Sciences* 14 (2014) 292–303.
- [110] S. Hong, E. Ergezen, R. Lec, K. A. Barbee, Real-time analysis of cell–surface adhesive interactions using thickness shear mode resonator, *Biomaterials* 27 (2006) 5813–5820.
- [111] A. A. Khalili, M. R. Ahmad, A review of cell adhesion studies for biomedical and biological applications, *International Journal of Molecular Sciences* 16 (2015) 18149–18184.
- [112] D. Salzig, J. Leber, K. Merkewitz, M. C. Lange, N. Köster, P. Czermak, Attachment, growth, and detachment of human mesenchymal stem cells in a chemically defined medium, *Stem Cells International* 2016 (2016) 1–10.
- [113] Q. A. Rafiq, K. Coopman, A. W. Nienow, C. J. Hewitt, Systematic microcarrier screening and agitated culture conditions improves human mesenchymal stem cell yield in bioreactors, *Biotechnology Journal* 11 (2016).
- [114] D. Schop, F. Janssen, E. Borgart, J. D. de Bruijn, R. van Dijkhuizen-Radersma, Expansion of mesenchymal stem cells using a microcarrier-based cultivation system: growth and metabolism, *Journal of Tissue Engineering and Regenerative Medicine* 2 (2008) 126–135.
- [115] A. M. Soure, A. Fernandes-Platzgummer, F. Moreira, C. Lilaia, S.-H. Liu, C.-P. Ku, Y.-F. Huang, W. Milligan, J. Cabral, C. L. Silva, Integrated culture platform based on a human platelet lysate supplement for the isolation and scalable manufacturing of umbilical cord matrix-derived mesenchymal stem/stromal cells, *Journal of Tissue Engineering and Regenerative Medicine* 11 (2017) 1630–1640.

- 
- [116] B. Ladoux, A. Nicolas, Physically based principles of cell adhesion mechanosensitivity in tissues, *Reports on Progress in Physics* 75 (2012) 1–26.
- [117] L. Champion, M. I. Linder, U. Kutay, Cellular reorganization during mitotic entry, *Trends in Cell Biology* 27 (2017) 26–41.
- [118] N. Ramkumar, B. Baum, Coupling changes in cell shape to chromosome segregation, *Nature Reviews Molecular Cell Biology* 17 (2016) 511–521.
- [119] J. Leber, J. Barezai, M. Blumenstock, B. Pospisil, D. Salzig, P. Czermak, Microcarrier choice and bead-to-bead transfer for human mesenchymal stem cells in serum-containing and chemically defined media, *Process Biochemistry* 59 (2017) 255–265.
- [120] A. Pietuch, A. Janshoff, Mechanics of spreading cells probed by atomic force microscopy, *Open Biology* 3 (2013) 1–10.
- [121] A. Garg, D. D. Houlihan, V. Aldridge, S. Suresh, K. K. Li, A. L. King, R. Sutaria, J. Fear, R. H. Bhogal, P. F. Lalor, et al., Non-enzymatic dissociation of human mesenchymal stromal cells improves chemokine-dependent migration and maintains immunosuppressive function, *Cytotherapy* 16 (2014) 545–559.
- [122] M. Takeichi, T. Okada, Roles of magnesium and calcium ions in cell-to-substrate adhesion, *Experimental Cell Research* 74 (1972) 51–60.
- [123] C. R. Duffy, R. Zhang, S.-E. How, A. Lilienkampf, P. A. De Sousa, M. Bradley, Long term mesenchymal stem cell culture on a defined synthetic substrate with enzyme free passaging, *Biomaterials* 35 (2014) 5998–6005.
- [124] A. Tamura, J. Kobayashi, M. Yamato, T. Okano, Thermally responsive microcarriers with optimal poly (N-isopropylacrylamide) grafted density for facilitating cell adhesion/detachment in suspension culture, *Acta Biomaterialia* 8 (2012) 3904–3913.
- [125] K. D. Newman, M. W. McBurney, Poly (D, L lactic-co-glycolic acid) microspheres as biodegradable microcarriers for pluripotent stem cells, *Biomaterials* 25 (2004) 5763–5771.
- [126] Q. A. Rafiq, M. P. Hanga, T. R. Heathman, K. Coopman, A. W. Nienow, D. J. Williams, C. J. Hewitt, Process development of human multipotent stromal cell microcarrier culture using an automated high-throughput microbioreactor, *Biotechnology and Bioengineering* 114 (2017) 2253–2266.
- [127] H. S. Yang, O. Jeon, S. H. Bhang, S.-H. Lee, B.-S. Kim, Suspension culture of mammalian cells using thermosensitive microcarrier that allows cell detachment without proteolytic enzyme treatment, *Cell Transplantation* 19 (2010) 1123–1132.
- [128] S. Frauenschuh, E. Reichmann, Y. Ibold, P. M. Goetz, M. Sittinger, J. Ringe, A microcarrier-based cultivation system for expansion of primary mesenchymal stem cells, *Biotechnology Progress* 23 (2007) 187–193.



- [129] S. R. Caruso, M. D. Orellana, A. Mizukami, T. R. Fernandes, A. M. Fontes, C. A. Suazo, V. C. Oliveira, D. T. Covas, K. Swiech, Growth and functional harvesting of human mesenchymal stromal cells cultured on a microcarrier-based system, *Biotechnology Progress* 30 (2014) 889–895.
- [130] L.-Y. Sun, D.-K. Hsieh, W.-S. Syu, Y.-S. Li, H.-T. Chiu, T.-W. Chiou, Cell proliferation of human bone marrow mesenchymal stem cells on biodegradable microcarriers enhances in vitro differentiation potential, *Cell Proliferation* 43 (2010) 445–456.
- [131] S. Kaiser, V. Jossen, C. Schirmaier, D. Eibl, S. Brill, C. van den Bos, R. Eibl, Fluid flow and cell proliferation of mesenchymal adipose-derived stem cells in small-scale, stirred, single-use bioreactors, *Chemie Ingenieur Technik* 85 (2013) 95–102.
- [132] M. Chen, X. Wang, Z. Ye, Y. Zhang, Y. Zhou, W.-S. Tan, A modular approach to the engineering of a centimeter-sized bone tissue construct with human amniotic mesenchymal stem cells-laden microcarriers, *Biomaterials* 32 (2011) 7532–7542.
- [133] A. K.-L. Chen, Y. K. Chew, H. Y. Tan, S. Reuveny, S. K. W. Oh, Increasing efficiency of human mesenchymal stromal cell culture by optimization of microcarrier concentration and design of medium feed, *Cytotherapy* 17 (2015) 163–173.
- [134] T. K.-P. Goh, Z.-Y. Zhang, A. K.-L. Chen, S. Reuveny, M. Choolani, J. K. Y. Chan, S. K.-W. Oh, Microcarrier culture for efficient expansion and osteogenic differentiation of human fetal mesenchymal stem cells, *BioResearch Open Access* 2 (2013) 84–97.
- [135] Q. A. Rafiq, K. M. Brosnan, K. Coopman, A. W. Nienow, C. J. Hewitt, Culture of human mesenchymal stem cells on microcarriers in a 5 L stirred-tank bioreactor, *Biotechnology Letters* 35 (2013) 1233–1245.
- [136] T. R. Heathman, A. Stolzing, C. Fabian, Q. A. Rafiq, K. Coopman, A. W. Nienow, B. Kara, C. J. Hewitt, Scalability and process transfer of mesenchymal stromal cell production from monolayer to microcarrier culture using human platelet lysate, *Cytotherapy* 18 (2016) 523–535.
- [137] Y. Yuan, M. S. Kallos, C. Hunter, A. Sen, Improved expansion of human bone marrow-derived mesenchymal stem cells in microcarrier-based suspension culture, *Journal of Tissue Engineering and Regenerative Medicine* 8 (2014) 210–225.
- [138] C. Ferrari, F. Balandras, E. Guedon, E. Olmos, I. Chevalot, A. Marc, Limiting cell aggregation during mesenchymal stem cell expansion on microcarriers, *Biotechnology Progress* 28 (2012) 780–787.
- [139] S. Sart, Y.-J. Schneider, S. N. Agathos, Ear mesenchymal stem cells: an efficient adult multipotent cell population fit for rapid and scalable expansion, *Journal of Biotechnology* 139 (2009) 291–299.
- [140] J. Hupfeld, I. H. Gorr, C. Schwald, N. Beaucamp, K. Wiechmann, K. Kuentzer, R. Huss, B. Rieger, M. Neubauer, H. Wegmeyer, Modulation of mesenchymal stromal cell characteristics by microcarrier culture in bioreactors, *Biotechnology and Bioengineering* 111 (2014) 2290–2302.

- 
- [141] K. Siddiquee, M. Sha, Billion-cell hypoxic expansion of human mesenchymal stem cells in bioBLU® 5c single-use vessels, *BioProcessing* 14 (2015) 1538–8786.
- [142] Y. Yu, K. Li, C. Bao, T. Liu, Y. Jin, H. Ren, W. Yun, Ex vitro expansion of human placenta-derived mesenchymal stem cells in stirred bioreactor, *Applied Biochemistry and Biotechnology* 159 (2009) 110–118.
- [143] A. E. Turner, C. Yu, J. Bianco, J. F. Watkins, L. E. Flynn, The performance of decellularized adipose tissue microcarriers as an inductive substrate for human adipose-derived stem cells, *Biomaterials* 33 (2012) 4490–4499.
- [144] G. Zhao, F. Liu, S. Lan, P. Li, L. Wang, J. Kou, X. Qi, R. Fan, D. Hao, C. Wu, et al., Large-scale expansion of wharton’s jelly-derived mesenchymal stem cells on gelatin microbeads, with retention of self-renewal and multipotency characteristics and the capacity for enhancing skin wound healing, *Stem Cell Research & Therapy* 6 (2015) 38–54.
- [145] M. Gadelorge, M. Bourdens, N. Espagnolle, C. Bardiaux, J. Murrell, L. Savary, S. Ribaud, B. Chaput, L. Sensebé, Clinical-scale expansion of adipose-derived stromal cells starting from stromal vascular fraction in a single-use bioreactor: proof of concept for autologous applications, *Journal of Tissue Engineering and Regenerative Medicine* 12 (2018) 129–141.
- [146] F. Petry, J. R. Smith, J. Leber, D. Salzig, P. Czermak, M. L. Weiss, Manufacturing of human umbilical cord mesenchymal stromal cells on microcarriers in a dynamic system for clinical use, *Stem Cells International* 2016 (2016).
- [147] M. Hervy, J. L. Weber, M. Pecheul, P. Dolley-Sonneville, D. Henry, Y. Zhou, Z. Melkounian, Long term expansion of bone marrow-derived hMSCs on novel synthetic microcarriers in xeno-free, defined conditions, *PLOS One* 9 (2014) 1–7.
- [148] A. Mizukami, A. Fernandes-Platzgummer, J. G. Carmelo, K. Swiech, D. T. Covas, J. M. Cabral, C. L. da Silva, Stirred tank bioreactor culture combined with serum-/xenogeneic-free culture medium enables an efficient expansion of umbilical cord-derived mesenchymal stem/stromal cells, *Biotechnology Journal* 11 (2016) 1048–1059.
- [149] J. G. Carmelo, A. Fernandes-Platzgummer, M. M. Diogo, C. L. da Silva, J. Cabral, A xeno-free microcarrier-based stirred culture system for the scalable expansion of human mesenchymal stem/stromal cells isolated from bone marrow and adipose tissue, *Biotechnology Journal* 10 (2015) 1235–1247.
- [150] T. R. Heathman, A. W. Nienow, Q. A. Rafiq, K. Coopman, B. Kara, C. J. Hewitt, Agitation and aeration of stirred-bioreactors for the microcarrier culture of human mesenchymal stem cells and potential implications for large-scale bioprocess development, *Biochemical Engineering Journal* 136 (2018) 9–17.
- [151] B. Cunha, T. Aguiar, S. B. Carvalho, M. M. Silva, R. A. Gomes, M. J. Carrondo, P. Gomes-Alves, C. Peixoto, M. Serra, P. M. Alves, Bioprocess integration for human mesenchymal stem cells: From up to downstream processing scale-up to cell proteome characterization, *Journal of Biotechnology* 248 (2017) 87–98.

- [152] S. Gottipamula, M. Muttigi, U. Kolkundkar, R. Seetharam, Serum-free media for the production of human mesenchymal stromal cells: a review, *Cell Proliferation* 46 (2013) 608–627.
- [153] M. S. Croughan, J.-F. Hamel, D. I. Wang, Hydrodynamic effects on animal cells grown in microcarrier cultures, *Biotechnology and Bioengineering* 29 (1987) 130–141.
- [154] T. M. Maul, D. W. Chew, A. Nieponice, D. A. Vorp, Mechanical stimuli differentially control stem cell behavior: morphology, proliferation, and differentiation, *Biomechanics and Modeling in Mechanobiology* 10 (2011) 939–953.
- [155] A. Tamburini, A. Brucato, A. Cipollina, G. Micale, M. Ciofalo, CFD predictions of sufficient suspension conditions in solid-liquid agitated tanks, *International Journal of Nonlinear Sciences and Numerical Simulation* 13 (2012) 427–443.
- [156] S. Ibrahim, A. Nienow, Suspension of microcarriers for cell culture with axial flow impellers, *Chemical Engineering Research and Design* 82 (2004) 1082–1088.
- [157] T. N. Zwietering, Suspending of solid particles in liquid by agitators, *Chemical Engineering Science* 8 (1958) 244–253.
- [158] M.-L. Collignon, A. Delafosse, M. Crine, D. Toye, Axial impeller selection for anchorage dependent animal cell culture in stirred bioreactors: methodology based on the impeller comparison at just-suspended speed of rotation, *Chemical Engineering Science* 65 (2010) 5929–5941.
- [159] I. Pieralisi, G. Rodriguez, M. Micheletti, A. Paglianti, A. Ducci, Microcarriers suspension and flow dynamics in orbitally shaken bioreactors, *Chemical Engineering Research and Design* 108 (2016) 198–209.
- [160] A. Delafosse, C. Loubière, S. Calvo, D. Toye, E. Olmos, Solid-liquid suspension of microcarriers in stirred tank bioreactor-experimental and numerical analysis, *Chemical Engineering Science* (2018) 52–63.
- [161] P. Liovic, I. D. Šutalo, R. Stewart, V. Glattauer, L. Meagher, Fluid flow and stresses on microcarriers in spinner flask bioreactors, in: *Proceedings of the 9th International Conference on MSC in the Minerals and Process Industries*, pp. 1–6.
- [162] P. Liovic, I. D. Šutalo, L. Meagher, G. O. Lovrecz, Computations of flow environments in medium-scale stirred-tank bioreactors for stem cell expansion, in: *ASME 2014 4th Joint US-European Fluids Engineering Division Summer Meeting collocated with the ASME 2014 12th International Conference on Nanochannels, Microchannels, and Minichannels*, American Society of Mechanical Engineers, pp. 1–7.
- [163] A. Delafosse, M.-L. Collignon, A. Marc, D. Toye, E. Olmos, Revisiting the determination of hydromechanical stresses encountered by microcarriers in stem cell culture bioreactors, in: *BMC Proceedings*, volume 9, BioMed Central, p. 41.

- 
- [164] M.-L. Collignon, A. Delafosse, S. Calvo, C. Martin, A. Marc, D. Toye, E. Olmos, Large-eddy simulations of microcarrier exposure to potentially damaging eddies inside mini-bioreactors, *Biochemical Engineering Journal* 108 (2016) 30–43.
- [165] E. Olmos, K. Loubiere, C. Martin, G. Delaplace, A. Marc, Critical agitation for microcarrier suspension in orbital shaken bioreactors: experimental study and dimensional analysis, *Chemical Engineering Science* 122 (2015) 545–554.
- [166] A. Lavrentieva, I. Majore, C. Kasper, R. Hass, Effects of hypoxic culture conditions on umbilical cord-derived human mesenchymal stem cells, *Cell Communication and Signaling* 8 (2010) 18–27.
- [167] L. F. Richardson, *Weather prediction by numerical process*, Cambridge University Press, 2007.
- [168] A. N. Kolmogorov, The local structure of turbulence in incompressible viscous fluid for very large reynolds numbers, in: *Dokl. Akad. Nauk SSSR*, volume 30, pp. 299–303.
- [169] A. N. Kolmogorov, Dissipation of energy in locally isotropic turbulence, in: *Dokl. Akad. Nauk SSSR*, volume 32, pp. 16–18.
- [170] M. S. Croughan, J.-F. Hamel, D. I. C. Wang, Hydrodynamic effects on animal cells grown in microcarrier cultures, *Biotechnology and Bioengineering* 29 (1987) 130–141.
- [171] A. W. Nienow, C. J. Hewitt, T. R. Heathman, V. A. Glyn, G. N. Fonte, M. P. Hanga, K. Coopman, Q. A. Rafiq, Agitation conditions for the culture and detachment of hMSCs from microcarriers in multiple bioreactor platforms, *Biochemical Engineering Journal* 108 (2016) 24–29.
- [172] H.-J. Henzler, Particle stress in bioreactors, in: *Influence of Stress on Cell Growth and Product Formation*, Springer, 2000, pp. 35–82.
- [173] G. Zhou, S. M. Kresta, Impact of tank geometry on the maximum turbulence energy dissipation rate for impellers, *AIChE Journal* 42 (1996) 2476–2490.
- [174] A. W. Nienow, M. Edwards, N. Harnby, *Mixing in the process industries*, Butterworth-Heinemann, 1997.
- [175] N. Ma, K. W. Koelling, J. J. Chalmers, Fabrication and use of a transient contractional flow device to quantify the sensitivity of mammalian and insect cells to hydrodynamic forces, *Biotechnology and Bioengineering* 80 (2002) 428–437.
- [176] L. A. Cutter, Flow and turbulence in a stirred tank, *AIChE Journal* 12 (1966) 35–45.
- [177] A. W. Nienow, Impeller selection for animal cell culture, *Encyclopedia of Industrial Biotechnology: Bioprocess, Bioseparation, and Cell Technology* (2009) 1–25.

- [178] R. V. Venkat, L. R. Stock, J. J. Chalmers, Study of hydrodynamics in microcarrier culture spinner vessels: a particle tracking velocimetry approach, *Biotechnology and Bioengineering* 49 (1996) 456–466.
- [179] R. Godoy-Silva, J. J. Chalmers, S. A. Casnocha, L. A. Bass, N. Ma, Physiological responses of CHO cells to repetitive hydrodynamic stress, *Biotechnology and Bioengineering* 103 (2009) 1103–1117.
- [180] P. Jüsten, G. Paul, A. Nienow, C. Thomas, Dependence of mycelial morphology on impeller type and agitation intensity, *Biotechnology and Bioengineering* 52 (1996) 672–684.
- [181] A. Amanullah, R. Blair, A. Nienow, C. Thomas, Effects of agitation intensity on mycelial morphology and protein production in chemostat cultures of recombinant *Aspergillus oryzae*, *Biotechnology and Bioengineering* 62 (1999) 434–446.
- [182] L. Reppel, T. Margossian, L. Yaghi, P. Moreau, N. Mercier, L. Leger, S. Hupont, J.-F. Stoltz, D. Bensoussan, C. Huselstein, Hypoxic culture conditions for mesenchymal stromal/stem cells from Wharton’s jelly: a critical parameter to consider in a therapeutic context, *Current Stem Cell Research & Therapy* 9 (2014) 306–318.
- [183] M. Schneider, I. W. Marison, U. von Stockar, The importance of ammonia in mammalian cell culture, *Journal of Biotechnology* 46 (1996) 161–185.
- [184] R. S. Cherry, E. T. Papoutsakis, Physical mechanisms of cell damage in microcarrier cell culture bioreactors, *Biotechnology and Bioengineering* 32 (1988) 1001–1014.
- [185] S. Stolberg, K. E. McCloskey, Can shear stress direct stem cell fate?, *Biotechnology Progress* 25 (2009) 10–19.
- [186] L. Liu, B. Yu, J. Chen, Z. Tang, C. Zong, D. Shen, Q. Zheng, X. Tong, C. Gao, J. Wang, Different effects of intermittent and continuous fluid shear stresses on osteogenic differentiation of human mesenchymal stem cells, *Biomechanics and Modeling in Mechanobiology* 11 (2012) 391–401.
- [187] G. Montante, F. Magelli, Mixed solids distribution in stirred vessels: experiments and computational fluid dynamics simulations, *Industrial & Engineering Chemistry Research* 46 (2007) 2885–2891.
- [188] A. Tamburini, A. Cipollina, G. Micale, A. Brucato, M. Ciofalo, MSC simulations of dense solid–liquid suspensions in baffled stirred tanks: Prediction of suspension curves, *Chemical Engineering Journal* 178 (2011) 324–341.
- [189] D. Wadnerkar, R. P. Utikar, M. O. Tade, V. K. Pareek, MSC simulation of solid–liquid stirred tanks, *Advanced Powder Technology* 23 (2012) 445–453.
- [190] D. Guha, P. Ramachandran, M. Dudukovic, J. Derksen, Evaluation of large eddy simulation and Euler–Euler MSC models for solids flow dynamics in a stirred tank reactor, *AIChE Journal* 54 (2008) 766–778.

- [191] B. Blais, M. Lassaing, C. Goniva, L. Fradette, F. Bertrand, Development of an unresolved MSC–DEM model for the flow of viscous suspensions and its application to solid–liquid mixing, *Journal of Computational Physics* 318 (2016) 201–221.
- [192] K. Ponnuru, J. Wu, P. Ashok, E. Tzanakakis, E. P. Furlani, Analysis of stem cell culture performance in a microcarrier bioreactor system, *Proceedings International NSTI Nanotech Conference 2* (2014) 132–5.
- [193] V. Jossen, S. C. Kaiser, C. Schirmaier, J. Herrmann, A. Tappe, D. Eibl, A. Siehoff, C. van den Bos, R. Eibl, Modification and qualification of a stirred single-use bioreactor for the improved expansion of human mesenchymal stem cells at benchtop scale, *Pharmaceutical Bioprocessing 2* (2014) 311–322.
- [194] J. Berry, P. Liovic, I. Sutalo, R. Stewart, V. Glattauer, L. Meagher, Characterisation of stresses on microcarriers in a stirred bioreactor, *Applied Mathematical Modelling* 40 (2016) 6787–6804.

# Chapter 2

## Improvement of WJ-MS-C culture on microcarriers

### Contents

---

<b>2.1</b>	<b>Introduction</b>	<b>92</b>
<b>2.2</b>	<b>Preliminary results</b>	<b>94</b>
2.2.1	WJ-MS-C culture using a culture medium supplemented with hPL	94
2.2.2	Microcarrier coating impact on cell attachment	97
<b>2.3</b>	<b>Development of an automatic cell counting method on microcarriers using image analysis</b>	<b>99</b>
2.3.1	Automatic cell and microcarrier recognition and counting	99
2.3.2	Method advantages and limits	101
<b>2.4</b>	<b>Impact of the type of microcarrier in different agitation modes on the expansion performances</b>	<b>104</b>
2.4.1	Context	105
2.4.2	Material and methods	107
2.4.3	Results and discussion	115
2.4.4	Conclusion	133
2.4.5	Acknowledgements	133
<b>2.5</b>	<b>Cell culture on home-made microcarriers</b>	<b>135</b>
2.5.1	Macroscopic observations	135
2.5.2	hPL coating relevance and indirect cell kinetics	137
2.5.3	Cell distribution on microcarriers	137
2.5.4	Cell detachment	138
<b>2.6</b>	<b>Chapter conclusions</b>	<b>140</b>

---

## 2.1 Introduction

As mentioned in the literature review, the MSC expansion process must be intensified in order to reach the high cell dose requirements for MSC-based clinical trials and drugs development [1]. Different strategies were investigated, such as the use of microcarriers. These particles indeed present significant advantages, such as higher specific adherence surface available for cell expansion or the possibility to work in controlled and monitored STR, in accordance with GMP specifications. Perspectives for the expansion process scale-up are also considered. However, despite various culture conditions are available in the literature for BM-MSC culture in a medium supplemented with FBS, only a few studies were focused on WJ-MSC cultures in a clinical grade medium. Cell physiological responses should be thus investigated in more details in order to determine how culture conditions should be adapted (microcarriers, agitation mode...).

In this context, this first result chapter is focused on the improvement of WJ-MSC expansion process on microcarriers in stirred bioreactors, and is divided into four parts, as illustrated in Fig. 2.1. They take advantage of preceding works of two thesis performed in the laboratory and from the literature data. The first thesis, conducted by Caroline Ferrari (2012), involved the expansion of bone marrow MSC from pig, while the second one, defended by Céline Martin (2016), used human bone marrow MSC, both using culture media supplemented with FBS. With the support of the IMoPA laboratory (Nancy, France), displaying strong expertise in MSC expansion and directly involved into MSC clinical applications, culture conditions were partially adapted according to the current clinical requirements (GMP guidelines). Hence, the FBS was replaced by human platelet lysate (hPL) and MSC from Wharton's jelly were used in order to take profit of the numerous advantages presented in section 1.3.2.

These modifications led to the need of adapted culture conditions for dynamic microcarrier-based cultures, which are presented in the first part of this chapter (section 2.2).

In parallel, a novel, direct, robust, and *in situ* counting method was developed to improve cell counting analysis. The second part of this chapter presents the validation of the method and some perspectives (section 2.3).

Using all these preliminary results, a comparative study was performed between various commercial microcarriers for different culture modes, namely static and dynamic cultures involving either a mechanical or an orbital agitation. Culture performances were esta-



blished according to three criteria taking into account the cell adhesion ability, the cell expansion and the ease of detachment. This study led to the third part of this chapter and is presented in section 2.4 as its submission format to *Biochemical Engineering Journal*.

The last part of this chapter consists in a collaborative work with the LCPM laboratory (Nancy, France), partner of the STEMCellREACTOR ANR project. Their skills in material formulation permitted to develop new microcarriers dedicated to MSC cultures. In the present work, comparative results between these home-made microcarriers and selected commercial microcarriers are presented (section 2.5).

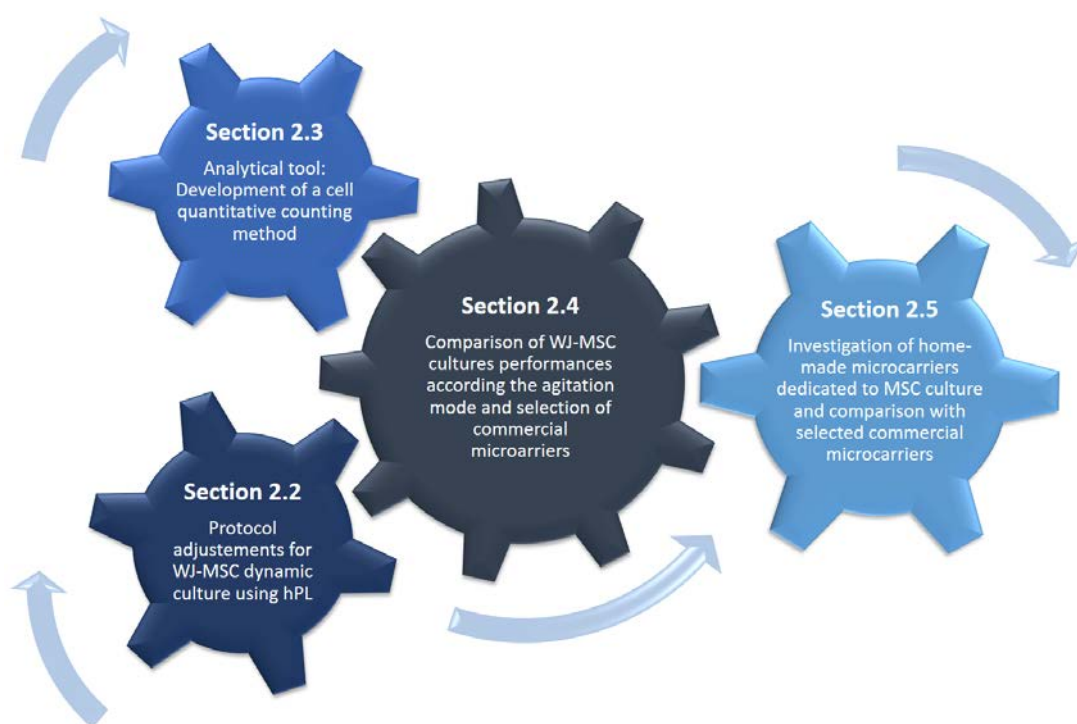


Figure 2.1: Presentation of the different steps of this work for the improvement of a WJ-MSC expansion process on microcarriers.

## 2.2 Preliminary results

This first section is dedicated to the MSC culture process adaptations arising from the impact of Wharton’s jelly cell source and the use of a culture medium containing hPL, suitable for clinical applications. It will also deal with the microcarrier coating step before dynamic cultures. Studies indeed reported better cell attachments when microcarriers were coated using for example fibronectin, FBS or hPL [2, 3, 4], whereas other studies displayed successful MSC cultures without coating [5, 6]. Cell expansions were thus compared with and without a hPL-coating, for two commercial microcarriers (Cytodex-1 and Star-Plus). Materials and methods about this study are presented in more detail in Appendix A.

### 2.2.1 WJ-MSC culture using a culture medium supplemented with hPL

#### Planar static culture

WJ-MSC culture using a medium supplemented with 5 % hPL was initially compared to cultures using a medium supplemented with 10 % FBS, in planar culture flasks. In parallel, WJ-MSC cultures were compared to BM-MSC cultures, both using a 5 % hPL supplemented culture medium. Main observations during cell detachment steps and the number of harvested cells, based on an equal surface  $A = 525 \text{ cm}^2$ , are reported in Table 2.1. In accordance with the literature, the cell growth was found higher using hPL in the culture medium, than with FBS [7]. Here, in average, 1.9-fold more cells were obtained with cultures supplemented with hPL. This number was notably affected by a better ease of detachment. Almost all cells were harvested with a reduced incubation time. However, cell dispersion after the centrifugation step required more pipette aspirations and discharges to separate cells and avoid aggregates. This step must be carefully performed in order to limit the hydromechanical stress and preserve cell quality.

Table 2.1: Comparison of the number of cells harvested and the ease of detachment according to the cell origin and the culture medium used ( $n=2$ ).

Conditions	WJ / hPL	BM / hPL	WJ / FBS
Part of detached cells		Quasi-totality	2/3 to 3/4
TrypLE incubation time		< 1 min	5 min
Pellet dispersion		Necessity of several aspirations and discharges to disperse cells	Directly dispersed
Number of harvested cells $N_{cell}$ ( $10^5$ )	$133 \pm 38$	$91 \pm 19$	$69 \pm 6$
$N_{cell}/S$ ( $10^3$ ) (cells / $\text{cm}^2$ )	$25 \pm 7$	$17 \pm 4$	$13 \pm 1$

Concerning cell origin, MSC from the Wharton's jelly were found to present a higher number of cells, with 1.5-fold more harvested cells than for cultures using bone marrow MSC. This was probably due to the age of the donor, considering WJ-MSC age as the one of the newborn. An undesired phenomenon was nevertheless observed for longer cultures, with two cell behaviours. In the first case, cells left some areas and presented delineated colonized zones with a very tight organization, as shown in Fig. 2.2 (A). In the second case, cells tended to gather together despite some surfaces were still free around, and then formed a macroscopic cell cluster whose size reached up to hundreds micrometers, as presented in Fig. 2.2 (B). Without knowledge on cell stemness from this cluster, cultures presenting this phenomenon were separated from the others and not used for the following studies. Moreover, to limit it, static cell expansion was restrained to 70 % of the confluence. The adhesion surface was thus systemically replaced when reached 70 % of the confluence.

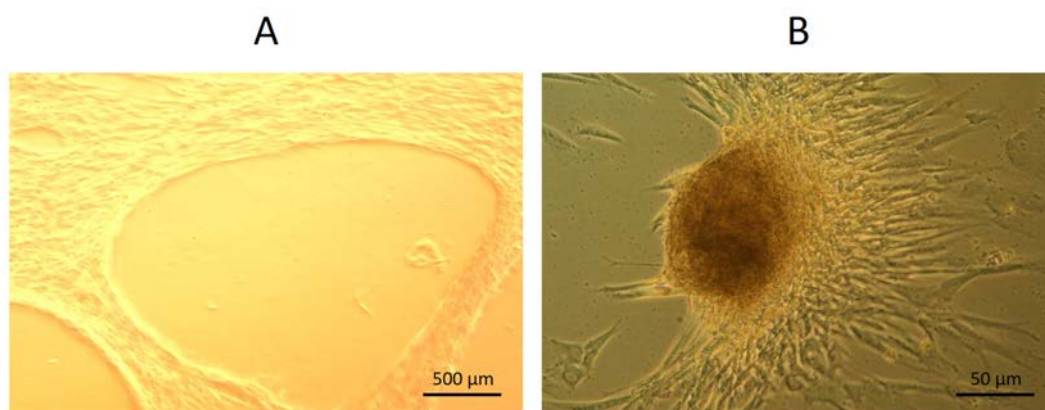


Figure 2.2: Non-systematic WJ-MSC behaviour in planar static cultures when cells are locally close to confluence: Cells can leave certain surface areas and form tight organizations (A), or clusters (B).

### From static to dynamic culture on microcarriers

When applying usual protocols for MSC cultures on microcarriers, but using hPL instead of FBS, **a jelly matrix was observed after a few minutes of agitation**, following the cell inoculation. As shown in Fig. 2.3, this jelly matrix entrapped all microcarriers and led to a high variability on cell attachment and cell expansion, even using cells from the same donor cultivated in parallel with the same operating conditions. This created an important technical bottleneck and needed advanced preliminary experiments to limit the cultures variability due to the jelly matrix, which made difficult the cultures comparison from one condition to another. Different operating conditions were compared in order to determine which factors were related to this jelly matrix. Table 2.2 presents the results

and suggests that the source of this matrix comes from the hPL. However, this matrix was not observed in cultures using hPL, but without microcarriers or MSC. Hence, these two elements were found to be also required for the jelly matrix formation.



Figure 2.3: Jelly matrix formation entrapping all microcarriers during dynamic cultures at  $t_0 + 1$  day.

Table 2.2: Potential of jelly matrix formation for different sets of culture conditions.

Medium		Microcarriers		Agitation mode		MSC		Jelly matrix ?
FBS	hPL	Cytodex-1	Star-Plus	Orbital	Mechanical	WJ	BM	
	X	X		X		None		No
	X	X		X		X		Yes
	X	X		X			X	Yes
	X		None	X		X		No
X		X		X		X		No
	X	X			X	X		Yes
	X		X	X		X		Yes
	X		X		X	X		Yes

Regarding hPL composition, involving notably thrombocyte-derived factors and plasma with fibrinogen and clotting factors, reactions with the calcium present in the basal culture medium may occur and lead to gel formation. Heparin is usually used to avoid this gel but, in the present dynamic cultures, the recommended concentration of 2 IU / mL was found to be not sufficient. The increase of the heparin concentration was not considered, due to the negative effect of higher concentrations of heparin on MSC [8]. Consequently, two strategies were developed to avoid this jelly matrix formation. First, cells were passed through a 40  $\mu\text{m}$  filter in order to retain the potential cell aggregates, as presented in Fig. 2.2. The risk to form the jelly matrix was reduced from 50 %, but was not totally avoided. The second strategy consisted in **a fibrin-depletion of the culture medium**. In this case, the hPL was added to the basal culture medium without heparin. The protocol of this fibrin-depletion is detailed in Appendix A. Briefly, successive mechanical

and thermal shocks were applied, leading to the gel formation, which was then removed. A centrifugation step and a filtration step were finally performed to get the final fibrin-depleted culture medium, called here  $FD - M$ , in contrast to the usual culture medium containing heparin and called here  $hep - M$ . Cell expansion performances were compared within these two culture media, for various operating conditions (microcarrier, WJ-MSC donor), that are not developed here for clarity reasons. To do that, the total glucose consumption was determined for each culture medium, assuming it to be related to the cell expansion. Table 2.3 presents these glucose consumption ratios between the two culture media  $GLU_{FD-M}^{tot. cons.} / GLU_{hep-M}^{tot. cons.}$ . In all cases, and thus whatever the other conditions applied, the  $FD - M$  culture medium led to lower glucose consumption, than the  $hep - M$  one. During the induced fibrin precipitation, some elements enhancing cell attachment and / or cell expansion may thus also be trapped and removed from the medium. However, the  $FD - M$  culture medium led to more reproducible results than with the  $hep - M$  medium, which led to more variability of the culture results. So, despite slightly reduced cell expansion performances, the  $FD - M$  culture medium was chosen for dynamic cultures in the present work, in order to avoid jelly matrix formation.

Table 2.3: Glucose consumption ratios between the two culture media  $FD - M$  and  $hep - M$  for paired cultures at various operating conditions.

Culture number	1	2	3	4	5	6
$GLU_{FD-M}^{tot. cons.} / GLU_{hep-M}^{tot. cons.}$	0.95	0.68	0.72	0.70	0.19	0.78

## 2.2.2 Microcarrier coating impact on cell attachment

The microcarrier coating may enhance cell attachment and expansion performances as reported by Heathman *et al.* with fibronectin [9], and De Soure *et al.* with hPL [4]. In the present study, an hPL-based coating was compared to uncoated microcarriers, in order to determine if this coating step was necessary for different microcarriers. In this way, 2 microcarriers with different materials were compared: (i) Cytodex-1 made of dextran and (ii) Star-Plus made of polystyrene. Cultures were first performed with the previously described  $hep - M$  culture medium. Glucose and lactate concentrations are presented in Fig. 2.4. It was shown that the metabolite concentration kinetics with coated and uncoated Cytodex-1 remained similar with both culture media. Hence, the hPL coating was found unnecessary for this specific microcarrier. In the other hand, glucose and lactate concentrations presented significant deviations between coated and uncoated Star-Plus microcarriers, with respectively 1.0 and 0.4 mmol L<sup>-1</sup> d<sup>-1</sup> glucose consumptions and 2.0 and 0.9 mmol L<sup>-1</sup> d<sup>-1</sup> lactate production over seven days. In this

case, coated Star-Plus would be highly recommended. In the same way, cultures were then performed using the  $FD - M$  culture medium, leading to the results presented in Fig. 2.5. Similarly to the previous case, no coating was required for culture on Cytodex-1, but the hPL coating was still recommended with Star-Plus microcarriers.

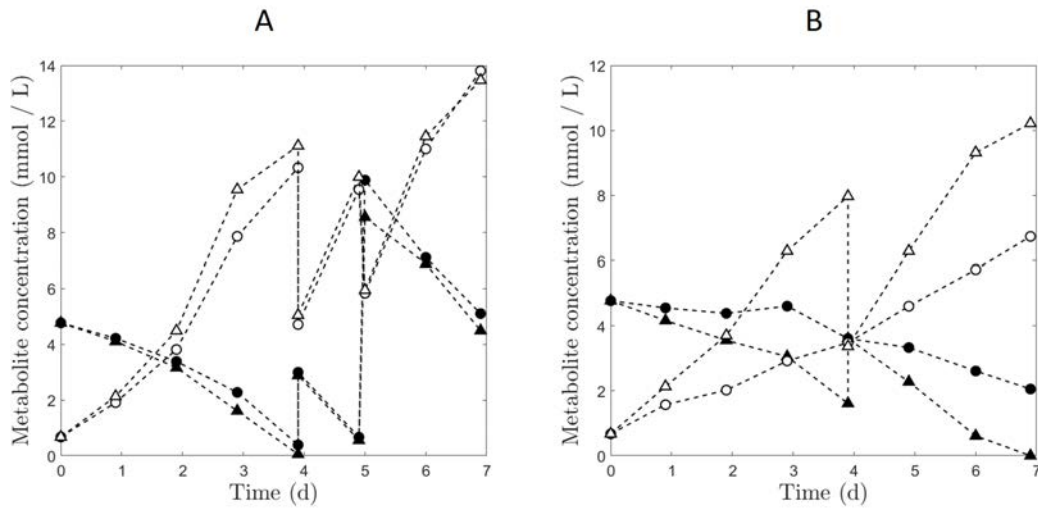


Figure 2.4: Kinetics of the metabolite concentrations using the  $hep - M$  culture medium, and according to the type of microcarrier: Cytodex-1 (A) and Star-Plus (B). Filled - Glucose, Empty - Lactate, (o) - Non-coated microcarriers, ( $\Delta$ ) - hPL-coated microcarriers.

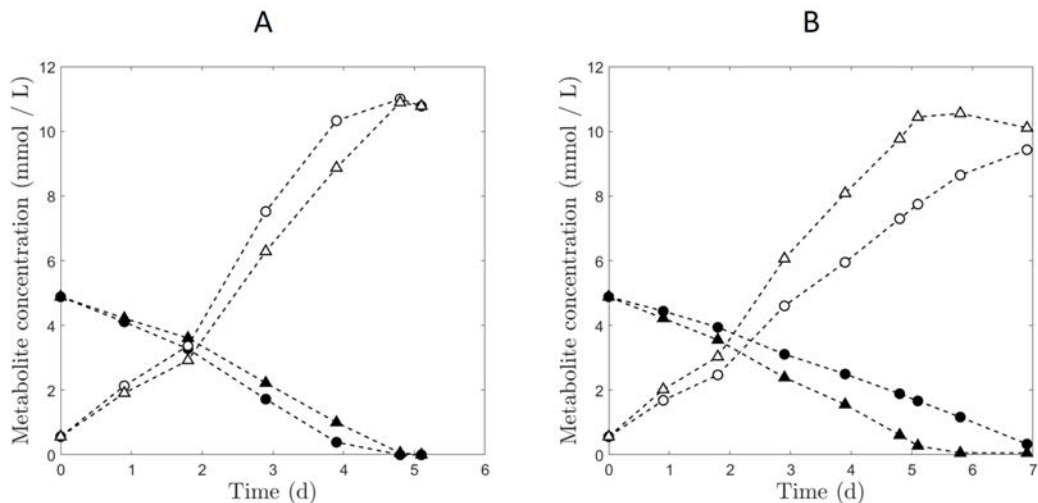


Figure 2.5: Kinetics of the metabolite concentrations using the  $FD - M$  culture medium, and according to the type of microcarrier: Cytodex-1 (A) and Star-Plus (B). Filled - Glucose, Empty - Lactate, (o) - Non-coated microcarriers, ( $\Delta$ ) - hPL-coated microcarriers.

## 2.3 Development of an automatic cell counting method on microcarriers using image analysis

Cell counting methods are complex to apply in the case of MSC adhered on microcarriers, with generally limited current quantitative methods. Because MSCs may be difficult to detach and as the filtration step may retain a fraction of cells, cell counting using usual cell counters for suspended cells may show significant errors. Despite this uncertainty on results, this method is still widely used to compare culture conditions [6, 4]. Other quantitative methods were also employed to determine the cell concentration, such as nuclei counting after cell lysis [10] or indirect measurements like WST-1 and MTT assays [5, 2], or fluorescence emission intensity with an alamarBlue assay [11]. However, they only provide volume-averaged data. No information is available on cell distribution on microcarriers, which may be crucial to understand cell attachment and expansion mechanisms, and to enhance the culture process thereafter. Frauenschuh *et al.* reported the use of a light microscope to manually count cells on 60 microcarriers during the first hours of the cultures, with the aim of evaluating the seeding procedure applied on different microcarriers [12], but such method is too time-consuming to be applied for cell expansion measurement. A robust quantitative method was thus developed to directly count MSC cells on microcarriers, considered '*in situ*', without any detachment step needed. This method was based on microscopic analysis, and image post-treatments performed by a Matlab script for automatic cell counting.

### 2.3.1 Automatic cell and microcarrier recognition and counting

Thresholds for colour detection were validated with no interference for each microcarrier, as presented in Fig. 2.6 and 2.7 for cells on Cytodex-1 microcarriers. Hue, saturation and value masks were modified until cell spot detection and counting were validated with less than 5 % of deviation, compared with the human visual counting. In the case of Plastic-Plus, Star-Plus and Hillex II, microcarriers may also produce blue light after DAPI staining. It was thus necessary to adjust thresholds in order to correctly detect the blue colour emitted by cells from the blue colour coming from particles. Final values of these thresholds are presented in Table 2.4. It should be nevertheless noticed that after a few seconds of laser light, Hillex II emission increased, requiring fast photo recording in order to detect cells thereafter.

Since cells and their location on each microcarrier were validated, the counting step was investigated. Cytodex-1 and Hillex II were found to let light passing through the material.

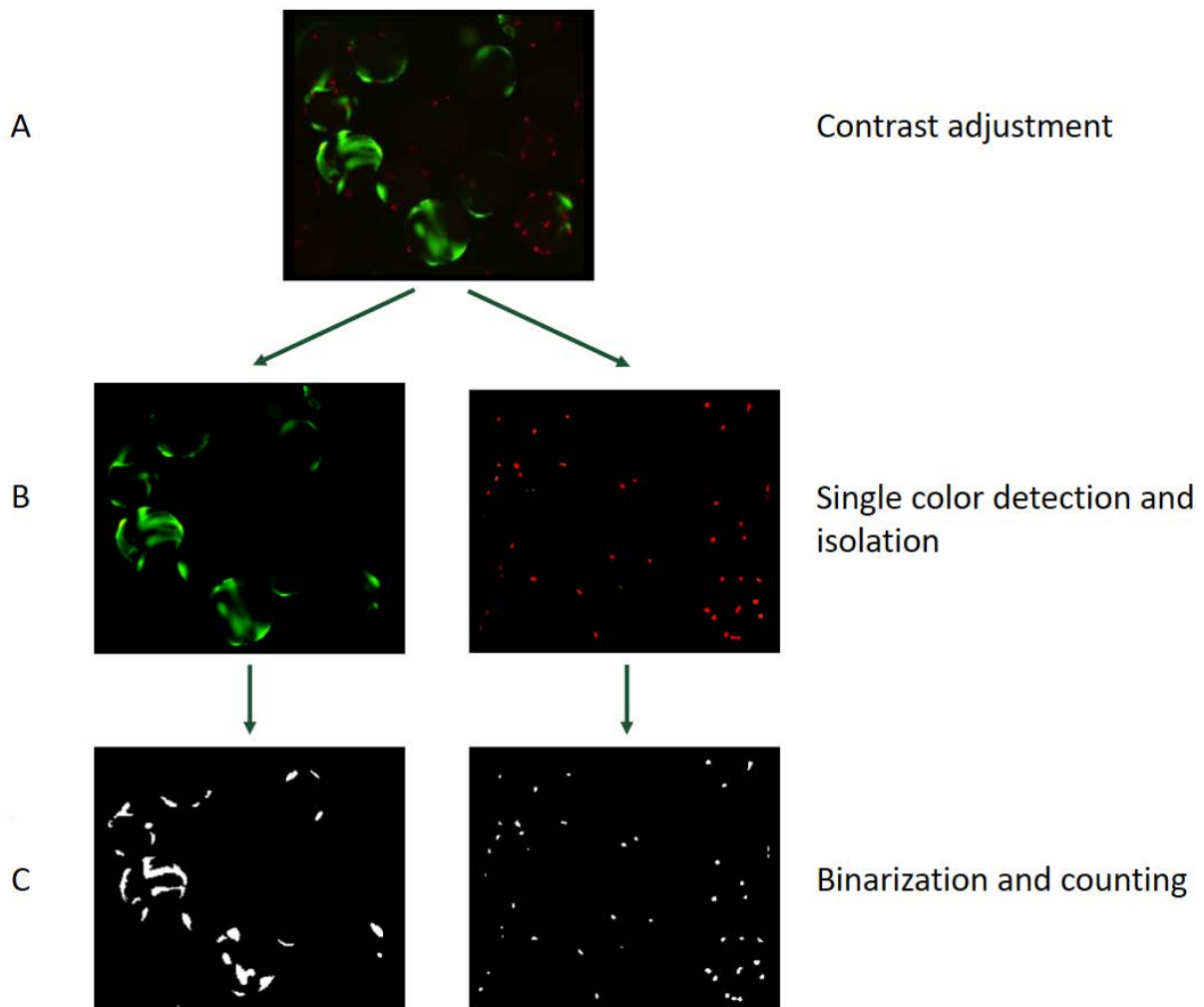


Figure 2.6: Photo post-treatment to detect and count cells after Live / Dead staining: Contrast adjustment (A), green and red elements isolations characterizing living and dead cells respectively (B) and binarization and counting of the selected elements (C). Microcarrier recognition is performed in parallel, but not shown in the present photos for better visualization.

Consequently, all cells could be directly counted. On contrary, Plastic-Plus and Star-Plus were found opaque. It was supposed that limiting the colonization fraction with only microcarrier visible sides may under-estimate the real value. A microcarrier with no cell on the visible side may hide one or more cells on the other side. A probability distribution was thus applied in order to predict the number of cell on the hidden side of the microcarrier. Hu *et al.* provided evidence of the Poisson distribution in the case of human foreskin fibroblast cell culture on microcarriers [13], which was thus chosen for the present study. The characteristic parameter of this type of distribution is the average number of events, namely here the mean number of cells per microcarrier counted in a photo during the post-treatment.

Concerning cell staining strategy, more cells were globally counted with DAPI staining than by summing all cells of the Live (calcein-AM) / Dead (ethidium homodimer) stain-



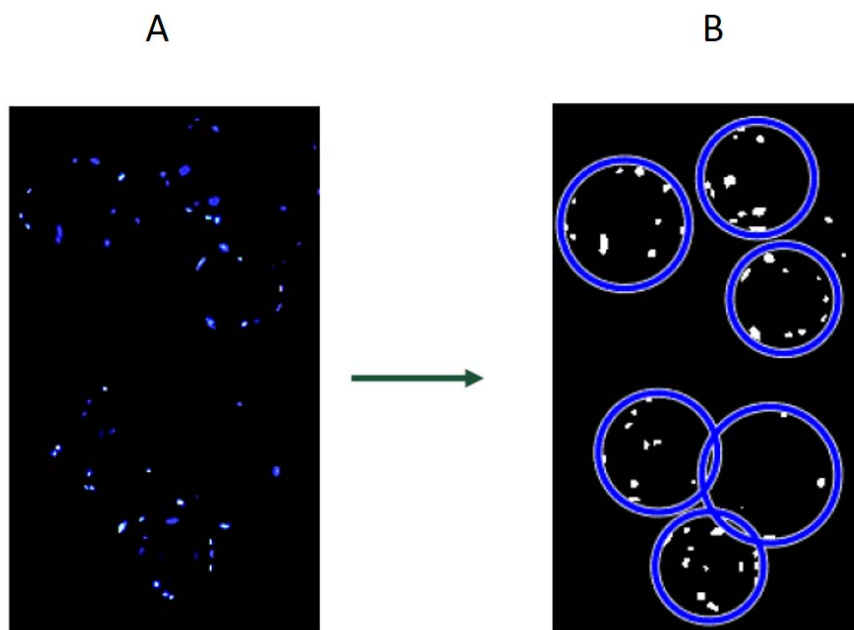


Figure 2.7: Photo treatment to detect and count microcarriers and cells after DAPI staining: Contrast adjustment and blue elements isolation characterizing either living and dead cells (A), and binarization and counting of the selected elements before recording according to the corresponding microcarrier location (B).

ing. Up to 50 % and 45 % deviations were indeed obtained for respectively Star-Plus and Plastic-Plus microcarriers. As living cells emission came from cell membrane, and regarding cell fibroblast morphology, two very close cells were difficult to distinguish, either by the human eye or by the Matlab script. So, due to large emissions from cell membranes, the total number of cells may only be qualitatively estimated or bounded by a minimal value, living cells being expected to be under-estimated. As dots are clearly delineated, nuclei staining (DAPI) led to a better accuracy, but did not provide data about cell viability.

### 2.3.2 Method advantages and limits

The proposed method presented two main advantages regarding counting methods:

- Cell counting was performed *in situ*. No detachment step was required.
- The method provided both global (total number of cells, mean number of cells per microcarrier, fraction of colonized microcarriers) and local (distribution of the number of cells per microcarrier) values characterizing cell numbers and the potentially heterogeneous distribution on microcarriers. It was notably demonstrated that cell distribution on microcarriers became wider over time (Fig. 2.8).

### 2.3. DEVELOPMENT OF AN AUTOMATIC CELL COUNTING METHOD ON MICROCARRIERS USING IMAGE ANALYSIS

---

Table 2.4: Thresholds values for cell recognition according to the staining and the type of microcarrier used.

	Cytodex-1	Plastic-Plus	Star-Plus	Hillex II
<hr/> Green emission <hr/>				
Hue threshold low	0.15	0.15	0.15	0.15
Hue threshold high	1	0.60	0.60	0.60
Saturation threshold low	0	0.36	0.36	0.36
Saturation threshold high	1	1	1	1
Value threshold low	0	0	0	0
Value threshold high	1	0.8	0.8	0.8
<hr/> Red emission <hr/>				
Hue threshold low	0	0	0	0
Hue threshold high	0.1	0.1	0.01	0.1
Saturation threshold low	0.4	0.4	0.58	0.4
Saturation threshold high	1	1	1	1
Value threshold low	0.4	0.4	0.55	0.4
Value threshold high	1	1	1	1
<hr/> Blue emission <hr/>				
Hue threshold low	0	0	0.55	0.45
Hue threshold high	1	1	0.64	0.8
Saturation threshold low	0	0	0.99	0.3
Saturation threshold high	1	1	1	1
Value threshold low	0	0.8	0.8	0.3
Value threshold high	1	1	1	1

It was nevertheless not applicable in the following situations:

- When cell density became high and close to microcarrier confluence, cell number may be under-estimated, due to cell membranes or cell nuclei spots getting too close to be clearly distinguished.
- In the case of cell aggregates, for the same preceding reasons.

So, the present method would be recommended during the first days of cultures, especially when data on cell distribution on microcarriers are required, but may lead to higher deviations when confluence is nearly reached. It could still give information on microcarrier colonization fractions, but not on the number of cells per microcarrier, and on the total number of cells. For this purpose, indirect methods would be more suitable, such as the kinetics of metabolite concentrations, nuclei counting after cell lysis, WST-1 (based on a DNA synthesis monitoring) or MTT (based on the MTT reduction into formazan into living cells by NAD(P)H-dependent cellular oxidoreductase enzymes).

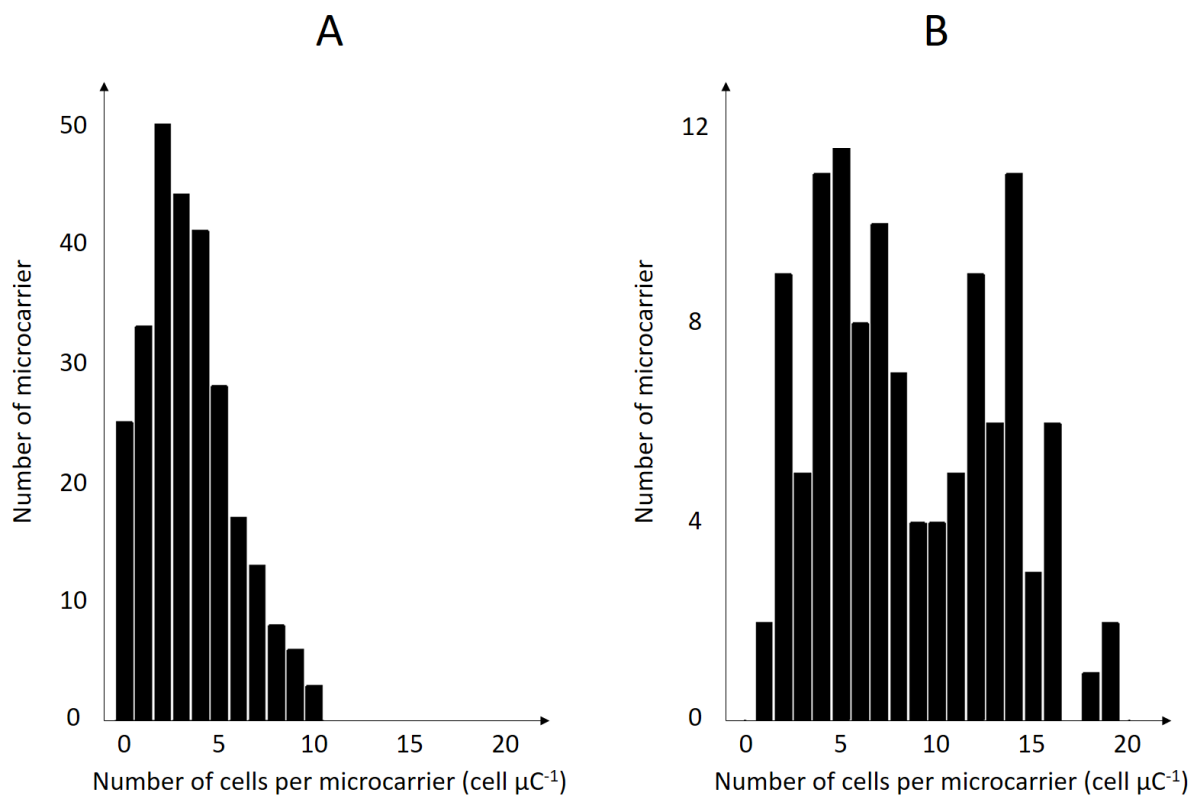


Figure 2.8: Distributions of the number of cells per microcarrier, calculated by the Matlab script, after 3 days of culture (A) and 13 days of culture (B).

## 2.4 Impact of the type of microcarrier in different agitation modes on the expansion performances

Based on the culture conditions determined in section 2.2, and the analytical method developed in section 2.3, culture performances were compared for different commercial microcarriers, and according to different agitation modes. Because MSC are the final product, the ease of cell detachment was also investigated, in the same way as the cell attachment capability and the cell expansion ; these three phases of the process were considered equally important. This part will present the results of this study in the form of a scientific paper.

### Impact of the type of microcarrier and agitation modes on the expansion performances of stem cells derived from umbilical cord

C. Loubière<sup>a</sup>, I. Chevalot<sup>a</sup>, N. De Isla<sup>b</sup>, C. Sion<sup>a</sup>, L. Reppel<sup>b,c,d</sup>, E. Guedon<sup>a</sup>, E. Olmos<sup>a</sup>

<sup>a</sup>Laboratoire Réactions et Génie des Procédés, Université de Lorraine, CNRS, LRGP, F-54000 Nancy, France

<sup>b</sup>CNRS, IMoPA, UMR 7365, Vandoeuvre-lès-Nancy, France

<sup>c</sup>CHRU de Nancy, Unité de Thérapie cellulaire et Tissus and FR 3209, Vandoeuvre-Lès-Nancy, France

<sup>d</sup>Université de Lorraine, Faculté de Pharmacie, Département de Microbiologie-Immunologie, Nancy, France

Keywords: Mesenchymal stromal / stem cells, Wharton's jelly, microcarrier, human platelet lysate, mixing.

### Publication abstract

Mesenchymal stem cells isolated from the Wharton's jelly of umbilical cords (WJ-MS) are promising due to their abundance and their high proliferative and immunomodulatory properties. MSC culture on microcarriers are performed to overcome the surface limitation of 2D planar culture and to improve culture processes. Before the proposal of robust bioreactor scale-up rules, the impact of the agitation modes should be studied, which has not been done yet. The present study proposed to compare different xeno-free microcarriers for WJ-MS cultures, in a clinical grade culture medium using human platelet lysate, according to three culture modes: (i) static, (ii) orbital agitation and (iii) mechanical agitation. Attachment and expansion performances were notably characterized using a

method coupling microscopic analysis and a Matlab script allowing an *in situ* cell counting without detachment step. The cell detachment was also considered for microcarrier comparisons. Results showed that performances obtained in static mode were not necessarily representative of culture performances in dynamic mode. Moreover, the environment was found to have an impact on the nutrient / metabolite consumptions and productions, such as a higher glutamine consumption when Cytodex-1 microcarriers were used. The detachment strategy used was found relatively efficient for Star-Plus, Plastic-Plus and Hillex II, but not sufficient for Cytodex-1. Despite Cytodex-1 presented promising attachment and expansion performances, Star-Plus and Plastic-Plus were found to be better compromises, respectively for the orbital and the mechanical agitation modes.

### 2.4.1 Context

In recent years, Mesenchymal Stem / Stromal Cells (MSCs) are increasingly used in regenerative medicine. According to the U.S. National Institute of Health, the number of completed or ongoing MSC-based studies passed from around 500 in 2016 to 854 in July 2018 [14]. This is mainly due to the promising application of MSCs in cell therapies with actions as trophic mediators and displaying bioactive factors secretion [15]. Their immunomodulatory properties also present a great interest for this medical purpose, allowing either autologous and allogenic treatments. They are notably involved into treatments for type I and II Diabetes, cancers and heart failures in some others [16].

MSCs were firstly isolated from bone marrow by Friedenstein *et al.* and identified as a population of anchorage cells with a fibroblast behavior and the capacity to regenerate bone cells [17]. Since then, other parts of the body were identified as MSCs sources, such as adipose-tissues [18], synovium [19], lung [20], muscles [21], umbilical-cord blood [22] or umbilical-cord matrix (Wharton's jelly) [23]. In order to establish robust criteria to define MSCs, the International Society for Cellular Therapy (ISCT) proposed three minimalist conditions: (i) the capacity to adhere on plastic in standard culture conditions, (ii) the expression or non-expression of specific surface antigens (positive for CD105, CD73 and CD90; negative for CD45 CD34, CD14 or CD11b, CD79a or CD19 and HLA-DR), and the *in vitro* differentiation ability into osteoblasts, adipocytes and chondrocytes [24].

These cells are nevertheless present in limited quantities in the body, which decrease with ageing [25]. *In vitro* expansions are thus necessary to reach the high cell dose requirements for the medical purposes, between  $10^9$  and  $10^{12}$  cells/lot [1]. To improve their performance, expansion processes have been investigated from static planar cultures to stirred tank bioreactors, taking into account both the quantity and the quality of the harvested cells [26, 27, 28].

Concerning the quality, MSCs have the particularity to be the drug itself, directly in-

jected into the patient, meaning that, in addition to the process itself (robust control and monitoring), all components involved in the culture medium must be suitable for clinical applications. This led to the use of chemically defined culture media displaying much higher costs [29], or to the serum replacement by human blood-derived alternatives like the human platelet lysate (hPL) [30]. The use of hPL has notably been validated for MSC cultures, with higher expansion rates than with fetal bovine serum, making it a good substitute at an affordable cost [7]. It also presents the advantage to be rich in proteins and growth factors, avoiding the need of bFGF addition.

For the large-scale production of MSC, the technology of microcarriers, developed by Van Wezel *et al.* in 1967, is today widely used to allow adherent-dependent cell cultures. They consist in micro-spheres from 90 to 400  $\mu\text{m}$  diameter with a density slightly higher than water [31]. Cells adhere on these beads, which are then suspended in a stirred tank bioreactor. Agitation allows homogenization of the culture medium, mass transfers and limits concentration gradients. For applications with MSCs, it has been demonstrated that cultures on microcarriers provided a higher number of cells than in mono- or multi-layer planar cultures, although they require more efforts in investments and R&D [32, 33]. Recently, MSC cultures have been successfully conducted at a few liter-scale [10, 34]. A stirred system allows thus to cultivate MSCs in a more robust, effective and scalable system, but investigations are still necessary to understand the impact of the agitation on cell biological responses [35, 36]. Studies recently pointed out the lack of robust and transferable methodology for microcarrier selection. As reported by Jung *et al.*, very few studies reported the comparison of growth depending on the type of microcarriers, and studies are difficult to compare one to each other due to various cell sources and culture conditions [37]. For instance, a systematic microcarrier screening was described, involving 13 microcarriers under both static and dynamic conditions [5], but this study was based on bone marrow MSC.

During last years, efforts have been made to perform and study cultures of MSCs derived from umbilical cords and more specifically from the Wharton's jelly (WJ-MS). These studies reported some relevant advantages in comparison to other sources. For instance, cell isolation procedure is non-invasive and provides a higher number of cells with up to  $5 \cdot 10^6$  cells / cm of cord [38]. This criterion becomes important with the increasing needs of MSCs for clinical trials and for a potential industrial implementation. Another advantage concerns the higher *in vitro* proliferative and immunomodulatory properties of WJ-MS in comparison to bone marrow MSCs [39, 40, 41]. Moreover, considering that WJ-MS have the age of the newborn, less impact due to the donor age is expected. Until now, WJ-MS have been successfully isolated and cultivated, in culture scales up to 800 mL [42, 43, 44, 45].

Recently, two studies explored the culture of WJ-MS on microcarriers in a medium sup-

plemented with hPL, adapted for clinical use [6, 4]. Petry *et al.* compared five different microcarriers (Hillex II, ProNectin F-coated, Plastic, Plastic-Plus and Glass-coated) in static mode and validated the dynamic culture in Spinner flasks with Plastic-Plus, which gave the best growth and attachment performance in static mode. In parallel, de Soure *et al.* validated cell isolations and also dynamic cultures in spinner flasks with Plastic microcarriers coated with a culture medium supplemented with 50 % hPL. To our knowledge, the comparison of microcarriers has only been performed in static mode for WJ-MSC cultures in a hPL-supplemented medium. However, it was previously demonstrated that MSC growth in stirred systems was not necessarily correlated to the growth in static microcarrier culture, and that early cell attachment and spreading on microcarriers was not necessarily representative of the efficiency of MSC expansion in agitated microcarrier cultures [46].

The objective of the present study is to determine a standardized method to cultivate WJ-MSCs on microcarriers in a serum-free culture medium, supplemented with hPL. To do that, five animal product-free microcarriers were compared, both in static and dynamic modes. Two different agitation modes were studied: Erlenmeyer flasks mixed by an orbital agitation, and spinner flasks involving mechanical agitation. The best microcarrier was determined, regarding three criteria characterizing the different culture steps: (*i*) the adhesion ability, (*ii*) the growth rate and cell expansion, and (*iii*) the ease of detachment. In parallel, as MSCs can be difficult to detach and as the filtration step, requiring to separate cells from microcarriers, may retain a fraction of cells, significant errors by usual cell counter may occur. Consequently, to estimate and compare the number of cells per microcarrier *is situ*, and in a reproducible and objective way, a counting method has been developed, providing a direct measurement without cell detachment.

## 2.4.2 Material and methods

### Cell source

WJ-MSC were recovered from a healthy donor. The human umbilical cord was collected after informed mother consent, according to the national legislation regarding human sample collection, manipulation and personal data protection. MSC isolation was performed using mechanical migration: The umbilical cord was dissected in small sections (around 1 or 2 mm thickness), washed with Dulbesco Phosphate buffer saline solution (DPBS, Sigma) and plated as explants on planar plastic surfaces. After migration and expansion on the surface, cells were recovered and frozen in a container filled with liquid nitrogen at  $-196^{\circ}\text{C}$ . By concern of senescence limitation and stem phenotype alteration, cells used in all cultures of the present study did not exceed 5 passages. Static cell expansions were performed after 3 passages and cultures on microcarriers after 5 passages.

### Culture medium

The basal medium used was  $\alpha$ -MEM Eagle solution (Lonza), supplemented with 5 % human platelet lysate (MultiPL'30, Macopharma), 4 mM glutamine (Sigma) and 1 % antibiotic-antimycotic (Gibco). According to the manufacturer instructions, the hPL derived from screened normal human donor platelets, was pooled in large batch sizes of 10 L and was sterilized by filtration of 0.2  $\mu\text{m}$  before filling in closed systems.

Heparin (Sigma-Aldrich) was added to this basal medium for planar static cultures at a concentration of 2 IU / mL. Concerning dynamic cultures on microcarriers, first cultures led to the formation of a jelly matrix precipitate, entrapping microcarriers, even with 2 IU / mL heparin in the culture medium. This gel appeared during the first days and led to high variability of cell adhesion and expansion. The heparin was thus found to be not enough effective to avoid gel formation. Hence, it was chosen to use a mechanical fibrinogen-depletion instead of the increase of heparin concentration, which may have deleterious effects on cell expansion at higher concentrations [8]. Similar fibrinogen-depletion methods have already been described by other authors [47, 48]. For the present study, the culture medium was maintained between 4 and 6 hours at room temperature to allow clot formation. It was then stored at 4°C at least 18 hours. Before fibrin gel removing, the medium was brought to 37°C and submitted to mechanical shocks by agitation. The biogel was then physically collapsed and the precipitated fibrin was pelleted by centrifugation ( $670 \times g$ , 10 min, Jouan G 4.11). Finally, the medium was passed through a 0.22  $\mu\text{m}$  filter.

### Microcarrier preparation

Five microcarriers were compared, including Cytodex-1 (GE Healthcare), widely used for adherent dependent cell cultures, and the Pall Starter Kit composed of Plastic, Plastic-Plus, Hillex II and Star-Plus microcarriers (Pall, SoloHill). Microcarriers properties and culture concentrations are presented in Table 2.5. The different concentrations of microcarriers were calculated in order to display the same available surface for cell expansion, both in static ( $A = 30 \text{ cm}^2$ ) and dynamic ( $A = 250 \text{ cm}^2$ ) modes. Preliminary cultures showed that a coating with hPL enhanced cell attachment on microcarriers (data not shown). Only Cytodex-1 presented similar cell attachment with and without hPL coating. In the present work, all microcarriers were thus coated with hPL by incubating them in pure hPL at 37°C, 80 % humidity and 5 %  $\text{CO}_2$  during two hours. Then, microcarriers were washed with fresh culture medium before cell seeding.



### Cell culture under static conditions

After quick thawing, cells were seeded at 2000 cells / cm<sup>2</sup> in T175 flasks filled with 25 mL culture medium. The medium was changed every 2 or 3 days by complete medium removing and addition of the same volume of fresh medium. Once 60-70 % of the confluence was reached, the culture medium was removed and cells were washed with DPBS before the cell detachment, using 5 mL TrypLE (Gibco) per flask. TrypLE is composed of recombinant cell-dissociation enzymes that replace trypsin. Incubation did not exceed 5 min and the enzymatic digestion was stopped by adding 20 mL of fresh medium. The suspension was then centrifuged at  $130 \times g$  during 5 min, the supernatant was removed and the pellet was dispersed in fresh culture medium. A filtration step was performed with 40  $\mu\text{m}$  filters, in order to eliminate potential cell aggregates. 1 mL of the suspension was finally collected to determine the cell number and cell viability.

### Cell culture on microcarriers in static mode

Six well plates with ultra-low attachment surface (Corning) were used to perform static cultures on microcarriers. After addition of the microcarriers at the bottom of the well, cells were seeded at a concentration of  $3 \times 10^5$  cells / well in a working volume of 5 mL. After 5 days, the supernatant was removed and microcarriers were washed with DPBS. Cell detachments were finally performed by using 1 mL of TrypLE. A complementary agitation can be applied to promote cell detachment and to reduce the incubation time, as proposed by Nienow *et al.* [3]. An orbital agitation of 75 rpm (orbital diameter  $d_o = 10$  mm) was applied during 5 min, and 5 mL of fresh medium was then added to stop the enzymatic digestion. Cells were finally separated from microcarriers with a 70  $\mu\text{m}$  filtration step.

### Cell culture on microcarriers in agitated mode

The following protocol was established from preliminary cultures performed using both Cytodex-1 and Star-Plus microcarriers, in order to determine the suitable operating conditions for cell growth comparison on different microcarriers. Two stirred culture systems were used: (i) Erlenmeyer flasks and (ii) Spinner flasks. Properties of the two systems are presented in Table 2.6. Cells were recovered from planar cultures at around 70 % of the confluence and were passed through a 40  $\mu\text{m}$  filter to trap potential aggregates before seeding. 70 % of the confluence was found to be a good compromise to recover enough cells while avoiding the formation of aggregates. After counting, cells were inoculated at a concentration of  $0.8 \times 10^6$  cells / mL, namely  $2 \times 10^6$  cells per flask. In Erlenmeyer flasks, a gentle agitation was applied to homogenize cell and microcarrier suspension, and cultures

## 2.4. IMPACT OF THE TYPE OF MICROCARRIER IN DIFFERENT AGITATION MODES ON THE EXPANSION PERFORMANCES

Table 2.5: Microcarrier physical properties (based on manufacturer data) and concentrations used in this study.

Name	Manufacturer	Diameter range ( $\mu\text{m}$ )	Density ( $\text{g mL}^{-1}$ )	Static culture concentration ( $\text{g L}^{-1}$ )	Dynamic culture concentration ( $\text{g L}^{-1}$ )
Cytodex-1	GE Healthcare	147 - 248	1.03	1.4*	2.35*
Plastic	Pall SoloHill	125 - 212	1.02	15	N/A
Plastic-Plus	Pall SoloHill	125 - 212	1.02	15	25
Star-Plus	Pall SoloHill	125 - 212	1.02	15	25
Hillex II	Pall SoloHill	160 - 200	1.1-1.2	21	34.2

\*Cytodex-1 concentrations are given according to the particle dry weight.

were let without agitation during one hour to allow cell adhesion. Agitation rate was then fixed at the minimal agitation rate ensuring all particle suspension  $N = N_{js} = 75$  rpm ( $d_o = 10$  mm). In Spinner flasks, cultures performed at  $N = N_{js}$  led to cell lysis. It was thus decided to let cultures without agitation during one hour with gentle agitations at the beginning and at the mid-point, before working at a low agitation rate  $N = 40$  rpm, at which a sufficient number of particles were suspended without major hydromechanical stress [3]. Both cultures performed in Erlenmeyer and spinner flasks were limited to 5 days, with 50 % medium exchange performed at  $t_0 + 3d$  and  $t_0 + 4d$ , in order to ensure a sufficient glucose concentration for cell expansion and to reduce the lactate concentration. At the end of the culture, the supernatant was removed and particles were washed with DPBS. 10 mL of TrypLE were then added with a complementary agitation during 5 min. Fresh medium was used to stop the enzymatic digestion and cells were separated from microcarriers with a 70  $\mu\text{m}$  filtration step. Cell number and viability were determined before being frozen. Microcarriers were recovered from filters and microscopic analyses were performed to determine the number of cells remaining attached.

Table 2.6: Stirred systems and agitation conditions chosen for cultures in dynamic mode.

	Bioreactor	
	Erlenmeyer flask	Spinner flask
Manufacturer	Fisherbrand (Fisher Scientific)	DWK Life Sciences Inc. (Wheaton)
Mixing mode	Orbital	Mechanic
Material	Plastic (single-use)	Siliconized glass
Diameter (mm)	66	40
$V_{working}$ (mL)	25	25
$N$ (rpm)	75	40

### Detached cells counting

After each detachment, cell number and cell viability were determined from cell suspensions, using the Vi-Cell<sup>TM</sup> Cell Viability Analyzer Counter (Beckman Counter), based on a Trypan Blue Dye Exclusion method.

### In situ counting of cells adhered on microcarriers

A dedicated post-treatment was developed to dispose of a robust and quantitative method to directly count MSC cells attached on microcarriers, without detachment step. To do that, samples of 200  $\mu\text{L}$  were recovered from homogeneous particle suspensions. After supernatant removing for metabolite analysis, cells were stained using a DAPI-methanol

solution of 1  $\mu\text{g}$  / mL (DAPI from Sigma) during 15 min at room temperature. Cells were then washed with DPBS and microscopic analyses were performed. At least 5 photos per operating condition were recorded and loaded in a Matlab script for post-treatment. First, microcarriers were identified by contour recognition and their coordinates were recorded. Secondly, based on the simple colour detection by the hue function of Matlab, a mask was applied in order to only keep the blue elements concerning cell nuclei after the DAPI staining. After contrast adjustments, a binarization was performed and cell coordinates were compared to microcarrier coordinates in order to get the number of cells per microcarrier. Cytodex-1 and Hillex II microcarriers are transparent and were found to allow blue light to pass through the material. In this way, cells adhered in the whole bead surface were counted. On the contrary, Plastic, Plastic-Plus and Star-Plus microcarriers were found opaque and only cells present in half of the bead surface were counted. Furthermore, a half-face found empty did not necessarily mean that there was no cell on the other side. Consequently, in order to predict the number of cells on the non-visible surface, a Poisson distribution was integrated in the routine. The routine finally provided the following information: (i) The mean number of cell per microcarrier  $\langle N_{cell/\mu C} \rangle$ , (ii) the distribution of the number of cell per microcarrier, (iii) the standard deviation of this distribution  $\sigma$ , and (iv) the percentage of colonized microcarriers  $x_{colo}$ , namely the fraction of particles containing at least one cell. This method based on image analysis was preliminary validated by cell visual counting.

### Cell morphology investigation

As for cell counting, samples of 200  $\mu\text{L}$  were recovered from a homogeneous particle suspension. After removing the supernatant, cells were stained using a Live / Dead Cell double staining kit (Sigma) during 30 min at 37°C. It was composed of calcein-AM for living cell membrane staining, and ethidium homodimer for dead cell nuclei staining. Microscopic analyses were then performed in order to qualitatively determine cell morphology. This operation was performed at  $t_0 + 2$  days in order to ensure cell attachment and their final morphology, while no doubling population already occurred. The objective was to distinguish round from spreaded cells.

### Metabolites analysis

Everyday, glucose, lactate, glutamine, ammonia and lactate dehydrogenase (LDH) concentrations were measured from supernatant samples collected throughout the cultures, by using the Gallery multiparametric analyzer (Thermo Fisher Scientific). Glucose (GOD-POD), L-Lactic Acid and LDH (SCE) kits from Thermo Fisher Scientific and Glutamine V2 Bio and  $\text{NH}_3$  Bio kits from Roche were used.

### Kinetic parameters calculation

Based on the previous experimental measurements, different parameters were calculated to characterize cell culture kinetics. An expansion factor  $F^{exp}$ , expressed in Eq. (2.1), used data from cell counting by image analysis and compared the number of cell produced between  $t_0 + 2$  days and  $t_0 + 5$  days.

$$F^{exp} = \frac{\langle N_{cell/\mu C} \rangle_{t_0+5d} - \langle N_{cell/\mu C} \rangle_{t_0+2d}}{\langle N_{cell/\mu C} \rangle_{t_0+2d}} \quad (2.1)$$

Also based on image analysis results, the distribution of the number of cell per microcarrier was determined and the corresponding coefficient of variation  $c_v$  was calculated according to Eq. (2.2), with  $\sigma$  the standard deviation presented in Eq. (2.3). In this last parameter,  $N_{cell/\mu C} (i)$  corresponds to the number of cell counted on the  $i^{th}$  microcarrier and  $n$  represents the total number of microcarriers treated by image analysis.

$$c_v = \frac{\sigma}{\langle N_{cell/\mu C} \rangle} \cdot 100 \quad (2.2)$$

$$\sigma = \sqrt{\frac{1}{n-1} \sum_{i=1}^n (N_{cell/\mu C} (i) - \langle N_{cell/\mu C} \rangle)^2} \quad (2.3)$$

Two parameters based on metabolite concentrations were finally calculated. In one hand,  $Y_{Glu}$  yield was defined according to the Eq. (2.4), and described the concentration of glucose consumed on the cell concentration production, from  $t_0 + 2$  days to  $t_0 + 5$  days, with  $\Delta_{2 \rightarrow 5} C_{Glucose}^{consumption}$  corresponding to the cumulative glucose consumption between  $t_0 + 2$  days and  $t_0 + 5$  days,  $\Delta_{2 \rightarrow 5} \langle N_{cell/\mu C} \rangle$  for the mean number of cell produced between  $t_0 + 2$  days and  $t_0 + 5$  days, and  $C_{\mu C/L}$  the microcarrier concentration in the system. In the other hand, the  $Lac/Glu$  ratio was defined as the cumulative lactate production on the cumulative glucose consumption during the whole culture.

$$Y_{Glu} = \frac{\Delta_{2 \rightarrow 5} C_{Glucose}^{consumption}}{\Delta_{2 \rightarrow 5} \langle N_{cell/\mu C} \rangle \cdot C_{\mu C/L}} \quad (2.4)$$

### Phenotypic analysis

After trypsinization, cells were frozen before the flow cytometry analyses. They were then quickly thawed with fresh culture medium, pre-warmed at  $37^\circ$ . After centrifugation, cells were re-suspended in DPBS and their viability was validated using a Live / Dead kit assay. Cells were then incubated into DPBS-BSA 0.5 % (Gibco, Sigma-Aldrich) during 15 minutes and double marks were realized using antibodies targeting the specific antigen coupled with Phycoerythrin (PE) or Fluorescein isothiocyanate (FITC) during 45 minutes,

## 2.4. IMPACT OF THE TYPE OF MICROCARRIER IN DIFFERENT AGITATION MODES ON THE EXPANSION PERFORMANCES

---

at room temperature and out of direct light. Table 2.7 summarizes the antibodies used in this study. Cells were finally washed in DPBS and suspended in 300  $\mu$ L DPBS, before the injection into the flow cytometer Gallios (Beckman Coulter, Brea, CA, USA). The number of positive cells was obtained using the Kaluza software (Beckman Coulter, Brea, CA, USA).

Table 2.7: List of antibodies used for the flow cytometry analyses.

Antigen	Fluorophore	Manufacturer	Reference	Species	Isotype
Control isotype	FITC	DAKO	X0927	Mouse	IgG1 $\kappa$
Control isotype	PE	DAKO	X0928	Mouse	IgG1 $\kappa$
CD 90	FITC	Beckman Coulter	IM1838U	Mouse	IgG2a
CD 34	PE BD	Pharmlingen	555882	Mouse	IgG1 $\kappa$
HLA-DR	FITC	Beckman Coulter	IM0463U	Mouse	IgG2b
CD 73	PE BD	Pharmlingen	550257	Mouse	IgG1 $\kappa$
CD 45	FITC	DakoCytomation	F0861	Mouse	IgG1 $\kappa$
CD 166	PE	Beckman Coulter	A22361	Mouse	IgG1
CD 44	FITC	Beckman Coulter	IM1219U	Mouse	IgG1

### Multilineage differentiation studies

Cell multipotency was validated by using StemPro Differentiation Kits (Gibco).

#### *Adipogenesis differentiation*

As recommended by the manufacturer, cells were seeded at 10,000 cells /  $\text{cm}^2$  on 24-well plates with 1 mL of culture medium. After 24 h, culture medium was replaced with pre-warmed Complete Adipogenesis Differentiation Medium and re-feed every 3 days. After at least 40 days of culture, cells were washed with DPBS and fixed in a 4 % formaldehyde solution during 30 min. Thereafter, cells were twice washed with distilled water and incubated with Oil Red-O solution (0.5 % in isopropanol) at room temperature for 15 min. Cells were finally rinsed with distilled water before microscopic visualization.

#### *Osteogenesis differentiation*

As recommended by the manufacturer, cells were seeded at 5,000 cells /  $\text{cm}^2$  on 24-well plates with 1 mL of culture medium. After 24 h, culture medium was replaced with pre-warmed Complete Osteogenesis Differentiation Medium and re-feed every 3 days. After at least 40 days of culture, cells were washed with DPBS and fixed in a 4 % formaldehyde solution during 30 min. Thereafter, cells were twice washed with distilled water and stained with 2 % Alizirin Red S solution at room temperature for 2-3 min. Cells were finally rinsed with distilled water before microscopic visualization.

*Chondrogenesis differentiation*

Micromass cultures were performed in 24-well plates by seeding 5  $\mu\text{L}$  droplets of a cell solution of  $1.6 \cdot 10^7$  viable cells / mL. After 1 night in high humidity conditions, warmed chondrogenesis media was added and replaced every 3 days. After at least 40 days of culture, cells were washed with DPBS and fixed in a 4 % formaldehyde solution during 30 min. Thereafter, cells were twice washed with distilled water and incubated with 1 % Alcian Blue solution prepared in 0.1 HCl at room temperature for 30 min. Cells were finally rinsed three times with 0.1 HCl and distilled water before microscopic visualization.

**Data statistical analysis**

A one-way analysis of variance (ANOVA) test was used with a Fisher's Least Significant Difference (LSD) test admitting significance at  $p\text{-value} < 0.05$  to determine if the different groups were significantly different. For static cultures, standard deviations were calculated according to data from cultures performed in parallel ( $n=3$ ). Concerning dynamic cultures, standard deviations were calculated according to data of different cultures ( $n=2$ ). Higher variability may be thus expected than with cultures performed in the same time, with the same inoculum.

**2.4.3 Results and discussion*****In situ* cell counting on microcarriers validation**

Our original method to count cells *in situ* on microcarriers, without preliminary detachment, was first validated. Based on image analyses, cell nuclei emission from DAPI staining was recorded to distinguish and count cells on 584 microcarriers (18 photos processing). Thresholds for blue colour detection were validated with no interference, for each microcarriers, as shown in Fig. 2.9. Cell detection and counting were validated with 5 % mean deviation with the human visual counting, as presented in Fig 2.10. The method provided robust results up to 15 cells per microcarrier, which occurred in the photo displaying a mean number of 10 cells per microcarriers.

## 2.4. IMPACT OF THE TYPE OF MICROCARRIER IN DIFFERENT AGITATION MODES ON THE EXPANSION PERFORMANCES

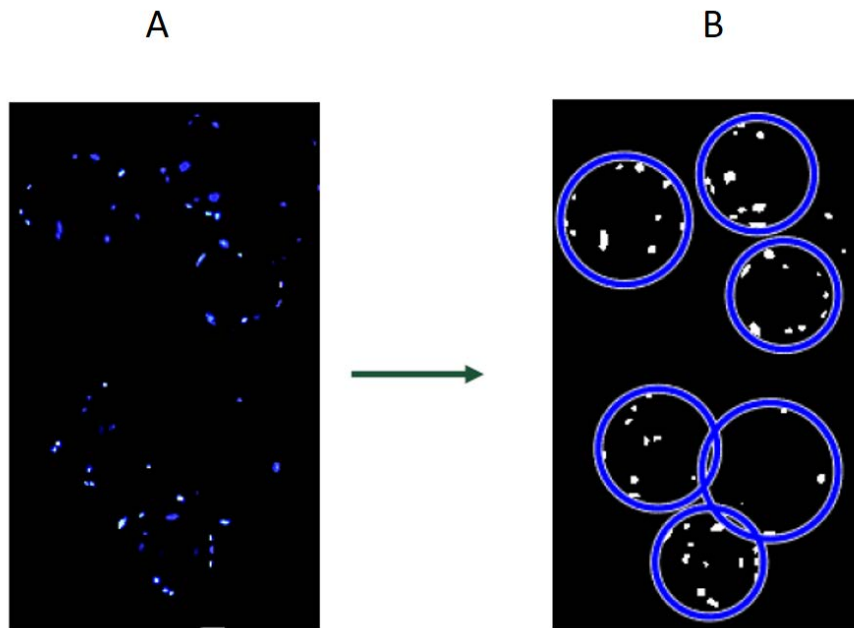


Figure 2.9: Example of photo treatment by image analysis after DAPI staining and microcarriers recognition: Contrast adjustment and blue colour isolation (A), and microcarrier detection and cell binarization and counting (B).

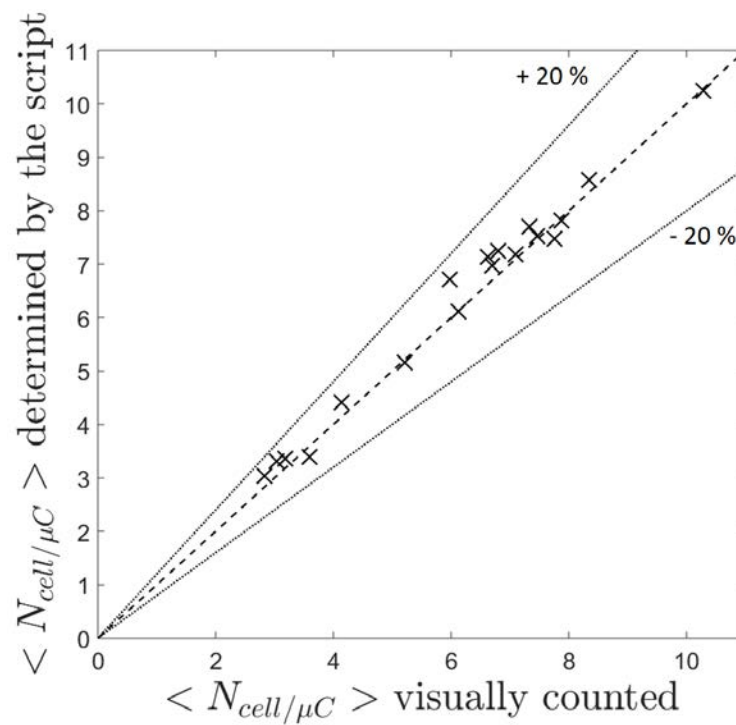


Figure 2.10: Comparison of the mean cell number per microcarrier determined by automatic post-treatment and by visual counting.



### Cell attachment and expansion on microcarriers

The number of cells attached at the beginning of the culture is closely linked to the cell expansion, since cell expansion latency may occur if a too low number of cells is adhered. However, a microcarrier presenting lower attachment capability than another may present a better expansion during the culture, and *vice versa*. Consequently, attachment and expansion are complementary. In the present study, cell adherence was described according to four parameters calculated during the first days of the cultures when possible: (i) the mean number of cells per microcarrier  $\langle N_{cell/\mu C} \rangle$ , (ii) the percentage of inoculated cells who adhered, (iii) the coefficient of variation  $c_v$  characterizing the cell number distribution (Eq. (2.2)) and (iv) the percentage of colonized microcarriers  $x_{colo}$ . Four additional parameters were also calculated to describe cell expansion: (i)  $Y_{Glu}$  (Eq. (2.4)), (ii)  $F^{exp}$  (Eq. (2.1)), (iii) LDH concentration kinetics, and (iv)  $Lac/Glu$  ratios. However, probably related to a lack of place, MSCs tended to gather together till some aggregates formation during longer cultivation durations. In some cases, microcarriers previously colonized were recovered empty, whereas a minority presented over-colonizations, as already reported by Ferrari *et al.* with porcine bone marrow MSCs [49]. Moreover, in dynamic mode, cell attachment was observed at  $t_0 + 48$  h in order to ensure cell adhesion and final morphology. During this duration, cell division was indeed negligible, with no population doubling, allowing to discuss on cell adhesion at the beginning of the cultures.

#### *Cell attachment and expansion comparison in static mode*

Without agitation, cells adhered on microcarriers may be found close one to each other with cell aggregates in some cases, making impossible the use of the *in situ* cell counting method. Consequently, microscopic analyses provided qualitative data and kinetics of metabolite concentration were used to quantitatively compare expansion performances. Different cell population behaviours and distributions on microcarriers were observed according to the type of microcarrier. Concerning Cytodex-1 and Plastic-Plus, cell bridges formed between microcarriers, as shown in Fig. 2.11 (A) and (D). Hence, heterogeneous cell distributions were observed at the end of the culture, with some microcarriers full of cells and others without cells in the case of Plastic-Plus, or with only one or two cells in the case of Cytodex-1. All Cytodex-1 were nevertheless colonized with at least one cell. Some cell colonies were observed on Plastic microcarriers, but the number of cells on microcarriers was significantly lower, as presented in Fig. 2.11 (C). Star-Plus and Hillex II qualitatively presented more homogeneous distributions without aggregates (Fig. 2.11 (D) and (E)).

Glucose consumption and lactate production kinetics showed that Cytodex-1, Star-Plus and Hillex II microcarriers led to higher cell expansions (Fig. 2.12). These microcarriers

## 2.4. IMPACT OF THE TYPE OF MICROCARRIER IN DIFFERENT AGITATION MODES ON THE EXPANSION PERFORMANCES

---

presented better fractions of colonized particles, which seemed to globally impact the cell expansion. On the contrary, Plastic microcarriers were notably unsuitable for MSC culture in comparison to other microcarriers regarding the low cell expansion after 5 days of culture and the LDH concentration. LDH concentration was indeed higher for the culture using Plastic microcarriers than with others, despite a lower number of cells observed on particles. This confirmed a lower cell viability in comparison to other microcarriers. Only Cytodex-1, Star-Plus, Plastic-Plus and Hillex II microcarriers were thus selected for the dynamic cultures.

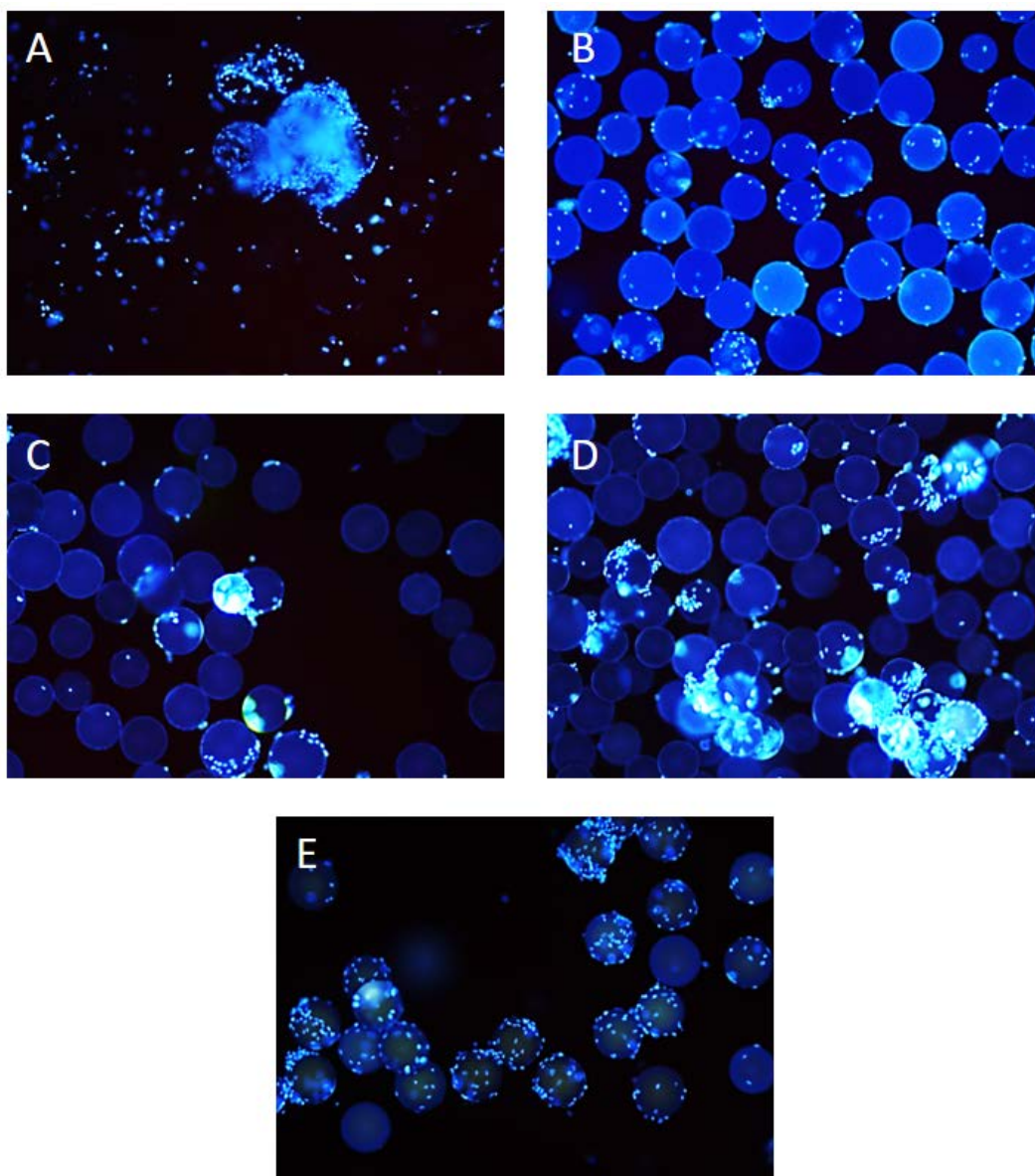


Figure 2.11: Cell nuclei DAPI coloration at  $t_0 + 5$  days in static mode: Cytodex-1 (A), Star-Plus (B), Plastic (C), Plastic-Plus (D) and Hillex II (E) microcarriers.

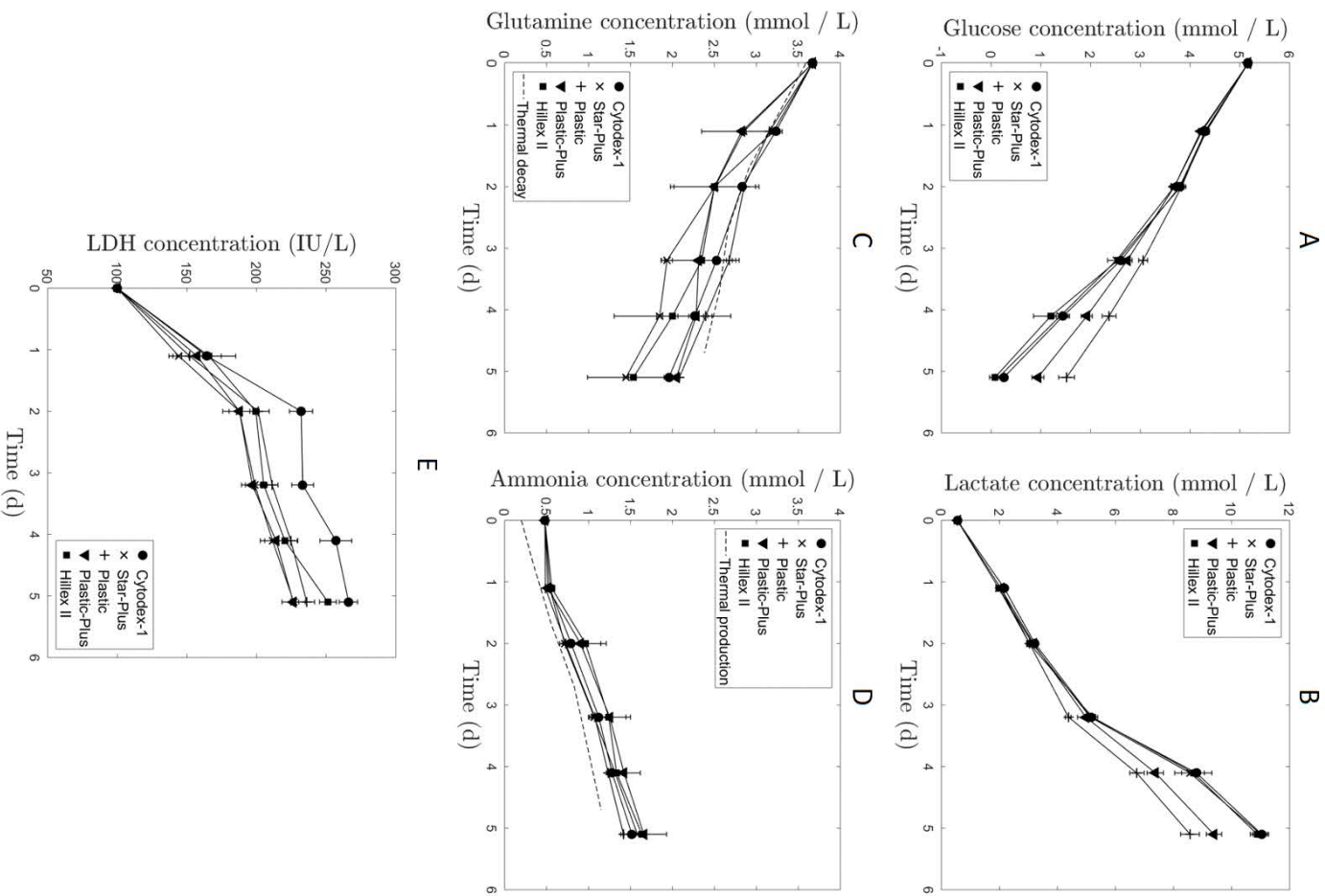


Figure 2.12: Kinetics of metabolite concentrations over time in static mode and according to the type of microcarrier used: Glucose (A), lactate (B), glutamine (C), ammonia (D) and LDH (E) ( $n = 3$ ).

*Cell attachment and expansion comparison with an orbital agitation*

Cultures in Erlenmeyer flasks were performed without agitation during the first two hours. Then, a continuous orbital agitation was applied to ensure particle suspension, but gathering most of particles inward. They led to different cell attachments depending on the type of microcarrier used. As presented in Fig. 2.13, Cytodex-1 presented the best capability with 59 % of inoculated cells adhered on microcarriers surfaces, whereas Star-Plus and Plastic-Plus presented lower values with 20 % and 37 % respectively. Concerning Hillex II, cell adhesion was found to be very low with only 9 % of adhered cells. The percentage of colonized microcarriers  $x_{colo}$ , represented in Fig. 2.14, was found to be related to the number of cells, with higher  $x_{colo}$  obtained with cultures displaying more attached cells. Fig. 2.15 showed that despite different mean cell numbers per microcarriers, the coefficients of variation of the cell distributions  $c_v$  remained similar for Cytodex-1, Star-Plus and Plastic-Plus, displaying tighter distributions than for Hillex II. Cell spreading was notably found larger and similar to fibroblasts for cells attached on Cytodex-1, as presented in Fig. 2.16. On the contrary, a significant fraction of cells adhered on the other microcarriers displayed round morphologies. Cell-microcarrier interactions are dependent on the microcarrier material and should be strong enough to maintain cells attached when subjected to hydromechanical stress.

After 5 days of culture, a higher number of cells was observed on Cytodex-1, as shown in Fig. 2.13, with at least 2.4 more cells than on other microcarriers. No cell expansion was observed using Plastic-Plus and Hillex II, making them unsuitable for cultures in Erlenmeyer flasks. In order to quantitatively compare expansion performances, the expansion factor  $F^{exp}$ , the cumulative glucose consumption  $Y_{Glu}$  (Eq. (2.4)) and the  $Lac/Glu$  ratio were calculated for each microcarrier and presented in Table 2.8. A higher expansion factor was found with Star-Plus. Hence, despite Cytodex-1 presented the best cell attachment capability, cell expansion performance was found better using Star-Plus microcarriers. As cell expansion is indeed limited by the free surface on microcarriers, a fraction of Cytodex-1 may already contain a too high number of cells from the beginning of the culture, that may reduce the substrate kinetics due to an early confluence.

The mean number of cells may also be related to the metabolite / substrate kinetics, presented in Fig. 2.17. As expected with a low cell adhesion, Hillex II presented low expansion performances. The mean number of cells per microcarrier, as well as the metabolite kinetics, declined, traducing cell death or detachment and limited cell proliferation. Regarding the LDH concentration, significantly more LDH was produced using Hillex II with 186 IU mL<sup>-1</sup>, in comparison to 169, 161 and 162 IU mL<sup>-1</sup> for respectively Cytodex-1, Star-Plus and Plastic-Plus, before the first culture medium exchange

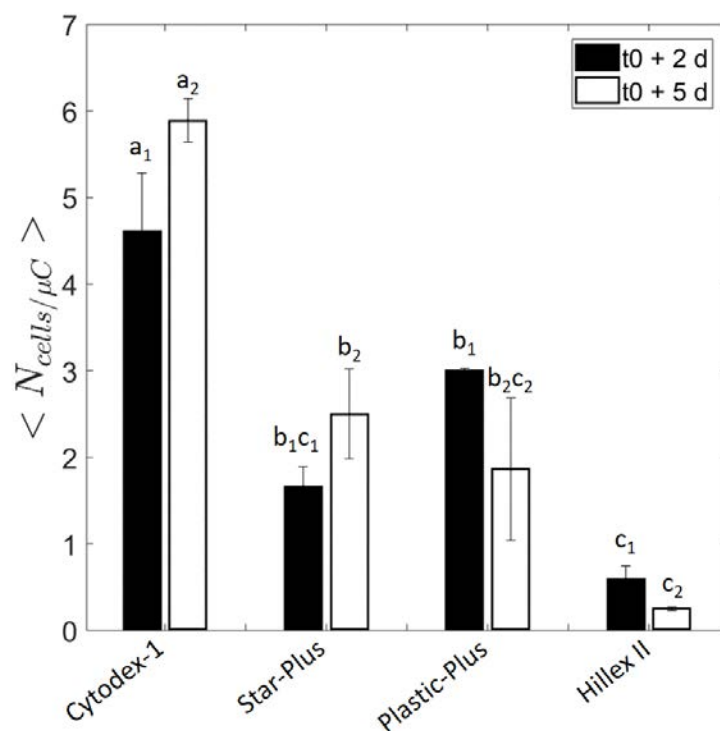


Figure 2.13: Mean number of cells per microcarrier cultivated with an orbital agitation and according to the type of microcarrier at  $t_0 + 2$  days (black bars) and  $t_0 + 5$  days (white bars) ( $n = 2$ ).

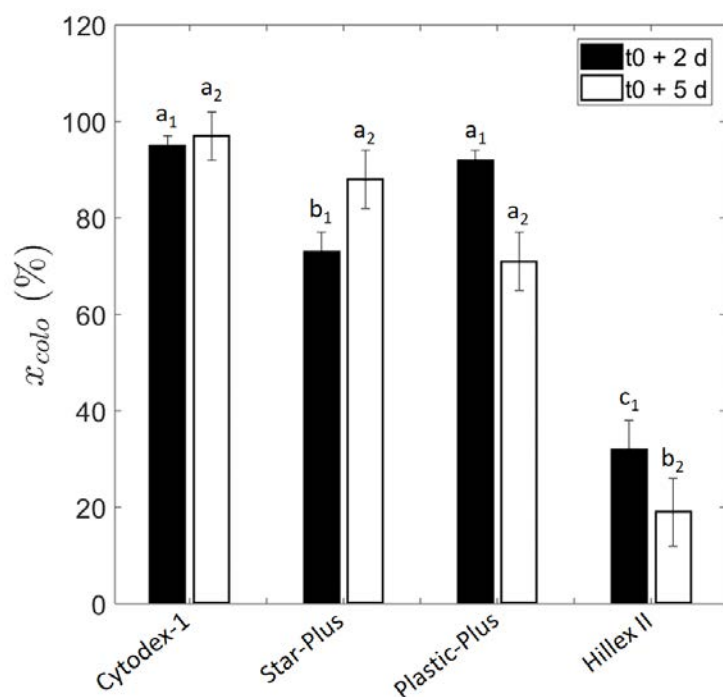


Figure 2.14: Fraction of microcarriers containing at least one cell in culture with an orbital agitation and according to the type of microcarrier at  $t_0 + 2$  days (black bars) and  $t_0 + 5$  days (white bars) ( $n = 2$ ).

## 2.4. IMPACT OF THE TYPE OF MICROCARRIER IN DIFFERENT AGITATION MODES ON THE EXPANSION PERFORMANCES

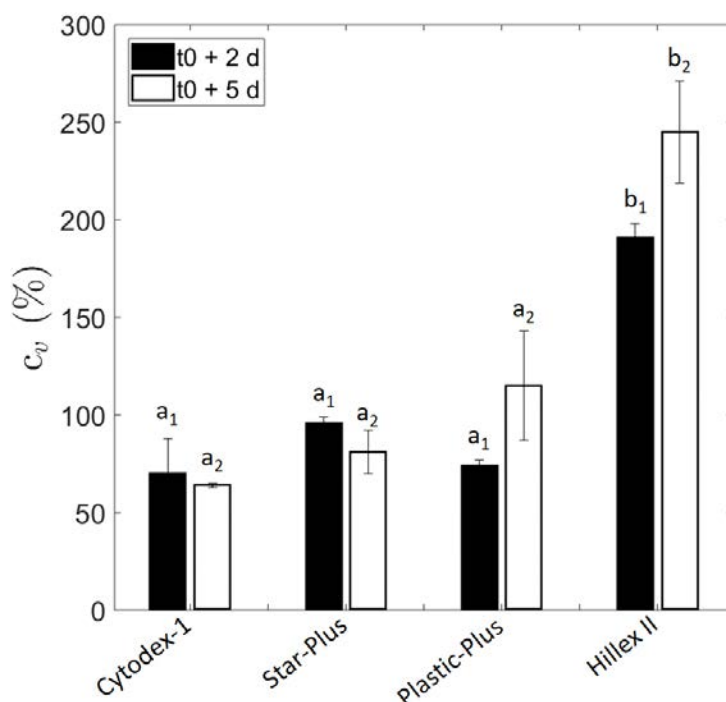


Figure 2.15: Coefficient of variation of the distribution characterizing the number of cell per microcarrier with an orbital agitation and according to the type of microcarrier at  $t_0 + 2$  days (black bars) and  $t_0 + 5$  days (white bars) ( $n = 2$ ).

(Fig. 2.17 (E)), whereas the total number of cells was found to be the lowest. It may be thus assumed that cell viability declined during the first days of the cultures. On the other hand, Cytodex-1 presented the highest  $Y_{Glu}$  yield of  $2.2 \cdot 10^{-10}$  mol cell<sup>-1</sup> in comparison to  $1.4 \cdot 10^{-10}$  mol cell<sup>-1</sup> calculated with Star-Plus. Due to a higher number of cells, the LDH concentrations was notably expected to be higher after 5 days of cultures (Fig. 2.17 (E)). Star-Plus presented a higher number of cells than on Plastic-Plus at  $t_0 + 2$  days and thus led to a higher metabolic activity during the first days. However, at  $t_0 + 5$  days, the mean number of cells on Plastic-Plus declined despite a metabolic activity. It may be supposed that a fraction of viable cell remained in suspension, without attachment possibility on microcarriers. However, cells in suspension would not be taken into account by the *in situ* counting method.

Cell distribution on microcarriers at  $t_0 + 2$  days and  $t_0 + 5$  days are presented in Fig. 2.15.  $c_v$  remained similar over time, except for Hilllex II. In this case, the deviation became significantly higher and may be related to the decrease of the colonized microcarrier fraction (Fig. 2.14).

Interesting results were obtained with *Lac/Glu* ratios, presented in Table 2.8. Values over 2 indicated the use of another carbon source than glucose into the different metabolic pathways, such as glutamine that may be a second source of carbon and energy. In static cultures performed without glutamine, cells exhibited round morphologies and finally de-

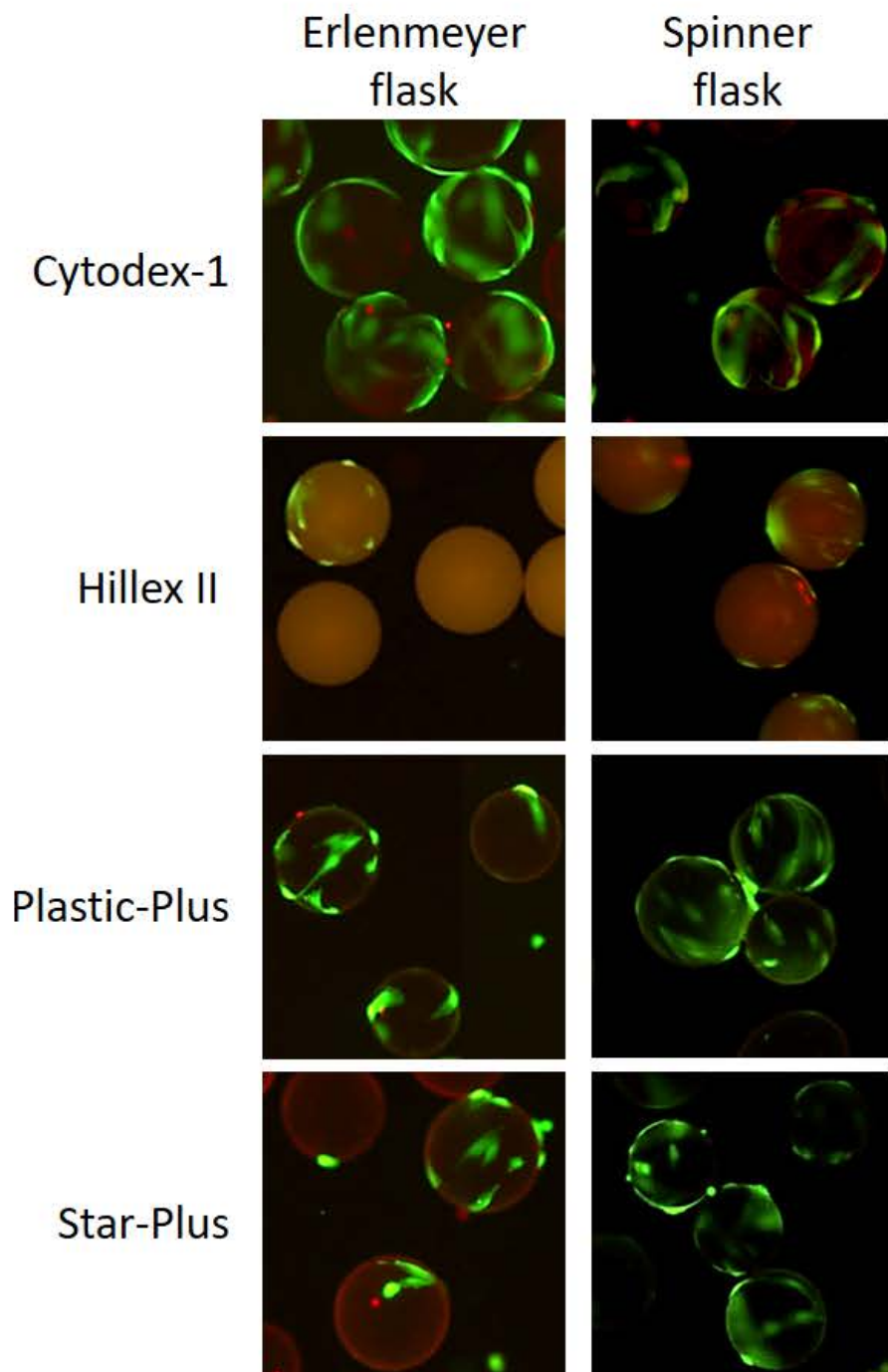


Figure 2.16: Cell morphology grown on microcarriers at  $t_0 + 2$  days according to the type of microcarrier and the agitation mode. Green staining for living cell membranes and red staining for dead cell nuclei.

## 2.4. IMPACT OF THE TYPE OF MICROCARRIER IN DIFFERENT AGITATION MODES ON THE EXPANSION PERFORMANCES

---

tached after a few days, without proliferation (data not shown). It was thus observed that glutamine was necessary for cell expansion. Hence, glutamine may be used by cells, even in low concentration and with limited cell respiratory activity. Such results were already reported in consistent other studies for Madin Darby Canine Kidney (MDCK) cells and Vero cells [50, 51]. So, the same metabolic adaptation may occur with WJ-MSK.

Table 2.8: Kinetic parameters calculated for cultures involving an orbital agitation and according to the type of microcarrier used ( $n = 2$ ).

Microcarrier	$F^{exp}$ (-)	$Y_{Glu}$ $\times 10^{-10}$ (mol cell $^{-1}$ )	$Lac/Glu$ (g g $^{-1}$ )
Cytodex-1	0.28	2.2	2.0
Star-Plus	0.51	1.4	2.0
Plastic-Plus	-0.38	N/A	2.1
Hillex II	-0.58	N/A	1.7

### *Cell attachment and expansion comparison with a mechanical agitation*

Cell cultures in spinner flasks started with one hour without agitation, except a gentle agitation at mid-time to promote cell homogenization on microcarriers. Particles were then dispersed by a mechanical agitation. In this system, cell attachment was similar for Cytodex-1, Star-Plus and Plastic-Plus microcarriers with 3.6 to 3.7 cells per microcarrier at  $t_0 + 2$  days, as presented in Fig. 2.18, and cell displayed similar fibroblast-like morphologies, as shown in Fig. 2.16. On the contrary, only 1.8 cells per microcarrier were counted on Hillex II microcarriers, with 30 % empty microcarriers as presented in Fig. 2.19. As a consequence, cells on Hillex II presented a more heterogeneous distribution than on Cytodex-1 and Plastic-Plus, with  $c_v = 105$  %, whereas 68 to 80 % were obtained with for the other microcarriers (Fig. 2.20).

In addition to the low cell attachment observed on Hillex II, no cell expansion was noticed at  $t_0 + 5$  days on Fig. 2.18. Cells adhered on Hillex II notably displayed more round morphologies than on other microcarriers, as shown in Fig. 2.16. Concerning the three other microcarriers, similar mean numbers of cells per microcarrier at  $t_0 + 5$  days were observed. However, the kinetics of metabolite concentrations, showed that cells used more glucose in cultures with Plastic-Plus microcarriers and more glutamine in cultures with Cytodex-1 (Fig. 2.21), despite no significant difference was observed on the mean number of cells per microcarriers on Cytodex-1, Star-Plus and Plastic-Plus at  $t_0 + 2$  days and  $t_0 + 5$  days. Hence, the metabolic activity, related to viable cells, was higher for cultures carried out with these two microcarriers, but with different metabolic pathways, involving different carbon sources for cell expansion. As for cultures in Erlenmeyer flasks,  $Lac/Glu$  ratios, and displaying values over 2, led to the hypothesis that glutamine was used by



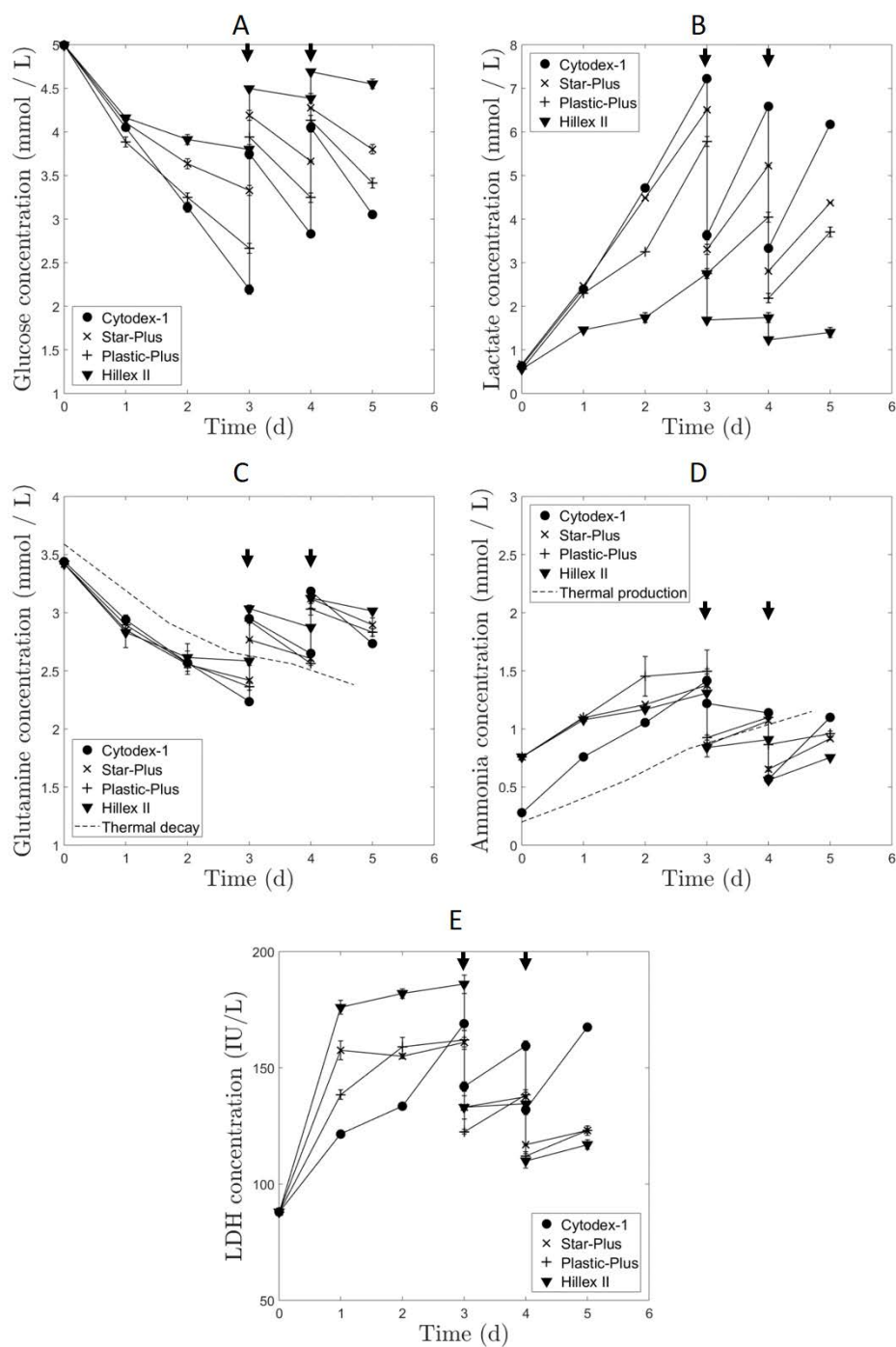


Figure 2.17: Kinetics of metabolite concentrations during cultures stirred with an orbital agitation and according to the type of microcarrier used: Glucose (A), lactate (B), glutamine (C), ammonia (D) and LDH (E). Vertical arrows correspond to an exchange of 50 % culture medium ( $n = 2$ ).

2.4. IMPACT OF THE TYPE OF MICROCARRIER IN DIFFERENT AGITATION MODES ON THE EXPANSION PERFORMANCES

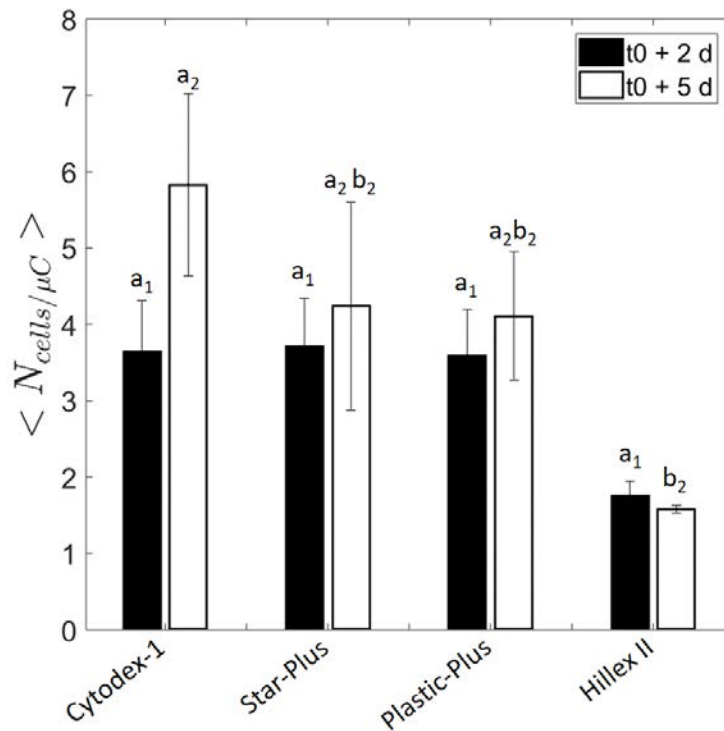


Figure 2.18: Mean number of cells per microcarrier cultivated with a mechanical agitation and according to the type of microcarrier at  $t_0 + 2$  days (black bars) and  $t_0 + 5$  days (white bars) ( $n = 2$ ).

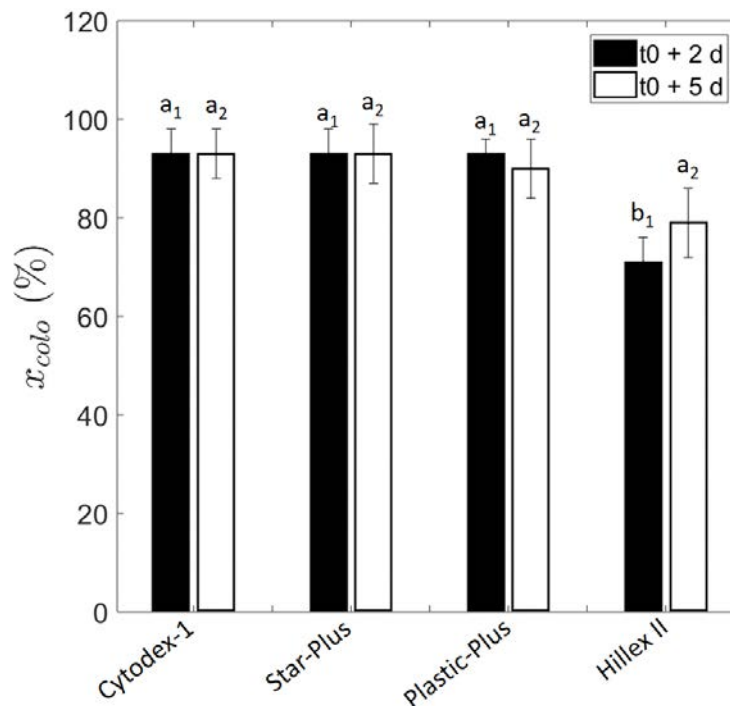


Figure 2.19: Fraction of microcarriers containing at least one cell in culture with a mechanical agitation and according to the type of microcarrier at  $t_0 + 2$  days (black bars) and  $t_0 + 5$  days (white bars) ( $n = 2$ ).

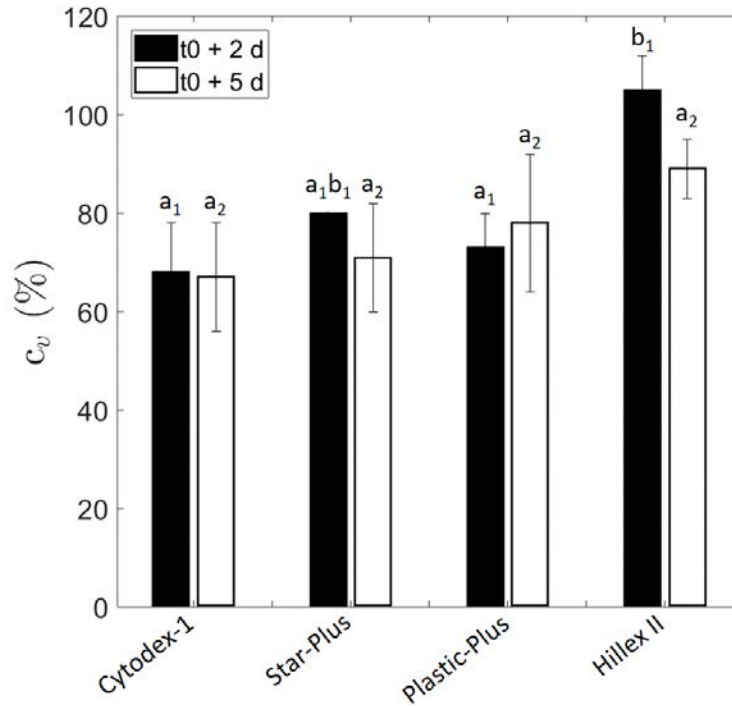


Figure 2.20: Coefficient of variation of the distribution characterizing the number of cell per microcarrier with a mechanical agitation and according to the type of microcarrier at  $t_0 + 2$  days (black bars) and  $t_0 + 5$  days (white bars) ( $n = 2$ ).

cells and led to the production of more lactate (Table 2.9). Here, this assumption was notably supported by the results on glutamine consumption with Cytodex-1.

It should nevertheless be noted that after 5 days, some broken Cytodex-1 were observed on microscopic analyses. The fraction of broken microcarriers remained low but may be expected to increase for longer cultures, and should thus be taken into account for cell quality. No broken particles were found in cultures performed with Star-Plus, Plastic-Plus and Hillex II, showing that these microcarriers are more robust in stirred systems than Cytodex-1.

Table 2.9: Kinetic parameters calculated for cultures involving a mechanical agitation and according to the type of microcarrier used ( $n = 2$ ).

Microcarrier	$F^{exp}$ (-)	$Y_{Glu}$ $\times 10^{-10}$ (mol cell <sup>-1</sup> )	$Lac/Glu$ (g gl <sup>-1</sup> )
Cytodex-1*	0.60	0.4	2.2
Star-Plus	0.14	1.7	2.1
Plastic-Plus	0.15	3.7	2.2
Hillex II	-0.10	N/A	1.9

## 2.4. IMPACT OF THE TYPE OF MICROCARRIER IN DIFFERENT AGITATION MODES ON THE EXPANSION PERFORMANCES

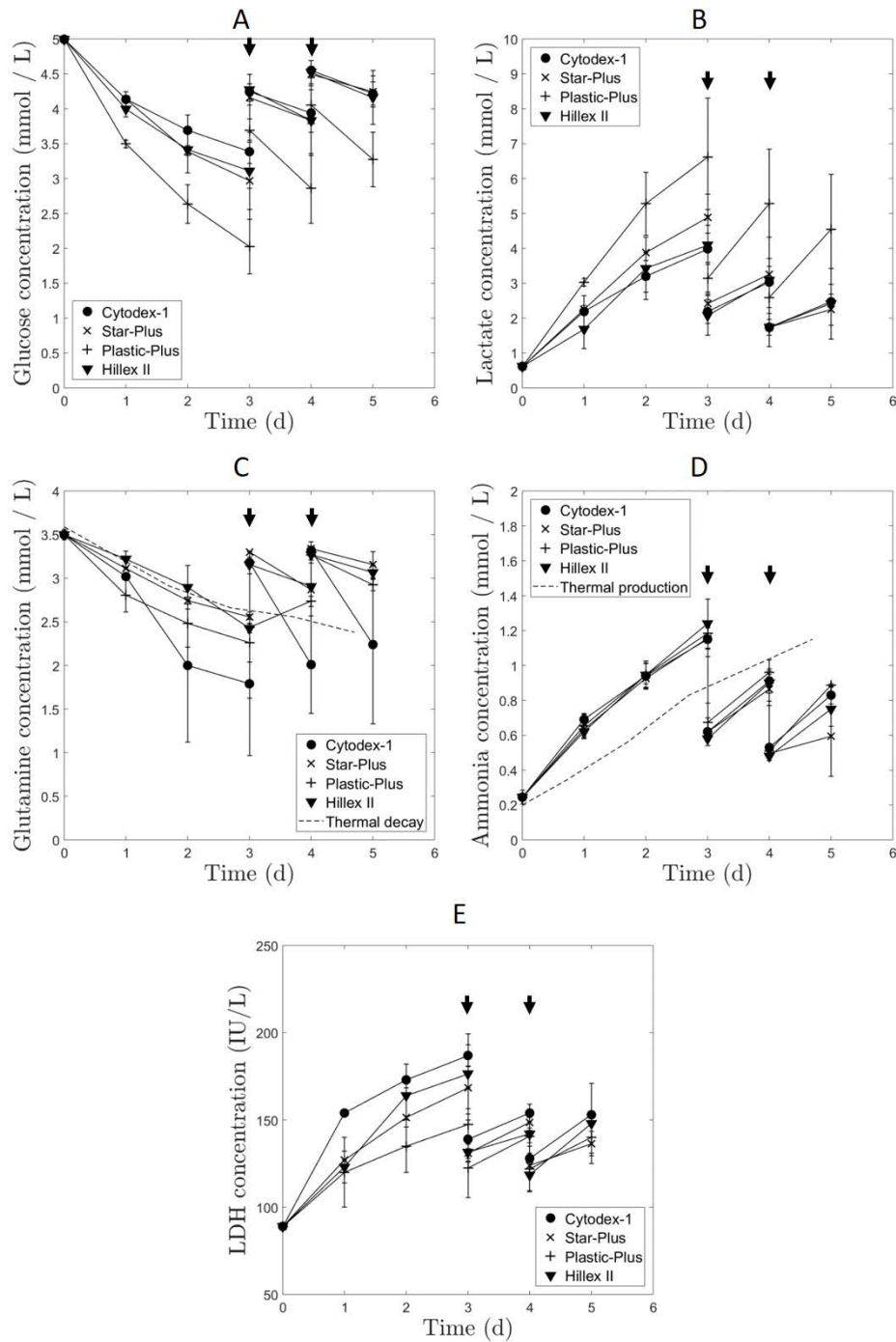


Figure 2.21: Kinetics of metabolite concentrations during cultures stirred with a mechanical agitation and according to the type of microcarrier used: Glucose (A), lactate (B), glutamine (C), ammonia (D) and LDH (E). Vertical arrows correspond to 50 % culture medium exchange ( $n = 2$ ).

To summarize the results related to the cell attachment and expansion criteria, the agitation mode used was found to have a significant impact on microcarrier performances. Static cultures of cells attached on microcarriers were found not representative of what could occur during dynamic cultures, in particular concerning Hillex II microcarriers. In the case of the orbital agitation, cells presented the best adhesion capability on Cytodex-1, the highest expansion rate on Star-Plus, and Plastic-Plus and Hillex II were found unsuitable for MSC cultures in Erlenmeyer flasks. By using a mechanical agitation, similar number of cells were obtained with Cytodex-1, Star-Plus and Plastic-Plus, but cell expansion seemed to involve different carbon sources with a higher glutamine consumption for cells on Cytodex-1 than with others. Hillex II was still found unsuitable with this agitation mode. As a result, microcarrier selection in static mode for applications in dynamic mode may be questionable, considering that performances in this condition could not be necessarily transposed to agitated cultures.

### **Cell detachment from microcarriers**

The last criterion to compare microcarriers adequacy for MSC cultures is the ease of detachment. Results of the microscopic analysis performed on microcarriers recovered after filtration used for the cell-particles separation are presented in Fig. 2.22. Cells presented good detachments from Star-Plus, Plastic-Plus and Hillex II, with almost no cells observed on microcarriers. On the contrary, many cells remained attached on Cytodex-1. Cell number and viability were controlled after cell detachment and filtration (Table. 2.10 and 2.11). In static mode, the cell viability was similar for all microcarriers, between 81 and 85 %. However, cells on Cytodex-1 presented lower viabilities of 83 % and 73 % after cultures with respectively both orbital and mechanical agitations, than those on Star-Plus and Plastic-Plus microcarriers. Concerning Hillex II, in stirred cultures, the detachment step damaged cells and led to cell viabilities of 61 % (orbital agitation) and 62 % (mechanical agitation), explaining the poor number of cells counted on microcarriers of only 0.5 to 0.6  $10^5$  cells.

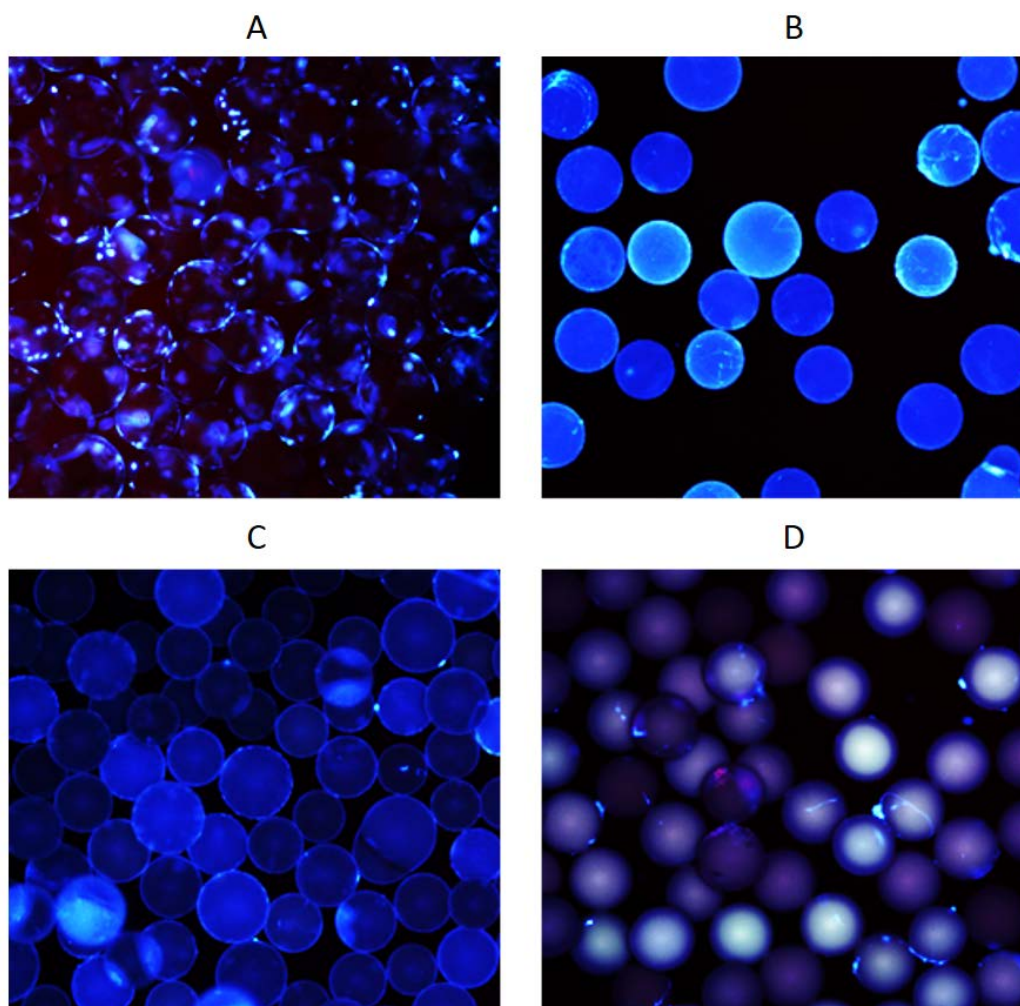


Figure 2.22: DAPI cell nuclei staining after cell detachment and filtration: Cytodex-1 (A), Star-Plus (B), Plastic-Plus (C) and Hillex II (D).

Table 2.10: Cell number counted after detachment according to the type of microcarrier ( $\times 10^5$ ,  $n = 2$ ).

Microcarrier	Static	Orbital agitation	Mechanical agitation
Cytodex-1	$1.3 \pm 0.2$	$3.4 \pm 1.8$	$0.5 \pm 0.1$
Star-Plus	$1.9 \pm 0.9$	$2.8 \pm 0.6$	$1.2 \pm 1.0$
Plastic	$1.1 \pm 0.3$	N/A	N/A
Plastic-Plus	$1.3 \pm 0.5$	$3.5 \pm 0.9$	$2.0 \pm 1.3$
Hillex II	$1.7 \pm 1.1$	$0.5 \pm 0.3$	$0.6 \pm 0.6$

### MSC identity validation

### Surface antigen expression

GW-MSC immunophenotype was characterized for various operating conditions in dynamic mode, involving the four microcarriers (Cytodex-1, Plastic-Plus, Star-Plus and

Table 2.11: Cell viability after detachment according to the type of microcarrier ( $n = 2$ ).

Microcarrier	Static	Orbital agitation	Mechanical agitation
Cytodex-1	82 % $\pm$ 7	83 % $\pm$ 1	73 % $\pm$ 4
Star-Plus	81 % $\pm$ 10	95 % $\pm$ 0	87 % $\pm$ 5
Plastic	78 % $\pm$ 5	N/A	N/A
Plastic-Plus	83 % $\pm$ 16	94 % $\pm$ 1	84 % $\pm$ 8
Hillex II	82 % $\pm$ 7	61 % $\pm$ 17	62 % $\pm$ 13

Hillex II) and the two agitation modes (orbital and mechanical) studied. Fig. 2.23 presented the percentage of expression obtained from MSC-specific cell surface markers. In all cases, less than 5 % expressed HLA-DR, CD45 and CD34. Concerning CD44, CD166, CD90 and CD73, more than 90 % cells expressed these markers, except in the cases of cultures on Cytodex-1 with an orbital agitation and on Star-Plus with a mechanical agitation, where CD90 markers were respectively expressed by 78 % and 75 % of the cell populations. All these values allow nevertheless to validate the cell immunophenotype for stem cell characterization.

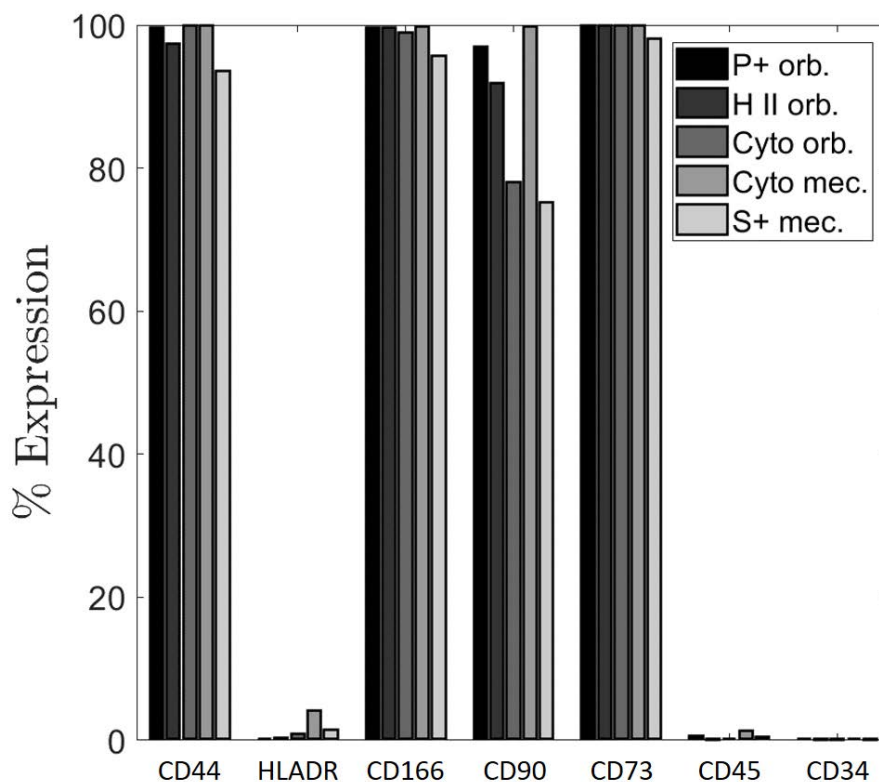


Figure 2.23: Characterization of GW-MSC immunophenotype, expanded under various dynamic conditions, by flow cytometry: Cells cultivated with an orbital agitation on Plastic-Plus (P+ orb.), Hillex II (H II orb.) and Cytodex-1 (Cyto orb.), and with a mechanical agitation on Cytodex-1 (Cyto mec.) and Star-Plus (S+ mec.).

### Cell differentiation validation

Differentiated cells into adipocytes, osteocytes and chondrocytes were observed after cell staining, as shown in Fig. 2.24. The type of microcarrier used and the agitation mode did not impact cell multipotency. However, in all cases the number of adipocyte differentiated cells was low, as already reported in the literature [52]. MSC from Wharton's jelly seemed to require more time than other MSC for adipocyte differentiation.

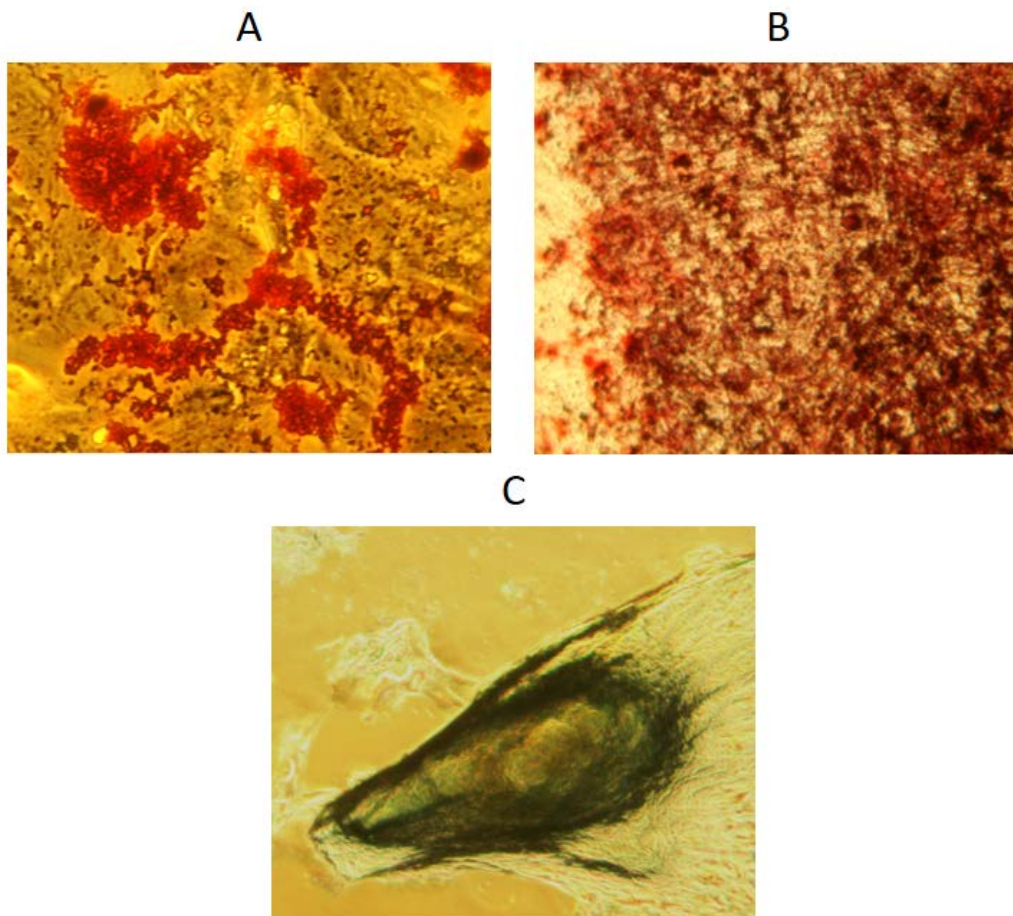


Figure 2.24: Differentiated WJ-MSC: (A) adipocytes stained with Oil Red, (B) osteocytes stained with Alizarin Red, (C) chondrocytes stained with Alcian blue.

### Microcarriers performances comparison

Microcarriers were finally compared according to the three criteria concerning cell attachment, expansion and ease of detachment. Each agitation mode led to the results summarized in Table 2.12. In the present study, the growth performance comparison was done relatively to the different microcarriers used, for each agitation mode. In static mode, Cytodex-1, Star-Plus, and Hillex II presented the best attachment and expansion



performances, but Cytodex-1 was found to be unsuitable for the cell detachment step. A significant fraction of cells remained attached, leading to cell loss at the end of the culture process. Using an orbital agitation, Cytodex-1 was preferred for attachment and expansion performances, but as for static cultures, the detachment step remained difficult. Consequently, Star-Plus microcarriers seemed to be the best compromise considering the three criteria of the study. In dynamic mode using mechanical agitation, Cytodex-1, and Plastic-Plus presented similar attachment and expansion performances, but the detachment step was still difficult for Cytodex-1, making Plastic-Plus more reliable. In both dynamic cases, Hillex II presented the lowest attachment and expansion performances, despite promising results in static mode.

### 2.4.4 Conclusion

Microcarriers were compared for three different agitation modes, namely static mode, orbital and mechanical agitation. Three culture steps were investigated, involving the attachment efficiency, the cell proliferation and the ease of detachment. It was assumed that all these three criteria were equally important for the cultivation process improvement. Results showed that performances obtained in static mode were not necessarily representative of culture performances in dynamic mode. They confirmed the need to already transpose the investigated agitation mode for microcarrier screening and selection before scale-up. Cell aggregates were notably observed in static cultures for Cytodex-1 and Plastic-Plus, but were found to be well dispersed in agitated mode.

This study demonstrated that the detachment step is still a challenge for the development of a robust process, especially when Cytodex-1 were used. Star-Plus and Plastic-Plus were found to be better compromises, respectively for the orbital and the mechanical agitation modes.

### 2.4.5 Acknowledgements

The authors would like to thank the French Agence Nationale de la Recherche (ANR) for its financial support. They also acknowledge Fabrice Blanchard (LRGP, Nancy) for his technical contribution to this work.

2.4. IMPACT OF THE TYPE OF MICROCARRIER IN DIFFERENT AGITATION MODES ON THE EXPANSION PERFORMANCES

Table 2.12: Microcarriers performances summary according to the agitation mode.

Microcarrier	Cytodex-1	Star-Plus	Plastic	Plastic-Plus	Hillex II
<b>Static mode</b>					
Cell attachment on microcarriers	++	++	-	++	++
Cell distribution and microcarrier occupancy	-	++	-	-	++
Cell expansion	++	++	-	+	++
Ease of detachment	-	++	-	++	++
<b>Orbital agitation</b>					
Cell attachment on microcarriers	++	+	N/A	+	-
Cell distribution and microcarrier occupancy	++	++	N/A	++	-
Cell expansion	+	++	N/A	+	-
Ease of detachment	-	++	N/A	++	+
<b>Mechanical agitation</b>					
Cell attachment on microcarriers	++	++	N/A	++	-
Cell distribution and microcarrier occupancy	++	++	N/A	++	-
Cell expansion	++	+	N/A	++	-
Ease of detachment	-	++	N/A	++	+

-: Lowest performances observed in the study.

+: Intermediate performances.

++: Best performances observed in the study.

N/A: Not applicable.

## 2.5 Cell culture on home-made microcarriers

Based on the results of the previous sections, commercial microcarriers were selected for comparison with home-made microcarriers developed by the LCPM laboratory. Cytodex-1 was chosen for its suitable attachment and expansion performances, but taking into account its poor detachment efficiency. Plastic-Plus was also selected as a good compromise between cell attachment, expansion and detachment. Cultures performances with these two commercial microcarriers and the microcarriers synthesized by the LCPM were compared in static mode. Concerning the home-made microcarriers, two different structures were compared, both with and without hPL coating, leading to a total of four home-made microcarriers: (i) PLA1, (ii) PLA1-hPL, (iii) PLA2 and (iv) PLA2-hPL. PLA-1 and PLA-2 both displays a polylactic acid (PLA) core, but differ from their surface composition, with a dextran- $C_{6,14}$  corona for PLA-1 and a dextran- $C\equiv C_{25}$  outer-layer for PLA-2 (Fig. 2.25) [53]. The LCPM production capacity was limited. Hence, the static mode was first chosen in order to validate cell-microcarrier interactions. Due to the low material needs in term of microcarriers and cells, cultures were performed in microplates. Dynamic cultures were then conducted, but results were inconclusive, and due to the limited microcarriers quantity, they could not be reproduced. The results presented in this last part will thus only focus on static cultures, despite a definitive comparison should be performed in dynamics mode, as demonstrated in section 2.4, where attachment and expansion differences may be observed between static and dynamic modes. The present work should thus be interpreted as preliminary data, suggesting that a low attachment efficiency in static mode would also led to low attachment with an agitation.

### 2.5.1 Macroscopic observations

No agitation was applied in order to validate the cell-substrate interactions leading to cell attachment on particles. At  $t_0 + 1 d$ , aggregates were observed with PLA2, PLA2-hPL and Plastic-Plus, despite the use of a fibrin-depleted culture medium, as shown in Fig. 2.26. It was suggested that, without agitation, and by using low attachment treated 6 well-plates, cells tended to gather during the attachment step to compensate a lack of available surface when they are present in a zone without microcarriers. It was indeed shown in the literature that MSC from bone marrow were able to grow in aggregate suspensions [54], but no expansion was *a priori* observed in the case of WJ-MSC aggregate suspensions. Then, cell bounding or matrix secreted by cells appeared to gather microcarriers together in one or more aggregates. This phenomenon was nevertheless found to be dependent

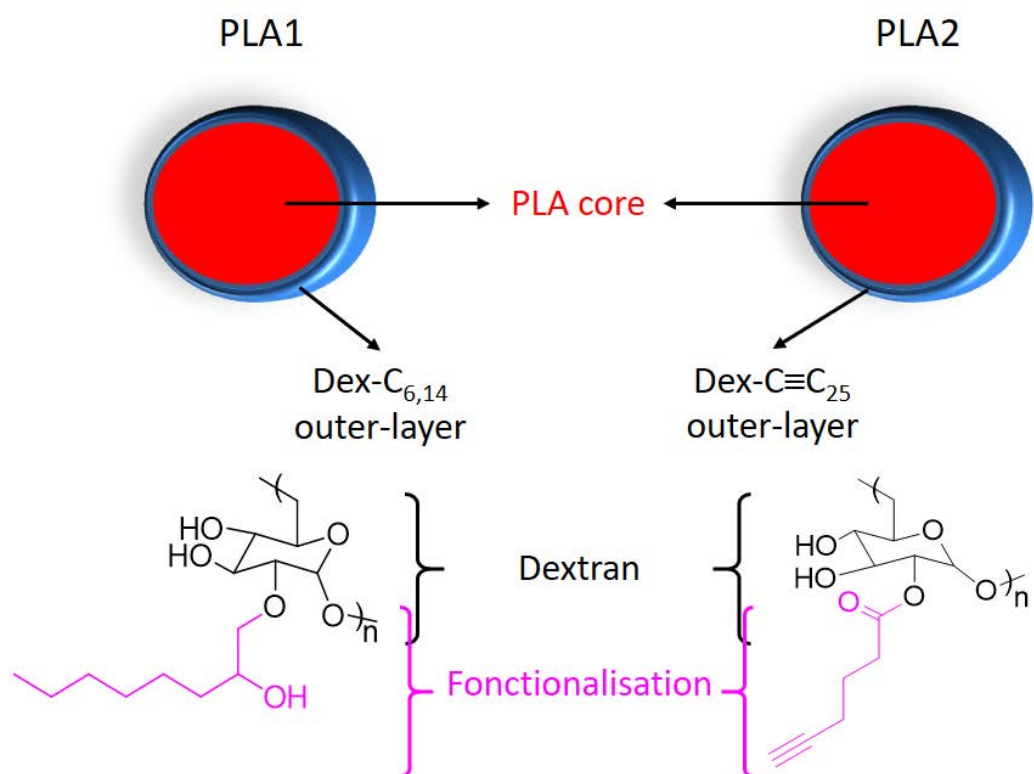


Figure 2.25: Home-made microcarriers formulation by the LCPM laboratory.

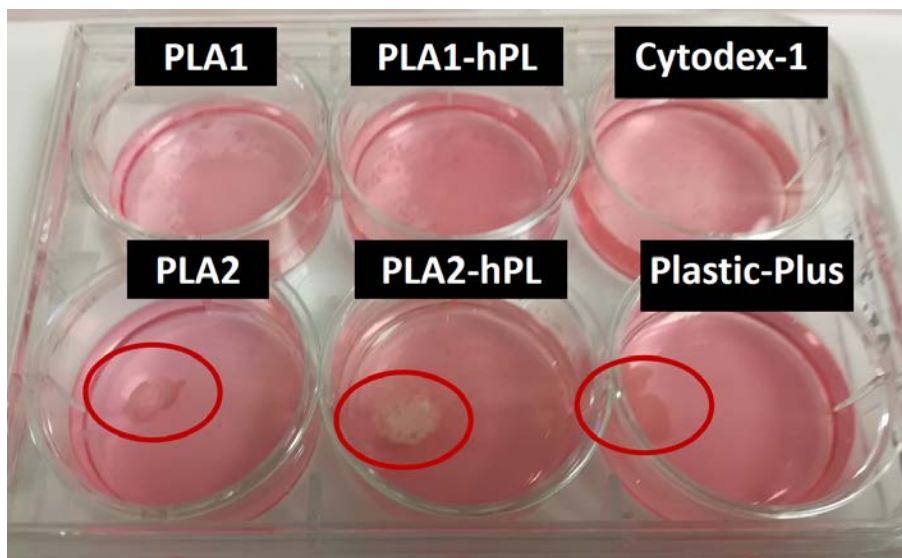


Figure 2.26: Macroscopic comparison of WJ-MSC static cultures in 6 well-plates with commercial and home-made microcarriers. Microcarriers aggregates are surrounded in red (representative results of 3 experiments are shown).

on the substrate material, as Cytodex-1, PLA1 and PLA1-hPL led to a well dispersed microcarriers behaviour.

## 2.5.2 hPL coating relevance and indirect cell kinetics

Figure 2.27 presents the kinetics of glucose consumption and lactate production. For all microcarriers, the substrate / metabolite kinetics validated cell expansion, and thus the preliminary cell attachment. Regarding the kinetics, it was observed that PLA1 and PLA2, namely the home-made microcarriers without hPL coating, presented similar glucose consumptions to those obtained with the commercial microcarriers. Only PLA1-hPL microcarrier was found to present significant lower glucose consumptions than all other and notably with its homologue without coating. On the contrary to most of commercial microcarriers, the home-made microcarriers presented the advantage to not require the coating step for microcarriers preparation. Removing this step would present relevant advantages, including operational costs and contamination risk reductions.

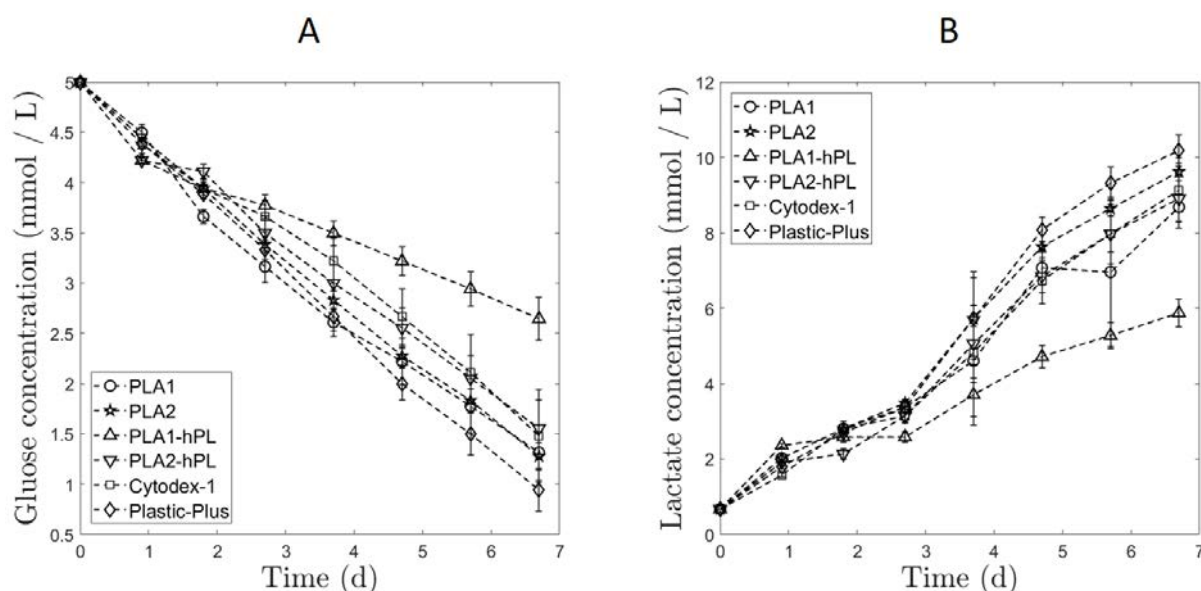


Figure 2.27: Kinetics of the metabolite concentrations WJ-MSC cultures on commercial and home-made microcarriers in static 6 well-plates: Glucose (A) and lactate (B) concentrations ( $n = 3$ ).

## 2.5.3 Cell distribution on microcarriers

Due to aggregate formations, no sampling was possible for cultures on Plastic-Plus, PLA2 and PLA2-hPL microcarriers without deleterious effects. Hence, microscopic analyses were only performed on Cytodex-1, PLA1 and PLA1-hPL microcarrier suspensions. Examples of photos are given in Fig. 2.28, presenting different cell distributions. Cells were found to be well dispersed on Cytodex-1, with all microcarriers containing at least one cell. Concerning PLA1 microcarriers, some of those were supposed empty but cells were

found to be mostly dispersed. In the case of the PLA1-hPL microcarriers, majority of microcarriers were empty and cells were gathered in small aggregates bounding a few particles together. Two hypotheses can be suggested. In one hand, it may be the result of high local cell expansion. In the other hand, cells may be gathered into aggregates since the beginning of the culture during the attachment step. By regarding the corresponding glucose consumption over time on Fig, 2.27, the second assumption is the most likely scenario, otherwise the kinetics of glucose consumption would present an exponential trend for several days. Here, the glucose consumption was found lower, probably as a consequence of the confluence. Moreover, without agitation, no potential bead-to-bead cell transfer was possible, limiting expansion on the empty, and thus available microcarriers.

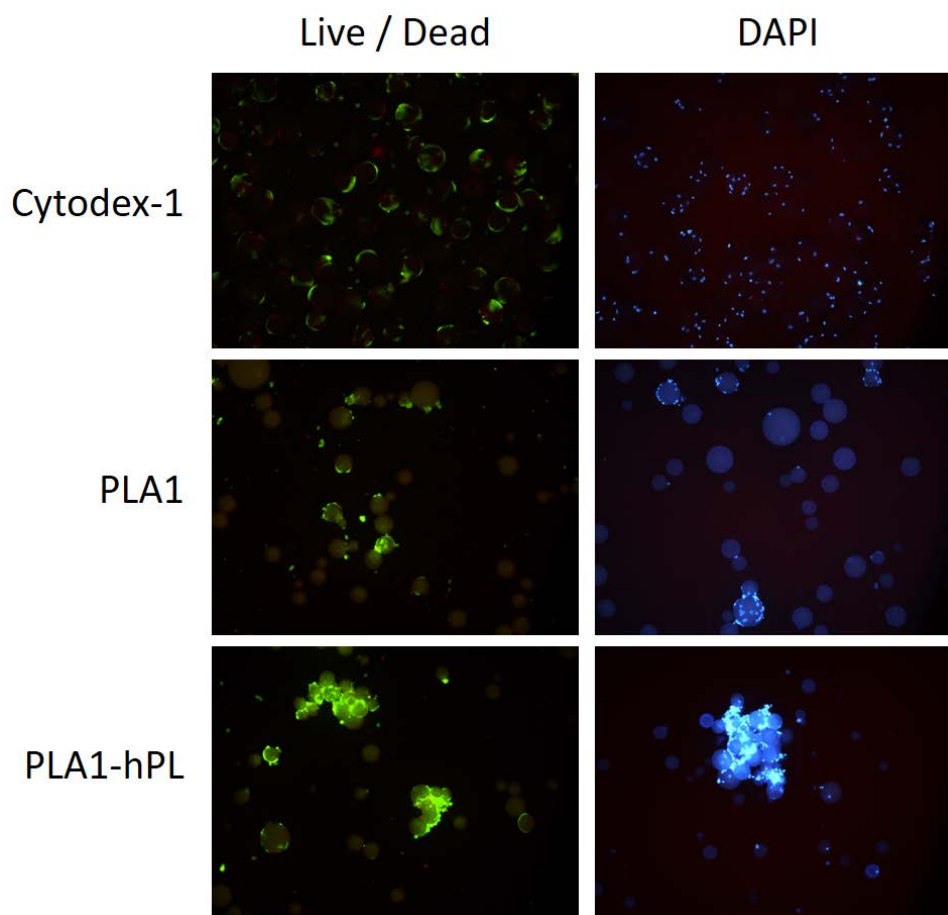


Figure 2.28: Live / Dead and DAPI cell staining on the commercial Cytodex-1 and the home-made PLA1 and PLA1-hPL microcarriers, from static cultures in 6 well-plates at  $t_0 + 7 d$ .

#### 2.5.4 Cell detachment

At  $t_0 + 7 d$ , cells were detached using TrypLE with a complementary agitation, and separated from microcarriers by a 40  $\mu\text{m}$  filtration. Figure 2.29 presented the number of

cells counted by a usual cell counter, cells being in suspension with a round morphology. The present numbers are only based on cells recovered at the end of the process, which may be considered as the final objective in some production fields. Some cells may still be attached on microcarriers as for Cytodex-1, or cell aggregates may be trapped during the filtration step. It is thus not necessarily representative of the cell expansion. Moreover, it was shown in section 2.4.3 that cell attachment on microcarriers in static mode was limited, with only 30 to 40 % of cells adhered on microcarriers. Because of macro- and micro- aggregate formations, no reliable data was obtained concerning the number of adhered cells at the beginning of the cultures, consequently no yield calculation on cell expansion could be performed. Cell number at the end of the culture may only be compared to their absolute value, leading to a similar quantity of harvested cells. As a result, the cell detachment protocol was validated for all home-made microcarriers.

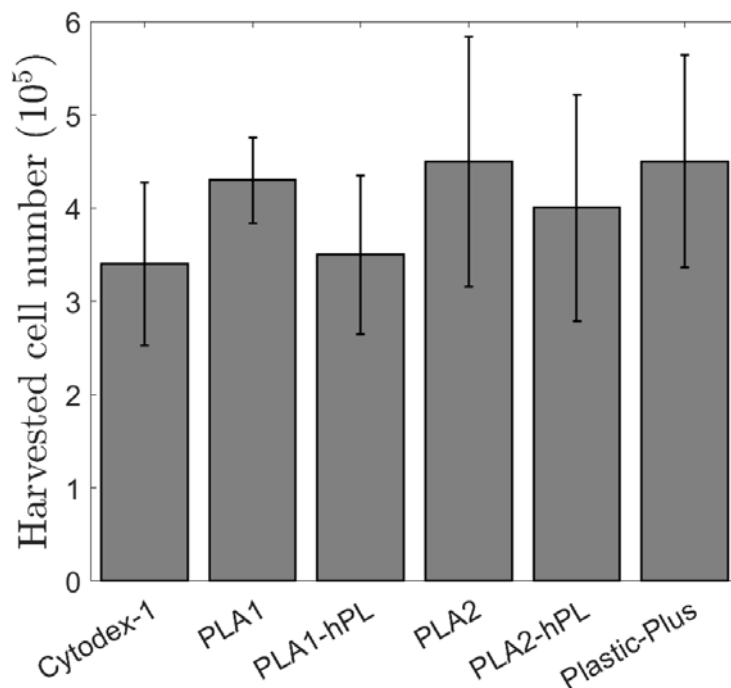


Figure 2.29: Number of harvested cells after the detachment and separation from microcarriers steps performed at  $t_0 + 7 d$  and from static cultures in 6 well-plates using commercial and home-made microcarriers ( $n = 3$ ).

## 2.6 Chapter conclusions

For WJ-MSK expansion, operating conditions required an adaptation of the usual protocols, previously validated for BM-MSK culture in a culture medium supplemented by FBS. WJ-MSK dynamic cultures on microcarriers and in a culture medium involving hPL led to gel formation despite the use of heparin. A mechanical and thermal fibrin-depletion avoided this jelly matrix formation, but cell expansion was slightly delayed. In parallel, the hPL-based coating was recommended for microcarriers as Star-Plus, but did not enhance cell attachment and expansion on Cytodex-1.

Once dynamic cell culture protocols were established, methods for performances comparison needed to be defined. With the aim of a robust quantitative method to directly count cells on microcarriers, a method coupling microscopic analysis and a Matlab script was developed. This method was consistent with DAPI staining, and led to both local and global data of the number of cells adhered on microcarriers. Cell distribution on microcarriers was notably quantified. However, this method presented deviations with the Live / Dead staining, from which light emission came from cell membrane instead of nuclei spots, indicating that the dye choice is crucial for the method accuracy.

Based on the two previous results, WJ-MSK cultures were performed with different commercial microcarriers and in systems involving different agitation modes. The objective was to compare culture performances for the three culture phases: (*i*) the attachment efficiency, (*ii*) the cell expansion and (*iii*) the ease of detachment. It was hence shown that microcarriers displayed different efficiencies, with no optimal microcarrier simultaneously for the three steps. Cytodex-1 could notably be recommended for cell attachment and expansion, but cell detachment was more difficult to perform. In parallel, the environment had an impact on the substrate consumptions, such as a higher glutamine consumption when Cytodex-1 microcarriers were used.

The last part of this chapter focused on cell culture comparison between selected commercial microcarriers and home-made microcarrier dedicated to MSK cultures, provided by the LCPM laboratory. This study was performed in static mode in order to validate cell attachment through interactions between cells and microcarrier material. The microcarrier PLA1, composed of a PLA core surrounded by a C6<sub>14</sub> dextran corona, presented the best results, by avoiding aggregates formation and by allowing a correct cell expansion, quantified by the metabolic activities. However, dynamic cultures should be performed in order to definitively validate this microcarrier comparison.



Main contributions of Chapter 2

- **WJ-MSC cultures on microcarriers were validated in a medium supplemented with hPL.** However, a mechanical **fibrin-depletion was required** to avoid a jelly matrix formation impacting cell expansion.
- **An automatic and *in situ* cell counting method on microcarriers** was developed using microscopic analysis and a Matlab script. It provided data on the **local cell distribution on microcarriers.**
- No optimal microcarrier was simultaneously found for static and dynamic cultures, according to cell adhesion, expansion and detachment capabilities. **When a new cell expansion process is investigated, a preliminary microcarrier screening would thus be recommended using the same agitation mode as the final process.**
- **Cytodex-1 is recommended for cell attachment and expansion, but cell detachment is more difficult to perform** than with other microcarriers. As a **compromise** between cell attachment, expansion and detachment, the **Star-Plus** and **Plastic-Plus** microcarriers are suggested, including the **orbital and the mechanical agitations** for each respectively.
- A **home-made microcarrier (PLA-1)**, that require no coating step, was synthesized for MSC culture applications. **In static mode, similar expansion performances than with Cytodex-1 and Plastic-Plus** were observed.

---

## References

- [1] J. Rowley, E. Abraham, A. Campbell, H. Brandwein, S. Oh, Meeting lot-size challenges of manufacturing adherent cells for therapy, *BioProcess International* 10 (2012) 16–22.
- [2] G. Eibes, F. dos Santos, P. Z. Andrade, J. S. Boura, M. M. Abecasis, C. L. da Silva, J. M. Cabral, Maximizing the ex vivo expansion of human mesenchymal stem cells using a microcarrier-based stirred culture system, *Journal of Biotechnology* 146 (2010) 194–197.
- [3] A. W. Nienow, C. J. Hewitt, T. R. Heathman, V. A. Glyn, G. N. Fonte, M. P. Hanga, K. Coopman, Q. A. Rafiq, Agitation conditions for the culture and detachment of hMSCs from microcarriers in multiple bioreactor platforms, *Biochemical Engineering Journal* 108 (2016) 24–29.
- [4] A. M. Soure, A. Fernandes-Platzgummer, F. Moreira, C. Lilaia, S.-H. Liu, C.-P. Ku, Y.-F. Huang, W. Milligan, J. Cabral, C. L. Silva, Integrated culture platform based on a human platelet lysate supplement for the isolation and scalable manufacturing of umbilical cord matrix-derived mesenchymal stem/stromal cells, *Journal of Tissue Engineering and Regenerative Medicine* 11 (2017) 1630–1640.
- [5] Q. A. Rafiq, K. Coopman, A. W. Nienow, C. J. Hewitt, Systematic microcarrier screening and agitated culture conditions improves human mesenchymal stem cell yield in bioreactors, *Biotechnology Journal* 11 (2016).
- [6] F. Petry, J. R. Smith, J. Leber, D. Salzig, P. Czermak, M. L. Weiss, Manufacturing of human umbilical cord mesenchymal stromal cells on microcarriers in a dynamic system for clinical use, *Stem Cells International* 2016 (2016).
- [7] N. B. Azouna, F. Jenhani, Z. Regaya, L. Berraeis, T. B. Othman, E. Ducrocq, J. Domenech, Phenotypical and functional characteristics of mesenchymal stem cells from bone marrow: comparison of culture using different media supplemented with human platelet lysate or fetal bovine serum, *Stem Cell Research & Therapy* 3 (2012) 6–20.
- [8] H. Hemeda, J. Kalz, G. Walenda, M. Lohmann, W. Wagner, Heparin concentration is critical for cell culture with human platelet lysate, *Cytotherapy* 15 (2013) 1174–1181.
- [9] T. R. Heathman, A. W. Nienow, Q. A. Rafiq, K. Coopman, B. Kara, C. J. Hewitt, Agitation and aeration of stirred-bioreactors for the microcarrier culture of human mesenchymal stem cells and potential implications for large-scale bioprocess development, *Biochemical Engineering Journal* 136 (2018) 9–17.
- [10] Q. A. Rafiq, K. M. Brosnan, K. Coopman, A. W. Nienow, C. J. Hewitt, Culture of human mesenchymal stem cells on microcarriers in a 5 L stirred-tank bioreactor, *Biotechnology Letters* 35 (2013) 1233–1245.
- [11] D. Schop, F. Janssen, E. Borgart, J. D. de Bruijn, R. van Dijkhuizen-Radersma, Expansion of mesenchymal stem cells using a microcarrier-based cultivation system:

- growth and metabolism, *Journal of Tissue Engineering and Regenerative Medicine* 2 (2008) 126–135.
- [12] S. Frauenschuh, E. Reichmann, Y. Ibold, P. M. Goetz, M. Sittinger, J. Ringe, A microcarrier-based cultivation system for expansion of primary mesenchymal stem cells, *Biotechnology Progress* 23 (2007) 187–193.
- [13] W. Hu, J. Meier, D. Wang, A mechanistic analysis of the inoculum requirement for the cultivation of mammalian cells on microcarriers, *Biotechnology and Bioengineering* 27 (1985) 585–595.
- [14] N. I. of Health, US national library of medicine, <https://www.clinicaltrials.gov>, cited July 2018.
- [15] A. I. Caplan, J. E. Dennis, Mesenchymal stem cells as trophic mediators, *Journal of Cellular Biochemistry* 98 (2006) 1076–1084.
- [16] M. Mimeault, R. Hauke, S. Batra, Stem cells: a revolution in therapeutics: recent advances in stem cell biology and their therapeutic applications in regenerative medicine and cancer therapies, *Clinical Pharmacology & Therapeutics* 82 (2007) 252–264.
- [17] A. Friedenstein, R. Chailakhjan, K. Lalykina, The development of fibroblast colonies in monolayer cultures of guinea-pig bone marrow and spleen cells, *Cell Proliferation* 3 (1970) 393–403.
- [18] B. Puissant, C. Barreau, P. Bourin, C. Clavel, J. Corre, C. Bousquet, C. Taureau, B. Cousin, M. Abbal, P. Laharrague, et al., Immunomodulatory effect of human adipose tissue-derived adult stem cells: comparison with bone marrow mesenchymal stem cells, *British Journal of Haematology* 129 (2005) 118–129.
- [19] C. De Bari, F. Dell’Accio, P. Tylzanowski, F. P. Luyten, Multipotent mesenchymal stem cells from adult human synovial membrane, *Arthritis & Rheumatology* 44 (2001) 1928–1942.
- [20] M. J. Griffiths, D. Bonnet, S. M. Janes, Stem cells of the alveolar epithelium, *The Lancet* 366 (2005) 249–260.
- [21] W. Jackson, A. Aragon, F. Djouad, Y. Song, S. Koehler, L. Nesti, R. Tuan, Mesenchymal progenitor cells derived from traumatized human muscle, *Journal of Tissue Engineering and Regenerative Medicine* 3 (2009) 129–138.
- [22] K. Bieback, S. Kern, H. Klüter, H. Eichler, Critical parameters for the isolation of mesenchymal stem cells from umbilical cord blood, *Stem Cells* 22 (2004) 625–634.
- [23] H.-S. Wang, S.-C. Hung, S.-T. Peng, C.-C. Huang, H.-M. Wei, Y.-J. Guo, Y.-S. Fu, M.-C. Lai, C.-C. Chen, Mesenchymal stem cells in the wharton’s jelly of the human umbilical cord, *Stem Cells* 22 (2004) 1330–1337.

- 
- [24] M. Dominici, K. Le Blanc, I. Mueller, I. Slaper-Cortenbach, F. Marini, D. Krause, R. Deans, A. Keating, D. Prockop, E. Horwitz, Minimal criteria for defining multipotent mesenchymal stromal cells. the international society for cellular therapy position statement, *Cytotherapy* 8 (2006) 315–317.
- [25] A. Stolzing, E. Jones, D. McGonagle, A. Scutt, Age-related changes in human bone marrow-derived mesenchymal stem cells: consequences for cell therapies, *Mechanisms of Ageing and Development* 129 (2008) 163–173.
- [26] K. Cierpka, C. L. Elseberg, K. Niss, M. Kassem, D. Salzig, P. Czermak, hMSC production in disposable bioreactors with regards to GMP and PAT, *Chemie Ingenieur Technik* 85 (2013) 67–75.
- [27] K. M. Panchalingam, S. Jung, L. Rosenberg, L. A. Behie, Bioprocessing strategies for the large-scale production of human mesenchymal stem cells: a review, *Stem Cell Research & Therapy* 6 (2015) 225–234.
- [28] C. Martin, É. Olmos, M.-L. Collignon, N. De Isla, F. Blanchard, I. Chevalot, A. Marc, E. Guedon, Revisiting MSC expansion from critical quality attributes to critical culture process parameters, *Process Biochemistry* 59 (2017) 231–243.
- [29] F. d. Santos, P. Z. Andrade, M. M. Abecasis, J. M. Gimble, L. G. Chase, A. M. Campbell, S. Boucher, M. C. Vemuri, C. L. d. Silva, J. M. Cabral, Toward a clinical-grade expansion of mesenchymal stem cells from human sources: a microcarrier-based culture system under xeno-free conditions, *Tissue Engineering Part C: Methods* 17 (2011) 1201–1210.
- [30] C. Tekkatte, G. P. Gunasingh, K. Cherian, K. Sankaranarayanan, Humanized stem cell culture techniques: the animal serum controversy, *Stem Cells International* 2011 (2011) 1–14.
- [31] A. Van Wezel, Growth of cell-strains and primary cells on micro-carriers in homogeneous culture, *Nature* 216 (1967) 64–65.
- [32] A. S. Simaria, S. Hassan, H. Varadaraju, J. Rowley, K. Warren, P. Vanek, S. S. Farid, Allogeneic cell therapy bioprocess economics and optimization: Single-use cell expansion technologies, *Biotechnology and Bioengineering* 111 (2014) 69–83.
- [33] T. Ma, A.-C. Tsai, Y. Liu, Biomanufacturing of human mesenchymal stem cells in cell therapy: Influence of microenvironment on scalable expansion in bioreactors, *Biochemical Engineering Journal* 108 (2016) 44–50.
- [34] T. Lawson, D. E. Kehoe, A. C. Schnitzler, P. J. Rapiejko, K. A. Der, K. Philbrick, S. Punreddy, S. Rigby, R. Smith, Q. Feng, J. R. Murrell, M. S. Rook, Process development for expansion of human mesenchymal stromal cells in a 50 L single-use stirred tank bioreactor, *Biochemical Engineering Journal* 120 (2017) 49–62.
- [35] M. S. Croughan, J.-F. Hamel, D. I. Wang, Hydrodynamic effects on animal cells grown in microcarrier cultures, *Biotechnology and Bioengineering* 29 (1987) 130–141.

- [36] T. M. Maul, D. W. Chew, A. Nieponice, D. A. Vorp, Mechanical stimuli differentially control stem cell behavior: morphology, proliferation, and differentiation, *Biomechanics and Modeling in Mechanobiology* 10 (2011) 939–953.
- [37] S. Jung, K. M. Panchalingam, R. D. Wuerth, L. Rosenberg, L. A. Behie, Large-scale production of human mesenchymal stem cells for clinical applications, *Biotechnology and Applied Biochemistry* 59 (2012) 106–120.
- [38] A. Bongso, C.-Y. Fong, The therapeutic potential, challenges and future clinical directions of stem cells from the wharton? jelly of the human umbilical cord, *Stem Cell Reviews and Reports* 9 (2013) 226–240.
- [39] T. Nagamura-Inoue, H. He, Umbilical cord-derived mesenchymal stem cells: Their advantages and potential clinical utility, *World Journal of Stem Cells* 6 (2014) 195–202.
- [40] D.-W. Kim, M. Staples, K. Shinozuka, P. Pantcheva, S.-D. Kang, C. V. Borlongan, Wharton’s jelly-derived mesenchymal stem cells: phenotypic characterization and optimizing their therapeutic potential for clinical applications, *International Journal of Molecular Sciences* 14 (2013) 11692–11712.
- [41] D. L. Troyer, M. L. Weiss, Concise review: Wharton’s jelly-derived cells are a primitive stromal cell population, *Stem Cells* 26 (2008) 591–599.
- [42] I. N. Simões, J. S. Boura, F. dos Santos, P. Z. Andrade, C. M. Cardoso, J. M. Gimble, C. L. da Silva, J. Cabral, Human mesenchymal stem cells from the umbilical cord matrix: Successful isolation and ex vivo expansion using serum-/xeno-free culture media, *Biotechnology Journal* 8 (2013) 448–458.
- [43] W. C. Pereira, I. Khushnooma, M. Madkaikar, K. Ghosh, Reproducible methodology for the isolation of mesenchymal stem cells from human umbilical cord and its potential for cardiomyocyte generation, *Journal of Tissue Engineering and Regenerative Medicine* 2 (2008) 394–399.
- [44] J. R. Smith, K. Pfeifer, F. Petry, N. Powell, J. Delzeit, M. L. Weiss, Standardizing umbilical cord mesenchymal stromal cells for translation to clinical use: selection of gmp-compliant medium and a simplified isolation method, *Stem Cells International* 2016 (2016) 1–14.
- [45] A. Mizukami, A. Fernandes-Platzgummer, J. G. Carmelo, K. Swiech, D. T. Covas, J. M. Cabral, C. L. da Silva, Stirred tank bioreactor culture combined with serum-/xenogeneic-free culture medium enables an efficient expansion of umbilical cord-derived mesenchymal stem/stromal cells, *Biotechnology Journal* 11 (2016) 1048–1059.
- [46] K. Y. Tan, K. L. Teo, J. F. Lim, A. K. Chen, S. Reuveny, S. K. Oh, Serum-free media formulations are cell line-specific and require optimization for microcarrier culture, *Cytherapy* 17 (2015) 1152–1165.

- 
- [47] S. Laner-Plamberger, T. Lener, D. Schmid, D. A. Streif, T. Salzer, M. Öller, C. Hauser-Kronberger, T. Fischer, V. R. Jacobs, K. Schallmoser, et al., Mechanical fibrinogen-depletion supports heparin-free mesenchymal stem cell propagation in human platelet lysate, *Journal of Translational Medicine* 13 (2015) 354.
- [48] K. Pachler, T. Lener, D. Streif, Z. A. Dunai, A. Desgeorges, M. Feichtner, M. Öller, K. Schallmoser, E. Rohde, M. Gimona, A good manufacturing practice-grade standard protocol for exclusively human mesenchymal stromal cell-derived extracellular vesicles, *Cytotherapy* 19 (2017) 458–472.
- [49] C. Ferrari, F. Balandras, E. Guedon, E. Olmos, I. Chevalot, A. Marc, Limiting cell aggregation during mesenchymal stem cell expansion on microcarriers, *Biotechnology Progress* 28 (2012) 780–787.
- [50] Y. Sidorenko, A. Wahl, M. Dauner, Y. Genzel, U. Reichl, Comparison of metabolic flux distributions for mdck cell growth in glutamine-and pyruvate-containing media, *Biotechnology Progress* 24 (2008) 311–320.
- [51] E. Petiot, E. Guedon, F. Blanchard, C. Gény, H. Pinton, A. Marc, Kinetic characterization of vero cell metabolism in a serum-free batch culture process, *Biotechnology and Bioengineering* 107 (2010) 143–153.
- [52] L. Reppel, T. Margossian, L. Yaghi, P. Moreau, N. Mercier, L. Leger, S. Hupont, J.-F. Stoltz, D. Bensoussan, C. Huselstein, Hypoxic culture conditions for mesenchymal stromal/stem cells from wharton’s jelly: a critical parameter to consider in a therapeutic context, *Current Stem Cell Research & Therapy* 9 (2014) 306–318.
- [53] A. Roy, M. A. M. Valderrama, V. Daujat, K. Ferji, M. Léonard, A. Durand, J. Babin, J.-L. Six, Stability of a biodegradable microcarrier surface: physically adsorbed versus chemically linked shells, *Journal of Materials Chemistry B* 6 (2018) 5130–5143.
- [54] D. Baksh, J. E. Davies, P. W. Zandstra, Adult human bone marrow-derived mesenchymal progenitor cells are capable of adhesion-independent survival and expansion, *Experimental Hematology* 31 (2003) 723–732.

# Modelling of microcarriers just-suspended state in a stirred tank bioreactor

## Contents

---

<b>3.1</b>	<b>Introduction</b>	<b>148</b>
<b>3.2</b>	<b>CFD models investigation for simulation of microcarriers suspension in stirred-tank bioreactors</b>	<b>150</b>
3.2.1	Culture systems geometries and meshing	150
3.2.2	Material properties	151
3.2.3	Multiphase modelling by CFD	151
3.2.4	Initialization and convergence criteria	152
3.2.5	Navier-Stokes equations	152
3.2.6	Turbulence modelling	153
3.2.7	Near-wall turbulence modelling	155
3.2.8	Drag force model investigation	156
3.2.9	Turbulent dispersion force impact	160
3.2.10	Granular temperature modelling	161
3.2.11	Models selection synthesis	162
<b>3.3</b>	<b>Dimensional analysis and CFD simulations of microcarrier just-suspended state</b>	<b>163</b>
3.3.1	Context	164
3.3.2	Experimental approach	166
3.3.3	Particle suspension modelling	168
3.3.4	Results and discussions	174
3.3.5	Conclusion	183
3.3.6	Acknowledgements	184
<b>3.4</b>	<b>Chapter conclusions</b>	<b>185</b>

---

## 3.1 Introduction

**M**ICROCARRIERS are more and more used for MSC culture intensification. However, in order to guarantee cells quality during cultures and to allow a process scale-up based on well-chosen and robust parameters, the bioreactor hydrodynamics must be carefully taken into account. This notably passes through the development and validation of reliable descriptive models.

Microcarrier suspension during dynamic cultures is induced by an agitation, leading to hydromechanical stress onto bead surfaces, and consequently to potential cell damages. In order to minimize this stress, the minimal agitation rate ensuring all particles suspension  $N = N_{js}$  is generally looked for. **A first study was performed to develop experimental measurements based on light attenuation in order to characterize the spatial distribution of microcarrier concentration at different suspension states.** Based on these experimental analyses, Euler-Euler CFD simulations were validated to predict the spatial distribution of microcarriers within the vessel. **This work, which can be found in Appendix A, investigated the microcarrier distribution at different agitation rates.** Nevertheless, simulations run at  $N = N_{js}$  led to higher solid concentration at the tank bottom, despite the suspension was experimentally nearly uniform.

As previously demonstrated, in the case of MSC cultures, focus on the particle just-suspended state, namely at  $N = N_{js}$  is pertinent. In that manner, this chapter deals with the modelling of the microcarrier just-suspended state in stirred tank bioreactors. Until now, the Zwietering visual method has been widely used at the beginning of experiments to determine the just-suspended state. This critical state is considered to be reached when particles do not stay longer than 1 or 2 seconds in the bottom of the bioreactor. This method would be nevertheless tricky to apply in the case of large cultures over tens of liters or for cultures performed in non-transparent bioreactors. The aim of this chapter, illustrated in Fig. 3.1, is hence to present two scalable methods to predict the just-suspended state, developed in collaboration with the university of Liège (ULg, Belgium). These models were notably developed in order to be applicable for all three axial, mixed-flow and radial flows.

First, preliminary results will be presented in order to justify the models chosen for the further CFD simulations (section 3.2). Attention will be paid to the turbulence and liquid-solid interaction forces.



In a second time, the two modelling approaches will be presented as a submitted publication in *Chemical Engineering Science* (section 3.3). The first one consisted in a dimensional analysis based on numerous experimental  $N_{js}$  measurements using different impeller geometries and particle properties. In parallel, the second method was established using CFD simulations and validated using the experimental measurements.

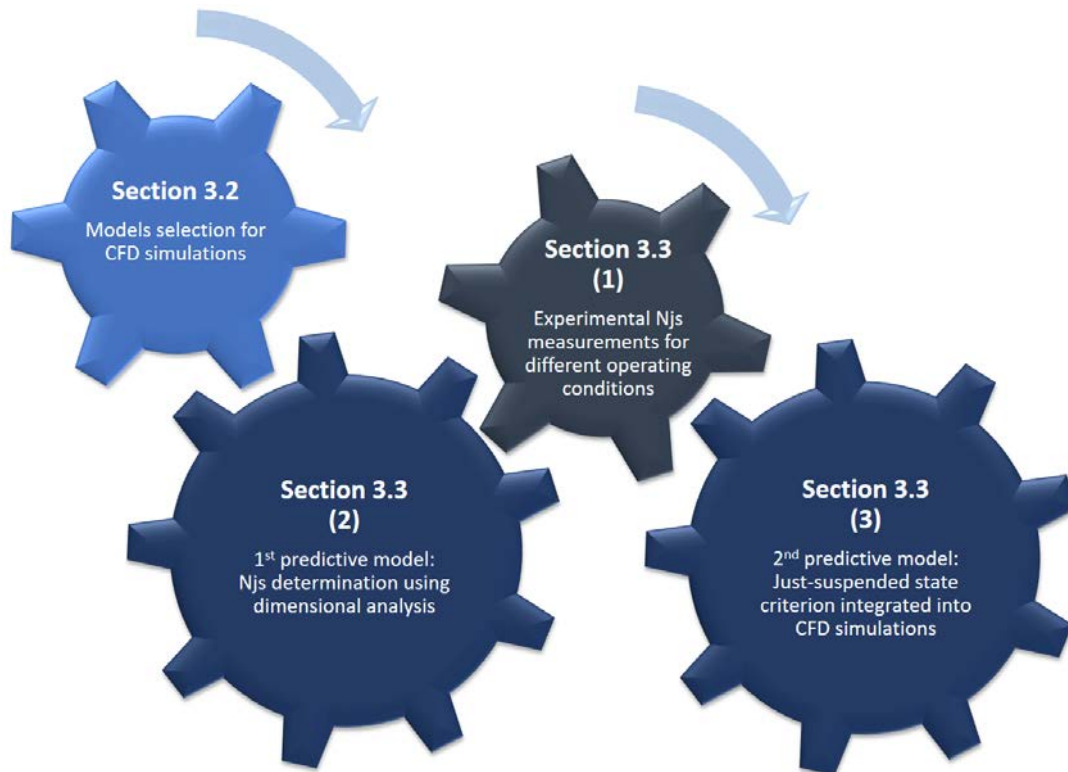


Figure 3.1: Presentation of the different steps of this work for the establishment of methods to predict microcarriers just-suspended state in stirred tank bioreactors.

## 3.2 CFD models investigation for simulation of microcarriers suspension in stirred-tank bioreactors

### 3.2.1 Culture systems geometries and meshing

Two bioreactors were investigated using CFD simulations: (*i*) the minibioreactor (Global Process Concept, La Rochelle, France) and (*ii*) the TRYTON bioreactor (Pierre Guérin SAS, Mauzé-sur-le-Mignon, France). In the first case, a working volume of 200 mL was considered, discretized into 120,000 to 200,000 tetrahedral meshes (Fig. 3.2). Concerning simulations in the TRYTON bioreactor, displaying a working volume of 1.12 L, the calculation domain was discretized using between 230,000 and 275,000 tetrahedral meshes of around 5 mm, except in a zone in the vessel bottom, where the size was refined at a maximum of 2 mm, as presented in Fig. 3.3. These numbers of mesh cell were chosen as a good compromise between a reasonable calculation time and a sufficient accuracy for the results analysis.

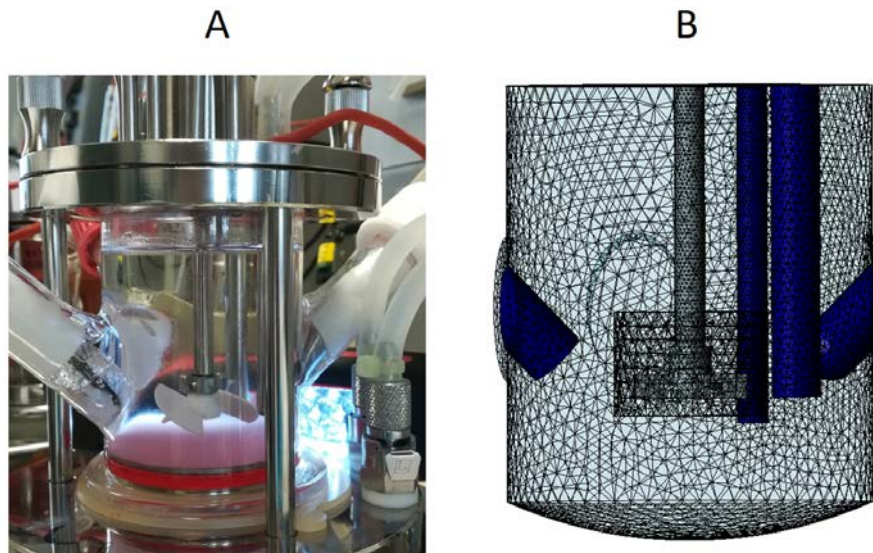


Figure 3.2: Minibioreactor used for CFD simulations: Experimental apparatus (A) and example of mesh discretization (B).

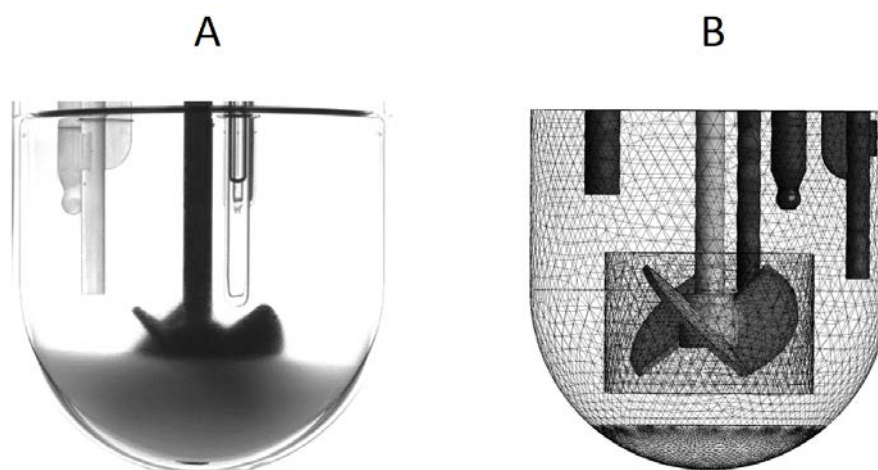


Figure 3.3: TRYTON bioreactor used for CFD simulations: Experimental apparatus (A) and example of mesh discretization (B).

### 3.2.2 Material properties

Cytodex-1 particles and water were respectively chosen as reference particles and continuous phase for the simulations. Concerning simulations performed in the minibioreactor, material property values were reproduced from Collignon *et al.* (2016) [1], where the temperature was controlled at  $T = 37^\circ\text{C}$ . In the case of simulations in the TRYTON bioreactor (1 L), material properties were experimentally determined and simulations were performed at a temperature  $T = 20^\circ\text{C}$ . Data are summarized in Table 3.1. In accordance to experimental observations, the solid packing limit was fixed to 0.6 for all simulations.

Table 3.1: Water and microcarriers material properties for CFD simulations.

Bioreactor	Thesis sections	$\rho_L$ ( $\text{kg m}^{-3}$ )	$\mu_L$ ( $\text{Pa s}$ )	$d_p$ ( $\mu\text{m}$ )	$\rho_S$ ( $\text{kg m}^{-3}$ )
Minibioreactor	4.2 - 5.2 - 5.3	993	0.000692	190	1030
TRYTON	4.3	998.2	0.001003	170	1020

### 3.2.3 Multiphase modelling by CFD

Numerical approaches are based on previous studies using an Euler-Euler granular approach to describe microcarrier suspension at the just-suspended state [2, 3, 4, 5]. Due to the very low density difference between the fluid phase and the granular phase, the impact of the lift force, as the virtual mass force were neglected in the governing equations. At least two interaction forces were found dominant, namely the drag and the turbulent dispersion forces. At the microcarrier just-suspended state, Reynolds numbers may be found in the transition regime ( $\text{Re} \approx 10^3$ ), but the use of the  $k - \varepsilon$  turbulence model was

found to display the best results in terms of just-suspended agitation rate and solid spatial distribution [5]. Hence, preliminary CFD simulations were performed in order to choose adapted models for the two main solid / liquid interaction forces, namely the drag and the turbulent dispersion forces, and for turbulence modelling. Simulations were performed by using the commercial finite-volume solver ANSYS Fluent. Based on the previous work of Delafosse *et al.*, presented in Appendix B, the two-phase Euler-Euler liquid-solid granular (RANS) approach was applied [5], as successfully validated for sand or glass bead suspensions [6, 7, 8, 9, 10, 11]. This was also previously validated for microcarrier suspensions in STR [2, 3, 4].

Adapted models for CFD simulations of microcarrier suspensions were initially chosen in the minibioreactor configuration, with a working volume of 200 mL. This configuration choice was motivated by the clear indications given by Collignon *et al.* for  $N_{js}$  experimental measurements with 5 different impeller designs [1]. These different geometries, involving a Rushton turbine, marine propellers and Elephant Ear impellers both in up- and down-pumping modes, were investigated and models were compared from simulations performed with the agitation rate corresponding to the experimentally established just-suspended state.

### 3.2.4 Initialization and convergence criteria

The present strategy, based on a relatively coarse meshing, a steady-state solver and using the Euler-Euler RANS and MRF approaches, allowed to perform simulations with a reasonable calculation time, namely 10 to 30 hours per configuration using 14 CPU Xeon 2.8 GHz. All particles were initially quasi-settled ( $\alpha_S = 0.5$ ). Higher particle concentrations led to divergence during the first iterations. By this way, 0.5 was thus found to be a good compromise, allowing particles settling during the first iterations and avoiding divergence. Convergence of the simulations was supposed when equation residuals were less than  $10^{-5}$  and when liquid velocities and solid volume fractions in the impeller vicinity were stabilized.

### 3.2.5 Navier-Stokes equations

The continuity and momentum equations were solved for each phase at the steady-state by using the Moving Reference Frame (MRF) approach to model the impeller rotation. The Reynolds stress tensor  $\bar{\tau}$  was modelled by the standard k- $\epsilon$  turbulence model with a standard wall function for near-wall function modelling. In the case of the minibioreactor geometry, dimensionless distance  $y^+$  were found under 15. The standard wall function was thus replaced by the scalable wall function. This choice validation is presented in more details in section 3.2.3. The drag and the turbulent dispersion forces were considered as

the dominant fluid / solid interactions. The two conservation equations are developed in Eqs. (3.1) and (3.2) for the liquid phase, and Eqs. (3.3) and (3.4) for the solid phase.

$$\begin{cases} \nabla \cdot (\alpha_L \rho_L \mathbf{v}_L) = \nabla(\gamma_L \nabla \alpha_L) & (3.1) \\ \nabla \cdot (\alpha_L \rho_L \mathbf{v}_L \mathbf{v}_L) = -\alpha_L \nabla p + \nabla \cdot \bar{\bar{\tau}}_L & (3.2) \\ \quad \quad \quad + \alpha_L \rho_L \mathbf{g} + K_{SL}(\mathbf{v}_S - \mathbf{v}_L) \end{cases}$$

$$\begin{cases} \nabla \cdot (\alpha_S \rho_S \mathbf{v}_S) = \nabla(\gamma_S \nabla \alpha_S) & (3.3) \\ \nabla \cdot (\alpha_S \rho_S \mathbf{v}_S \mathbf{v}_S) = -\alpha_S \nabla p - \nabla p_S + \nabla \cdot \bar{\bar{\tau}}_S & (3.4) \\ \quad \quad \quad + \alpha_S \rho_S \mathbf{g} + K_{LS}(\mathbf{v}_L - \mathbf{v}_S) \end{cases}$$

Where  $\mathbf{v}$  is the velocity of the corresponding phase,  $p$  the pressure shared by all phases and  $\mathbf{g}$  the acceleration due to gravity. The interphase drag force involved the interphase momentum exchange coefficient  $K_{LS}$ , modelled by the Huilin-Gidaspow equations presented in Eqs. (3.5) to (3.9) [12]. This model allowed to weight two models according to the local particle volume fraction in the mesh cell, involved in the smoothing function  $\Psi$  (Eq. (3.6)). In one hand, the Ergun model is suitable for particles beds, whereas in the other hand, the Wen & Yu model is more suitable for dilute systems. The diffusion-in-VOF equation was used to model the turbulent dispersion, which was included in the mass conservation equations. Interaction forces models choice is detailed in section 3.2.

$$K_{LS} = \Psi \cdot K_{LS-Ergun} + (1 - \Psi) \cdot K_{LS-Wen\&Yu} \quad (3.5)$$

$$\Psi = \frac{1}{2} + \frac{\arctan(262.5(\alpha_s - 0.2))}{\pi} \quad (3.6)$$

Ergun model:

$$K_{LS} = \frac{3}{4} \cdot C_D \cdot \frac{\alpha_S \alpha_L \rho_L |\mathbf{v}_S - \mathbf{v}_L|}{d_p} \cdot \alpha_L^{2.65} \quad (3.7)$$

$$C_D = \frac{24}{\alpha_S Re_S} \left[ 1 + 0.15(\alpha_L Re_S)^{0.687} \right] \quad (3.8)$$

Wen & Yu model:

$$K_{LS} = 150 \frac{\alpha_S (1 - \alpha_L) \mu_L}{\alpha_L d_p^2} + 1.75 \frac{\rho_L \rho_S [1 + 0.15(\alpha_L Re_S)^{0.687}]}{d_p} \quad (3.9)$$

### 3.2.6 Turbulence modelling

Despite relatively low Reynolds numbers calculated in the systems described in this thesis ( $Re \approx 10^3$ ), models were previously validated in a robust way, through the confronta-

tion of different sets of models with experimental measurements of particle concentration gradients, using a light scattering technique [5]. For more details on this work, please refer to the appendix A. The  $k - \varepsilon$  mixture turbulence model is suitable for multiphase flows with a density ratio between phases close to 1. In the case of microcarrier suspensions  $\rho_S/\rho_L \approx 1.02$ , consequently the mixture approach was considered suitable. In that manner, mixture properties and velocities are sufficient to collect the main features of the turbulent flow [12].

The  $k$  and  $\varepsilon$  equations, presented in Eqs. (3.10) to (3.15) were solved, with constants given in Table 3.2, and with  $G_{k,m}$  as the production of turbulence kinetic energy.

$$\nabla \cdot (\rho_m \mathbf{v}_m k) = \nabla \cdot \left[ \left( \mu_m + \frac{\mu_{t,m}}{\sigma_k} \right) \nabla k \right] + G_{k,m} - \rho_m \varepsilon \quad (3.10)$$

$$\nabla \cdot (\rho_m \mathbf{v}_m \varepsilon) = \nabla \cdot \left[ \left( \mu_m + \frac{\mu_{t,m}}{\sigma_\varepsilon} \right) \nabla \varepsilon \right] + \frac{\varepsilon}{k} (C_{1\varepsilon} G_{k,m} - C_{2\varepsilon} \rho_m \varepsilon) \quad (3.11)$$

$$\rho_m = \alpha_S \rho_S + \alpha_L \rho_L \quad (3.12)$$

$$\mu_m = \alpha_S \mu_S + \alpha_L \mu_L \quad (3.13)$$

$$\mathbf{v}_m = \frac{\alpha_S \rho_S \mathbf{v}_S + \alpha_L \rho_L \mathbf{v}_L}{\alpha_S \rho_S + \alpha_L \rho_L} \quad (3.14)$$

$$\mu_{t,m} = \rho_m C_\mu \frac{k^2}{\varepsilon} \quad (3.15)$$

Table 3.2: Constants involved in the  $k$  and  $\varepsilon$  equations during CFD simulations.

Cosntant	Value
$C_{1\varepsilon}$	1.44
$C_{2\varepsilon}$	1.92
$C_\mu$	0.09
$\sigma_k$	1.0
$\sigma_\varepsilon$	1.3

It should be noticed that no source term modelling the turbulent interaction between the dispersed phase and the continuous phase was implemented in the  $k$  and  $\varepsilon$  equations. The turbulent dispersion force was indeed directly integrated into the mass conservation equation (Eqs. (3.1) and (3.3)), through the  $\nabla(\gamma_L \nabla \alpha_L)$  and the  $\nabla(\gamma_S \nabla \alpha_S)$  terms from the diffusion-in-VOF model, where  $\gamma_L$  and  $\gamma_S$  are the liquid and solid diffusion coefficients (Eqs. (3.16) and (3.17)), and  $\mu_{t,S}$  the solid turbulent viscosity.

$$\nabla(\gamma_L \nabla \alpha_L) = -\nabla(\gamma_S \nabla \alpha_S) \quad (3.16)$$

$$\gamma_S = \frac{\mu_{t,m}}{0.75} \quad (3.17)$$

### 3.2.7 Near-wall turbulence modelling

Based on the previous work of Delafosse *et al.*, the mixture standard k- $\varepsilon$  model was chosen for turbulence modelling (see Appendix A) [5]. Despite some deviations on the microcarrier solid distribution between experimental measurements and the CFD simulations were observed, especially in the bottom zone, it provided the most reliable results in comparison to other turbulence models proposed with the Euler-Granular modelling. However, in the specific configuration of the minibioreactor, the Standard Wall Function for near-wall treatment was found to present dimensionless distance  $y^+$  values below 15, as shown in Fig. 3.4.  $y^+$  is presented in Eq. (3.18), with  $u_*$  the friction velocity,  $y_p$  the distance between the mesh cell centroid and the nearest wall, and  $\nu$  the kinematic viscosity. This critical value is described to result in unbounded errors in wall shear stress [12]. The use of the Scalable Wall Function was investigated in order to avoid such errors. It indeed allows to produce consistent results for grids or arbitrary refinement. This function implementation is based on the dimensionless distance  $y^*$  calculation, defined in Eq. (3.19), where  $\rho_L$  and  $\mu_L$  are the liquid density and dynamic viscosity,  $C_\mu$  is an empirical constant used for the turbulent viscosity calculation and  $k_p$  is the turbulent kinetic energy in the mesh cell. The scalable wall function approach allows to go below 11, by forcing a value  $y^* = y_{limit}^* = 11.225$ .

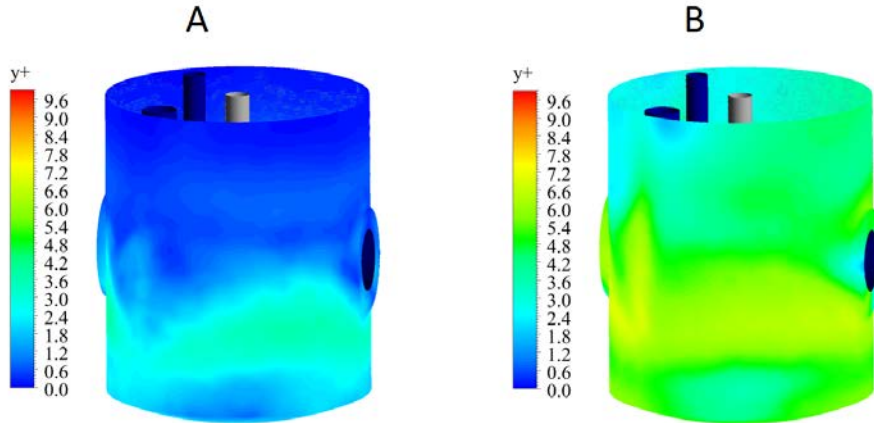


Figure 3.4: Comparison of the impact of the wall function selected for near-wall treatment with the k- $\varepsilon$  model on  $y^+$  values displayed on the vessel wall: Standard Wall Function (A) and Scalable Wall Function (B).

$$y^+ = \frac{u_* y_p}{\nu} \quad (3.18)$$

$$y^* = \frac{\rho_L C_\mu^{1/4} k_p^{1/2} y_p}{\mu} \quad (3.19)$$

The Scalable Wall Function was compared to the Standard Wall Function at the just-suspended state for an Elephant Ear impeller, as presented in Fig. 3.5. Transitions between the moving zone around the impeller and the steady zone in the rest of the vessel were notably found better with the Scalable Wall Function. The transition on the upper part of the vessel, where velocities and energy dissipations are the lowest, was also found to be affected by the near-wall treatment. Reynolds numbers of the different configurations and with both wall functions were calculated and are presented in Table 3.3, with the corresponding volume-averaged and minimal values of the Kolmogorov length scale  $\lambda_K$  and the turbulent energy dissipation rate  $\varepsilon$ . Relatively low Reynolds values were found, but immersed probes act as baffles in the system, promoting eddy subdivisions. It may be also noticed that the Standard Wall Function displayed higher  $\varepsilon_{max}$  values than with the Scalable Wall Function. In the case of the EEU, a 57-fold increase was obtained. The five configurations were found to display volume-averaged  $\lambda_K$  length scales of the same size as microcarriers and the impact of the near-wall turbulence model on  $\lambda_K$  was not significant.

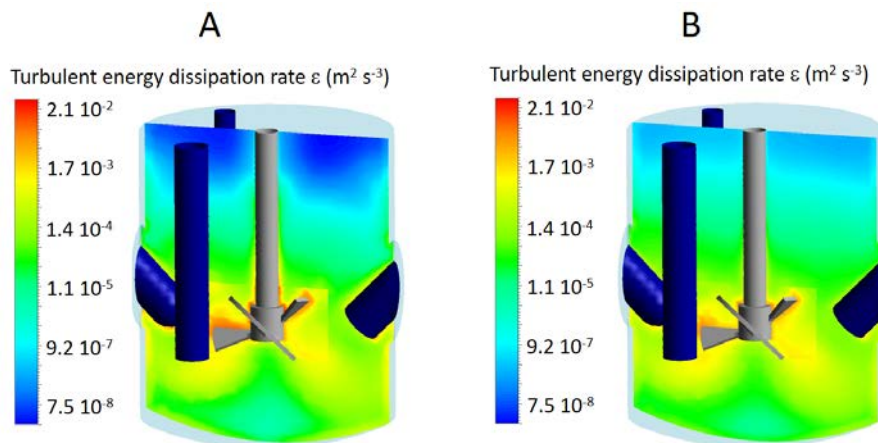


Figure 3.5: Comparison of the impact of the wall function selected for near-wall treatment with the k- $\varepsilon$  model on the turbulent energy dissipation rate: Standard Wall Function (A) and Scalable Wall Function (B).

### 3.2.8 Drag force model investigation

The drag force modelling is crucial for microcarrier suspension. At the just-suspended state, particle concentration gradients are notably observed in the bioreactor, with a dense dispersion in the bottom of the vessel, whereas a dilute dispersion is observed in the rest of the system. Hence, simulations should be able to describe these two behaviours. Some models are based on strong hypothesis on particle concentration, and are briefly



Table 3.3: Impact of near-wall turbulence modelling on CFD results at the microcarrier just-suspended state and for different impeller designs in a minibioreactor.

Impeller design	$N_{js}$ (rpm)	Re (-)	$\langle \lambda_K \rangle$ ( $\mu\text{m}$ )	$\langle \varepsilon \rangle$ $10^{-3}$ ( $\text{m}^2 \text{s}^{-3}$ )	$\lambda_{K,min}$ ( $\mu\text{m}$ )	$\varepsilon_{max}$ ( $\text{m}^2 \text{s}^{-3}$ )
<b>Standard k-<math>\varepsilon</math> model with the Standard Wall Function</b>						
MPD	140	970	210	0.17	37	0.19
MPU	340	2350	117	1.8	17	4.2
RT	163	1560	161	0.51	36	0.21
EED	75	1030	225	0.13	54	0.04
EEU	130	1790	133	1.1	15	6.6
<b>Standard k-<math>\varepsilon</math> model with the Scalable Wall Function</b>						
MPD	140	970	221	0.14	49	0.06
MPU	340	2350	119	1.7	19	2.4
RT	163	1560	163	0.48	38	0.17
EED	75	1030	215	0.16	61	0.02
EEU	130	1790	133	1.1	41	0.12

presented in Table 3.4. For each model, the interphase momentum exchange coefficient  $K_{SL}$  was calculated in function of the local particle volume fraction in the case of the minibioreactor equipped with a marine propeller in down-pumping mode at  $N = N_{js}^{exp} = 140$  rpm. Equations corresponding to each model are listed below, with  $C_D$  the drag coefficient:

Schiller Naumann [13]:

$$K_{SL} = \frac{3}{4} \cdot \frac{C_D}{d_p} \alpha_S \rho_L |\mathbf{v}_S - \mathbf{v}_L| \quad (3.20)$$

$$\begin{cases} C_D = 24(1 + 0.15Re^{0.687})/Re & \text{if } Re \leq 1,000 \\ C_D = 0.44 & \text{if } Re > 1,000 \end{cases} \quad (3.21)$$

$$\quad (3.22)$$

Syamlal O'Brien [14]:

$$K_{SL} = \frac{3\alpha_S\alpha_L\rho_L}{4v_{r,S}^2d_p} C_D \frac{Re_S}{v_{r,S}} |\mathbf{v}_S - \mathbf{v}_L| \quad (3.23)$$

With  $v_{r,S}$  the terminal velocities of particles in settling beds:

$$v_{r,S} = 0.5(A - 0.06Re_S + \sqrt{(0.06Re_S)^2 + 0.12Re_S(2B - A) + A^2}) \quad (3.24)$$

With  $A = \alpha_L^{4.14}$  and  $B = 0.8\alpha_L^{1.28}$  for  $\alpha_L \leq 0.85$  or  $B = \alpha_L^{2.65}$  for  $\alpha_L > 0.85$ .

Ergun [15]:

$$K_{SL} = 150 \frac{\alpha_S(1 - \alpha_L)\mu_L}{\alpha_L d_p^2} + 1.75 \frac{\rho_L \alpha_S |\mathbf{v}_S - \mathbf{v}_L|}{d_p} \quad (3.25)$$

Wen & Yu [16]:

$$K_{SL} = \frac{3}{4} C_D \frac{\alpha_S \alpha_L \rho_L |\mathbf{v}_S - \mathbf{v}_L|}{d_p} \alpha_L^{-2.65} \quad (3.26)$$

### 3.2. CFD MODELS INVESTIGATION FOR SIMULATION OF MICROCARRIERS SUSPENSION IN STIRRED-TANK BIOREACTORS

---

$$C_D = \frac{24}{\alpha_L Re_S} \left[ 1 + 0.15(\alpha_L Re_S)^{0.687} \right] \quad (3.27)$$

Gidaspow [17]:

$$\begin{cases} K_{SL} = K_{SL, Wen\&Yu} & \text{if } \alpha_S < 0.2 \\ K_{SL} = K_{SL, Ergun} & \text{if } \alpha_S \geq 0.2 \end{cases} \quad (3.28)$$

$$\quad (3.29)$$

Huilin Gidaspow [18]:

$$K_{SL} = \Psi K_{SL, Ergun} + (1 - \Psi) K_{SL, Wen\&Yu} \quad (3.30)$$

With  $\Psi$  the stitching function:

$$\Psi = \frac{1}{2} + \frac{\arctan(262.5(\alpha_S - 0.2))}{\pi} \quad (3.31)$$

Gibilaro [19]:

$$K_{SL} = \left( \frac{18}{Re} + 0.33 \right) \frac{\rho_f |\mathbf{v}_S - \mathbf{v}_L|}{d_p} \alpha_S \alpha_L^{-1.8} \quad (3.32)$$

Table 3.4: Brief description of the drag force models proposed in Fluent and compared for microcarrier just-suspended state.

Method	Application
Schiller Naumann	Initially developed for laminar flow. Considered as the standard model for fluid-fluid interactions.
Syamlal O'Brien	Based on measurements of the terminal velocities of particles in fluidized beds.
Ergun	Appropriate for dense fluidized beds.
Wen & Yu	Appropriate for dilute systems.
Gidaspow	Combination of the Wen & Yu model and the Ergun equation. Model switching occurs at $\alpha_L = 0.8$ .
Huilin Gidaspow	Combination of the Wen & Yu model and the Ergun equation. Model switching depends on a smooth function (models are weighted).
Gibilaro	Appropriate for circulating fluidized beds.

Results are presented in Fig. 3.6. For all these  $K_{SL}$  calculations, the mean value of  $|\mathbf{v}_s - \mathbf{v}_l|$  was fixed at  $1.2 \cdot 10^{-4} \text{ m s}^{-1}$ , based on data determined from a CFD simulation. It led to a Reynolds number on the solid phase  $Re_S = \rho_L d_p |\mathbf{v}_S - \mathbf{v}_L| / \mu_L$  of 0.034.

As expected, the Ergun model differed from the other for very dilute concentrations, as the assumption of packed bed systems was not respected and so the model may be considered unsuitable for low values of  $\alpha_S$ . In the same way, the model from Syamlal

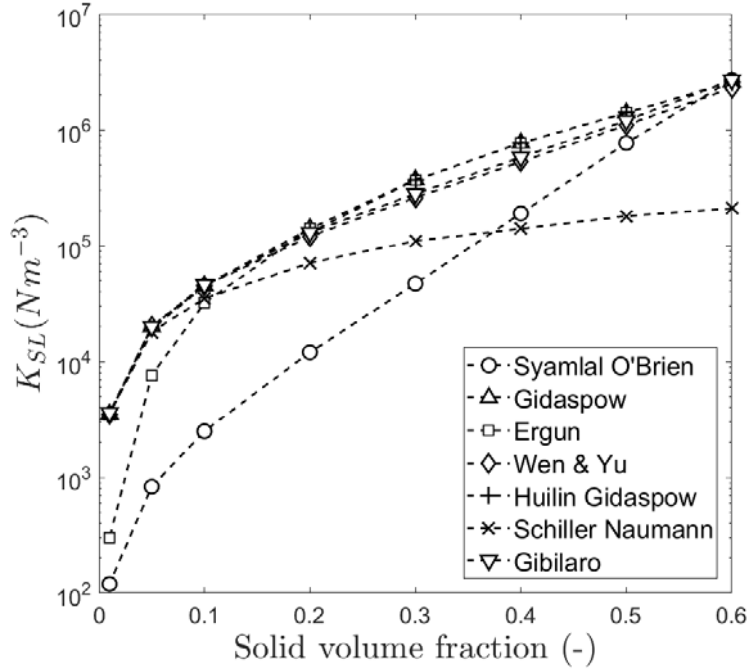


Figure 3.6: Interphase momentum exchange coefficient  $K_{SL}$  evolution with the particle volume fraction from different models.

O'Brien also deviated from the other models for dilute solid concentrations. For high particle concentrations, only the model of Schiller Naumann presented deviations from the others. For the next simulations, the model of Huilin Gidaspow will be applied. It presents the advantage of using models suitable for both dilute and dense dispersions, by weighting them according to the local particle volume fraction in each mesh cell.

It has been however highlighted that drag coefficients issued from single particles settling in a still fluid did not well expressed the one investigated for a particle in a stirred turbulent fluid. Corrective coefficients were developed with the integration to the drag force of the turbulent eddy sizes on particle diameter ratio  $\lambda_K/d_p$  [20, 21]. In Fluent software,  $K_{SL}$  is replaced by  $K'_{SL}$ , calculated according to Eq. (3.33). Table 3.5 presents the corrective coefficients calculated with the Brucato correlation (Eq. (3.34)) [20] and the Pinelli correlation (Eq. (3.35)) [21]. Due to the heterogeneous turbulent eddy sizes through the whole bioreactor, different representative points were chosen, with smaller or larger eddy sizes according to the location. Even in the zones displaying the smallest eddies (impeller region), the two corrective coefficient were found close to 1. Hence, no drag force modification was applied.

$$K'_{SL} = f_t K_{SL} \quad (3.33)$$

$$f_{t,Brucato} = \left[ 1 + 8.76 \times 10^{-4} \left( \frac{d_p}{\lambda_K} \right)^3 \right] \quad (3.34)$$

$$f_{t,Pinelli} = \left[ 0.6 + 0.4 \tanh \left( 16 \frac{\lambda_K}{d_p} - 1 \right) \right]^{-2} \quad (3.35)$$

Table 3.5: Calculation of the Brucato and Pinelli corrections for drag force models at different vessel levels.

Localisation	$\lambda_K$ (m)	$\lambda_K/d_p$	$f_{t,Brucato}$	$f_{t,Pinelli}$
Impeller wall	$7.7 \cdot 10^{-5}$	0.4	1.01	1.00
Liquid surface	$2.2 \cdot 10^{-3}$	11.5	1.00	1.00
Vessel bottom	$6.7 \cdot 10^{-4}$	3.5	1.00	1.00
Vessel lower half	$1.2 \cdot 10^{-4}$	0.6	1.00	1.00
Vessel top half	$1.0 \cdot 10^{-3}$	5.3	1.00	1.00

### 3.2.9 Turbulent dispersion force impact

The turbulent dispersion force represents the interphase turbulent momentum transfer. It plays a role into particles dispersion, notably by driving them away from their initial location. In the present case, the Diffusion in VOF model was chosen. It presented the particularity to involve this force in the governing equations of phase volume fractions, with the terms  $\nabla(\gamma_L \nabla \alpha_L)$  and  $\nabla(\gamma_S \nabla \alpha_S)$  in the right side of Eqs. (3.1) and (3.3), where  $\gamma_L$  and  $\gamma_S$  are the liquid and solid diffusion coefficients (Eqs. (3.36) and (3.37)), and  $\mu_{t,S}$  the solid turbulent viscosity.

$$\nabla(\gamma_L \nabla \alpha_L) = -\nabla(\gamma_S \nabla \alpha_S) \quad (3.36)$$

$$\gamma_S = \frac{\mu_{t,S}}{0.75} \quad (3.37)$$

The necessity of the turbulent dispersion force was verified by comparison between simulations with and without the diffusion in VOF model at  $N = N_{js}$ . It was assumed, that at the just-suspended state, only a few particles would tend to a higher concentration in the bottom of the bioreactor. Fig. 3.7 (A) presents the solid volume fraction distribution without turbulent dispersion force modelling. In this case, 37 % of particles were found to be close from each other, with a local particle volume fraction in mesh cells between 0.55 and the packing limit 0.6. Particle dispersion was found to be not representative of what was expected in this case. Fig. 3.7 (B) presented the solid volume fraction distribution for the same configuration, but modelling the turbulent dispersion force with

the diffusion in VOF model. This turbulent dispersion force was found to highly impact particle dispersion, with a maximal particle volume fraction of 0.31 in the bottom of the vessel. This distribution was closer to the observations established during experimental  $N_{js}$  measurements, for which a small fraction of particles stayed in the bottom with very slow circular movements. The local particle volume fraction was not quantitatively established, but it could be confirmed that it was more dispersed than a packed bed configuration. The diffusion in VOF model was hence selected for the following simulations. **Its validation will be confirmed in a more robust way with the  $N_{js}$  criterion definition, presented in section 3.3.**

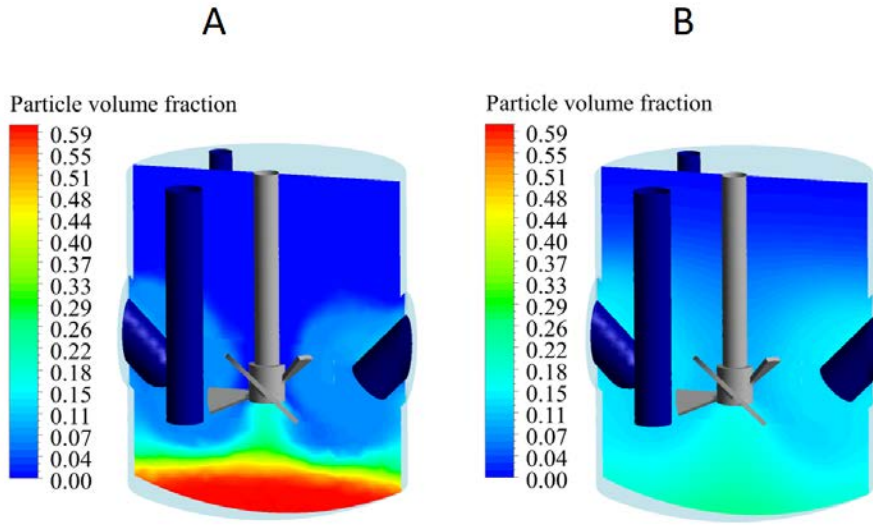


Figure 3.7: Comparison of the impact of the turbulent dispersion force on the particle volume fraction distribution in the bioreactor: Solid volume fraction fields from simulations run without turbulent dispersion model (A) and with the diffusion in VOF model (B).

### 3.2.10 Granular temperature modelling

The granular temperature of the solid phase is proportional to the kinetic energy of the particle motion, as expressed in Eq. (3.38), where  $u_{s,i}$  is the fluctuating solid velocity related to the  $i^{th}$  component. The system is here defined as an ensemble average of the particles' random velocity within a finite volume and time period.

$$\theta_S = \frac{1}{3} u_{s,i} u_{s,i} \quad (3.38)$$

Based on the kinetic theory, the transport equation can be written as follow :

$$\frac{3}{2} \left[ \frac{\partial}{\partial t} (\rho_S \alpha_S \theta_S) + \nabla \cdot (\rho_S \alpha_S \mathbf{v}_S \theta_S) \right] = (-p_S \bar{\bar{I}} + \bar{\bar{B}}) : \nabla \mathbf{v}_S + \nabla \cdot (k_{\theta_S} + \nabla \theta_S) - \gamma_{\theta_S} + \Phi_{l_S} \quad (3.39)$$

Where  $\gamma_{\theta_S}$  is the collisional dissipation of energy, with  $g_{0,ss}$  the radial distribution function and  $e_{ss}$  the coefficient of restitution for particle collisions set at 0.9, from the Lun *et al.* model :

$$\gamma_{\theta_S} = \frac{12(1 - e_{ss}^2)g_{0,ss}}{d_p\sqrt{\pi}}\rho_S\alpha_S^2\theta_S^{3/2} \quad (3.40)$$

And where  $\Phi_{ls}$  represents the transfer of kinetic energy of random fluctuations in particle velocity from the solid phase to the liquid phase :

$$\Phi_{ls} = -3 \cdot K_{ls}\theta_S \quad (3.41)$$

The left part of the transport equation represented the transient and convective transport and the right part is divided into terms respectively related to the generation of energy by the solid stress tensor, to the diffusive flux of fluctuating of granular energy, to the collisional dissipation of energy and to an energy exchange between the liquid and the solid phase. In the present work, the algebraic formulation was selected and neglected convection and diffusion terms in Eq. (3.39).

### 3.2.11 Models selection synthesis

Based on the preliminary investigations, the final models selection for turbulence and main liquid / solid interaction forces modelling is summarized in Table 3.6.

Table 3.6: Summary of the final models selection for microcarrier just-suspended state during CFD simulations.

Force / Phenomenon	Chosen model
Turbulence	k- $\varepsilon$ model with the Standard Wall Function or the Scalable Wall Function according to $y^*$ values.
Drag force	Huilin-Gidaspow model.
Turbulent dispersion force	Diffusion in VOF model.
Granular temperature	Algebraic model.
Solid pressure	Lun <i>et al.</i> model.
Granular viscosity	Syamlal O'Brien model.
Radial distribution	Lun <i>et al.</i> model.

### 3.3 Dimensional analysis and CFD simulations of microcarrier just-suspended state

The particle just-suspended state is a crucial parameter for MSC cultures on microcarriers. The agitation rate is generally chosen depending on this condition. Then, depending on the bioreactor and the impeller designs, turbulence is generated by the agitation and lead to potential hydromechanical stress on particles. It is therefore important to understand how the different parameters related to the solid just-suspended suspension equilibrium (agitation design, agitation rate  $N_{js}$ , particles and liquid properties...) are related one to each other. For this purpose, the present study was focused on the impact of the impeller geometrical characteristics and design, and of the material properties of the solid and the liquid phase on the  $N_{js}$  value. Two methods, based on a dimensional analysis [22] and on CFD simulations using models presented in section 3.2, were investigated in order to model  $N_{js}$ . This part will present the results of this study in the form of a scientific paper.

#### Dimensional analysis and CFD simulations of microcarrier 'just-suspended' state in Mesenchymal Stromal Cells bioreactors

C. Loubière<sup>a</sup>, A. Delafosse<sup>b</sup>, E. Guedon<sup>a</sup>, I. Chevalot<sup>a</sup>, D. Toye<sup>b</sup>, E. Olmos<sup>a</sup>

<sup>a</sup>Laboratoire Réactions et Génie des Procédés, Université de Lorraine, CNRS, LRGP, F-54000 Nancy, France

<sup>b</sup>Laboratory of Chemical Engineering, Université de Liège, Allée de la Chimie 3, B6C, 4000 Liège, Belgium

Keywords: Microcarrier suspension, bioreactor, critical just-suspended agitation rate, Computational Fluid Dynamics (CFD), dimensional analysis.

#### Publication abstract

Large-scale Mesenchymal stem / stromal cells culture uses 3D culture systems involving spherical solid particles, called microcarriers. Cells adhere on these spheres, which are then set in suspension in stirred tank bioreactors. This work is more particularly focused on the determination of the critical impeller agitation rate  $N_{js}$ , at which complete beads suspension is ensured. It is indeed generally assumed that this value is a good compromise between sufficient nutrients homogenization, mass transfer and the minimization of hydromechanical stress encountered by the cells. However, no robust correlation predicting  $N_{js}$  in the case of microcarriers can be found in literature. To fill this lack, a design

of experiments was carried out, dealing with geometrical variables and two different microcarriers, and  $N_{js}$  were experimentally determined for 140 operating conditions. An empirical correlation was established and a dimensional analysis was performed, showing that the impact of the particle concentration on  $N_{js}$  was function of the impeller design. Moreover, two dimensionless numbers characterizing the number of particle and an Archimede number applied on the particle cloud were found to better describe the impact of particle diameter and density on  $N_{js}$ . Simultaneously, a strategy based on Computational Fluid Dynamics simulations was conducted in order to predict  $N_{js}$  and was validated with the  $N_{js}$  experimental values.

### 3.3.1 Context

Today, still growing attention is paid to mesenchymal stem / stromal cell (MSC) culture for applications in regenerative medicine, with 843 MSC-based clinical completed or ongoing trials identified in May 2018 ([www.clinicaltrials.gov](http://www.clinicaltrials.gov)). Nevertheless, these cells are present in limited quantities in the human body, and this number decreases with the age of the donor [23]. An *ex-vivo* expansion phase is thus necessary to get sufficient cells quantities to meet the medical needs which are generally estimated between  $10^9$  and  $10^{12}$  cells/lot [24]. As some other cell sources, MSCs are anchorage-dependent, namely they need to adhere on a surface to proliferate. Thus, MSCs are typically cultivated in static mode in 2D monolayer systems such as planar culture flasks. However, these devices hold some significant disadvantages for expansion process scale-up such as the storage of numerous flasks in incubators, the difficulty of operating conditions control, as well as the operational costs and the contamination risks.

To overcome these limits, cultures are now being transposed on microcarriers, consisting of spheres of about 200  $\mu\text{m}$  diameter with a density close to water one [25]. Once cells adhere on the surface of these particles, they are suspended in a bioreactor filled with the culture medium by mechanical agitation. The specific adherence surface available for cell expansion is greatly enhanced in comparison with 2D static culture, and the addition of monitoring / control loop is made easier, in accordance with GMP specifications. Moreover, mixing allows a better culture homogenization, limiting  $\text{O}_2$ , pH and nutrients gradients, enhancing mass transfer and available liquid-solid interfacial area maximization. It has been demonstrated that growth on microcarriers allow a higher number of cells recovered by lot, despite requiring more efforts and investments in R&D for a company currently using T-flasks to change to microcarrier based cultures [26, 27]. Recently, microcarrier MSC cultures have been successfully conducted at a few liter-scale [28, 29]. However, while a too low agitation would lead to microcarriers settling in the bottom of the vessel and aggregation [30], a too high agitation may generate damages to the cells



[31], induce their differentiation [32] or led to a failure of the cells to attach efficiently to the particles [33]. These damages may result from three separate mechanisms [34]: collisions with another microcarrier, collisions with bioreactor internals (wall, probes, other immersed equipment, and particularly the impeller) and interactions with turbulent eddies whose size is close to microcarriers one [35]. One reasonable strategy to get a sufficient mixing performance and minimization of hydromechanical stress is to operate at the impeller just-suspended agitation rate  $N_{js}$  at which complete bead suspension is ensured. This means that bioreactor hydrodynamics have to be therefore intensively studied to guarantee cells viability and allow a process scale-up [36], leading to the need of reliable model and numerical tools. Many methods have been established to estimate  $N_{js}$ , and some of them are well-developed in [11]. They were classified in 4 categories: (i) 'direct methods' like the Zwietering visual method [37, 38, 39] stating that when  $N_{js}$  is reached, particles do not stay longer than 1 or 2 seconds in the vessel bottom, (ii) 'indirect methods' like the cloud height method [40], the particle concentration determination using light attenuation technique [5] or the power number method [41], (iii) 'numerical methods' based on data recovered from CFD simulations [42, 43], and (iv) finally 'theoretical methods'. In the last case, investigations were mainly based on the assumption of an equilibrium between particle settling and the off-bottom lifting [44, 45, 46] and led to models derived from experimental results, according to limited ranges of geometries and particle properties. The most commonly used was developed by Zwietering [37] and is presented in Eq. (3.42).

$$N_{js} = S \cdot \nu_L^{0.1} \cdot \left( \frac{g \cdot (\rho_p - \rho_L)}{\rho_L} \right)^{0.45} \cdot X^{0.13} \cdot d_p^{0.2} \cdot D^{-0.85} \quad (3.42)$$

Where  $S$  is a dimensionless parameter related to the geometry of the vessel and the impeller, via the ratio of the impeller diameter on the tank diameter  $D/T$ , the ratio of the off-bottom clearance on the tank diameter  $C/T$  and the impeller design. With these dimensionless parameters,  $S$  is independent of the scale of the system but not of the system geometry. However, this correlation has been established and validated for particles that were significantly denser than microcarriers, like sand or glass beads. It has been shown by [47] that the calculation of the  $S$  coefficients using Eq. (3.42), in the same operational conditions, could present up to 50 % overestimation for microcarriers. This difference was attributed to the low density difference between the solid and the liquid phases (around  $40 \text{ kg m}^{-3}$ ) in the case of microcarriers, which facilitates the lifting of particles from the tank bottom.

Complementary studies have been conducted on the determination of  $N_{js}$  and its dependence on geometrical, physical and operational variables like, among others, the effects of the low off-bottom impeller clearance or the bottom shape on flow patterns evolution

[48, 49], the impacts of the solid volume fraction incorporated in the reactor [50], or in the specific case of microcarriers, the type of microcarrier used [51] and the impeller design leading to different possible agitation modes [1]. Recently, microcarrier suspension has also been characterized in orbital shakers and led to the establishment of a new correlation predicting  $N_{js}$ . A dimensional analysis furnished the most appropriate geometrical characteristics for cell cultures [52]. However, despite all of these efforts, no robust correlation predicting  $N_{js}$  can be found in the literature for microcarrier suspension in stirred tank bioreactors.

To fill this lack, the present study was focused on the numerical prediction of  $N_{js}$  in the specific case of microcarriers. To do that, the critical agitation rate  $N_{js}$  was experimentally determined for 140 operating conditions in the case of a hemispherical-bottom shape bioreactor. A dimensionless equation was then established using these data. Simultaneously, a strategy based on Computational Fluid Dynamics (CFD) simulations was conducted in order to predict  $N_{js}$  for specific operating conditions of the cell culture. The  $N_{js}$  values obtained by numerical simulations were thereafter validated with the previous experimental data.

### 3.3.2 Experimental approach

#### Design of experiment

The bioreactor investigated was a hemispherical-bottom transparent glass vessel equipped with three probes (dissolved oxygen, pH and temperature) on the head plate. It was filled with Dulbecco's Phosphate Buffered Saline solution (DPBS) for a working volume of 1.12 L, at which the liquid height corresponded to the vessel diameter  $H = T = 0.12$  m. The temperature was controlled and regulated at 20°C, at which the liquid properties were considered to be the same as water, and a baffle was added to the pH probe in order to avoid vortex formation during the agitation. A design of experiments of five parameters, involving the impeller and the microcarriers, has been set up to guide the experiments (Fig. 3.8).

Firstly, the impeller geometry impact has been investigated by changing the impeller design and two geometrical ratios:  $D/T$ , defining the impeller diameter on the vessel diameter, and  $C/T$ , defining the off-bottom clearance on the vessel diameter ratio. More specifically, three impeller designs were studied: a radial four-blade Rushton Turbine (RT), an axial 3-blade impeller (HTPG) and an Elephant Ear impeller (EE). Both axial impellers were studied in up-pumping and down-pumping modes, allowing at least five agitation types. Each impeller was available at three  $D/T$  ratios: 0.33, 0.4 and 0.5, and placed according to three possible  $C/T$  ratios: 0.5, 0.33 and 0.25. In this study, the

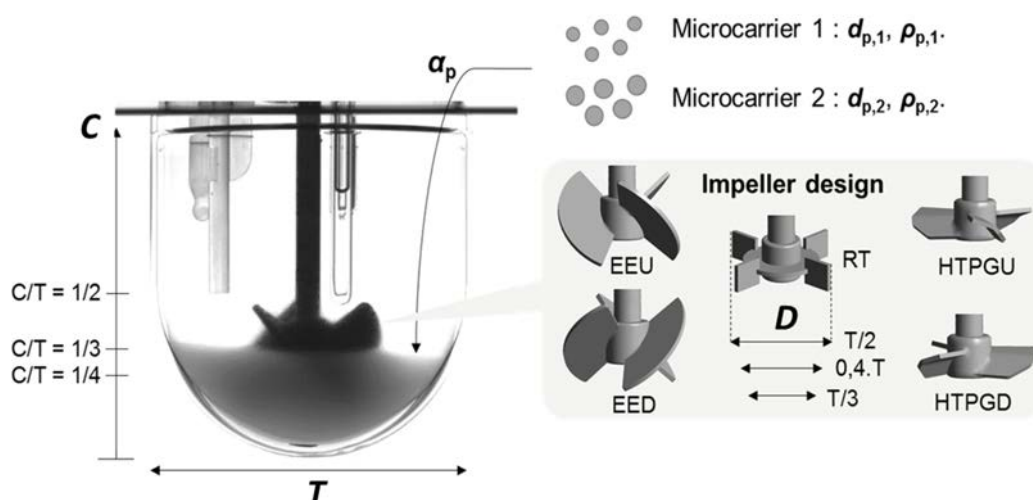


Figure 3.8: Variables used in the design of experiments: the off-bottom clearance  $C$  and the impeller diameter  $D$  in function of the tank diameter  $T$ , the type of microcarrier with their specific diameters and density, the particle volume fraction  $\alpha_S$ , and the impeller design with the Elephant Ear in up-pumping (EEU) and down-pumping (EED) modes, the HTPG impeller up-pumping (HTPGU) and down-pumping (HTPGD) and the Rushton turbine (RT).

off-bottom clearance  $C$  was considered as the distance between the vessel bottom and the bottom side of the impeller hub.

Secondly, microcarrier properties impact was determined by varying the particle volume fraction  $\alpha_S$  and the type of microcarrier used. Two different microcarriers were investigated: the Cytodex-1 (GE Healthcare) composed of a cross-linked dextran matrix with positively charged N, N-diethylaminoethyl groups, and the Star-Plus (Pall SoloHill) composed of a polystyrene core and featuring a surface chemistry with a net positive charge. Cytodex-1 microcarriers swell when put in solution. Their swelling factor, and thus their diameter and density, depends on the salt concentration of the solution. After spending a night in a phosphate buffer saline (DPBS) solution, the diameter distributions were established from microscope images and their density was estimated from their swelling factor and the density of the dry microcarriers (see [5] for details). The same procedure was also applied to Star-Plus microcarriers. The physical properties assumed for all the study are the experimental data given in Table 1. For comparison, the values provided by the manufacturer are also reported. Five microcarrier volume fractions ranging from 1 to 12 % were investigated, corresponding to the concentrations classically used during cell cultures.

### Experimental suspension criterion and $N_{js}$ visual determination

The vessel was placed in an aquarium with a mirror added below, permitting a better visualization and  $N_{js}$  was visually established by particle movements at the bottom of

Table 3.7: Microcarrier physical properties: manufacturer and experimental data.

	Manufacturer data			Experimental data			
	$\rho_P$ kg m <sup>-3</sup>	$d_{50}$ μm	$d_{5-95}$ μm	$\rho_P$ kg m <sup>-3</sup>	$d_{50}$ μm	$d_{5-95}$ μm	$d_{mean}$ μm
Microcarrier							
Cytodex-1	1.03	190	147-248	1.018	165	139-201	167
Star-Plus	1.02-1.03	N/A	125-212	1.020	139	116-173	142

the vessel using the protocol of Zwietering criterion [5]. For each  $N_{js}$  determination, two measurements were performed. For the first one, all particles were settled in the vessel bottom with no agitation followed by a slow increase of the agitation rate until just-suspended state  $N_{js, up}$ . For the second one, agitation rate was progressively reduced from complete suspension to just-suspended state  $N_{js, down}$ . For all operating conditions, it was noted that these two agitation rate values remained close one from each other (mostly 2 rpm difference). Thus,  $N_{js, up}$  will be used as  $N_{js}$  in the rest of the study to mimic the  $N_{js}$  investigation during cultures. According to the design of experiments, 95 operating conditions were used for the model resolution. The model was then validated using 45 other operating conditions.

### 3.3.3 Particle suspension modelling

#### Zwietering correlation validity

First, the  $N_{js}$  experimentally collected were used to verify the Zwietering correlation given in Eq. 3.42, by calculating the experimental  $S$  coefficients which are a function of the impeller design,  $D/T$  and  $C/T$  ratios and the vessel bottom shape. It is also assumed that  $S$  is independent of other parameters, such as the solid volume fraction  $\alpha_S$  or the particle physical properties  $\rho_p$  and  $d_p$ . Since not all  $S$  coefficients of the experimental conditions presented in the present study are available in the literature, particularly with a hemispherical vessel bottom shape, experimental  $S$  could not be directly compared to their theoretical values. However, if it is assumed that they are not dependent of the particle volume fraction and particles diameter and density,  $S$  should stay constant while only these parameters were varied. This was verified for two different microcarriers at particle volume fractions between 1 % and 12 %. If significant variations were observed between the different experimental values, it would deny the model proposed by Zwietering (Eq. 3.42) for microcarrier suspension.

#### Dimensional analysis

The targeted variable  $N_{js}$  was determined according to the 9 following physical parameters:

- Geometrical parameters including  $T$  the tank diameter,  $D$  the impeller diameter and  $C$  the off-bottom clearance.
- Material properties of the liquid phase (density  $\rho_L$  and dynamic viscosity  $\mu_L$ ) and of the solid phase (density  $\rho_p$ , diameter  $d_p$  and volume fraction  $\alpha_S$ ).
- Gravity acceleration  $g$ .

These parameters were considered independent and involved 3 fundamental dimensions, namely mass, length and time. According to the Vachy-Buckingham theorem, these 10 variables may be related by a relationship between 7 dimensionless numbers. The following dimensionless ratios  $\pi_i$  were thus constructed:

$$\pi_1 = \frac{N_{js} \cdot T^2 \cdot \rho_L}{\mu_L}, \quad \pi_2 = \frac{C}{T}, \quad \pi_3 = \frac{D}{T}, \quad \pi_4 = \frac{d_p}{T},$$

$$\pi_5 = \alpha_S, \quad \pi_6 = \frac{g \cdot T^3 \cdot \rho_L^2}{\mu_L^2}, \quad \pi_7 = \frac{\rho_p}{\rho_L}.$$

By looking for their physical meaning, they were adapted into the 6 following dimensionless ratios:

- Geometrical ratios:  $\frac{C}{T}$ ,  $\frac{D}{T}$  and  $\frac{d_p}{D}$ .
- Reynolds number:  $\frac{\rho_L \cdot N_{js} \cdot D^2}{\mu_L}$ .
- Solid volume fraction:  $\alpha_S$ .
- Liquid viscosity ratio  $\mu^* = \frac{\mu_L}{(\rho_p - \rho_L) \cdot g^{0.5} \cdot T^{1.5}}$ .

The last parameter  $\mu^*$  was adapted from Olmos *et al.* [52]. A second set of dimensionless parameters was proposed with the following ratios:

- Geometrical ratios:  $\frac{C}{T}$  and  $\frac{D}{T}$ .
- Reynolds number:  $\frac{\rho_L \cdot N_{js} \cdot D^2}{\mu_L}$ .
- Solid volume fraction:  $\alpha_S$ .
- Archimede number of the particle cloud:  $\frac{g \cdot \alpha_S \cdot T^3 \cdot \rho_L \cdot (\rho_p - \rho_L)}{\mu_L^2}$ .
- Number of particles:  $\left[ \alpha_S \cdot \left( \frac{T}{d_p} \right) \right]^3$ .

On the basis of the experimental data, three monomial models were build and the most robust  $N_{js}$  model was determined. The first one, given in Eq. (3.43) expressed  $N_{js}$  directly as a function of  $\alpha_S$ ,  $C$ ,  $D$  and  $d_p$ , whereas the two others presented in Eqs. (3.44)

and (3.45) involved the two set of dimensionless ratios, with the targeted variable  $N_{js}$  through the Reynolds number  $Re_{js}$ .

Model 1

$$N_{js} = K_1 \cdot \alpha_S^{a_1} \cdot C^{b_1} \cdot D^{c_1} \cdot d_p^{d_1} \quad (3.43)$$

Model 2

$$Re_{js} = K_2 \cdot \alpha_S^{a_2} \cdot \left(\frac{C}{T}\right)^{b_2} \cdot \left(\frac{D}{T}\right)^{c_2} \cdot \left(\frac{d_p}{D}\right)^{d_2} \cdot \left(\frac{\mu_L}{(\rho_p - \rho_L) \cdot g^{0.5} \cdot T^{1.5}}\right)^{e_2} \quad (3.44)$$

Model 3

$$Re_{js} = K_3 \cdot \alpha_S^{a_3} \cdot \left(\frac{C}{T}\right)^{b_3} \cdot \left(\frac{D}{T}\right)^{c_3} \cdot \left[\alpha_S \cdot \left(\frac{T}{d_p}\right)^3\right]^{d_3} \cdot \left(\frac{g \cdot \alpha_S \cdot T^3 \cdot \rho_L \cdot (\rho_p - \rho_L)}{\mu_L^2}\right)^{e_3} \quad (3.45)$$

In Eqs. (3.43) - (3.45),  $K_i$  are constants characterizing the impeller design and  $a_i$ ,  $b_i$ ,  $c_i$ ,  $d_i$  and  $e_i$  are the exponents to which the parameters or dimensionless numbers were raised to. It is important to emphasize that in this study  $d_p$ ,  $\rho_p$  and the liquid properties,  $\rho_L$  and  $\mu_L$ , are specific to microcarriers and chosen in the industrial context of animal cell culture. Hence,  $d_p$  and  $\rho_p$  belong to a narrow range of values, with a density close to the liquid phase similar to water. The phase density difference was found very sensitive in the model resolution, caused by very low values and inaccuracies. So,  $(\rho_p - \rho_L)$  was not included in the first model (Eq. (3.43)), and  $e_i$  exponents for model 2 and 3 (Eqs. (3.44) and (3.45)) were not possible to determine by experimental data fit. Consequently, another strategy was adopted to calculate these values. It has been indeed demonstrated by Mersmann *et al.* that particles suspensions occurred at constant  $(P/V)$  ratios for systems with geometrical similarities [44]. The model proposed should thus respect this assumption to be consistent, so  $e_i$  coefficients were calculated in order to keep constant the  $(P/V)_{js}$  ratio defined in Eq. (3.46).

$$\left(\frac{P}{V}\right)_{js} = \frac{N_p \cdot \rho_L \cdot N_{js}^3 \cdot D^5}{V} \quad (3.46)$$

In the present study, Reynolds number were calculated between 1000 and 12000. Without reliable  $N_p$  measurements in a such small volume,  $N_p$  was nevertheless considered steady in this flow regime. A constant  $(P/V)_{js}$  would lead to the equation (3.47).

$$\frac{N_{js}^3 \cdot D^5}{T^3} \propto 1 \quad (3.47)$$

In order to reduce the number of exponents to be solved,  $(D/T)$  exponent determination was based on the literature. In one hand, the Zwietering model (Eq. (3.42)) proposed a value of -0.85, admitting that the model constant was also function of the impeller diameter. In the other hand, Nienow *et al.* extracted the impeller variable from the constant and obtained a final exponent of -2.21 [38]. The present models were thus solved for different values comprised between these two bounds. They were solved by using an optimization algorithm (non-linear, GRC, Excel, Microsoft) in order to get the last exponent values  $a_i$ ,  $b_i$  and  $d_i$ . The objective of this optimization consisted in minimizing the criterion  $\omega = \sum_{i=0}^{n_{exp}} (N_{js}^{mod} - N_{js}^{exp})^2$  with  $N_{js}^{mod}$  and  $N_{js}^{exp}$  are respectively the modeled and the experimental values of  $N_{js}$ . Models were finally validated for 40 operating conditions chosen out of the previous design of experiments, involving different impellers at different particle volume fractions between 1 and 19 %. An additional  $N_{js}$  data (Cytodex-1 at a volume fraction of 18.5 %) was recovered from the literature for the case of an Elephant Ear impeller ( $D/T = 1/2$  and  $C/T = 1/3$ ) in down-pumping mode placed in a 20 L hemispherical bioreactor, geometrically similar to the one used in the present study [53]. Models were applied for these operating conditions to verify their scalability. A last validation at the temperature of 37°C, generally used in cell culture, was performed by comparing experimental  $N_{js}$  values to the predicted values at 20 and 37°C and for 4 different impellers.

## Multiphase modelling by CFD

### CFD simulations

CFD simulations were performed by using the commercial finite volume solver ANSYS Fluent (ANSYS Inc., version 16.1). A granular Euler-Euler RANS (Reynolds Averaged Navier-Stokes) approach was applied, considering two interpenetrating phases. The continuity and momentum equations were solved for each phase in steady-state by using the Moving Reference Frame (MRF) approach to model the impeller rotation. The Reynolds stress tensor  $\bar{\tau}$  was modelled by the standard k- $\epsilon$  turbulence model, and the two dominant fluid/solid interactions considered were the drag and the turbulent dispersion forces. These two conservation equations are developed in Eqs. (3.48) and (3.49) for the liquid phase, and Eqs. (3.50) and (3.51) for the solid phase.

$$\left\{ \begin{array}{l} \nabla \cdot (\alpha_L \rho_L \mathbf{v}_L) = \nabla(\gamma_L \nabla \alpha_L) \\ \nabla \cdot (\alpha_L \rho_L \mathbf{v}_L \mathbf{v}_L) = -\alpha_L \nabla p + \nabla \cdot \bar{\tau}_L \\ \qquad \qquad \qquad + \alpha_L \rho_L \mathbf{g} + K_{SL}(\mathbf{v}_S - \mathbf{v}_L) \end{array} \right. \quad \begin{array}{l} (3.48) \\ (3.49) \end{array}$$

$$\left\{ \begin{array}{l} \nabla \cdot (\alpha_S \rho_S \mathbf{v}_S) = \nabla(\gamma_S \nabla \alpha_S) \\ \nabla \cdot (\alpha_S \rho_S \mathbf{v}_S \mathbf{v}_S) = -\alpha_S \nabla p - \nabla p_S + \nabla \cdot \bar{\bar{\tau}}_S \\ \qquad \qquad \qquad + \alpha_S \rho_S \mathbf{g} + K_{LS}(\mathbf{v}_L - \mathbf{v}_S) \end{array} \right. \quad (3.50)$$

$$\qquad \qquad \qquad (3.51)$$

Where  $\mathbf{v}$  is the velocity of the corresponding phase,  $p$  the pressure shared by all phases and  $\mathbf{g}$  the acceleration due to gravity. The interphase drag force involves the interphase momentum exchange coefficient  $K_{LS}$ , modelled by the Huilin-Gidaspow equations (ANSYS Fluent theory guide [12]). The diffusion-in-VOF equation was used to model the turbulent dispersion and was included in the mass conservation equation.

Cytodex-1 particles were chosen as reference particles for the simulations, defined by the experimental mean diameter and density. In accordance with experimental observations, the solid packing limit was fixed to 0.6 as recommended by Delafosse *et al.* [5]. Calculation domain was discretized using between 230,000 and 275,000 tetrahedral meshes of around 5 mm, except in a zone in the vessel bottom, where the size was refined at a maximum of 2 mm, as presented in Fig. 3.9 to allow a better description of particle just-suspended state. This number of mesh cells was chosen as a compromise between a reasonable calculation time and a sufficient accuracy for the results analysis.

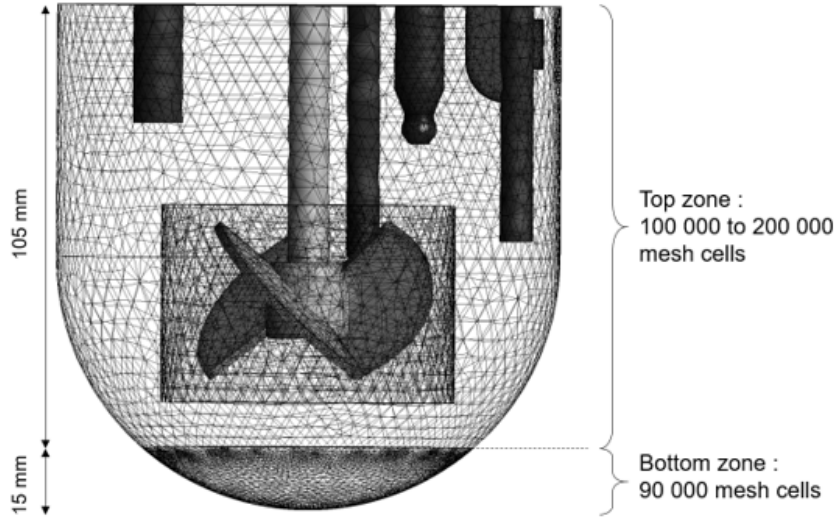


Figure 3.9: Mesh discretization of the vessel for the CFD simulations.

The simulation was initialized, considering all particles quasi-settled ( $\alpha_S = 0.5$ ) at the bottom of the bioreactor. Higher particle concentrations led to divergence during the first



iterations. Consequently, 0.5 was found to be a good compromise, allowing particles settling during the first iterations and avoiding divergence. Convergence of the simulations was supposed when equation residuals were less than  $10^{-5}$  and when liquid velocities and solid volume fractions in the impeller vicinity were stabilized. This second validation was necessary to ensure the stabilization of the  $N_{js}$  determination criterion presented in the next following part.

### $N_{js}$ determination strategy by using CFD

To model the subjective experimental determination of  $N_{js}$ , two simulation outputs were proposed.

The first one Packed Fraction  $PF$  relates the volume of packed particles to the total volume of particles. To determine the value of  $PF$ , particles were supposed packed if their local volume fraction was between  $\alpha_{ref} = 0.55$  and the packing limit 0.6 (Eq. 3.52).

$$PF = \frac{V_p (\alpha_S > \alpha_{ref})}{V_{p, tot}} \quad (3.52)$$

The second one, Still Fraction  $SF$  (Eq. 3.53), relates the volume of 'quasi-motionless' particles on the total volume of particles. It is based on the determination of the local particle residence time  $\tau_p$  in mesh cells in the bottom of the system. If this value was smaller than a reference residence time based on a time of 1 second to pass through a cube with 2 mm sides, then particles were considered to be almost motionless in the mesh cell. Experimentally, the last microcarriers to be lifted seemed to stay closely together by forming a little cone with a slow circular movement.  $SF$  reflects this phenomenon and corresponds to the percentage of particles in this situation.

$$SF = \frac{V_P (\tau_p < \tau_{ref})}{V_{p, tot}} \quad (3.53)$$

As considered by Tamburini *et al.* with the development of their CFD method *Unsus-pended Solids Criterion*, the results were dependent of the grid and the volume discretization [42]. A coarse grid could lead to uncertainties and to underestimations of  $N_{js}$  values. In the present study, the finer meshing in the bottom zone permitted to limit this effect. Using these two criteria, a CFD-based strategy was developed to reach the value of  $N_{js}$  by a progressive decrease of the agitation rate  $N$  until a predefined critical value of  $PF$  or  $SF$  was reached. Preliminary simulations were performed in a 200 mL minibioreactor with the experimental data obtained from Collignon *et al.* works [1]. This step allowed to validate the chosen models and to define the critical values of the two parameters defining the just-suspended state of particles:  $PF^{crit}$  and  $SF^{crit}$ . After this first validation, the

method was transferred to the geometry of the 1.12 L reactor of this study. The approach was validated for various geometrical conditions and particle concentrations in the case of the HTPG and the Elephant Ear impellers in down-pumping mode. Then, this method was applied at one or two operating conditions of the Rushton turbine and the HTPG and Elephant Ear impellers in up-pumping mode.

### 3.3.4 Results and discussions

#### Suspension modelling

First,  $S$  coefficients of the Zwietering correlation presented in Eq. (3.42) were calculated from 8 experimental  $N_{js}$  measurements. They all shared the same impeller conditions: an HTPG impeller in down-pumping mode, at a  $D/T$  ratio of 0.5 and a  $C/T$  ratio of 0.5. These  $S$  values are presented in function of the microcarrier volume fraction  $\alpha_S$  in Fig. 3.10. On the contrary to what is commonly admitted, it can be noted that, in the case of microcarriers,  $S$  depended on the value of  $\alpha_S$  with a 27 % deviation between the lowest and the highest values of  $S$ . Thus, exponents of the Zwietering correlation should be revisited, especially concerning the terms involving the microcarrier properties.

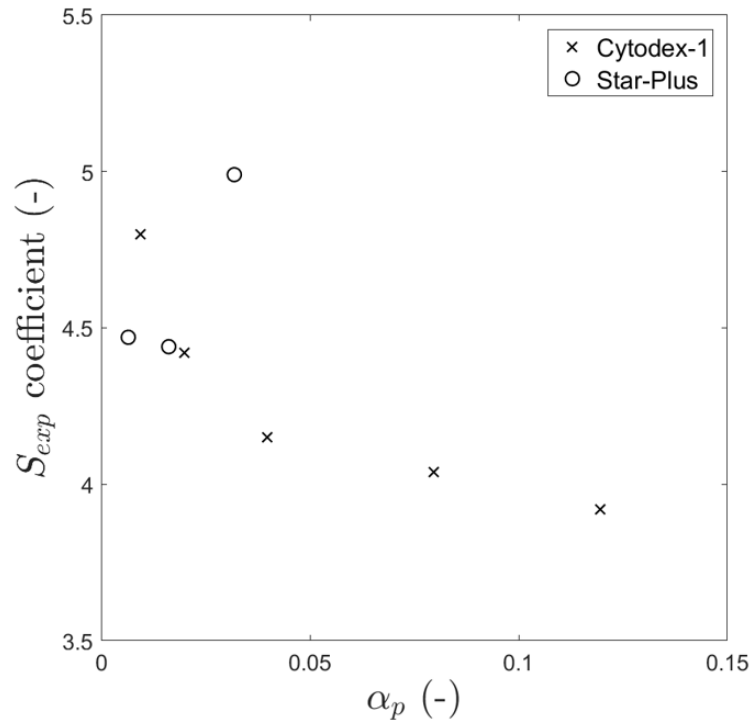


Figure 3.10: Evolution of the experimentally determined  $S$  coefficients from the Zwietering correlation with the microcarrier volume fraction in the bioreactor, for Cytodex-1 and Star-Plus.

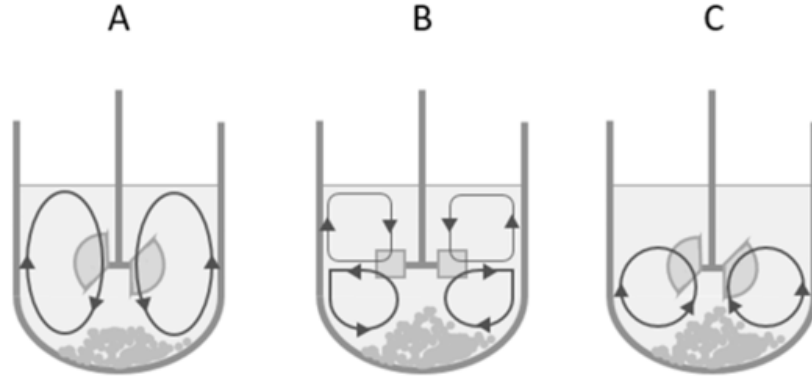


Figure 3.11: Flow patterns and particle bed shapes observed at agitation rates  $N < N_{js}$  depending on mixing structures: axial flow with EED and HTPGD (A), radial flow with RT (B) and mixed-flow with EEU and HTPGU (C).

The five impellers could be classified in three types, according to the flow patterns induced and microcarrier bed shapes. With increasing agitation rates, the bed progressively evolved from a planar-surface volume to a cone shape for both radial flow (RT) and mixed-flow (EEU and HTPGU) impellers, as presented in Fig. 3.11 (B and C). Particles were pushed inward and driven by the impeller. With axial flow (EED and HTPGD) the bed was a peakless cone as shown in Fig. 3.11 (A). In this case, particles were pushed down and suspended after sliding along the side wall. Thus, these three flow patterns involved different suspensions phenomena, which were taken into account for the model establishment. The consequence on parameter fitting was that, despite it could be possible to determine a unique set of parameters  $b_i$ ,  $c_i$  and  $d_i$  for the three flow patterns, the exponents related to particle volume fraction had to be specific to each of them. The model constants  $K_i$  logically depended on impeller geometry. Best fitted models are given in Eqs. (3.54) - (3.56) and the parameters  $K_i$  given in Table 3.8, are only dependent on the impeller design. The coefficients  $a_1$ ,  $a_2$  and  $a_3$  displayed three values according to the flow pattern and are given in table 3.8.  $a_1$  and  $a_2$  are the only exponents involving  $\alpha_S$ . Considering Model 3 (Eq. (3.56)),  $\alpha_S$  is involved in three terms, with  $\alpha_S^{0.3}$ ,  $\alpha_S^{0.4/3}$  and  $\alpha_S^{14/45}$ , consequently, a total exponent *Tot.  $\alpha_S$  exponent* has been calculated as  $Tot. \alpha_S \text{ exponent} = a_3 + 0.4/3 + 14/45$ .

Model 1

$$N_{js} = K_1 \cdot \alpha_S^{a_1} \cdot C^{1/3} \cdot D^{-1} \cdot d_p^{-0.4} \quad (3.54)$$

Model 2

$$Re_{js} = K_2 \cdot \alpha_S^{a_2} \cdot \left(\frac{C}{T}\right)^{1/3} \cdot \left(\frac{D}{T}\right)^{0.6} \cdot \left(\frac{d_p}{D}\right)^{-0.4} \cdot \left(\frac{\mu_L}{(\rho_p - \rho_L) \cdot g^{0.5} \cdot T^{1.5}}\right)^{-28/75} \quad (3.55)$$

Model 3

$$Re_{js} = K_3 \cdot \alpha_S^{a_3} \cdot \left(\frac{C}{T}\right)^{1/3} \cdot \left(\frac{D}{T}\right)^1 \cdot \left[ \alpha_S \cdot \left(\frac{T}{d_p}\right)^3 \right]^{0.4/3} \cdot \left( \frac{g \cdot \alpha_S \cdot T^3 \cdot \rho_L \cdot (\rho_p - \rho_L)}{\mu_L^2} \right)^{14/45} \quad (3.56)$$

Table 3.8:  $K_i$  and  $a_i$  parameters of the three models predicting  $N_{js}$ , according to the impeller design.

Flow pattern	Impeller	$K_1$ ( $\times 10^{-3}$ )	$K_2$	$K_3$	$a_1$	$a_2$	$a_3$	<i>Tot. <math>\alpha_S</math> exponent</i> (model 3)
(A)	HTPGD	7.9	8.2	2.4	0.07	0.07	-0.37	0.07
(A)	EED	4.9	5.0	1.5	0.07	0.07	-0.37	0.07
(B)	RT	6.3	6.4	2.0	0.1	0.1	-0.34	0.1
(C)	HTPGU	6.7	6.8	2.0	0.2	0.2	-0.24	0.2
(C)	EEU	4.9	5.1	1.5	0.2	0.2	-0.24	0.2

These three models were applied on 40 operating configurations out of the design of experiments. The experimental measurements were performed by three different operators to include the potential subjective  $N_{js}$  determination, and involved the HTPG impeller in down-pumping mode, the Elephant Ear impeller in up-pumping mode and the Rushton turbine at different  $C/T$  ratios and at different particle volume fractions. Results are presented in Fig. 3.12 for model 3. Models were globally validated but presented deviations for high particle volume fractions with the Elephant Ear impeller. The model establishment was based on data involving particle volume fractions up to 12 % and does not seem thus suitable for higher concentrations with this type of impeller. However, these high microcarrier volume fractions are seldom used in animal cell culture bioreactors. Considering the 95 configurations of the design of experiments and the 40 complementary measurements, mean relative errors under 10 % were obtained for the three models. Mean errors obtained with each model are presented for the different impeller designs in Table 3.9.

In order to determine the most robust model between the three proposed, the validity of each model was verified at the cell culture working temperature of 37°C and for a scale-up application in a 20 L vessel. Concerning the temperature stability, fluid properties were admitted to be the same as water, with both density and viscosity dependent of the temperature. Results for four impeller designs are given in Table 3.10. All models presented mean deviations of less than 20 % between the experimental values and the predicted values, but model 2 (Eq. (3.55)) was found to be more robust than the others.

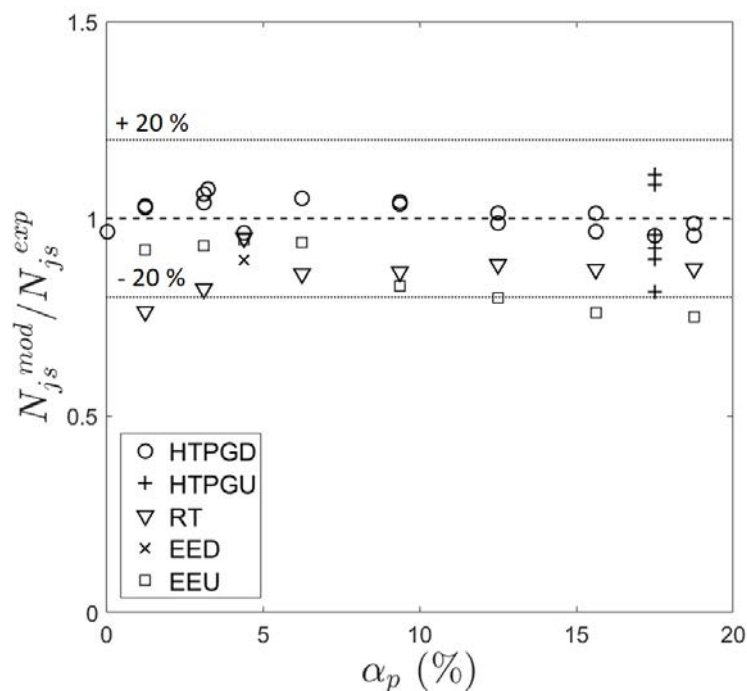


Figure 3.12: Comparison of the deviation between the experimental  $N_{js}$  and the  $N_{js}$  predicted by the model for operating conditions out of the design of experiment and model resolution, according to the impeller design.

Table 3.9: Mean errors between  $N_{js}$  predicted by the models and experimental values at  $T = 20^\circ\text{C}$ , according to the impeller design and the model used.

	Model		
	1	2	3
HTPGD	6.0 %	6.0 %	5.8 %
EED	8.6 %	8.4 %	8.6 %
RT	11.1 %	12.8 %	11.5 %
HTPGU	9.3 %	8.9 %	8.9 %
EEU	12.3 %	13.2 %	12.5 %
Mean error	8.7 %	9.1 %	8.7 %

Concerning the model scalability, results are presented in Table 3.11. In this case, the model 2 presented the highest deviation of 34 %. Consequently, model 1 (Eq. (3.54)) and model 3 (Eq. (3.56)) were found to be more suitable.

Regarding the mean relative error, the temperature validity, the scalability, and the physical meanings of each parameters, model 3 (Eq. (3.56)) was considered to be the best compromise. The comparison between the predicted values  $N_{js}^{mod}$  and the experimental values  $N_{js}^{exp}$  is reported in Fig. 3.13 for particle volume fractions under 12 %. A Student's t-test was performed with a statistical significance chosen at 0.05. Due to the distinct values of  $K_3$  and  $a_3$  coefficients according to the impeller design, t-tests were applied separately for each impeller design. For each of them, a regression analysis led to  $p$ -values

of less than 0.01, indicating that all parameters of the model were statistically significant. This model will be used for the following discussion on the impact of each parameter of the design of experiment on  $N_{js}$ . For the sake of clarity,  $K_3$  and  $a_3$  will be respectively renamed  $K$  and  $a$ .

Table 3.10: Mean errors between  $N_{js}$  predicted by the models and experimental values, at 37°C according to the impeller design and the model used.

	Model		
	1	2	3
HTPGD	18.5 %	0.5 %	15.1 %
EED	22.5 %	6.1 %	20 %
RT	15.1 %	7.2 %	11.3 %
EEU	19.1 %	0.9 %	15.3 %
Mean error	18.8 %	3.7 %	15.4 %

Table 3.11: Mean errors between  $N_{js}$  predicted by the models and experimental values at 20 rpm, in a 20 L vessel equipped with a EE down-pumping impeller, according to the impeller design and the model used.

Model	$N_{js}^{mod}$ (rpm)	Deviation
1	21	5 %
2	27	34 %
3	22	11.2 %

### Effect of the impeller geometry on $N_{js}$

First, the off-bottom impeller clearance  $C$  was raised to the power of 1/3 which is in accordance with literature data, stating that  $N_{js}$  become lower as the  $C/T$  ratio is reduced [38, 46]. In this study, the lowest value of  $C/T$  was 0.25, so it is admitted that flow patterns respected a 'double-eight' regime in the case of radial impellers. There was no pattern modification with the decrease of  $C/T$  [54, 55, 56].

Concerning the effect of the impeller diameter, it was found that  $N_{js}$  was proportional to  $D^{-1}$ , with the three models (Eqs. (3.54) to (3.56)). This trend is also in accordance with the literature [37, 38, 39]. A larger impeller presents a higher surface in contact with the continuous phase, and thus delivers a higher discharge stream, which facilitates the solids suspension. Moreover, our results showed that the impact of  $D/T$  ratio was much more significant than that of  $C/T$ , which is in agreement with previous works [39]. However, the -1 coefficient identified in our work was significantly lower than the one proposed by Nienow *et al.* [38], with a value of -2.21, or the -3.45 estimated by Arvinth

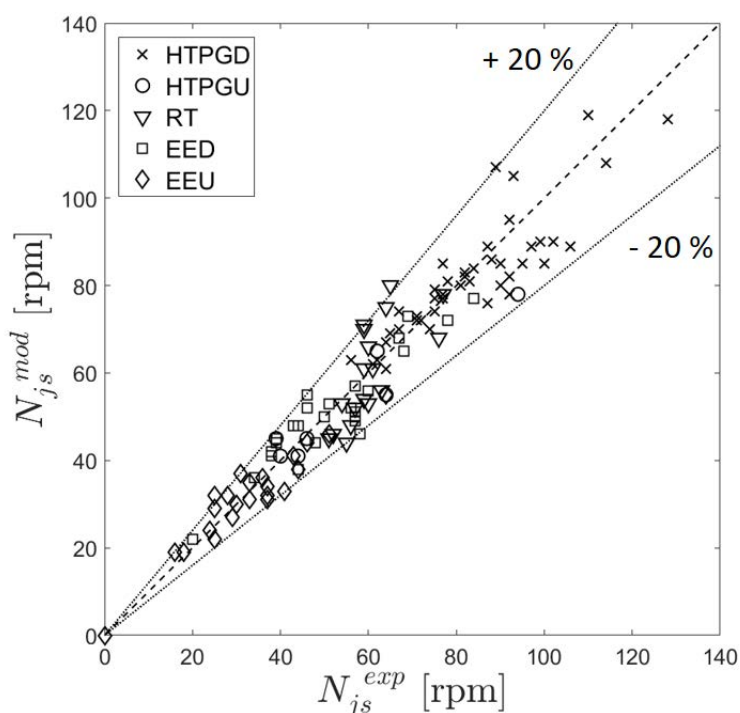


Figure 3.13: Comparison of experimental  $N_{js}^{exp}$  and modeled  $N_{js}^{mod}$  with the equation 3.56, depending on the impeller design.

*et al.* [39]. The low density difference of the particles used in our study probably explains these differences.

The last geometrical parameter considered in the models was the impeller shape, independently of its size. Depending on this shape, different model parameters were then determined for the constant  $K$  and the exponent  $a$  of particle volume fraction  $\alpha_S$  to improve model precision. This choice is justified by the macroscopic structures of flow, promoting particle suspension either by particle aspiration or particle down-pushing according to the impeller design, and leading to different power dissipation gradients within the vessel. In order to compare the different impellers used, both  $\alpha_S$  and  $K$  effects on  $N_{js}$  were taken into account, and the  $K \cdot \alpha_S^a$  product was calculated for each impeller design. Products values are given in Table 3.12.

Table 3.12: Impact of the impeller design on  $N_{js}$  and classification.

Impeller design	$K \cdot \alpha_S^a$		
	$\alpha_S=4 \%$	$\alpha_S=8 \%$	$\alpha_S=12 \%$
HTPGD	8.1	6.3	5.4
RT	5.0	3.9	3.3
EED	5.9	4.7	4.0
HTPGU	4.3	3.7	3.3
EEU	3.3	2.6	2.6

These values showed that the radial Rushton turbine and the impellers operating in mixed-flow regime displayed lower values, reflecting that it requires less energy to lift particles by pushing them inward and aspirating them through the impeller direction than pushing them outward and making them slide along the wall, as it was represented in Fig. 3.11. Impellers could thus be classified, according to their efficiency to minimize  $N_{js}$ : the Elephant Ear impeller displayed lower  $N_{js}$  than the other impeller, especially at high solid concentrations and in up-pumping mode, whereas the HTPG impeller in down-pumping mode presented the highest value for  $N_{js}$ . But for cell culture applications, the impeller design has to be carefully chosen as displaying a lower  $N_{js}$  does not necessarily imply a minimization of hydromechanical stress induced. It was indeed shown by Collignon *et al.* that the Elephant impeller Ear displayed a lower  $N_{js}$ , but also higher Energy Dissipation / Circulation function than the Rushton turbine and the Marine propellers at the same power input indicating a higher exposition frequency of microcarriers to mechanical stresses with the Elephant Ear impeller [1]. For the investigation of an optimal impeller design, a parameter involving frequency exposure to hydromechanical stress should thus be taken into account, in addition to the  $N_{js}$  minimization.

#### **Effect of the microcarrier concentration on $N_{js}$**

As it was previously described, the particle concentration term was found to be a function of the impeller design in the  $\alpha_S^{a_3}$  term, where  $a_3$  displayed at least three values according to the agitation mode. An increase of  $N_{js}$  was observed with the solid volume fraction. The exponents obtained after the model resolution were close to the one proposed in the Zwietering correlation, where the solid mass fraction was raised to 0.13 (Eq. (3.42)). For microcarrier density, it corresponds to a solid volume fraction raised to 0.12. In the present study, the three values proposed by the new model were 0.07, 0.1 and 0.2, leading to a mean value of 0.12. The new model was thus broadly in accordance with the Zwietering correlation, but provided more precision with distinct values for each agitation modes.

#### **Effect of microcarrier properties**

Regarding only the particle diameter  $d_p$  effect on  $N_{js}$ , a negative value of -0.4 was found, which is in contradiction with correlations in the literature, presenting positive values [37, 38, 39]. In the present study, the number of particles was proposed instead of a geometrical parameter. Hence, for a given particle concentration, larger beads led to lower number of particles, and thus to lower total interface area between the liquid and solid phases. For the case of microcarrier, more input power was required to suspend or avoid settling of a higher number of particles, despite their smaller diameter. Concerning particle density, it was involved through an Archimede number with a length scale characterizing



the microcarrier cloud. As expected, denser particles required more input power, and thus a higher agitation rate to be fully suspended.

### Comparison with the Zwietering correlation

In order to compare this new model (Eq. 3.56) with the Zwietering correlation, the  $S$  coefficient of the Eq. (3.42) has to be determined for each geometrical configuration of the study. To do that, experimental Zwietering coefficients  $S_{exp}$  were calculated from the experimental  $N_{js}$  measurements. The objective was then to gather all configurations varying the particle concentration or the microcarriers used, but displaying the same geometrical configuration, and determine a common  $S$  value. Because of the dispersed design of experiments, the majority of geometrical configurations had only one or two points. So, based on the results of this work, it was assumed that  $N_{js} \propto C^{1/3}$ , permitting to divide all measurements in 15 groups according to their common  $D/T$  value and impeller design. The ratio  $N_{js}$  was then expressed in function of the modified Zwietering function  $f_{Zwietering, m}$  presented in Eqs. (3.57) and (3.58), inspired from a modified Zwietering correlation with  $C^{1/3}$  extracted from the  $S$  coefficient (Eq. (3.57)). This  $f_{Zwietering, m}$  term should be linear to  $N_{js}$ , with a slope corresponding to the common  $S_{calc}$  value of a given group. The  $S_{calc}$  values obtained after linear regressions are presented in Table 3.13.

$$N_{js, Zwietering\ calc} = S_{calc} \cdot f_{Zwietering, m} \quad (3.57)$$

$$f_{Zwietering, m} = \nu_L^{0.1} \cdot \left( \frac{g \cdot (\rho_p - \rho_L)}{\rho_L} \right)^{0.45} \cdot X^{0.13} \cdot d_p^{0.2} \cdot D^{-0.85} \cdot C^{1/3} \quad (3.58)$$

Table 3.13: Adapted Zwietering coefficients  $S_{calc}$  values according to the impeller design and the  $D/T$  ratio.

Design	D / T		
	0.33	0.4	0.5
EED	7.1	7.1	6.3
HTPGD	11.8	11.3	11.1
RT	7.6	7.4	8.4
EEU	5.2	4.6	4.4
HTPGU	7.5	6.0	5.3

A comparison of this modified Zwietering model (Eq. (3.57)) with the new model (Eq. (3.56)) was finally performed and is represented in Fig. 3.14 The new model led to a relative error of 8.8 % with 96 % of points under 20 % deviation, whereas the adapted Zwietering model provided a relative error of 12.9 %, with 18 % of the absolute deviations over 20 % and leading up to 69 % deviation. The new model proposed thus better  $N_{js}$

prediction. Moreover, contrary to the Zwietering correlation, the constant  $K$  of the new model was only dependent of the impeller design.

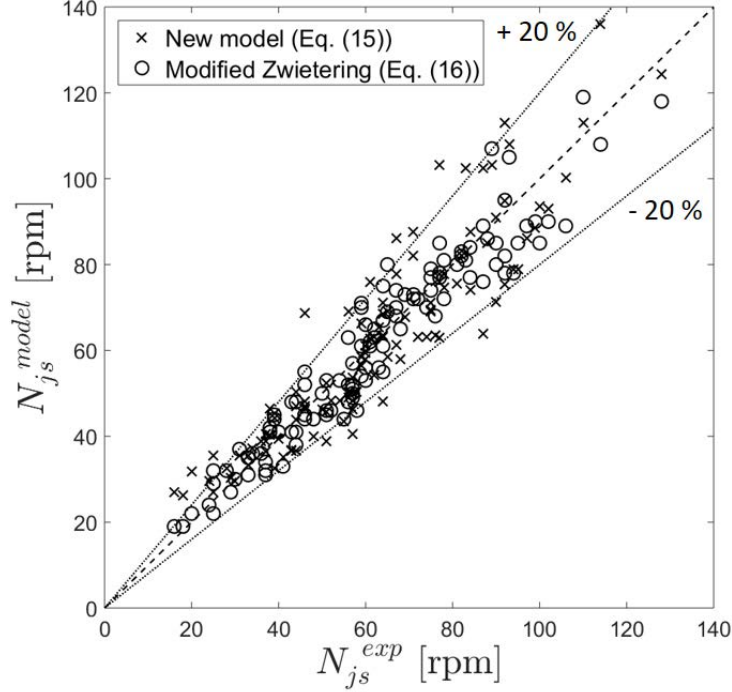


Figure 3.14: Comparison of modeled  $N_{js}$  and numerically adapted  $N_{js,Zwietering}$ .

### CFD-based method to predict $N_{js}$

Preliminary simulations were run to determine a suitable criterion to predict  $N_{js}$ . To do that, both  $PF$  and  $SF$  criteria (Eq. (3.52) and (3.53)) were calculated on the 200 mL minibioreactor geometry with 4 different impeller designs (EEU, EED, RT and Marine propeller in up-pumping mode). At the just-suspended state, the Reynolds numbers were comprised between 1000 and 1800, traducing a transitional regime. With a  $k-\varepsilon$  Standard Wall Function model, the turbulence was incorrectly solved at the boundary layers, probably due to not fully turbulent regime in the reactor. In that respect, the  $k-\varepsilon$  Scalable Wall Function was implemented instead of the Standard Wall Function to improve boundary layer modelling. Simulations run at the experimental critical agitation rate  $N_{js}^{exp}$  provided  $SF$  values comprised between 0.08 % and 0.13 % and null values for  $PF$ . The  $SF$  criterion was thus used for the study with a critical value  $SF^{crit}$  fixed at 0.10 %. Predicted critical agitation rates  $N_{js}^{simul}$  were then determined by looking for the agitation rate presented  $SF = SF^{crit}$ . Results are presented in Fig. 3.15 and led to a relative error of 9 %. This choice of criterion differed from the one of Tamburini *et al.* [42]. For glass bead suspension, they found that a solid volume fraction based criterion

presented better results than a one based on particle velocity. This second criterion was developed assuming that only particles presenting velocities equal to zero were considered to be unsuspended, unlike the  $SF$  criterion of the present study, in which particles with particles with a very low residence time were considered to be unsuspended. It was in accordance with microcarriers suspension observations. Probably due to a density close to the liquid phase, the last particles to be suspended, as defined by the Zwietering criterion, were not totally motionless when staying in the bottom of the reactor.

The CFD-based method to predict  $N_{js}$  was then applied on 20 operating conditions of the 1.12 L reactor described in the experimental approach part. The  $k-\varepsilon$  model adaptation was not necessary for this reactor scale, displaying higher Reynolds number values of about 5000, and so the Standard Wall Function was used. This system may be still considered in transitional regime, but the Standard Wall Function appeared to correctly solve the turbulent equations. As previously,  $SF^{crit}$  value was firstly determined from  $SF$  values obtained from simulations run at the experimental critical agitation rate  $N_{js}^{exp}$ . In this case,  $SF^{crit}$  was found at 0.20 %. This percentage indicated a quasi-motionless microcarrier volume of around  $0.2 \text{ cm}^3$ , which seemed to be representative of the experimental observations.  $N_{js}^{simul}$  were finally recovered according to  $SF^{crit}$  and compared to their corresponding experimental data. Comparison of the experimental and the predicted critical agitation rates are presented in Fig. 3.15 and displayed a mean relative error of 9 %. Deviations were observed with configurations presenting the lowest Reynolds number values, less than 2100, at which the chosen turbulent models seemed to be inadequate. By removing these configurations, a mean relative error of 9 % was obtained in this restricted domain.

### 3.3.5 Conclusion

A new empirical correlation has been established to predict  $N_{js}$  for microcarriers and was found to provide a better accuracy than the most commonly used Zwietering correlation. Another advantage displayed by the new model concerned the constant of the correlation. The traditional Zwietering correlation proposed a constant  $S$  function of the impeller design and both  $D/T$  and  $C/T$  ratios, which may be difficult to find in the literature. In the present study, the constants  $K$  were only dependent of the impeller design.

A dimensional analysis provided two other remarkable information. First, the influence of the particle volume fraction  $\alpha_S$  seemed to be a function of the regime applied by the impeller. The determination of the constants  $K$  permitted to classify impellers, showing that the up-pumping mode led to lower  $N_{js}$  values. Secondly, in the case of microcarriers, the number of particles was found to better suit than the  $d_p/D$  ratio.

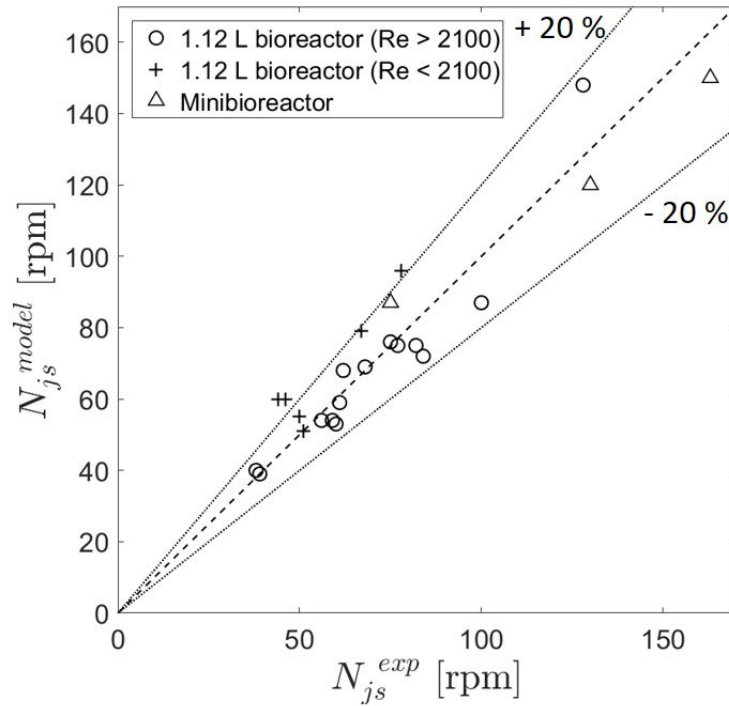


Figure 3.15: Comparison of experimental  $N_{js}$  and modeled  $N_{js}$  with the CFD-based method.

Finally, a CFD-based method was developed to numerically predict  $N_{js}$ . The models chosen and the method were validated according to two different working volumes, with 17 configurations for the specific vessel of this study. The particle residence time in the bottom was found to be the best criterion for microcarriers, with a critical value fixed at  $SF^{crit}$  of 0.20 %.

### 3.3.6 Acknowledgements

The authors would like to thank the French Agence Nationale de la Recherche (ANR) and the Interreg VA Grande Région program for their financial support. They also acknowledge Fabrice Blanchard (LRGP, Nancy) and Thierry Salmon (PEPs, Liège) for their technical contribution to this work.

### 3.4 Chapter conclusions

The present work aimed at providing a robust method for  $N_{js}$  determination, in the specific case of microcarrier suspensions. It was indeed verified that 'classic' models, initially developed using particles with higher densities, such as glass beads or sand, presented deviations between the modelled  $N_{js}$  and the experimental measurements. It notably concerned the Zwietering correlation [57] and the Unsuspended Solids Criterion proposed by Tamburini. *et al.* [42] during CFD simulations. These deviations may be explained by the low-density characteristics displayed by microcarriers.

First of all, 140  $N_{js}$  measurements were performed according to different operating conditions, including the impeller design, the particle properties, and the fluid properties at 20°C and 37°C.

The first model method was based on a dimensional analysis, performed using experimental measurements. An original model was found suitable for the different impeller designs, using a coefficient only dependent on the flow structures developed (axial, radial or mixed-flow). Moreover, this model was found more robust by using a term describing the number of particle instead of a geometrical ratio involving the particle diameter.

The second strategy used CFD simulations, through a screening approach. Based on the work of Delafosse *et al.* [5] and preliminary comparisons, models were carefully chosen for the particles just-suspended state determination. In this case, attention was paid to the drag and the turbulent dispersion forces and the near-wall turbulence modelling. A criterion based on particle residence time in the bottom of the vessel was finally developed for the just-suspended state prediction. Models and the related criterion were validated for two bioreactor scales and for different impeller geometries and particle concentrations. Some deviations were nevertheless observed for configurations with low  $N_{js}$  values, probably due to a lack of turbulence modelling, CFD turbulence models may be not suitable. For a  $Re > 2,100$ , both the numerical approach and the developed  $N_{js}$ -criterion demonstrated to be valid, with a reasonable calculation time. However, this approach focused on the particles in the bottom of the reactor to model the just-suspended state. Complementary investigations allowing a better accuracy to predict particle concentration gradients within the vessel. They should consist in a refined meshing as proposed by Delafosse *et al.* (2018) [58], and other strategies such as a Lagrangian approach or an unresolved CFD-DEM approach, limited to a low number of particles.

## Main contributions of Chapter 3

- **Current models to determine  $N_{js}$  may present up to 50 % deviations with experimental measurements**, probably due to the low density difference between the solid and the liquid phases.
- An **original model dedicated to microcarrier suspension** was provided. It was found to be **suitable for scale-up** and displayed a better accuracy in comparison to the Zwietering correlation, with a **constant value that only depends on the impeller design**.
- Based on a dimensional analysis, the **impact of the particle volume fraction on  $N_{js}$  was found to be a function of the regime applied by the impeller** (axial, radial, mixed-flow).
- A **CFD-based method** was also proposed using a **criterion based on the particle residence time in the bottom of the bioreactor**. A good accuracy was observed when  $Re > 2,100$ . However, under this value, the turbulence modelling was suggested to be unsuitable.

## References

- [1] M.-L. Collignon, A. Delafosse, S. Calvo, C. Martin, A. Marc, D. Toye, E. Olmos, Large-eddy simulations of microcarrier exposure to potentially damaging eddies inside mini-bioreactors, *Biochemical Engineering Journal* 108 (2016) 30–43.
- [2] S. Kaiser, V. Jossen, C. Schirmaier, D. Eibl, S. Brill, C. van den Bos, R. Eibl, Fluid flow and cell proliferation of mesenchymal adipose-derived stem cells in small-scale, stirred, single-use bioreactors, *Chemie Ingenieur Technik* 85 (2013) 95–102.
- [3] C. Schirmaier, V. Jossen, S. C. Kaiser, F. Jüngerkes, S. Brill, A. Safavi-Nab, A. Siehoff, C. Bos, D. Eibl, R. Eibl, Scale-up of adipose tissue-derived mesenchymal stem cell production in stirred single-use bioreactors under low-serum conditions, *Engineering in Life Sciences* 14 (2014) 292–303.
- [4] V. Jossen, S. C. Kaiser, C. Schirmaier, J. Herrmann, A. Tappe, D. Eibl, A. Siehoff, C. van den Bos, R. Eibl, Modification and qualification of a stirred single-use bioreactor for the improved expansion of human mesenchymal stem cells at benchtop scale, *Pharmaceutical Bioprocessing* 2 (2014) 311–322.
- [5] A. Delafosse, C. Loubière, S. Calvo, D. Toye, E. Olmos, Solid-liquid suspension of microcarriers in stirred tank bioreactor-experimental and numerical analysis, *Chemical Engineering Science* (2018) 52–63.
- [6] G. Montante, F. Magelli, Modelling of solids distribution in stirred tanks: analysis of simulation strategies and comparison with experimental data, *International Journal of Computational Fluid Dynamics* 19 (2005) 253–262.
- [7] A. Khopkar, G. Kasat, A. Pandit, V. Ranade, Computational fluid dynamics simulation of the solid suspension in a stirred slurry reactor, *Industrial & Engineering Chemistry Research* 45 (2006) 4416–4428.
- [8] G. Montante, F. Magelli, Mixed solids distribution in stirred vessels: experiments and computational fluid dynamics simulations, *Industrial & Engineering Chemistry Research* 46 (2007) 2885–2891.
- [9] D. Guha, P. Ramachandran, M. Dudukovic, J. Derksen, Evaluation of large eddy simulation and euler-euler MSC models for solids flow dynamics in a stirred tank reactor, *AIChE Journal* 54 (2008) 766–778.
- [10] D. Wadnerkar, R. P. Utikar, M. O. Tade, V. K. Pareek, MSC simulation of solid-liquid stirred tanks, *Advanced Powder Technology* 23 (2012) 445–453.
- [11] A. Tamburini, A. Brucato, A. Cipollina, G. Micale, M. Ciofalo, CFD predictions of sufficient suspension conditions in solid-liquid agitated tanks, *International Journal of Nonlinear Sciences and Numerical Simulation* 13 (2012) 427–443.
- [12] Fluent, ANSYS, Release 15.0, Theory Guide, November (2013).
- [13] L. Schiller, A drag coefficient correlation, *Zeit. Ver. Deutsch. Ing.* 77 (1933) 318–320.

- 
- [14] M. Syamlal, T. J. O'Brien, Computer simulation of bubbles in a fluidized bed, in: AICHE Symp. Ser, volume 85, Publ by AICHE, pp. 22–31.
- [15] S. Ergun, Fluid flow through packed columns, Chemical Engineering Progress 48 (1952) 89–94.
- [16] C. Y. Wen, Mechanics of fluidization, in: Chemical Engineering Progress, volume 62, pp. 100–111.
- [17] D. Gidaspow, R. Bezburuah, J. Ding, Hydrodynamics of circulating fluidized beds: kinetic theory approach, Technical Report, Illinois Institute of Technology, Chicago, IL (United States). Department of Chemical Engineering, 1991.
- [18] L. Huilin, D. Gidaspow, Hydrodynamics of binary fluidization in a riser: MSC simulation using two granular temperatures, Chemical Engineering Science 58 (2003) 3777–3792.
- [19] L. Gibilaro, R. Di Felice, S. Waldram, P. Foscolo, Generalized friction factor and drag coefficient correlations for fluid-particle interactions, Chemical Engineering Science 40 (1985) 1817–1823.
- [20] A. Brucato, F. Grisafi, G. Montante, Particle drag coefficients in turbulent fluids, Chemical Engineering Science 53 (1998) 3295–3314.
- [21] D. Pinelli, M. Nocentini, F. Magelli, Solids distribution in stirred slurry reactors: influence of some mixer configurations and limits to the applicability of a simple model for predictions, Chemical Engineering Communications 188 (2001) 91–107.
- [22] R. Hassan, K. Loubiere, J. Legrand, G. Delaplace, A consistent dimensional analysis of gas–liquid mass transfer in an aerated stirred tank containing purely viscous fluids with shear-thinning properties, Chemical Engineering Journal 184 (2012) 42–56.
- [23] A. Stolzing, E. Jones, D. McGonagle, A. Scutt, Age-related changes in human bone marrow-derived mesenchymal stem cells: Consequences for cell therapies, Mechanisms of Ageing and Development 129 (2008) 163–173.
- [24] J. Rowley, E. Abraham, A. Campbell, H. Brandwein, S. Oh, Meeting lot-size challenges of manufacturing adherent cells for therapy, BioProcess International 10 (2012) 16–22.
- [25] A. L. Van Wezel, Growth of Cell-strains and Primary Cells on Micro-carriers in Homogeneous Culture, Nature 216 (1967) 64–65.
- [26] A. S. Simaria, S. Hassan, H. Varadaraju, J. Rowley, K. Warren, P. Vanek, S. S. Farid, Allogeneic cell therapy bioprocess economics and optimization: Single-use cell expansion technologies, Biotechnology and Bioengineering 111 (2014) 69–83.
- [27] T. Ma, A.-C. Tsai, Y. Liu, Biomanufacturing of human mesenchymal stem cells in cell therapy: Influence of microenvironment on scalable expansion in bioreactors, Biochemical Engineering Journal 108 (2016) 44–50.



- [28] Q. A. Rafiq, K. M. Brosnan, K. Coopman, A. W. Nienow, C. J. Hewitt, Culture of human mesenchymal stem cells on microcarriers in a 5 l stirred-tank bioreactor, *Biotechnology Letters* 35 (2013) 1233–1245.
- [29] T. Lawson, D. E. Kehoe, A. C. Schnitzler, P. J. Rapiejko, K. A. Der, K. Philbrick, S. Punreddy, S. Rigby, R. Smith, Q. Feng, J. R. Murrell, M. S. Rook, Process development for expansion of human mesenchymal stromal cells in a 50 L single-use stirred tank bioreactor, *Biochemical Engineering Journal* 120 (2017) 49–62.
- [30] C. Ferrari, F. Balandras, E. Guedon, E. Olmos, I. Chevalot, A. Marc, Limiting cell aggregation during mesenchymal stem cell expansion on microcarriers, *Biotechnology Progress* 28 (2012) 780–787.
- [31] M. S. Croughan, J.-F. Hamel, D. I. C. Wang, Hydrodynamic effects on animal cells grown in microcarrier cultures, *Biotechnology and Bioengineering* 29 (1987) 130–141.
- [32] T. M. Maul, D. W. Chew, A. Nieponice, D. A. Vorp, Mechanical stimuli differentially control stem cell behavior: morphology, proliferation, and differentiation, *Biomechanics and Modeling in Mechanobiology* 10 (2011) 939–953.
- [33] T. R. Heathman, A. W. Nienow, Q. A. Rafiq, K. Coopman, B. Kara, C. J. Hewitt, Agitation and aeration of stirred-bioreactors for the microcarrier culture of human mesenchymal stem cells and potential implications for large-scale bioprocess development, *Biochemical Engineering Journal* 136 (2018) 9–17.
- [34] C. J. Hewitt, K. Lee, A. W. Nienow, R. J. Thomas, M. Smith, C. R. Thomas, Expansion of human mesenchymal stem cells on microcarriers, *Biotechnology Letters* 33 (2011) 2325–2335.
- [35] R. S. Cherry, E. T. Papoutsakis, Physical mechanisms of cell damage in microcarrier cell culture bioreactors, *Biotechnology and Bioengineering* 32 (1988) 1001–1014.
- [36] A. C. Schnitzler, A. Verma, D. E. Kehoe, D. Jing, J. R. Murrell, K. A. Der, M. Aysola, P. J. Rapiejko, S. Punreddy, M. S. Rook, Bioprocessing of human mesenchymal stem/stromal cells for therapeutic use: Current technologies and challenges, *Biochemical Engineering Journal* 108 (2016) 3–13.
- [37] T. N. Zwietering, Suspending of solid particles in liquid by agitators, *Chemical Engineering Science* 8 (1958) 244–253.
- [38] A. Nienow, Suspension of solid particles in turbine agitated baffled vessels, *Chemical Engineering Science* 23 (1968) 1453–1459.
- [39] S. Arvinth, P. G. Rao, T. Murugesan, Critical impeller speed for solid suspension in turbine agitated contactors, *Bioprocess and Biosystems Engineering* 14 (1996) 97–99.
- [40] M. Kraume, Mixing times in stirred suspensions, *Chemical Engineering & Technology* 15 (1992) 313–318.
- [41] K. Raghava Rao, V. Rewatkar, J. Joshi, Critical impeller speed for solid suspension in mechanically agitated contactors, *AIChE Journal* 34 (1988) 1332–1340.

- 
- [42] A. Tamburini, A. Cipollina, G. Micale, A. Brucato, M. Ciofalo, MSC simulations of dense solid–liquid suspensions in baffled stirred tanks: Prediction of suspension curves, *Chemical Engineering Journal* 178 (2011) 324–341.
- [43] N. Kee, R. B. Tan, MSC simulation of solids suspension in mixing vessels, *The Canadian Journal of Chemical Engineering* 80 (2002) 1–6.
- [44] A. Mersmann, F. Werner, S. Maurer, K. Bartosch, Theoretical prediction of the minimum stirrer speed in mechanically agitated suspensions1, *Chemical Engineering and Processing: Process Intensification* 37 (1998) 503–510.
- [45] K. Wichterle, Conditions for suspension of solids in agitated vessels, *Chemical Engineering Science* 43 (1988) 467–471.
- [46] G. Baldi, R. Conti, E. Alaria, Complete suspension of particles in mechanically agitated vessels, *Chemical Engineering Science* 33 (1978) 21–25.
- [47] S. Ibrahim, A. W. Nienow, Suspension of Microcarriers for Cell Culture with Axial Flow Impellers, *Chemical Engineering Research and Design* 82 (2004) 1082–1088.
- [48] P. M. Armenante, E. U. Nagamine, Effect of low off-bottom impeller clearance on the minimum agitation speed for complete suspension of solids in stirred tanks, *Chemical Engineering Science* 53 (1998) 1757–1775.
- [49] M. Chudacek, Solids suspension behaviour in profiled bottom and flat bottom mixing tanks, *Chemical Engineering Science* 40 (1985) 385–392.
- [50] M. S. Croughan, J.-F. P. Hamel, D. I. C. Wang, Effects of microcarrier concentration in animal cell culture, *Biotechnology and Bioengineering* 32 (1988) 975–982.
- [51] Q. A. Rafiq, K. Coopman, A. W. Nienow, C. J. Hewitt, Systematic microcarrier screening and agitated culture conditions improves human mesenchymal stem cell yield in bioreactors, *Biotechnology Journal* 11 (2016).
- [52] E. Olmos, K. Loubiere, C. Martin, G. Delaplace, A. Marc, Critical agitation for microcarrier suspension in orbital shaken bioreactors: experimental study and dimensional analysis, *Chemical Engineering Science* 122 (2015) 545–554.
- [53] M.-L. Collignon, A. Delafosse, M. Crine, D. Toye, Axial impeller selection for anchorage dependent animal cell culture in stirred bioreactors: methodology based on the impeller comparison at just-suspended speed of rotation, *Chemical Engineering Science* 65 (2010) 5929–5941.
- [54] P. M. Armenante, E. U. Nagamine, Effect of low off-bottom impeller clearance on the minimum agitation speed for complete suspension of solids in stirred tanks, *Chemical Engineering Science* 53 (1998) 1757–1775.
- [55] G. Montante, A. Brucato, K. Lee, M. Yianneskis, An experimental study of double-to-single-loop transition in stirred vessels, *The Canadian Journal of Chemical Engineering* 77 (1999) 649–659.

- [56] G. Montante, K. Lee, A. Brucato, M. Yianneskis, Numerical simulations of the dependency of flow pattern on impeller clearance in stirred vessels, *Chemical Engineering Science* 56 (2001) 3751–3770.
- [57] T. N. Zwietering, Suspending of solid particles in liquid by agitators, *Chemical Engineering Science* 8 (1958) 244–253.
- [58] A. Delafosse, C. Loubière, S. Calvo, E. Olmos, D. Toye, Experimental validation of solid-liquid simulations of microcarrier suspensions in a stirred-tank bioreactor, 16th European Conference on Mixing (MIXING), Toulouse, France (2018).



# Optimization of the impeller design for MSC culture on microcarriers in a stirred tank bioreactor

## Contents

---

<b>4.1 Introduction</b>	<b>194</b>
<b>4.2 Impeller design comparison according to the hydromechanical stress encountered by the microcarriers</b>	<b>196</b>
4.2.1 Impeller design selection	196
4.2.2 Hydromechanical stress based on all the liquid volume	197
4.2.3 Hydromechanical stress encountered by microcarriers	199
4.2.4 Multi-parameter analysis	200
<b>4.3 CFD-based strategy to optimize the impeller design adapted to microcarrier suspension in a minibioreactor</b>	<b>203</b>
4.3.1 Introduction	204
4.3.2 Bioreactor description	206
4.3.3 Numerical approach	206
4.3.4 Hydrodynamics and mixing parameters	211
4.3.5 Experimental approach	213
4.3.6 Results and discussion	214
4.3.7 Conclusion of the publication	224
4.3.8 Acknowledgements	225
<b>4.4 WJ-MSC culture in STR using selected EE impeller designs</b>	<b>226</b>
4.4.1 Validation of the MSC culture in a minibioreactor	226
4.4.2 WJ-MSC cultures using impeller designs from the Elephant Ear design optimization study	227
<b>4.5 Chapter conclusions</b>	<b>232</b>

---

## 4.1 Introduction

**S**IMILARLY to continuous cell lines, mesenchymal stem / stromal cells are shear sensitive, namely they can accept lower levels of stresses in comparison with microbial cultures. In addition, it was demonstrated that mechanical stimuli may promote cell differentiation, which unintended for cell therapies, where stemness properties must be ensured. Consequently, process intensification in STR must be attentive to the hydrodynamics and the turbulence generated by the agitation. But today, most of the current studies on microcarrier suspensions in STR based their analysis on the volume-averaged and / or the maximal turbulent energy dissipation rate in the whole bioreactor. However, the cell history along its 'lifelines' should be taken into account, within the time exposure to the potentially damaging zones and the potential rest time in other part of the vessel. Today, it is still unknown whether cell physiological response in bioreactor will be more impacted by a moderate shear stress during a long time duration or by a shorter but with higher shear stress.

This chapter aims at improving the geometrical characteristics of an impeller design for MSC cultures on microcarriers (Fig. 4.1). To achieve this, CFD simulations were run in order to get both global and local data on the turbulence dissipation particle distributions within the vessel.

A first study about the comparison of the impact of different impeller designs at the just-suspended state is presented in section 4.2. It uses the CFD models investigated in Chapter 3 (section 3.2), as well as the CFD-based method developed to model  $N_{js}$  (section 3.3). A comparison based on the turbulent energy dissipation rate in all the liquid volume will be first introduced. In a second time, the particle spatial distribution will be taken into account and another comparison will be developed, based on the local dissipated energy. Local hydromechanical stress encountered by the solid phase is then determined using the Kolmogorov theory of isotropic turbulence.

In a second time, using pre-established geometrical ratios, the impeller design found to generate the lowest stress onto particles was selected for a geometrical optimization. Based on a compromise between reasonable calculation times and a sufficient accuracy on the results, a screening approach is presented by varying three geometrical parameters ( $D/T$ ,  $C/T$  and the blade slope angle). CFD was coupled with a multi-objective method in order to determine the final design that should be used to minimize the particle exposure to zones displaying critical turbulent energy dissipation rates, and consequently to minimize

the potential cell damages. The second part of this chapter will detail this strategy and results of a sensitivity analysis in a scientific paper format (section 4.3). That will be submitted to *Chemical Engineering Science*.

The last part will be focused on WJ-MSC expansion in minibioreactors equipped with selected impeller designs. It will use the culture conditions validated in Chapter 2 (section 2.2), the automatic *in situ* cell counting method as an analytical tool for expansions comparison (section 2.3), and the Cytodex-1 microcarriers, found to be suitable for both cell attachment and expansion (section 2.4). According to a step-by-step investigation, the cell attachment and the ease of detachment were not investigated in this work, but will be done in the near future. Here, validation of the culture conditions in the minibioreactor is presented, and first results on cell expansions using impellers with different geometrical configurations are presented (section 4.4) as a scoping study ; further complementary cultures are needed to complete this study. The forthcoming investigations on this part are then discussed.

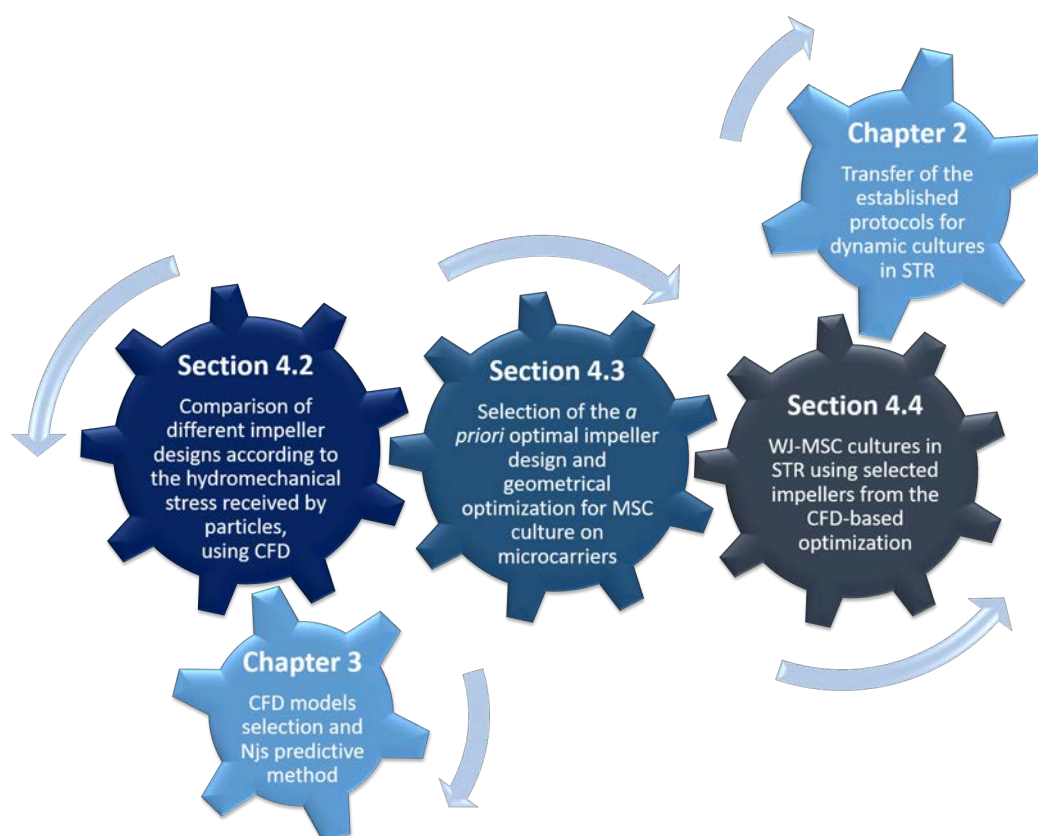


Figure 4.1: Presentation of the different steps of this work for the geometrical optimization of an impeller design, in order to improve MSC culture on microcarriers in STR.

## 4.2 Impeller design comparison according to the hydromechanical stress encountered by the microcarriers

### 4.2.1 Impeller design selection

Before investigating the improvement of the geometrical characteristics of an impeller design dedicated to MSC cultures on microcarriers, a preliminary comparison was performed on five impeller designs in a minibioreactor: (*i*) a marine propeller in up-pumping mode (MPU), (*ii*) a marine propeller in down-pumping mode (MPD), (*iii*) a Rushton turbine (RT), (*iv*) an Elephant Ear impeller in up-pumping mode (EEU) and (*v*) an Elephant Ear impeller in down-pumping mode (EED). Three flow structures were investigated with axial flow (MPU and EEU), radial flow (RT) and mixed-flow (MPD and EED). Experimental  $N_{js}^{exp}$  values were recovered from the previous study of Collignon *et al.* (2016) [1]. The different impeller designs are presented in Fig. 4.2.



Figure 4.2: Impeller designs used for CFD simulations. Left to right: four-blade Rushton turbine, three-blade Elephant Ear impeller and three-blade marine propeller. Picture reproduced from Collignon *et al.* (2016) [1].

Models used for the present CFD simulations are detailed in Appendix A, and discussed in chapter 3. It will be here emphasized that models were selected and the meshing was built, both in order to have a compromise between a reasonable calculation time for CFD simulations and a sufficient accuracy on results for post-treatment, focused on the hydromechanical stress encountered by the particles. The aim of this work was indeed to provide a robust screening method for the further impeller design investigation. The modelled minimal agitation rate ensuring all particle suspension  $N_{js}^{mod}$  was considered to be reached when 0.10 % of the total solid volume was quasi-motionless in the bottom of the vessel ( $\tau_p < \tau_{p, ref}$ ). For more details, please refer to section 3.3. Based on the results presented in Table 4.1,  $N_{js}^{mod}$  was found to be in good agreement with  $N_{js}^{exp}$  for MPU, RT, EED and EEU impeller designs. Only estimation of  $N_{js}$  for MPD displayed a significant difference. In this last case, the particle concentration obtained by CFD simulations at  $N = N_{js}^{exp}$  would be over-estimated in the bottom and under-estimated in the rest of the



vessel leading to a biased particle spatial distribution estimation. On the other hand, CFD simulations with a  $N = N_{js}^{mod} \gg N_{js}^{exp}$  would strongly over-estimate the turbulent energy dissipation rate in the system. It was thus chosen to remove the MPD from the present comparison study, and following sections will only compare MPU, RT, EEU and EED, which were validated according to  $N_{js}$  modelling.

Table 4.1: Comparison of the experimental  $N_{js}^{exp}$  and the modelled  $N_{js}^{mod}$  and fluid turbulence characteristics at the microcarrier just-suspended state for different impeller designs in a minibioreactor, according to  $\langle \varepsilon \rangle$  ascending order.

Impeller design	$N_{js}^{exp}$ (rpm)	$N_{js}^{mod}$ (rpm)	Deviation	Re (-)	$\langle \varepsilon \rangle$ $10^{-3} \text{ (m}^2 \text{ s}^{-3}\text{)}$	$\varepsilon_{max}$ $\text{(m}^2 \text{ s}^{-3}\text{)}$
MPD	140	240	71 %	970	N/A	N/A
EED	75	80	6.7 %	1030	0.16	0.02
RT	163	160	1.8 %	1560	0.48	0.17
EEU	130	140	7.7 %	1790	1.1	0.12
MPU	340	340	0.0 %	2350	1.7	2.4

## 4.2.2 Hydromechanical stress based on all the liquid volume

In order to determine the local stress encountered by the particles, and also by cells, CFD simulations were combined to the Kolmogorov's isotropic turbulence theory. It was indeed shown by Henzler *et al.* (2000) that particle stress would be related to the turbulent energy dissipation rate  $\varepsilon$  and particle diameter only [2]. The volume-averaged and the maximal turbulent energy dissipation rates were thus calculated using CFD simulations for the four impeller designs at the experimental just-suspended state, and are presented in Table 3.3 (section 3.2). These values are recalled in Table 4.1 according to the  $\langle \varepsilon \rangle$  ascending order.  $\langle \varepsilon \rangle$  was found to be the highest for impellers operating in up-pumping mode (EEU and MPU), whereas the impeller in down-pumping mode (EED) presented the lowest value. The radial Rushton turbine displayed an intermediate value. Fig. 4.3 presents the volume distribution of  $\varepsilon$  related to the 4 impeller designs. In accordance with the volume-averaged  $\langle \varepsilon \rangle$  comparison, MPU promoted a wider fluid zone displaying highest  $\varepsilon$  values ( $\varepsilon > 0.1 \text{ m}^2 \text{ s}^{-3}$ ), and the EED the recommended design to reduce the turbulence dissipation into the fluid.

It was noticed that EED and RT presented two distinct peaks in Fig. 4.3, with the first found close to the corresponding  $\langle \varepsilon \rangle$  values (on the right), and the other presenting much lower  $\varepsilon$  values (on the left). Indeed, the peaks on the left corresponds to the volume of fluid near the surface, but through which particles do not necessarily pass through. These impellers led to a solid compartmentalisation, as it was observed during the experimental  $N_{js}$  measurements performed by Collignon *et al.* (2016), in Fig. 4.4

## 4.2. IMPELLER DESIGN COMPARISON ACCORDING TO THE HYDROMECHANICAL STRESS ENCOUNTERED BY THE MICROCARRIERS

[1]. Hence, the EED supposed to limit the turbulent dissipation rate, considering all the liquid height, may be not the impeller leading the lowest turbulent dissipation rate in the zones more specifically visited by the microcarriers. To characterize the solid phase exposure to the potentially damaging zones, the particle pathways inside the vessel must thus, *a priori*, be taken into account.

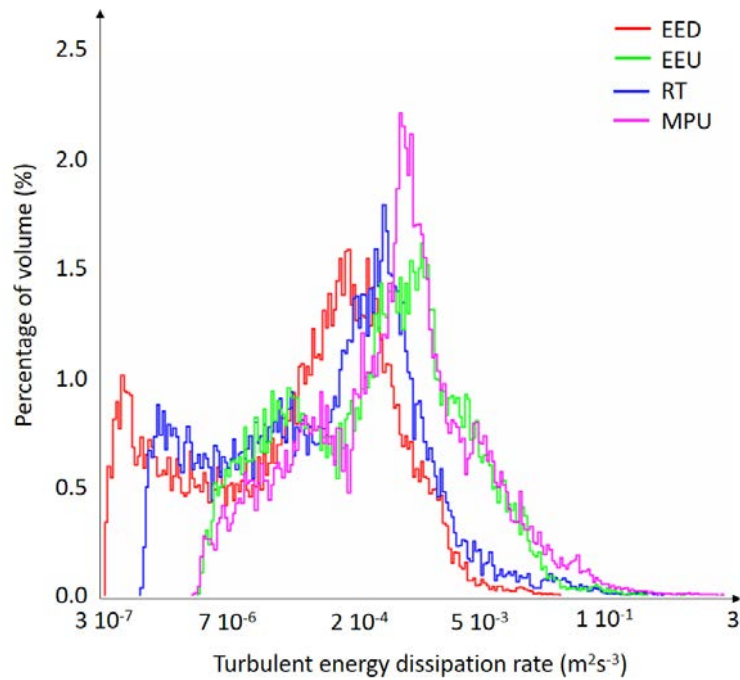


Figure 4.3: Volumetric distributions of the turbulent energy dissipation rate  $\varepsilon$  in the whole fluid volume in the bioreactor, at  $N = N_{js}$  for different impeller designs.

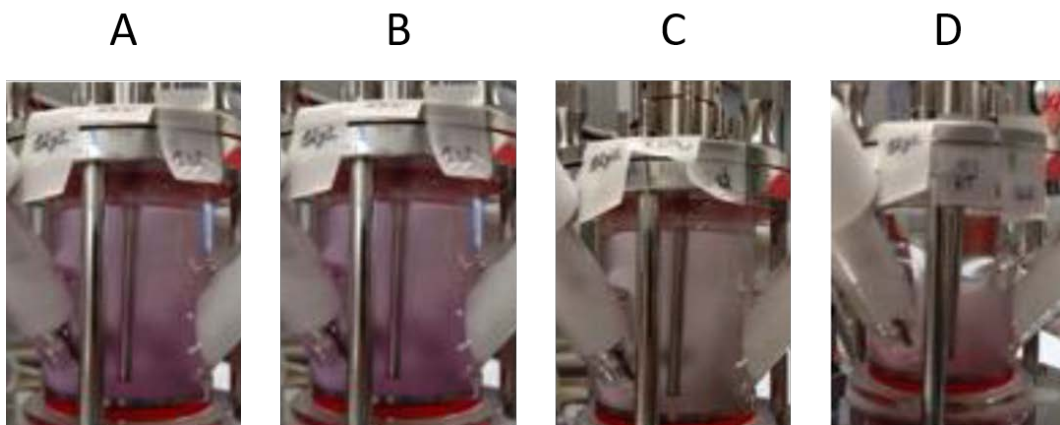


Figure 4.4: Experimental spatial distribution of microcarriers at  $N = N_{js}$  with the EED (A), the EEU (B), the MPU (C) and the RT (D). Figure reproduced from Collignon *et al.* (2016) [1].

### 4.2.3 Hydromechanical stress encountered by microcarriers

The objective of the present work is to determine which impeller should be recommended to minimize the cell damages due to fluid shear stress. In this way, two parameters involving the solid phase are proposed to compare the different impeller designs: (i) the dissipated power received by the particles  $\langle (P/V)_{@p} \rangle$  and (ii) an energy dissipation / circulation function  $EDC$ .

#### Estimation of the dissipated power received by the particles $\langle (P/V)_{@p} \rangle$

The power encountered by the solid phase was calculated according to Eq. 4.1, for each impeller design and at both experimental and modelled  $N_{js}$  values, with  $\rho_m$  the mixture density (Eq. (4.19)) Results are summarized in Table 4.2.  $\langle \epsilon \rangle$  values based on the whole fluid volume are recalled for comparison.

$$\left\langle \left( \frac{P}{V} \right)_{@p} \right\rangle = \rho_m \langle \epsilon \rangle_{@p} = \frac{\rho_m}{V_p} \iiint_{V_p} \epsilon(V) dV \quad (4.1)$$

$$\rho_m = \alpha_S \rho_S + \alpha_L \rho_L \quad (4.2)$$

Table 4.2: Fluid turbulence determination at the microcarrier just-suspended state for different impeller designs in a minibioreactor, according to  $\langle \epsilon \rangle$  ascending order.

Impeller design	Simulations at $N = N_{js}^{exp}$		Simulations at $N = N_{js}^{mod}$	
	$\langle \epsilon \rangle$ $\times 10^{-3} \text{ (m}^2 \text{ s}^{-3}\text{)}$	$\langle (P/V)_{@p} \rangle$ $\text{(W m}^{-3}\text{)}$	$\langle \epsilon \rangle$ $\times 10^{-3} \text{ (m}^2 \text{ s}^{-3}\text{)}$	$\langle (P/V)_{@p} \rangle$ $\text{(W m}^{-3}\text{)}$
MPU	1.7	1.91	1.7	1.91
RT	0.48	0.60	0.45	0.58
EED	0.16	0.20	0.19	0.23
EEU	1.1	1.17	1.4	1.44

Based on the experimental  $N_{js}$ , simulations indicated that MPU displayed a significantly higher  $\langle (P/V)_{@p} \rangle$ , almost ten times higher than the value obtained with the EED impeller. Overall, the two highest values were obtained with the impeller operating in up-pumping mode.

#### Estimation of the energy dissipation / circulation function $EDC$

The energy dissipation / circulation function  $EDC$  established in this work (Eq. (4.3)) was inspired by the energy function developed by Justen *et al.* to study the simultaneous impact of circulation times and power dissipation on fungi morphology [3], and by the

## 4.2. IMPELLER DESIGN COMPARISON ACCORDING TO THE HYDROMECHANICAL STRESS ENCOUNTERED BY THE MICROCARRIERS

---

modified function proposed by Collignon *et al.* to compare different impeller designs for MSC culture [1]. Here, the main difference is that the stress duration is integrated through the energy encountered by the particles. This energy is taken into account only if, locally potentially damaging zones are expected. Based on the work of Croughan *et al.* (1988), this was suggested to occur when the Kolmogorov length scale  $\lambda_K$  was found below the particle diameter, here  $d_p = 190 \mu\text{m}$  [4]. In Eq. (4.3),  $Q_{p,net}$  is the local microcarrier volume flow rate in the mesh cell.  $EDC$  values are presented for the four impeller designs in Table 4.3, with the corresponding volume-averaged Kolmogorov length scale, calculated using the whole fluid volume.

$$EDC = \iiint_{V_L(\lambda_K < d_p)} \frac{\rho_m \varepsilon(V)}{Q_{p,net}(V)} dV \quad (4.3)$$

Table 4.3: Fluid turbulence characterization at the microcarrier just-suspended state for different impeller designs in a minibioreactor, according to  $\langle \varepsilon \rangle$  ascending order.

Impeller design	Simulations at $N = N_{js}^{exp}$		Simulations at $N = N_{js}^{mod}$	
	$\langle \lambda_K \rangle$ ( $\mu\text{m}$ )	$EDC$ ( $\text{kJ m}^{-3}$ )	$\langle \lambda_K \rangle$ ( $\mu\text{m}$ )	$EDC$ ( $\text{kJ m}^{-3}$ )
MPU	119	4.3	118	4.3
RT	163	0.91	166	0.86
EED	215	0.36	205	0.45
EEU	133	2.8	126	3.3

Similarly to  $\langle (P/V)_{@p} \rangle$ , higher  $EDC$  values were obtained with up-pumping impeller designs. Based on the results from simulations performed at  $N = N_{js}^{exp}$ , an almost 12-fold difference was observed between the MPU, displaying the highest value, and the EED impeller, which led to the lowest  $EDC$ . Concerning  $\langle \lambda_K \rangle$  determination, only the EED impeller displayed a volume-averaged eddy size of approximately the same size as the particles. All other impeller designs led to lower values indication, and more risks of cell damages in these configurations.

### 4.2.4 Multi-parameter analysis

Comparisons of the impellers according to  $\langle (P/V) \rangle$ ,  $\langle (P/V)_{@p} \rangle$  and  $EDC$  are summarized in Fig. 4.5. First of all, more potential cell damages would be expected using impellers in up-pumping mode. Despite these axial impellers are widely used for suspended animal cell cultures, with the aim of promoting axial blending, air dispersion and aerated power characteristics with low power numbers, they are not recommended for microcarrier-based cultures. The present results are in accordance with the observations

of Ibrahim and Nienow (2004) and Nienow (2006). More precisely, axial impellers in down-pumping mode, such as the three-blade hydrofoil HE3 or the Lightnin' A310, were found to be more suitable for cell culture on microcarriers [5, 6], but their results were based on the global parameter  $\langle \varepsilon \rangle$  determined at the just-suspended state. The present study thus completes this assumption, by validating that the part of the dissipated turbulent energy received by the solid phase was also found lower in the case of down-pumping impellers. In addition, power and energy were distinguished in the present work. Despite comparisons led to the same impeller design order according to the  $\langle (P/V) \rangle$ ,  $\langle (P/V)_{@p} \rangle$  or  $EDC$  values, differences between these values led to slightly different relative comparisons between impellers. Here, between EED and RT, a 2.5-fold increase was found between  $\langle (P/V)_{@p} \rangle$  values, whereas only a 1.9-fold increase was obtained between  $EDC$  values. These two parameters must be thus considered together, as complementary one to each other. Moreover, comparison between  $\langle (P/V) \rangle$  and  $\langle (P/V)_{@p} \rangle$  values in Fig. 4.5 showed that all impeller designs of this study displayed  $\langle (P/V)_{@p} \rangle$  values 1.1- to 1.3-fold higher than their corresponding values in all the fluid volume. This is due to the particle concentration gradient within the vessel, which are mainly concentrated in the lower part of the bioreactor. **Calculations based on the whole fluid thus underestimate the turbulent energy dissipation rate actually encountered by the microcarriers.**

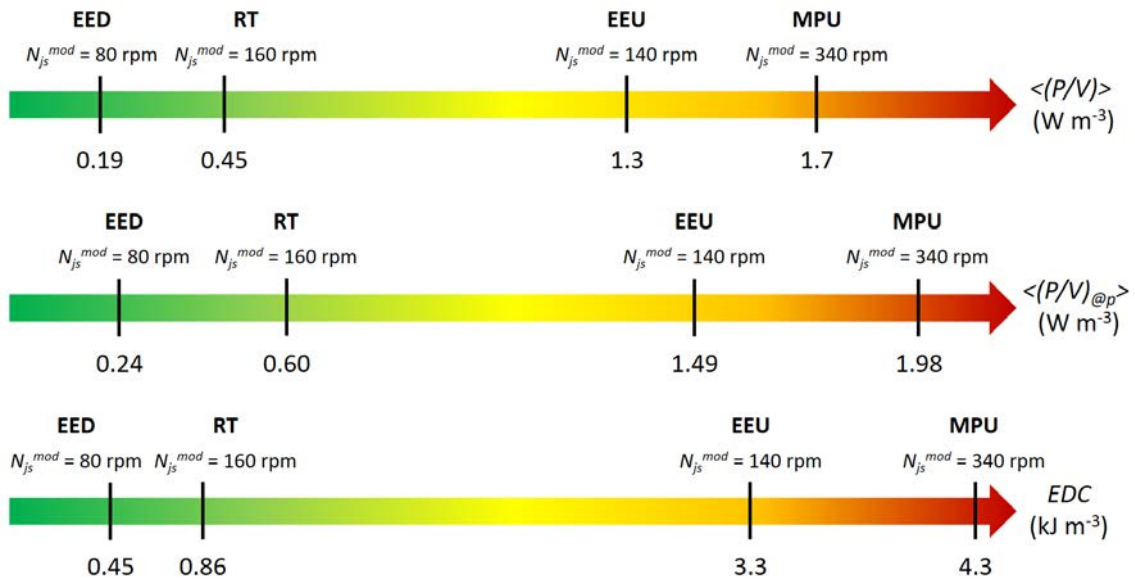


Figure 4.5: Relative comparison between four impeller designs (EED, RT, EEU and MPU) at  $N = N_{js}$ , according to the power per unit of volume based on the whole liquid volume  $\langle (P/V) \rangle$  and encountered by the microcarriers  $\langle (P/V)_{@p} \rangle$ , and the Energy Dissipation / Circulation function  $EDC$ .

#### 4.2. IMPELLER DESIGN COMPARISON ACCORDING TO THE HYDROMECHANICAL STRESS ENCOUNTERED BY THE MICROCARRIERS

---

The study of Collignon *et al.* also reported a comparison between the hydrodynamics data from CFD simulations to a visual / experimental particle distribution, with the same impeller as in the present study [1]. They calculated the frequency of microcarriers exposure to the potentially damaging zones ( $\lambda_K < d_p$ ) and the time and volume fraction of microcarrier exposures in these zones, all based on the same power input equal to  $10^{-3}$  W kg<sup>-1</sup>. They demonstrated that, the MPU impeller displayed both the lowest exposure frequency to maximal mechanical stress areas, with a frequency of 0.055 s<sup>-1</sup> and the lowest temporal fraction of exposure to these critical zones, with a fraction of 22.5 %. Hence, based on a fixed power input, the MPU impeller was recommended. However, in this situation, the agitation rates of MPU and EED were respectively equal to 308 and 150 rpm. At the just-suspended state, MPU agitation rate was found higher ( $N_{js}^{exp} = 340$  rpm) and EED agitation rate was found lower ( $N_{js}^{exp} = 75$  rpm). **Our work thus showed that a comparison based on the just-suspended state, instead of the same power input, led to different trends and we recommended the use of EED impellers rather than the MPU.** For microcarrier-based cell cultures operating at the particle just-suspended criterion, it is thus recommended to compare impeller designs at the just-suspended state instead of a defined input power criterion.

### 4.3 CFD-based strategy to optimize the impeller design adapted to microcarrier suspension in a minibioreactor

The previous section (4.2) presented the EED impeller as the most suitable for cell culture on microcarriers at the just-suspended state. This impeller design was thus selected for a geometrical optimization. CFD simulations may be coupled to this optimization with the integration of  $\langle (P/V)_{@p} \rangle$  and  $EDC$  as optimization criteria. For this purpose, the variation of the  $D/T$  ratio, related to the impeller size, and the  $C/T$  ratio, related to the impeller off-bottom clearance, were investigated, as these parameters were demonstrated to have an impact on the particle suspension in section 3.3. In addition, the blade slope angle was studied as a third geometrical parameter. This part will present the results of this work in the form of a scientific paper.

#### CFD-based strategy to optimize the impeller design adapted to microcarrier suspension in stirred tank bioreactors

C. Loubière<sup>a</sup>, A. Delafosse<sup>b</sup>, E. Guedon<sup>a</sup>, I. Chevalot<sup>a</sup>, D. Toye<sup>b</sup>, E. Olmos<sup>a</sup>

<sup>a</sup>Laboratoire Réactions et Génie des Procédés, Université de Lorraine, CNRS, LRGP, F-54000 Nancy, France

<sup>b</sup>Laboratory of Chemical Engineering, Université de Liège, Allée de la Chimie 3, B6C, 4000 Liège, Belgium

Keywords: Impeller design, particle suspension, Computational Fluid Dynamics (CFD), bioreactor, multi-objective optimization.

#### Publication abstract

In mixed bioreactors, adherent-dependent mesenchymal stem cells are cultivated on 100-300  $\mu\text{m}$  diameter solid particles, called microcarriers. When mixing this solid-liquid suspension, a compromise has to be found to allow sufficient mixing to suspend the microcarriers and minimization of potentially damaging hydromechanical stresses. The present study proposes a strategy to improve the design of an Elephant Ear impeller at the just-suspended state ( $N = N_{js}$ ), by varying its relative size, blade slope angle and its position in the reactor. To do that, Computational Fluid Dynamics simulations could be coupled with a multi-objective optimization. Simulations successfully predict  $N_{js}$  according to a

method based on the particle minimal velocity. A set of impeller designs were 3D-printed to experimentally validate the  $N_{js}$  values. To characterize the damaging zones, the turbulent energy dissipation rate was locally integrated, and the power per unit of volume 'seen' by the solid phase, and also a fluid energy dissipation circulation function were calculated. On the basis of 114 simulations, response surfaces were built and a multi-optimization was performed by minimizing the hydromechanical stress encountered by the particles. Regarding these objectives, the impeller ( $C/T = 0.5$ ,  $D/T = 0.4$ ,  $\beta = 57^\circ$ ) was found to be the optimal geometry.

### 4.3.1 Introduction

During the last decades, a particular attention has been paid to mesenchymal stem cells (MSC) for their application in regenerative medicine, to cure diseases for which current treatments were found not sufficiently effective (heart failures, cancers, type I and II diabetes...). According to the U.S. National Institute of Health, more than 800 clinical trials are indeed completed or ongoing to treat cancers, heart failures and Parkinson's disease as some of many examples. However, *in vitro* cell expansion is necessary in order to reach the high cell dose requirements, between  $10^9$  and  $10^{12}$  cells / lot [7]. A way to improve the expansion of these adherent-dependent cells is the suspension of microcarriers in agitated bioreactors. These particles consists in 100-300  $\mu\text{m}$  diameter solid particles with a density around  $1020 \text{ kg m}^{-3}$ , thus close to the culture medium one. When mixing this solid-liquid suspension, a compromise has to be found, between a sufficient mixing to suspend the microcarriers and a moderate hydromechanical stress to avoid cell damages (cell differentiation, detachment or death) [8, 9, 10]. Adherent-dependent animal cells are known to be more particularly sensitive to shear stress than cells in suspension [11]. In this way, cultures are generally performed at the just-suspended state, as defined by the Zwietering criterion, namely when particles does not stay motionless one or two seconds in the bottom of the vessel [12].

Previous studies demonstrated that both the bioreactor and the impeller designs had an impact on the hydrodynamics in the vessel [1, 13, 14, 15, 16]. Hence, the design may be specifically chosen to reduce the hydromechanical stress in the bioreactor. In the case of MSC cultures, a minimization of cell damages due to this stress is looked for, since cells quality must be preserved during all the expansion process. Based on the Kolmogorov's isotropic turbulence theory [17], the Kolmogorov length scale  $\lambda_K$  and the turbulent energy dissipation rate  $\varepsilon$ , are key-parameters used to characterize the hydrodynamics in STR, and to compare the impact of different impeller designs on the potential cell damages induced by the agitation [2].

Considering the preceding facts, axial impellers are generally advised for animal cell cul-



ture. Following this assessment, two studies based on Computational Fluid Dynamics (CFD) were performed with axial impellers to compare microcarrier suspensions at the just-suspended state. On one hand, Collignon *et al.* compared 7 impellers in a 20 L bioreactor, involving 4 designs (TTP Mixel, A310 Lightning, 3 streamed-blades VMI-Rayneri, Elephant Ear Applikon) with different diameters [16]. At  $N = N_{js}$ , impellers inducing the largest swept volumes led to the lowest agitation rates. They finally proposed the TTP Mixel with a small diameter and the Elephant Ear impellers as the most suitable for cell cultures, by presenting the lowest mechanical stress. On the other hand, Jossen *et al.* performed the optimization of a dual-impeller design in the 2 L UniVessel® SU Bioreactor [18]. They started from the standard design of the UniVessel® SU Bioreactor and compared 9 geometrical configurations, varying the impeller diameter, the blade slope angle and the off-bottom clearance. They finally demonstrated that the agitation rate required to reach the just-suspended state was reduced by only slight modifications of the blade slope angle and the off-bottom clearance.  $N_{js}$  passed from 122 rpm to 77 rpm after the optimization, and as a consequence,  $\varepsilon$  was significantly reduced and  $\lambda_K$  found larger. These two studies demonstrated the significance of the impeller design selection for the investigation of systems leading to reduced hydromechanical stress. They were however limited to axial impellers and did not consider particle-particle interactions.

Recently, other impellers were investigated using CFD, as in the work of Delafosse *et al.*, comparing a down-pumping HTPG impeller, an up-pumping Elephant Ear impeller and a radial Rushton turbine [19]. The local stress related to the particle collisions was notably added to the criterion ; this phenomenon is rarely taken into account in CFD studies, as it remains complex to determine. The HTPG impeller in down-pumping mode led to more potential damaging zones and was found to generate more collisions, making the up-pumping Elephant Ear impeller a better choice for MSC cultures. Collignon *et al.* also compared microcarrier suspension at the just-suspended state with 5 different impeller designs [1]. Hydrodynamics using a Rushton turbine, an Elephant Ear impeller and a marine propeller, both in up-pumping and down-pumping modes, were investigated in single-phase Large-Eddy-Simulations CFD simulations run a  $\langle (P/V) \rangle$  value of  $10^{-3}$  W  $\text{kg}^{-1}$ . For a given  $\langle \varepsilon \rangle$  value, the Elephant Ear design led to higher exposures to both frequency and intensity of hydromechanical stress in comparison to the Rushton turbine or the Marine propeller.

Investigation of an optimal design through an experimental screening would be expensive and time-consuming. In the case of MSC cultures, it would be also limited by the number of cells available from the same donor. Hence, the use of CFD simulations may permit to reduce the final number of experiments and to better understand the impact of the different geometrical parameters studied on the hydrodynamics. The use of a multi-objective optimization on response surfaces coupled with CFD has already been validated for gas

dispersion maximization through required power minimization in an aerated reactor [20], and for particle suspension homogeneity while minimizing the power consumption induced by the agitation [21]. They both revealed a promising tool for screening and for sensitivity analysis. In the present study, a CFD-multi-objective optimization strategy was applied to predict an impeller design *a priori* dedicated to stem cell cultures in bioreactors.

Current production scales remain low (a few liters) [22] and low O<sub>2</sub> consumptions are observed [23]. So, unlike some other bioprocesses, homogeneity and O<sub>2</sub> transfer are today not limiting phenomena ; investigations are thus mainly focused on the particle suspension and the related hydromechanical stress. Criteria that should be considered for the present multi-objective optimization locally integrated the turbulent energy dissipation rate according to the solid phase concentration. This novel feature is even more important that at the just suspended state, particle concentration is not homogeneous in the whole bioreactor, and that the stress received by particles is dependent on particle pathways in the reactor. In this way, cumulative power received by the particles and dissipated energy in the potentially damaging zones were both taken into account, as well as the volume-averaged Kolmogorov length scale.

### 4.3.2 Bioreactor description

The bioreactor used was the 250 mL minibioreactor from Global Process Concept (GPC, La Rochelle, France), presented in Fig. 4.6. This bioreactor was developed according to a scale-down approach from a traditional bench top 2 L stirred tank bioreactor, using a constant power dissipation per unit of volume ( $P/V$ ). In the present study, the working volume was set to 200 mL, and the bioreactor was equipped with two lateral probes (pH, dissolved O<sub>2</sub>) and two immersed tubes for the temperature probe and the sampling system. These elements avoided vortex formation, so no additional baffle was necessary. Stirring was ensured by a mechanical agitation using a 3-blades Elephant Ear impeller operating in down-pumping mode.

### 4.3.3 Numerical approach

The global strategy developed here may be divided into four main steps, summarized in the flowchart of Fig. 4.7. With the aim of a numerical screening, a Design Of Experiments (DOE) varying the EE impeller geometry was firstly established. Then, CFD simulations were run for each design points, and specific parameters characterizing the hydromechanical stress received by the particles were recorded. Based on these results, response surfaces were built and experimentally validated using a set of 3D printed impellers. Once the range of validity was defined, an optimization was performed to determine the most

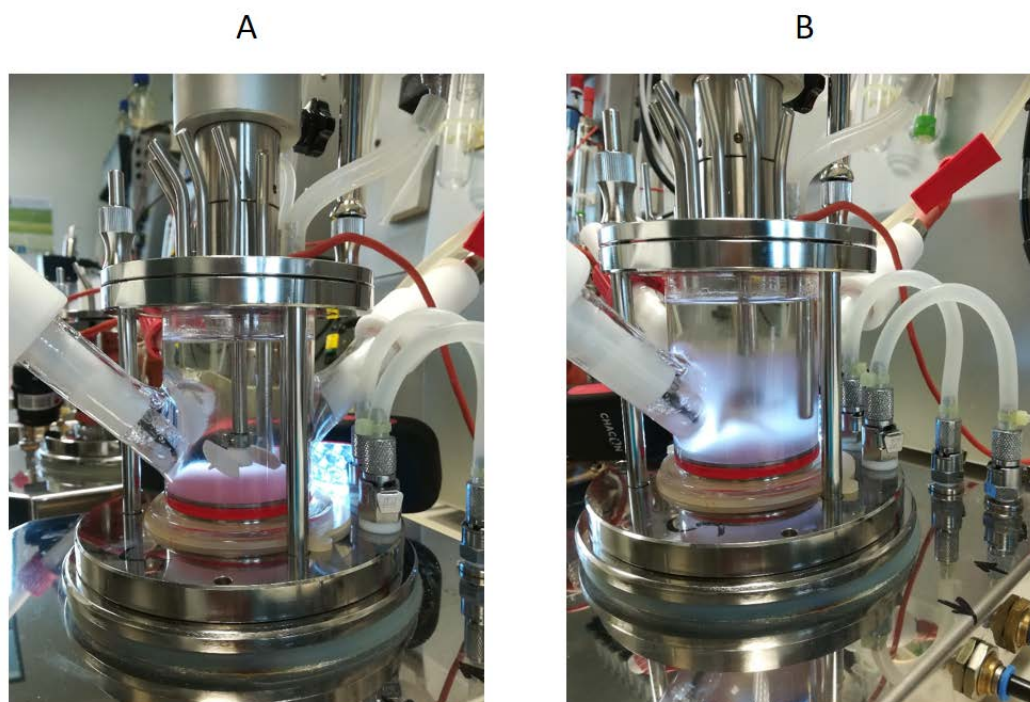


Figure 4.6: Microcarrier distribution within the minibioreactor equipped with an EE impeller ( $C/T = 0.41$ ,  $D/T = 0.4$ ,  $\beta = 45^\circ$ ) at  $N = 0$  rpm (A) and  $N = N_{js} = 75$  rpm (B).

suitable design for MSC cultures on microcarriers. The following sections will detail each of these steps.

### Design of experiments

The optimal EE impeller design was investigated by varying 3 geometrical parameters. The  $D/T$  ratio, defined as the impeller diameter on the tank diameter, characterized the impeller size and was set between 0.25 and 0.5. The  $C/T$  ratio, defined as the off-bottom clearance on the tank diameter, described the impeller position in the bioreactor and was chosen between 0.2 and 0.5. In this study,  $C$  was defined as the length between the tank bottom and the bottom side of the impeller hub. The blade slope angle  $\beta$  was finally studied with values comprised between 0 and  $90^\circ$ .

Based on these three parameters and their boundaries, a DOE was established according to a Box-Behnken design, as proposed in the ANSYS DesignXplorer package. It was then completed with personalized design points to refine the response surfaces obtained after CFD solving, until the response surface building was found robust, namely that the addition of a new design point did not modify the response surfaces resolution. In this manner,  $N_{DOE} = 31$  different geometries were used (Appendix C).

Impeller designs were build by using the Computational-aided design software DesignMod-eler and meshes were generated using Meshing software, both from ANSYS. The same

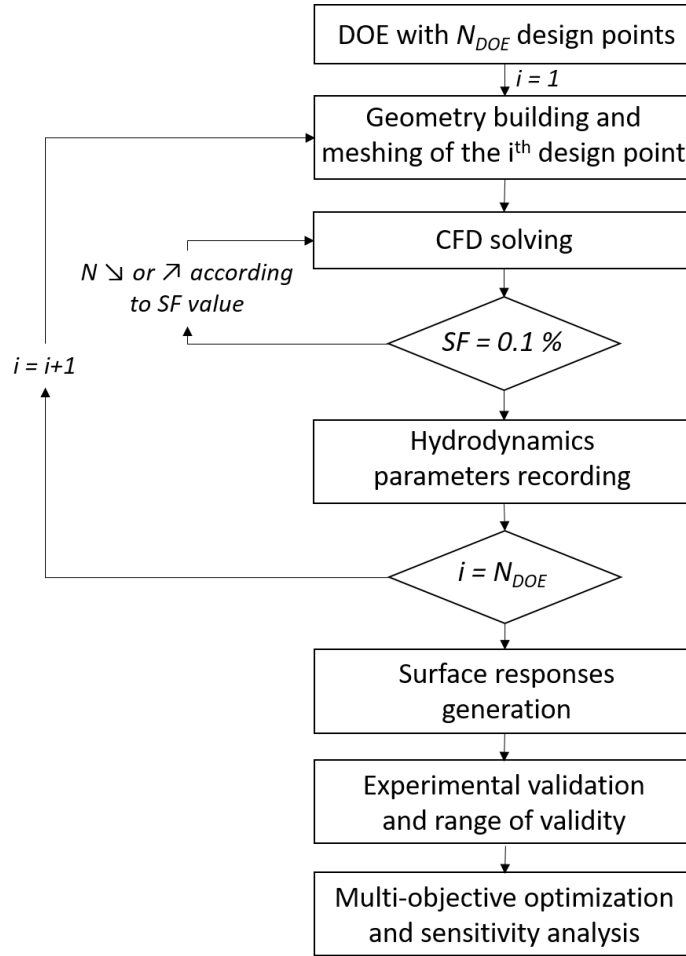


Figure 4.7: Flowchart presenting the global strategy applied for the impeller design optimization coupling CFD simulations with a multi-objective optimization.

meshing algorithm was used for all configurations with a calculation domain involving 120,000 to 200,000 tetrahedral meshes (Fig. 4.8). This coarse grid mesh was previously validated to be a good compromise between the calculation time requirements adapted for a screening approach, and the results relevance (Section 3.3). In addition to these preliminary validations, CFD simulations were validated by experimental measurements of  $N_{js}$ .

### Multiphase modelling by CFD

CFD simulations were performed by using the commercial finite-volume solver ANSYS Fluent. Based on the previous work of Delafosse *et al.*, the two-phase Euler-Euler liquid-solid granular (RANS) approach was applied [24]. The continuity and momentum equations were solved for each phase at the steady-state by using the Moving Reference Frame (MRF) approach to model the impeller rotation. The Reynolds stress tensor  $\bar{\tau}$  was

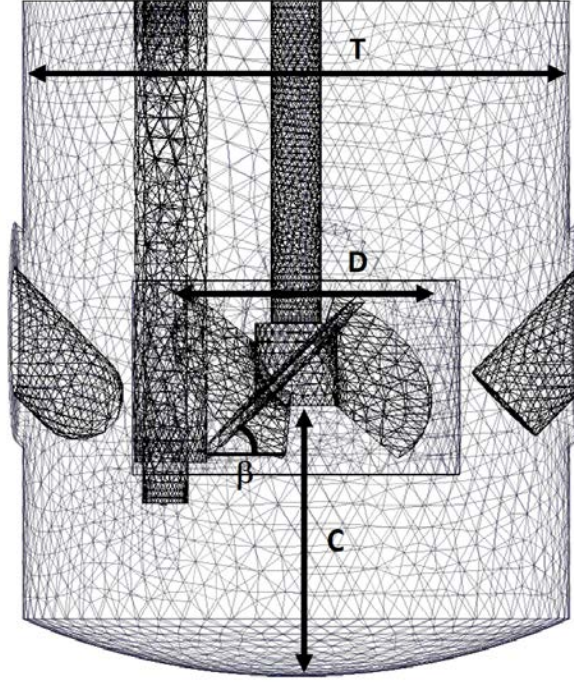


Figure 4.8: Mesh discretization of the vessel for the CFD simulations and visualization of the geometrical variables involved in the design optimization.

modelled by the standard  $k-\epsilon$  turbulence model with a scalable wall function for near-wall function modelling. The drag and the turbulent dispersion forces were considered as the dominant fluid / solid interactions. The two conservation equations are developed in Eqs. (4.4) and (4.5) for the liquid phase, and Eqs. (4.6) and (4.7) for the solid phase.

$$\left\{ \begin{array}{l} \nabla \cdot (\alpha_L \rho_L \mathbf{v}_L) = \nabla(\gamma_L \nabla \alpha_L) \\ \nabla \cdot (\alpha_L \rho_L \mathbf{v}_L \mathbf{v}_L) = -\alpha_L \nabla p + \nabla \cdot \bar{\tau}_L \\ \quad \quad \quad + \alpha_L \rho_L \mathbf{g} + K_{SL}(\mathbf{v}_S - \mathbf{v}_L) \end{array} \right. \quad \begin{array}{l} (4.4) \\ (4.5) \end{array}$$

$$\left\{ \begin{array}{l} \nabla \cdot (\alpha_S \rho_S \mathbf{v}_S) = \nabla(\gamma_S \nabla \alpha_S) \\ \nabla \cdot (\alpha_S \rho_S \mathbf{v}_S \mathbf{v}_S) = -\alpha_S \nabla p - \nabla p_S + \nabla \cdot \bar{\tau}_S \\ \quad \quad \quad + \alpha_S \rho_S \mathbf{g} + K_{LS}(\mathbf{v}_L - \mathbf{v}_S) \end{array} \right. \quad \begin{array}{l} (4.6) \\ (4.7) \end{array}$$

Where  $\mathbf{v}$  is the velocity of the corresponding phase,  $p$  the pressure shared by all phases and  $\mathbf{g}$  the acceleration due to gravity. The interphase drag force involved the interphase momentum exchange coefficient  $K_{LS}$ , modelled by the Huilin-Gidaspow equations presented in Eqs. (4.8) to (4.12). This model allowed to weight two models according to the local particle volume fraction. In one hand, the Ergun model is suitable for particles beds, whereas in the other hand, the Wen & Yu model is suitable for dilute systems. The

diffusion-in-VOF equation was used to model the turbulent dispersion, with  $\gamma_S$  and  $\gamma_L$  the diffusion coefficients of the solid and liquid phases, which was included in the mass conservation equation through the turbulent dispersion terms  $\nabla(\gamma_L \nabla \alpha_L)$  and  $\nabla(\gamma_S \nabla \alpha_S)$ .

$$K_{LS} = \Psi \cdot K_{LS-Ergun} + (1 - \Psi) \cdot K_{LS-Wen\&Yu} \quad (4.8)$$

$$\Psi = \frac{1}{2} + \frac{\arctan [262.5(\alpha_s - 0.2)]}{\pi} \quad (4.9)$$

Ergun model:

$$K_{LS} = \frac{3}{4} \cdot C_D \cdot \frac{\alpha_S \alpha_L \rho_L |\mathbf{v}_S - \mathbf{v}_L|}{d_p} \cdot \alpha_L^{2.65} \quad (4.10)$$

$$C_D = \frac{24}{\alpha_S Re_S} \left[ 1 + 0.15(\alpha_L Re_S)^{0.687} \right] \quad (4.11)$$

Wen & Yu model:

$$K_{LS} = 150 \frac{\alpha_S (1 - \alpha_L) \mu_L}{\alpha_L d_p^2} + 1.75 \frac{\rho_L \rho_S [1 + 0.15(\alpha_L Re_S)^{0.687}]}{d_p} \quad (4.12)$$

Cytodex-1 particles were chosen as reference particles for the simulations, defined by their experimental mean diameter  $d_p = 170 \mu\text{m}$  and density  $\rho_S = 1020 \text{ kg m}^{-3}$ . The global solid volume fraction  $\langle \alpha_S \rangle$  was fixed at 0.1. In accordance to experimental observations, the solid packing limit was fixed to 0.6. Based on cell culture conditions, water at 37°C was chosen for the liquid phase.

Despite relatively low Reynolds numbers describing a transition regime,  $Re \approx 10^3$ , models were previously validated in a robust way, through the confrontation of different set of models with experimental particle concentration gradients measurements using a light scattering technique [24]. Other studies also reported the use of Euler-Euler simulations with  $k - \varepsilon$  turbulence models, for microcarrier suspension investigation at the just-suspended state in stirred systems, with satisfactory results [25, 26]. Here, this strategy allowed to perform simulations with a reasonable calculation time, namely between 10 and 30 hours per configuration using 14 CPU Xeon 2.8 GHz.

All particles were initially quasi-packed ( $\alpha_S = 0.5$ ) before  $N_{js}$  investigation using a particle velocity-based method. For each bioreactor configuration, successive simulations were run by progressively decreasing agitation rates; the percentage of particles considered as almost motionless in the bottom of the vessel was recovered till it reached the critical value of 0.1 %, which was defined as the just-suspended state. For more detail on this method, authors would recommend to refer to the related previous work (section 3.3 in the present thesis). Convergence of the simulations was supposed when equation residuals were less than  $10^{-5}$  and when liquid velocities and solid volume fractions in the impeller vicinity were stabilized. This second validation was necessary to ensure the stabilization

of the  $N_{js}$  determination criterion. A total number of 114 simulations were performed.

#### 4.3.4 Hydrodynamics and mixing parameters

Before presenting the parameters chosen to characterize the system and to perform the design optimization, it should be emphasized that, in the case of microcarrier-based cultures, the hydromechanical stress is particularly studied through its impact on cells adhered on particles. Hence, the solid phase was defined as the targeted phase for the optimization, also related to the parameters chosen to characterize the hydrodynamics. In order to determine the local stress encountered by the particles, and also by cells, CFD simulations were combined to the Kolmogorov isotropic turbulence theory. It was indeed shown by Henzler *et al.* (2000) that this stress was related to the turbulent energy dissipation rate  $\varepsilon$  [2]. Two different optimization criteria were proposed. The first one,  $\langle (P/V)_{@p} \rangle$ , presented in Eq. (4.13), characterized the volume-averaged power dissipation encountered by the particles in the bioreactor. The turbulent energy dissipation rate was integrated according to the local particle volume fraction in each mesh cell. The second one,  $EDC$ , was inspired by the Energy dissipation / Circulation function introduced by Justen *et al.* for filamentous fungi morphology investigation [3], and by the modified function proposed by Collignon *et al.* [1] to compare different impeller designs for MSC cultures. In the present work, this  $EDC$  parameter was defined according to Eq. (4.14), and described an energy function that takes into account the time spent by particles in the potentially damaging zones, using  $Q_{p,net}$  the local particle volume flow rate. Here, only mesh cells with local Kolmogorov length scale  $\lambda_K = (\nu^3/\varepsilon)^{1/4}$  lower than the particle diameter  $d_p$  were considered. It was indeed assumed that in mesh cells displaying  $\lambda_K > d_p$ , no cell damages due to hydromechanical stresses occurred [9, 27, 28]. It is thus admitted that the cumulative effect should be taken into account for particles that stay in potentially damaging zones, whereas the turbulent energy dissipation rate should not be integrated in zones displaying eddy sizes larger than the particle size. The turbulent energy dissipation rate was thus locally integrated.

$$\langle \left( \frac{P}{V} \right)_{@p} \rangle = \frac{\rho_m}{V_p} \iiint_{V_p} \varepsilon(V) dV \quad (4.13)$$

$$EDC = \iiint_{V_L(\lambda_K < d_p)} \frac{\rho_m \varepsilon(V)}{Q_{p,net}(V)} dV \quad (4.14)$$

In addition to these three criteria, two other parameters defined at the just-suspended state were also determined: (i) The agitation rate  $N_{js}$  and (ii) the power number  $N_{p,js}$  (Eq. (4.15)), with  $P_{js}$  the dissipated power at the particle just-suspended state, (iii) the power per unit of volume  $\langle (P/V) \rangle$  calculated within all the fluid, and (iv) and (v) the volume-averaged Kolmogorov length scale 'seen' by particles  $\langle \lambda_{K,@p} \rangle$  and within all the

fluid  $\langle \lambda_K \rangle$ . Complementary CFD simulations were also run at agitation rates leading to fully turbulent regime ( $Re = 10^5$ ) in order to obtain the asymptotic power number  $N_p$  in such regime.

$$N_{p,js} = \frac{P_{js}}{\rho N_{js}^3 D^5} \quad (4.15)$$

### Response surfaces and experimental validation

Response surfaces were build for the six previous parameters by comparing 4 algorithms and solved using the Surface Response device of ANSYS Design Exploration toolbox (DesignXplorer). The four method principles used here are briefly described below:

- Kriging (constant kernel) is a non-parametric method fitting through all current data points and modelling the spatial interpolations using stochastic variables and covariances calculations.
- Non-parametric regression is based on Support Vector Regression (SVR). On the contrary to Kriging, only the most important data points are used for the prediction.
- Neuronal network (10 cells) is defined as a non-linear mapping from input data to the output (objective functions), through weighted functions. The design point selection is issued from 'learning', with the minimization of the distance between interpolation and known values.
- Genetic aggregation expresses an optimized weighted metamodells assembly (polynomial regression, kriging, SVR, moving least squares with different available settings). The most effective assembly is obtained after metamodells evolution through crossover and mutation operators and selection of the best models after each iteration.

In the first instance, these different methods were compared according to the coefficient of determination  $R^2$ , related the difference between the  $N_{js}$  and objectives predictions by the surface response and the parameters values from CFD simulations. In a second time, experimental measurements, detailed in section 4.3.5, were used to calculate the deviations between the  $N_{js}$  predicted by the response surface and the corresponding experimental value. These two comparison steps allowed to define the range of validity of the response surfaces, which were not necessarily robust for all design points. Once the most robust algorithm was determined, final response surfaces were established using only design points of the range of validity.

### Design optimization

Two optimization methods from the ANSYS Goal Driven Optimization tool were compared: (*i*) a non-iterative Screening approach allowing to compared 10,000 quasi-randomly



generated designs (Hammersley algorithm) and (ii) an iterative Multi-Objective Genetic Algorithm (MOGA, based on a hybrid variant of the Non-dominated Sorted Genetic Algorithm-II, NSGA-II). They both shared the same optimization objectives, namely both  $\langle (P/V_{@p}) \rangle$  and  $EDC$  minimization.

### 4.3.5 Experimental approach

3D-Printing was used to generate EE impellers with different geometrical configurations, chosen according to the numerical results obtained from the response surfaces build, using the 31 design points of the DOE. Geometrical characteristics are summarized in Table. 4.4, corresponding to the nine impeller designs presented in Fig. 4.9. Three of them belonged to the DOE, whereas six impellers were built out of the DOE.

Table 4.4: Geometrical characteristics of the 3D-printed impeller designs.

Impeller number	$\beta$ (°)	$D/T$ (-)	$C/T$ (-)
1	5	0.5	0.38
2	16	0.36	0.42
3	20	0.5	0.4
4	37	0.48	0.4
5	38	0.41	0.38
6	45	0.4	0.41
7	45	0.45	0.2
8	46	0.5	0.39
9	70	0.37	0.41

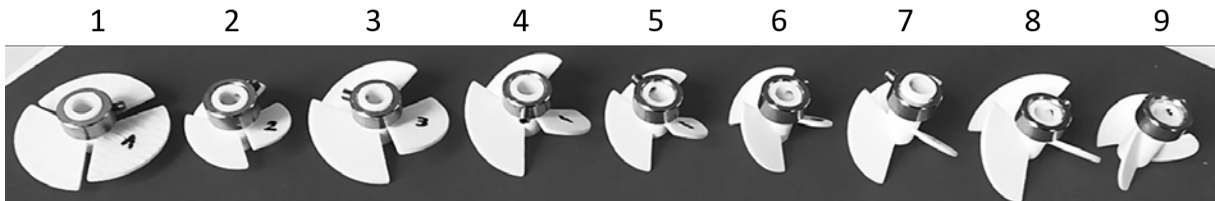


Figure 4.9: EE impellers built using 3D-printing for  $N_{js}$  experimental measurements.

As for CFD simulations, Cytodex-1 suspensions were investigated with a mean particle volume fraction of 0.1. The liquid phase consisted in a Dulbesco Phosphate buffer saline solution (DPBS, Sigma). For better visualization, particles were stained by using Rose Bengal dye as recommended and validated by Collignon *et al.* [1]. A backlight system enhanced visual observations, as shown in Fig. 4.6.  $N_{js}$  investigations were based on the Zwietering visual determination, stating that the just-suspended state is reached when

particles do not remain more than 1 or 2 seconds in the bottom [12]. Looking for a more robust determination, two measurements were performed. First, particles were settled and the agitation rate was slowly increased until the last particles to be just suspended began to move. The corresponding agitation rates were defined as  $N_{js, up}$ . Then, particles were completely suspended with  $N \gg N_{js}$  and the agitation rate was progressively reduced until some particles just began to stay motionless 1 or 2 seconds in the bottom. The agitation rate leading to this state was called  $N_{js, down}$ . The experimental  $N_{js}^{exp}$  chosen for comparison with numerical results was the mean value between  $N_{js, up}$  and  $N_{js, down}$ .

### 4.3.6 Results and discussion

#### Response surfaces algorithm

The different algorithms for the building of the response surfaces were compared to determine the most robust one. The  $R^2$  values based on the 31 design points are given in Table 4.5. Kriging, non-parametric regression and genetic aggregation presented very good fittings for all hydrodynamic parameters. This was expected with Kriging, as this method imposes the fitting function to pass through all the design points. On the contrary, the neuronal network used in the present work did not provide satisfactory outcomes. Table 4.5 also presents the mean deviations between  $N_{js}$  predicted by the corresponding surface responses and the experimentally measured  $N_{js}^{exp}$  from the 6 geometrical configurations out of the DOE and thus not used for response surfaces establishment. The genetic aggregation was then found to be the most suitable. It was notably verified that graph trends remained consistent with parameter variations.

Table 4.5: Comparison of the robustness of the response surfaces obtained with the different algorithms.

Response surface algorithm	Coefficient of determination $R^2$					Mean deviation
	$N_{js}$	$\langle (P/V)_{@p} \rangle$	$EDC$	$N_{p,js}$	$\langle \lambda_K \rangle$	
Kriging	1	1	1	1	1	18 %
Non-parametric regression	1	1	1	1	1	27 %
Neuronal network	0.94	0.57	0.43	0.99	0	14 %
Genetic aggregation	0.99	0.99	1	1	1	15 %

#### Validation of $N_{js}$ prediction

The range of validity of  $N_{js}$  prediction was investigated by comparing calculated  $N_{js}^{predicted}$  with the experimental  $N_{js}^{exp}$ . Values and deviations obtained with the genetic aggregation are presented in Fig. 4.10. Firstly, comparison was performed using response surfaces

solved with the 31 configurations of the DOE. A mean standard deviation of 15 % was obtained, but deviations higher than 20 % were observed for impellers with slope angles  $\beta$  lower than  $25^\circ$ . Hence, in a second time, these design points were eliminated from the design of experiments, limiting the optimization to impellers with blade slope angles comprised between  $25^\circ$  and  $90^\circ$ . New response surfaces were determined for this new range of validity. A better accuracy was obtained for  $N_{js}$  prediction with a mean standard deviation of 5 %. In the next parts of this study, results will be presented based on these second DOE and response surfaces, admitting that the strategy is not sufficiently robust for geometries with low  $\beta$  values.

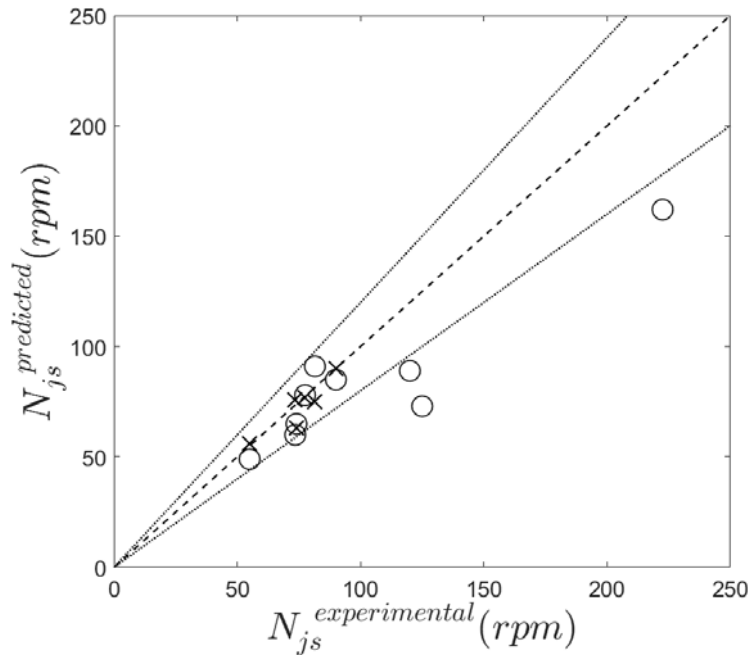


Figure 4.10: Comparison between experimental  $N_{js}^{exp}$  and modelled  $N_{js}^{predicted}$  using the 31-design points response surfaces ( $0^\circ < \beta < 90^\circ$ ) (o) and using the reduced-design points response surface ( $25^\circ < \beta < 90^\circ$ ) (x).

### Power number validation

A sensitivity analysis demonstrated that, in the range of parameters studied, the power number at the just-suspended state  $N_{p,js}$  was linearly related to the blade slope angle  $\beta$  (Fig. 4.11), with  $N_p$  values comprised between 1.0 for low blade slope angles ( $\beta = 25^\circ$ ) and 8.2 for vertical blades ( $\beta = 90^\circ$ ). Tsui *et al.* investigated the blade slope angle effect on the flow in STR equipped with a pitched-blade turbine [29]. They showed that for low blade slopes  $\beta$ ,  $D/T$  and  $C/T$  impact on the power number was negligible in comparison to  $\beta$  impact. However, for higher  $\beta$  values, slight differences were observed by varying  $D/T$  and  $C/T$ . In the present study, involving an Elephant Ear impeller, a

linear relationship relating  $\beta$  and  $N_{p,js}$ , regardless the impeller size ( $D/T$ ) and position in the bioreactor ( $C/T$ ), and even for  $\beta$  up to  $90^\circ$  was obtained. It should nevertheless be noticed, that Reynolds numbers were comprised between 700 and 1800, describing a transition regime, and more particularly with low  $\beta$  values, whereas the work of Tsui *et al.* was based on a fully turbulent flow. Here, impellers with low  $\beta$  values displayed a lower power dissipation capability from the impeller. As a consequence, higher agitation rates were necessary to reach full particle suspensions, leading to higher Reynolds numbers  $Re_{js}$ .

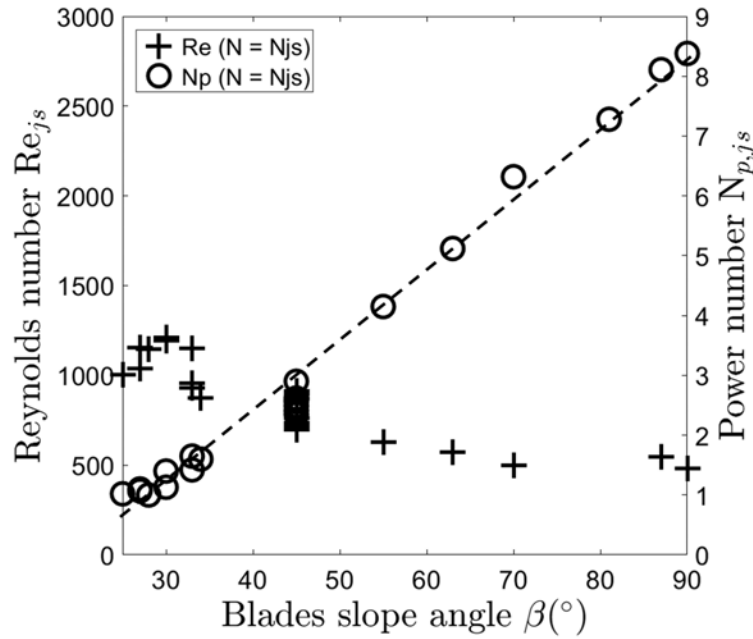


Figure 4.11: Linear relationship between the Power number  $N_{p,js}$  and the blade slope angle  $\beta$ , regardless the impeller size and position in the reactor.

Based on CFD simulations,  $(N_p; Re)$  pairs from different blade slope angles were calculated and compared to common impellers, both at the just-suspended state and in fully-turbulent regime, in Fig. 4.12. In the case of a fully turbulent flow, the EE impeller with vertical blades presented similar  $N_p$  as a radial Rushton turbine, whereas EE impellers with gently sloped blades were found close to values obtained with axial impellers. At the just-suspended state, a wide range of  $N_p$  values, comprised between 1.0 and 8.2, was also obtained, with the highest values for the vertical blades.  $N_p$  values were confirmed by the flow patterns displayed by the different  $\beta$  values. For low  $\beta$ , one main circulation loop reaching the vessel bottom was observed, in accordance with an axial flow pattern. In contrast, for high  $\beta$  values, a second small circulation loop in the low part of the bioreactor was obtained, similarly to a radial flow pattern.

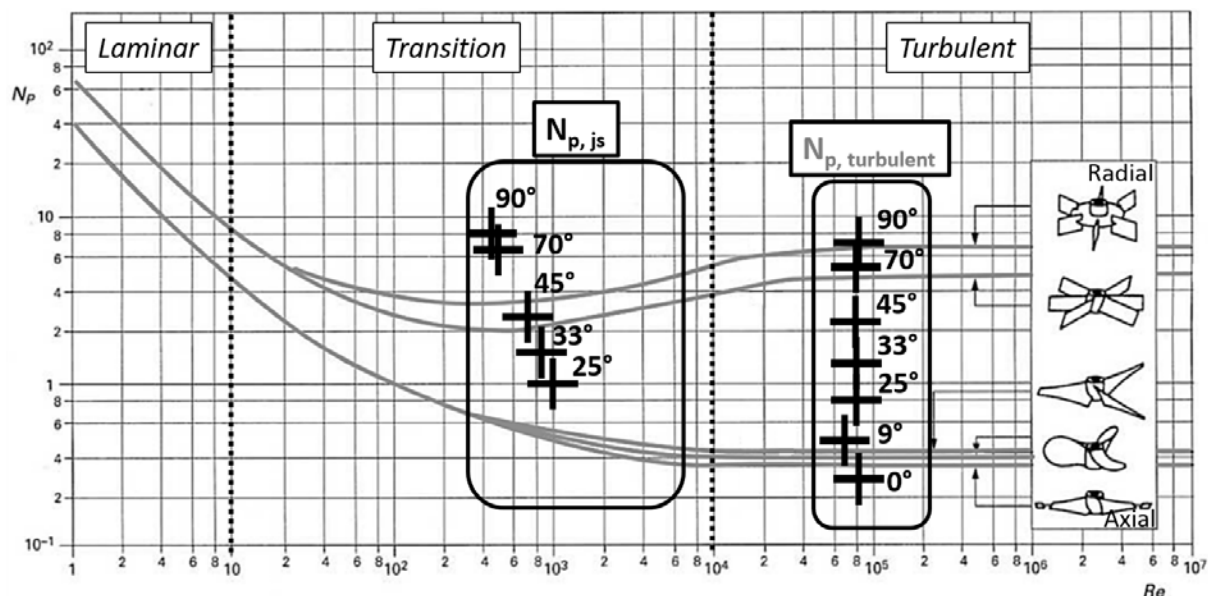


Figure 4.12: Comparison of the calculated Power numbers at the just-suspended state  $N_{p, js}$  according to the blade slope angle of EE impellers with values from common impellers in fully-turbulent regime. Figure adapted from Roustan (2005) [30].

### Particle distribution impact on the hydrodynamics parameter calculations

In the case of microcarrier-based cell cultures, studies demonstrated that turbulent eddies with approximatively the same size than the particles may lead to potential cell damages. Croughan *et al.* reported a critical value of  $2/3 \times d_p$  for fibroblasts [9], whereas Nienow *et al.* found no deleterious effect on MSC culture till  $1/3 \times d_p$  [27]. In this second study, significantly lower cell growths were however observed for  $\lambda_K \approx 1/4 \times d_p$ . In the present study,  $\lambda_K$  may fall as low as 40  $\mu\text{m}$ , below  $1/4 \times d_p$ , in the impeller influence zone. Hence, the agitation design must be carefully designed in order to avoid such low values.

Fig. 4.13 compares the values of  $\langle \lambda_K \rangle$ , based on the turbulent energy dissipation rate in all the fluid volume, to  $\langle \lambda_{K, @p} \rangle = (\nu^3 / \langle \varepsilon_{@p} \rangle)^{1/4}$ . In these two cases, all impeller designs leading to the highest  $\langle \lambda_K \rangle$  displayed relatively lower  $N_{js}$  values. However, low  $N_{js}$  values are not a guarantee of both  $\langle \lambda_K \rangle$  and  $\langle \lambda_{K, @p} \rangle$  maximizations. Differences were nevertheless observed between the volume-averaged  $\langle \lambda_K \rangle$  in the whole fluid volume and the  $\langle \lambda_{K, @p} \rangle$  encountered by the microcarriers. According to the impeller design,  $\langle \lambda_K \rangle$  was comprised between 170 and 220  $\mu\text{m}$ , but particles seemed to 'see' a lower volume-averaged Kolmogorov length scale, between 150 and 215  $\mu\text{m}$ . Thus, calculations based on the whole fluid under-estimate the energy dissipation to which microcarriers are really submitted.

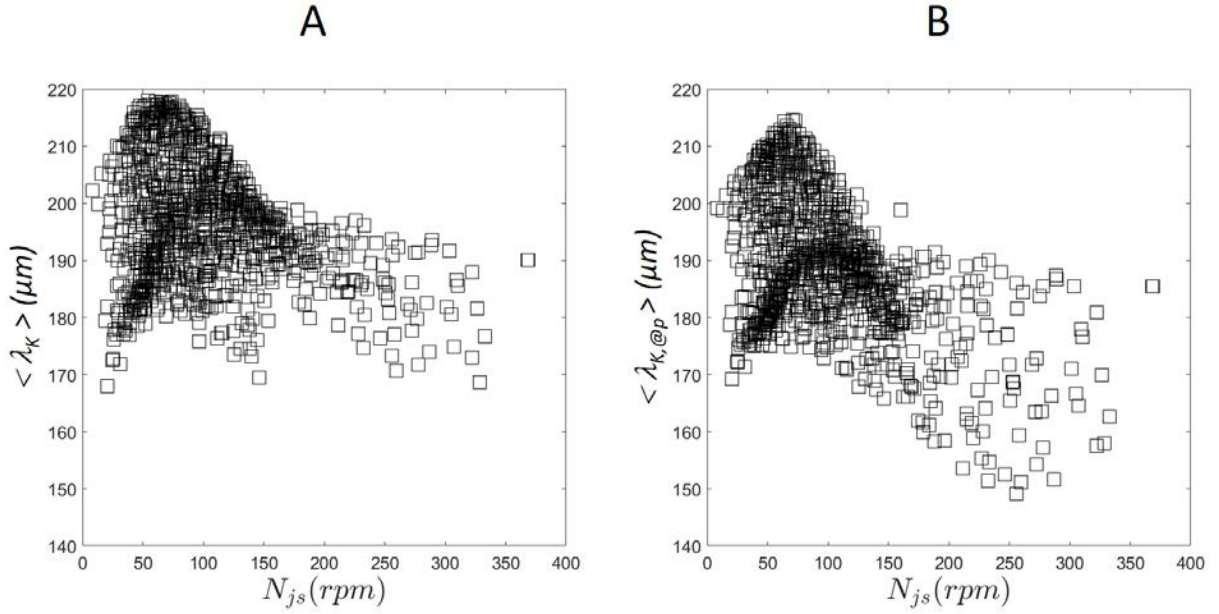


Figure 4.13: Relationship between  $N_{js}$  and  $\langle \lambda_K \rangle$  calculated within all the fluid volume (A), and  $\langle \lambda_{K,@p} \rangle$  calculated according to the local particle concentration within the bioreactor. Data are based on modelled values from the response surfaces, obtained from a 1,000 design points sampling.

### Sensitivity analysis

Results of four sensitivity analysis are presented in the next sections. They aim at determining which geometrical parameters significantly impact the different hydrodynamics parameters. First, results on the minimal agitation rate ensuring all particle suspension  $N_{js}$  will be presented. This parameter is indeed important for microcarrier-based cell cultures, as it is directly related to the particle just-suspended state which is generally looked for during cultures. Then, the two objective functions of the optimization strategy will be addressed.

#### *Just-suspended agitation rate $N_{js}$*

$N_{js}$  range of values is relatively large, by displaying values from approximately 40 rpm till over 200 rpm. Fig. 4.14 presents these values according to a heatmap layout in a 3-D graphic to reflect the impact of all three geometrical parameters of the study.  $N_{js}$  was notably sensitive to the  $D/T$  ratio and the blade slope angle  $\beta$ . The position of the impeller in the vessel ( $C/T$ ) seemed to be less significant. In agreement with the literature, lower agitation rates are indeed necessary to suspend particles with larger impellers [12, 31, 32]. Models developed to predict  $N_{js}$  also showed that the  $C/T$  ratio had a negligible impact in comparison with  $D/T$ , for  $C/T$  ratios over 0.2. Concerning the blade slope angles, vertical blades furnished lower values. It should be related to the previous calculations of Power number confirming that impellers with vertical blades

displayed a better power dissipation capability.

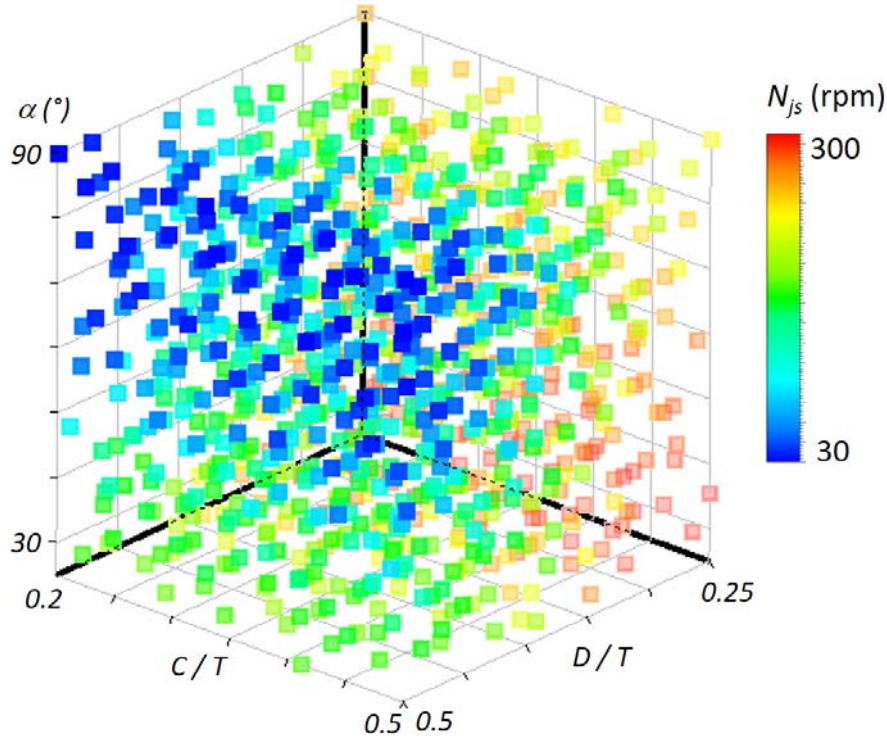


Figure 4.14: 3-D heatmap graphic displaying  $N_{js}$  value according to the 3 impeller geometrical parameters.

*Power per unit of volume encountered by particles*  $\langle (P/V)_{@p} \rangle$

The impact of the three geometrical parameters on  $\langle (P/V)_{@p} \rangle$  value are presented in Fig. 4.15. It is important to remember that this parameter calculation was based on the hydromechanical stress encountered by the solid phase in the vessel. In this way, the particle concentration gradients in the vessel were also integrated in the calculation. A higher particle concentration is indeed expected in the vessel bottom, and potentially in the impeller zone influence, whereas particles may not necessarily reach the fluid surface zone, where the turbulent dissipation rate is expected lower. In the present study,  $\langle (P/V)_{@p} \rangle$  was found to be particularly sensitive to  $D/T$  and  $C/T$  ratios, but the blade slope angle  $\beta$  impact was found negligible.

Larger volume-averaged values of the dissipation eddies size were indeed observed for impellers placed in the upper part of the bioreactor, namely for high  $C/T$  ratios. Regarding the  $D/T$  ratio, a compromise had to be found, directly related to the turbulent energy dissipation rate, with  $\lambda_K \propto \varepsilon^{-1/4}$ .  $\langle \varepsilon \rangle$  may also be related to the impeller diameter according to  $\langle \varepsilon \rangle \propto N_{js}^3 D^5$ . On one hand, a large impeller would induce a larger impeller influence zone, which is known to display the highest local  $\varepsilon$  values in the system [13].

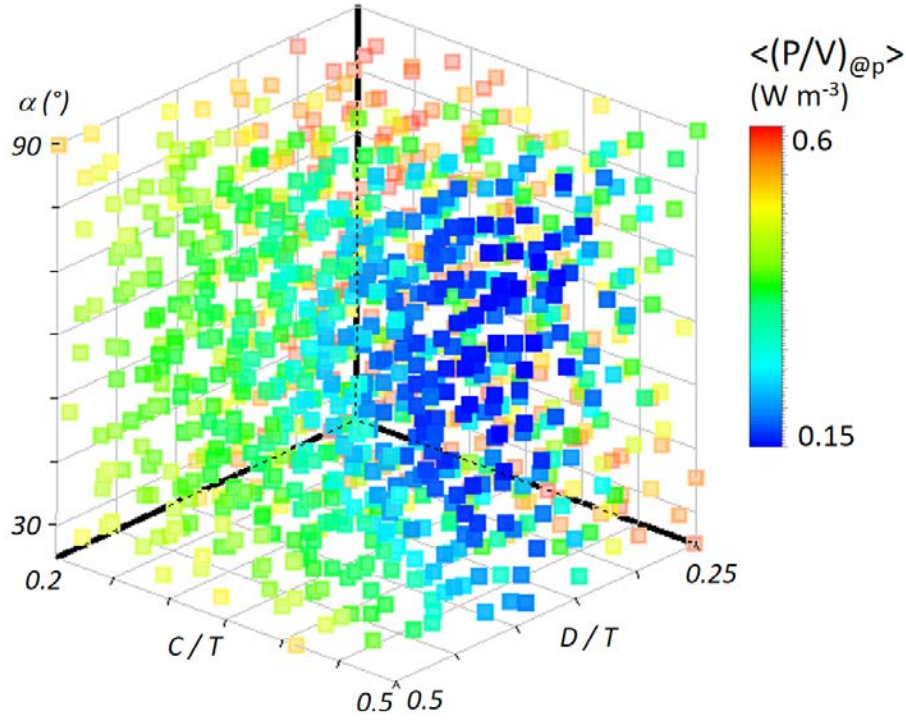


Figure 4.15: 3-D heatmap graphic displaying  $\langle (P/V)_{@p} \rangle$  value according to the 3 impeller geometrical parameters.

On the other hand, it was demonstrated that a smaller impeller would require a higher agitation rate  $N_{js}$  to ensure all particle suspension. The sensitivity analysis allowed to determine a compromise between the impeller diameter and its related agitation rate  $N_{js}$ , in order to minimize  $\langle \varepsilon_{@p} \rangle$  and thereby maximize  $\langle \lambda_{K,@p} \rangle$ . The optimal value was found to be  $D/T \approx 0.38$ .

The comparison of these results with the graph established for  $N_{js}$  in Fig. 4.14 confirmed that looking for the lowest  $N_{js}$  did not necessarily lead to the lowest hydromechanical stress received by the particles. Large impellers placed in the vessel bottom displayed lower  $N_{js}$ , but the impeller influence zone became larger. Hence, the fraction of particles close to the impeller, and thus present in the zone displaying the highest hydromechanical stress, is higher when the impeller get close to the bottom. It can be thus established that, despite an  $\varepsilon$  increase, induced by a higher agitation rate due to the higher position of the impeller in the vessel, the power encountered by the particles was reduced by a lower particle fraction in the impeller vicinity.

Fig. 4.16 compares  $\langle (P/V)_{@p} \rangle$  values calculated for the impeller designs of the DOE to their corresponding  $\langle (P/V) \rangle$  values, and shows that for all impeller designs,  $\langle (P/V)_{@p} \rangle$  was higher than  $\langle (P/V) \rangle$ . For instance, up to 22 % difference between  $\langle (P/V)_{@p} \rangle$  and  $\langle (P/V) \rangle$  was observed in the case of the EED ( $\beta = 45^\circ$ ,  $D/T = 0.25$ ,  $C/T = 0.2$ ), namely with the lowest size and position calculated in the DOE.



This confirms the need to integrate the local particle concentration in order to avoid an under-estimation of the particle exposure to the power dissipation.

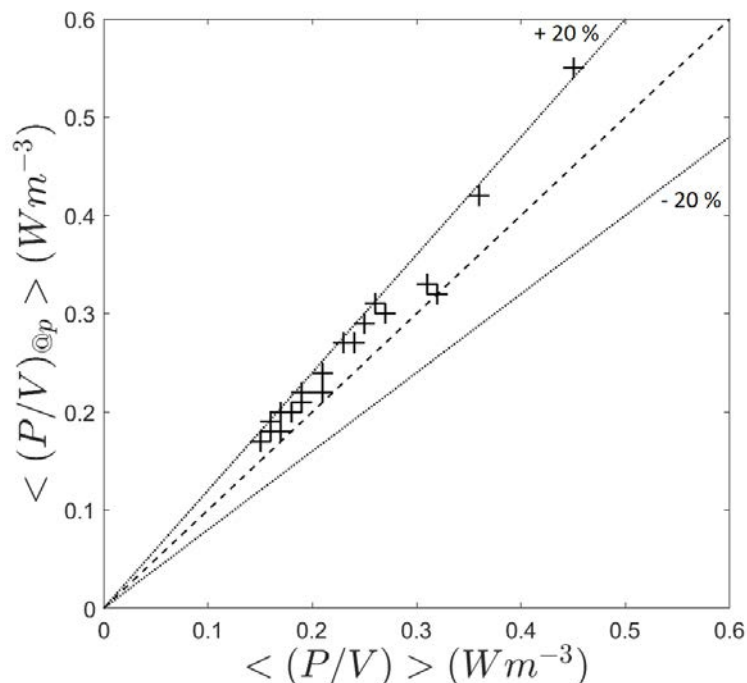


Figure 4.16: Comparison of  $\langle (P/V)_{@p} \rangle$  and  $\langle (P/V) \rangle$  calculated for the impeller designs of the DOE.

#### *Energy function EDC*

$EDC$  depended on all the three geometrical parameters, as shown in Fig. 4.17. As for the two other objective functions, dependent on  $\varepsilon$ , a compromise had to be found on  $D/T$ . However,  $EDC$  differed from these two previous parameters by involving a time effect. In a zone found as potentially damaging for particles and cells, the local value of  $EDC$  indeed depends on the local suspension flow rate. In the present case, the compromise on the impeller size to minimize  $EDC$  was found for  $D/T \approx 0.4$ .

The study of  $C/T$  impact on  $EDC$  revealed that impellers placed near the bottom of the bioreactor led to higher  $EDC$  values up to  $1 \text{ kJ m}^{-3}$ , which could be explained by the particle accumulation in the bottom of the bioreactor at the just-suspended state.

Finally, the blade slope angle  $\beta$  had an impact on  $EDC$ , by displaying an  $EDC$  increase from  $\beta \approx 60^\circ$ . This transition may be related to the flow pattern modification observed when  $\beta$  became higher, as discussed in the  $N_p$  validation section. An EE impeller presenting a high  $\beta$  value was found to display two circulation loops, similarly to radial flows. The second circulation loop affected the fluid velocity in the bottom of the reactor and involved higher turbulent energy dissipation rate in this area. As presented for the  $C/T$

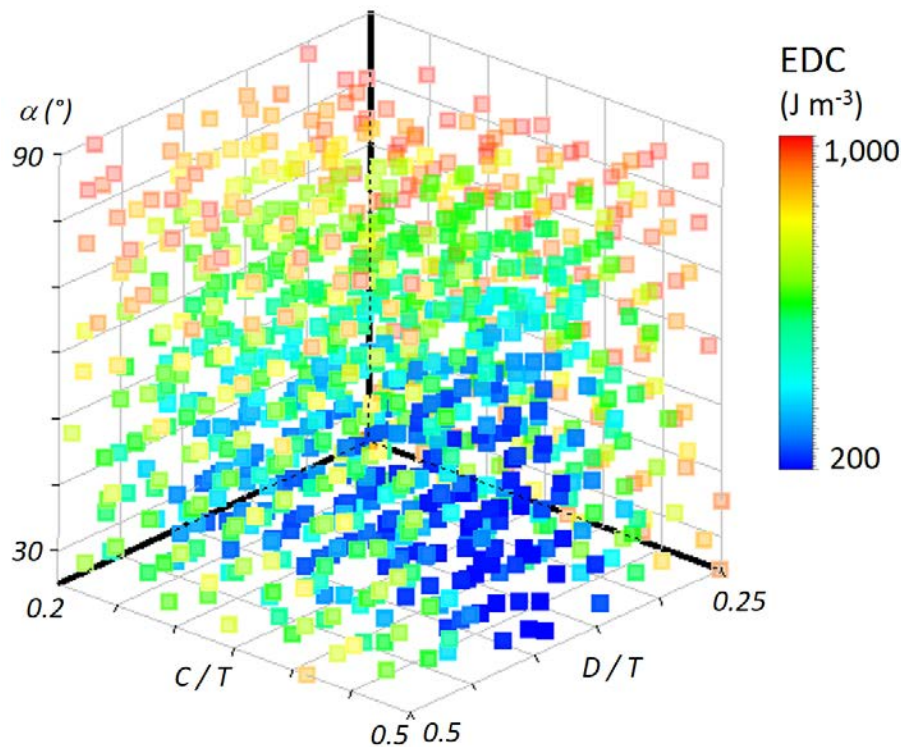


Figure 4.17: 3-D heatmap graphic displaying  $EDC$  value according to the 3 impeller geometrical parameters.

parameter impact, this zone is particularly important for the  $EDC$  calculation, since particle exposure to damaging zones may be expected higher.

### Impeller design optimization

A first outlook on Fig. 4.15 and 4.17 demonstrated the need to perform a multi-objective optimization to minimize the particle exposure to zones displaying critical turbulent energy dissipation rates, and consequently minimize the potential cell damages. It was indeed found that the impellers displaying the lowest  $\langle (P/V)_{@p} \rangle$  values presented higher  $\beta$  values than the impellers displaying the lowest  $EDC$ . However, without knowledge on which parameter would be the most critical for cell culture applications, it was here chosen to apply the same weight on these two objective functions, namely on both  $\langle (P/V)_{@p} \rangle$  and  $EDC$  minimizations.

The two optimization methods investigated, the sampling and the MOGA approaches, led to close geometrical configurations and were both validated for the global optimization strategy. Table 4.6 and Fig. 4.18 present the designs obtained from an optimization using each criteria separately and a multi-objective optimization. Based on these results, the most adapted impeller design for stem cell culture was found to display a blade slope angle of  $57^\circ$  which is the compromise between the two values independently obtained to

minimize  $\langle (P/V)_{@p} \rangle$  ( $\beta = 77^\circ$ ) and  $EDC$  ( $\beta = 42^\circ$ ). Concerning the impeller size and position in the reactor, optimal values for the three single-objective optimizations were relatively close and led to the definitive value of  $D/T = 0.4$  and  $C/T = 0.5$  in the multi-objective optimization outcome. A CFD simulation was run with this optimal impeller at  $N = N_{js}^{mod}$ , predicted by the response surface. Particle volume fraction and turbulent energy dissipation rate gradients are presented in Fig. 4.19. Due to the high impeller position in the bioreactor, namely  $C/T = 0.5$ , the impeller vicinity, leading to the highest local  $\varepsilon$  values, is far from the bottom of the bioreactor, where particle concentrations are the highest. In this case, the lowest Kolmogorov length scale  $\lambda_{K,min}$  is equal to  $77 \mu\text{m}$ , which corresponds to  $0.45 \times d_p$ . Based on the observations of Nienow *et al.*, where no damages were observed for  $\lambda_K < 1/3 \times d_p$  for MSC cultures on microcarriers, the optimal impeller proposed would be thus suitable for MSC culture [27].

Table 4.6: Geometrical parameters and corresponding  $N_{js}$  and objective function values predicted as optimal impellers. Results are presented from single-objective optimizations and from the final multi-objective function.

Optimization criteria	$\beta$ °	$D/T$ (-)	$C/T$ (-)	$N_{js}$ (rpm)	$\langle (P/V)_{@p} \rangle$ ( $\text{W m}^{-3}$ )	$EDC$ ( $\text{J m}^{-3}$ )	$\langle \lambda_{K,@p} \rangle$ ( $\mu\text{m}$ )
Min ( $\langle (P/V)_{@p} \rangle$ )	77	0.38	0.5	54	0.15	389	219
Min ( $EDC$ )	42	0.4	0.45	79	0.19	290	208
Multi-objective	57	0.4	0.5	59	0.15	312	218

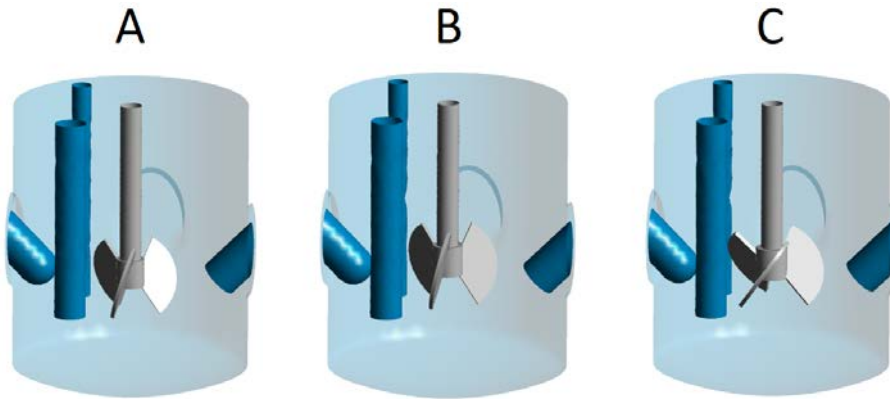


Figure 4.18: Geometry of the optimal impeller designs:  $\langle (P/V)_{@p} \rangle$  minimization (A),  $EDC$  minimization (B) and multi-objective optimization (C).

This optimization result may be compared to the dual 3-blade segment impeller design modification performed by Jossen *et al.* for MSC culture on microcarriers [18]. They reported the use of single-phase CFD simulations in order to minimize the fluid shear stress and enhance the axial discharge in a UniVessel SU bioreactor. Two  $D/T$  ratios of

0.41 and 0.55 ; two  $C/T$  ratios of 0.26 and 0.26 (with  $C$  the off-bottom clearance of the bottom-impeller) and three blade slope angles  $\beta$  of  $20^\circ$ ,  $30^\circ$  and  $45^\circ$  were investigated. The best  $D/T$  ratio was found very close to the optimal  $D/T$  ratio of the present study, namely  $D/T=0.4$ . Concerning the blade slope angle  $\beta$ , the highest angle from the range of values was selected, with  $\beta = 45^\circ$ . Here,  $\beta = 57^\circ$  was recommended, but without higher values of  $\beta$  used in the work of Jossen *et al.*, the comparison remains difficult. Concerning the  $C/T$  ratio, our results showed important disparities with the study of Jossen *et al.*, which advised to place the impeller near the bottom of the bioreactor, whereas the present optimization recommended to place it far from the bottom. However, it should be noticed that, in the study of Jossen *et al.*, the objective functions for the impeller design were based on single-phase CFD simulations. Moreover, no sparging device was included in the present study on contrary to the UniVessel SU configuration, and the use of two impellers instead of one may highly impact the circulation flow within the bioreactor.

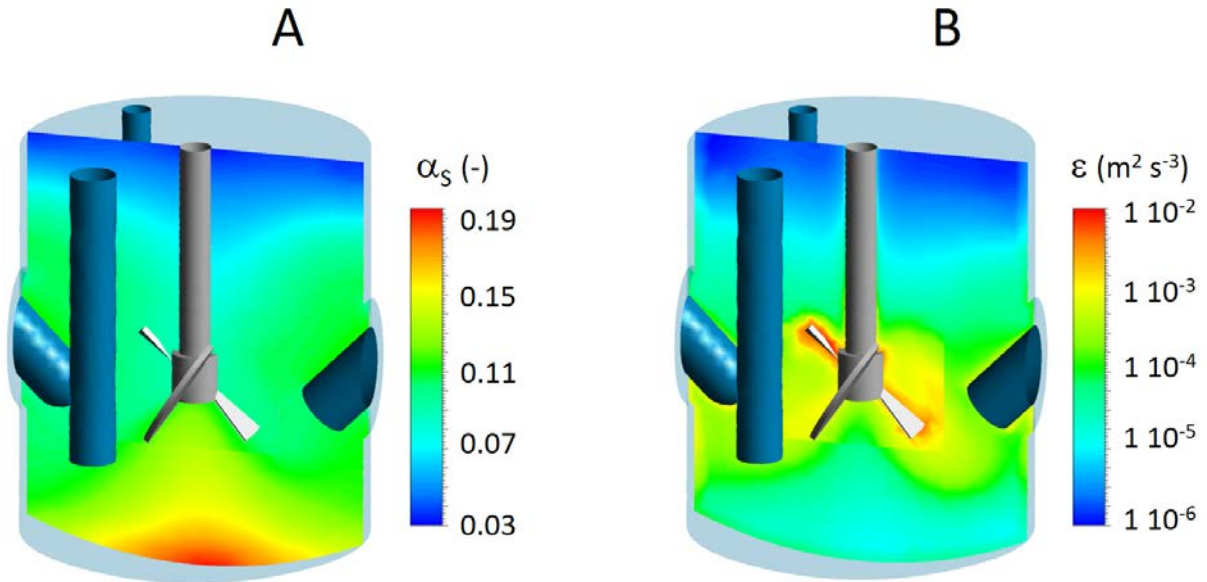


Figure 4.19: Particle volume fraction  $\alpha_S$  (A) and turbulent energy dissipation rate  $\varepsilon$  (B) distributions within the mini-bioreactor equipped with the optimal impeller design.

### 4.3.7 Conclusion of the publication

Coupling of CFD simulations with a multi-objective optimization was successfully applied in the case of the Ear-Elephant impeller in a mini-bioreactor. It was demonstrated that the optimization objectives should be focused on the solid phase, namely the microcarriers. Up to 22 % difference was indeed observed between the power per unit of volume in all the fluid  $\langle (P/V) \rangle$  and received by the particles  $\langle (P/V)_{@p} \rangle$ . Hence, an optimization based on hydrodynamics parameters calculated on all the fluid phase may under-estimate

the turbulent energy dissipation encountered by the particles.

The optimal impeller design displayed a blade slope angle  $\beta$  of  $57^\circ$ . The recommended position inside the bioreactor is relatively high in the vessel, with a  $C/T$  ratio of 0.5. Concerning the impeller size, a compromise between the volume swept and the value of  $N_{js}$  was found at  $D/T = 0.4$ .

The proposed method presents great capabilities for design optimization, especially to adapt bioreactor geometry to the cultivated cells. It will be next generalized to other impeller designs or to *ex-nihilo* designs, without hypothesis on impeller architecture.

### 4.3.8 Acknowledgements

The authors would like to thank the French Agence Nationale de la Recherche (ANR) and the Interreg VA Grande Région program for their financial support. They also acknowledge Fabrice Blanchard (LRGP, Nancy) for its technical contribution to this work.

## 4.4 WJ-MSC culture in STR using selected EE impeller designs

By concern of MSC expansion scale-up, WJ-MSC cultures were validated in a mini-bioreactor filled up with 200 mL of culture medium. As previously described in section 2.4, three steps may be distinguished during the culture: (i) the attachment, (ii) the expansion and (iii) the detachment phases. Following a step-by-step strategy, expansion performance was first characterized. Cell attachment and the ease of detachment in minibioreactors will be not presented in this thesis. In this section, preliminary results about the expansion performance comparison using different EED geometrical designs are introduced. However, it should be pointed out that the present results come from only one culture per condition. Further complementary cultures will be necessary to propose significant comparisons.

### 4.4.1 Validation of the MSC culture in a minibioreactor

In order to validate cell culture in the minibioreactor, presented in Fig. A.3, cell expansion was compared to a 8-days control culture in an Erlenmeyer flask. To achieve this, a quantitative comparison was based on the kinetics of metabolite concentrations, completed by a qualitative comparison based on microscopic image analyses. The impeller design used for this study the EED n°6 ( $\beta = 45^\circ$ ,  $D/T = 0.4$  and  $C/T = 0.41$ ).

#### Cell adhesion and expansion validation

Glucose and lactate concentrations are presented in Fig. 4.20. Both stirred systems were found suitable for cell expansion, but glucose consumption and lactate production seemed to be higher in the minibioreactor. Concerning the glutamine degradation and the ammonia production, no significant difference was observed between the cultures performed in the two systems.

#### Qualitative estimation of the cell distribution and viability on microcarriers

A Live / Dead staining was performed on cells adhered on microcarriers in order to determine their morphology and their viability. Representative photos are given in Fig. 4.21 after 1 and 5 days of culture and according to the two stirred systems. First, viable cells displayed fibroblast morphologies, providing evidence of a good cell spreading, both at  $t_0 + 1$  day and  $t_0 + 5$  days. A higher number of dead cells was however qualitatively observed after 5 days of culture in both the minibioreactor and the Erlenmeyer flask,

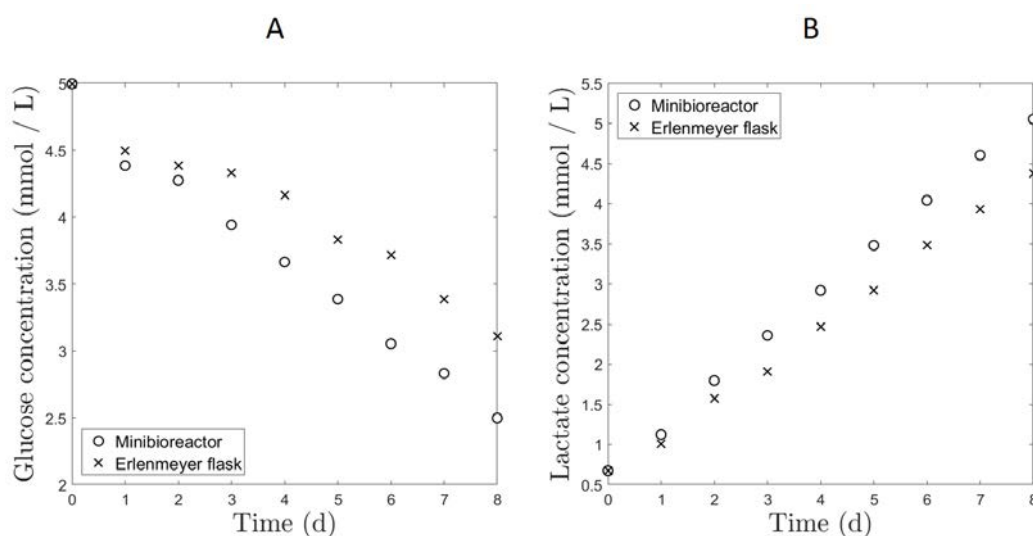


Figure 4.20: Kinetics of glucose (A) and lactate (B) concentrations according to the stirred system.

but the majority of cells were found viable. The minibioreactor was hence considered to be suitable for cell expansion, without impairing the cell viability in comparison to the control stirred system (Erlenmeyer flask).

#### 4.4.2 WJ-MSC cultures using impeller designs from the Elephant Ear design optimization study

##### Hydrodynamics characteristics

The impact of the geometrical characteristics of an Elephant Ear impeller design on MSC physiological response in the minibioreactor was investigated. To do that, three EED impellers, among the 3D-printed impellers presented in section 4.3, were selected for WJ-MSC expansions. It concerned impellers n°5 ( $\beta = 38^\circ$ ,  $D/T = 0.41$ ,  $C/T = 0.38$ ), n°6 ( $\beta = 45^\circ$ ,  $D/T = 0.4$ ,  $C/T = 0.41$ ) and n°9 ( $\beta = 70^\circ$ ,  $D/T = 0.37$ ,  $C/T = 0.41$ ), as presented in Fig. 4.22. This choice was motivated by the different  $EDC$  they generate, from 295 to 410  $\text{J m}^{-3}$ , for their close  $\langle (P/V)_{@p} \rangle$  values of 0.18 to 0.19  $\text{W m}^{-3}$ . Different particle distributions were observed at the just-suspended state. Their geometrical and modelled hydrodynamics characteristics are summarized in Table 4.7.

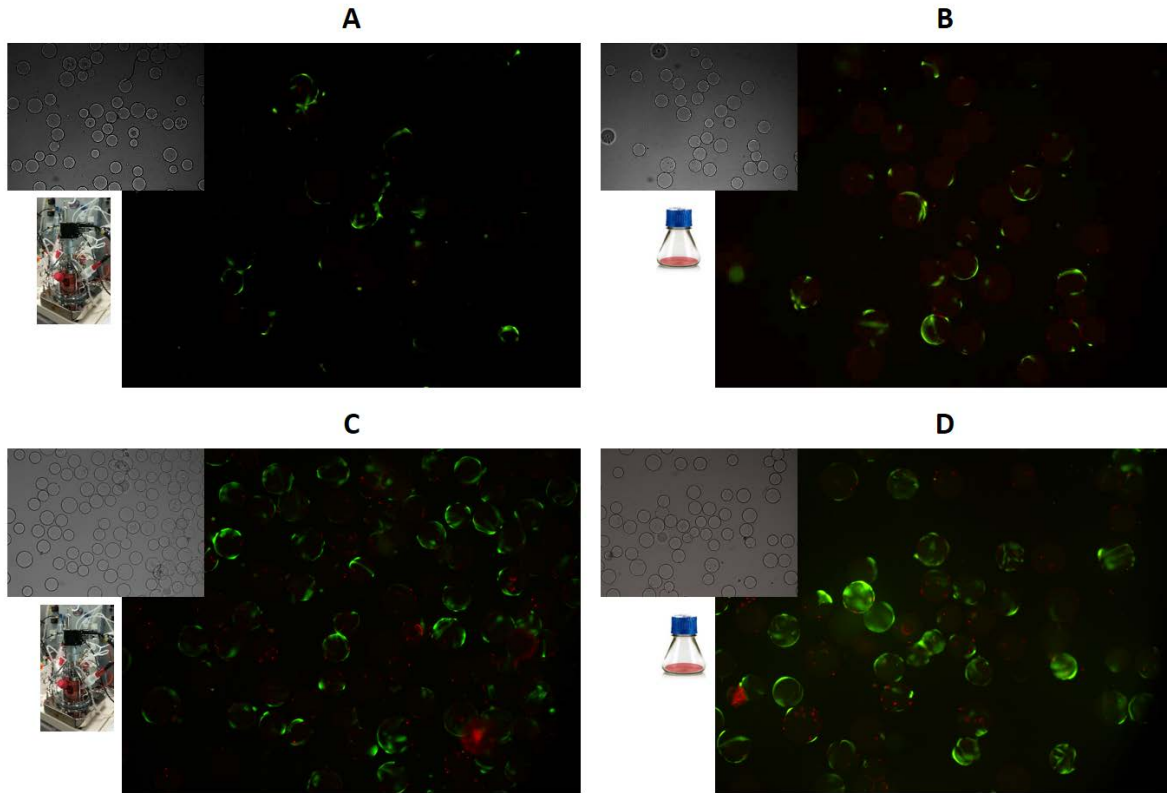


Figure 4.21: Cell morphology on microcarriers at  $t_0 + 1$  day (A and B) and  $t_0 + 5$  days (C and D), and according to the stirred system used: Minibioreactor (A and C) and Erlenmeyer flask (B and D). Green staining for living cell membranes and red staining for dead cell nuclei.

Table 4.7: Geometrical characteristics of the selected EED impellers and modelled parameters related to the hydromechanical stress encountered by the particles at the just-suspended state.

Impeller reference	$\beta$ ( $^\circ$ )	$D/T$ (-)	$C/T$ (-)	$N_{js}^{mod}$ (rpm)	$\langle (P/V)_{@p} \rangle$ ( $\text{W m}^{-3}$ )	$EDC$ ( $\text{J m}^{-3}$ )
5	38	0.41	0.38	90	0.19	295
6	45	0.4	0.41	77	0.19	330
9	70	0.37	0.41	63	0.18	410

### Cell expansions comparison

Fig. 4.23 presents the glucose and lactate concentration over time in minibioreactors equipped with the three EED impellers. Glucose consumption and lactate production were measured for all culture conditions, validating a cell activity in these three cultures. However, this glucose consumption was found slightly lower with the EED n°9, which displayed the highest  $EDC$  value. Replicates are however necessary to validate the significance of this trend. Residual glutamine and accumulation of ammonia displayed similar concentrations during the cultures with all impellers. However, due to the low glutamine consumption by the MSC, the glutamine concentration decrease and ammonia



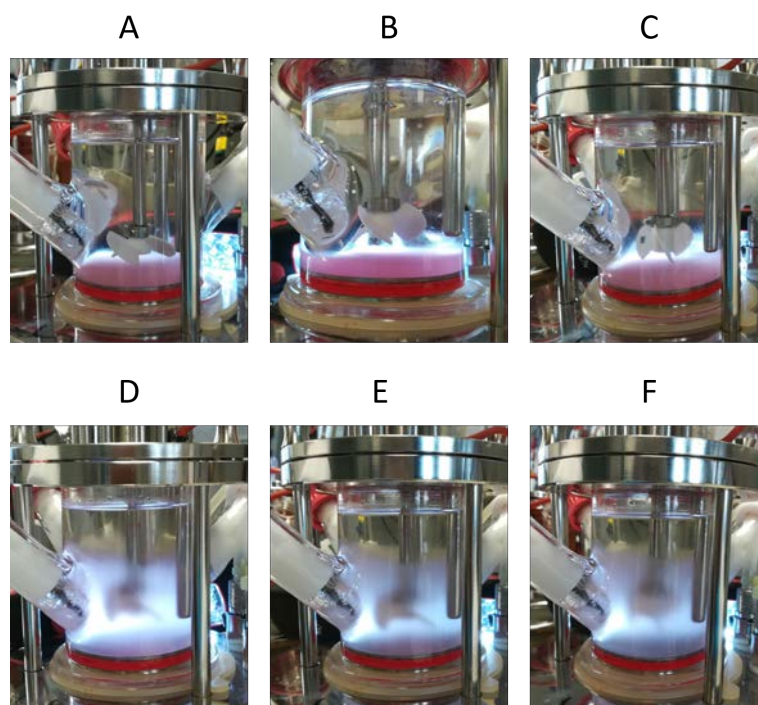


Figure 4.22: Selected EED impellers in mini-bioreactors, without agitation: EED n°5 (A), EED n°6 (B) and EED n°9 (C) ; and at the just-suspended state ( $N = N_{js}$ ): EED n°5 (D), EED n°6 (E) and EED n°9 (F). Microcarriers are stained using Rose bengal dye.

concentration increase over time could be mainly explained by the thermal degradation of glutamine. Hence, differences due to the impact of the impeller design may be negligible in comparison to this spontaneous degradation.

Based on the *in situ* cell counting method, presented in more details in section 2.3, the mean number of cell per microcarrier  $\langle N_{cell/\mu C} \rangle$  was recovered each two days and compared for the three cultures. Results are presented in Fig. 4.24. Cell expansions were validated with a 1.3-fold, a 1.4-fold and a 1.3-fold increases in 6 days, respectively with EED n°5, n°6 and n°9. 98 % to 100 % microcarriers were always colonized, namely that they contained at least one cell. However, as described in Appendix A, cell attachment on microcarriers was performed before inoculation into the mini-bioreactor.

### Conclusion and perspectives

To sum up, these preliminary cultures validated MSC expansion in the mini-bioreactor set-up. However, complementary cultures are necessary to deeper study the impact of EED geometry on cell expansion. In the future, more EED designs may be compared in order to determine if threshold values for  $\langle (P/V)_{@p} \rangle$  and  $EDC$  may be identified to guarantee

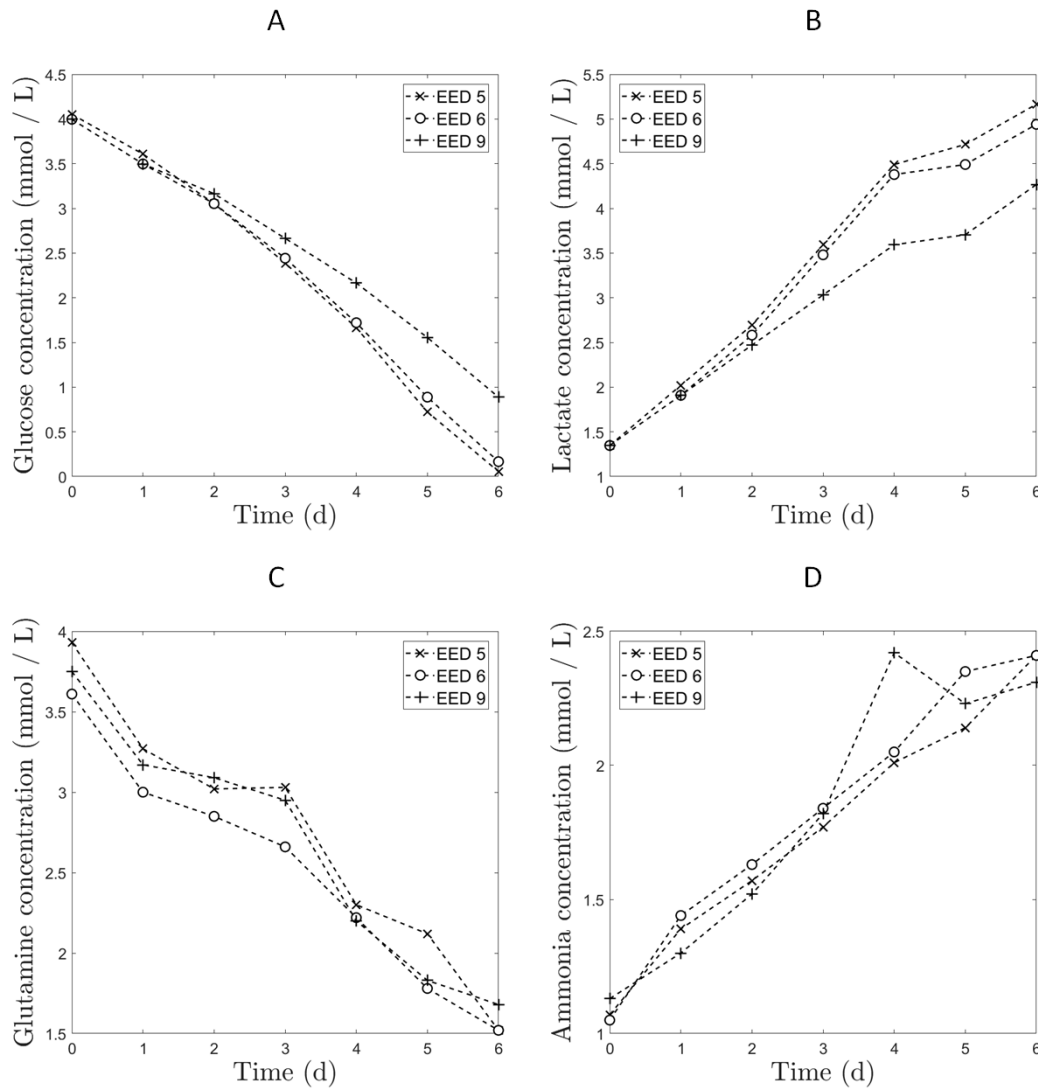


Figure 4.23: Kinetics of metabolite concentrations according to the EED impeller used in minibioreactor: Glucose (A), lactate (B), glutamine (C), ammonia (D).

cell quality during cultures in the minibioreactor. It would be notably interesting to include designs displaying much higher  $\langle (P/V)_{@p} \rangle$  and  $EDC$  values as negative controls, and the optimal design found in section 4.3. Moreover, Cherry and Papoutsakis (1988) demonstrated the need to consider particle collisions [33]. This phenomenon, which has also an impact on the potential cell damages, should be thus also taken into account in the multi-objective optimization algorithm.

Concerning further WJ-MSC cultures in minibioreactors, it would be recommended to seed cultures with less cells on microcarriers. In the present study, approximately 7.5 cells per microcarrier were counted at the beginning. As for all adherent-dependent cells, the expansion is however limited by the available surface. A compromise should be defined at the beginning of the cultures, between a sufficient number of cells per microcarrier to allow cell expansion and limit latency, and a low number of cells to delay

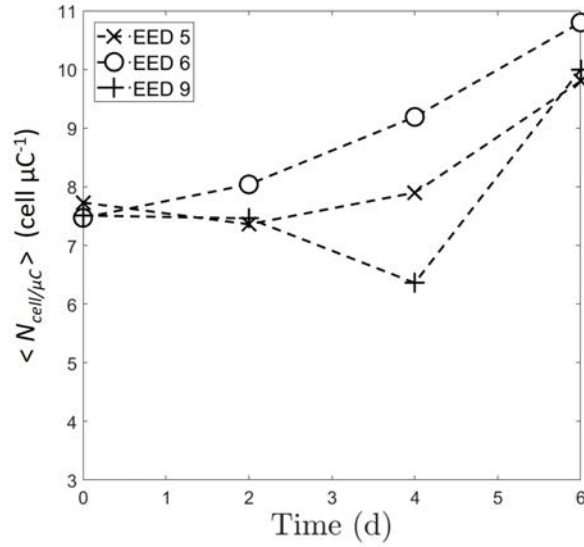


Figure 4.24: Evolution of the mean number of cells per microcarrier  $\langle N_{cell/\mu C} \rangle$  over time with the three EED impeller designs.

cell confluence. Moreover, a longer culture duration would stress the differences between culture conditions. To do that, other culture media and microcarriers feeding strategies should be applied, such as a feed / harvest or a continuous perfusion [34, 35, 36]. Cell quality should be also validated, through differentiation assays and a phenotypic analysis, as it was demonstrated that hydromechanical stress may lead to cell differentiation [37]. Finally, these investigations should be completed by validation of both cell attachment and cell detachment in the minibioreactor. Cell-microcarrier interactions are notably weaker during the attachment step. The hydromechanical stress have to be controlled to allow cell adhesion process until the strong focal adhesion establishment. In the same way, the impeller design would impact the cell detachment step. It was indeed shown that a high agitation of  $5 \times N_{js}$  improved the cell detachment, by decreasing the incubation time in trypsin [27]. A similar strategy may be applied in the minibioreactor, but should be first characterized to ensure the quality of both suspended and still adhered cells.

## 4.5 Chapter conclusions

This last chapter aimed at validating a CFD-based strategy coupled to a multi-objective optimization taking into account the particle spatial distribution integration. To do that, specific hydrodynamics parameters were defined. At the just-suspended state, the solid concentration gradients were calculated in order to determine if some culture conditions would maintain cells in potentially damaging zones or, on the contrary, would avoid it. In this way, CFD simulations were advantageously used to calculate  $\langle (P/V)_{@p} \rangle$  and  $EDC$ , defined as a power and an energy function per unit of volume.

First, four different impeller designs were compared according to particle time accumulation to potential damaging zones at the just-suspended state. Both two impellers operating in up-pumping mode (marine propeller, Elephant Ear) were found to display higher  $\langle (P/V)_{@p} \rangle$  values of 1.4 and 1.9  $\text{W m}^{-3}$  and  $EDC$  values of 3.3 and 4.3  $\text{kJ m}^{-3}$ , than the impeller in down pumping mode (Elephant Ear) and the radial Rushton turbine, displaying respectively  $\langle (P/V)_{@p} \rangle$  values of 0.23 and 0.58  $\text{W m}^{-3}$  and  $EDC$  values of 0.45 and 0.86  $\text{kJ m}^{-3}$ . The 'Elephant Ear' generic impeller in down-pumping mode displayed the lowest values and was thus selected for the design optimization. It is nevertheless admitted that this selection was based on the comparison of only one set of geometrical parameters for MPU, EEU, EED and RT. Hence, there is no guarantee that the optimal EED is more suitable than the optimal MPU, EEU or RT.

Based on the EED design, a numerical screening approach was investigated in order to predict the optimal geometrical parameters, by varying the impeller size, the off-bottom clearance and the blade slope angle. CFD simulations were run in order to predict the just-suspended state and get the corresponding  $\langle (P/V)_{@p} \rangle$  and  $EDC$ . Up to 22 % difference was observed between the power per unit of volume in all the fluid  $\langle (P/V) \rangle$  and encountered by the particles  $\langle (P/V)_{@p} \rangle$ . Hence, an optimization based on hydrodynamics parameters calculated on all the fluid phase may under-estimate the turbulent energy dissipation encountered by the particles. The minimization of the particle exposure to damaging zones was obtained for a  $D/T$  ratio equal to 0.4, and a large off-bottom clearance, with  $C/T = 0.5$ . Concerning the blade slope angle,  $\beta = 57^\circ$  was found to be a good compromise between  $77^\circ$  recommended to minimize  $\langle (P/V)_{@p} \rangle$  and  $42^\circ$  found for the  $EDC$  minimization.

In the last part of this study, WJ-MSD expansion using impeller designs that display various  $EDC$  values, were compared. Similar cell expansions were observed between 1.3- and 1.4-fold cell increase after 6 days of culture. However, the highest value was not

observed for the impeller displaying the lowest  $EDC$  values of  $295 \text{ J m}^{-3}$ , but with an intermediate value of  $330 \text{ J m}^{-3}$ . Complementary cultures are thus clearly necessary to discuss significantly the results obtained.

Main contributions of Chapter 4

- Up to 22 % difference was observed between  $\langle (P/V) \rangle$  and  $\langle (P/V)_{@p} \rangle$ . Hence, **an optimization based on hydrodynamics parameters calculated on all the fluid phase may under-estimate the turbulent energy dissipation encountered by the particles.**
- **Impellers operating in down-pumping mode are recommended for microcarrier-based cultures.**
- An original **optimization method** was proposed to determine the **best geometrical parameters for MSC cultures**, by minimizing the hydromechanical stress encountered by the solid phase.
- **WJ-MSD expansion was validated in a minibioreactor with up to 1.4-fold cell increase after 6 days. However, complementary study are still necessary to display significant results on the expansion comparison with various impeller designs, displaying different  $\langle (P/V)_{@p} \rangle$  and / or  $EDC$  values.**

---

## References


- [1] M.-L. Collignon, A. Delafosse, S. Calvo, C. Martin, A. Marc, D. Toye, E. Olmos, Large-eddy simulations of microcarrier exposure to potentially damaging eddies inside mini-bioreactors, *Biochemical Engineering Journal* 108 (2016) 30–43.
- [2] H.-J. Henzler, K. Schügerl, G. Kretzmer, P. Kieran, P. MacLoughlin, D. Malone, W. Schumann, P. Schamlou, S. Yim, Influence of stress on cell growth and product formation, volume 67, Springer Science & Business Media, 2000.
- [3] P. Jüsten, G. Paul, A. Nienow, C. Thomas, Dependence of mycelial morphology on impeller type and agitation intensity, *Biotechnology and Bioengineering* 52 (1996) 672–684.
- [4] M. S. Croughan, J.-F. P. Hamel, D. I. C. Wang, Effects of microcarrier concentration in animal cell culture, *Biotechnology and Bioengineering* 32 (1988) 975–982.
- [5] S. Ibrahim, A. W. Nienow, Suspension of Microcarriers for Cell Culture with Axial Flow Impellers, *Chemical Engineering Research and Design* 82 (2004) 1082–1088.
- [6] A. W. Nienow, Reactor engineering in large scale animal cell culture, *Cytotechnology* 50 (2006) 9–33.
- [7] J. Rowley, E. Abraham, A. Campbell, H. Brandwein, S. Oh, Meeting lot-size challenges of manufacturing adherent cells for therapy, *BioProcess International* 10 (2012) 16–22.
- [8] T. M. Maul, D. W. Chew, A. Nieponice, D. A. Vorp, Mechanical stimuli differentially control stem cell behavior: morphology, proliferation, and differentiation, *Biomechanics and Modeling in Mechanobiology* 10 (2011) 939–953.
- [9] M. S. Croughan, J.-F. Hamel, D. I. Wang, Hydrodynamic effects on animal cells grown in microcarrier cultures, *Biotechnology and Bioengineering* 29 (1987) 130–141.
- [10] R. S. Cherry, E. T. Papoutsakis, Physical mechanisms of cell damage in microcarrier cell culture bioreactors, *Biotechnology and Bioengineering* 32 (1988) 1001–1014.
- [11] N. Ma, K. W. Koelling, J. J. Chalmers, Fabrication and use of a transient contractional flow device to quantify the sensitivity of mammalian and insect cells to hydrodynamic forces, *Biotechnology and Bioengineering* 80 (2002) 428–437.
- [12] T. N. Zwietering, Suspending of solid particles in liquid by agitators, *Chemical Engineering Science* 8 (1958) 244–253.
- [13] G. Zhou, S. M. Kresta, Impact of tank geometry on the maximum turbulence energy dissipation rate for impellers, *AIChE Journal* 42 (1996) 2476–2490.
- [14] S. Ibrahim, A. Nienow, Suspension of microcarriers for cell culture with axial flow impellers, *Chemical Engineering Research and Design* 82 (2004) 1082–1088.

- [15] A. W. Nienow, Impeller selection for animal cell culture, *Encyclopedia of Industrial Biotechnology: Bioprocess, Bioseparation, and Cell Technology* (2009) 1–25.
- [16] M.-L. Collignon, A. Delafosse, M. Crine, D. Toye, Axial impeller selection for anchorage dependent animal cell culture in stirred bioreactors: methodology based on the impeller comparison at just-suspended speed of rotation, *Chemical Engineering Science* 65 (2010) 5929–5941.
- [17] A. N. Kolmogorov, Dissipation of energy in locally isotropic turbulence, in: *Dokl. Akad. Nauk SSSR*, volume 32, pp. 16–18.
- [18] V. Jossen, S. C. Kaiser, C. Schirmaier, J. Herrmann, A. Tappe, D. Eibl, A. Siehoff, C. van den Bos, R. Eibl, Modification and qualification of a stirred single-use bioreactor for the improved expansion of human mesenchymal stem cells at benchtop scale, *Pharmaceutical Bioprocessing* 2 (2014) 311–322.
- [19] A. Delafosse, M.-L. Collignon, A. Marc, D. Toye, E. Olmos, Revisiting the determination of hydromechanical stresses encountered by microcarriers in stem cell culture bioreactors, in: *BMC Proceedings*, volume 9, BioMed Central, p. 41.
- [20] M. Chen, J. Wang, S. Zhao, C. Xu, L. Feng, Optimization of dual-impeller configurations in a gas–liquid stirred tank based on computational fluid dynamics and multiobjective evolutionary algorithm, *Industrial & Engineering Chemistry Research* 55 (2016) 9054–9063.
- [21] N. Spogis, J. Nunhez, Design of a high-efficiency hydrofoil through the use of computational fluid dynamics and multiobjective optimization, *AIChE Journal* 55 (2009) 1723–1735.
- [22] A. C. Schnitzler, A. Verma, D. E. Kehoe, D. Jing, J. R. Murrell, K. A. Der, M. Aysola, P. J. Rapiejko, S. Punreddy, M. S. Rook, Bioprocessing of human mesenchymal stem/stromal cells for therapeutic use: Current technologies and challenges, *Biochemical Engineering Journal* 108 (2016) 3–13.
- [23] A. Lavrentieva, I. Majore, C. Kasper, R. Hass, Effects of hypoxic culture conditions on umbilical cord-derived human mesenchymal stem cells, *Cell Communication and Signaling* 8 (2010) 18–27.
- [24] A. Delafosse, C. Loubière, S. Calvo, D. Toye, E. Olmos, Solid-liquid suspension of microcarriers in stirred tank bioreactor-experimental and numerical analysis, *Chemical Engineering Science* (2018) 52–63.
- [25] S. Kaiser, V. Jossen, C. Schirmaier, D. Eibl, S. Brill, C. van den Bos, R. Eibl, Fluid flow and cell proliferation of mesenchymal adipose-derived stem cells in small-scale, stirred, single-use bioreactors, *Chemie Ingenieur Technik* 85 (2013) 95–102.
- [26] C. Schirmaier, V. Jossen, S. C. Kaiser, F. Jüngerkes, S. Brill, A. Safavi-Nab, A. Siehoff, C. Bos, D. Eibl, R. Eibl, Scale-up of adipose tissue-derived mesenchymal stem cell production in stirred single-use bioreactors under low-serum conditions, *Engineering in Life Sciences* 14 (2014) 292–303.

- 
- [27] A. W. Nienow, C. J. Hewitt, T. R. Heathman, V. A. Glyn, G. N. Fonte, M. P. Hanga, K. Coopman, Q. A. Rafiq, Agitation conditions for the culture and detachment of hMSCs from microcarriers in multiple bioreactor platforms, *Biochemical Engineering Journal* 108 (2016) 24–29.
- [28] T. R. Heathman, A. W. Nienow, Q. A. Rafiq, K. Coopman, B. Kara, C. J. Hewitt, Agitation and aeration of stirred-bioreactors for the microcarrier culture of human mesenchymal stem cells and potential implications for large-scale bioprocess development, *Biochemical Engineering Journal* 136 (2018) 9–17.
- [29] Y.-Y. Tsui, J.-R. Chou, Y.-C. Hu, Blade angle effects on the flow in a tank agitated by the pitched-blade turbine, *Journal of Fluids Engineering* 128 (2006) 774–782.
- [30] M. Roustan, Agitation. mélange: Caractéristiques des mobiles d’agitation, *Techniques de l’Ingénieur. Génie des procédés* 4 (1997) J3802–1.
- [31] A. Nienow, Suspension of solid particles in turbine agitated baffled vessels, *Chemical Engineering Science* 23 (1968) 1453–1459.
- [32] S. Arvinth, P. G. Rao, T. Murugesan, Critical impeller speed for solid suspension in turbine agitated contactors, *Bioprocess and Biosystems Engineering* 14 (1996) 97–99.
- [33] R. S. Cherry, E. T. Papoutsakis, Physical mechanisms of cell damage in microcarrier cell culture bioreactors, *Biotechnology and Bioengineering* 32 (1988) 1001–1014.
- [34] G. Eibes, F. dos Santos, P. Z. Andrade, J. S. Boura, M. M. Abecasis, C. L. da Silva, J. M. Cabral, Maximizing the ex vivo expansion of human mesenchymal stem cells using a microcarrier-based stirred culture system, *Journal of Biotechnology* 146 (2010) 194–197.
- [35] F. dos Santos, A. Campbell, A. Fernandes-Platzgummer, P. Z. Andrade, J. M. Gimble, Y. Wen, S. Boucher, M. C. Vemuri, C. L. da Silva, J. Cabral, A xenogeneic-free bioreactor system for the clinical-scale expansion of human mesenchymal stem/stromal cells, *Biotechnology and Bioengineering* 111 (2014) 1116–1127.
- [36] B. Cunha, T. Aguiar, M. M. Silva, R. J. Silva, M. F. Sousa, E. Pineda, C. Peixoto, M. J. Carrondo, M. Serra, P. M. Alves, Exploring continuous and integrated strategies for the up-and downstream processing of human mesenchymal stem cells, *Journal of Biotechnology* 213 (2015) 97–108.
- [37] T. M. Maul, D. W. Chew, A. Nieponice, D. A. Vorp, Mechanical stimuli differentially control stem cell behavior: morphology, proliferation, and differentiation, *Biomechanics and Modeling in Mechanobiology* 10 (2011) 939–953.



# Conclusions

 THE present PhD thesis aimed at improving the MSC culture expansion on microcarriers in stirred systems, including a focus on the impact of the hydrodynamics on the cell physiological response. This process must be indeed intensified in order to reach the high cell dose requirements for medical applications, but with a special attention to the cell quality. Hence, the present work proposed a cross-disciplinary strategy, involving the impact of various operating conditions (microcarrier type, agitation) on cell expansion, and investigations on the hydrodynamics in stirred tank bioreactors. Relying on numerical simulations (CFD) performed at  $N = N_{js}$ , particle concentration gradients were integrated into hydrodynamics parameters in order to determine suitable impeller designs minimizing the stress encountered by the microcarriers.

## Concluding remarks

### Improvement of WJ-MS C culture on microcarriers

The scientific strategy to improve the MSC expansion performances on microcarriers is remembered in Fig. 4.25, completed by the main contributions of this study (in red).

*Macroscopic interactions between the hPL and the suspension of colonized microcarriers*  
The human platelet lysate supplemented into the culture medium led to the formation of a jelly-matrix entrapping microcarriers during dynamic cultures, despite heparin addition. In order to ensure robust and reproducible culture conditions, and without supplementary heparin addition, this phenomenon was successfully avoided by a fibrin mechanical depletion. However cell expansion in this culture medium was slightly delayed.

### *Quantitative data robustness to compare cell expansion on microcarriers*

An automatic, robust and *in situ* cell counting method was validated with a mean deviation of 5 % in comparison with a manual counting. Based on photos from microscopic

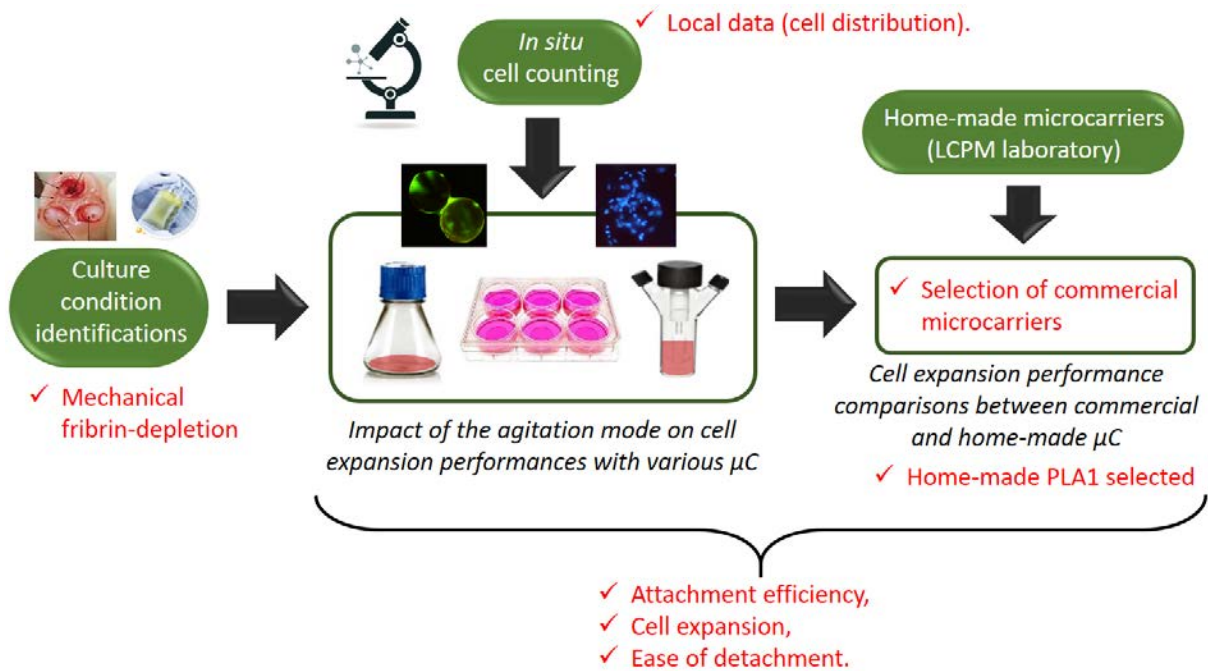


Figure 4.25: Global methodology and main contributions on the improvement of WJ-MS C cultures on microcarriers (Chapter 2 summary).

analyses after cell nuclei DAPI staining, the Matlab script correctly detected cells and microcarriers contours. While current approaches for cell kinetics establishment are indirect (substrate / metabolite kinetics, nuclei counting after cell lysis, WST1, MTT), the present method provided statistic data, such as the distribution of the number of cells per microcarriers and the fraction of colonized microcarriers. Distributions were notably compared after 3 and 13 days of cultures and led to a larger standard deviation after several days of culture, with 1 to 20 cells /  $\mu\text{C}$  at day 13 instead of 0 to 10 cells /  $\mu\text{C}$  at day 3. However, due to proximity of cell nuclei spots, a lack of accuracy was observed when cell density get close to the microcarrier confluence. **To sum up, a quick and robust method was developed to count cells directly on microcarriers. A probabilistic approach allowed then to presume the number of cells adhered on the non-visible side of opaque particles.**

*Microcarrier type and agitation mode impact on MSC expansion*

Based on the validated culture conditions on microcarriers and using the *in situ* cell counting method, WJ-MS C cultures performances were compared for various microcarriers and with different agitation modes. No optimal microcarrier was simultaneously found for static and dynamics cultures, including both orbital and mechanical agitations. A preliminary microcarrier screening would thus be recommended when a new cell expansion process is investigated. Nonetheless, Cytodex-1 was recommended for cell attachment and expansion, with an expansion factor  $F^{exp}$  of 0.6 in spinner flasks, but cell detachment was

more difficult to perform than with other microcarriers. Qualitative observations indeed showed that a significant fraction of cells remained attached after the trypsinization. **As a compromise between cell attachment, expansion and detachment, the hPL-coated Star-Plus ( $F^{exp} = 0.5$ ) and Plastic-Plus ( $F^{exp} = 0.2$ ) microcarriers were suggested, with respectively an orbital and a mechanical agitations applied.**

### *Validation of a home-made microcarrier dedicated to MSC culture*

Cytodex-1 and hPL coated Plastic-Plus microcarriers were selected to compare the cell expansion performances with a home-made microcarrier [1]. In static mode, the microcarrier PLA1, composed of a PLA core surrounded by a C<sub>6,14</sub> dextran corona, did not require any coating and presented similar performances than the commercial microcarriers. However, as previously recommended, a validation in dynamic mode should be performed to confirm these microcarriers capability for MSC cultures.

### **Modelling of microcarriers just-suspended state in a STR**

The second part of this PhD thesis dealt with modelling of the microcarrier just-suspended state in a STR. The global scientific strategy is reminded in Fig. 4.26, completed by the main contributions of the present study (in red).

### *Revisiting Zwietering model for particles with relative density close to 1*

The minimal agitation rate ensuring all particle suspension  $N_{js}$  was measured for 140 different operating conditions, varying the impeller geometrical parameters (design, size, position) and the microcarrier properties (concentration, density, viscosity, diameter). The Zwietering model, currently used to model  $N_{js}$  displayed up to 50 % discrepancies, probably due to the low density difference between the solid and the liquid phases, in the case of microcarriers. To address these deviations, two models were developed, based either on dimensional analysis or CFD simulations.

### *$N_{js}$ modelling for microcarrier suspensions*

Based on a dimensional analysis, the first model related  $Re_{js}$  to a constant  $K$ , only dependent on the impeller design, and five monomials, involving two impeller geometrical parameters ( $C/T$ ,  $D/T$ ) as well as three parameters related to the particle properties (volume fraction  $\alpha_S$ , number of particles and Archimede number with a characteristic length based on the 'particle cloud'). In particular, the particle volume fraction had an impact on  $N_{js}$  according to the regime applied by the impeller (axial, radial, mixed-flow). This model was suitable for scale-up, with a validation in a 20 L bioreactor, and displayed a better accuracy of 8.8 % mean error, in comparison with the Zwietering model.

The second model was implemented into CFD simulations. The just-suspended state

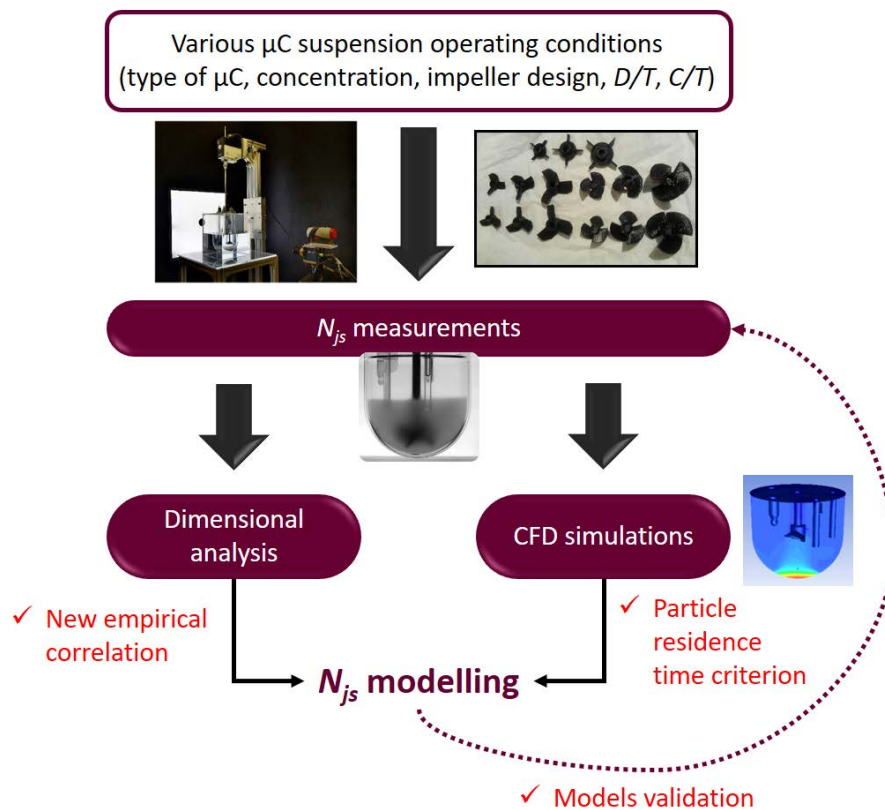


Figure 4.26: Global methodology and main contributions about the microcarrier just-suspended state modelling in a stirred tank bioreactor (Chapter 3 summary).

was determined by the particle residence time in the bottom of the bioreactor.  $N_{js}$  was reached when 0.1 % in volume of these particles presented a residence time under a critical value, corresponding to a time of 1 second to pass through a cube with 2 mm sides. A good accuracy, with a mean error of 9 %, was obtained when  $Re > 2,100$  at the 1 L scale (TRYTON bioreactor). For configurations below this value, over 20 % deviations were observed.  $y^+$  was suggested that the turbulence modelling was unsuitable in these cases.

### Optimization of the impeller design for MSC culture on microcarriers in a STR

Based on the results of both chapters 2 and 3, investigations were finally conducted in order to define an optimal impeller geometry for stem cell culture. Fig. 4.27 summarizes the global scientific strategy established, completed by the main contribution of this PhD thesis (in red).

#### *Integration of the particle concentration gradient into hydrodynamics parameters*

Liquid solid hydrodynamics in minibioreactors equipped with four impeller designs were compared using CFD simulations. The results showed significant differences between the

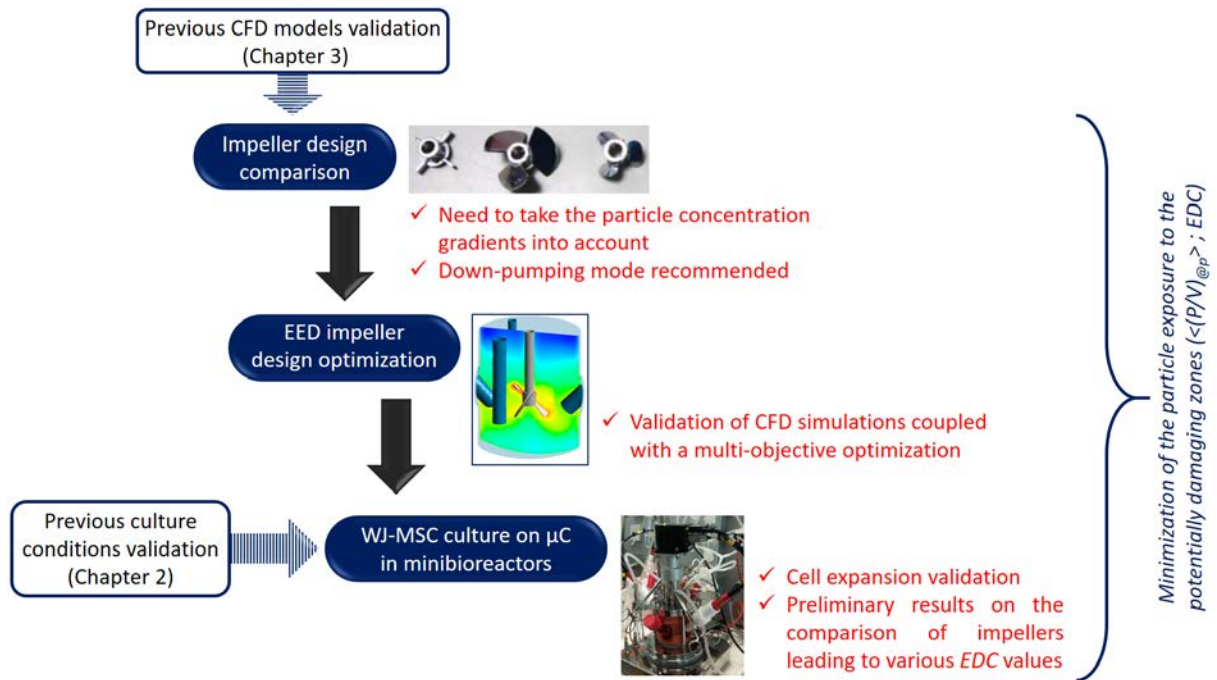


Figure 4.27: Global methodology and main contributions about the optimization of an impeller design for MSC culture on microcarriers in a stirred tank bioreactor (Chapter 4 summary).

power per unit of volume in the whole fluid volume  $\langle (P/V) \rangle$  and the one encountered by the microcarriers  $\langle (P/V)_{@p} \rangle$ , with a 1.1 to 1.3-fold increase when the particle distribution is taken into account. For the purpose of impeller designs comparison or optimization for MSC culture on microcarriers, it was thus recommended to calculate the hydrodynamics parameters by using the turbulent energy dissipation encountered by the particles  $\varepsilon_{@p}$ . In the present cases, the impeller operating in down-pumping mode (EED) was recommended, whereas the up-pumping mode led to the highest  $\langle (P/V)_{@p} \rangle$  and  $EDC$  values.

*CFD-based strategy to optimize an impeller design for MSC culture on microcarriers*

A strategy coupling CFD simulations with a multi-objective optimization (minimization of  $\langle (P/V)_{@p} \rangle$  and  $EDC$ ) was developed to determine the optimal geometrical parameters for MSC culture. In this study, the impeller blade slope angle  $\beta$ , the  $D/T$  ratio, and the  $C/T$  ratio were optimized in the case of a EED impeller, and led to a  $\beta$  value of  $57^\circ$ . The recommended position inside the bioreactor was far from the bottom, where particle concentration is the highest, with a  $C/T$  ratio of 0.5. Concerning the impeller size, a compromise between the volume swept and the value of  $N_{js}$  was found at  $D/T = 0.4$ .

### *Validation of WJ-MS C culture in a minibioreactor*

A set of impellers was finally selected with different  $EDC$ , but similar  $\langle (P/V)_{@p} \rangle$  values. WJ-MS C cultures were validated in the minibioreactor, with a higher glucose consumption and lactate production than in an Erlenmeyer flask. Up to a 1.4-fold increase of the mean number of cell per microcarrier was observed after 6 days. However, the highest expansion was not observed for the impeller design displaying the lowest  $EDC$  value of  $295 \text{ J m}^{-3}$ , but with an intermediate value of  $330 \text{ J m}^{-3}$ . Complementary cultures are thus clearly necessary to discuss significantly with the results.

### Future works

The present study allowed to define *a priori* suitable culture conditions and system design to ensure MS C quality during the expansion process. However, more investigations are still necessary to intensify the microcarrier-based MS C cultures.

- No commercial microcarrier was found optimal for all the three culture phases, namely cell attachment, expansion and detachment. Home-made microcarriers dedicated to MS C cultures are thus investigated, as the PLA-1 microcarrier displaying similar performances than the commercial Cytodex-1 and Plastic-Plus microcarriers when used in static mode. However, it was demonstrated that performances may depend on culture conditions. **In the short-term, dynamic cultures need to be performed with PLA-1 microcarriers**, in order to definitively validate their benefits. For long-term investigations, other microcarrier formulation may be developed, by taking into account the cell / material interactions (meso-modelling).
- The Euler-Euler approach used in CFD simulations is suitable for the screening application, and can be seen as a compromise between a reasonable calculation time and a sufficient accuracy for the results analysis. However due to a lack of available experimental data, parameters related to the particle / particle and particle / bioreactor collisions were not investigated (granular temperature), despite collisions are also responsible of cell detachment and damages [2]. A Lagrangian or a CFD-DEM approach would be suggested in order to take the individual particle motion into account. The use of unresolved **CFD-DEM simulations to build suspension curves** (fraction of suspended particles in function of the agitation rate) and predict  $N_{js}$  was recently validated for glass beads [3]. A similar approach may be applied in the case of microcarriers.
- In the present study, no significant difference was observed on the cell expansion

with EED impellers displaying various *EDC* values. **More designs should be compared** in order to determine if threshold values for  $\langle (P/V)_{@p} \rangle$  and *EDC* may be found to ensure cell quality during cultures in the minibioreactor. It is also suggested to include the optimal design found in Chapter 4 and designs displaying much higher  $\langle (P/V)_{@p} \rangle$  and *EDC* values as negative controls.

- Following a step-by-step strategy, only the expansion phase was investigated in the minibioreactors, but **it would be crucial to also characterize and optimize the hydrodynamics during the attachment and detachment phases**. During the first hours of the culture, suspended cells must be in contact with all microcarriers for a uniform cell distribution on the particles, but the electrostatic interactions between cells and the microcarrier surface, necessary before the integrin bounding and the focal adhesion, may be easily broken by an agitation. Similarly to cell attachments validated in Erlenmeyer and spinner flasks, a gentle or an intermittent agitation should be characterized. At the end of the culture, it was shown that a high agitation of  $5 \times N_{js}$  improved the cell detachment, by decreasing the incubation time in trypsin [4]. A similar strategy may be applied in the minibioreactor, but should be first characterized to ensure both suspended and still adhered cells quality.
- Due to cell aggregate formations, the WJ-MSK cultures performed in this work were limited to a few days. Longer culture durations, without aggregates, must thus be achieved to intensify the expansion process. To do that, **feeding strategies involving both fresh medium and microcarriers need to be applied**, such as a feed / harvest or a continuous perfusion [5, 6, 7, 8]. However, the addition of microcarriers would also promote more frequent particle collisions, and thus potential cell damages. Therefore, the collisions impact should be first characterized in order to define a suitable feeding strategy (perspective 2).


To conclude, the results obtained in the present PhD thesis open up long-term prospects for the scale-up of MSC expansion process, with promising applications in regenerative medicine. Complementary studies are still required in biomaterial and bioprocess fields in order to develop innovative and specific microcarriers (biodegradable or controlled degradation), as well as agitation designs or controlled and monitored bioreactors.

## References

- [1] A. Roy, M. A. M. Valderrama, V. Daujat, K. Ferji, M. Léonard, A. Durand, J. Babin, J.-L. Six, Stability of a biodegradable microcarrier surface: physically adsorbed versus chemically linked shells, *Journal of Materials Chemistry B* 6 (2018) 5130–5143.
- [2] R. S. Cherry, E. T. Papoutsakis, Physical mechanisms of cell damage in microcarrier cell culture bioreactors, *Biotechnology and Bioengineering* 32 (1988) 1001–1014.
- [3] B. Blais, O. Bertrand, L. Fradette, F. Bertrand, CFD-DEM simulations of early turbulent solid–liquid mixing: Prediction of suspension curve and just-suspended speed, *Chemical Engineering Research and Design* 123 (2017) 388–406.
- [4] A. W. Nienow, C. J. Hewitt, T. R. Heathman, V. A. Glyn, G. N. Fonte, M. P. Hanga, K. Coopman, Q. A. Rafiq, Agitation conditions for the culture and detachment of hMSCs from microcarriers in multiple bioreactor platforms, *Biochemical Engineering Journal* 108 (2016) 24–29.
- [5] C. Sion, C. Loubière, E. Guedon, I. Chevalot, E. Olmos, Control of microcarrier feed time by quantitative determination of bead-to-bead transfer during hMSC cultures, 12th European Symposium on Biochemical Engineering Sciences (ESBES), Lisbon, Portugal (2018).
- [6] G. Eibes, F. dos Santos, P. Z. Andrade, J. S. Boura, M. M. Abecasis, C. L. da Silva, J. M. Cabral, Maximizing the ex vivo expansion of human mesenchymal stem cells using a microcarrier-based stirred culture system, *Journal of Biotechnology* 146 (2010) 194–197.
- [7] F. dos Santos, A. Campbell, A. Fernandes-Platzgummer, P. Z. Andrade, J. M. Gimble, Y. Wen, S. Boucher, M. C. Vemuri, C. L. da Silva, J. Cabral, A xenogeneic-free bioreactor system for the clinical-scale expansion of human mesenchymal stem/stromal cells, *Biotechnology and Bioengineering* 111 (2014) 1116–1127.
- [8] B. Cunha, T. Aguiar, M. M. Silva, R. J. Silva, M. F. Sousa, E. Pineda, C. Peixoto, M. J. Carrondo, M. Serra, P. M. Alves, Exploring continuous and integrated strategies for the up-and downstream processing of human mesenchymal stem cells, *Journal of Biotechnology* 213 (2015) 97–108.



# Résumé détaillé du travail de thèse

ES dernières décennies ont vu une augmentation significative des investigations sur les potentialités des cellules souches mésenchymateuses (CSM) en thérapie cellulaire et, grâce à leur propriétés thérapeutiques (capacité de différenciation, potentiel immunomodulateur...), de nouvelles applications sont également en cours d'étude. Une partie des essais cliniques réalisés actuellement utilisent ces cellules pour soigner des maladies, pour lesquelles les traitements actuels se révèlent peu efficaces (insuffisance cardiaque, cancers, diabète de type I et II...). Pour se développer et proliférer, les CSM ont besoin d'adhérer sur une surface, ce qui constitue une contrainte technique importante lors du développement ou de l'extrapolation du procédé d'expansion cellulaire. En milieu clinique, la majorité des cultures sont encore réalisées dans des systèmes 2D planaires de type *T-flask*, malgré l'encombrement engendré dans les incubateurs, les risques de contaminations et les coûts opératoires (entretien des cultures) induits. Il est par ailleurs évident, aujourd'hui, que ce mode de culture ne permettra pas de répondre à la forte demande en CSM, à savoir entre  $10^9$  et  $10^{12}$  cellules par lot [1], et que le procédé d'expansion doit être intensifié en tenant compte à la fois de la quantité et de la qualité des cellules récoltées [2]. Ainsi, le procédé doit être élaboré et contrôlé avec précaution dans sa globalité, c'est-à-dire de l'extraction des cellules à leur distribution, et ce, de manière extrapolable, rentable et dans des systèmes fermés de grade GMP.

Les travaux de thèse présentés ici sont plus spécifiquement associés à la phase d'expansion des CSM sur des micro-sphères appelées microporteurs, présentant un diamètre d'environ  $200\ \mu\text{m}$  et une densité proche de la phase liquide, d'environ  $1020\ \text{kg m}^{-3}$ . L'utilisation de cette technologie a été motivée par leurs remarquables performances théoriques en comparaison des systèmes planaires 2D (Fig. 5.1). Les CSM adhèrent sur la surface de ces particules, qui sont ensuite mises en suspension par une agitation en bioréacteur. La production d'une dose contenant  $10^9$  cellules nécessiterait 150 boîtes de cultures de type T-175 (basées sur une densité finale de  $40\ 000$  cellules /  $\text{cm}^2$ ). La mise en œuvre de cultures de d'une telle ampleur se révélerait délicat à mettre en place. La surface

d'adhérence pour l'expansion cellulaire est significativement augmentée lors de cultures utilisant des microporteurs, où  $10^9$  cellules pourraient être produites dans un bioréacteur de 2,4 L. D'autre part, l'implémentation de boucles de contrôle et commande est facilitée, conformément aux spécifications GMP. Toutefois, la réponse des cellules à leur environnement doit encore être étudié dans de tels systèmes [3]. Lors des cultures de CSM, les critères suivants doivent être considérés :

- La composition du milieu de culture, qui doit être de grade clinique [4].
- Les propriétés des microporteurs (matériau, diamètre, porosité, revêtement...) et leur concentration [5].
- Les paramètres physico-chimiques de l'environnement, tels que la température, le pH ou le taux d'oxygène dissous [2].
- Les concentrations en substrats et métabolites [6].
- L'hydrodynamique mise en place et les contraintes générées par l'agitation [7, 8, 9].

Les réponses biologiques et physiologiques des cellules vis-à-vis de leur environnement doivent être d'abord comprises et contrôlées avant de pouvoir extrapoler le procédé d'expansion. Cette finalité implique la conception du bioréacteur, les stratégies d'alimentation en milieu et / ou microporteurs, ainsi que les conditions de culture choisies. Dans ce contexte, trois objectifs centraux ont été définis et traités au cours de ces trois années de thèse. Le premier visait l'amélioration des performances d'expansion de CSM issues de cordons ombilicaux (gelée de Wharton, GW) sur microporteurs, dans un milieu de grade clinique. Dans une seconde phase, l'hydrodynamique en bioréacteur agité a été caractérisée à l'état correspondant à une mise en suspension minimale des microporteurs (défini comme l'état de « juste mise en suspension »), et ce, pour diverses conditions opératoires (type de mobile, taille, position, propriétés des particules). Le dernier objectif consistait en la détermination d'une géométrie de mobile optimale pour la culture de CSM sur microporteurs en bioréacteur, par la minimisation de l'exposition des particules aux zones potentiellement dommageables.

Ces travaux se sont inscrits dans le cadre du projet pluri-disciplinaire STEMCellREACTOR (2014-2018, <http://stemcreator-project.com>), financé par l'ANR. Des études collaboratives ont été mises en place avec les partenaires de ce projet, impliquant trois laboratoires nationaux et internationaux (LCPM - Nancy, ULg - Liège, IBC - Moscou), et deux PME (Global Process Concept - La Rochelle, Bio-Inox - Bergerac). Ces études se sont plus particulièrement orientées sur le couplage hydrodynamique / performances de culture de CSM. Les cellules adhérentes étant connues pour être particulièrement sensibles aux contraintes de cisaillement [11], des études ont été menées afin de disposer de données sur

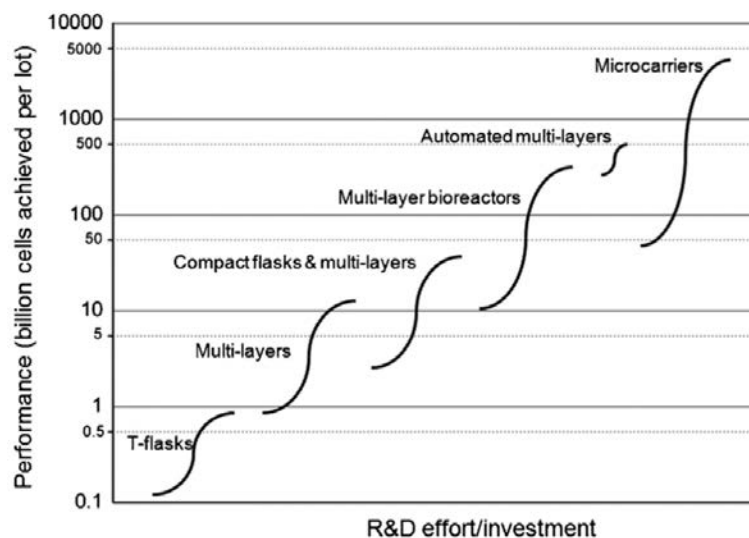


Figure 5.1: Illustration conceptuelle de type courbe en S, des technologies de culture de CSM. Figure reproduite de Simaria *et al.* (2014) [10].

l'hydrodynamique lors de la « juste mise en suspension » de microporteurs en bioréacteur agité. L'impact de cette agitation et des zones potentiellement dommageables dans le bioréacteur ont ensuite été reliées à la réponse physiologique des CSM lors du procédé d'expansion. Les cultures de CSM ont été menées, avec le support du laboratoire IMoPA (Nancy), directement impliqué dans des applications cliniques utilisant les CSM, et se sont basées sur les travaux de deux thèses précédemment effectuées au sein du laboratoire. La première thèse, réalisée par Caroline Ferrari (2012) concernait l'expansion de CSM de moelle osseuse porcine, tandis que la seconde thèse, soutenue par Céline Martin, (2016) utilisait des CSM de moelle osseuse humaine. Une approche pluri-disciplinaire a été mise en œuvre pour intensifier le procédé d'expansion de CSM, impliquant à la fois la validation de cultures cellulaires selon différentes conditions opératoires (type de microporteurs, agitation), et la caractérisation de l'hydrodynamique en bioréacteur agité. A l'issue de cette étude, reposant notamment sur des simulations numériques (CFD), les zones potentiellement dommageables pour les particules à  $N = N_{js}$  ont été mises en évidence, afin de déterminer la géométrie du mobile la mieux adaptée pour minimiser les contraintes perçues par les microporteurs.

Le manuscrit a été divisé en cinq chapitres, résumés dans la Figure 5.2:

- Le **Chapitre 1** présente un état de l'art global autour du procédé d'expansion de CSM et de l'impact de l'hydrodynamique sur les performances d'expansion.
- Le **Chapitre 2** introduit les résultats obtenus autour de l'amélioration des performances de culture de GW-CSM sur microporteurs. Afin de pallier un manque de robustesse et d'informations sur la distribution des cellules sur les microporteurs avec les techniques de comptage classiques actuelles, une méthode automatique et *in situ*

de comptage, basée sur l'analyse d'images, a été développée et validée, fournissant la distribution du nombre de cellules par microporteur. Grâce à cette méthode, l'impact du type de microporteur sur les performances d'expansion a été étudié selon différents modes d'agitation. Deux microporteurs commerciaux ont ainsi pu être sélectionnés et comparés à des microporteurs synthétisés par le laboratoire LCPM, en termes d'attachement, d'expansion et de détachement des cellules.

- Le **Chapitre 3** expose les résultats portant sur la modélisation de l'état de « juste mise en suspension » de microporteurs en bioréacteur agité. À l'issue de cette étude, deux modèles ont été établis pour prédire la fréquence minimale nécessaire pour mettre en suspension toutes les particules ( $N_{js}$ ). Le premier a été formulé à partir d'une analyse dimensionnelle, tandis que le second est basé sur des simulations CFD, dont le choix des modèles a préalablement été justifié.
- Le **Chapitre 4** vise finalement la comparaison de différents types de mobiles selon les contraintes hydromécaniques rencontrées par les microporteurs, à partir de simulations CFD. Pour cela, ces comparaisons sont basées sur l'exposition des particules aux zones potentiellement dangereuses. Les résultats ont ensuite permis de développer une stratégie couplant les simulations CFD avec une optimisation multi-critères pour prédire les paramètres géométriques optimaux (angle d'inclinaison des pales, taille, position) minimisant les potentiels dommages cellulaires dûs à l'agitation. Des cultures de GW-CSM ont finalement été menées en minioréacteurs de 200 mL équipés de différents mobiles d'agitation impliquant différents niveaux d'énergies subies par les particules.

## Principales contributions

### Amélioration du procédé de culture de CSM sur microporteurs

Ces premiers travaux peuvent être divisés en quatre phases. Tout d'abord des conditions de culture impliquant des CSM issues de la gelée de Wharton de cordons ombilicaux sur microporteurs et dans un milieu de grade clinique ont été établies. L'utilisation de lysat de plaquettes humaines (LPH), utilisé lors de cultures planaires pour des applications cliniques, a été retenue.

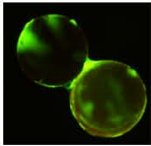
#### *Phénomènes macroscopiques générés par le LPH lors de la culture dynamique de CSM sur microporteurs*

Lors des cultures dynamiques sur microporteurs, le remplacement du sérum de veau foetal par du lysat de plaquettes humaines a mené à la formation d'une composante gélifiée

### Impact des conditions opératoire lors de cultures de GW-CSM sur microporteurs

#### Chapitre 2

- Validation des conditions de culture sur  $\mu$ P.
- Validation de la méthode de comptage cellulaire *in situ*.
- Comparaison et sélection de  $\mu$ P (commerciaux / synthétisés).

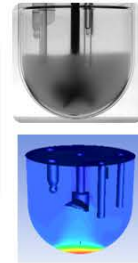


Quelle conditions  
de culture  
modéliser ?

### Caractérisation de l'hydrodynamique à l'état de juste mise en suspension

#### Chapitre 3

- Modélisation de l'état de juste mise en suspension de microporteurs:
  - ✓ Analyse dimensionnelle.
  - ✓ Simulations CFD.



### Couplage hydrodynamique-biologique pour déterminer un mobile d'agitation dédié à la culture de CSM

#### Chapitre 4

- Comparaison de différents mobiles selon les potentiels dommages cellulaires induits.
- Optimisation de la géométrie d'un mobile d'agitation.
- Comparaison d'expansions de CSM sur  $\mu$ P selon différents mobiles.

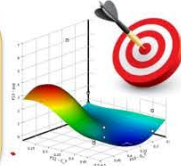
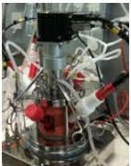


Figure 5.2: Méthodologie globale appliquée dans les présents travaux de thèse, reliant les résultats expérimentaux aux résultats numériques.

piégeant les microporteurs, malgré la présence d'héparine (Fig. 5.3). Il en résultait alors

une variabilité de l'expansion cellulaire entre différentes cultures. Une alternative à un ajout supplémentaire d'héparine a donc été recherchée, afin d'éviter un effet néfaste de cet anti-coagulant sur l'expansion cellulaire. Finalement, la défibrination mécanique a été validée de manière robuste et reproductible, en absence d'héparine, mais un léger retard d'expansion a été constaté.



Figure 5.3: Formation de matrice gélifiée piégeant les microporteurs lors d'une culture dynamique à  $t_0 + 1$  jour.

*Développement d'une méthode robuste et quantitative de comptage in situ du nombre de cellules par microporteur*

Aujourd'hui, les méthodes de comptage de CSM à l'issue d'une culture sur microporteurs se révèlent limitées. Il est en effet difficile de détacher les CSM des microporteurs, entraînant une sous-estimation du résultat lorsque le nombre de cellules est déterminé à partir d'une suspension de CSM détachées. Parmi les méthodes quantitatives actuellement employées, on distingue le comptage direct des noyaux après une lyse des cellules sur microporteurs, des techniques indirectes, telles que le suivi des cinétiques de substrats et de métabolites, les dosages WST-1 et MTT, ou encore l'intensité d'émission fluorescente lors d'un test d'AlamarBlue. Cependant, l'ensemble de ces méthodes ne fournissent qu'un nombre moyen de cellules par microporteurs sur l'ensemble de la culture. Une nouvelle méthode de comptage automatique, robuste et *in situ* a donc été développée à partir d'analyses microscopiques suite à une coloration DAPI des noyaux des cellules, et d'un script Matlab détectant les cellules et les contours des microporteurs (Fig. 5.4). Cette méthode a permis de dénombrer le nombre de cellules par microporteur avec une erreur moyenne de 5 % par rapport à un comptage manuel. Par ailleurs, la distribution du nombre de cellules par porteur a pu être déterminée, démontrant une évolution lors des cultures, avec des distributions de plus en plus larges au cours du temps. Des déviations ont cependant été observées au-delà d'un nombre moyen de 10 cellules par microporteur, dans les cas où la densité cellulaire se rapprochait de la confluence : les noyaux étant alors trop proches les uns des autres pour être formellement distingués.

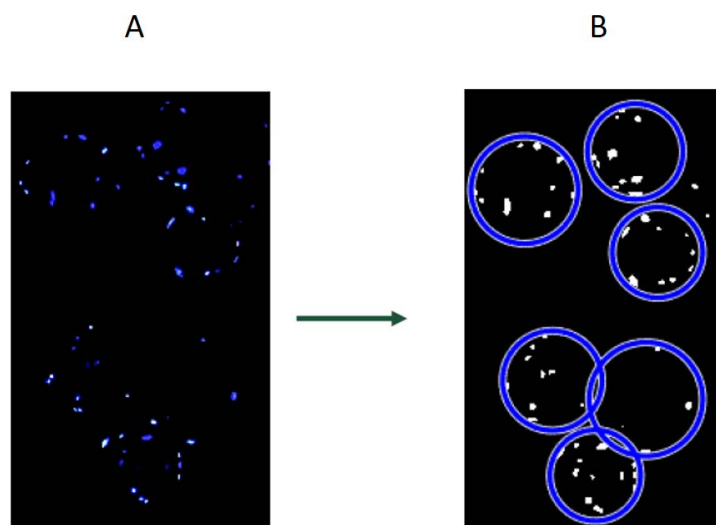


Figure 5.4: Traitement d'une photo par le script Matlab pour détecter et compter les cellules et microporteurs, après coloration DAPI.

#### *Impact du type de microporteur et du mode d'agitation sur l'expansion de CSM*

A partir des conditions de culture validées et de la méthode de comptage décrite précédemment, les performances de culture de GW-CSM ont été comparées pour différents microporteurs, et selon différents modes d'agitation. Le tableau 5.1 résume les performances observées. Aucun microporteur simultanément optimal en conditions statiques et dynamiques (agitation orbitale ou mécanique) n'a pu être déterminé. Au vu des différences observées entre les cultures statiques et dynamiques, une étape de criblage de microporteurs est recommandée dans des conditions d'agitation similaires à celles mises en place pour l'établissement d'un procédé d'expansion. Malgré tout, Cytodex-1 est adapté pour l'attachement et l'expansion cellulaire, bien que le détachement cellulaire soit plus difficile à mettre en œuvre comparativement aux autres microporteurs testés. Un compromis entre l'attachement, l'expansion et le détachement des cellules est l'utilisation de Star-Plus pour une agitation orbitale, et de Plastic-Plus pour une agitation mécanique.

#### *Validation de microporteurs synthétisés en laboratoire et dédiés à la culture de CSM*

Les microporteurs Cytodex-1 et Plastic-Plus ont été sélectionnés pour comparer les performances d'expansion cellulaire avec des microporteurs synthétisés par le laboratoire partenaire LCPM [12]. Des cultures statiques ont mis en évidence des performances similaires entre les microporteurs PLA1, composés d'un cœur en PLA et d'une couronne de dextran  $C_{6,14}$ , avec les microporteurs commerciaux. Cependant, comme indiqué précédemment, une validation définitive en mode agité est nécessaire pour confirmer le potentiel de ces microporteurs pour la culture de CSM.

Table 5.1: Résumé des performances obtenues avec différents microporteurs selon le mode de culture.

Microporteur	Cytodex-1	Star-Plus	Plastic	Plastic-Plus	Hillex II
<b>Culture statique</b>					
Capacité d'attachement sur les microporteurs	++	++	-	++	++
Distribution des cellules et taux de colonisation des microporteurs	-	++	-	-	++
Expansion cellulaire	++	++	-	+	++
Facilité de détachement	-	++	-	++	++
<b>Agitation orbitale</b>					
Capacité d'attachement sur les microporteurs	++	+	N/A	+	-
Distribution des cellules et taux de colonisation des microporteurs	++	++	N/A	++	-
Expansion cellulaire	+	++	N/A	+	-
Facilité de détachement	-	++	N/A	++	+
<b>Agitation mécanique</b>					
Capacité d'attachement sur les microporteurs	++	++	N/A	++	-
Distribution des cellules et taux de colonisation des microporteurs	++	++	N/A	++	-
Expansion cellulaire	++	+	N/A	++	-
Facilité de détachement	-	++	N/A	++	+

-: Plus faibles performances observées dans l'étude.

+: Performances intermédiaires.

++: Meilleures performances observées dans l'étude.

N/A: Non applicable.



L'ensemble de ces résultats est résumé Fig. 5.5.

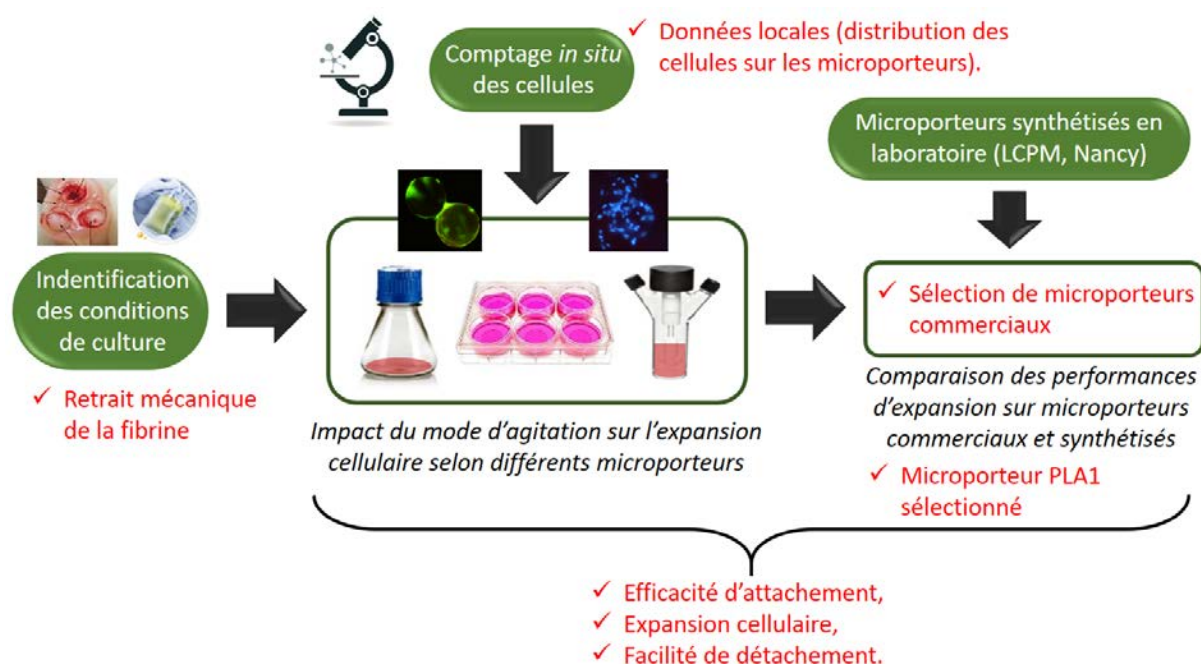


Figure 5.5: Stratégie scientifique mise en place pour l'amélioration des performances du procédé d'expansion cellulaire de CSM sur microporteurs (chapitre 2).

## Modélisation de l'état de juste mise en suspension de microporteurs en bioréacteur agité

La seconde partie de cette thèse s'est focalisée sur la « juste mise en suspension » des microporteurs en bioréacteur. En effet, la mise en œuvre de cultures de CSM en bioréacteur nécessite de connaître au préalable la fréquence nécessaire pour mettre en suspension les porteurs, afin d'éviter d'engendrer des dommages cellulaires si cette agitation est trop élevée ou la formations d'agrégats si celle-ci est trop faible. Par ailleurs, cette agitation doit permettre l'accessibilité du milieu de culture (nutriments), le transfert de matière, ainsi qu'une limitation des gradients de pH, d'O<sub>2</sub> et de substrats. Cette suspension peut être influencée par différents paramètres, présentés Fig. 5.6.

*Validité de la corrélation de Zwietering pour prédire la juste-suspension de particules à faible densité*

La fréquence d'agitation minimale nécessaire pour mettre en suspension toutes les particules  $N_{js}$  a été mesurée pour 140 conditions opératoires différentes, en faisant varier les

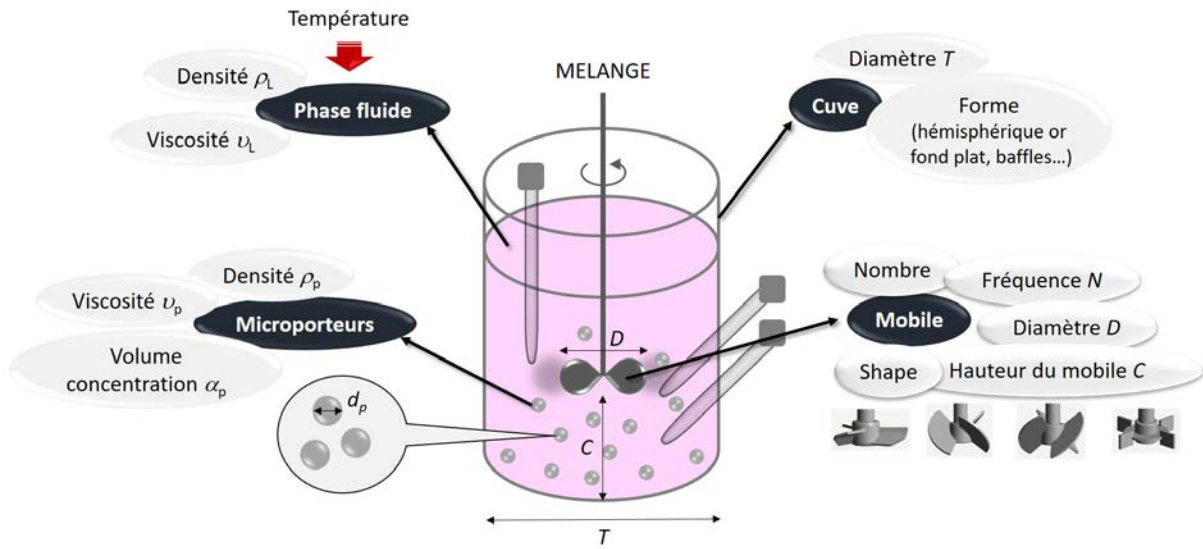


Figure 5.6: Paramètres influençant la suspension de particules en bioréacteur agité.

paramètres géométriques liés à l'agitation (type de mobile, taille, position) et les propriétés des microporteurs (concentration, densité, viscosité, diamètre). La corrélation de Zwietering, usuellement utilisée pour modéliser  $N_{js}$  a présenté jusqu'à 50 % d'erreur, probablement dûe à la faible différence de densité entre les phases solide et liquide, dans le cas des microporteurs ( $\rho_p - \rho_L \approx 40 \text{ kg m}^{-3}$ ). Afin de pallier ces incertitudes, deux nouveaux modèles ont été développés.

#### *Etablissement de modèles pour prédire $N_{js}$ lors de la suspension de microporteurs*

Une analyse dimensionnelle a été mise en œuvre pour développer un modèle reliant  $Re_{js}$  à une constante  $K$ , dépendant uniquement du type de mobile, et cinq monômes, impliquant deux paramètres géométriques ( $C/T$ ,  $D/T$ ) et trois paramètres liés aux propriétés des microporteurs (fraction volumique  $\alpha_S$ , nombre de particules, nombre d'Archimède avec une longueur caractéristique basée sur le « nuage de particules ») (Eq. 4.16, tableau 5.2). Il a été montré que  $N_{js}$  était impacté par la fraction volumique en particules  $\alpha_S$ , selon le régime d'écoulement induit par l'agitation (axial, radial, mixte). Ce modèle a finalement présenté une erreur moyenne de 8,8 %, avec une validation de l'extrapolation dans un bioréacteur de 20 L.

$$Re_{js} = K_3 \cdot \alpha_S^{a_3} \cdot \left(\frac{C}{T}\right)^{1/3} \cdot \left(\frac{D}{T}\right)^1 \cdot \left[\alpha_S \cdot \left(\frac{T}{d_p}\right)^3\right]^{0.4/3} \cdot \left(\frac{g \cdot \alpha_S \cdot T^3 \cdot \rho_L \cdot (\rho_p - \rho_L)}{\mu_L^2}\right)^{14/45} \quad (4.16)$$

Table 5.2: Paramètres  $K_3$  et  $a_3$  du modèle prédisant  $N_{js}$ , selon le type de mobile.

Écoulement	Mobile	$K_3$	$a_3$	$Tot. \alpha_S \text{ exponent}$
Mixte	HTPGD	2.4	-0.37	0.07
Mixte	EED	1.5	-0.37	0.07
Radial	RT	2.0	-0.34	0.1
Axial	HTPGU	2.0	-0.24	0.2
Axial	EEU	1.5	-0.24	0.2

Le second modèle a été établi à partir de simulations CFD. L'état de « juste mise en suspension » a été évalué à partir d'un critère basé sur le temps de passage des particules en fond de cuve.  $N_{js}$  était considéré comme atteint lorsque 0,1 % du volume des particules présentait un temps de passage inférieur à une valeur critique (1 s pour passer au travers d'une maille de 2 mm de côté). Ce modèle a été validé avec une erreur moyenne de 9 %, pour des conditions impliquant un nombre de Reynolds  $Re > 2\ 100$ . En-dessous de cette valeur, des déviations supérieures à 20 % ont été observées. Il a été suggéré que le modèle de turbulence appliqué n'était pas adapté pour ces configurations.

L'ensemble de ces résultats est résumé sur la Figure 5.7.

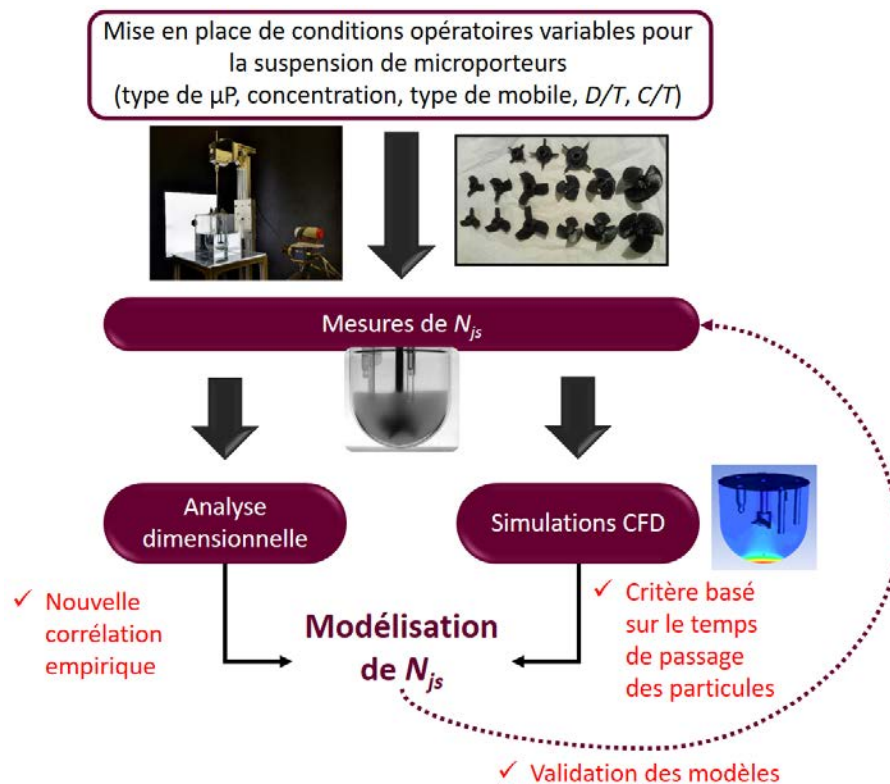


Figure 5.7: Stratégie scientifique mise en place et contributions pour modéliser l'état de juste mise en suspension de microporteurs en bioréacteur agité (chapitre 3).

## Optimisation de la géométrie d'un mobile d'agitation pour la culture de CSM sur microporteurs en bioréacteur agité

A partir des résultats établis précédemment, des études ont été conduites pour définir une géométrie optimale de mobile d'agitation dédié à la culture de CSM.

*Intégration du gradient de concentration en particules au sein des paramètres caractérisant l'hydrodynamique*

L'hydrodynamique liquide-solide en minibioréacteurs équipés de quatre mobiles d'agitation différents a été comparée à partir de simulations CFD. Les résultats ont montré des différences significatives entre la puissance par unité de volume dans l'ensemble du fluide  $\langle (P/V) \rangle$  et celle perçue par les microporteurs  $\langle (P/V)_{@p} \rangle$  (Eq. (4.17)), avec des valeurs 1,1 à 1,3 fois plus élevées lorsque la distribution spatiale des particules était prise en compte (Fig. 5.8). Il est donc recommandé de calculer les paramètres hydrodynamiques à partir de la dissipation de l'énergie turbulente rencontrée par les particules  $\varepsilon_{@p}$ , pour comparer ou optimiser un mobile d'agitation pour la culture de CSM. Dans le cas présent, le mobile opérant en pompage bas (EED) est recommandé, tandis que les mobiles opérant en pompage haut (EEU, MPU) ont présenté les plus hautes valeurs de  $\langle (P/V)_{@p} \rangle$  et  $EDC$  (Eq. (4.18)).

$$\langle \left( \frac{P}{V} \right)_{@p} \rangle = \rho_m \langle \epsilon \rangle_{@p} = \frac{\rho_m}{V_p} \iiint_{V_p} \varepsilon(V) dV \quad (4.17)$$

$$EDC = \iiint_{V_L(\lambda_K < d_p)} \frac{\rho_m \varepsilon(V)}{Q_{p,net}(V)} dV \quad (4.18)$$

$$\rho_m = \alpha_S \rho_S + \alpha_L \rho_L \quad (4.19)$$

*Mise en place d'une stratégie couplant des simulations CFD avec une optimisation multi-critères pour optimiser la géométrie d'un mobile d'agitation*

Une stratégie couplant des simulations CFD à une optimisation multi-paramétrique (minimisation de  $\langle (P/V)_{@p} \rangle$  et  $EDC$ ) a été mise en œuvre afin de déterminer la géométrie optimale d'un mobile pour la culture de CSM. Au cours de cette étude, l'angle d'inclinaison des pales  $\beta$ , le ratio  $D/T$  et le ratio  $C/T$ , ont été optimisés dans le cas d'un mobile EED. Les résultats ont mené à une valeur de  $\beta$  de  $57^\circ$ , une position recommandée assez haute dans la cuve, où les microporteurs sont moins concentrés, avec un ratio  $C/T$  de 0,5, et une taille de mobile suivant un compromis entre le volume de fluide brassé par le mobile et la valeur de  $N_{js}$ , avec un ratio  $D/T = 0,4$  (Fig. 5.9).

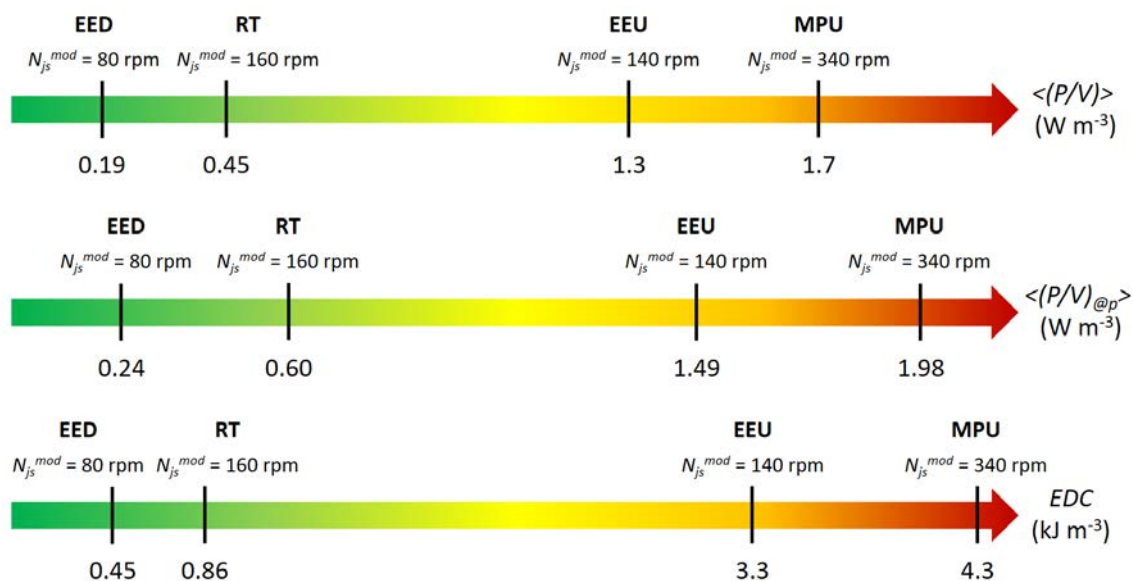


Figure 5.8: Comparaison relative entre quatre types de mobiles (EED, RT, EEU and MPU) à  $N = N_{js}$ , selon la puissance par unité de volume calculée sur l'ensemble du fluide  $\langle (P/V) \rangle$  et perçue par les microporteurs  $\langle (P/V)_{@p} \rangle$ , et la fonction  $EDC$ .

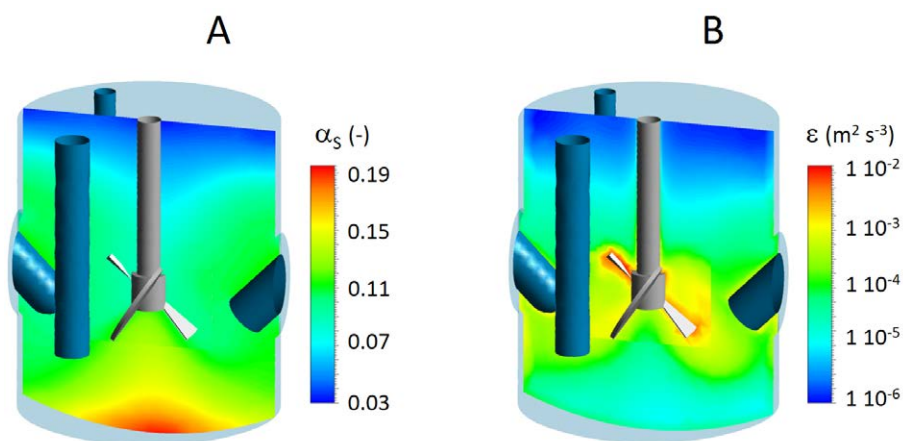


Figure 5.9: Distributions de la fraction volumique en microporteurs  $\alpha_S$  (A) et du taux de dissipation de l'énergie turbulente  $\varepsilon$  (B) dans le bioréacteur équipé du mobile optimisé.

## Validation de cultures de GW-CSM en minibioreacteur

Un set de mobiles présentant différentes valeurs de  $EDC$ , mais des valeurs de  $\langle (P/V)_{@p} \rangle$  similaires, a finalement été sélectionné. Des cultures de GW-CSM ont été validées en minibioreacteurs, avec des consommations de glucose et des productions de lactate plus élevées qu'en fiole d'Erlenmeyer. Une expansion d'un facteur 1,4 a été observée à partir du nombre moyen de cellules par microporteur après 6 jours de culture. Cependant, la plus forte expansion n'a pas été constatée avec le mobile présentant la plus faible valeur de  $EDC$  de  $295 J m^{-3}$ , mais pour une valeur intermédiaire de  $330 J m^{-3}$ .

Des cultures complémentaires sont nécessaires pour discuter des résultats de manière significative.

L'ensemble de ces résultats est résumé Fig. 5.10.

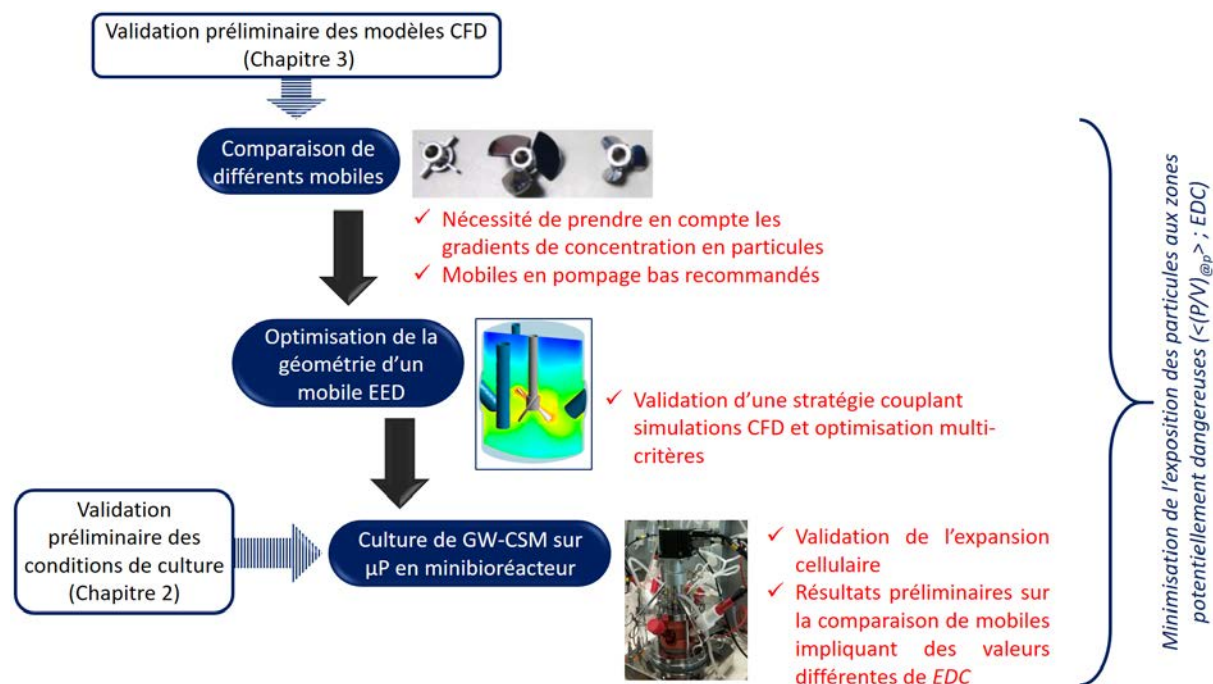


Figure 5.10: Stratégie scientifique mise en place et contributions autour de l'optimisation de la géométrie d'un mobile d'agitation pour la culture de CSM sur microporteurs en bioréacteur agité (chapitre 4).

## Perspectives

Les travaux effectués ont permis de définir des conditions de culture et un *design* d'agitation *a priori* adaptés à l'expansion de CSM, tout en assurant leur qualité durant le procédé de culture. Cependant, des études supplémentaires sont encore nécessaires pour intensifier les cultures sur microporteurs. Des pistes de perspectives ont ainsi été mises en évidence:

- Une validation définitive des performances de culture sur les microporteurs synthétisés PLA-1 devrait s'effectuer en conditions agitées. Par la suite, la formulation de nouveaux microporteurs dédiés à la culture de CSM pourrait être développée en prenant en compte les interactions entre les cellules et le matériau composant le microporteur (méso-modélisation).
- L'approche Euler-Euler utilisée en CFD a été développée pour une application de présélection (*screening*), mais n'a pas permis de prendre en compte les dommages

provoqués par les collisions entre particules et avec les parois du réacteur, pourtant significatifs [13]. Une approche lagrangienne ou basée sur la CFD-DEM peut être envisagée pour prendre en compte le mouvement des particules individuellement. L'application de la CFD-DEM dite *unresolved* a notamment permis la construction de courbes de suspension (fraction de particules en suspension en fonction de la fréquence d'agitation) et de prédire  $N_{js}$ , dans le cas de billes en verre [14]. Une approche similaire pourrait être appliquée dans le cas des microporteurs.

- Au cours de la présente étude, les mobiles présentant différentes valeurs de  $EDC$  n'ont pas mené à des différences significatives d'expansion cellulaire. D'autres géométries devraient être comparées afin de déterminer si des valeurs seuils de  $\langle (P/V)_{@p} \rangle$  et  $EDC$  peuvent être définies, à partir desquelles la qualité des cellules serait assurée. Il serait ainsi suggéré d'inclure le mobile optimal défini dans le chapitre 4, mais aussi des mobiles présentant des valeurs plus élevées de  $\langle (P/V)_{@p} \rangle$  et  $EDC$ , en tant que contrôles négatifs.
- L'études des cultures en minibioreacteurs s'est limitée à la phase d'expansion cellulaire. Pour tenir compte de l'ensemble du procédé, les étapes d'attachement et de détachement des cellules doivent aussi être validées dans le bioréacteur. Pour cela, une caractérisation de l'hydrodynamique est nécessaire pour assurer la qualité des cellules en suspension, mais aussi des cellules encore adhérentes.
- Les résultats présentés ici sont issus de cultures limitées à quelques jours, afin d'éviter la formation d'agrégats de cellules. Des cultures de plus longue durée, sans agrégats, sont néanmoins nécessaires dans l'optique d'intensification du procédé. Il est donc suggéré de mettre en place des stratégies d'alimentation en milieu de culture et microporteurs, de type recharge / récolte ou perfusion [15, 16, 17, 18]. Cependant, l'addition de microporteurs entraînerait une hausse des collisions particulières, et donc de potentiels dommages cellulaires. Ces collisions devront donc être caractérisées dans un premier temps afin de déterminer les conditions d'alimentation adaptées.

## References

- [1] J. Rowley, E. Abraham, A. Campbell, H. Brandwein, S. Oh, Meeting lot-size challenges of manufacturing adherent cells for therapy, *BioProcess International* 10 (2012) 16–22.
- [2] C. Martin, É. Olmos, M.-L. Collignon, N. De Isla, F. Blanchard, I. Chevalot, A. Marc, E. Guedon, Revisiting MSC expansion from critical quality attributes to critical culture process parameters, *Process Biochemistry* 59 (2017) 231–243.

- [3] A. C. Schnitzler, A. Verma, D. E. Kehoe, D. Jing, J. R. Murrell, K. A. Der, M. Aysola, P. J. Rapiejko, S. Punreddy, M. S. Rook, Bioprocessing of human mesenchymal stem/stromal cells for therapeutic use: Current technologies and challenges, *Biochemical Engineering Journal* 108 (2016) 3–13.
- [4] S. Gottipamula, M. Muttigi, U. Kolkundkar, R. Seetharam, Serum-free media for the production of human mesenchymal stromal cells: a review, *Cell Proliferation* 46 (2013) 608–627.
- [5] Q. A. Rafiq, K. Coopman, A. W. Nienow, C. J. Hewitt, Systematic microcarrier screening and agitated culture conditions improves human mesenchymal stem cell yield in bioreactors, *Biotechnology Journal* 11 (2016).
- [6] C. Ferrari, E. Olmos, F. Balandras, N. Tran, I. Chevalot, E. Guedon, A. Marc, Investigation of growth conditions for the expansion of porcine mesenchymal stem cells on microcarriers in stirred cultures, *Applied Biochemistry and Biotechnology* 172 (2014) 1004–1017.
- [7] C. J. Hewitt, K. Lee, A. W. Nienow, R. J. Thomas, M. Smith, C. R. Thomas, Expansion of human mesenchymal stem cells on microcarriers, *Biotechnology Letters* 33 (2011) 2325–2335.
- [8] A. W. Nienow, C. J. Hewitt, T. R. Heathman, V. A. Glyn, G. N. Fonte, M. P. Hanga, K. Coopman, Q. A. Rafiq, Agitation conditions for the culture and detachment of hMSCs from microcarriers in multiple bioreactor platforms, *Biochemical Engineering Journal* 108 (2016) 24–29.
- [9] T. R. Heathman, A. W. Nienow, Q. A. Rafiq, K. Coopman, B. Kara, C. J. Hewitt, Agitation and aeration of stirred-bioreactors for the microcarrier culture of human mesenchymal stem cells and potential implications for large-scale bioprocess development, *Biochemical Engineering Journal* 136 (2018) 9–17.
- [10] A. S. Simaria, S. Hassan, H. Varadaraju, J. Rowley, K. Warren, P. Vanek, S. S. Farid, Allogeneic cell therapy bioprocess economics and optimization: Single-use cell expansion technologies, *Biotechnology and Bioengineering* 111 (2014) 69–83.
- [11] N. Ma, K. W. Koelling, J. J. Chalmers, Fabrication and use of a transient contractional flow device to quantify the sensitivity of mammalian and insect cells to hydrodynamic forces, *Biotechnology and Bioengineering* 80 (2002) 428–437.
- [12] A. Roy, M. A. M. Valderrama, V. Daujat, K. Ferji, M. Léonard, A. Durand, J. Babin, J.-L. Six, Stability of a biodegradable microcarrier surface: physically adsorbed versus chemically linked shells, *Journal of Materials Chemistry B* 6 (2018) 5130–5143.
- [13] R. S. Cherry, E. T. Papoutsakis, Physical mechanisms of cell damage in microcarrier cell culture bioreactors, *Biotechnology and Bioengineering* 32 (1988) 1001–1014.
- [14] B. Blais, O. Bertrand, L. Fradette, F. Bertrand, CFD-DEM simulations of early turbulent solid–liquid mixing: Prediction of suspension curve and just-suspended speed, *Chemical Engineering Research and Design* 123 (2017) 388–406.



- [15] C. Sion, C. Loubière, E. Guedon, I. Chevalot, E. Olmos, Control of microcarrier feed time by quantitative determination of bead-to-bead transfer during hMSC cultures, 12th European Symposium on Biochemical Engineering Sciences (ESBES), Lisbon, Portugal (2018).
- [16] G. Eibes, F. dos Santos, P. Z. Andrade, J. S. Boura, M. M. Abecasis, C. L. da Silva, J. M. Cabral, Maximizing the ex vivo expansion of human mesenchymal stem cells using a microcarrier-based stirred culture system, *Journal of Biotechnology* 146 (2010) 194–197.
- [17] F. dos Santos, A. Campbell, A. Fernandes-Platzgummer, P. Z. Andrade, J. M. Gimble, Y. Wen, S. Boucher, M. C. Vemuri, C. L. da Silva, J. Cabral, A xenogeneic-free bioreactor system for the clinical-scale expansion of human mesenchymal stem/stromal cells, *Biotechnology and Bioengineering* 111 (2014) 1116–1127.
- [18] B. Cunha, T. Aguiar, M. M. Silva, R. J. Silva, M. F. Sousa, E. Pineda, C. Peixoto, M. J. Carrondo, M. Serra, P. M. Alves, Exploring continuous and integrated strategies for the up-and downstream processing of human mesenchymal stem cells, *Journal of Biotechnology* 213 (2015) 97–108.



# Appendices



# Appendix A:

## Supplementary materials and methods

### Cell culture

#### Cell source

WJ-MSC were recovered from a healthy donor. The human umbilical cords were collected after informed mother consent, according to the national legislation regarding human sample collection, manipulation and personal data protection. MSC isolation was performed using mechanical migration: The umbilical cord was dissected in small sections (around 1 or 2 mm thickness), washed with Dulbesco Phosphate Buffer Saline solution (DPBS, Sigma) and plated as explants on planar plastic surfaces. After migration and expansion on the surface, cells were recovered by trypsinization and frozen in a container filled with liquid nitrogen at  $-196^{\circ}\text{C}$ . By concern of senescence limitation and stem phenotype alteration, cells used in all cultures of the present study did not exceed 5 passages.

#### Culture medium

The basal medium used was  $\alpha$ -MEM Eagle solution (Lonza), supplemented with 5 % human platelet lysate (hPL, MultiPL'30, Macopharma), 4 mM glutamine (Sigma) and 1 % antibiotic-antimycotic (Gibco). According to the manufacturer instructions, the hPL derived from screened normal human donor platelets, was pooled in large batch sizes of 10 L and was sterilized by  $0.22\ \mu\text{m}$  filtration before filling in closed systems. Heparin (Sigma-Aldrich) was added to this basal medium for planar static cultures at a concentration of 2 IU / mL. Concerning dynamic cultures on microcarriers, first cultures led to the formation of a jelly matrix precipitate, entrapping microcarriers, even with 2 IU / mL heparin in the culture medium. This gel appeared during the first days and led to high variability of cell adhesion and expansion. The heparin was thus found to be not enough effective to avoid gel formation. Hence, it was chosen to use a mechanical fibrinogen-depletion method

instead of the increase of heparin concentration, which may have deleterious effects on cell expansion at higher concentrations [1]. Similar fibrinogen-depletion methods have already been described by other authors [2, 3]. In this thesis, the culture medium was maintained between 4 and 6 hours at room temperature and without agitation, to allow clot formation. It was then stored at 4°C at least 18 hours. The medium was then put at a temperature of 37°C during 1 hour and submitted to mechanical shocks by manual shaking. The biogel was then physically collapsed and the precipitated fibrin was pelleted by centrifugation ( $670 \times g$ , 10 min, Jouan G 4.11). Finally, the medium was passed through a 0.22  $\mu\text{m}$  filter.

### **Cell culture under planar static conditions**

After quick thawing, cells were seeded at 2000 cells /  $\text{cm}^2$  in T175 flasks filled with 25 mL culture medium. The medium was changed every 2 or 3 days by complete medium removing and addition of the same volume of fresh medium. Once 60-70 % of the confluence was reached, the culture medium was removed and cells were washed with DPBS before the cell detachment, using 5 mL TrypLE (Gibco) per flask. TrypLE is composed of recombinant cell-dissociation enzymes that replace trypsin. Incubation did not exceed 5 min and the enzymatic digestion was stopped by adding 20 mL of fresh medium. The suspension was then centrifuged at  $130 \times g$  during 5 min, the supernatant was removed and the pellet was dispersed in fresh culture medium. A filtration step was performed with 40  $\mu\text{m}$  filters, in order to eliminate potential cell aggregates. 1 mL of the suspension was finally collected to determine the cell number and cell viability.

### **Cell culture on microcarriers in static mode**

Six well plates with ultra-low attachment surface (Corning) were used to perform static cultures on microcarriers. After addition of the microcarriers at the bottom of the well, cells were seeded at a concentration of  $3 \times 10^5$  cells / well in a working volume of 5 mL. At the end of the cultures, the supernatant was removed and microcarriers were washed with DPBS. Cell detachments were finally performed by using 1 mL of TrypLE. A complementary agitation can be applied to promote cell detachment and to reduce the incubation time, as proposed by Nienow *et al.* [4]. In this study, an orbital agitation of 75 rpm (orbital diameter  $d_o = 10$  mm) was thus applied during 5 min, and 5 mL of fresh medium was then added to stop the enzymatic digestion. Cells were finally separated from microcarriers with a 70  $\mu\text{m}$  filtration step.

## Cell culture on microcarriers in dynamic mode

Three different stirred bioreactors were used for MSC cultures on microcarriers. Their characteristics are summarized in Table A.1. In all cases, cells were first recovered from planar cultures at around 70 % of the confluence and were passed through a 40  $\mu\text{m}$  filter to trap potential cell aggregates before seeding. 70 % of the confluence was found to be a good compromise to recover enough cells while avoiding the formation of aggregates. Suspended cell concentration was determined, before inoculation in the stirred systems.

Table A.1: Stirred systems and agitation conditions chosen for cultures in dynamic mode in this thesis.

Bioreactor	Erlenmeyer flask	Spinner flask	Minibioreactor
Manufacturer	Fisherbrand (Fisher Scientific)	DWK Life Sciences Inc. (Wheaton)	Global Process Concept (GPC)
Mixing mode	Orbital	Mechanical	Mechanical
Material	Plastic (single-use)	Siliconized glass	Siliconized glass
Diameter (mm)	66	40	60
$V_{working}$ (mL)	25	25	200
$N$ (rpm)	$N_{js} = 75$	$40 (< N_{js})$	$N_{js}^*$

\* $N_{js}$  value depends on the impeller design and is specified in result chapters.

### *MSC culture in Erlenmeyer flasks (orbital agitation)*

Cells were inoculated at a concentration of  $0.8 \cdot 10^6$  cells / mL, namely  $2 \cdot 10^6$  cells per flask. A gentle agitation was then applied to homogenize cell and microcarrier suspensions, and cultures were let without agitation during one hour to allow cell adhesion. The agitation rate was then fixed at the minimal agitation rate ensuring all particle suspension  $N = N_{js} = 75$  rpm (orbital diameter  $d_o = 10$  mm) (Fig. A.1). If indicated, 50 % of medium volume was exchanged, in order to ensure a sufficient glucose concentration for cell expansion and to reduce the lactate concentration.

At the end of the culture, the supernatant was removed and particles were washed with DPBS. 10 mL of TrypLE were then added with a complementary agitation at  $N = 75$  rpm, during 5 min. Fresh medium was used to stop the enzymatic digestion and cells were separated from microcarriers with a 70  $\mu\text{m}$  filtration step. Cell number and viability were determined before being frozen.

### *MSC culture in spinner flasks (mechanical agitation)*

Cells were inoculated at a concentration of  $0.8 \cdot 10^5$  cells / mL, namely  $2 \cdot 10^6$  cells per



Figure A.1: WJ-MSC culture in Erlenmeyer flasks.

flask, for 25 mL cultures (Fig. A.2). Because cultures performed at  $N = N_{js}$  led to cell lysis, it was decided to let cultures without agitation during one hour with gentle agitations at the beginning and at the mid-point, before working at a low agitation rate  $N = 40$  rpm, at which a sufficient number of particles were suspended without major hydromechanical stress [4]. If indicated, 50 % medium exchanges were performed, in order to ensure a sufficient glucose concentration for cell expansion and to reduce the lactate concentration.



Figure A.2: Spinner flask used for MSC culture on microcarriers.

At the end of the culture, the supernatant was removed and particles were washed with DPBS. 10 mL of TrypLE were then added with a complementary agitation at  $N = 40$  rpm, during 5 min. Fresh medium was used to stop the enzymatic digestion and cells were separated from microcarriers with a 70  $\mu\text{m}$  filtration step. Cell number and viability were determined before being frozen.



### *MSC culture in minibioreactors (mechanical agitation)*

MSC cultures in minibioreactors aimed at validating experimental conditions determined for cell expansion. Cell attachment phase on microcarriers was hence performed outside the minibioreactor. For four MSC cultures in minibioreactors, cells were initially inoculated at a concentration of  $1.5 \cdot 10^5$  cells / mL in 400 mL divided in  $2 \times 200$  mL in 500 mL Erlenmeyer flasks. A gentle agitation was then applied to homogenize cell and microcarrier suspension, and cultures were let without agitation during one hour to allow cell adhesion. Agitation rate was then fixed at  $N = 75$  rpm (orbital diameter  $d_o = 50$  mm). After one night, cells were considered to be completely adhered on microcarriers. The culture medium and the microcarrier suspension were equally distributed in the minibioreactors with 100 mL per reactor, completed by 100 mL pre-warmed fresh culture medium. Minibioreactors were previously equipped as shown in Fig. A.3, and an autoclave sterilization was performed at  $121^\circ\text{C}$  under 1 bar, during 20 min.

During MSC cultures, the temperature was regulated by a 20 W heat jacket and a cooling network at  $37^\circ\text{C}$ , the dissolved oxygen was maintained at 20 % of the air saturation by addition of  $\text{O}_2$  and  $\text{N}_2$  via a surface aeration, and the pH set-point was fixed at 7.3, controlled by  $\text{CO}_2$  addition. A 0.1 M NaOH solution was also prepared and connected to the minibioreactors, but no injection was needed during cultures performed in this work. Agitation rates were set at  $N = N_{js}$ , which depended on the impeller design. Values are given in more detail in result chapters, for each impeller design used.

Suspension samplings for cell expansion investigation were performed in a sterile area using a flame heat. Two consecutive aspirations and back-flows with the pipette were performed in order to disperse particles in the bottom of the bioreactor and recover a representative sample (homogenization). Suspension homogenization strategy using a higher agitation in the reactor was rejected in order to avoid supplementary hydromechanical stress on particles.

## **Analytical tools**

### **Cell morphology observation**

#### *Light microscopy*

Cell morphology and percentage of confluence of planar static cultures were determined using an inverse phase-contrast optical microscope (Axiovert-10, Zeiss, Germany), using LD Achrostat (Zeiss) lenses, displaying  $\times 5$  and  $\times 10$  magnifications, and based on white light. Photos were recorded using a numeric camera (Canon 400D Digital, Canon, Japan).

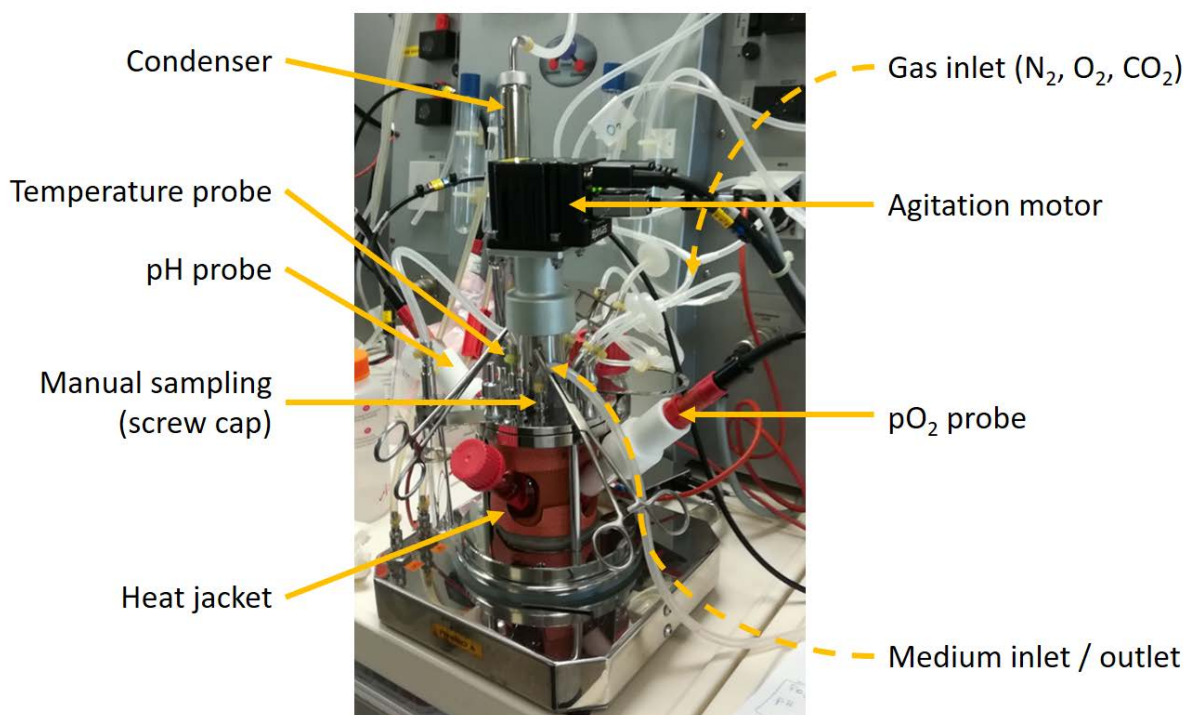


Figure A.3: WJ-MS culture in a minibioreactor.

### *Fluorescence microscopy*

Cell morphology on microcarriers and qualitative data on cell viability were obtained using a Live / Dead Cell double staining kit (Sigma). Calcein-AM is used to stain living cell membranes, whereas ethidium homodimer allows to stain dead cell nuclei. 200  $\mu\text{L}$  samples were recovered from a homogeneous particle suspension. After removing the supernatant, cells were stained using the Live / Dead kit (2  $\mu\text{L}$  EthD1 and 2  $\mu\text{L}$  Calcein-AM), during 30 min at 37°C. A fluorescence microscope was then used to qualitatively determine cell morphology. It was equipped with a HCX PI Fluostar, with a  $\times 5$  magnification, coupled to a Leica DFC450C camera and the integrated software LASV4.3 for photo post-treatment and recording.

### **Suspended cell counting**

After each detachment, cell number and cell viability were determined from cell suspensions of at least 0.7 mL, using the Vi-Cell<sup>TM</sup> Cell Viability Analyzer Counter (Beckman Counter), based on a Trypan Blue Dye Exclusion method.

### ***In situ* cell counting on microcarriers**

A dedicated analysis was developed to have a robust and quantitative method to directly count MSC cells attached on microcarriers, without detachment step. To do that, samples

of 200  $\mu\text{L}$  were recovered from homogeneous particle suspensions. After supernatant removing for metabolite analyses, cells were stained using a DAPI-methanol solution of 1  $\mu\text{g} / \text{mL}$  (DAPI from Sigma) during 15 min at room temperature. Cells were then washed with DPBS and microscopic analyses using the fluorescence microscope previously described, were performed. At least 5 photos per operating condition were recorded and loaded in a Matlab script for image post-treatment. First, microcarriers were identified by contour recognition and their coordinates were recorded. Secondly, based on the simple colour detection by the hue function of Matlab, a mask was applied in order to only keep the blue elements concerning cell nuclei after the DAPI staining. After contrast adjustments, a binarization was performed and cell coordinates were compared to microcarrier coordinates in order to get the number of cells per microcarrier. Validation of this method is detailed in section 2.3.

### Metabolite analysis

Glucose, lactate, glutamine, ammonia and lactate dehydrogenase (LDH) concentrations were measured from supernatant samples collected throughout the cultures, by using the Gallery multiparametric analyzer (Thermo Fisher Scientific). Glucose (GOD-POD), L-Lactic Acid and LDH (SCE) kits from Thermo Fisher Scientific and Glutamine V2 Bio and  $\text{NH}_3$  Bio kits from Roche were used.

## References

- [1] H. Hemedat, J. Kalz, G. Walenda, M. Lohmann, W. Wagner, Heparin concentration is critical for cell culture with human platelet lysate, *Cytotherapy* 15 (2013) 1174–1181.
- [2] S. Laner-Plamberger, T. Lener, D. Schmid, D. A. Streif, T. Salzer, M. Öller, C. Hauser-Kronberger, T. Fischer, V. R. Jacobs, K. Schallmoser, et al., Mechanical fibrinogen-depletion supports heparin-free mesenchymal stem cell propagation in human platelet lysate, *Journal of Translational Medicine* 13 (2015) 354.
- [3] K. Pachler, T. Lener, D. Streif, Z. A. Dunai, A. Desgeorges, M. Feichtner, M. Öller, K. Schallmoser, E. Rohde, M. Gimona, A good manufacturing practice-grade standard protocol for exclusively human mesenchymal stromal cell-derived extracellular vesicles, *Cytotherapy* 19 (2017) 458–472.
- [4] A. W. Nienow, C. J. Hewitt, T. R. Heathman, V. A. Glyn, G. N. Fonte, M. P. Hanga, K. Coopman, Q. A. Rafiq, Agitation conditions for the culture and detachment of hMSCs from microcarriers in multiple bioreactor platforms, *Biochemical Engineering Journal* 108 (2016) 24–29.
- [5] A. Delafosse, C. Loubière, S. Calvo, D. Toye, E. Olmos, Solid-liquid suspension of microcarriers in stirred tank bioreactor-experimental and numerical analysis, *Chemical Engineering Science* (2018) 52–63.

- [6] G. Montante, F. Magelli, Modelling of solids distribution in stirred tanks: analysis of simulation strategies and comparison with experimental data, *International Journal of Computational Fluid Dynamics* 19 (2005) 253–262.
- [7] A. Khopkar, G. Kasat, A. Pandit, V. Ranade, Computational fluid dynamics simulation of the solid suspension in a stirred slurry reactor, *Industrial & engineering chemistry research* 45 (2006) 4416–4428.
- [8] G. Montante, F. Magelli, Mixed solids distribution in stirred vessels: experiments and computational fluid dynamics simulations, *Industrial & Engineering Chemistry Research* 46 (2007) 2885–2891.
- [9] D. Guha, P. Ramachandran, M. Dudukovic, J. Derksen, Evaluation of large eddy simulation and euler-euler MSC models for solids flow dynamics in a stirred tank reactor, *AIChE Journal* 54 (2008) 766–778.
- [10] D. Wadnerkar, R. P. Utikar, M. O. Tade, V. K. Pareek, MSC simulation of solid–liquid stirred tanks, *Advanced Powder Technology* 23 (2012) 445–453.
- [11] A. Tamburini, A. Brucato, A. Cipollina, G. Micale, M. Ciofalo, CFD predictions of sufficient suspension conditions in solid-liquid agitated tanks, *International Journal of Nonlinear Sciences and Numerical Simulation* 13 (2012) 427–443.
- [12] S. Kaiser, V. Jossen, C. Schirmaier, D. Eibl, S. Brill, C. van den Bos, R. Eibl, Fluid flow and cell proliferation of mesenchymal adipose-derived stem cells in small-scale, stirred, single-use bioreactors, *Chemie Ingenieur Technik* 85 (2013) 95–102.
- [13] C. Schirmaier, V. Jossen, S. C. Kaiser, F. Jüngerkes, S. Brill, A. Safavi-Nab, A. Siehoff, C. Bos, D. Eibl, R. Eibl, Scale-up of adipose tissue-derived mesenchymal stem cell production in stirred single-use bioreactors under low-serum conditions, *Engineering in Life Sciences* 14 (2014) 292–303.
- [14] V. Jossen, S. C. Kaiser, C. Schirmaier, J. Herrmann, A. Tappe, D. Eibl, A. Siehoff, C. van den Bos, R. Eibl, Modification and qualification of a stirred single-use bioreactor for the improved expansion of human mesenchymal stem cells at benchtop scale, *Pharmaceutical Bioprocessing* 2 (2014) 311–322.
- [15] s. n. Fluent, *Ansys fluent theory guide 15.0*, Inc, Canonsburg, PA (2013).
- [16] M.-L. Collignon, A. Delafosse, S. Calvo, C. Martin, A. Marc, D. Toye, E. Olmos, Large-eddy simulations of microcarrier exposure to potentially damaging eddies inside mini-bioreactors, *Biochemical Engineering Journal* 108 (2016) 30–43.

Appendix B:  
Solid-liquid suspension of microcarriers in  
stirred tank bioreactor - Experimental and  
numerical analysis



## Solid-liquid suspension of microcarriers in stirred tank bioreactor – Experimental and numerical analysis

Angélique Delafosse<sup>a,b,c,\*</sup>, Céline Loubière<sup>b,c</sup>, Sébastien Calvo<sup>a</sup>, Dominique Toye<sup>a</sup>, Eric Olmos<sup>b,c</sup>

<sup>a</sup> Laboratory of Chemical Engineering, Université de Liège, Allée de la Chimie 3, B6C, 4000 Liège, Belgium

<sup>b</sup> CNRS, Laboratoire Réactions et Génie des Procédés, UMR 7274, 2 avenue de la forêt de Haye, TSA 40602, Vandœuvre-lès-Nancy F-54518, France

<sup>c</sup> Université de Lorraine, LRGP, UMR 7274, 2 avenue de la forêt de Haye, TSA 40602, Vandœuvre-lès-Nancy F-54518, France

### HIGHLIGHTS

- Experimental and numerical analysis of microcarrier suspension in STR.
- Cytodex-1 microcarriers with  $d_p = 162.2 \mu\text{m}$  and  $\rho_s = 1020 \text{ kg m}^{-3}$  at 10%v.
- Solid spatial distributions are obtained from light attenuation measurements.
- Analysis of spatial distribution enables the determination of  $N_{js}$ .
- CFD simulation predicts  $N_{js}$  but not the solid spatial distributions.

### ARTICLE INFO

#### Article history:

Received 25 July 2017

Received in revised form 15 December 2017

Accepted 2 January 2018

Available online 11 January 2018

#### Keywords:

Microcarrier suspension

Bioreactor

CFD

Granular-Eulerian model

Light attenuation experiments

Spatial distribution

### ABSTRACT

Solid-liquid suspensions in stirred tank reactors are common operations in many processes, including bioprocesses such as animal or stem cell cultures. These cells are often anchorage-dependent, i.e. they need to adhere to a surface to grow. Typically, they are cultivated on the surface of small spherical microbeads, the so-called microcarriers, suspended in stirred-tank bioreactors.

As far as we know, no extensive experimental characterization, and thus no validated simulation approach, of microcarrier suspensions in stirred-tank reactor exists in the literature. Therefore, the first aim of this work is to develop an experimental technique based on light attenuation to characterize the spatial distribution of particle concentration for various particle suspension states. The second aim is to determine the validity of Euler-Euler CFD simulations to predict the spatial distribution of low density particles, such as microcarriers, in a stirred tank bioreactor.

Experiments and simulations were performed in a small hemispherical bottom bioreactor stirred with a down-pumping axial impeller. The particles used were Cytodex-1 microcarriers ( $d_p = 162 \mu\text{m}$  and  $\rho_s = 1020 \text{ kg m}^{-3}$ ) at a solid concentration of 10% in volume.

The light attenuation technique enabled the characterization of the spatial distribution of the solid phase in the whole bioreactor, even for very dense suspensions by advantageously using the optical properties of the Cytodex-1 microcarriers. The analysis of the solid spatial distribution shows that the bioreactor volume can be divided in three distinct zones: a clear layer below the free surface where  $\alpha_{s,layer}$  tends to 0, a bulk zone where the solid phase is homogeneously distributed ( $\alpha_{s,bulk} \leq \langle \alpha_s \rangle$ ) and a packed bed of motionless particles at the bottom ( $\alpha_{s,bed} = \alpha_{s,max}$ ). One very interesting finding is that the evolution of the bulk solid concentration is directly proportional to the agitation rate and its value equals the averaged volume fraction  $\alpha_{s,bulk} = \langle \alpha_s \rangle$  at  $N = N_{js}$ .

Concerning the simulation results, the modeling approach presented in this work enables a reasonable estimation of the just-suspended agitation rate  $N_{js}$ . Nevertheless, the solid spatial distributions are not well predicted for agitation rates below or above  $N_{js}$ . The solid concentration at the vessel bottom is underestimated for  $N < N_{js}$  but overestimated for  $N \geq N_{js}$ .

© 2018 Elsevier Ltd. All rights reserved.

\* Corresponding author at: Department of Chemical Engineering, Université de Liège, Allée de la Chimie 3, B6C, 4000 Liège, Belgium.

E-mail address: [angelique.delafosse@uliege.be](mailto:angelique.delafosse@uliege.be) (A. Delafosse).

## Nomenclature

### Variables

$d_p$	particle diameter (m)
$k$	turbulent kinetic energy ( $\text{m}^2 \text{s}^{-2}$ )
$u$	instantaneous velocity ( $\text{m s}^{-1}$ )
$u_{T,0}$	terminal velocity of an isolated particle ( $\text{m s}^{-1}$ )
$u_{T,\alpha_s}$	terminal velocity of a particle swarm ( $\text{m s}^{-1}$ )
$V$	volume ( $\text{m}^3$ )
$x_{\text{susp}}$	fraction of particles in suspension ( )

### Greek letters

$\alpha$	solid volume fraction ( )
$\langle \alpha \rangle$	volume-averaged solid volume fraction ( )
$\varepsilon$	turbulent dissipation rate ( $\text{m}^2 \text{s}^{-3}$ )
$\rho$	density ( $\text{kg m}^{-3}$ )
$\mu$	dynamic viscosity (Pa s)

### dimensionless number

$C_D$	drag coefficient ( )
$Re_p$	terminal Reynolds number ( )
$Re_s$	particulate Reynolds number ( )

### Subscripts

bed	particles in the bottom zone
bulk	bulk zone
js	just-suspended
L	liquid phase
layer	layer of liquid near the surface
$m$	mixture
P	particle
S	solid phase

## 1. Introduction

Chemical and biochemical processes that involve solid-liquid suspension in stirred tank reactors are quite common in many applications. Among these, the culture of anchorage-dependent animal cells has recently found new interest for the culture of mesenchymal stromal cells (MSC), for cell therapies purpose. These anchorage-dependent cells need a support to grow. While in 2D systems such as T-flasks, these surfaces are planar, for large-scale culture, the preferred supports are small spheres, the so-called microcarriers (Martin et al., 2017; Ferrari et al., 2012). In order to maximize the adherence surface and to limit cell-cell aggregation, it is necessary to ensure the dispersion of these particles by mechanical stirring.

Beside this, animal cell bioreactor design and scale-up rules usually include upper limits for agitation rates as these cells are potentially damaged by hydromechanical stresses due to collisions or to interactions with turbulent eddies. One way to predict the occurrence of these damaging eddies is to compare the Kolmogorov scale  $l_K$  to the characteristic cell size (Nienow, 2006). Whereas this criterion is well defined for animal cells cultivated in suspension mode, in the case of anchorage-dependent animal cell culture, it is not clear whether the characteristic length scale to consider should be the cell,  $d_c \approx 10\text{--}20 \mu\text{m}$ , or the microcarrier size,  $d_c \approx 100\text{--}300 \mu\text{m}$  (Nienow et al., 2014). Nevertheless, to minimize damages, anchorage-dependent animal cell cultures are usually operated at the 'just-suspended' agitation rate  $N_{js}$  that ensures a complete suspension of the particles (namely, particles do not stay static more than a few seconds at the vessel bottom).

Because the ratio of microcarrier and culture medium density is close to 1 ( $\rho_s \approx 1010\text{--}1100 \text{kg m}^{-3}$ ), allowing a relatively easy suspension of the particles but also preventing their flotation (Ibrahim and Nienow, 2004), the bioreactor operates at low power dissipation per unit of mass  $\varepsilon$  thus entailing relatively large Kolmogorov scales ( $l_K = (v^3/\varepsilon)^{0.25}$ ), even in the impeller region. In most cases, the Kolmogorov scale is expected to be very close to the microcarrier diameter.

The 'just-suspended' agitation rate  $N_{js}$  is classically determined by using the relationship of Zwietering (1958), which was built using dimensional analysis. Its dimensional form is given by:

$$N_{js} = S \cdot v^{0.1} \cdot d_p^{0.2} \left( \frac{g \cdot (\rho_s - \rho_L)}{\rho_L} \cdot X^{0.13} \cdot D^{-0.85} \right) \quad (1)$$

where  $S$  is a dimensionless parameter that depends on impeller design and geometric ratios,  $N$  ( $\text{s}^{-1}$ ) the agitation rate,  $D$  (m) the impeller diameter,  $X$  ( $\text{g g}^{-1}$ ) the mass fraction of particles,  $\rho_L$  and  $\rho_s$  ( $\text{kg m}^{-3}$ ) the liquid and solid densities respectively and  $d_p$  (m) the particle diameter.

Eq. (1) offers robust precision for relatively heavy particles, but it was previously shown that, for microcarriers, a 50% overestimation of  $N_{js}$  was obtained, due to the low density gradient between the particles and the liquid phase (Ibrahim and Nienow, 2004).

Furthermore, the  $N_{js}$  criterion is not sufficient to characterize the spatial distribution of microcarriers. Indeed, operating a mixing vessel at an agitation rate of  $N_{js}$  does not imply that the microcarriers are homogeneously distributed in the whole liquid volume or even that some of them have at least reached the liquid surface. The direct consequence of heterogeneous distribution of microcarriers in the bioreactor is that the trajectories of the cells attached on the microcarriers differ from the liquid phase streamlines, meaning that the distribution of the hydromechanical stress on the microcarriers does not match with the distributions in the liquid phase as qualitatively demonstrated by Collignon et al. (2016). Thus, to bring new knowledge on microcarrier suspension in stirred tank bioreactor but also to refine the design and scale-up rules of these systems, it is necessary to accurately determine the spatial distribution of the microcarriers as a function of the bioreactor and impeller design, of the operating conditions and of the solid properties and concentrations, with a special attention paid to the just-suspended state. This characterization may be based either on experiments, either on numerical modeling or on a combination of both.

Various experimental techniques have been developed and used these last few years to access the local concentration of particles suspended in a mixing vessel (Tamburini et al., 2013). However, experimental techniques were usually used with particles of significantly higher density and/or diameter than microcarriers (typically glass beads or sand particles with density  $\rho = 2500 \text{kg m}^{-3}$ ). These techniques can be either intrusive or not and measure particle concentration punctually or on two-dimensional planes. Most of intrusive local measurements are based on the use of probes whose principles of operation were based on impedance (Micheletti et al., 2003), acoustic attenuation (Zheng and Zhang, 2004) or light (Angst and Kraume, 2006). These intrusive techniques present the disadvantages of potentially disturbing the liquid and solid flows and of providing only local information on particle concentration. In parallel to these techniques,

non-intrusive measurements such as Positron Emission Particle Tracking (Barigou, 2004), Electrical Tomography (Hosseini et al., 2010) or Computer Aided Particle Tracking (Dudukovic, 2002) have also found great interest to characterize liquid-solid flows, but they generally raise safety and costs issues. The complexity of data post-treatment also makes the generalization of their use difficult. More recently, Tamburini et al. (2009), Tamburini et al. (2013) and Peralisi et al. (2016) have developed laser techniques coupled with image analysis which provided the particle concentration distributions maps in stirred reactors and shaking flasks. This last technique brought new knowledge on the solid flow in liquid-solid suspensions, but as most of the techniques based on light, it is limited to very low particle concentrations (<1%v) for the study of Tamburini et al. (2013). More details concerning the advantages and drawbacks of the preceding methods can be found in the exhaustive study of Tamburini et al. (2013). Concerning the use of numerical modeling, a number of works have been conducted on simulations of solid-liquid suspensions in stirred tanks by Computational Fluid Dynamics. To model solid-liquid flow, two approaches can be used: the Euler-Lagrange approach, which considers the particles as a discrete phase and solves their individual motion, and the Euler-Euler approach, which models the dispersed solid phase as a continuum. Due to its high computational demand, the Euler-Lagrange approach is limited to very low solid volume fractions ( $\alpha_s \ll 1\%$ ) and has only been used by few authors (Derksen, 2003; Guha et al., 2008; Berry et al., 2016). Note that in the study of Berry et al. (2016) an Euler-Lagrange approach with Large Eddy Simulation was used to model the suspension of microcarriers in a spinner flask bioreactor. Similarly to Collignon et al. (2016), these authors have showed that the spatial distribution of the microcarriers has a significant impact on the prediction of the shear stress they could encounter in the mixing vessel. However, their study was limited to only 10,000 particles which appears insufficient when higher solid volume fractions or larger bioreactors should be characterized.

The Euler-Euler approach, often coupled with a granular description of the solid phase, allows the simulation of significantly denser suspensions than the Euler-Lagrange approach. Turbulence is modeled using RANS decomposition of transport equations and widely-used turbulence models such as  $k-\varepsilon$ -based models (Guha et al., 2008; Sardeshpande et al., 2010; Khopkar et al., 2006; Montante and Magelli, 2005, 2007; Tamburini et al., 2012a,b; Wadnerkar et al., 2012, 2016). Literature data thus show that, for the determination of just-suspended agitation rates or spatial distributions of solid concentrations, the Euler-Euler approach can bring valuable predictions as far as closure and interfacial forces (drag, turbulent dispersion) are carefully chosen. However, in most cases, and similarly to experimental measurements, the particles considered in available literature have a significantly higher density than the microcarriers used in cell cultures, with the exception of the works of Kaiser et al. (2013) and Schirmaier et al. (2014). They used a RANS Euler-Euler approach to simulate the microcarrier dispersion in various bioreactor designs (spinner flask, 2L and 50 STR). The agreement between calculated axial liquid velocities and PIV measurements was very good but no comparison with solid phase distribution was proposed. Moreover, the model of drag force used was not mentioned by these authors and they did not precise whether other forces were also considered in the simulations.

As far as we know, no extensive experimental characterization, and thus no validated simulation approach, of microcarrier suspensions in stirred-tank reactor exists in the literature. Therefore, the first aim of this work is to develop an experimental technique based on light attenuation to characterize the spatial distribution of particle concentration for various particle suspension states,

i.e. from partial to homogeneous suspension. Such a technique is usually limited to low volume fraction of solids (Tamburini et al., 2013) but, in the present study, industrially widely used Cytodex-1 microcarriers are used. As these microcarriers are transparent, their optical properties are *a priori* compatible with the use of an optical technique to characterize their distribution in liquid up to high volume fractions.

The second aim of the present study is to determine the validity of Euler-Euler CFD simulations to predict the spatial distribution of low density particles, such as microcarriers, in a stirred tank bioreactor. To do this, simulations are performed with the commercial CFD code ANSYS Fluent for several agitation rates (below and above the just-suspended rate  $N_{js}$ ) in a vessel equipped with an axial flow impeller.

## 2. Experimental approach

### 2.1. Bioreactor configuration

The bioreactor studied is an hemispheric-bottom glass bioreactor of working volume  $V = 1.12$  L ( $H = T = 0.12$  m) and designed to be used for animal cell culture (see Fig. 1). For this purpose, it is equipped with three probes (dissolved oxygen, pH and temperature) and an oxygen sparger; these internal parts were kept during the experiments and the CFD simulations to take their impact on the solid-liquid suspension into account. Two flat baffles are attached to the sparger and to the probe diametrically opposite to the sparger. The bioreactor is stirred by an axial down-pumping 3-blade impeller (commercially referenced as HTPG, Pierre Guérin). Its diameter is  $D = T/2 = 0.06$  m and it is located at a clearance  $C = D = 0.06$  m from the tank bottom.

### 2.2. Microcarrier characteristics

The particles used in this work are the commercial microcarriers Cytodex-1<sup>TM</sup> (GE Healthcare), widely used in cell culture applications. Cytodex-1 is made of cross-linked dextran matrix which is substituted with positively charged N, N-diethylaminoethyl groups. These microcarriers are commercialized in dry form and swell when placed in a saline solution. It is important to note that microcarrier diameter and density significantly depend on the salt concentration in the solution. In this work, the microcarriers are swelled in a phosphate buffer saline (PBS) solution of concentration 0.01 M which is classically used in animal cell culture. To ensure a homogeneous swelling of the microcarriers, the solutions are placed during one night under low agitation before their use in the bioreactor.

The mean value of microcarrier diameter has been measured from microscope image analysis, in solution (wet form) as well as in dry form. In both states (dry and wet), the particle shape is

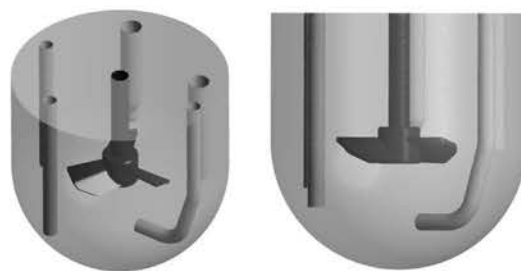
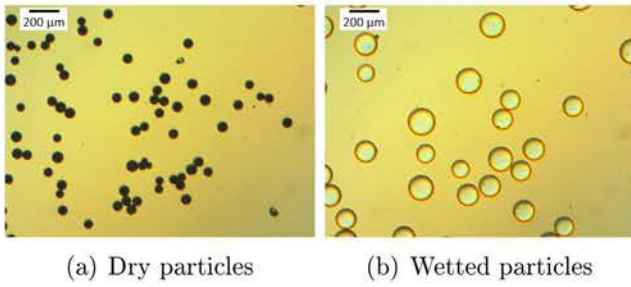


Fig. 1. Stirred-tank bioreactor used in this work.





**Fig. 2.** Microscope images of Cytodex-1 microcarriers in (a) dry form and (b) swelled in PBS solution.

found to be perfectly spherical (Fig. 2). The measured mean diameter of wet particles is  $d_p = 162 \mu\text{m}$ .

Their wet density is estimated using two methods. First, the density of the dry particles is measured by weighing a known volume of particles. Assuming a solid volume fraction of 0.63 (maximum value for a random packing of spheres of equal diameter) and using the solution density and the swelling factor between the dry and wet particles computed from their measured diameters, the wet particles density could be estimated (Eq. (2)). Due to measurement imprecision and to the uncertainty relative to the bed void fraction, the estimated values of the swelled microcarrier density range between  $1015$  and  $1025 \text{ kg m}^{-3}$ .

$$\rho_s = \frac{d_{p,dry}^3}{d_{p,wet}^3} \rho_{s,dry} + \left(1 - \frac{d_{p,dry}^3}{d_{p,wet}^3}\right) \rho_L \quad (2)$$

In a second step, the settling velocity is measured as a function of the microcarrier volume fraction ( $0.025 < \alpha_s < 0.2$ ). The hindered settling velocity  $u_{T,\alpha_s}$  of particles in a quiescent liquid can be related to the terminal settling velocity of a single particle  $u_{T,0}$  and to the solid volume fraction  $\alpha_s$  using the Richardson and Zaki law (Richardson and Zaki, 1997) as follows:

$$u_{T,\alpha_s} = u_{T,0}(1 - \alpha_s)^n \quad (3)$$

$$u_{T,0} = \sqrt{\frac{4d_p g(\rho_s - \rho_L)}{3C_D \rho_L}} \quad (4)$$

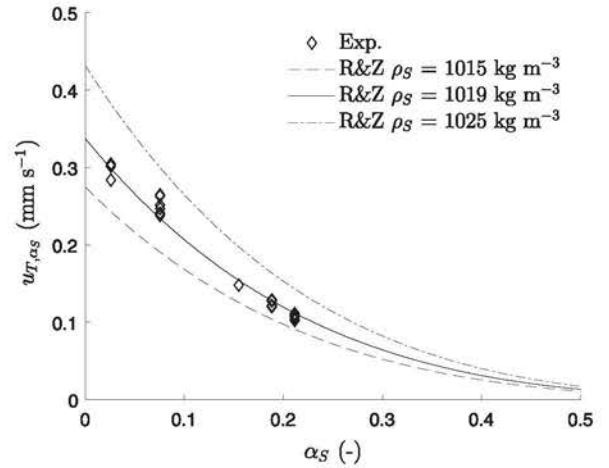
$$C_D = \frac{24}{Re_p} \text{ for } Re_p < 1 \quad (5)$$

$$Re_p = \frac{\rho_L d_p u_{T,0}}{\mu_L} \quad (6)$$

As the particle Reynolds number is  $Re_p < 0.2$ , the Richardson and Zaki index is  $n = 4.65$  (Richardson and Zaki, 1997).

The measured hindered settling velocity is plotted in Fig. 3 (diamond symbols). The hindered settling velocity computed from the Richardson and Zaki model (Eq. (3)) is also plotted considering  $d_p = 162.2 \mu\text{m}$  and  $\rho_s = 1019 \text{ kg m}^{-3}$  (continuous black line), as well as  $\rho_s = 1015 \text{ kg m}^{-3}$  and  $\rho_s = 1025 \text{ kg m}^{-3}$  (dashed gray lines). The sensitivity of the hindered settling velocity, and thus of the drag coefficient  $C_D$ , to the solid density is quite significant, due to the low density difference between the liquid and solid phase.

The properties of the microcarriers used in this study, i.e. density and diameters, in dry as well as wet form are summarized in Table 1.



**Fig. 3.** Impact of microcarrier volume fraction  $\alpha_s$  on hindered settling velocity  $u_{T,\alpha_s}$ .

**Table 1**

Wet and dry properties of the microcarriers used in this study.

	Dry	In solution
$\rho_s$ ( $\text{kg m}^{-3}$ )	1250	1019
$d_{50}$ ( $\mu\text{m}$ )	68.2	162.2
$d_{5-95}$ ( $\mu\text{m}$ )	55–81	133–194



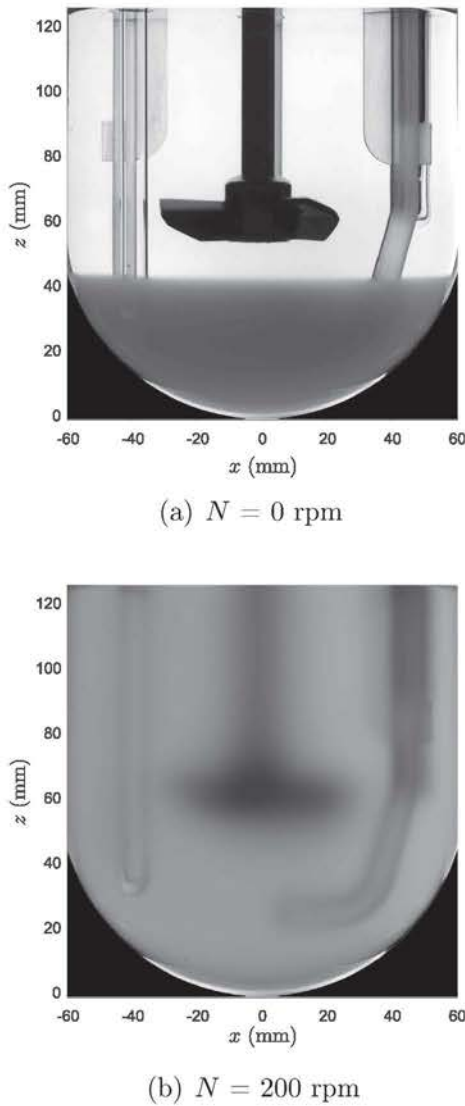
**Fig. 4.** Configuration of the experimental apparatus for light attenuation measurements.

### 2.3. Light attenuation technique

The setup used to measure the solid phase distribution is presented in Fig. 4. It is based on the measurements of light attenuation through the microcarrier suspension.

During measurements, the bioreactor is placed in a square aquarium filled with water to minimize optical deformation. A white LED backlight (Phlox s.a.,  $70\,000 \text{ cd m}^{-2}$ ) is placed against one side of the aquarium in order to illuminate the bioreactor containing the suspension of microcarriers and a CMOS camera is placed on the opposite side of the bioreactor (Fig. 4).

In order to relate the gray levels of each pixel in the images recorded by the camera to the local volume fraction of particles, the technique has to be calibrated by measuring the light attenuation through homogeneous microcarrier suspensions. For this purpose, averaged volume fractions  $\langle \alpha_s \rangle$  ranging between 0.01 and 0.44 have been used. For all solid concentrations, an agitation rate of  $N = 200 \text{ rpm}$  allows to obtain an homogeneous solid suspension.



**Fig. 5.** Gray level images at (a)  $N = 0$  rpm (packed bed) and (b)  $N = 200$  rpm (homogeneous suspension) for a volume-averaged volume fraction of  $\langle \alpha_S \rangle = 0.1$ .

The measurements of solid volume fractions by light attenuation techniques are usually limited to low particle volume fractions, namely approximately a few percents (Tamburini et al., 2013). However, Cytodex-1 microcarriers are transparent and do not reflect or refract light as plastic or glass beads do. As a consequence, the light is not completely attenuated even for volume fractions close to the microcarrier packing limit ( $\alpha_{S,max} = 0.51$ ), as it can be seen in Fig. 5a.

One drawback of this technique is that the measured light attenuations are integrated over the bioreactor thickness. Thus, solid concentration gradients along the horizontal light paths will not be measured. However, experimental and numerical results indicate that gradients are mostly observed in the vertical direction and that horizontal gradients are not present, except at the bioreactor bottom when a bed of motionless particles is present.

### 3. Numerical approach

#### 3.1. Multiphase modeling

Simulations of the solid-liquid suspension for an average volume fraction of 10% are performed with the commercial CFD code Ansys Fluent 16.2 for agitation rates between 40 and 100 rpm. The

Euler-Euler approach considering the two phases as interpenetrating continua is used. Continuity and momentum equations are solved for each phase separately (Eqs. (7)–(10)). The granular model is also included in the simulations. It enables to take into consideration the maximum packing limit achievable ( $\alpha_{S,max} = 0.51$ ). It also takes the interactions between the particles into account, through the introduction of a solid pressure term  $\nabla p_S$  in the solid phase momentum transport equation. The simulations are performed in steady state using the Moving Reference Frame approach to model the impeller rotation. Continuity and momentum conservation equations are then established as:

*Liquid phase*

$$\nabla \cdot (\alpha_L \rho_L \vec{u}_L) = 0 \quad (7)$$

$$\begin{aligned} \nabla \cdot (\alpha_L \rho_L \vec{u}_L \otimes \vec{u}_L) = & -\alpha_L \nabla p + \alpha_L \rho_L \vec{g} + \vec{F}_{LS} \\ & + \nabla \cdot (\alpha_L (\mu_L + \mu_{t,L}) (\nabla \vec{u}_L + (\nabla \vec{u}_L)^T)) \end{aligned} \quad (8)$$

*Solid phase*

$$\nabla \cdot (\alpha_S \rho_S \vec{u}_S) = 0 \quad (9)$$

$$\begin{aligned} \nabla \cdot (\alpha_S \rho_S \vec{u}_S \otimes \vec{u}_S) = & -\alpha_S \nabla p - \nabla p_S + \alpha_S \rho_S \vec{g} - \vec{F}_{LS} + \vec{F}_{SS} \\ & + \nabla \cdot (\alpha_S (\mu_S + \mu_{t,S}) (\nabla \vec{u}_S + (\nabla \vec{u}_S)^T)) \end{aligned} \quad (10)$$

where  $\vec{g}$  is the acceleration due to gravity,  $p$  the pressure shared by both phases and  $p_S$  the solid pressure.  $\vec{F}_{LS}$  is the interaction forces between phases L and S arising from drag force (Eq. (11)).  $\vec{F}_{SS}$  is the solid-solid interaction force modeled according to Syamlal (1987).

$$\vec{F}_{LS} = K_{LS} (\vec{u}_S - \vec{u}_L) \quad (11)$$

where  $K_{LS}$  is the momentum exchange coefficient between phases L and S.

The liquid-solid exchange coefficient  $K_{LS}$  is modeled using the Huilin-Gidaspow model (12), which is a combination of the Wen and Yu model (Eq. (14)) for solid volume fractions less than 0.2 and the Ergun equation (Eq. (17)) for higher solid volume fractions.

$$K_{LS} = \phi K_{LS,Ergun} + (1 - \phi) K_{LS,Wen/Yu} \quad (12)$$

with the switching function  $\phi$  given by:

$$\phi = \frac{1}{2} + \frac{\arctan(262.5(\alpha_S - 0.2))}{\pi} \quad (13)$$

The liquid-solid exchange coefficient for low volume fractions is obtained by:

$$K_{LS,Wen/Yu} = \frac{3}{4} C_D \frac{\alpha_S \alpha_L \rho_L |\vec{u}_S - \vec{u}_L|}{d_p} \alpha_L^{-2.65} \quad (14)$$

with the drag coefficient  $C_D$  given by:

$$C_D = \frac{24}{\alpha_L Re_S} \left[ 1 + 0.15 (\alpha_L Re_S)^{0.687} \right] \quad (15)$$

and the Reynolds number  $Re_S$  by:

$$Re_S = \frac{\rho_L d_p |\vec{u}_S - \vec{u}_L|}{\mu_L} \quad (16)$$

For high volume fraction, the liquid-solid exchange coefficient is obtained by:

$$K_{LS, Ergun} = 150 \frac{\alpha_s(1-\alpha_L)\mu_L}{\alpha_L d_p^2} + 1.75 \frac{\rho_L \alpha_s |\vec{u}_s - \vec{u}_L|}{d_p} \quad (17)$$

The turbulent quantities are solved using the 'mixture' standard k-epsilon model, meaning the turbulence quantities are calculated for the mixture of liquid and solid phases at the mixture density  $\rho_m$  and viscosity  $\mu_m$ . This model is especially adapted when the density ratio between phases is close to 1, which is the case in this work. By solving the transport equations of the turbulent kinetic energy  $k$  and turbulent dissipation rate  $\varepsilon$  for the mixture phase, the turbulence model then provides the mixture turbulent viscosity  $\mu_{t,m}$ :

$$\mu_{t,m} = 0.09 \rho_m \frac{k^2}{\varepsilon} \quad (18)$$

which further allows the determination of the turbulent viscosity of phase  $i$  by  $\mu_{t,i} = (\rho_i/\rho_m)\mu_{t,m}$  used in Eqs. (8) and (10).

### 3.2. Solution strategy

Transport equations are discretized on a mesh containing approximately one million of tetrahedral cells. The mesh is refined in the impeller zone as well as at the bottom of the bioreactor where a packed bed of motionless particles may be expected. Second order Upwind discretization schemes are used for the momentum and turbulence equations and the QUICK scheme is used for the discretization of the volume fraction transport equation.

Simulations are initialized with a uniform volume fraction  $\alpha_s = 10\%$  for all simulated agitation rates ( $40 < N < 100$  rpm).

## 4. Results

### 4.1. Experimental results

#### 4.1.1. Calibration of the light attenuation technique

Following the Beer-Lambert law, the light attenuation, measured in terms of gray level ratio in each pixel of an image, can be related to the averaged solid volume fraction as follows:

$$-\log\left(\frac{A}{A_0}\right) = k\langle\alpha_s\rangle \quad (19)$$

where  $A$  is the gray level measured for a homogeneous microcarrier suspension of average volume fraction  $\langle\alpha_s\rangle$  and  $A_0$  is the gray level measured in pure water ( $\langle\alpha_s\rangle = 0$ ).

As an example, the calibration curve obtained for a given pixel located below the impeller ( $x = 0$  mm;  $z = 25$  mm) is plotted in Fig. 6. for solid volume fractions up to  $\langle\alpha_s\rangle = 0.15$ , the volume fraction is found to be directly proportional to the logarithm of the gray level ratio for all pixels. However, for solid volume fractions  $\langle\alpha_s\rangle > 0.15$ , the experimental data have to be modeled using a third-order polynomial. For  $\langle\alpha_s\rangle < 0.15$ , the differences between the two fits are negligible and so the 3rd degree polynomial law may be used to convert gray level ratios to solid volume fractions for the whole range of solid volume fraction.

To validate the calibration procedure, the volume-averaged solid volume fraction computed on local values obtained from attenuation images are compared to the expected solid concentrations. This validation has been done for agitation rates below and above  $N_{js}$  and for the whole range of solid concentrations used. For all conditions tested, the measured values are in excellent agreement with the expected values (Fig. 7). The mean and maximum absolute errors observed between the expected and

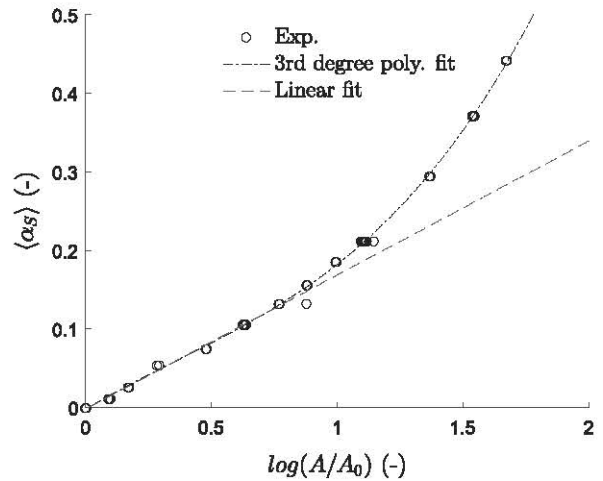


Fig. 6. Calibration curve in a pixel located below the impeller, at mid distance between the tank bottom and the impeller bottom ( $x = 0$  mm and  $z = 25$  mm).

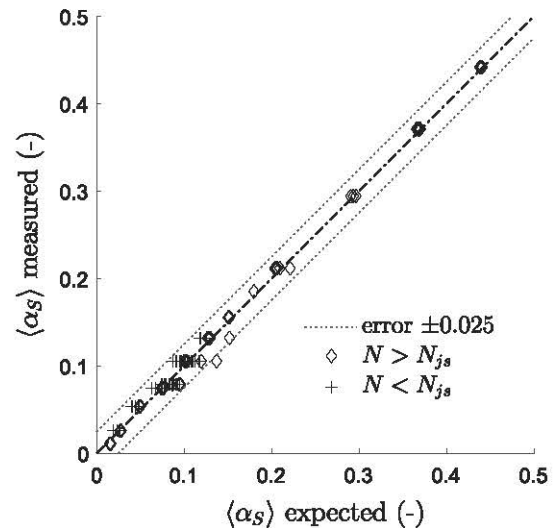


Fig. 7. Plot of the volume-averaged volume fractions of microcarriers  $\langle\alpha_s\rangle$  in the bioreactor measured by the light attenuation technique against the modeled values.

measured values of the average volume fraction are equal to 0.4 and 2.5%, respectively. Moreover, for homogeneous suspensions ( $N \gg N_{js}$ ) the standard deviation computed between expected  $\langle\alpha_s\rangle$  and measured  $\alpha_s$  in each pixel of an image do not exceed 2.2% and its average value computed from all homogeneous suspensions is equal to 1%.

#### 4.1.2. Suspension results

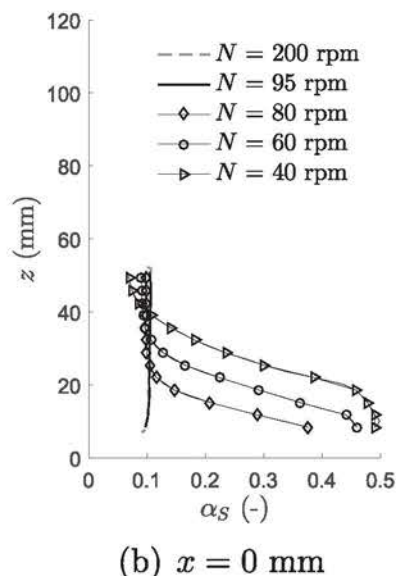
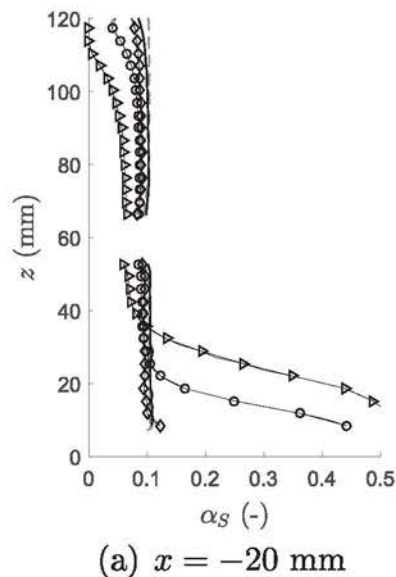
The spatial distribution of microcarriers was characterized for various agitation rates varying from 30 to 200 rpm for a solid concentration  $\langle\alpha_s\rangle = 0.1$ . In parallel, the minimal agitation rate required to just suspend all the particles,  $N_{js}$ , was visually determined according to the Zwietering criterion. Because of its simplicity, the visual method is still widely used for the determination of  $N_{js}$ , despite a number of drawbacks. For examples, it is a subjective criterion that can lead to significant differences depending on the observer, it is limited to transparent vessels and this method becomes difficult to apply with dense suspension of opaque particles. As the microcarriers used in this work are transparent, the last point was not really an issue. For an average volume fraction  $\langle\alpha_s\rangle = 0.1$ ,  $N_{js} = 95 \pm 2$  rpm. Nevertheless, a method to determine

$N_{js}$  in a more 'robust' objective way was developed using the results obtained with the light attenuation technique.

Fig. 8 presents two vertical profiles (see Fig. 1) of the measured volume fractions for several agitation rates: (a) at 20 mm (on the left of the impeller axis) and (b) at  $x = 0$  mm, below the impeller.

From the analysis of the spatial distribution of microcarriers in the bioreactor as a function of agitation rates, the solid-liquid suspension could schematically be decomposed into three distinct zones:

1. Just below the liquid surface, a clear layer where the volume fraction is significantly lower than in the bulk such as  $\alpha_{S,layer} \approx 0$ .
2. On the tank bottom, below the impeller, a packed bed of motionless particles, where the volume fraction is close to the packing limit ( $\alpha_{S,bed} \approx \alpha_{S,max}$ ).
3. In the rest of the bioreactor volume, a bulk zone where the solid volume fraction is uniform but inferior or equal to the average volume fraction ( $\alpha_{S,bulk} \leq \langle \alpha_S \rangle$ ).



These zones are depicted in Fig. 9 (a) for an agitation rate  $N = 50$  rpm. The corresponding contours of volume fraction are also plotted in Fig. 9 (b).

For agitation rates  $N \leq 80$  rpm, the presence of a bed with high solid fractions is clearly visible at the bioreactor bottom. Unfortunately, because of the light reflection of the vessel bottom and the presence of a shadow, approximately 7 mm of the bottom is masked on the recorded images. As a consequence, for agitation rates between  $N = 80$  rpm and  $N_{js} = 95$  rpm, no clear bed is detected on the images, although its presence is attested by visual observations up to  $N_{js}$ . The packed bed observed on the tank bottom has a "bell curve" shape (Fig. 9). But, it was not possible to directly determine its shape or its volume from recorded images because the volume fractions obtained with the light attenuation are integrated over the bioreactor thickness. Therefore, a direct measurement of  $N_{js}$ , based on the identification of the minimal agitation rate for which the volume of the packed bed becomes zero, is not possible from the light attenuation results.

Nevertheless,  $N_{js}$  can also be defined as the minimal agitation rate for which all particles are suspended. The fraction of particles which are suspended can be estimated from the experimental results by solving a simple mass balance based on the three zones identified previously. Knowing the volume of the clear layer below the surface  $V_{layer}$ , as well as the volume fraction in the bulk  $\alpha_{S,bulk}$

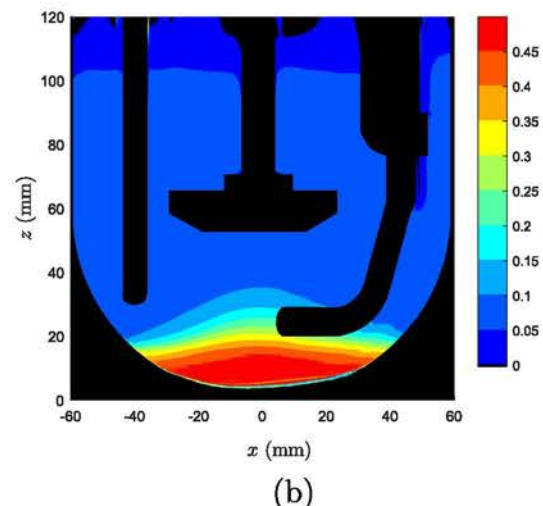
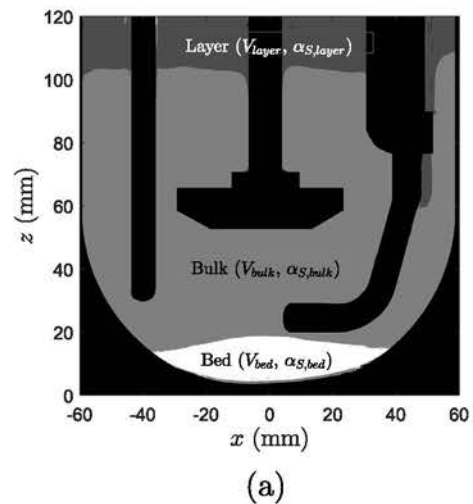


Fig. 8. Vertical profiles of solid volume fractions measured by the light attenuation technique at various agitation rates for an averaged volume fraction  $\langle \alpha_S \rangle = 0.1$ .

Fig. 9. Schematic decomposition of the liquid-solid suspension into three zones (a) and corresponding contours of microcarrier volume fraction  $\alpha_S$  (b) for  $N = 50$  rpm.

(Fig. 11) and assuming that the volume fraction in the bed is equal to the packing limit ( $\alpha_{S,bed} = \alpha_{S,max} = 0.51$ ), the bed volume  $V_{bed}$  and the fraction of suspended particles  $x_{susp}$  can then be estimated by Eq. (20).

$$\langle \alpha_S \rangle = \frac{\alpha_{S,layer} V_{layer} + \alpha_{S,bed} V_{bed} + \alpha_{S,bulk} V_{bulk}}{V}$$

$$V = V_{layer} + V_{bulk} + V_{bed} \quad (20)$$

$$x_{susp} = 1 - \frac{\alpha_{S,bed} V_{bed}}{\langle \alpha_S \rangle V} = \frac{\alpha_{S,bulk} V_{bulk}}{\langle \alpha_S \rangle V}$$

The height of the clear layer, and thus its volume, has been measured from the volume fraction contours. Its evolution as a function of the normalized agitation rate  $N/N_{js}$  is plotted in Fig. 10. From  $N = 40$  rpm ( $N/N_{js} \approx 0.4$ ), the clear layer volume decreases linearly with increasing  $N$  to become negligible for  $N = 80$  rpm ( $N/N_{js} \approx 0.85$ ), before the complete suspension is achieved. A very thin layer is still present even at complete suspension and slightly above, but it is too thin (<1 mm) to allow its robust measurement. Moreover, its contribution to the mass balance is negligible.

In the bulk of the bioreactor, *i.e.* in the volume between the surface layer and the bed of settled particles, the solid concentration ( $\alpha_{S,bed}$ ) is nearly homogeneous as it can be seen on the axial profiles plotted in Fig. 8a, even for very low agitation rates. This observation is in contradiction with most of previous studies in which solid concentrations are measured at different locations (Micheletti et al., 2003; Spidla et al., 2005; Hosseini et al., 2010; Jafari et al., 2012; Carletti et al., 2014). In the case of heavier particles, such as glass beads or sand, significant radial and vertical concentration gradients are indeed measured, even at complete suspension. However, Micheletti et al. (2003) observed that the solid concentration gradients decrease with the particle size. Moreover, no significant concentration gradients were present at  $N = N_{js}$  with particles lighter than glass beads (polystyrene  $\rho_s = 1050 \text{ kg m}^{-3}$ ; Diakon  $\rho_s = 1180 \text{ kg m}^{-3}$ ). They however observed concentration gradient below the complete suspension, but the particle sizes ( $d_p > 500 \mu\text{m}$ ) were significantly higher than in the present work.

The solid bulk concentration increase linearly with the agitation rate between  $N = 50$  rpm and  $N_{js} = 95$  rpm, where the bulk volume fraction becomes equal to the volume-averaged volume fraction (Fig. 11). The linear interpolation of the values measured between 50 and 95 rpm led to  $N_{js,bulk} = 94$  rpm. Thus, our results suggest that the variation of  $\alpha_{S,bulk}$  with  $N$  may be used to quantitatively determine the just-suspended agitation rate, at least for similar

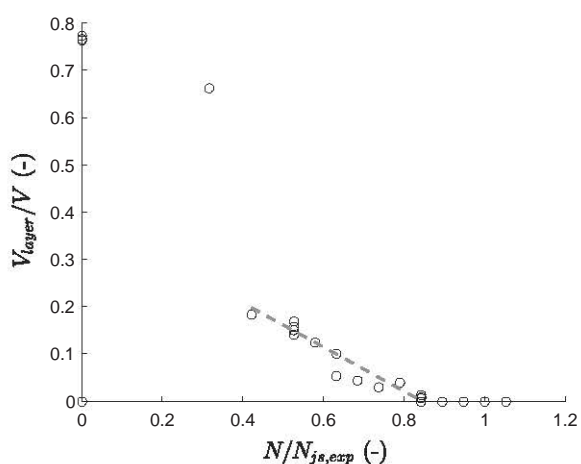


Fig. 10. Variation of the relative volume of the clear layer in function of normalized agitation rates  $N/N_{js}$ .

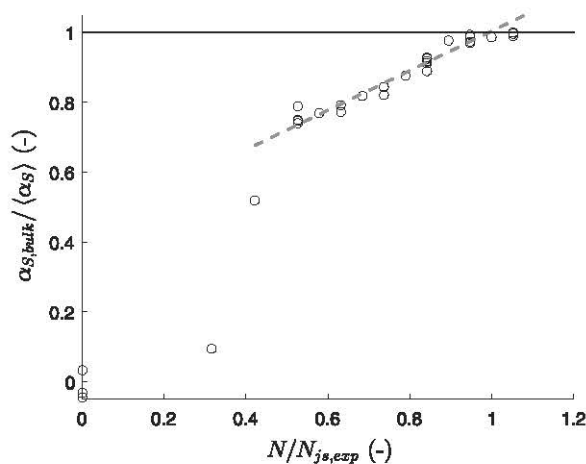


Fig. 11. Impact of normalized agitation rate on the relative bulk volume fraction  $\alpha_{S,bulk}$ .

impellers that induce the disappearance of the clear layer before the complete suspension.

Using the results presented in Figs. 10 and 11 and Eqs. (20), the fraction of suspended particles  $x_{susp}$  may be computed as a function of agitation rate. In Fig. 12, the evolution of  $x_{susp}$  is plotted as a function of the normalized agitation rate  $N/N_{js}$ .

The fraction of suspended particles increased linearly with the agitation rate between  $N = 50$  and 95 rpm. Using the curve of Fig. 12, it could be possible to determine the just-suspended agitation rate  $N_{js,susp} = 93$  rpm at the break of its slope.

Other works performed with heavier particles (around  $2500 \text{ kg m}^{-3}$ ) using the Pressure Gauge Technique suggest that the evolution of  $x_{susp}$  with  $N$  is not linear but rather follows a sigmoid function (Brucato et al., 1997; Micale et al., 2002; Selima et al., 2008; Tamburini et al., 2012b). If a sharp increase of  $x_{susp}$ , more or less linear, has also been observed with increasing  $N$ , as  $x_{susp}$  became close to 1, its increase with the agitation rate slowed down considerably. Indeed, if the majority of the particles were suspended, some particles tended to stay motionless in regions of low liquid velocities and the agitation rate has to be greatly increased to allow all the particles to be suspended. Based on that observation, Micale et al. (2002) proposed an alternative to the Zwietering criterion, the sufficient suspension agitation rate  $N_{ss}$  defined as the agitation rate at which 98% of the solids are sus-

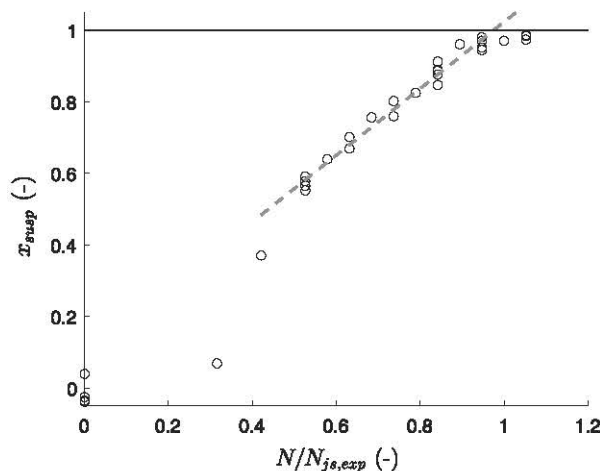


Fig. 12. Evolution of the fraction of suspended microcarriers  $x_{susp}$  as a function of normalized agitation rates  $N/N_{js}$ .

pended. Brucato et al. (1997) and Micale et al. (2002) found that  $N_{js}$  values were higher than  $N_{ss}$  up to 50%. However, the differences between  $N_{js}$  and  $N_{ss}$  depends on the tank bottom shape, as Selima et al. (2008) found a 5% difference between the two criteria in a conical bottom reactor. The bioreactor hemispherical bottom used in this work probably prevents the formation of dead zones at the tank bottom. Moreover, the microcarrier density being very close to the liquid density, the microcarriers do not require as much power input to suspend.

It should also be noted that the bed volume computed using Eqs. (20) is overestimated because it does not account of the layer around the particle bed where the volume fraction increases gradually between the bulk volume fraction and the packing limit. Nevertheless, despite these approximations, the approach proposed here enabled a very satisfactory estimation of the just-suspended agitation rate.

#### 4.2. Numerical results

The aims of the CFD simulations of the solid-liquid suspension are two fold: (1) to evaluate the capability of CFD to predict the minimal agitation rate for complete suspension  $N_{js}$  and (2) to identify a validated numerical tool which can be used to predict solid spatial distributions at various  $N$ , especially in the bioreactor bottom where experimental data are usually scarce. Several modeling approaches have been evaluated but only the one that gives the best results in terms of  $N_{js}$  and solid spatial distribution is presented here (multiphase model: Euler-Granular; turbulence model: mixture standard  $k$ - $\epsilon$ ; drag model: Huilin-Gidaspow).

Unlike with experiments, the fraction of suspended particles in the stirred tank bioreactor, and thus  $N_{js}$ , are easily obtained with the CFD results because the solid concentration  $\alpha_s$  is known in each element of the mesh. Considering that particles are suspended for values of  $\alpha_s$  smaller than the maximum packing limit allowed ( $\alpha_{s,max} = 0.51$ ), the value of  $x_{susp}$  can be computed from CFD data by simply summing the contribution of all suspended mesh elements (Eq. (21)) as proposed by Tamburini et al. (2011). The evolution of  $x_{susp}$  as a function of the normalized agitation rate ( $N/N_{js}$ ) is plotted in Fig. 13 with black triangle symbols.

$$x_{susp} = \frac{1}{V} \sum_i \alpha_s(i)V(i) \quad (21)$$

$\alpha_s(i) < \alpha_{s,max}$

where  $\alpha_s(i)$  is the solid volume fraction in grid cell  $i$  and  $V(i)$  the volume of cell  $i$ .

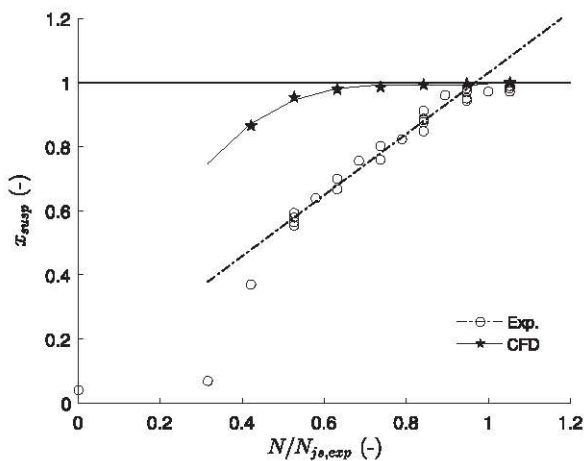


Fig. 13. Evolution of the fraction of suspended microcarriers as a function of the normalized agitation rate  $N/N_{js}$  (black star: simulations; blank circle: experiments).

The fraction of particles in suspension predicted by CFD tends to 1 between 95 and 100 rpm, indicating that CFD simulations could indeed predict  $N_{js}$  with a reasonable accuracy. However, for  $N < N_{js}$  the predicted values of  $x_{susp}$  are significantly higher than the ones estimated experimentally from Eqs. (20) and its evolution as a function of the agitation rate is far from being linear.

In order to compare in more details the CFD results to the experimental one, the local solid volume fractions computed by CFD were exported and averaged over the tank thickness. Two vertical profiles at  $x = -20$  mm and  $x = 0$  mm are presented in Figs. 14 for agitation rates  $N = 60, 80$  and  $100$  rpm, alongside the corresponding experimental profiles.

For  $N \leq 80$  rpm ( $N/N_{js} \leq 0.85$ ), the solid concentration at the tank bottom is underestimated but becomes overestimated for  $N > 80$  rpm. Even for  $N > N_{js}$ , the solid volume fractions predicted by CFD at the tank bottom are still significantly higher than  $\langle \alpha_s \rangle$ , even if the maximum packing limit is not reached anymore.

Fig. 15 shows that the height of the clear layer is significantly underestimated for  $N \leq 80$  rpm ( $N/N_{js} \leq 0.85$ ), but a fine clear layer persists even for agitation rates above the experimental  $N_{js}$ . This could be partly related to the modeling of the free surface in the CFD simulations (flat and unmoving surface modeled by a symmetry condition).

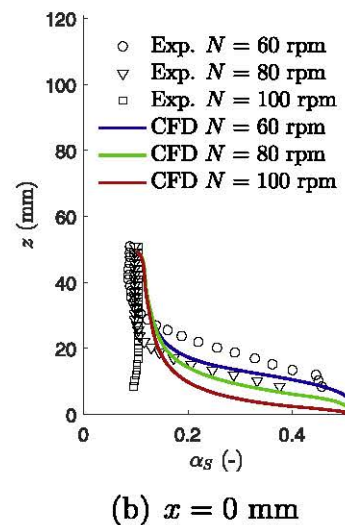
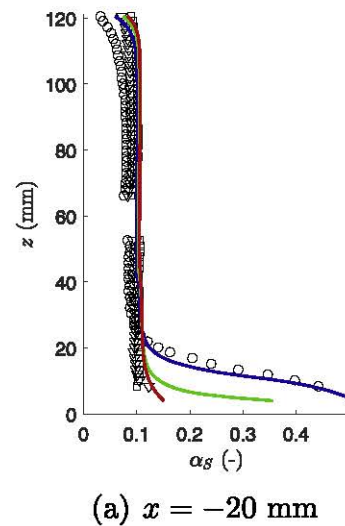


Fig. 14. Axial profiles of solid volume fractions  $\alpha_s$  obtained by CFD (continuous lines) and the experimental technique (symbols) at various agitation rates for an volume-averaged volume fraction ( $\alpha_g$ ) = of 0.1.

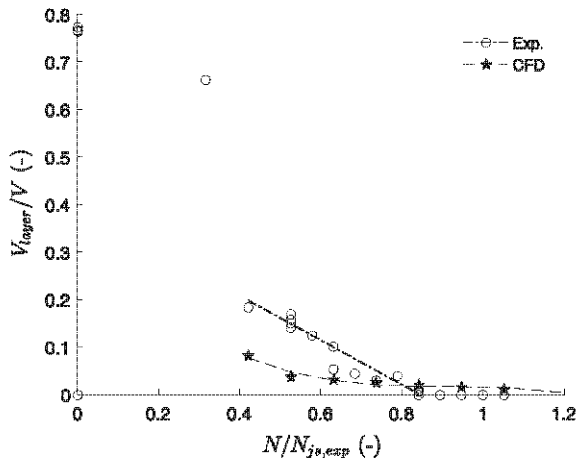


Fig. 15. Evolution of the volume of the clear layer in function of agitation rates.

Conversely, Fig. 16 shows that the bulk solid concentration is significantly overestimated for  $N \leq 80$  rpm ( $N/N_{js} \leq 0.85$ ), and underestimated  $N > 80$  rpm ( $N/N_{js} > 0.85$ ). Nevertheless, as for the experimental observations, Fig. 14 shows that the solid concentration predicted by CFD in the bulk is homogeneous, except in the region between the impeller bottom and the particle bed where the solid concentration is 2 times higher than in the bulk.

Several assumptions can be made to explain the discrepancies between the experimental and numerical results. Firstly, the flow is not fully turbulent, even at  $N_{js}$ , as  $Re_{js} = \rho_L N_{js} D^2 / \mu_L = 6000$ . Although the standard *k-epsilon* model is in theory not suited for this 'just-turbulent' flow regime, the best results in terms of solid spatial distribution and  $N_{js}$  are achieved compared to the other RANS models tested.

The turbulence can influence the particle motion. This influence can be modeled in two ways: by correcting the drag coefficient to take the influence of the free-stream turbulence on the settling velocity into account and/or by including a turbulence dispersion force in the momentum equations.

Several correction terms for the drag coefficient are proposed in the literature in the specific case of solid-liquid suspension in stirred-tank reactors (Brucato et al., 1998; Pinelli et al., 2001; Khopkar et al., 2006). Those correlations increase the drag coefficient for values of the ratio of the particle diameter to the Kolmogorov scale  $d_p/l_k$  greater than 1. However, in the present case, regarding the very low values of power dissipation per unit of

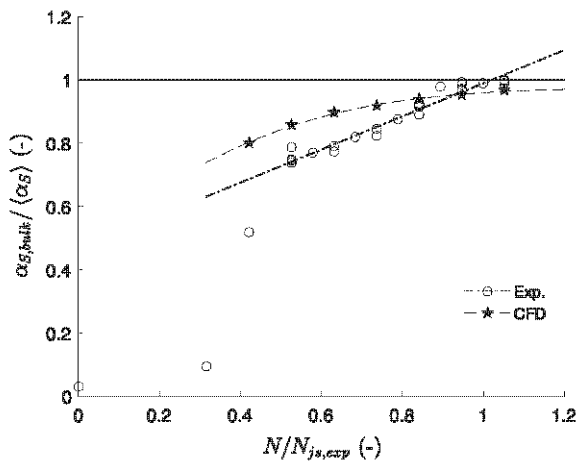


Fig. 16. Evolution of the bulk volume fraction as a function of normalized agitation rate ( $N/N_{js}$ ).

volume required to suspend microcarriers ( $P/V \propto 1 \text{ W m}^{-3}$ ) and their small size, a ratio  $d_p/l_k < 1$  is obtained. So, none of the above mentioned corrections for the drag coefficient are here significant.

Many authors have shown that the inclusion of turbulent dispersion force can significantly enhance the simulation accuracy (Kasat et al., 2008; Fletcher and Brown, 2009; Wadnerkar et al., 2012, 2016), at least in the case of heavy particles. In the present simulations, including the turbulent dispersion force leads to a uniform spatial distribution of solid concentration, even for  $N < N_{js}$ .

Finally, the presence of particles can alter the turbulence properties (Unadkat et al., 2009; Gabriele et al., 2011; Montante et al., 2012). Such influence can be included via source terms in the turbulence equations using the turbulent interaction force proposed by Simonin and Viollet (1990). But no significant improvement was observed neither in the bulk, nor in the packed bed when this additional force was considered.

## 5. Discussion and conclusions

The light attenuation technique presented in this work enabled the characterization of the spatial distribution of the solid phase in a solid-liquid stirred vessel, even for very dense suspensions by advantageously using the optical properties of the Cytodex-1 microcarriers. The analysis of the solid spatial distributions for agitation rates below and above  $N_{js}$  have highlighted that the suspension in the bioreactor could be divided in three zones: a clear layer below the free surface where  $\alpha_{s,layer}$  tends to 0, a bulk zone where the solid phase is homogeneously distributed ( $\alpha_{s,bulk} \leq \langle \alpha_s \rangle$ ) and a packed bed of motionless particles at the bioreactor bottom ( $\alpha_{s,bed} = \alpha_{s,max}$ ). The evolutions of the relative importance of the three zones, in terms of solid volume fraction and occupied volume, are directly proportional to the agitation rate.

One very interesting result is that the solid concentration is uniform in the bulk region. This is in contradiction with previous works performed with heavier particles in which significant solid concentration gradients were observed. This could be related to the microcarrier size and density, which are small compared to the particles usually used (sand or glass beads). As already discussed in Micheletti et al. (2003), the presence of concentration gradients is partly related to the particle inertia, characterized by the Stokes number (Eq. (22)). If  $St < 1$ , particles will follow closely the liquid flow, and thus will be more easily dispersed. On the contrary, if  $St > 1$ , the particles do not have time to adjust to a sudden change in the flow and thus concentration gradients can appear, especially in the impeller vicinity such as it is observed with glass beads in the work of Micheletti et al. (2003). In the present work, the Stokes number is inferior or close to unity for all conditions tested.

$$St = \frac{\tau_p}{\tau_K} \quad (22)$$

where  $\tau_p$  is the particle relaxation time and  $\tau_K$  the characteristic time related to the Kolmogorov scales.

$$\tau_p = \frac{\rho_s d_p^2}{18\mu} \quad (23)$$

$$\tau_K = \left(\frac{\nu}{\epsilon}\right)^{0.5} \quad (24)$$

The homogeneous solid concentration in the bulk, and its relationship with  $N_{js}$  could also be geometry related and need to be studied further. But if confirmed, a simple method could be designed in order to measure  $N_{js}$ , even in opaque systems: a single probe, soundly positioned, could be sufficient to follow the evolution of the bulk solid concentration as a function of the agitation rate.

In the near future, the light attenuation technique will be used to study in details the influence of the impeller design and of the tank bottom on the suspension of microcarriers. It appears to be a valuable tool to better understand the suspension mechanisms, to design and optimize suspension processes and to validate numerical simulations.

The experimental results have also been used for the validation of CFD simulations of the liquid-solid suspension in the stirred-tank bioreactor. Various modeling approaches, in terms of multiphase, turbulence and drag models, have been tested but only the most robust set of models was presented in this study. The choice of interaction forces included in the multiphase approach is crucial to reach a satisfactory validation of the numerical results. Among these forces, turbulent dispersion and drag forces are known to be the most important when RANS turbulent simulations of liquid-solid flows are realized. The presented CFD results were performed using the Eulerian-Granular model, the "mixture" standard *k-epsilon* model and the Huilin-Gidaspow drag model. This choice of model set enables a good prediction of  $N_{js}$  using the suspension curve. However, the agreement between experimental results and CFD simulations in terms of solid spatial distribution is less satisfactory. Especially at  $N = N_{js}$ , the CFD simulation predicts high solid concentration at the tank bottom, although the experimental results show that the suspension is nearly uniform.

As already mentioned before, the discrepancies between experiments and CFD could be explained by several reasons. One of the main is that the flow is not fully turbulent and, theoretically, the *k-epsilon* closure model is not adapted in this case. It gives however the best results in terms of just-suspended agitation rate and solid spatial distributions. Other closure models were also tested, such as the Reynolds Stress Model and the SST *k-omega* models but they led to convergence and stability issues. Single-phase Particle Image Velocimetry (PIV) experiments could be used to validate the CFD simulations at the low Reynolds number found in small-scale bioreactors. Two-phase PIV could also be considered to better comprehend the influence of particles on the flow, but it is unfortunately limited to very low solid loading (<1%v).

In the case of light particles such as microcarriers, literature data remains sparse and no general consensus could yet be found. For heavier particles, new very promising numerical strategies were recently developed to allow the finer description of dilute liquid-solid suspensions in stirred-tank reactors using lattice-Boltzmann simulations (Ayranci et al., 2013). In particular, Derksen (2012) used highly resolved simulations in denser suspensions (volume fraction of 8%) but in a small STR. Finally, Blais et al. (2016) developed an interesting approach based on DEM modelling, which allowed an accurate simulation of granular dynamics in dense liquid-solid suspension. Its transposition to microcarrier suspensions would thus be an interesting perspective.

## Acknowledgments

The authors would like to thank the French Agence Nationale de la Recherche, the Interreg VA Grande Région program and the Région Wallone for their financial support. They are also grateful to Fabrice Blanchard and Thierry Salmon for their technical support.

## References

- Angst, R., Kraume, M., 2006. Experimental investigations of stirred solid-liquid systems in three different scales: particle distribution and power consumption. *Chem. Eng. Sci.* 61 (9), 2864–2870.
- Ayranci, I., Kresta, S.M., Derksen, J.J., 2013. Experiments and simulations on bidisperse solids suspension in a mixing tank. *Chem. Eng. Technol.* 36 (11), 1957–1967.
- Barigou, M., 2004. Particle tracking in opaque mixing systems: an overview of the capabilities of PET and PEPT. *Chem. Eng. Res. Des.* 82 (9), 1258–1267.
- Berry, J., Liovic, P., Sutalo, I., Stewart, R., Glattauer, V., Meagher, L., 2016. Characterisation of stresses on microcarriers in a stirred bioreactor. *Appl. Math. Model.* 40 (15–16), 6787–6804.
- Blais, B., Lassaingne, M., Goniva, C., Fradette, L., Bertrand, F., 2016. Development of an unresolved CFD-DEM model for the flow of viscous suspensions and its application to solid-liquid mixing. *J. Comput. Phys.* 318, 201–221.
- Brucato, A., Grisafi, F., Montante, G., 1998. Particle drag coefficients in turbulent fluids. *Chem. Eng. Sci.* 53 (18), 3295–3314.
- Brucato, A., Micale, G., Rizzuti, L., 1997. Determination of the amount of unsuspended solid particles inside stirred tanks by means of pressure measurements. In: *Rec Progr Genie des Proc.*, vol. 11, pp. 3–10.
- Carletti, C., Montante, G., Westerlund, T., Paglianti, A., 2014. Analysis of solid concentration distribution in dense solid-liquid stirred tanks by electrical resistance tomography. *Chem. Eng. Sci.* 119, 53–64.
- Collignon, M.-L., Delafosse, A., Calvo, S., Martin, C., Marc, A., Toye, D., Olmos, E., 2016. Large-eddy simulations of microcarrier exposure to potentially damaging eddies inside mini-bioreactors. *Biochem. Eng. J.* 108, 30–43.
- Derksen, J., 2003. Numerical simulation of solids suspension in a stirred tank. *AIChE J.* 49 (11), 2700–2714.
- Derksen, J., 2012. Highly resolved simulations of solids suspension in a small mixing tank. *AIChE J.* 58 (10), 3266–3278.
- Dudukovic, M., 2002. Opaque multiphase flows: experiments and modeling. *Exp. Thermal Fluid Sci.* 26 (6), 747–761.
- Ferrari, C., Balandras, F., Guedon, E., Olmos, E., Chevalot, I., Marc, A., 2012. Limiting cell aggregation during mesenchymal stem cell expansion on microcarriers. *Biotechnol. Prog.* 28 (3), 780–787.
- Fletcher, D.F., Brown, G.J., 2009. Numerical simulation of solid suspension via mechanical agitation: effect of the modelling approach, turbulence model and hindered settling drag law. *Int. J. Comput. Fluid Dyn.* 23 (2), 173–187.
- Gabriele, A., Tsofigkas, A., Kings, I., Simmons, M., 2011. Use of PIV to measure turbulence modulation in a high throughput stirred vessel with the addition of high stokes number particles for both up- and down-pumping configurations. *Chem. Eng. Sci.* 66 (23), 5862–5874.
- Guha, D., Ramachandran, P., Dudukovic, M., Derksen, J., 2008. Evaluation of large eddy simulation and euler-euler CFD models for solids flow dynamics in a stirred tank reactor. *AIChE J.* 54 (3), 766–778.
- Hosseini, S., Patel, D., Ein-Mozaffari, F., Mehrvar, M., 2010. Study of solid liquid mixing in agitated tanks through electrical resistance tomography. *Chem. Eng. Sci.* 65 (4), 1374–1384.
- Ibrahim, S., Nienow, A., 2004. Suspension of microcarriers for cell culture with axial flow impellers. *Chem. Eng. Res. Des.* 82 (9), 1082–1088.
- Jafari, R., Tanguy, P.A., Chaouki, J., 2012. Experimental investigation on solid dispersion, power consumption and scale-up in moderate to dense solid-liquid suspensions. *Chem. Eng. Res. Des.* 90 (2), 201–212.
- Kaiser, S., Jossen, V., Schirmaier, C., Eibl, D., Brill, S., van den Bos, C., Eibl, R., 2013. Fluid flow and cell proliferation of mesenchymal adipose-derived stem cells in small-scale, stirred, single-use bioreactors. *Chem. Ing. Tech.* 85 (1–2), 95–102.
- Kasat, G., Khopkar, A., Ranade, V., Pandit, A., 2008. CFD simulation of liquid-phase mixing in solid-liquid stirred reactor. *Chem. Eng. Sci.* 63 (15), 3877–3885.
- Khopkar, A., Kasat, G., Pandit, A., Ranade, V., 2006. Computational fluid dynamics simulation of the solid suspension in a stirred slurry reactor. *Indus. Eng. Chem. Res.* 45 (12), 4416–4428.
- Martin, C., Olmos, E., Collignon, M.-L., De Isla, N., Blanchard, F., Chevalot, I., Marc, A., Guedon, E., 2017. Revisiting msc expansion from critical quality attributes to critical culture process parameters. *Process Biochem.* 59 (B), 231–243.
- Micale, G., Grisafi, F., Brucato, A., 2002. Assessment of particle suspension conditions in stirred vessels by means of pressure gauge technique. *Chem. Eng. Res. Des.* 80 (8), 893–902. *fluid Mixing VII*.
- Micheletti, M., Nikiforaki, L., Lee, K.C., Yianneskis, M., 2003. Particle concentration and mixing characteristics of moderate-to-dense solid-liquid suspensions. *Indus. Eng. Chem. Res.* 42 (24), 6236–6249.
- Montante, G., Magelli, F., 2005. Modelling of solids distribution in stirred tanks: analysis of simulation strategies and comparison with experimental data. *Int. J. Comput. Fluid Dyn.* 19 (3), 253–262.
- Montante, G., Magelli, F., 2007. Mixed solids distribution in stirred vessels: experiments and computational fluid dynamics simulations. *Indus. Eng. Chem. Res.* 46 (9), 2885–2891.
- Montante, G., Paglianti, A., Magelli, F., 2012. Analysis of dilute solid-liquid suspensions in turbulent stirred tanks. *Chem. Eng. Res. Des.* 90 (10), 1448–1456.
- Nienow, A.W., 2006. Reactor engineering in large scale animal cell culture. *Cytotechnology* 50 (1–3), 9–33.
- Nienow, A.W., Rafiq, Q.A., Coopman, K., Hewitt, C.J., 2014. A potentially scalable method for the harvesting of HMSCS from microcarriers. *Biochem. Eng. J.* 85, 79–88.
- Pieralisi, I., Rodriguez, G., Micheletti, M., Paglianti, A., Ducci, A., 2016. Microcarriers suspension and flow dynamics in orbitally shaken bioreactors. *Chem. Eng. Res. Des.* 108 (suppl. C), 198–209. *the 15th European Conference on Mixing*.
- Pinelli, D., Nocentini, M., Magelli, F., 2001. Solids distribution in stirred slurry reactors: influence of some mixer configurations and limits to the applicability of a simple model for predictions. *Chem. Eng. Commun.* 188 (1), 91–107.
- Richardson, J., Zaki, W., 1997. Sedimentation and fluidisation: Part I. *Chem. Eng. Res. Des.* 75, S82–S100.
- Sardeshpande, M.V., Juvekar, V.A., Ranade, V.V., 2010. Hysteresis in cloud heights during solid suspension in stirred tank reactor: experiments and CFD simulations. *AIChE J.* 56 (11), 2795–2804.



- Schirmaier, C., Jossen, V., Kaiser, S.C., Jüngerkes, F., Brill, S., Safavi-Nab, A., Siehoff, A., Bos, C., Eibl, D., Eibl, R., 2014. Scale-up of adipose tissue-derived mesenchymal stem cell production in stirred single-use bioreactors under low-serum conditions. *Eng. Life Sci.* 14 (3), 292–303.
- Selima, Y.S., Fangary, Y.S., Mahmoud, N.A., 2008. Determination of minimum speed required for solids suspension in stirred vessels using pressure measurements. *Can. J. Chem. Eng.* 86 (4), 661–666.
- Simonin, O., Viollet, P., 1990. Modelling of turbulent two-phase jets loaded with discrete particles. *FG Hewitt, et al. Phenom. Multiphase Flow*, 259–269.
- Spidla, M., Sinevic, V., Jahoda, M., Machon, V., 2005. Solid particle distribution of moderately concentrated suspensions in a pilot plant stirred vessel. *Chem. Eng. J.* 113 (1), 73–82.
- Syamlal, M. (1987). The particle-particle drag term in a multiparticle model of fluidization (No. DOE/MC/21353-2373). EG and G Washington Analytical Services Center, Inc., Morgantown, WV (USA).
- Tamburini, A., Brucato, A., Cipollina, A., Micale, G., Ciofalo, M., 2012a. CFD predictions of sufficient suspension conditions in solid-liquid agitated tanks. *Int. J. Nonlinear Sci. Numer. Simul.* 13 (6), 427–443.
- Tamburini, A., Cipollina, A., Micale, G., Brucato, A., 2013. Particle distribution in dilute solid liquid unbaffled tanks via a novel laser sheet and image analysis based technique. *Chem. Eng. Sci.* 87, 341–358.
- Tamburini, A., Cipollina, A., Micale, G., Brucato, A., Ciofalo, M., 2011. CFD simulations of dense solid-liquid suspensions in baffled stirred tanks: prediction of suspension curves. *Chem. Eng. J.* 178, 324–341.
- Tamburini, A., Cipollina, A., Micale, G., Brucato, A., Ciofalo, M., 2012b. CFD simulations of dense solid-liquid suspensions in baffled stirred tanks: prediction of the minimum impeller speed for complete suspension. *Chem. Eng. J.* 193, 234–255.
- Tamburini, A., Gentile, L., Cipollina, A., Micale, G., Brucato, A., 2009. Experimental investigation of dilute solid-liquid suspension in an unbaffled stirred vessels by a novel pulsed laser based image analysis technique. *Chem. Eng. Trans.* 17, 1.
- Unadkat, H., Rielly, C., Hargrave, G., Nagy, Z., 2009. Application of fluorescent PIV and digital image analysis to measure turbulence properties of solid-liquid stirred suspensions. *Chem. Eng. Res. Des.* 87 (4), 573–586. 13th European Conference on Mixing: New developments towards more efficient and sustainable operations.
- Wadnerkar, D., Tade, M.O., Pareek, V.K., Utikar, R.P., 2016. CFD simulation of solid-liquid stirred tanks for low to dense solid loading systems. *Particuology* 29, 16–33.
- Wadnerkar, D., Utikar, R.P., Tade, M.O., Pareek, V.K., 2012. CFD simulation of solid-liquid stirred tanks. *Adv. Powder Technol.* 23 (4), 445–453. special Issue Featuring Articles from Chemeca 2011.
- Zheng, Y., Zhang, Q., 2004. Simultaneous measurement of gas and solid holdups in multiphase systems using ultrasonic technique. *Chem. Eng. Sci.* 59 (17), 3505–3514.
- Zwietering, T.N., 1958. Suspending of solid particles in liquid by agitators. *Chem. Eng. Sci.* 8 (3–4), 244–253.



Appendix C:  
Design of experiments of the impeller design  
optimization

$\beta$	D/T	C/T	N/s	Re	$\langle P/V \rangle @ p$	$\langle P/V \rangle$	EDC	Np	$\lambda K min$	$\langle \lambda K \rangle$	$\langle \lambda K \rangle @ p$	$\epsilon max$	$\langle \epsilon \rangle$	$\langle \epsilon \rangle @ p$
(°)	(-)	(-)	(rpm)	(-)	(W m-3)	(W m-3)	(kJ m-3)	(-)	( $\mu m$ )	( $\mu m$ )	( $\mu m$ )	(m2 s-3)	(m2 s-3)	(m2 s-3)
90	0.37	0.41	60	786	0.21	0.19	0.54	8.2	69	204	200	0.02	1.95E-04	2.11E-04
87	0.26	0.3	135	785	0.41	0.36	0.95	8.0	43	175	170	0.10	3.58E-04	4.02E-04
81	0.45	0.425	45	719	0.20	0.19	0.51	7.2	76	205	204	0.01	1.91E-04	1.96E-04
70	0.37	0.41	61	827	0.17	0.15	0.33	6.3	72	217	214	0.01	1.51E-04	1.63E-04
63	0.4	0.4	60	907	0.19	0.17	0.38	5.1	72	211	206	0.01	1.72E-04	1.87E-04
55	0.45	0.45	52	1,318	0.18	0.16	0.34	4.1	78	213	211	0.01	1.64E-04	1.72E-04
45	0.25	0.2	245	1,308	0.54	0.45	0.78	3.9	37	165	159	0.19	4.55E-04	5.26E-04
45	0.45	0.25	75	1,064	0.28	0.25	0.45	2.3	57	191	187	0.03	2.55E-04	2.76E-04
45	0.45	0.5	61	1,255	0.18	0.17	0.36	2.9	54	210	211	0.04	1.75E-04	1.72E-04
45	0.45	0.33	72	1,006	0.26	0.24	0.42	2.4	57	194	191	0.03	2.37E-04	2.55E-04
45	0.4	0.4	73	1,025	0.17	0.15	0.24	2.6	62	219	214	0.02	1.47E-04	1.63E-04
45	0.37	0.47	87	1,261	0.20	0.18	0.34	2.7	64	208	205	0.02	1.80E-04	1.91E-04
34	0.36	0.46	113	1,679	0.20	0.18	0.27	1.6	46	208	204	0.08	1.81E-04	1.95E-04
33	0.5	0.2	78	1,412	0.29	0.27	0.53	1.4	60	188	185	0.03	2.70E-04	2.88E-04
33	0.45	0.5	81	1,382	0.21	0.21	0.38	1.6	49	200	200	0.06	2.12E-04	2.11E-04
33	0.35	0.45	131	1,787	0.23	0.21	0.35	1.4	45	200	196	0.09	2.11E-04	2.30E-04
30	0.5	0.5	83	1,747	0.31	0.32	0.67	1.4	37	180	182	0.18	3.20E-04	3.06E-04
30	0.42	0.25	115	1,650	0.30	0.26	0.36	1.1	51	190	184	0.05	2.60E-04	2.97E-04
28	0.37	0.41	140	1,782	0.26	0.23	0.32	1.1	39	194	190	0.14	2.37E-04	2.58E-04
27	0.3	0.5	230	1,532	0.32	0.31	0.46	1.3	25	181	181	0.82	3.17E-04	3.16E-04
27	0.37	0.47	130	1,487	0.20	0.19	0.28	1.1	43	204	203	0.10	1.94E-04	2.01E-04
25	0.35	0.47	141	1,785	0.18	0.16	0.22	1.0	45	213	209	0.08	1.66E-04	1.77E-04
16	0.36	0.42	160	1,846	0.19	0.17	0.20	0.7	38	211	206	0.16	1.70E-04	1.88E-04
15	0.35	0.43	175	2,426	0.19	0.17	0.20	0.7	37	211	208	0.18	1.70E-04	1.82E-04
9	0.35	0.275	230	1,937	0.37	0.31	0.29	0.6	25	181	175	0.82	3.17E-04	3.64E-04
5	0.5	0.4	90	1,787	0.15	0.11	0.15	0.5	42	233	220	0.11	1.15E-04	1.44E-04
5	0.5	0.38	83	2,045	0.12	0.10	0.12	0.6	54	242	233	0.04	9.88E-05	1.15E-04
5	0.5	0.35	95	1,796	0.19	0.15	0.18	0.6	44	218	208	0.09	1.50E-04	1.82E-04
5	0.45	0.38	103	2,389	0.17	0.13	0.16	0.6	34	225	214	0.26	1.32E-04	1.63E-04
2.4	0.34	0.49	240	3,702	0.33	0.28	0.31	0.5	24	186	180	0.99	2.82E-04	3.25E-04
0	0.5	0.2	172	-	0.56	0.47	0.93	0.3	31	163	158	0.39	4.76E-04	5.46E-04

# Abstract

Mesenchymal stem cells (MSC) are becoming increasingly involved in the regenerative medicine field, particularly to treat diseases that are not effectively curable with the current therapies. Two scientific barriers are nevertheless responsible for MSC use and commercialization limitations. On one side, large amounts of cells are needed to reach the high cell dose requirements. On the other side, cells being the final product themselves, directly injected into the patient, their quality have to be controlled (stem cell phenotype, differentiation capability). MSC cultivation on microcarriers in a stirred bioreactor seems to meet these challenges. However, a precise knowledge about the impact of the technologies and the hydrodynamics generated, on the physiological cell response, is necessary to improve the scale-up of MSC cultures in bioreactors. In this context, present work is dedicated to the study of the impact of the agitation mode (orbital or mechanical) on the cell attachment, expansion and detachment on various microcarrier types, in the case of MSC derived from the Wharton's jelly (WJ-MSC) of umbilical cords. To quantify more precisely cell distribution and expansion on microcarriers, an automatic and in situ counting method was developed, which need no detachment step. This allowed the identification of commercial microcarriers suitable for WJ-MSC cultures, which were then compared to home-made microcarriers, synthesized by a partner laboratory, in terms of cell attachment and expansion, and detachment efficiency. In parallel to these works, the impact of the impeller design on the microcarrier suspension in stirred tank bioreactors was investigated. Based on a dimensional analysis and CFD simulations, it resulted in the establishment of two models relating the minimal agitation rate to ensure all particle suspension ( $N_{js}$ ) with the impeller geometrical characteristics (design, size, off-bottom clearance) and the material properties of both the solid and the liquid phases. CFD models validation allowed then to develop a strategy to optimize the geometrical configuration of an impeller, dedicated to MSC cultures on microcarriers in a minibioreactor. Parameters characterizing the hydromechanical stress encountered by the solid phase were wisely chosen and integrated into CFD simulations. Based on a design of experiments, and the hydrodynamics data recovered from simulations, response surfaces were built and a multi-objective optimization was achieved in order to determine the geometry minimizing the particle stress, and also by adhered cells. WJ-MSC cultures in minibioreactors equipped with impellers displaying various geometries were finally validated, with a preliminary comparison of the impact of these geometries on the cell expansion.

*Keywords:* Stem cell culture, bioreactor, hydrodynamics, Computational Fluid dynamics (CFD).

# Résumé

Les cellules souches mésenchymateuses (CSM) interviennent de plus en plus dans le domaine de la médecine régénérative, notamment pour traiter des maladies aujourd'hui difficilement curables avec les moyens actuels. Deux verrous scientifiques limitent pourtant leur utilisation et leur commercialisation. D'une part, de grandes quantités de cellules sont nécessaires pour répondre à la forte demande médicale. D'autre part, les cellules étant elles-mêmes le médicament final, délivré chez le patient, leur qualité doit être préservée (phénotype souche, capacité de différenciation). La mise en culture de ces cellules, sur des microporteurs, en bioréacteur agité, semble répondre à ces enjeux. Cependant, une connaissance plus précise de l'impact, sur la réponse physiologique des cellules, des technologies utilisées et de l'hydrodynamique générée est nécessaire pour améliorer les lois d'extrapolation des bioréacteurs de culture de CSM. Dans ce contexte, des travaux ont été mis en œuvre pour étudier l'influence du mode d'agitation (orbitale ou mécanique) sur l'attachement, l'expansion et le détachement de CSM issues de la gelée de Wharton (GW-CSM) de cordons ombilicaux, sur des microporteurs de différentes compositions. Pour contribuer à la quantification de l'expansion cellulaire, une méthode de comptage automatique in situ a été développée pour estimer le nombre de cellules par microporteur, ainsi que leur répartition, sans avoir à procéder à leur détachement. Cela a permis d'identifier des microporteurs commerciaux adaptés à la culture de GW-CSM, qui ont ensuite pu être comparés à des microporteurs synthétisés dans un laboratoire partenaire, en termes d'attachement et expansion cellulaire, ainsi que de facilité de détachement. En parallèle de ces travaux, l'impact de la conception du mobile d'agitation, en bioréacteur mécaniquement agité, sur la mise en suspension de microporteurs a été analysé. A l'issue de cette étude, une analyse dimensionnelle et des simulations CFD ont été mises en place et deux modèles reliant la fréquence minimale de juste mise en suspension ( $N_{js}$ ) avec la géométrie du mobile d'agitation (forme, taille, position dans la cuve) et les propriétés matérielles des particules et de la phase liquide ont été proposés. La validation des modèles CFD a par la suite permis de développer une stratégie d'optimisation des paramètres géométriques d'un mobile en minibioreacteur, dédié à la culture de CSM sur microporteurs. Des paramètres caractérisant les contraintes hydromécaniques perçues par la phase solide ont été judicieusement choisis et intégrés lors des simulations CFD. A partir d'un plan d'expérience, et des données sur l'hydrodynamique issues des simulations, des surfaces de réponse ont été construites et une optimisation multi-objective a été réalisée afin de déterminer la géométrie minimisant les contraintes perçues par les particules, et donc par les cellules adhérentes. Des cultures de GW-CSM en minibioreacteurs équipés de mobiles de différentes géométries ont finalement été validées, avec une comparaison préliminaire de l'impact de ces géométries sur l'expansion cellulaire.

*Mots-clés:* Culture de cellules souches, bioréacteur, hydrodynamique, Mécanique des fluides numériques ('CFD').